51/2/2019
ISSN 1338-3523
ISSN 0369-2086

Mineralia Slovaca

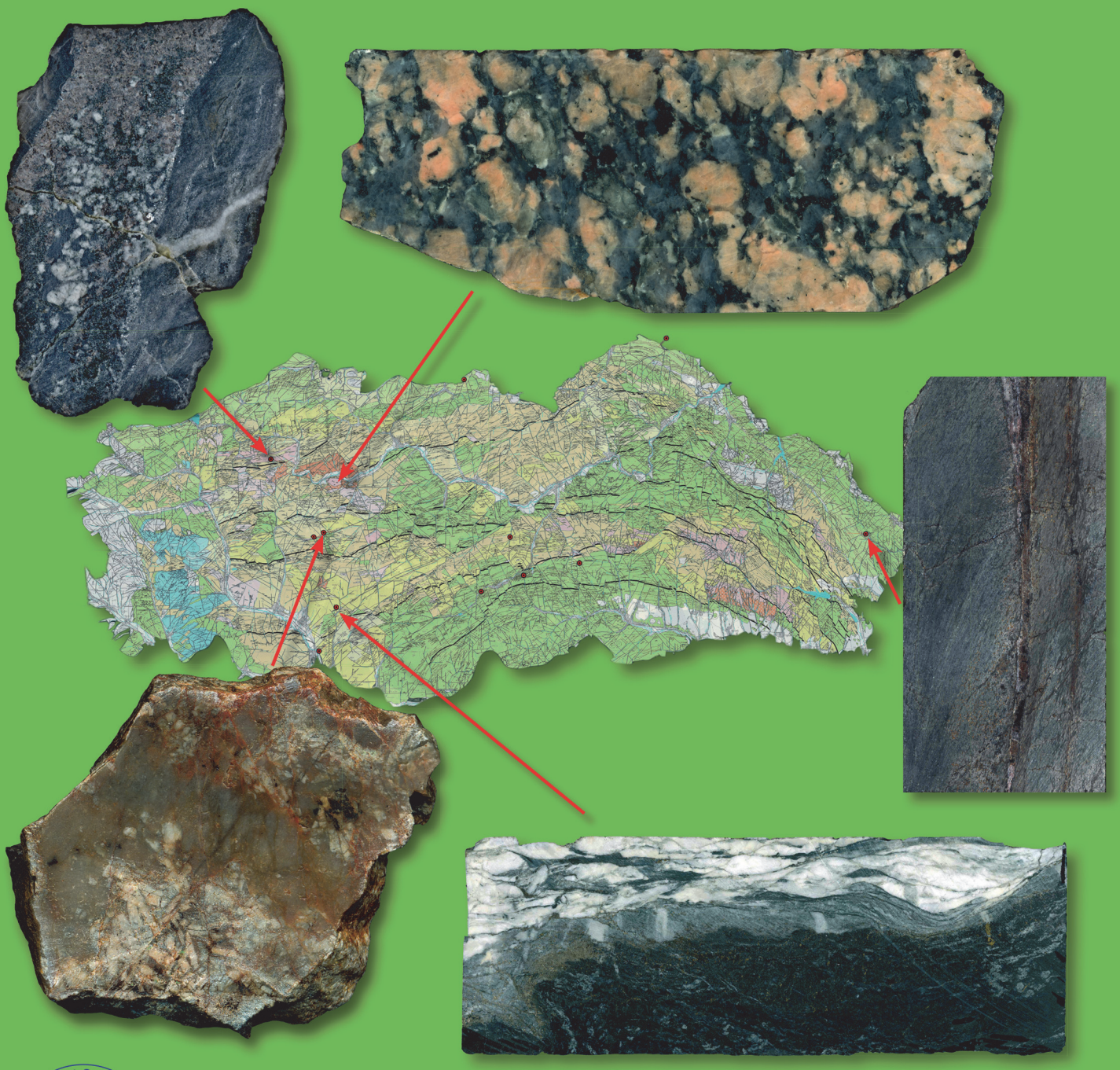

Štátny geologický ústav Dionýza Štúra Bratislava

Mineralia Slovaca

Časopis pre regionálnu a environmentálnu geológiu
a aktivity Slovenskej geologickej spoločnosti a geologických asociácií

PREDSEDA VYDAVATEĽSKEJ RADY – CHAIRMAN OF EDITORIAL BOARD

BRANISLAV ŽEC
Štátny geologický ústav Dionýza Štúra Bratislava

VEDECKÝ REDAKTOR – SCIENTIFIC EDITOR

ZOLTÁN NÉMETH
Štátny geologický ústav Dionýza Štúra
Regionálne centrum Košice
Jesenského 8, 040 01 Košice
zoltan.nemeth@geology.sk

REDAKČNÁ RADA – EDITORIAL BOARD

Klement Fordinál, Štátny geologický ústav D. Štúra Bratislava
Ľubomír Hraško, Štátny geologický ústav D. Štúra Bratislava
Vlasta Jánová, Ministerstvo životného prostredia SR Bratislava
Peter Malík, Štátny geologický ústav D. Štúra Bratislava
Jozef Michalík, Ústav vied o Zemi SAV Bratislava
Ľubomír Petro, Štátny geologický ústav D. Štúra Košice
Dušan Plašienka, Prírodovedecká fakulta UK Bratislava
Marián Putiš, Prírodovedecká fakulta UK Bratislava
Igor Slaninka, Štátny geologický ústav D. Štúra Bratislava
Ján Soták, Ústav vied o Zemi Banská Bystrica
Ladislav Šimon, Štátny geologický ústav D. Štúra Bratislava
Pavel Uher, Prírodovedecká fakulta UK Bratislava

REDAKCIA – EDITORIAL STAFF

Vedúci oddelenia vydavateľstva ŠGÚDŠ a propagácie – Head of the Department of ŠGÚDŠ Publishers and Promotion

LADISLAV MARTINSKÝ
ladislav.martinsky@geology.sk

Jazykoví redaktori – Lingual editors

Janka Hrtusová – Zoltán Németh
janka.hrtusova@geology.sk

Grafická úprava a technické spracovanie – DTP processing

Slávka Žideková
slavka.zidekova@geology.sk

Mineralia Slovaca (Web ISSN 1338-3523, ISSN 0369-2086), EV 3534/09, vychádza dvakrát ročne. Vydavateľ a tlač: Štátny geologický ústav Dionýza Štúra, Mlynská dolina 1, 817 04 Bratislava, IČO 31 753 604. Dátum vydania čísla 51/2/2019: december 2019.
Predplatné v roku 2019 vrátane DPH, poštovného a balného pre jednotlivcov 22,00 €, pre členov SGS a geologických asociácií 20,90 €, pre organizácie v SR 31,90 €, pre organizácie v ČR 55,00 €. Cena jednotlivého čísla pri osobnom nákupe v predajniach ŠGÚDŠ v Bratislave a v Košiciach je 6,05 € vrátane DPH. Časopis možno objednať v redakcii a v knižnici regionálneho centra v Košiciach.
Adresa redakcie: Štátny geologický ústav D. Štúra – RC Košice (Mineralia Slovaca), Jesenského 8, 040 01 Košice. Telefón: 055/625 00 43; fax: 055/625 00 44, e-mail: mineralia.slovaca@geology.sk, e-mail knižnica: secretary.ke@geology.sk

Mineralia Slovaca (Web ISSN 1338-3523, ISSN 0369-2086) is published twice a year by the State Geological Institute of Dionýz Štúr Bratislava, Slovak Republic. The date of issuing of the number 51/2/2019: December 2019.
Subscription for the whole 2019 calendar year (two numbers of the journal): 66.00 € (Europe), 77.00 € (besides Europe), including VAT, postage and packing cost. Claims for nonreceipt of any issue will be filled gratis.
Order of the Editorial Office: Štátny geologický ústav D. Štúra – RC Košice (Library), Jesenského 8, SK-040 01 Košice, Slovak Republic. Phone: +421/55/625 00 43; fax: +421/55/625 00 44, e-mail: mineralia.slovaca@geology.sk, library: secretary.ke@geology.sk

© Štátny geologický ústav Dionýza Štúra Bratislava

www.geology.sk/mineralia

Mineralia Slovaca 51 (2019) • 2

Obsah – Content

PÔVODNÉ ČLÁNKY – ORIGINAL PAPERS

Radvanec, M. & Gonda, S.
Genetic model of Permian hydrothermal mineralization in Gemericum (W. Carpathians) from the deep-seated zone of anatectic melting to volcanic-exhalative SedEx mineralization on the surface
Genetický model permskej hydrotermálnej mineralizácie gemerika od zóny anatektického tavenia v hĺbke po vulkanicko-exhalačnú SedEx mineralizáciu na povrchu 109

Aliyev, A. A. & Abbasov, O. R.
Mineralogical and geochemical proxies for the Middle Eocene oil shales from the foothills of the Greater Caucasus, Azerbaijan: Implications for depositional environments and paleoclimate
Aplikácia mineralogických a geochemických údajov zo strednoeocénnych roponosných bridlíc na úpätí Veľkého Kaukazu v Azerbajdžane pri rekonštrukcii environmentálnych a paleoklimatických podmienok ich genézy 157

Marko, F., †Túnyi, I. & Beniaková, E.
Block rotations in the Carpathian Shear Corridor – a paleomagnetic record
Rotácie blokov v karpatskom strižnom koridore – paleomagnetický záznam 175

Malík, P., Máša, B., Bottlik, F., Švasta, J., Bahnová, N., Vasilenková, A., Bajtoš, P. & Černák, R.
Hidden groundwater inflows from the Slovenský kras Mts. to the Slaná River identified by thermometric and resistivimetric measurements
Skryté prestupy podzemných vôd Slovenského krasu do rieky Slaná medzi Brzotínom a Gombasekom identifikované termometrickými a rezistivimetrickými meraniami 187

Štyriaková, I., Danková, Z., Košuth, M., Šuba, J., Nováková, J. & Kollárová, V.
Removal of toxic elements from the minerals particles of contaminated soil by chemical and biological leaching
Odstraňovanie toxických prvkov z minerálnych častíc kontaminovanej pôdy chemickým a biologickým lúhovaním 205

Jurkovič, Ľ., Juhásová, J., Kulikova, T., Faragó, T., Méres, Š., Klimko, T., Šottník, P., Hiller, E., Nemček, L. & Bujdoš, M.
Geochemicko-mineralogický prieskum pôd ovplyvnených banskou činnosťou v oblasti opusteného Sb ložiska Čučma
Geochemical and mineralogical exploration of soils affected by mining activities at the abandoned Sb-deposit Čučma 217

OBÁLKA:

Mapa metamorfnej zonálnosti gemerika s vyznačením pozície študovaných vzoriek granitu a permskej hydrotermálnej mineralizácie. Mapa je zmenšená z podkladu 1 : 25 000 podľa práce Radvanec et al. (2019). Minerálne zloženie a veľkosť vzoriek sú na obrázkoch v článku Radvanca a Gondu v tomto čísle časopisu.

Vzorka vľavo hore – greisen s kasiteritom, lokalita Hnilec; obr. 7 a 9.

Vzorka vpravo hore – porfyrický Bt/Kfs granit s ružovými živcami, lokalita Delava, vrt DP-1, hĺbka 553 m; obr. 4.

Vzorka v strede vpravo – uránonosná SedEx mineralizácia z lokality Košice-Kurišková; obr. 28 a 30.

Vzorka vľavo dole – žilník apatitovo-xenotímovej mineralizácie, lokalita Čučma; obr. 19 a 20.

Vzorka vpravo dole – skarn z lokality Dlhá dolina, vrt VDD-43, hĺbka 266 m; obr. 16, 17 a 18.

COVER:

Map of metamorphic zonality in the Gemeric unit showing the position of studied samples of granite and Permian hydrothermal mineralization. The map is scaled down from the base version 1 : 25 000 (Radvanec et al., 2019). Mineral compositions and sample dimensions are shown in figures presented in the paper by Radvanec and Gonda in this number of the journal, as listed below:

Top left sample – greisen with cassiterite, Hnilec locality; Figs. 7 and 9.

Top right sample – porphyric Bt/Kfs granite with pink feldspars, Delava locality, borehole DP-1, depth 553 m; Fig. 4.

Sample in the middle right – U-bearing SedEx mineralization from the Košice-Kurišková locality; Figs. 28 and 30.

Bottom left sample – stockwork with apatite-xenotime mineralization, Čučma locality; Figs. 19 and 20.

Bottom right sample – skarn from the Dlhá dolina locality, borehole VDD-43, depth 266 m; Figs. 16, 17 and 18.

Mineralia Slovaca, Web ISSN 1338-3523, ISSN 0369-2086
52 (2019), 109 – 156, © Authors 2019. CC BY 4.0

Genetic model of Permian hydrothermal mineralization in Gemeric unit (W. Carpathians) from the deep-seated zone of anatectic melting to volcanic-exhalative SedEx mineralization on the surface

MARTIN RADVANEC and STANISLAV GONDA

State Geological Institute of Dionýz Štúr, Mlynská dolina 1, SK-817 04 Bratislava, Slovakia

Abstract: The hydrothermal mineral assemblages of Permian age were studied in rocks of immediate contact with Permian granite, as well as of granite exocontact, rocks in the granite wider surrounding, as well as Permian volcanosedimentary sequences and volcanic breccia in Gemeric unit (Internal Western Carpathians). Presented evolution of Permian mineralization in closed metamorphic-magmatic-hydrothermal (MMH) cycle is based on new mineralogical and geochemical studies of various mineralization etalons, distinguished by their genetic succession and location within the anatectic melting zone in amphibolite facies (amphibolite, granite) through epidote-amphibolite facies to biotite zone with cassiterite-tourmaline bearing greisen in the Hnilec locality. In the chlorite-apatite zone there were studied the cassiterite-tourmaline-Fe carbonates-bearing greisen in the Dlhá dolina valley and tourmaline-molybdenite-Fe carbonates-bearing greisen of the Hnilec locality. The apatite-xenotime bearing mineralization of chlorite-apatite zone occurs in stockwork of the Čučma locality and Sb-rich sulfides-tourmaline-Fe carbonates in Rozabela vein. The sedimentary exhalative U-rich SedEx mineralization was studied in localities of Kurišková and Poráč in the Permian volcanosedimentary sequences of chlorite-apatite zone. In the stilpnomelane-chlorite zone, skarns were formed at the boundary of magnesite-dolomite and calcite-ankerite bodies in locality of Dlhá dolina. The body of Ca-Mg-Fe carbonates was separately formed by Mg and Fe-rich fluids that had replaced the former Silurian limestone. In these metasomatites the skarn consists of assemblage of maghemite-cassiterite-Fe carbonate-FeZnCuBiTeIn sulfides. The siderite-sulfides bearing veins having an etalon of Konštancia and Strieborná veins are distributed in the chlorite zone.
Permian metamorphic-magmatic and hydrothermal cycle in the Gemeric region was a product of the final (collisional) stage of earlier subduction and related to the volcanic arc magmatism, having two stages: (1) Older cycle (281–273 Ma) producing porphyric granite (VAG), cassiterite greisen, apatite-xenotime stockworks, maghemite-cassiterite-ankerite skarn, as well as andesite (K-CAB) and U-rich SedEx mineralization in the North-Gemeric zone, having source in the upper crust. (2) Younger cycle (263–251 Ma) had the mantle influence and produced differentiated granite (syn-COLG) with cassiterite-tourmaline-Fe, as well as tourmaline-molybdenite-Fe carbonates greisens, maghemite-cassiterite-Fe carbonate-FeZnCuBiTeIn sulfides bearing skarn and related Mg-Fe metasomatites, Sb-rich sulfides-tourmaline-Fe carbonates veins, siderite-sulfides veins and rhyolite (K-CAB) with related U-Mo-Cu-rich SedEx breccia. According to the Re-Os dating of molybdenite and cassiterite there has been found that mineralization in the Permian cycle formed within an interval of 268–256 Ma and lasted 12 Ma. The igneous cycle lasted 30 Ma from 281 to 251 Ma. The primary source for Permian mineralization was represented by the lydites and stratabound sulfidic mineralization (Silurian and Devonian). Gemeric granites are of S-type and K, P, Rb, Li, Ta, Nb and mainly Sn, B and Sb-bearing. The study is focussed exclusively on Permian (late Variscan) metallogeny and does not treat with the younger Alpine period metallogenesis.

Key words: metallogenesis, granite of S-type, Sn greisen, skarn, In-rich sulfides, apatite-xenotime stockwork, Fe carbonate veins, U-SedEx mineralization, volcanic arc magmatism, Gemeric unit

Graphical abstract

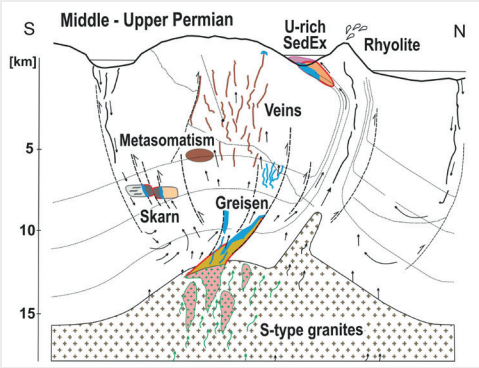

Highlights

- Metamorphic-magmatic and hydrothermal cycle in Permian of the Gemeric region was a product of collisional stage, terminating the subduction, with exceeded volcanic arc magmatism of two cycles: (1) Older cycle (281–273 Ma) producing porphyric granite (VAG), Cst greisen, Ap-Xtm stockworks, Mgh-Cst-Ank skarn – andesite (K-CAB) and U-SedEx, having source in upper crust; (2) Younger cycle (269–251 Ma) – differentiated granite (syn-COLG) – Cst-Tur-Mo-Sd/Ank-greisens – Mgh-Cst-Sd/Ank-FeZnCuBiTeIn sulf. skarn – Mg and Fe metasomatites – Sb-sulf.-Tur-Sd/Ank veins – Sd-sulf. veins – rhyolite (K-CAB) and U-Mo-Cu SedEx breccia of mantle influence.
- Primary source of fluids for Permian mineralization are lydites and stratabound sulfidic mineralization (Silurian–Devonian)
- Gemeric granites of S-type are K, P, Rb, Li, Ta, Nb and mainly Sn, B and Sb-bearing.

Introduction

Presented model of the mineralization origin within the Gemeric region during the closed Permian metamorphic-magmatic-hydrothermal (MMH) cycle summarizes new mineralogical, petrological and geochemical findings, evaluates and completes the recent knowledge about the evolution of hydrothermal mineralization in Gemeric unit and its geotectonic background and time succession (Radvanec et al., 2010; Radvanec & Grecula, 2016). This study is focussed exclusively on Permian (late Variscan) metallogeny and does not treat with the younger metallogenesis, related to Alpine metamorphic core complex in Upper Cretaceous (metamorphism **M2** and deformation phase **AD2**; Németh in Radvanec, Németh & Bajtoš – eds., 2010; Németh et al., 2016 – Fig. 1G ibid).

In the type localities of Hnilec, Delava, Dlhá dolina, Čučma, Rozabela-Štofova dolina, Strieborná vein, Konštancia vein, Poráč, Krompachy, Kurišková, the hydrothermal mineral assemblages of Permian MMH cycle were studied in granite, as well as in the rocks at direct contact with granite, in the granite exocontact, in the wider mantle of granite, as well as in Permian volcanites and volcanic breccias (Fig. 1). In precisely localized samples from boreholes, workings and outcrops in these type localities, the crystallization successions of mineral assemblages in relation on P-T conditions of their origin were revealed.

New findings explain the relation of sedimentary-exhalative (SedEx) mineralization to further metamorphic-anatectic-hydrothermal mineralization types, occurring in Gemeric unit in greisen bodies, skarns, stockworks and veins (Bartalský et al., 1973; Grecula et al., 1995). The SedEx U-Mo-Fe-Cu sulfidic mineralization originated in basins with evaporites and is genetically interconnected with andesite-rhyolite volcanisms, or forms matrix in Permian volcanogene-pneumatolytic and tectonic breccias. First demonstrations of this SedEx type mineralization occur in volcano-sedimentary sequences of Lower and Middle Permian (Cisuralian; the Knola Fm.). The first occurrences of economically significant mineralization occur in the Middle and Upper Permian (Novotný & Miháľ, 1987; Vozárová & Vozár, 1988; Grecula et al., 1995; Kohút et al., 2013).

The etalons of various mineralization types were selected by succession of their occurrence and location from the anatectic zone in amphibolite facies (amphibolite, granite) through the epidote-amphibolite facies or biotite zone with greisens. In the chlorite-apatite zone in stockworks, the quartz-apatite-tourmaline mineralization with REE-P-U-Ti minerals occurs, similarly as greisen and Fe carbonate veins with Sb sulfides. In stilpnomelane-chlorite zone the Mg/Fe metasomatites and skarns were found. In the chlorite zone numerous siderite veins with sulfides occur. In this succession the Sn-Nb/Ta mineralization we have newly studied in localities of Hnilec and Dlhá dolina. The REE-P-U-Ti mineralization was studied in localities of Čučma and Betliar. The Fe-Sn-In-Bi-Te skarn mineralization was studied in locality of Dlhá dolina and Fe carbonate mineralization with Sb

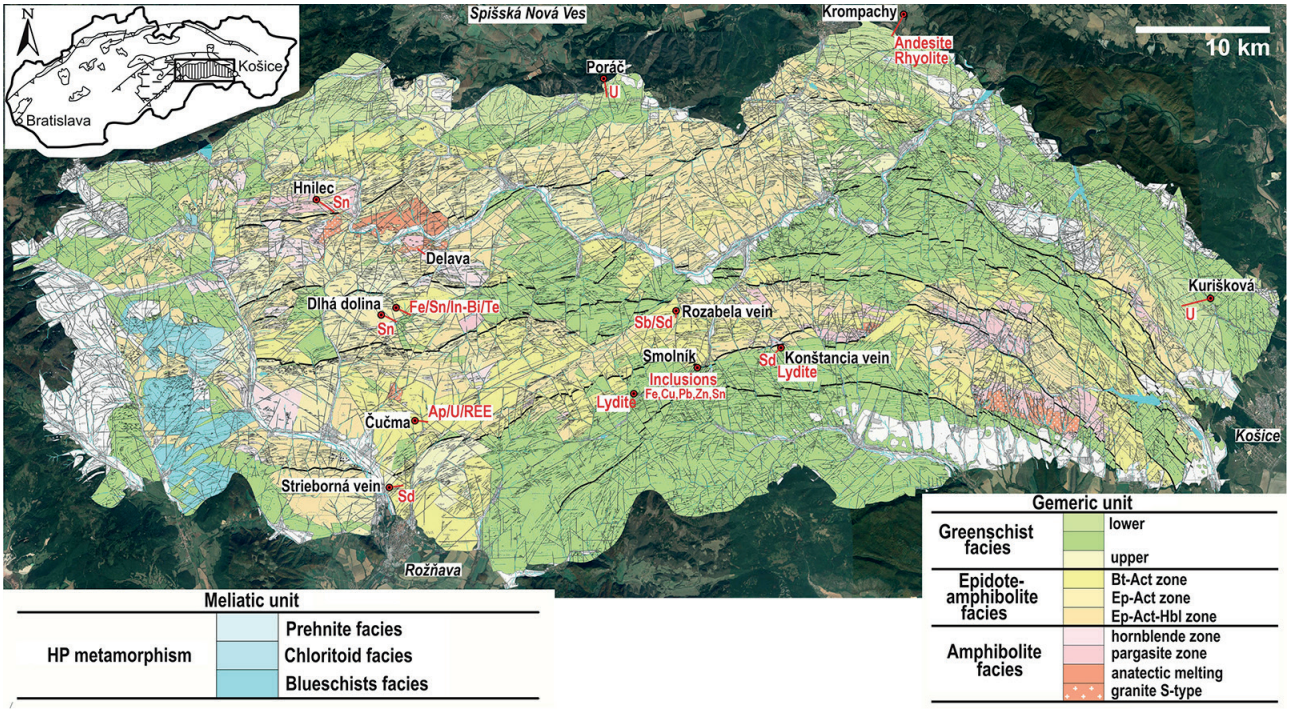

Fig. 1. Metamorphic zonality of Meliatic and Gemeric units from the anatectic zone in amphibolite facies through the epidote-amphibolite facies or biotite zone to greenschists facies and relation of etalon mineralizations to metamorphic facies in the 3D model.

sulfides in Rozabela vein, as well as the siderite sulfidic mineralization in Konštancia and Strieborná veins. In Permian volcano-sedimentary sequences, the SedEx mineralization, forming a matrix in tectonic breccias, was newly studied in localities of Kurišková and Poráč (Fig. 1).

Methodology

Mineralogical, geochemical and petrological research was done on etalons of various mineralization genetic types in known localities of Gemeric unit.

Greisen mineralization was newly studied in locality of Hnilec – samples from trenches R-HC-2a (48° 49' 34.44"N, 20° 29' 0.17"E) and R-HC-3a (48° 49' 35.23"N, 20° 29' 2.86"E) as well as mining levels 1 and 2: samples HN-10 (48° 49' 35.79"N, 20° 29' 11.15"E), HN-133 (48° 49' 33.36"N, 20° 28' 15.11"E) and HN-1253/27 (48° 49' 34.77"N, 20° 29' 0.46"E), including the outcrop in the Dlhá dolina valley (48° 46' 7.30"N, 20° 31' 54.56"E).

Apatite-xenotime mineralization was studied in locality of Čučma (superficial flat-lying outcrop; 48° 43' 0.10"N, 20° 33' 20.87"E and adit), as well as in locality of Betliar.

Skarn mineralization was studied in locality of Dlhá dolina, applying samples from the borehole V-DD-43 (266.8 m; 48° 46' 19.16"N, 20° 32' 35.16"E) and the Elisabeth adit (borehole VSV05-2, 43.0–43.3 m, 48° 46' 19.26"N, 20° 32' 43.39"E).

Sb sulfidic, tourmaline and Fe carbonate mineralization was studied in the samples from the dumps of Rozabela vein in the Štofova dolina valley (dumps; 48° 46' 8.21"N, 20° 45' 19.01"E; 48° 46' 4.65"N, 20° 45' 5.90"E; 48° 46' 4.64"N, 20° 45' 3.84"E; 48° 46' 4.61"N, 20° 45' 1.83"E; 48° 44' 57.59"N, 20° 49' 37.99"E).

Siderite-sulfidic mineralization was studied in veins of Konštancia vein (Jedľovec locality; dumps located in the distance 150.6 m in profile PF 53 of earlier project SGR – Geophysics (Grecula & Kucharič, 1985; 48° 44' 57.59"N, 20° 49' 37.99"E), as well as the 6th deep level of the Strieborná vein at the Rožňava town.

U-rich SedEx mineralization in Permian volcano-sedimentary rocks in the Kurišková locality (borehole LE-K-29, 150.0 m; 48° 46' 4.90"N, 21° 9' 1.41"E), as well as Poráč locality (48° 53' 4.70"N, 20° 42' 0.90"E), where SedEx occurs in the matrix of the tectonic breccia.

In locality of Smolník (near the former Pech shaft; 48° 4' 23.62"N, 20° 45 '57.57"E) the representative samples of **stratabound sulfidic mineralization** of Devonian age were taken:

- from the former central zone of ore-bearing fluid effluence on sea bottom – Cu zone
- from the transitional zone – the Zn-Pb fluid effluence
- from the external zone – the Ba-Sn-Mo fluid effluence

The **Sn-Mo mineralization** was sampled (48° 43' 24.51"N, 20° 44' 53.42"E) in external zone of Devonian stratiform sulfidic mineralization of the Smolník type (Radvanec & Grecula, 1985).

Silurian lydite/volcanosilicite of the Betliar Fm. was sampled in the Jedľovec locality and in locality between Smolník and Úhorná settlements (48° 43' 40.03"N, 20° 43' 5.99"E; 48° 43' 22.17"N, 20° 43' 0.36"E; 48° 43' 21.16"N, 20° 42' 58.90"E).

Representative varieties of Permian S-type granites were studied in Hnilec and Delava localities – from the mine HN-Sn-128 (48° 49' 34.77"N, 20° 29' 0.46"E), borehole HD-41, 1037.9 m (48° 49' 46.79"N, 20° 28' 39.59"E) and borehole HD-28, 380.0 m (48° 50' 3.50"N, 20° 30' 22.68"E).

Representative samples of Permian andesite and rhyolite, including samples with mineralization were studied in the Krompachy area from boreholes 953 (38.4 m, 48° 55' 1.61"N, 20° 53' 46.80"E) and 1113 (99.0 m, 502.1 m; 48° 54' 55.28"N, 20° 53' 28.73"E).

The relations between minerals were studied in polished thin sections. Chemical composition of minerals was determined by EMPA analyses. All above listed type rocks and mineralizations were analysed by quantitative analyses encompassing 62 elements (Tab. 11). Chemical analyses were done in SGIDŠ GAL Laboratories in Spišská Nová Ves, Slovakia. The EMPA mineral analyses and their crystallization succession were obtained in the SGIDŠ Department of microanalysis, Bratislava. The Cameca SX-100 electron microscope was equipped by three spectrometers and Kevex delta IV EDS system. The natural and synthetic standards were used for calibration. Measuring conditions: acceleration voltages 15 KV, 25 KV and 80 KV, current 10 nA at analyses of carbonates or 20 nA at silicate analyses. The diameter of the electron beam was changed according to the type and size of minerals. Micas were measured by widened beam 7–10 µm, carbonates 10–15 µm and other minerals by 2–5 µm beam. The measurement time from 10 to 35 s was chosen for the best measurement accuracy of given element. Detection limit for individual elements is smaller than 0.05 wt.% with an error 1-sigma. The area distribution of element contents (X-Ray map) was determined at the same measurement conditions as analyses of individual minerals.

All above stated type localities were mineralogically and economically evaluated also in the past, being a part of extended metallogenetic investigation in the Gemeric region, lasting from the Middle Ages. The mineralogical-geological results from these localities were evaluated in extended studies by Bartalský et al. (1973, 1993), Grecula et al. (1995), a.o. Earlier mineralogical research in these localities was not done systematically. Authors usually described in details only main mineral association.

For example – the carbonates (siderite, Mn ankerite, ankerite) in greisens of Hnilec and Dlhá dolina localities were not found, or were described only marginally and mineralogical investigation was focussed only on Sn-Nb-Ta mineralization. Similarly, in veins with prevailing Sb-sulfides the co-existing, from the viewpoint of mineralogists "subsidiary" Fe carbonate mineralization with tourmaline, white mica and apatite was evaluated only as Sb sulfidic mineralization without a comprehensive evaluation. This Sb mineralization from other vein mineralizations (siderite veins) of Gemeric unit differs by the content of Sb sulfides. More than 1200 veins prevailingly of siderite-sulfidic composition are known in Gemeric unit. In these veins the same Sb and other minerals occur as in Sb veins. Though in siderite-sulfidic veins these minerals are subsidiary and revealed were in lower parts of veins (Bartalský et al., 1973; Grecula et al., 1995).

The above stated mineralogical discrepancy was a reason for a new mineralogical-geochemical-petrological investigation of etalon localities, being presented in this study. New mineralogical data in above listed localities were classified in the same way. After study in optical microscope the EMPA results for all revealed minerals were projected in triangle and tetrahedron diagrams. These projections were done for carbonates, sulfides, REE-P-U-Ti mineralization and further matrix minerals in each etalon locality (Figs. 9, 11, 15, 18, 20, 22, 24, 25, 30, 31).

Carbonates were projected in triangle diagrams magnesite-siderite-calcite, resp. with the end-member rhodochrosite. The projection of silicate analyses after re-calculation to chemical formula was shown in CFA triangle diagram (Fig. 6). Chemical analyses of projections of the matrix minerals were shown in tetrahedron diagram K=KfsFCaA. The projections of chemical analyses of minerals intended their exact view in crystallization system. In KAl=KfsFCA projection the critical minerals are shown, classifying individual mineralizations to zones from the biotite zone of epidote-amphibolite facies through the chlorite-apatite, stilpnomelane-chlorite to chlorite zones (Figs. 6, 9, 11, 15, 18, 20, 22, 24, 25, 30, 31).

The projection of sulfides, arsenides and other minerals (halides, oxyhalides) analyses after recalculation for chemical formula was visualized in projection of individual tetrahedron diagrams:

- in AsPbFeZn projection
- in ZnPbFe projection (alternatively Sb or Cu or Te – in further text an alternative)
- in PbBiFe (Cu/Sb/Te alternative) projection
- in ZnFeIn (Cu/Sb/Te alternative) projection.

The S and F contents were in these projections ignored. The analyses projections were joined into a single unit aiming to show sulfides in crystallization system according to above stated end elements.

The REE-P-U-Ti minerals were visualized in two individual tetrahedron projections PCaUREE and PCaTiU. Similarly as at sulfides, arsenides and other minerals processing they were joined to one entity PCaUREETi. In the case when a mineral contains a significant amount of another element of the above projections, this element is highlighted by the name of the mineral. For example, gersdorffite Co, U-kobeite, Ta-polycrase, etc. (Figs. 6, 9, 11, 15, 18, 20, 22, 24, 25, 30, 31).

The bulk chemical analyses of etalon mineralizations, lydites, S-types of granites and their effusive equivalents in Permian (andesite, rhyolite) were normalized according to REE standards. There were found two groups. Older group of investigated samples suits to upper crust normalization and the second, younger group of samples suits to primitive mantle normalization (Fig. 33). By this REE normalization the etalon mineralization were divided into two groups fully compliant with geotectonic background and model of the origin of two groups of granites in hot lines above subduction zone during Permian evolution of Paleo-Gemericum according to Radvanec et al. (2009; Fig. 2). In subsequent processing the group of bulk analyses of the "upper crust" was normalized on porphyric granite, representing the source non-differentiated anatectic melt. This anatectic melt generated the fluid phase, from which in the granite exocontact the mineralization originated with the upper crust characteristics. According to REE normalization this mineralization complies with the source porphyric granite. Variation of 62 elements contents from the group of "upper crust" after normalization to porphyric granite were visualized in isocones (isoconcentrations) and in the logarithmic scale they were evaluated as enrichment or deficiency in the element content (Fig. 35).

The second – younger group, having the influence of primitive mantle, was normalized on younger differentiated granite, which correspondingly was displayed as enrichment or deficiency of the element content (Figs. 36, 37). This approach was used also for characterization of pre-Permian, i.e. Early Paleozoic mineralizations, being after anatectic process in hot line the source of metals for fluid phase in Permian. Such source of elements is represented by stratabound sulfidic mineralization of Smolník type (Silurian–Devonian) and the Betliar Fm. with lydites (Silurian; Fig. 34).

In our geotectonic model of the mineralization origin in Gemeric unit in closed Permian MMH cycle, the until published zircon ages (SHRIMP) and Re-Os ages of molybdenite were used (see following text). These methods of dating determine the real age of these minerals without their possible younger rejuvenation or their "substitution" contamination during their origin (see references in further text). The monazite, uraninite and xenotime ages derived from EMPA are directly dependent on the quality of WD analyses.

Determining ages of these minerals, the Pb content measurement preciseness is principal and in the calculations of ages also U and Th contents from highly precise analyses play an important role (Suzuki & Adachi, 1991, 1994; Suzuki et al., 1994, Montel, 1996; Nagy, 2002; Konečný et al.; 2004). From the total number of 100 monazite analyses from above stated mineralizations, altogether 42 % were without Pb and Th. It means that the age of this monazite generation was not found and further derived ages were variable, similarly and in xenotime. The xenotime from the Čučma locality was analysed in the "dating area" in Fig. 19. In this chemically homogeneous grain in area 100 m x 50 m the xenotime was precisely analysed, applying focussed beam of 5 mm in 21 points. Analysed points are well visible. Chaotic dating results were as follows: Permian 290–247 Ma (n = 2), average 268.5 Ma; Triassic 226–204 Ma (n = 2), 215 Ma; Jurassic 282–151 Ma (n = 4), 166 Ma; Cretaceous 137–68 Ma (n = 9), 101 Ma; Paleogene 56–25 Ma (n = 2), 41 Ma; Paleocene 23–5 Ma (n = 2), 14 Ma. Points of analyses with totally differing ages 290 Ma and 5 Ma were mutually distant 10 µm. Monazite at the place does not contain Pb and Th (Tab. 6).

Uraninites, encosed in hosting cassiterite and molybdenite of the Hnilec greisen, by the EMPA dating provide ages around 185 Ma (Fig. 7). According to mineralogical criteria cassiterite, filling also small fractures in uraninite, must be younger that uraninite. But the cassiterite provides ages of 268 Ma and hosting molybdenite 263 Ma, so both minerals are older than uraninite enclosing them (Fig. 7). It is probable that the Pb content is influenced also by the total balance of Pb in hydrothermal solution. The primary content of Pb in the fluid is probable variously substitutionally bound and distributed among coexisting galena, monazite, uraninite, xenotime and other minerals. Possibly the Pb content derived by the uranium decomposition is influenced also by the fluid, from which monazite, uraninite and xenotime had crystallized. In analysed xenotime in the Čučma locality numerous small inclusions of galena were found (Fig. 19). Distribution of Pb in this system is until not well studied and will be a topic for further research. Due to this reason the dating results by means of the total content of Pb in monazite, uraninite and xenotime cannot be interpreted. The dating results derived from the analyses (EMPA) of monazite, uraninite and xenotime as well as from until published works were not taken into consideration in this study.

The position of mineralization etalons in vertical cross-section through the upper crust was determined by the P-T conditions at origin of mineralization etalons. All above described approached were taken into account in metallogenetic model of the gradual origin of mineralization from the Lower to Upper Permian in Paleo-Gemericum (Figs. 38, 39). According to individual mineral etalons the existing databases were reevaluated. New analyses from our mineralogical-petrographical study are presented in Tables 1–12 as Supplement to this paper.

Permian metamorphic-magmatic cycle in Gemeric unit

The Permian metamorphic-magmatic cycle is represented by individual facies of orogenic metamorphism, S-type granites and their effusive equivalents (andesite, dacite, rhyolite, basalt) on the surface (Grecula et al., 2009; Radvanec & Grecula, 2016; Vozárová & Vozár, 1988). Permian period is characterized by the low- to medium-pressure metamorphism with high temperature gradients in the range of 40–50 °C/km (Radvanec et al., 2007, 2009, 2017; Radvanec & Grecula, 2016; Radvanec & Németh, 2018). This extreme overheating of the Paleo-Gemeric region in Permian caused regional metamorphism and culminated with S-type anatectic granite magmatism. The Gemeric granites as anatectic products have increased SiO_2 contents (73–78 wt.%) and are weakly peraluminous (Shand`s index – A/CNK = 1.2–1.6), having high concentration of F, B, Rb, Li, Cs, Sn, Mo, Be, as well as low concentrations of Sr, Ba, Zr and V (Tauson et al., 1977; Petrík & Kohút, 1997; Broska & Uher, 2001). The high Sr initial isotopic ratios (I_{Sr} = 0.711–0.715), together with negative values $e_{Nd(i)}$ = –4.6 and increased values of stable isotopes $d^{18}O_{(VSMOW)}$ = 10 ‰, $d^{34}S_{(CDT)}$ = 4.48 ‰, indicate the mature continental protolith, rich in rocks with high content of feldspars and muscovite (Kovách et al., 1986; Cambel et al., 1989; Kohút et al., 1999, 2001; Kohút & Recio, 2002). The presence of residual fluids rich in volatile substances in short distance from the anatexic zone allowed the crystallization of the rare-element Sn-Li-Nb-Ta-B-F-U-Bi-Mo-As mineralization (Drnzík et al., 1981; Drnzík, 1982). The numerous group of radiometric ages within the range of 300–230 Ma for Gemeric granites (Kovách et al., 1981) was refined by the zircon (SHRIMP) and monazite dating to 275–258 Ma (Radvanec et al., 2009) and the Re-Os molybdenite ages to 263 Ma (Kohút et al., 2005).

The high temperature gradients are characteristic for metamorphic events, related to large region overheating during the volcanism of the island-arc type (Spear, 1995), or they underwent overheating during the calc-alkaline and K-calc-alkaline volcanic activity in continental arc. The Permian period in Gemeric unit has signs of the island arc magmatism with accompanied low- to medium-pressure metamorphism from amphibolite to greenschist facies (Fig. 1). In this period of the Gemeric and South Veporic evolution the granite melt originated in amphibolite facies metamorphism having its effusive andesite-rhyolite volcanic equivalents on the surface (Radvanec et al., 2007, 2009, 2017; Grecula et al., 2009; Radvanec & Németh, 2018; Radvanec & Grecula, 2016; Novotný & Mihál',

1987; Vozárová & Vozár, 1988). The geochemical classification of andesite-dacite-rhyolite, calc-alkaline and K-calc-alkaline type of volcanism is in diagrams evaluated as equivalent of granites of volcanic arc (VAG). Part of chemical analyses is in the field of syn-collisional granites (syn-COLG; Fig. 3). The source of volcanism is represented by melting of prevailingly continental crust (Vozárová et al., 2015). Permian volcanic suite of andesite, dacite and rhyolite has two zircon generations. Older one is derived prevailingly from andesites, having ages ranging from 287 to 273 Ma (SHRIMP). Younger group of zircons is prevailingly from dacites to rhyolites, having ages from 269 to 251 Ma (Vozárová et al., 2009, 2009a, 2010, 2012, 2013, 2015).

The geotectonic back-ground of anatectic melting of pre-Permian rocks, origin of S-type granites and volcanites (andesite-rhyolite) of island arc in Permian in the Paleo-Gemeric zone is related to the heat input and melting of the crust in two hot lines above subduction zone (Radvanec et al., 2007, 2009; Fig. 2). This subduction started with compression in Lower Carboniferous between subducted plate and the mantle accretion prism ("hanging wall", Radvanec & Grecula, 2016). Tectonic blocks of Cpx-SrEp-rich metagabbros registered gradual "exhumation" metamorphism from the eclogite facies, through blueschist to pumpellyite-actinolite facies. During subduction, in Upper Carboniferous the blocks of these metagabbros were exhumed to accretion prism (Radvanec & Németh, 2018). Followingly in Permian the heat transfer from this subduction zone to the Earth crust above it caused the melting of the crust and origin of above stated association of S and A-type Early- to Late Permian granites. Above granites this magmatism caused the bulging of the crust and its extension as a result of subduction dipping to the north (Radvanec et al., 2007, 2009; Fig. 2). During the culmination of subduction since Middle Permian the fractures, formed in the upper crust by extension, were used by the acid (including granitic) as well as basic magma penetration towards the surface, as well as facilitated the heat flow in two parallel "hot lines" (l.c.) The heat ascend in upper crust of the Paleo-Gemeric fundament is demonstrated by metamorphic differentiation (seggregation) to local partial melting of metapelites, metapsammites and acid Early Paleozoic metavolcanites (Grecula et al., 2009). Granites were melted from the crustal and partly also the under-crust protoliths during extensional régime and intrusively entered up to upper crust, where they increased the thermal gradient to such level that the synmetamorphic differentiation/seggregation of metapelites, metapsammites and metavolcanites occurred, being originally metamorphosed in the pumpellyite-actinolite facies and in biotite zone of the orogenic (Upper Carboniferous–Lower Permian) metamorphism (Radvanec et al., 2017; Radvanec & Németh, 2018).

In Gemeric unit, the S-type granite varieties are divided into two different belts (lines) or groups (Figs. 2, 3, 4). Southern hot line is older and according to granite dating

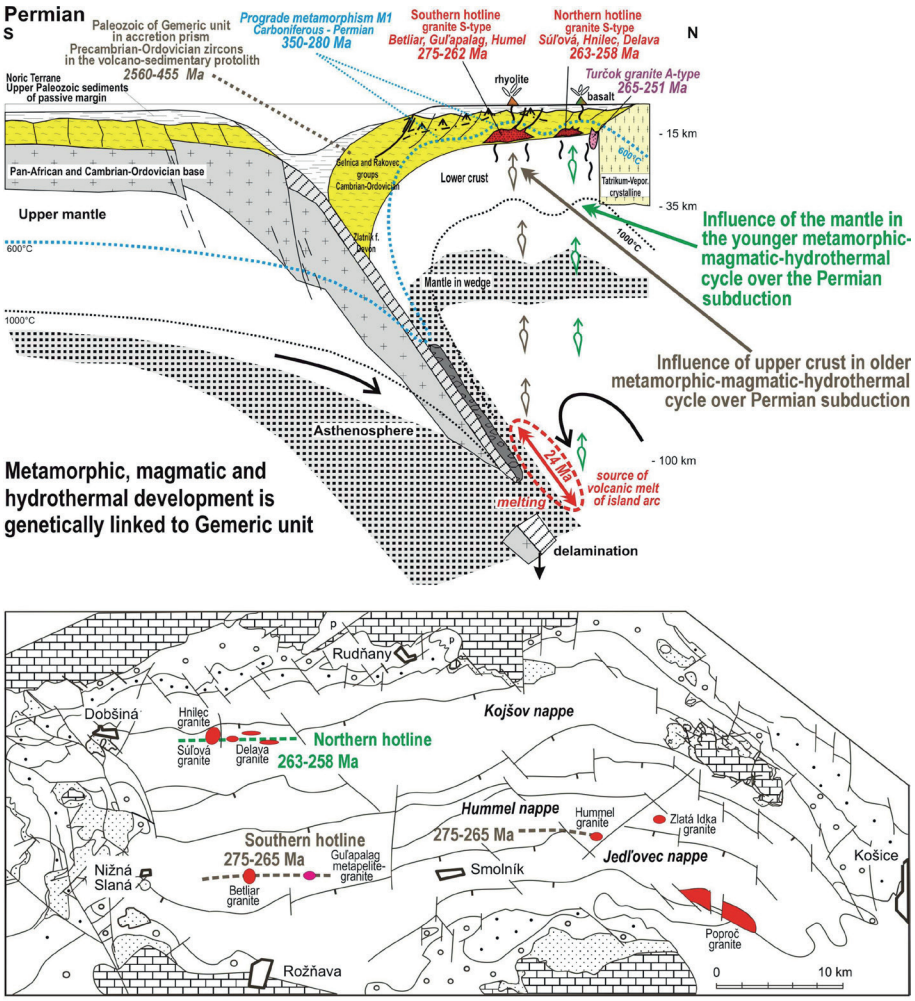

Fig. 2. Permian geodynamic evolution of Paleo-Gemericum over subduction zone and the zircon dating in granites, metamorphites and sediments of accretion prism (Radvanec et al., 2007, 2009; Putiš et al., 2009).

it originated within the ages 275–262 Ma. Northern line is younger and anatectic granites there originated within interval 263–258 Ma (Radvanec et al., 2009; Fig. 2). The age shift of granites of "southern hot line" (275–262 Ma) comparing to granites of the "northern hot line" (S-type – 263–258 Ma; A-type – 265–251 Ma) accounts around 12 Ma with ca 24 Ma total duration of granite magmatism in hot lines (Radvanec et al., 2009; Fig. 2). The age shift of the granite melt origin, and by this way also the age of extension in the crust, relates to submerging of subducting plate and the depth of subduction in the direction from the south to north. Above the plate the collapse of late-Variscan accretion prism occurred due to extension of the crust and mantle lithosphere.

The age of a part of zircons in the Betliar (484 Ma) and Súľová (458 Ma) granites indicates that the S-type granite protolith was represented by Ordovician volcanosedimentary rocks. The metamorphic differentiated metapelite to "metatectic granite" from the Gul'apalag locality contains besides the Ordovician zircon (455 Ma and 467 Ma; average ages) also of zircon with inherited Late Proterozoic (560 Ma) and Late Archaic (2560 Ma) cores (Radvanec et al., 2007, 2009). The same ages of pre-magmatic zircon we found in the "southern", as well as "northern" hot lines. It confirms that prevailingly Ordovician protolith (volcanosedimentary complex of the Gelnica Group and the **lower crust sequences of Ordovician age** partially melted in Devonian (Putiš et al., 2008, 2009) had in the pre-Variscan "Gemericum" the whole area distribution and were from the Upper Carboniferous to Lower Permian again metamorphosed during the late-Variscan subduction-collision metamorphism. In "hot lines" the late-Variscan metamorphism in the Middle and Upper Permian gradually reached P-T conditions of synmetamorphic (metatectic) seggregation of metamorphosed prevailingly pelitic protolith.

After Alpine folding, the arrangement of tectonic blocks of variably metamorphosed rocks in Paleo-Gemericum has preserved its original Permian metamorphic zonality of two above stated parallel "lines" (Fig. 1). In the amphibolite facies zones there originated the anatectic granites. The distribution of tectonic blocks of metamorphites of epidote-amphibolite and greenschists facies represents the gradual vertical cooling along hot line from the anatexic zone to greenschists facies rocks (Figs. 1, 2).

The magmatic activity on hot line is superficially manifested by Permian volcanism of island-arc type, which, similarly as Permian granites is characterized by two volcanic periods with volcanoes situated in two parallel lines. At the northern margin of Gemeric unit the andesite-dacite and dacite-rhyolite volcanism prevails, starting from Lower Permian and having linear arrangement of volcanoes in E-W direction (Novotný & Mihál', 1987; Vozárová & Vozár, 1988). Furthermore to the north – at the boundary of Gemeric and Veporic units and in souther Veporic unit – the younger volcanic chain

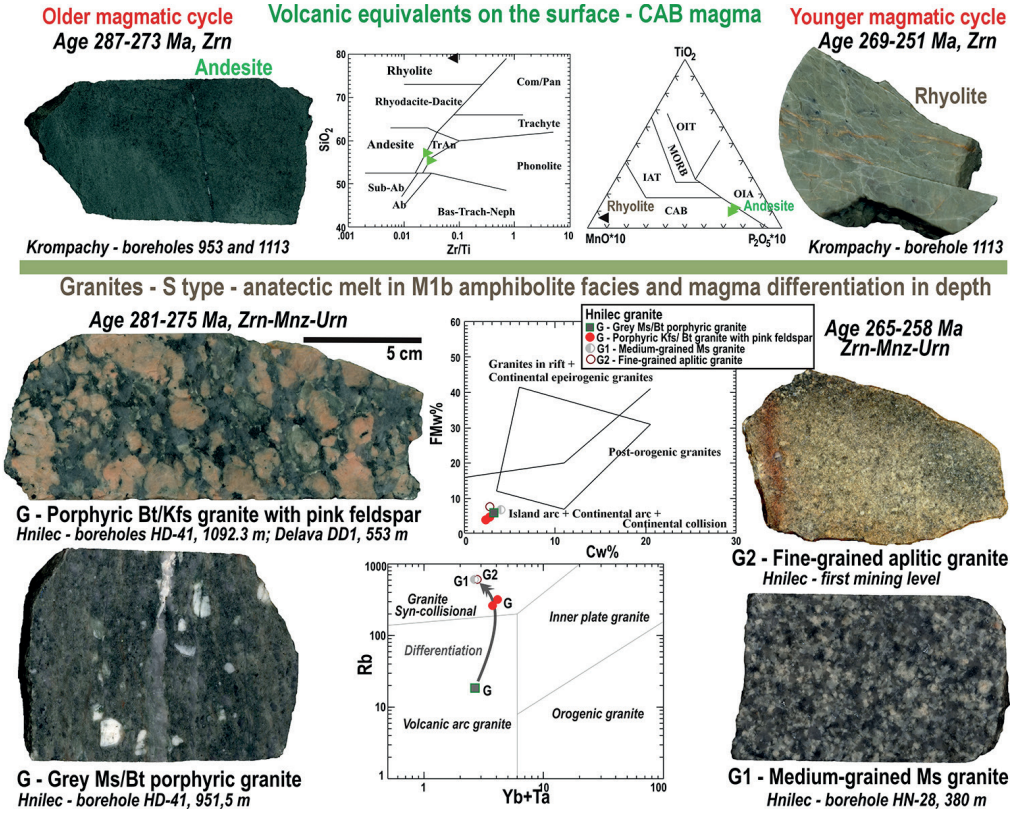

Fig. 3. Geochemical characteristics and dating of two groups of abyssal rocks and their volcanic equivalents in Permian magmatic cycle in type localities. Porphyric S-type granite and andesite represent older pair and the medium- to fine-grained S-type granite and rhyolite represent the younger pair.

prevailingly of Upper Permian age has also E-W trending linear arrangement, consisting of dacite-rhyolite as well as individual basalt volcanic bodies (Novotný & Mihál', 1987; Vozárová et al., 1988; Grecula et al., 2009). According to stratigraphic position and dating results, the older andesite–dacite volcanic suite has the ages within the range of 287 to 273 Ma and younger suite of dacites to rhyolites the ages 269–251 Ma (Novotný & Mihál', 1987; Vozárová et al., 2012, 2013, 2015).

Older magmatic cycle on hot line had produced a porphyric granite with andesite as its main effusive equivalent on the surface. Younger magmatic cycle produced medium- and fine-grained granite with rhyolite as its main effusive equivalent (Fig. 3). The REE contents normalized on upper crust and primitive mantle clearly demonstrate the upper crust influence during the anatectic melting in the case of older magmatites, producing a pair of porphyric granite and andesite as its effusive equivalent (Fig. 4). The influence of primitive mantle in younger magmatites is represented by differentiated medium- and fine-grained granites and rhyolite as their effusive equivalent. The influence of upper crust in the period of **281–273 Ma in older magmatic cycle** relates to the shallower melting depth of the rocks in subduction zone. In this period the heat was transferred from shallower melting zone (southern hot line), where the fluid phase prevailed over magma. The influence of primitive mantle in **younger magmatic cycle in the period of 269–251 Ma** indicates that in this period the subducted rocks were melted in deeper part of subduction zone together with mantle (Fig. 2). This deep-located melting in the mantle results in differenciated granitic melt with the mantle influence, found in medium- and fine-grained granites and their effusive equivalent – rhyolite (Figs. 3, 4). The individual basalt bodies in Permian reflect direct melting of the mantle, when the subduction reached in the astenosphere the deepest level (Fig. 2). The basalt effusions are younger than two above stated magmatic cycles on hot lines and recently are located further north and away of andesite, dacite and rhyolite bodies (Vozárová & Vozár, 1988; Grecula et al., 2009).

Relation of metamorphism, granites, residual fluid phase and matrix index minerals in hot line

The gradual origin and position of porphyric, medium- and fine-grained granites and relation of these varieties to exocontact were investigated in details by the borehole and mine surveys in type occurrences located between the Babiná hill and the Hnilec village (Drnzík et al., 1981; Drnzík, 1982; Fig. 5). Here, the exocontact of granites is formed by chlorite-muscovite phyllites, metabasalt/amphibolite, as well as (Cpx/Sr) clinopyroxene metagabbro, containing Sr-rich epidote (Drnzík et al.,

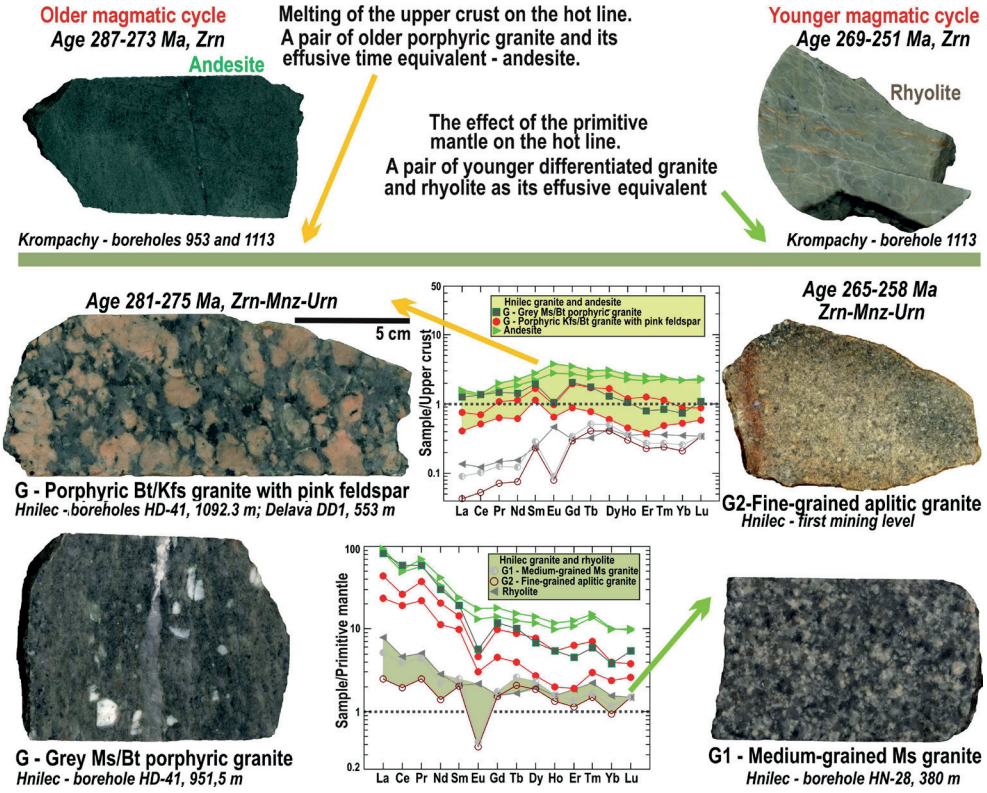

Fig. 4. Normalization of two groups of abyssal magmatic rocks and their volcanic equivalents in Permian magmatic cycle in type localities according to REE courses. Older magmatic pair of porphyric S-type granite and andesite originated due to melting of upper crust. Younger magmatic pair – medium- to fine-grained S-type granite and rhyolite indicate the mantle influence. Both magmatic groups originated gradually on hot lines in Permian. The source of heat above subduction zone initiated firstly anatectic melting in the upper crust and younger hot line has transported besides heat also REE characteristics of the mantle, which is in agreement with the subduction depth more than 100 km as well as the melting of subducted rocks in the mantle of the Earth according to model of subduction in Permian (Radvanec et al., 2009, cf. Fig. 2).

1981; Radvanec & Németh, 2018; Fig. 5). SHRIMP zircon dating indicates the polystadial metamorphism of these rocks during (1) the earlier Carboniferous metamorphism of Variscan orogenic phase **M1a (348–307 Ma)** and (2) later Permian metamorphic overprint **M1b (261 Ma)**. During Carboniferous metamorphism **M1a**, the Cpx-Sr Ep metagabbro exhumed in subduction zone was gradually metamorphosed – firstly in epidote-eclogite facies and later the blueschist facies retrograde metamorphism, being followed by pumpellyite-actinolite facies (Radvanec & Németh, 2018). In Permian the Cpx-Sr Ep metagabbro, metabasalt/amphibolite and chlorite-muscovite phyllites were newly metamorphosed in orogenic metamorphism **M1b**. In the area of localities Babiná and Hnilec the orogenic metamorphism **M1b** reached the conditions of amphibolite (600–700 °C, ~8 kbar) and epidote-amphibolite facies (~550 °C, ~5 kbar; l.c.; Fig. 1). In chlorite-muscovite phyllites the equivalents of amphibolite and epidote-amphibolite facies were revealed, being present in the biotite zone (cross-section in Fig. 7). These new **M1b** mineral assemblages **M1b** originated in the exocontact of the Hnilec granite body during the brittle-ductile deformation, when this new association infilled the joints in metabasalt, which had underwent also earlier Carboniferous overprint in the pumpellyite-actinolite facies **M1a** (Fig. 6). Along the hot line in investigated Hnilec area the Permian metamorphism of amphibolite and epidote-amphibolite facies reached the same P-T conditions (600–650 °C, 3–6 kbar) as the biotite zone metamorphism in metapelites. In biotite zone there originated the granite magma of S-type during anatectic melting of metapelites, lydites and the Lower Paleozoic metavolcanites (Radvanec et al., 2007, 2009; Grecula et al., 2009; Radvanec & Németh, 2018).

According to mineralogical investigation, the micas, apatite, tourmaline and Mn/Fe carbonates represent index minerals of granites, metamorphism and simultaneously represent also index minerals of residual fluid phase, which source was derived from anatectic melt.

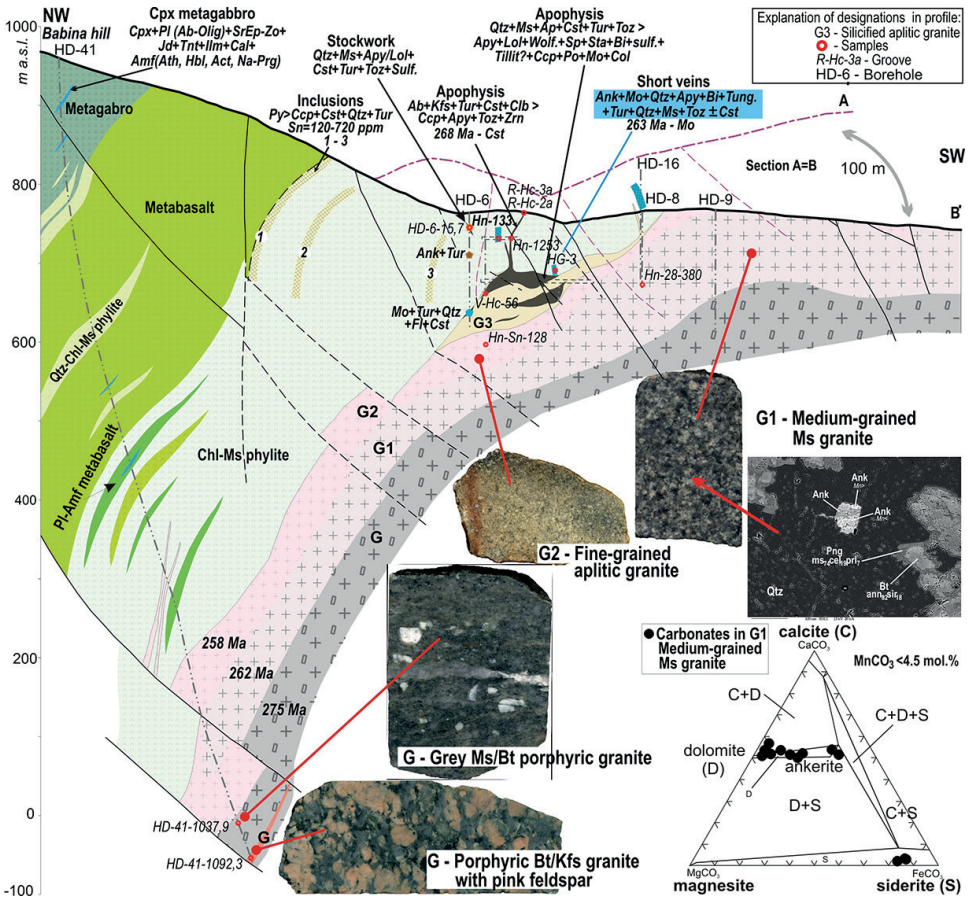

Fig. 5. Relation of anatectic zone with various S-types granites and epidote-amphibolite/amphibolite facies in granite exocontact in locality of Hnilec. Mineral assemblages in the greisen and granite exocontact were taken from boreholes and are shown in cross-section (Drnzík et al., 1981). Main minerals of S-type granites are: albite (Ab), quartz (Qtz), biotite (Bt), phengite/muscovite (Ms), K feldspar (Kfs), apatite-F (Ap), tourmaline (Tur), fluorite (Fl), chlorite (Chl), ilmenite (Ilm), rutile (Rt). In the medium-grained granite the inclusions of zonal dolomite (Dol) to ankerite (Ank) and siderite (Sd) in quartz-albite matrix were found. Biotite (Bt) is at margin changed to phengite (Png). Chemical classification of carbonates is provided by triangle diagram magnesite-siderite-calcite.

Tourmaline

Tourmaline in the Babiná – Hnilec area was found in the granite exocontact in epidote-amphibolite facies in all granite types from porphyric to aplitic type, in apophyses and in greisens (Figs. 5, 6; Drnzík et al., 1981; Drnzík, 1982). Tourmaline registered the genetically conditioned relation among granite melt, metamorphism and residual fluid phase. Tourmaline belongs to schorl-dravite series and has two main stages of its origin. The major part of the tourmaline grains crystallized in the first M-stage forming the zonal grains, which centre has a higher content of Fe, Al and Mn than its margin. During second L-stage there originated second generation of tour-

maline, which fills tiny cracks at brittle-ductile deformation in the granite exocontact (Fig. 6; Tab. 1). Tourmaline from L-stage is richer in Mg and poorer in Fe, Al and Mn as tourmaline from M-stage. In granites the tourmaline from L-stage has similar composition as younger tourmaline margin from M-stage. The contents of $d^{11}B$ boron isotopes from M-stage range from –10.3 ‰ to -15.4 ‰, so there is not possible to distinguish the centre and rim of the grain, though some tourmaline grains from the granite exocontact (biotite zone) have higher values of $d^{11}B$ in the centre than in the margin. Younger tourmalines from L-stage have lower values of $d^{11}B$ (from –16.0 ‰ to –17.1 ‰; Jiang et al., 2008). Revealed isotopic ranges and trends indicate the change of the source from the dominant magmatic-hydrothermal fluid phase to late stage, where in the granite exocontact (epidote-amphibolite facies, amphibolite facies or biotite zone) the B source prevails from metamorphic fluid phase of orogenic metamorphism. The significantly higher content of Fe^{3+} in tourmaline from L-stage reflects the change of redox conditions towards the oxidation in younger L-stage (Jiang et al., 2008). This change of redox conditions significantly influences the origin of hydrothermal greisen Sn mineralization in investigated area. Re-Os age of molybdenite 263 Ma dates the origin of this greisen mineralization to Middle Permian (Kohút & Stein, 2005). Dated molybdenite in the greisen is in coexistence with Mn ankerite, apatite-F and tourmaline (Fig. 21).

Tourmaline of schorl-dravite series occurs in type localities of Hnilec, Dlhá dolina, Čučma, Rozabela and Kurišková in greisen, skarn, veinlets, Fe carbonate veins with Sb sulfides and in U-SedEx mineralization (Tab. 1). In these localities, tourmaline from epidote amphibolite facies, from biotite zone up to greenschists facies has approximately corresponding chemical composition and is a part of KAl=KfsFCA crystallization system (Figs. 9, 11, 15, 18, 20, 22, 24, 30). The values of the ratio Al/(Al + Fe + Mg) tourmaline was within the range 0.60–0.77 and values Na/(Na + Ca) within the range 0.63–0.99. In localities with zonal tourmaline, the Mg/(Mg + Fe) ratio in the centre of tourmaline ranges from 0 to 0.34 and at the margin from 0.59 to 0.89 (Tab. 1). Mineralogical investigation revealed that the tourmaline of schorl-dravite series is a part of mineral assemblage in the root and lower parts of numerous siderite-sulfidic veins of Gemeric unit (Bartalský et al., 1973; Grecula et al., 1995).

Micas, Mn/Fe carbonates, topaz and apatite-F

Next index minerals, originating during Permian metamorphism and anatectic melting in **M1b** from residual fluid phase, represent white micas, Mn/Fe carbonates, topaz and apatite. Mn/Fe carbonates and phengite originated by the reaction of biotite in granite with residual fluid phase. It was found in Hnilec locality in younger medium-grained granite, containing isolated and zonal ankerite and Mn ankerite grains (Fig. 5). Biotite in this granite consists of molecules of annite (82 %) and siderophyllite (18 %). Its margin was changed to phengite with the content of muscovite (74 %), seladonite (15 %) and pyrophyllite (7 %) molecule (Fig. 5). This change of the dark mica to white mica porphyroblast has shown that the granite varieties from the younger magmatic cycle were altered by residual fluid phase with high CO_2 content. At the P-T boundary for anatectic melting, this fluid phase has destructed the former biotite and from it deliberated Mg and Fe were bound in ankerite, dolomite or siderite (Fig. 5). In other places in the quartz and albite matrix of this granite, the separated dolomite and siderite grains were found. Mn-Fe-Mg carbonates were not found in older porphyric granite.

Similarly, within the biotite zone of locality Rožňava-Turecká (35th mining level), in the metapelite with psammitic component (quartz clasts) the manifestations of local corrosion of allanite by fluid phase were found. This fluid phase had a high content of Mn and CO_2. Allanite from this biotite zone is in the margin changed to Mn siderite and bastnäsite. Mn siderite fills the fractures in the allanite grain (Radvanec et al., 2004, 2007). This metapelite with allanite from the Rožňava-Turecká area is metamorphosed in the P-T boundary for anatectic melting, correspondingly as there were metamorphosed rocks in the area Babiná – Hnilec.

In the exocontact of the Hnilec granite in biotite zone of epidote-amphibolite facies the following gradual metamorphism of chlorite-muscovite phyllite (sample HG-3, geological cross-section in Figs. 7, 8, 21) took place: Former white mica in phyllite originated in Carboniferous pumpellyite-actinolite facies **M1a** (Radvanec et al., 2017; Radvanec & Németh, 2018). In the biotite zone of Permian metamorphism **M1b** this white mica recrystallized to fine-grained phengite and subsequently to muscovite. This replacement was controlled by residual fluid phase and during the metamorphism of white mica there originated also topaz and apatite. The reaction, which formed phengite, muscovite and topaz in the sample HG-3 is directly related with the origin of Fe/Ca carbonates and metamorphism of former sedimentary intercalations of calcite-limestone in phyllite to ankerite and siderite, as well as apatite-F according to reactions 1–2:

$$\underbrace{2K_{1.65}Mg_{0.80}Fe_{0.13}^{2+}Fe_{0.75}^{3+}Al_{4.34}Si_{6.24}O_{20}(OH)_4}_{\text{Fe-rich white mica}} +$$

$$+ \underbrace{CaCO_3}_{\text{calcite}} + \underbrace{0.38KCl}_{\text{sylvite}} + \underbrace{0.77SiO_2}_{\text{quartz}} + \underbrace{2.73AlO(OH)}_{\text{boehmite-diaspore}} +$$

$$+ 2CO_2 \rightarrow \underbrace{K_{1.80}Mg_{0.53}Fe_{0.18}^{2+}Al_{4.59}Si_{6.72}O_{20}(OH)_4}_{\text{phengite}} +$$

$$\underbrace{K_{1.88}Mg_{0.18}Fe_{0.55}^{2+}Al_{4.82}Si_{6.53}O_{20}(OH)_4}_{\text{muscovite}} + \underbrace{Al_2O_3}_{\text{in topaz}} +$$

$$\underset{\text{ankerite}}{Fe_{0.26}Mg_{0.70}Ca_{1.04}(CO_3)_2} + \underset{\text{siderite}}{Fe_{0.77}Mg_{0.19}CO_3} + H_2O + OH^- + 0.38Cl^- \quad (1)$$

$$\underset{\text{from reaction 1}}{Al_2O_3} + \underset{\text{quartz}}{SiO_2} + 2HF \rightarrow \underset{\text{topaz}}{Al_2SiO_4F_2} + H_2O \quad (2)$$

Reaction (1) explains the relation between a former (probably sedimentary?) Fe-rich white mica in the core and the mixture of phengite and muscovite at the rim of the white mica porphyroblast (Figs. 8, 21). In agreement with increasing temperature on hot line in Permian metamorphism **M1b**, the former Fe content in the core of porphyroblast lowered and in the mixture of phengite and muscovite at the rim the Fe content is low. During this recrystallization of the white mica porphyroblasts, the main part of Fe content from original Fe-rich white mica deliberated to fluid phase and subsequently caused the replacement of neighbouring sedimentary calcite to Fe/Ca carbonates, which is expressed by the reaction (1). After this heat exchange there followed the exchange of Fe in retrograde phase **M1b**, which started with the origin of ankerite and later continued with the carbonate phase, rich in Mn-Fe-Mg-Ca and siderite. The exchange of calcite to ankerite was found only locally, because the primary sedimentary calcite represented only insignificant admixture in primary phyllite (Figs. 8, 21). The primary sediment contained mainly quartz and Fe-rich white mica. This local Fe metasomatism, or replacement of calcite to ankerite in phyllite, is comparable with identical process of the metamorphism of large bodies of Lower Paleozoic limestone to ankerite and siderite, e.g. in the deposit Mano at the village of Nižná Slaná (Iró & Radvanec, 1997; Radvanec at al., 2004). Metasomatic ankerite and siderite by this way originated also in the contact of former limestone with skarn in the borehole V-DD-43 (Dlhá dolina, Fig. 18).

White mica of phengite-muscovite composition and Fe/Ca carbonates originated by the replacement of biotite and recrystallization of former sedimentary Fe-rich white micas in metapelite according to reaction 1 and reactions in KAl=KfsFCA crystallization system. The phengite-muscovite represents a significant part of matrix mineral assemblage in granites, greisens, skarn, in apatite-xenotime stockworks, Sb-sulfide-tourmaline-Fe carbonate veins, in siderite-sufidic veins and U-rich SedEx mieralizaion as well. Values of the ratio Fe/(Fe + Mg) in phengite-muscovite occur within the range 0.24–0,91 (Tab. 2). According to mineralogical investigation and projection of chemical composition of phengite-muscovite in KAl=KfsFCA system, phengite-muscovite from chlorite-apatite zone occur in two generations, which agrees with reaction 1. These two generations were found in the greisen in locality Hnilec and in SedEx mineralization (Figs. 22, 30). In other zones there was found only one phengite generation (Figs. 9, 11, 15, 18, 20, 24, 25).

Apatite-F

In locality of Hnilec (sample HG-3) part of original calcite in phyllite reacted with residual fluid phase with H_3PO_4 content forming apatite-F according to reaction (3):

$$5Calcite + 3H_3PO_4 + HF \rightarrow Apatite\text{-}F + 5H_2O + 5CO_2 \quad (3)$$

The origin of apatite-F is conditioned by the existence of original calcite or limestone, reacted to this mineral. Reaction 3 runs simultaneously with Fe metasomatism of calcite to ankerite. Apatite-F and ankerite represent coexisting minerals (Fig. 21). Mineral assemblage phengite, muscovite, tourmaline, topaz, ankerite, apatite-F and dated molybdenite in the sample HG-3 characterize greisen from apatite-chlorite zone in the Hnilec locality (Figs. 21, 22).

Apatite-F occurs in all type localities – Hnilec, Dlhá dolina, Čučma, Rozabela, Poráč and Kurišková. It occurs in granites, greisens, skarns, Mg-Fe metasomatites in the contact with skarns, in apatite-xenotime stockworks, Sb-sulfidic-tourmaline-Fe carbonate veins, in siderite-sulfidic veins and U-SedEx mineralization. In all these localities from greisens to U-SedEx mineralization, apatite-F does not contain any admixture of other elements and its chemical formula is $Ca_5(PO_4)_3F$ (Tab. 3). The same apatite-F occurs in assemblage with tourmaline, biotite, phengite, margarite, topaz, stilpnomelane, chlorite, quartz, fluorite, calcite, ankerite, dolomite, kutnahorite, rodochrozite, siderite, magnesite, allanite, goyazite and represents a part of KAl=KfsFCA crystallization system (Figs. 9, 11, 15, 18, 20, 22, 24, 30). According to metamorphic zones and the distance from the zone of anatectic melting on the hot line, the above stated mineral assemblages in KAl=KfsFCA system change, with an exception of stable chemical composition of apatite-F. The metamorphic zone, where the apatite-F occurs with dominant phengite and chlorite, was named the apatite-chlorite zone (Figs. 11, 20, 22, 24, 30).

Minerals crystallizing in KAl=KfsFCA system represent matrix minerals. According to projections of minerals chemical composition in KAl=KfsFCA system the matrix assemblage well characterizes the metamorphic-mineralization zones. In locality of Hnilec the classification of matrix minerals in ACF diagram and KAl=KfsFCA system revealed epidote-amphibolite and biotite zones, where originated the greisens (Figs. 6–9). In locality of Dlhá dolina the chlorite-apatite zone was revealed with the greisen occurrence (Figs. 10, 11). In

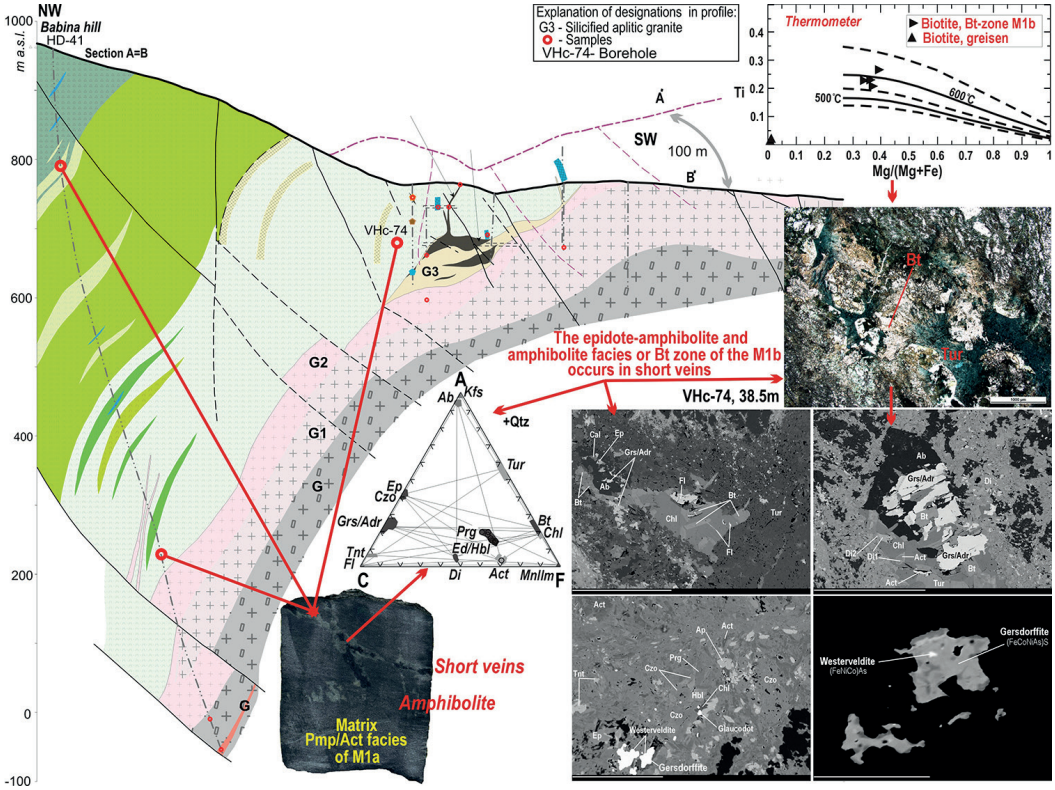

Fig. 6. The exocontact of the Hnilec granite prevailingly consists of the Lower Paleozoic basalt protolith, which underwent orogenic polyphase metamorphism. The matrix of metabasalt or amphibolite was firstly metamorphosed in Carboniferous in the pumpellyite-actinolite facies **M1a** and later in Permian in biotite zone or epidote-amphibolite and amphibolite facies **M1b** (Radvanec & Németh, 2018). Permian mineral assemblage **M1b** originated during brittle-plastic deformation in fractures, where minerals are in equilibrium with the matrix (actinolite Act). The same mineral filling of fractures was found in the granite exocontact in three places in boreholes HD-41 and V-Hc-74. Samples of the granite exocontact from boreholes were studied in cross-section (Drnzík et al., 1981). Fractures are filled with two gradual assemblages: 1 – diopside (Di), pargasite (Prg), edenite-hornblende (Ed/Hbl), epidote-clinozoisite (Ep/Czo), grossular-andradite (Grs/Adr), biotite (Bt), albite, (Ab) and Mn ilmenite (MnIlm); 2 – tourmaline (Tur), fluorite (Fl), apatite (Ap), chlorite (Chl), titanite (Tnt), calcite (Cal), westerveldite (Wes), gersdorffite (Ges) and glaucodote (Gla) sulphides. Mineral assemblage 1 is older in fracture, being enveloped by assemblage 2 (see relation of blue tourmaline and other minerals in reflected electrons). According to biotite thermometer, the mineral assemblage 1 originated at 550–600 °C. In CFA diagram the minerals of Permian assemblage **M1b** from the brittle-ductile fractures characterize the epidote-amphibolite and amphibolite facies of orogenic metamorphism, but not contact metamorphism. Relatively younger assemblage of minerals 2 represents the crystallization from the residual fluid phase and encompasses arsenides, sulfide, tourmaline, fluorite, apatite-F and calcite. BSE.

the same locality the skarns were found in stilpnomelane-chlorite zone (Figs. 12–18). In localities Čučma, Hnilec, Rozabela, Poráč and Kurišková in chlorite-apatite zone the variegated mineralization was found in the greisen, in stockworks, veins and in the form of disseminations in volcanosedimentary sequences on the surface (Figs. 19–24 and 27–30). In mineral deposits of Strieborná vein and Konštancia vein, their vein-type mineralization was found in the chlorite zone (Fig. 25).

In all these metamorphic zones together with matrix minerals there crystallized the variegated "ore" hydrothermal mineralization. The recent distribution and classification of "ore" mineralization on hot lines revealed, in Gemeric unit, has not been comprehensively evaluated yet from the viewpoint of succession of the magmatic and metamorphic zones origin. In previous models the hydrothermal mineralization was evaluated from the viewpoint of P-T conditions of orogenic metamorphism in the range of anatectic melting zone in the depth up to greenschists facies towards the surface (Grecula et al., 1995; Radvanec et al., 2004, 2010; Radvanec & Grecula, 2016). The relations of disseminated U-SedEx mineralization on the surface to hydrothermal mineralization, generated in the depth, were not evaluated in previous genetic models of the Permian development. These relations represent the main goal of this study.

Greisen of the biotite and epidote-amphibolite zones in the line of anatectic melting in the Hnilec type locality

Greisen in the Hnilec locality originated in the zone of anatectic melting and in the area of S-type granite magma differentiation. In the granite exocontact the greisen was found in amphibolite and epidote-amphibolite facies, as well as in biotite zone. Greisen originated in the granite cupola, where the residual fluid phase changed the original granite to so-called "internal greisen". It occurs also in the immediate contact of granite with amphibolite and phyllite (Figs. 6, 7, 8).

The greisen mineralization was found also in short apophyses reaching max. 100 m distance from the granite

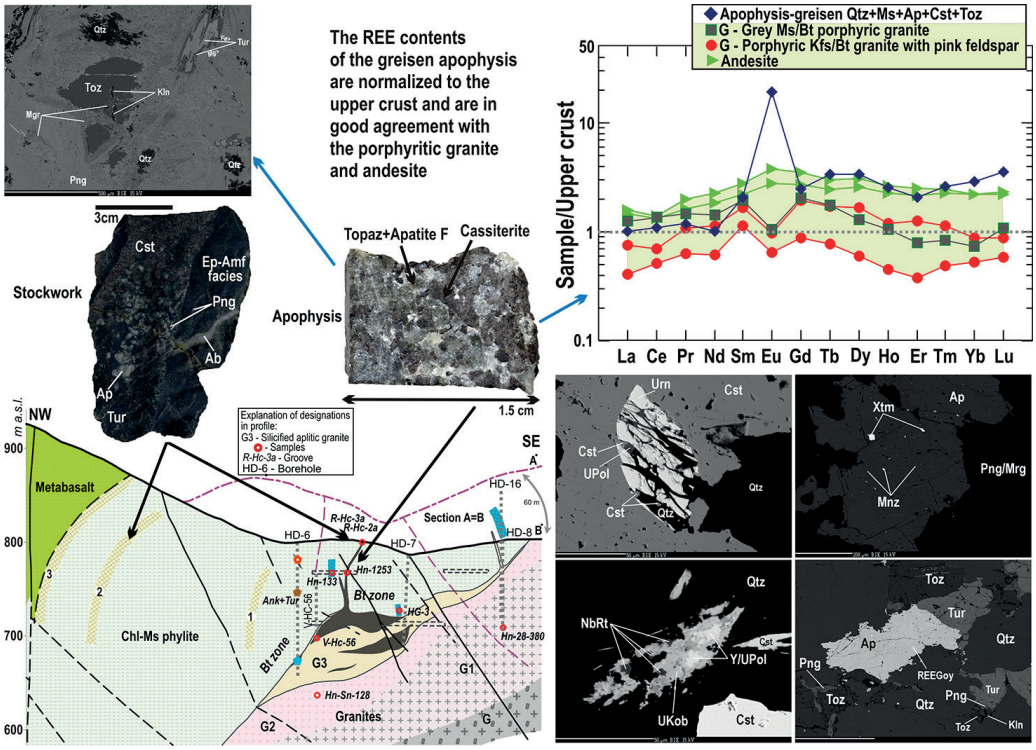

Fig. 7. The greisen samples from the stockwork and apophysis in the Hnilec locality with assemblage of cassiterite (Cst), topaz (Toz), apatite-F (Ap), tourmaline (Tur), phengite (Png), margarite (Mrg), kaolinite (Kln), albite (Ab), uraninite (Urn), kobeite-U (UKob), polycrase-U/Y (U/YPol), monasite (Mnz), xenotime (Xtm), rutile-Nb (NbRt), REE goyazite (REEGoy), quartz (Qtz). BSE image. Greisen occurs in the granite exocontact and originated in epidote-amphibolite facies and biotite zone of **M1b** metamorphism. Samples are from the exploration trench, borehole and the mine. In cross-section they are marked by red circles (Drnzík et al., 1981). Normalization of the REE contents of the greisen has positive Eu anomly and corresponds with older magmatic pair of porphyric granite and andesite. The REE normalization shows that the greisen mineralization has the upper crust source.

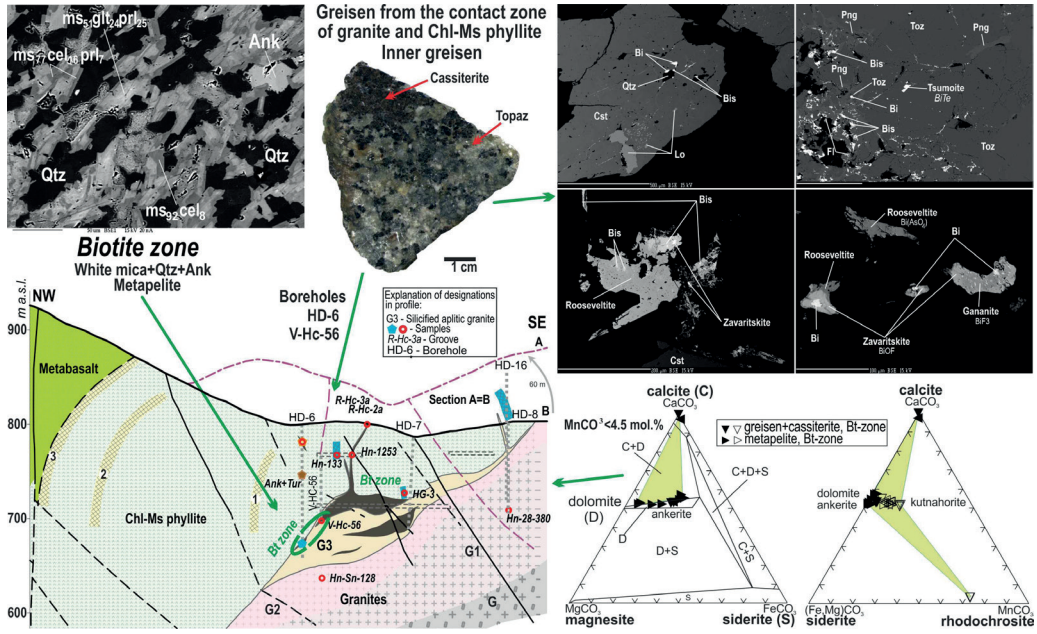

Fig. 8. Greisen from the inner zone of the granite contact with phyllites of epidote-amphibolite facies or biotite zone in the Hnilec locality. In the cross-section the sampling place is marked by the green ellipse. Samples were taken from boreholes Hn-6 and V-Hc-56 (Drnzík et al., 1981). Mineral assemblage of the greisen: cassiterite (Cst), topaz (Toz), apatite-F (Ap), tourmaline (Tur), phengite (Png), fluorite (Fl), albite (Ab), quartz (Qtz), Fe/Mn carbonates (kutnahorite, rodochrosite, dolomite, ankerite), calcite (Cal), löllingite (Lo), bismuthinite (BiS), tetradymite (BiTe). Native Bi (Bi) is at the margin changed to roosveltite, gananite and zavaritskite. BSE image. Triangle diagrams for carbonates show projections of ankerite, dolomite and calcite from metapelite of the biotite zone and projections of kutnahorite and rodochrosite from greisen of biotite zone.

(Figs. 7, 8; Drnzík et al., 1981). In amphibolites and chlorite-muscovite phyllites it fills the fractures originating in brittle-ductile deformation and in this environment it has the stockwork to pseudo-disseminated form, being found by the mine and borehole survey in three mineralization zones (Figs. 6–8; Drnzík et al., 1981). Mineralized zones 1, 2 and 3 originated to the max. distance of 300 m from the granite and their shape copies parallel the cupola of granite

magma (Fig. 7). In these zones there prevails the pyrite above assemblage of chalcopyrite, cassiterite, quartz, tourmaline, Fe oxides. Individual zones contain varying Sn content of 0.012–0.072 wt.% (Drnzík et al., 1981). The normalization of REE contents in this greisen has positive Eu anomaly and is corresponding with older magmatic pair of porphyric granite and andesite. According to REE normalization, the source of greisen mineralization occurred in the upper crust and mineralization originated by rocks melting (Fig. 7).

The greisen mineralization of the stockwork, apophyses, inner greisen and pseudodisseminations in mineralized zones 1, 2 and 3 originated in one gradual event and chemically is classified by various crystallization systems: In the KAl=KfsFA system there originated a matrix assemblage of K feldspar, phengite, biotite, tourmaline, kaolinite and albite. Biotite, margarite and K feldspar represent index minerals of the biotite zone or epidote-amphibolite facies. In FCA system there originated the matrix assemblage apatite-F, fluorite, calcite, dolomite, ankerite, kutnahorite, rhodochrosite, margarite, REE goyazite and topaz. Mineral matrix minerals in KAl=KfsFA and FCA systems represent coexisting associations and their projections are shown in joint system KAl=KfsFCA (Fig. 9). Matrix minerals and relations among them in KAl=KfsFA and FCA system describe the process of greisenization in the biotite zone and in epidote-amphibolite facies. Muscovite-phengite and quartz originated by reaction of K-feldspar with residual fluid phase, produced by the melting of the upper crust. Reaction of muscovite-phengite with HF produced topaz and quartz. Reaction of margarite and quartz with HF produced kaolinite, topaz, fluorite and quartz. Kaolinite reacted with fluid phase to topaz and quartz. The origin of topaz, muscovite-phengite, ankerite, siderite and quartz is well described by reactions 1 and 2. Assemblage cassiterite, maghemite, siderite, Mn/Mg/Fe carbonates, quartz and muscovite-phengite originated by decomposition of biotite with residual fluid phase, containing $SnCl_2$, CO_2 and water. Biotite represents one of main minerals in the S-type granite. Its decomposition during greisenization of granite cupolas conditiones not only the origin of cassiterite, but during its decomposition a significant amount of Fe was released into residual fluid phase. Released Fe then

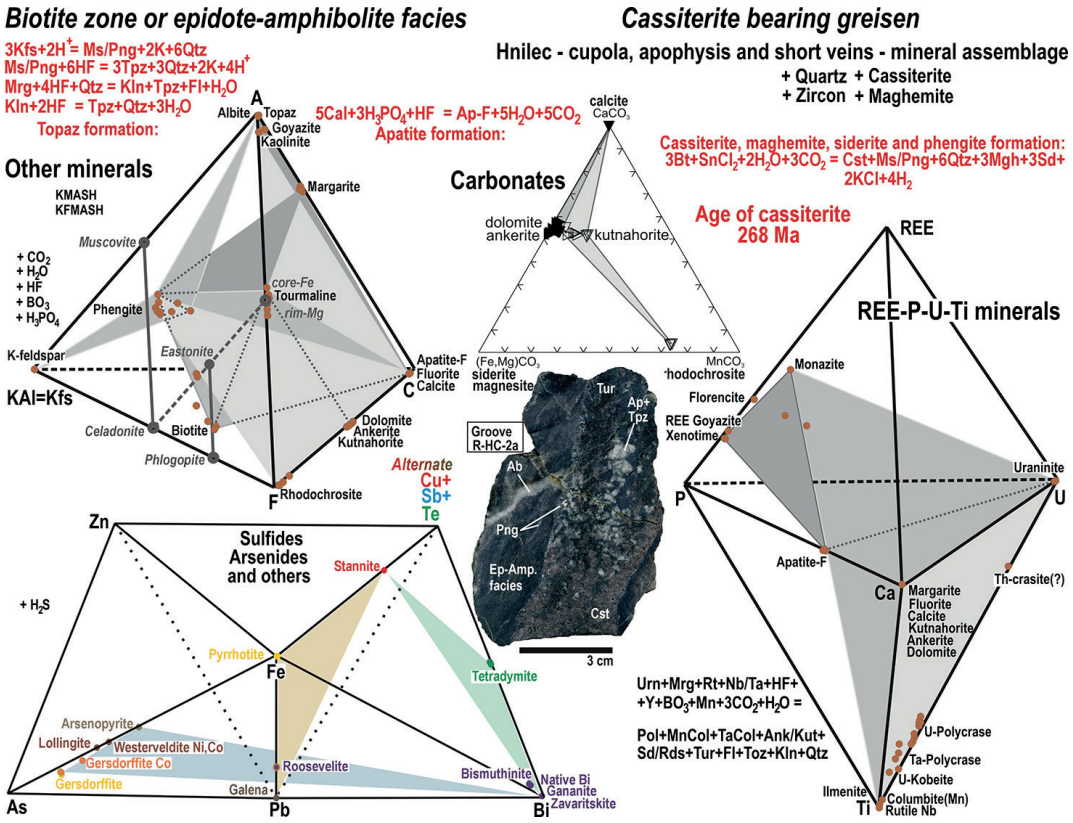

Fig. 9. Projections of the cassiterite greisen mineral assemblages on hot line in the zone of anatectic melting in epidote-amphibolite facies or biotite zone **M1b** in the Hnilec locality. Chemical composition of carbonates is projected in triangle diagram siderite/magnesite-rhodochrosite-calcite. REE-P-U-Ti mineralization is projected intetrahedrons PCaUREE as well as PCaUTi. The greisen matrix minerals are in KAl=KfsFCA projection and sulfides, arsenides and tellurides in tetrahedrous projections FePbBi(Cu/Sb/Te), ZnFePb(Cu/Sb/Te) and ZnFePbAs. Reactions describe the origin of topaz, apatite-F and cassiterite. The age of cassiterite is 268 Ma (M. Kohút, personal information). Further minerals are quartz, cassiterite, molybdenite, zircon and maghemite.

bounds together with CO_2 in Fe/Ca carbonates. These carbonates were found in younger differentiates of granite melt in medium-grained Ms granite-G1 and in greisen (Figs. 5, 8, 9). Apatite-F originated by reaction of calcite with residual fluid phase, containing H_3PO_4 (reaction 3). Besides this, calcite represented a part of Lower Paleozoic sediments of upper crust (Grecula et al., 2009) and these sediments suffered anatectic melting on hot line. This means that anatectic melt contained sufficient amount of Ca for the origin of apatite-F in granite and greisen. The reactions of greisenization and matrix mineral assemblage are shown in Fig. 9.

Next minerals, originating in greisen, are shown in PCaUREE system, where originated xenotime, REE goyazite, florencite, monazite and apatite-F. In the PCaUTi system it is assemblage of uraninite, Th crasite(?), U/Ta polycrase, U-kobeite, Mn columbite, Nb rutile and ilmenite. In FeAsPb system there originated pyrrhotine, arsenopyrite, löllingite, Ni/Co westerveldite, Co gersdorffite, gersdorffite, galena and rooseveltite. In FePbBiCu/Te system it is a native bismuth, gananite, zavaritskite, bismuthinite, tetradymite and staninite. Besides mineral assemblages in these crystallization systems in greisen there was found the main mineral of the greisen – cassiterite, next zircon, maghemite and quartz (Fig. 9). Altogether – the found minerals, equilibria reactions 1–3 and reactions in Fig. 9 allowed to reveal that residual fluid phase of the hot line, in the area close to anatectic melting, contained H_2S, H_2O, CO_2, HF, BO_3, $SnCl_2$, H_3PO_4, Na, K, Ca, Al, Si, Ni, Co, As, Fe, Mn, Mg Sn, REE, U, Ti, Y, Ta, Nb, Cu, Te, Bi, Pb and Sr (Fig. 9). According to the amount of found minerals this greisen mineralization can be designated as cassiterite-topaz-apatite-tourmaline-mica-quartz-Mn/Fe carbonate As-Bi mineralization. According to cassiterite dating, the age of this mineralizatiom is 268 Ma (M. Kohút, personal information).

Greisen mineralization of chlorite-apatite zone in the Dlhá dolina type locality

The greisen mineralization in the type locality of Dlhá dolina was revealed in outcrop of dimensions 70 x 5–10 m. The borehole and mine survey did not found the depth continuation of this mineralization (Fig. 10). Greisen represents a tectonic block of the apophyse or stockwork-type. Mineralization has fine- to medium-grained texture with frequent albite and quartz veinlets. It originated and is localized in chlorite-apatite zone (Fig. 10). The REE contents in greisen and their normalization to primitive mantle suits to group of younger magmatic cycle, being in Permian represented by differentiated medium- and fine-grained granite and its effusive equivalent rhyolite. Though, the light REE contents from La to Eu are deficiet in this comparison (Fig. 10). According to mineralogical study, Mg siderite and ankerite occur together with tourmaline, apatite-F, quartz, bastnäsite, chlorite, thorianite and gersdorffite, representing a coexsisting assemblage in the greisen (Fig. 10). In the ankerite clusters the assemblage sphalerite, galena, pyrite, chalcopyrite, Sb-rich gersdorffite and gersdorffite was found. Siderite fills the tiny cracks in cassiterite and phengite. These cracks with siderite in cassiterite do not continue to surrounding quartz matrix and at the boundary of phengite and quartz the bartonite was revealed. In cassiterite, an assemblage columbite – Ta-Fe columbite, U polycrase and U kobeite often was found. The position of chemical composition of these oxides in UNbCaTi projection has revealed the origin of U polycrase and U kobeite from the reaction of rutile-columbite-meta-autunite-scheelite end members (Fig. 10).

Greisen in locality of Dlhá dolina is formed by mineralization, originating gradually in one event, chemically classified in various crystallization systems. In KAl=KfsFCA system there originated the matrix association of phengite, bartonite, chlorite, tourmaline, kaolinite, albite, apatite-F, fluorite, scheelite, ankerite, Mn ankerite and siderite. Tourmaline belongs to schorl-dravite series similarly as in the Hnilec locality and bartonite, chlorite and apatite-F represent index minerals of chlorite-apatite zone. In PCaUREE system there originated xenotime, bastnäsite, monazite and apatite-F. In the system PCaUTi it is an assemblage of uraninite, U polycrase, Ta-Fe columbite, U kobeite, rutile and ilmenite. In FeZnAsPb it is pyrrhotite, pyrite, sphalerite, arsenopyrite, Sb gersdorffite, Co gersdorffite, gersdorffite and galena. In FePbBiCu/Te system there originated native bismuth, bismuthinite, tetradymite and chalcopyrite. Besides mineral assemblages in above listed crystallization systems, cassiterite, zircon, huttonite and quartz were found in the greisen as the main minerals (Fig. 11). Using equilibrium reactions for the formation of apatite-F, cassiterite and Fe/Mn carbonates there was detected that residual fluid phase on hot line in the chlorite zone area contained H_2S, H_2O, CO_2, HF, BO_3, $SnCl_2$, H_3PO_4, Na, K, Ca, Al, Si, Ni, Co, As, Fe, Mg Sn, REE, U, Ti, Y, Ta, Nb, Cu, Sb, Te, Bi, Pb and Zn (Fig. 11). Comparing with the biotite zone greisen of the Hnilec locality, in the Dlhá dolina chlorite-apatite greisen the Fe carbonates do not contain a distinct share of Mn, and Mn carbonates are missing. Within the element association, Zn and Sb appeared in the fluid phase. Zn is bound in sphalerite and the Sb balance is isomorphically bound in Sb gersdorffite. Individual Sb minerals in greisen were not found. The variability of the Bi binding on minerals was restricted to native Bi and bismuthinite. The Mn, Zn and Sb ± Bi difference in the biotite zone element assemblage is explained by the temperature decrease at the greisen origin in the chlorite-apatite zone. Further elements and molecules in the Dlhá dolina greisen are the same like in the biotite zone Hnilec greisen. According to amount of minerals, the Dlhá dolina greisen mineralization can be designated as the cassiterite, tourmaline, ankerite-

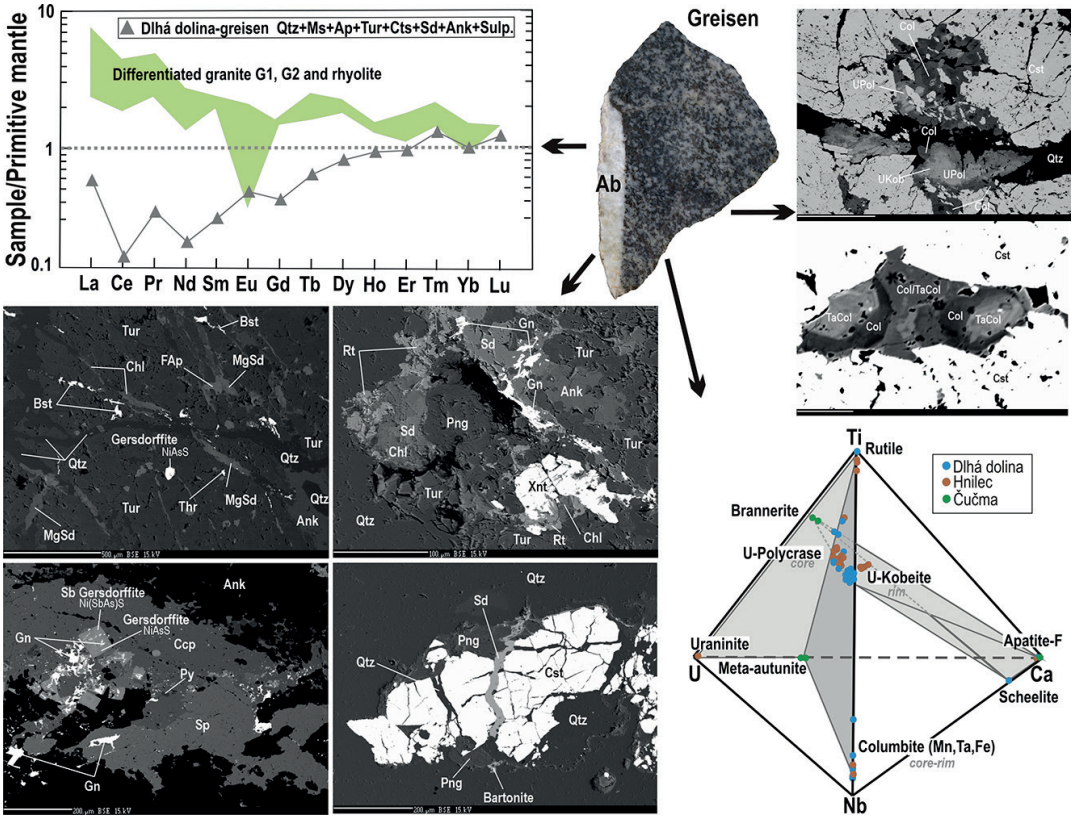

Fig. 10. Greisen apophysis of chlorite-apatite zone with an assemblage of cassiterite (Cst), apatite-F (Ap), tourmaline (Tur), phengite (Png) and Nb/Ta/U oxides – polycrase, columbite (Col), quartz (Qtz), albite (Ab), chlorite (Chl), Mg siderite (MgSd), siderite (Sd), ankerite (Ank) in locality of Dlhá dolina. The REE contents of this greisen are normalized to primitive mantle, which associates the greisen with younger mineralization group – together with differentiated granite and its volcanic equivalent – rhyolite. Further greisen minerals are gersdorffite (Ger), Sb gersdorffite, galena (Gn), sphalerite (Sp), chalcopyrite (Ccp), pyrite (Py), bastnäsite (Bas), thorianite (Thr), Ta columbite (TaCol)-columbite (Col), polycrase-U (UPol), kobeite-U (UKob). Siderite is coexisting with cassiterite, phengite and bartonite. BSE image. The U-Ti-Nb-Ca mineralization in localities of Dlhá dolina, Hnilec and Čučma is projected in UNbCaTi tetrahedron.

siderite and quartz-bearing mineralization (Fig. 11). The comparison of projections of U-Ti-Nb-Ca mineralization from the biotite zone greisen (Hnilec) and chlorite-apatite zone greisen (Dlhá dolina) in tetrahedron projection UNbCaTi shows a gradual origin of zonal oxides from U kobeite in the middle of the grains to U polycrase at the margin. U kobeite and U polycrase originated in the chlorite-apatite zone greisen (Dlhá dolina) by the reaction between the end members rutile–columbite–meta-autunite. The same oxides in the higher temperature biotite zone (Hnilec), originated by the reaction among the end members rutile–columbite–meta-autunite and scheelite/aptite-F (Fig. 10).

Maghemite-cassiterite-Fe carbonate skarn with FeZnCuBiTeIn sulfides in stilpnomelane-chlorite zone in locality of Dlhá dolina

Skarn in locality of Dlhá dolina does not reach the surface. It was revealed by the survey boreholes DD-11 and DD-21 in the depth 283.9–285.4 m, resp. 353.2–354.5 m, where it reaches thickness 1.3–1.5 m (Malachovský et al., 1983, 1992, 2000). These boreholes surveyed the magnesite-talc deposit Gemerská Poloma, developed beneath the Dlhá dolina valley. Samples in this study are from the underground borehole VSV-05-2 in 43 m, drilled in this area for verification of continuation of magnesite-talc mineralization in Elisabeth exploration adit. Here the skarn thickness in the underground borehole VPSOB-2 reaches 5.3 m (Kilik et al., 1995). Further samples are from the superficial borehole V-DD-43, where skarn was verified in the depth of 266.8 m. The distance of both studied skarn bodies is 300 m. Skarn originated in the direct contact of former limestone lens, being a part of the Holec Beds. The Silurian Holec Beds belong to the Betliar Fm. (Grecula et al., 2009; Radvanec & Grecula, 2016). In both boreholes the sulfidic mineralization with prevailing pyrite forms the immediate contact of the skarn with carbonates or former limestone. The thickness of this sulfidic rim is up to 5 cm. Besides sulfides, the Fe/Mg carbonates, stilpnomelane, chlorite, phengite and locally also phlogopite were found in this immediate contact (Figs. 12, 16). In the skarn of

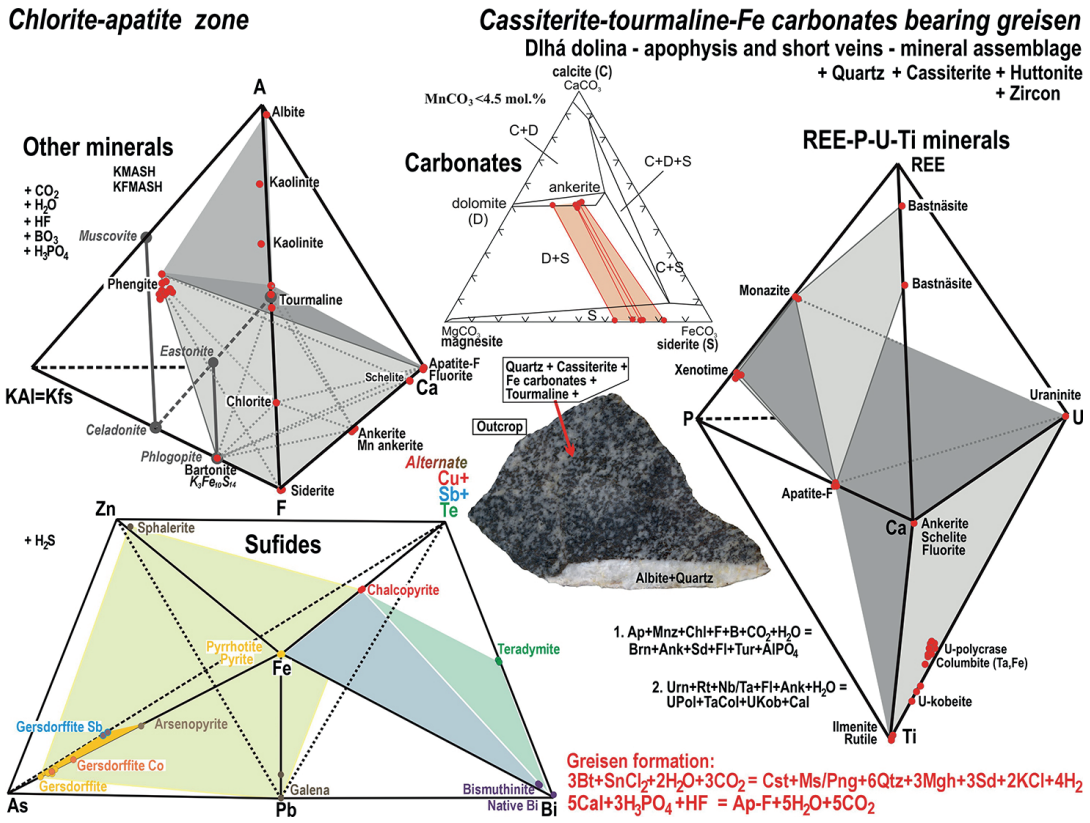

Fig. 11. Tectonic block of the greisen apophysis and stockwork in the outcrop of the Dlhá dolina locality. The greisen mineral assemblages belong to chlorite zone **M1b**. Projections of chemical composition of carbonates are in a triangle diagram magnesite-siderite-calcite. Projection of REE-P-U-Ti mineralization is in PCaUREE, as well as PCaUTi tetrahedron. Projections of matrix minerals are in KAl=KfsFCA tetrahedron. Projections of sulfides, arsenides and tellurides are in FePb(Cu/Sb/Te)Bi, ZnFe(Cu/Sb/Te)Pb and ZnFePbAs tetrahedron. Reactions describe the origin of apatite-F and cassiterite.

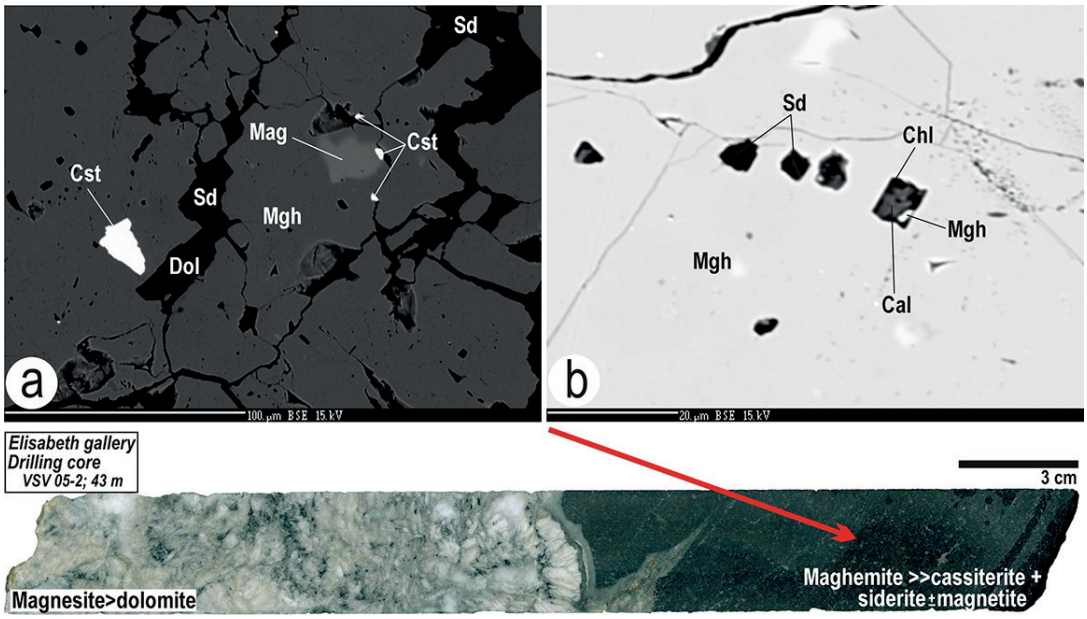

Fig. 12. Skarn in stilpnomelane-chlorite zone **M1b** in locality of Dlhá dolina (vicinity of Gemerská Poloma), borehole VSV-05-2, depth 43 m. Skarn is formed by the main association of maghemite (Mgh), cassiterite (Cst) and siderite (Sd). Magnetite (Mag), forms irregular inclusions in maghemite. Dolomite (Dol) was found together with siderite in maghemite cracks. The calcite (Cal), chlorite (Chl) with dolomite (Dol) relics were preserved in maghemite. BSE image.

both boreholes the maghemite strongly prevails above cassiterite and siderite. It is of black colour having pseudo-cast monomineral form and is weakly magnetic.

Maghemite is strongly prevailing in the skarn of the borehole VSV-05-2V and rarely contains magnetite. Cassiterite, native bismuth and bismuthinite form in maghemite irregular and frequent inclusions with size up to 50 µm, co-existing with maghemite and magnetite. In maghemite calcite is very rarely preserved together with chlorite. Siderite and dolomite were found in clusters and irregular fractures of maghemite. These three minerals are principal in the skarn (Fig. 12). The REE contents of the skarn and magnesite-dolomite metasomatite from the borehole VSV-05-2V and their normalization to primitive mantle classifies it to the group of younger magmatite cycle, originating in Permian hot line (Fig. 15). According to the REE contents normalization skarn belongs to the group of differentiated medium- and fine-grained S-type granites with rhyolite as their effusive equivalent (Fig. 4).

Sulfidic rim in immediate contact of the skarn with carbonates is formed by variegated association. Pyrite is the main mineral of this zone. At the pyrite margin, the tetradymite, pavoite and gladite often occur (Fig. 13a, b). In pyrite the inclusions of pyrrhotite, pavoite, bismuthinite, chalcopyrite, magnesite, dolomite and molybdenite were found. In the matrix, among pyrite grains the association of siderite, Mg siderite, Mg magnesite, dolomite, bismuthinite, stilpnomelane, phengite and chlorite was found. Stilpnomelane and chlorite represent index minerals defining the stilpnomelane-chlorite zone of **M1b** metamorphism, where skarn originated (Fig. 13c).

Mineral composition of the skarn and immediate contact of the skarn with sulfidic rim is in both boreholes approximately identical. Mineral composition of carbonates in the contact with skarn is differing (Figs. 12, 17).

In the borehole VSV-05-2 skarn originated in the contact with magnesite and dolomite (Figs. 12–14), which are relatively older than skarn and originated by gradual metasomatic replacement of former Silurian limestone lens. The chemical composition of fluid inclusions in magnesite and dolomite revealed that Mg-rich bitter brines represented the determining factor for the origin of Mg-carbonates (Radvanec & Prochaska, 2001; Koděra & Radvanec, 2002, 2003; Radvanec et al., 2004a, b). Analyses of leachates from fluid inclusions in magnesite and dolomite provided the Cl/Br ratio 107–185 and Na/Br ratio 48–135, which clearly indicates the fraccionated and evaporitic origin of Permian Mg-rich bitter brines due to advanced evaporation of the sea water (Radvanec et al., 2010). The Mg metasomatic replacement of former limestone/calcite took place during Variscan orogenic metamorphism **M1b** at temperature 300–420 °C: 3calcite + 2Mg-brine → dolomite + magnesite + 2Ca-in epidote/allanite/apatite/fluorite (Radvanec et al., 2010).

In borehole VSV-05-2 the magnesite and dolomite clusters at the skarn contact are covered and replaced by Mg siderite, siderite and ankerite. In other places of this contact Mg siderite mixes with Fe magnesite (Fig. 14). According to mineralogical investigation in the carbonate part of the contact with the skarn the Mg brine mixed with residual Fe-bearing fluid phase to the distance of 1 cm from the immediate contact. By this way there originated the mixture of Fe magnesite and Mg siderite (Fig. 14a). In external part, besides the distance of 1 cm from the contact, the influence of Fe residual fluid phase was not found and magnesite-dolomite mineralization does not contain Fe carbonates (Fig. 14). In this external part, the apatite-F of oval or aphanitic form often occurs in magnesite and dolomite. Similarly as in greisens from Hnilec and Dlhá dolina, apatite-F in Mg carbonates does not contain any admixture of other elements and its chemical formula is $Ca_5(PO_4)_3F$ (Tab. 3). Analysis of Mg/Fe carbonates from the contact of skarn on REE contents and their normalization on primitive mantle classifies the mixture of Mg/Fe carbonates, similarly as maghemite skarn, into a group of younger cycle of Permian magmatites in hot line (Fig. 14).

According to above stated division on three zones, the skarn mineralization in borehole VSV-05-2 has originated in one gradual event of Variscan metamorphic process **M1b**. In P-T conditions of biotite zone the Silurian limestones were replaced to magnesite and dolomite (Radvanec et al., 2010). In retrograde P-T conditions of stilpnomelane-chlorite zone, during the same **M1b** process the Fe carbonate, sulphidic and skarn mineralization originated. The gradual origin of mineral assemblages is chemically classified in various crystallization systems: In KAl=KfsFCA system there originated the matrix association of phengite, phlogopite, stilpnomelane, chlorite, apatite-F, fluorite, calcite, ankerite, dolomite, Fe magnesite, magnesite, Mg siderite, siderite and magnetite and tourmaline (Fig. 15). Tourmaline belongs to schorl-dravite series, similarly as in greisens localities of Hnilec and Dlhá dolina (Tab. 1). In classification triangle diagram magnesite-siderite-calcite there is in stages 1–2 expressed the gradual exchange of former Silurian limestone – calcite to dolomite–magnesite and dolomite–Fe magnesite. Younger stage 3 from the contact of skarn with Mg carbonates is in this triangle diagram classified among ankerite and Fe magnesite and Mg siderite. Ankerite, Fe magnesite and Mg siderite originated in the stilpnomelane-chlorite zone. In the skarn cracks the siderite with the $MgCO_3$ content of 14–22 mol. % crystallized (Fig. 15). In the ZnPbCuFe system there originated pyrrhotite, pyrite, sphalerite, chalcopyrite and tetrahedrite. In FePbBiTe system it was native bismuth, bismuthinite, pavoite, gladite and tetradymite. Besides above stated mineral assemblages, in skarn and in the contact of the skarn with Mg carbonates there was found cassiterite,

maghemite, molybdenite, zircon, huttonite, quartz, monazite, synchisite, bastnäsite and kobelite (Fig. 15). Talc originated by the replacement of magnesite in Alpine metamorphism **M2** (Radvanec et al., 2010).

The borehole V-DD-43 revealed the skarn in the contact with former Silurian limestone body (calcite), where limestone is locally replaced to dolomite. During the skarn origin the mixture of ankerite, stilpnomelane, chlorite and

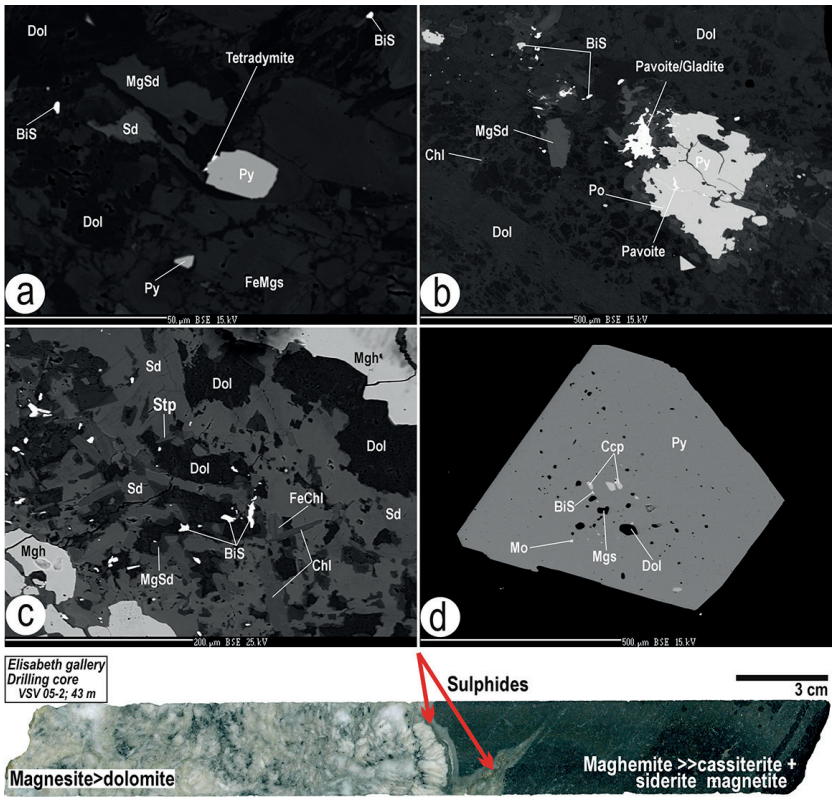

Fig. 13. Sulfidic contact of Mg carbonates with skarn in stilpnomelane-chlorite zone **M1b** in the Dlhá dolina locality, borehole VSV-05-2, 43 m. Direct contact is formed by association: ***a*** – pyrite (Py), tetradymite, bismuthinite (BiS) in matrix of Fe magnesite (FeMgs), dolomite (Dol) and Mg siderite (MgSd); ***b*** – pyrite encloses inclusions of pyrrhotite (Po) and pavoite. Dolomite contains individual grains of pavoite/gladite, Mg siderite, chlorite (Chl) and bismutinite; ***c*** – association of dolomite, siderite (Sd), stilpnomelane (Stp), Mg siderite, chlorite, bismuthinite in the contact with maghemite (Mgh); ***d*** – inclusions of molybdenite (Mo), bismuthinite and chalcopyrite (Ccp), magnesite (Mgs) and dolomite (Dol) in pyrite. BSE image.

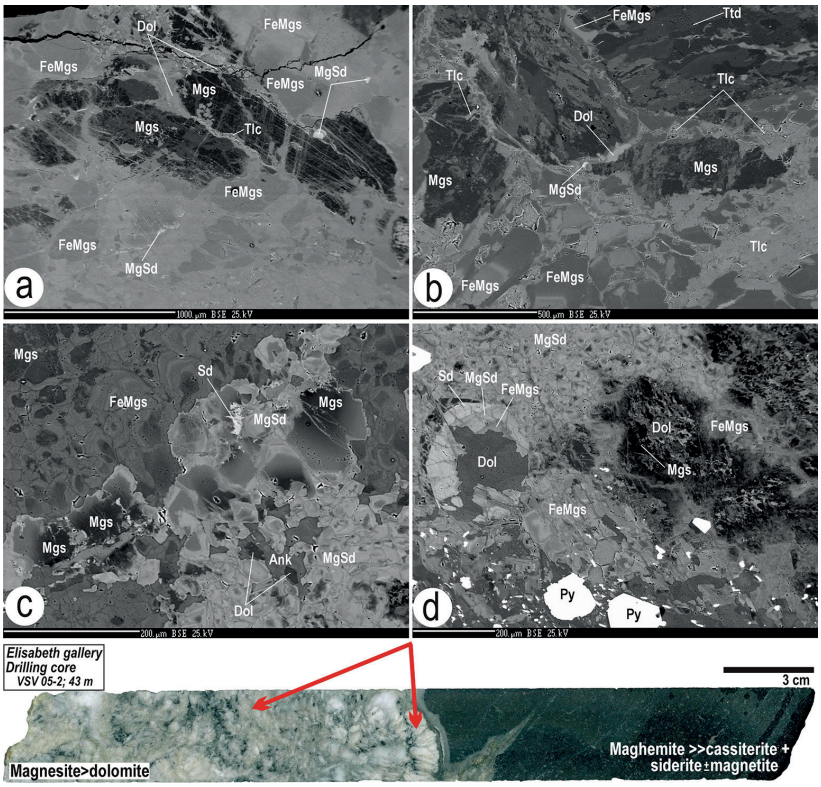

Fig. 14. Dolomite and magnesite body at the contact with skarn. Stilpnomelane-chlorite zone of **M1b** metamorphism in the Dlhá dolina locality, borehole VSV-05-2, 43 m. Dolomite and magnesite originated by metasomatic replacement of Silurian limestone by Mg bitter brine in Permian (Radvanec et al., 2010). ***a–d*** – the contact zone with skarn is formed of Mg/Fe carbonates. Magnesite (Mgs) and dolomite (Dol) rims and replaces Mg siderite (MgSd) and Fe magnesite (FeMgs). Carbonate closes tetrahedrite (Ttd) and pyrite (Py). BSE image.

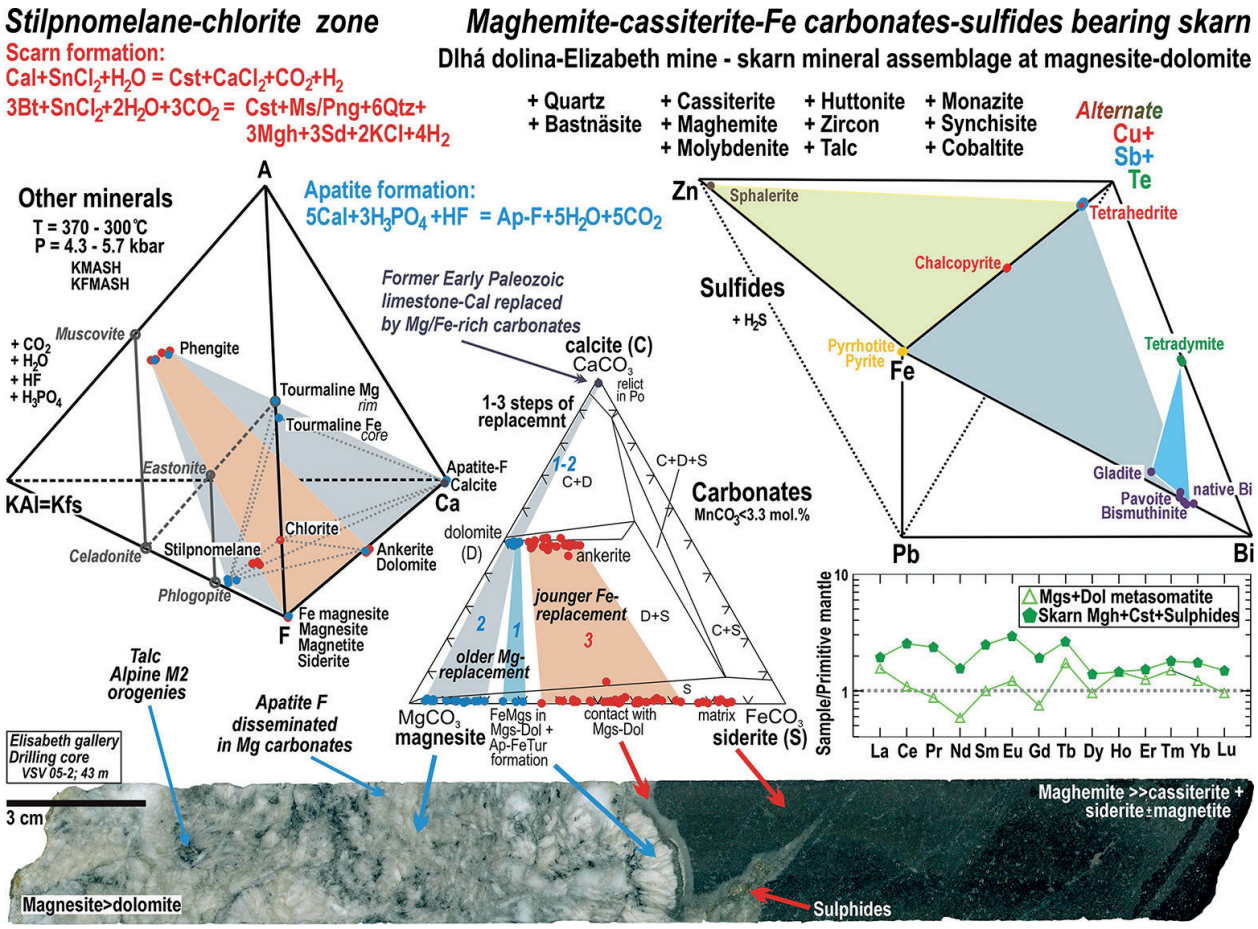

Fig. 15. Classifications of mineral associations in the contact of the skarn with a body of Mg carbonates (dolomite and magnesite) in locality of Dlhá dolina, borehole VSV-05-2, 43 m, the Elisabeth adit. Chemical composition of carbonates is projected in triangle diagram magnesite-siderite-calcite. Gradual process of the former calcite replacement to dolomite and magnesite in a limestone body (stages 1 and 2); younger stage 3 – ankerite and Mg siderite rim and replace earlier Mg carbonates from the stage 1–2 or form with them a crystallization mixture. This mixture of Mg and Fe carbonates was found only to the 1 cm distance from the contact with skarn. Siderite was found in the matrix of skarn, in a mass between maghemite. Minerals in KAl=KfsFCA projection characterize the stilpnomelane-chlorite and biotite zone of Variscan metamorphism **M1b**. The composition of sulfides is visualized in tetrahedron projection in combination of ZnFe(Cu/Sb/Te)Pb and FePb(Cu/Sb/Te)Bi. Reactions describe the origin of apatite-F and cassiterite. The phlogopite-biotite analyses are from Radvanec et al. (2010).

phengite originated in the limestone. Maghemite forms the pseudo-veinlets developed in the limestone cleavage (Fig. 16a). Borehole V-DD-43 has verified the external part of the limestone body, where, differing from findings in the borehole VSV-05-2, no metasomatic exchange of calcite to magnesite occurred.

Skarn in the borehole V-DD-43 is formed by maghemite. In the maghemite fractures bastnäsite was found and among the maghemite grains the mixture of Mn ilmenite and former calcite frequently occurs (Fig. 16b). Cassiterite, native bismuth, bimuthinite, ankerite and chalcopyrite form irregular inclusions in the maghemite, large up to 200 µm, being in co-existence with maghemite (Fig. 16a–b). Ankerite, allanite, chlorite, bimuthinite, monazite, cassiterite and chalcopyrite (Fig. 16d–e) were found among maghemite grains. These minerals form a skarn mass, where maghemite dominates.

The REE contents in the skarn from the borehole V-DD-43 and their normalization on upper crust provides a good agreement with the group of older cycle of Permian magmatites (Fig. 16). According to normalization of REE contents the skarn belongs to group of porphyric granites of S-type with andesite as effusive equivalent. The REE contents analyses of carbonates from partially changed limestone and their sulfidic rim after their normalization to primitive mantle manifest a good agreement of these skarn parts with younger Permian mineralization group, together with differentiated granite and its volcanic equivalent – rhyolite (Fig. 16).

In the boreholee V-DD-43 the sulfidic rim in the immediate skarn contact with carbonate is formed by the main association of pyrite and ankerite. Similarly as in the borehole VSV-05-2, pyrite forms a main mineral of

this zone. The inclusions and enclosures of cassiterite, maghemite, pyrrhotite, bismutinite, chalcopyrite, dolomite, Mg siderite, calcite, sakuraiite and electrum were found in pyrite (Fig. 17). In the pyrite cracks the association of chalcopyrite, bismutinite, bismuthinite with Pb content, tetradymite and electrum was found, where Au distinctly prevails above Ag (Fig. 17a, c). At the pyrite margin the tetrahedrite, chalcopyrite and apatite-F often occur (Fig. 17a, b). In the matrix among pyrite grains, the association of siderite, Mg siderite, dolomite, Mn ankerite, ankerite, cassiterite, bismuthinite was found and on pyrite margin occurred tetradymite, stilpnomelane, phengite, chlorite, chalcopyrite, apatite-F, uraninite, thorite, rutile, rutile with the content of W, bastnäsite, huttonite, zircon, talc, monazite and quartz. Also aggregates of sphalerite, bismutinite, pyrite, tetrahedrite and chalcopyrite were revealed there. In chalcopyrite and locally also in pyrite the enclosures of the sphalerite mixture with the content of In up to 5 wt.%, sakuraiite with Zn content and roquesite (Fig. 17d–f) occur. Rarely in pyrrhotite there were found fine enclosures of chalcopyrite and sakuraiite with Sn content. Stilpnomelane and chlorite represent the index minerals for defining the stilpnomelane-chlorite zone of the skarn origin (Figs. 16, 17).

Skarn and its contact in borehole V-DD-43 is characterized by gradual origin of mineral associations, being chemically classified in various crystallization systems. In KAl=KfsFCA system there originated the matrix association phengite, stilpnomelane, chlorite and allanite, apatite-F, calcite, ankerite, dolomite, Mg siderite and siderite. Apatite-F does not contain any admixture of other elements and its chemical formula is $Ca_5(PO_4)_3F$ (Tab. 3). Mineral associations in KAl=KfsFCA characterize the stilpnomelane-chlorite zone of Variscan metamorphism **M1b** (Fig. 18).

In the magnesite-siderite-calcite triangle the replacement of former Silurian limestone – calcite to dolomite and ankerite is expressed in two gradual stages. In this triangle, Fe carbonates from the contact of skarn with calcite are chemically classified between ankerite and coexisting Mg siderite to siderite. In the skarn mass there crystallized siderite with $MgCO_3$ content 22–25 mol. % and in pyrite and pyrrhotite the Mg siderite inclusions reach $MgCO_3$ content 46–50 mol. % (Fig. 18). Chemical composition of sulfides pyrrhotite, pyrite, sphalerite, chalcopyrite and tetrahedrite is projected in ZnPb(Cu or alt. Sb)Fe system. In FePbBi(Te or alt. Cu) system it is a projection of native bismuth, bismuthinite, bismuthinite Pb, bismuthinite Cu and tetradymite. In ZnFeCuIn system there was found the complete substitution row among the end members sphalerite–chalcopyrite–roquesite. According to chemical formula, in this substitution row of In sulfides there were found sphalerite with a content of In, sakuraiite Zn, ishiharaite Fe, roquesite, sakuraiite with Sn and chalcopyrite with In (Fig. 18).

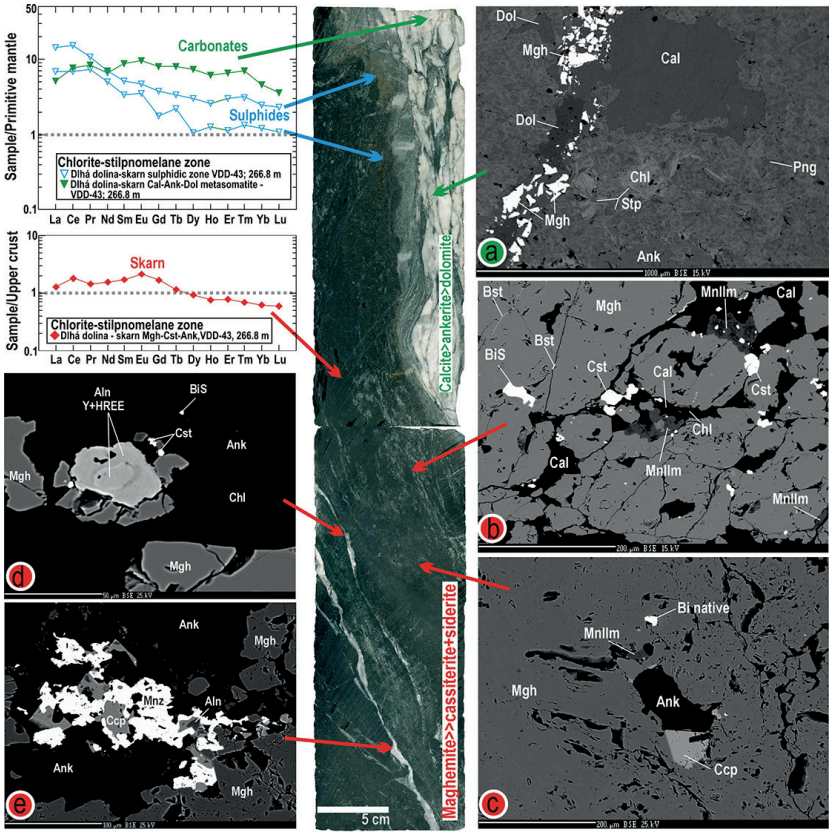

Fig. 16. Partial replacement of Silurian limestone from the Holec Beds of Betliar Fm. to dolomite and ankerite, sulfidic contact with skarn and skarn in locality of Dlhá dolina, borehole V-DD-43, 266.8 m. ***a*** – Relic of former calcite (Cal), dolomite (Dol), ankerite (Ank) and mixture of chlorite (Chl), stilpnomelane (Stp) and phengite (Png). In the vein of Mg/Fe carbonates the maghemite is present (Mgh). ***b–e*** – skarn is formed by the main association maghemite (Mgh), cassiterite (Cst) and ankerite (Ank). Rarely in the skarn the relics of former calcite are preserved. In the maghemite there are present numerous inclusions of bismuthinite (Bis). The occurrences of Mn ilmenite (MnIlm), bastnäsite (Bas), native bismuth (Bi), chalcopyrite (Ccp), allanite (Aln) and monazite (Mnz). BSE image. The REE contents from the sulfidic contact and partially changed limestone on Mg/Fe carbonates are in agreement with the primitive mantle. The changed limestone and sulfidic rim at the contact with skarn belong according to normalization of the REE contents to younger Permian mineralization group. Into the older Permian mineralization stage there belongs the maghemite skarn, which after REE normalization corresponds with upper crust.

The PCaUREE system shows projections of chemical composition of monazite, bastnäsite, allanite (Y, light REE), apatite-F, calcite, ankerite and dolomite. System PCaUTi shows association uraninite, rutile, rutile with W and illmenite. This mineralization was named REE-P-U-Ti (Fig. 18).

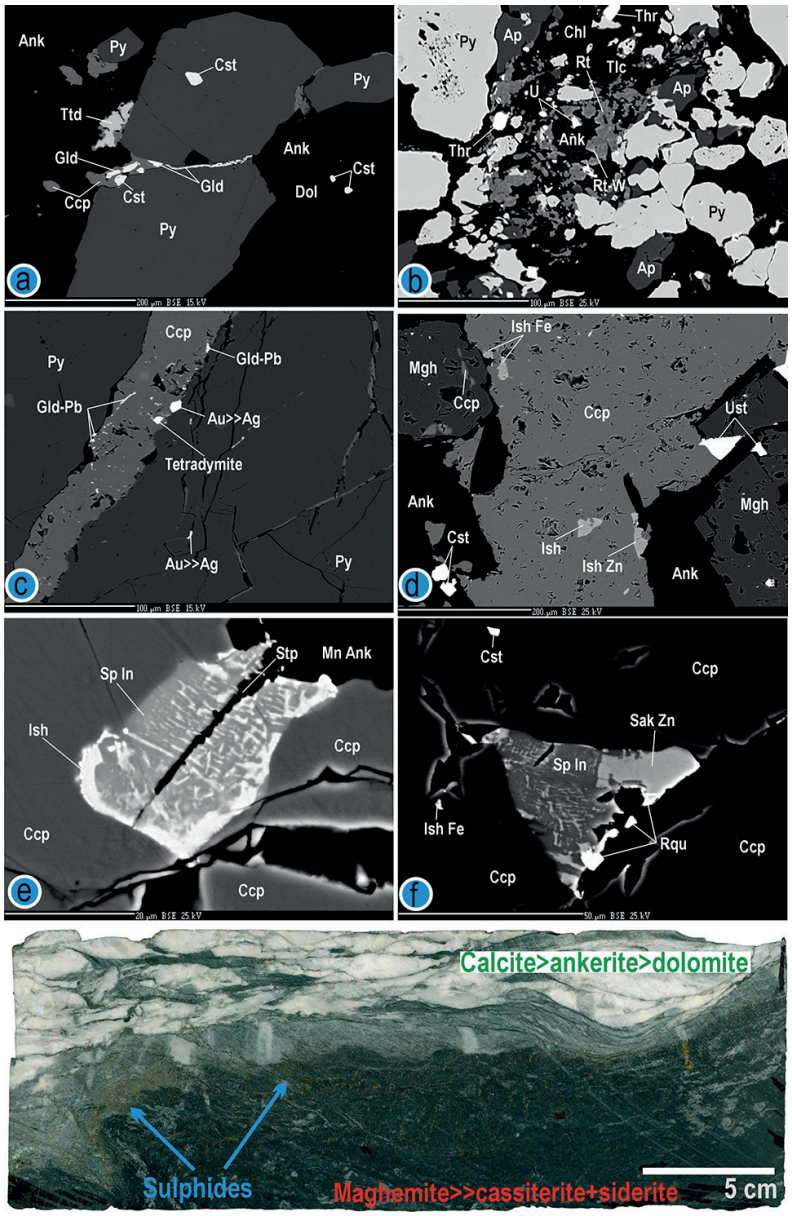

Fig. 17. Minerals in sulfidic rim of the skarn in immediate contact with Mg/Fe carbonates. Locality of Dlhá dolina, borehole VVD-43, 266.8 m. Main minerals of the sulfidic contact are represented by pyrite (Py), ankerite (Ank), chalcopyrite (Ccp), apatite-F (Ap) and bismuthinite (Bis). ***a–f*** – Cassiterite (Cst) inclusions in pyrite and ankerite. bismuthinite, tetrahedrite (Ttd) and cassiterite cover the chalcopyrite. In mixture with pyrite there was found thorite (Thr), chlorite (Chl), uraninite (U), apatite-F, rutile and rutile with the W content. Fractures in pyrite are filled with chalcopyrite and inclusions of electrum (Au >> Ag), bismuthinite with the content of Pb (BisPb) and tetradymite. In the immediate contact with maghemite (Mgh) chalcopyrite contains inclusions of ishiharaite Fe (IshFe), sakuraiite (Sak) and sakuraiite Zn (SakZn). Inclusions in sulfides are in chalcopyrite inhomogeneous and often form a mixture of sphalerite In (SpIn), sakuraiite and stilpnomelane. In other places in chalcopyrite it is a mixture of sphalerite In, sakuraiite Zn (SakZn) and roquesite (Rqu). In chalcopyrite the ishiharaite Fe forms also individual inclusions. BSE image.

The dividing of the skarn contact to carbonate zone, sulfidic zone and skarn characterizes the origin of skarn in the borehole V-DD-43, similarly as in VSV-05-2. Mineralogical study revealed the skarn origin in one gradual event together with the sulfidic zone. This mineralization crystallized from residual fluid phase with high Fe content. In the area of borehole VSV-05-2 the source of residual fluid phase was influenced by primitive mantle in all three zones from the skarn through sulfidic zone to body of Mg/Fe carbonates at the skarn contact. In the maghemite skarn around borehole V-DD-43 the source of fluid phase if influenced by the upper crust. The sulfidic zone of the skarn as well as body of carbonates (calcite, dolomite, ankerite) indicate the influence of the source by primitive mantle (Figs. 16, 17).

The skarn present in both boreholes originated in the same stilpnomelane-chlorite zone of **M1b** metamorphism (Figs. 15, 18). P-T conditions were derived from stilpnomelane–muscovite–quartz geothermometer and the stilpnomelane stability between 300–370 °C and 4.3–5.7 kbar (Tropper & Piber, 2012). Applying the classification of minerals, equilibria reactions for the origin of apatite-F, cassiterite and Fe carbonates, there was found that the residual fluid phase on hot line within the stilpnomelane-chlorite zone contained H_2S, H_2O, CO_2, HF, BO_3, $SnCl_2$, H_3PO_4, K, Ca, Al, Si, Fe, Mg, Sn, REE, U, Ti, Y, Cu, Sb, Te, Bi, Zn and In (Figs. 15, 18). In the element association in fluid phase there additionally occurred In. In the skarn of stilpnomelane-chlorite zone there are missing Na, Ta, Nb, Pb, Ni, Co and As in comparison with the greisen of biotite zone (Hnilec locality) and the greisen of chlorite-apatite zone (Dlhá dolina). Depletion of these elements was caused by the decrease of temperature in the stilpnomelane-chlorite zone to 300–370 °C. Mineralogical investigation revealed the P-T conditions of stilpnomelane–chlorite zone with the lower limit for the cassiterite and iron origin, being boun in maghemite and Fe carbonates and representing main elements of this zone (Figs. 12–18).

Similarly as in greisen, the presence of calcite is determining for the origin of apatite-F. At the contact of skarn, the

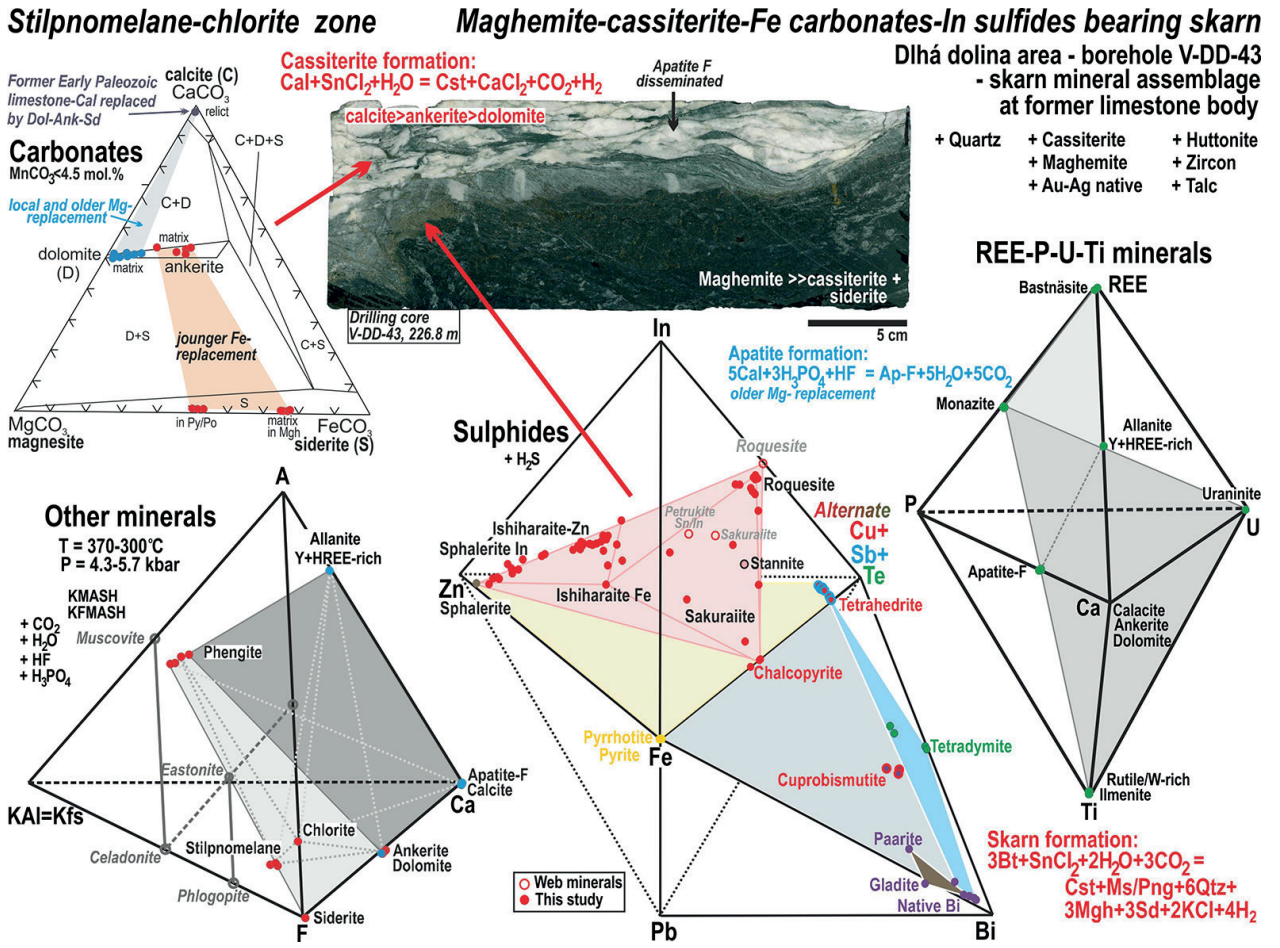

Fig. 18. Classifications of mineral associations of the skarn and the contact of skarn with a body of Silurian limestone, partially replaced to dolomite and ankerite. Locality of Dlhá dolina, borehole V-DD-43, 266.8 m. Chemical composition of carbonates is projected in triangle diagram magnesite-siderite-calcite. Older stage – partial Mg metasomatism of calcite to dolomite; younger stage – ankerite and Mg siderite replace the former calcite. Inclusions of Mg siderite were found in pyrite and pyrrhotite. Siderite was found in the matrix of the skarn – in a mass among maghemite. The matrix minerals in KAl=KfsFCA projection characterize stilpnomelane-chlorite zone of Variscan metamorphism **M1b**. The composition of sulfides is shown in tetrahedron projection in combination with ZnFe(Cu/Sb/Te) Pb, FePb(Cu/Sb/Te)Bi and ZnFe(Cu/Sb/Te)In. A complete substitution row of In sulfides – sphalerite In, sakuraiite Zn, ishiharaite Fe, sakuraiite and roquesite was found between sphalerite–chalcopyrite–roquesite end members. The sakuraiite with Sn content belongs also to this projection. REE-P-U-Ti mineralization is classified in PCaUREE and PCaUTi projections. Reactions describe the origin of apatite-F, cassiterite, maghemite and siderite.

calcite from the former limestone reacted with H_3PO_4 and the apatite-F has originated without the content of other elements (Figs. 15, 18). The occurrence of apatite-F was revealed in sulfidic zone mainly of Mg/Fe carbonatic part of the contact with the skarn (Figs. 15, 17a). So the skarn mineralization in locality Dlhá dolina (vicinity of the Gemerská Poloma village) can be named as maghemite–cassiterite–siderite–In-Bi-Te–sulfidic mineralization. It is a significant source of In, Bi and Te sulfides.

Stockwork apatite-xenotime-quartz-phengite-tourmaline mineralization in the chlorite-apatite zone in the Čučma locality

The apatite-xenotime-quartz-phengite-tourmaline mineralization in the Čučma locality forms short irregular stockworks thick up to 2 cm (Fig. 19). The depth range of the stockwork is several tens of meters, max. 70 m (Pecho, 1976). The stockwork was sampled in the outcrop and exploration adit No. 26 (Donát, 1998; Figs. 1, 19). The stockwork type of mineralization indicates that the separation of residual fluid phase from the rock, from which mineralization in small cracks crystallized, occurred close to the zone of anatectic melting.

The stockwork shape simultaneously indicates that P-T conditions of the chlorite-apatite zone and fluid phase crystallization were close to equilibrium with surrounding rock, where the stockwork at Čučma was revealed.

The mineral assemblages of the stockwork with apatite-xenotime-quartz-phengite-tourmaline mineralization was found in the "augen" metapelite. Macroscopically well recognizable "augens" in the metapelite are formed of

the admixture of clastic quartz large up to 3 mm. In the metapelite matrix these clasts have random distribution and locally form 20 % of the rock volume. Mineral composition of the metapelite beneath the stockwork was revealed by mining survey: quartz, albite, phengite, biotite, garnet-core ($Spess_{57-66}Alm_{21-23}Gross_{11-19}$), garnet-rim ($Gross_{42-54}Alm_{21-33}Spess_{21-26}$), Kfs (micrographic overgrowths Kfs + Qtz, micropertite Ab + Kfs + Qtz), chlorite, zoisite, epidote, allanite, actinolite, apatite, tourmaline, zircon, Mn ilmenite, ilmenite, rutile, titanite, xenotime, monazite, uraninite, thorianite, bastnäsite, graphite, calcite, siderite, Mn siderite and pyrite. This metapelite with biotite porphyroblasts and clastic quartz of psammitic fraction was designated as Bt metapelite (Radvanec et al., 2007). In earlier literature about Gemeric unit this rock was named "porphyroid". Bt metapelite was metamorphosed in the biotite zone (see cross-section in Fig. 19). The micrographic and micropertitic clusters indicate the P-T conditions of biotite zone close to metapelite melting. The peak temperature of low-pressure biotite zone was 600 °C (Fig. 19). At these P-T conditions in Gemeric unit the local anatectic metapelite melting occurred with the origin of the minimum-type granite melt (Radvanec et al., 2007, 2009). The assemblage of K-feldspar, quartz and albite after metamorphism of Bt metapelite in situ has an arrangement and textural signs of granite, shown in thin-sections by micrographic overgrowths of K-feldspar and quartz, as well as the presence of myrmekite and micropertite. The local textural signs of melting in thin-sections do not overreach 2 cm^2 and were found besides investigated locality of Čučma also in further localites – Guľapalag, Majerská dolina, Bystrý potok, Rožňava-Turecká, Hrelichov potok and Dlhá dolina (Radvanec et al., 2007).

Tourmaline represents the index and matrix mineral of the anatectic melting zone of the pelite in the immediate footwall of investigated stockwork. It crystallized in Bt metapelite in the same kinematic regime as matrix Bt metapelite. At the beginning of ductile regime the Fe > Mg tourmaline ($Srl_{76}Foi_{13}Drv_{35}$) had crystallized and at the end the Mg-Fe tourmaline ($Srl_{52}Foi_{11}Drv_{38}$), being relatively younger than Fe > Mg tourmaline (Radvanec et al., 2007). Based on chemical classification of Al, Mg, Fe and Ca this tourmaline belongs to groups of dravite, Al-dravite and schorl (sensu Henry & Guidotti, 1985). Schorl with the high content of foitite molecule was found in samples of Bt metapelite with indications of melting (micropertite and micrographic overgrowths of K-feldspar with quartz) and the Betliar granite. The Fe-tourmaline in Bt metapelite has the same chemical composition as tourmaline in the Hnilec granite (Radvanec et al., 2007).

The occurrence of the group of metamorphic minerals epidote, garnet and amphibole confirms the equivalence of the biotite zone in the Čučma stockwork underlier to the epidote-amphibolite facies, similar as in the Hnilec locality. According to biotite geothermometer the Bt metapelite metamorphism in the stockwork surrounding reached temperature 400–500 °C (Fig. 19). Age of Bt metapelite was revealed from monazite-uraninite isochrone within the range of 275–262 Ma, though also older Carboniferous ages 323–310 Ma were found (Radvanec et al., 2007).

The main minerals of the stockwork are apatite-F, xenotime, quartz, phengite, tourmaline and monazite. Apatite-F does not contain any admixture of other elements and its chemical formula is $Ca_5(PO_4)_3F$. The hypidiomorphic and idiomorphic apatite-F reaches the grain-size 1 cm and often encloses goethite and xenotime of grain-size up to 0.5 cm. This assemblage forms aggregates in quartz-phengite matrix (Fig. 19). Xenotime often encloses inclusions and admixtures of monazite, uraninite, galena and vyacheslavite. In the matrix there was found goyazite-REE, allanite, orthobrannerite, monazite, tourmaline (schorl–dravite), meta-autunite and rarely unknoun Ti-P-Fe-U-Ca-Pb phase, pyrite, chalcopyrite, gersdorffite-Co and jamesonite/boulangerite, at the rim being replaced by plumbogummite and evansite. Evansite in this rim makes a micture with corroded jamesonite/boulangerite, so the evansite has variegated contents of Sb, Fe and S (Fig. 19).

According to projections of chemical composition of the matrix assemblage in classification diagrams (Fig. 20), in the KAl=KfsFCA system the stockwork belongs to chlorite-apatite zone. The projections of REE-P-U-Ti mineralization are in PCaUREE and PCaUTi systems. Projection of sulfides are visualized in triangle diagrams PbFeAs and PbFe(Sb alternative Cu) and the matrix minerals in KAl=KfsFCA projection. Reaction describes the origin of apatite-F and four qualitative reactions described the origin of REE-U-Ti mineralization (Fig. 20). Using reactions for formation of apatite-F, goyazite-REE, vyacheslavite, meta-autunite and orthobrannerite we have derived that residual fluid phase contained H_2S, H_2O, HF, BO_3, H_3PO_4, K, Ca, Al, Si, Fe, REE, U, Ti, Ni, Co, As, Pb, Cu, Sb and Sr (Fig. 20). Besides the contents of $SnCl_2$, Mg, Ni, Co, As, Te, Bi, Zn and In, the composition of residual fluid phase is close to skarn mineralization and also originated in the chlorite-apatite zone.

Analyses of four stockwork samples to REE contents and their normalization to upper crust classify stockwork with apatite-quartz-phengite-tourmaline and REE-P-U-Ti mineralization, which is in good agreement with a group of older Permian magmatites. According to normalization of REE contents this mineralization belongs to group of S-type porphyric granites with andesite as their effusive equivalent (Fig. 19). The age 275–262 Ma of Bt metapelite, where stockwork occurs, is in good agreement with the age of Permian older magmatic cycle (Figs. 3, 4).

The accessoric occurrence of apatite-F, monazite, xenotime, chlorite, allanite, tourmaline, zircon, rutile,

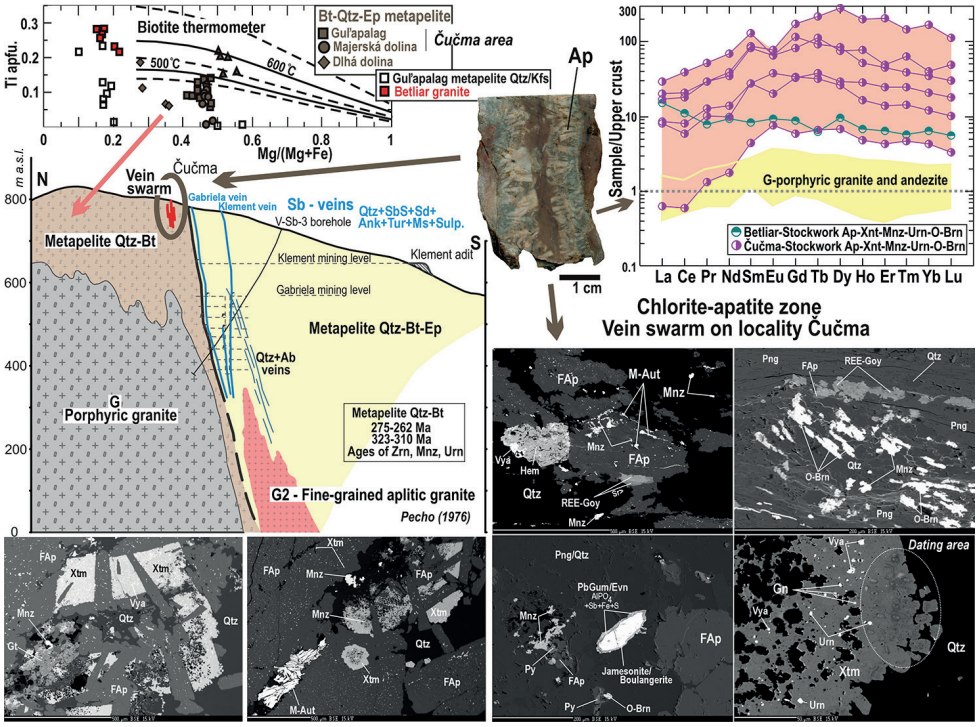

Fig. 19. Mineral assemblages of the stockwork with apatite-xenotime-quartz-phengite-tourmaline mineralization in chlorite-apatite zone of **M1b** metamorphism in locality of Čučma. Samples in the geological cross-section are from the adit 26 and are visualized by ellipse (Donát, 1998; Pecho, 1976). Abbreviations: Apatite-F (FAp), xenotime (Xtn), vyacheslavite (Vya), quartz (Qtz), monazite (Mnz), galena (Gn), uraninite (Urn), goethite (Gt), phengite (Png), goyazite REE (REE-Goy), orthobrannerite (O-Brn), pyrite (Py), meta-autunite (M-Aut), plumbogummite/evansite (PbGum/Evn). BSE image. The biotite thermometer indicates temperature 500 °C of metamorphism around the stockwork. According to normalization of REE on upper crust the origin of the stockwork belongs to earlier Permian mineralization period. Dating area – xenotime dating – see the chapter Methodology.

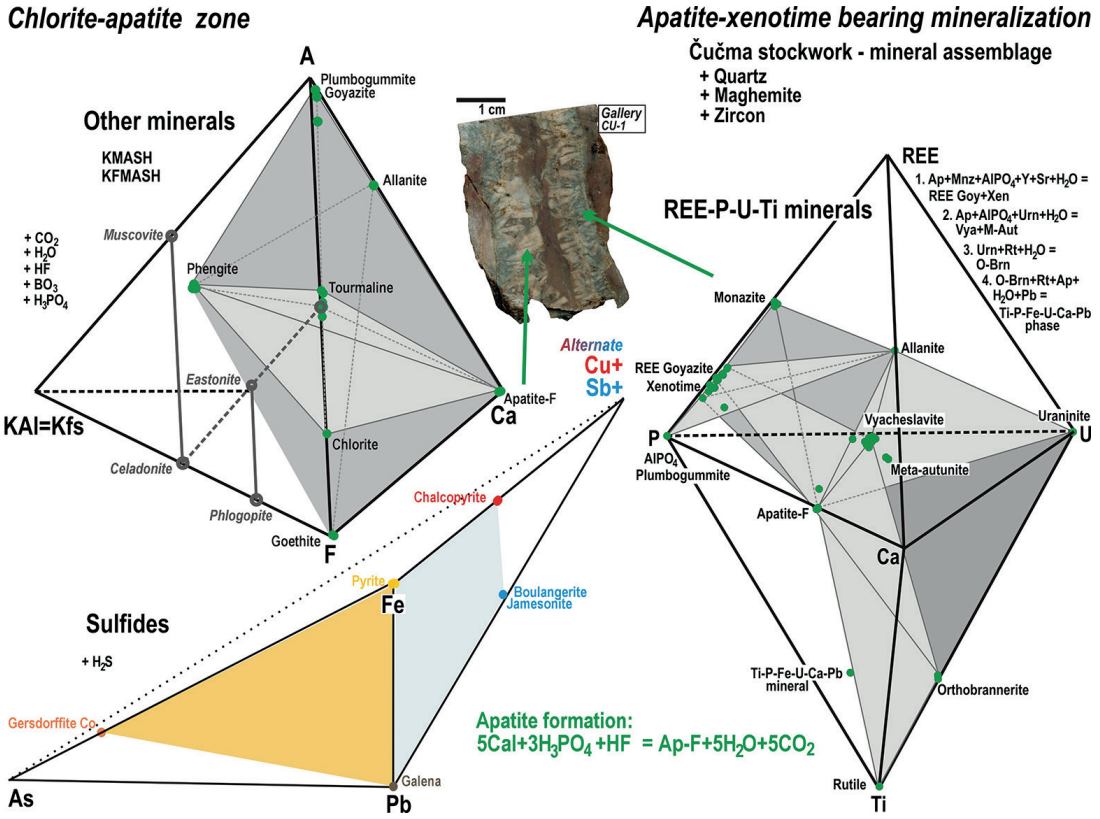

Fig. 20. Mineral assemblages of the stockwork with apatite-xenotime-quartz-phengite-tourmaline mineralization from the chlorite-apatite zone of metamorphism **M1b** in locality of Čučma. Classification diagrams show REE-P-U-Ti mineralization, sulfides and matrix minerals. Reaction describe the origin of apatite-F and REE-U-Ti mineralization.

uraninite and pyrite in Bt metapelite and the same minerals in stockwork characterize the same residual fluid phase, from which these equal assemblages originated.

Tourmaline-molybdenite-Fe carbonate and quartz-phengite-topaz-apatite-sulfidic mineralization in the greisen of chlorite-apatite zone from the granite exocontact in the Hnilec locality

From the granite exocontact in locality of Hnilec the samples of tourmaline-molybdenite-Fe carbonate and quartz-phengite-topaz-apatite-sulfidic mineralization were taken from the adit 1 (HG-133), adit 2 (HG-3) and boreholes (HD-16, HD-8). The sampling sites are visualized in cross-section (Fig. 21; Drnzík et al., 1981).

Mineralization occurs in the granite exocontact in the greenschists facies chlorite-muscovite phyllite. Greisen occurs in irregular form, in short pseudoveins, clusters and stockworks and often envelopes older greisen from the biotite zone (Fig. 22). This greisen mineralization is younger than mineralization in internal cassiterite greisene or cassiterite greisen in immediate contact of granite with its exocontact in the area of anatectic melting (Figs. 6, 7, 8). Greisenized phyllite contains irregular sedimentary carbonate interbeds, intercallations or thin beds. In the phyllite these interbeds of calcite – limestone are thick up to several cm (Fig. 22). Residual fluid phase in the granite exocontact changed this former phyllite to greisen type with prevailing matrix association of quartz, phengite, tourmaline, apatite-F, ankerite and siderite. The fluid phase metasomatically replaced the former calcite in phyllite to ankerite and siderite according to reaction 1 and coexisting apatite-F with ankerite originated according to reaction 3. Beside this main mineralization in greisen there was found topaz, bismuthinite, molybdenite, arsenopyrite, pyrite and rarely also pyrrhotite, jamesonite and garavellite (Figs. 21, 22). Topaz originated according to reaction 2.

REE contents from this greisen are normalized to primitive mantle, having corresponding course and the

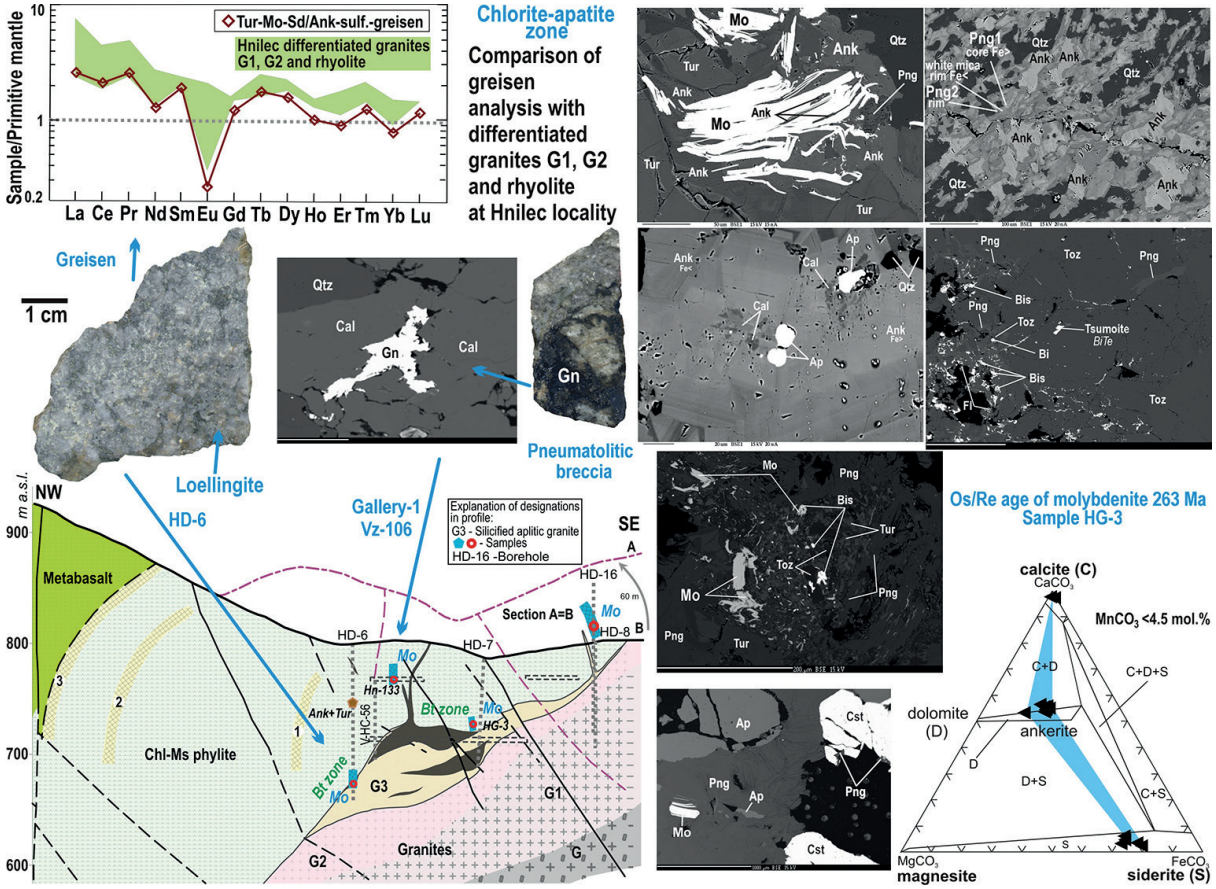

Fig. 21. Tourmaline-molybdenite-Fe carbonate mineralization with quartz-phengite-topaz-apatite and sulfides in the greisen of chlorite-apatite zone **M1b** in the granite exocontact of the Hnilec locality. Sampling sites: boreholes HD-8 and HD-16, adit 1 – HG-133, adit 2 – HG-3. Position of samples in cross-section according to Drnzík et al. (1981) is marked blue. Abbreviations: Quartz (Qtz), calcite (Cal), galena (Gn), topaz (Toz), molybdenite (Mo), bismuthinite (Bis), phengite 1–2 (Png1, Png2), tourmaline (Tur), apatite-F (Ap), ankerite (Ank). BSE image. REE contents from this greisen are normalized to primitive mantle. Greisen belongs to younger mineralization group of Permian together with differentiated granite and its volcanic equivalent – rhyolite. Molybdenite Re-Os age is 263 Ma (Kohút & Stein, 2005).

same negative Eu anomaly in concordance with the differentiated granites G1 and G2 (Fig. 21). Griesen belongs to younger mineralization group of Permian together with differentiated granites and their volcanic equivalent – rhyolite. Origin of the greisen from rezidual fluid phase was influenced by the mantle (Fig. 21). The Re-Os age of molybdenite from the sample HG-3 is ~263 Ma. The sulphur isotopic composition of dated molybdenite is $d^{34}S_{(CDT)}$ = 1.71 ± 0.2 ‰ and prefers its crustal origin connected with magmatic process (Kohút & Stein, 2005). In apatite-F of phengite matrix the sphalerite clusters with chalcopyrite and tetrahedrite were found. Galena was revealed in calcite and in other places of the greisen the galena forms the matrix of pneumatolytic breccia in the mass of apatite-F, phengite and topas (Fig. 22).

Greisen with tourmaline-molybdenite-Fe carbonate and quartz-phengite-topaz-apatite sulfidic mineralization ich characterized by gradual origin of mineral associations, chemically classified in crystallization systems. KAl=KfsFCA projection shows matrix association of phengite, chlorite, tourmaline, topaz, apatite-F, calcite, ankerite and siderite. Apatite-F does not contain any admixture of other elements and its chemical formula is $Ca_5(PO_4)_3F$. Projection of matrix association characterizes chlorite-apatite zone (Fig. 22). The projections of chemical composition of above stated sulfides are shown in Zn-Fe(Sb/Cu)Pb, ZnFePbAs and PbFe(Sb/Cu)Bi systems (Fig. 22). The classification of minerals and equilibrium reactions revealed that residual fluid phase in chlorite-apatite zone contained H_2S, H_2O, CO_2, HF, BO_3, H_3PO_4, Na, K, Ca, Al, Si, Fe, REE, As, Pb, Zn, Cu, Bi, Mo and Sb. Comparison with higher temperature fluid phase, producing greisen in epidote-amphibolite facies and in biotite zone revealed that the fluid phase of chlorite-apatite zone was deficient in $SnCl_2$, Mn, Mg, U, Ti, Y, Ni, Co, Ta, Nb and Te (Fig. 9). In this comparison we have found that in chlorite-apatite zone the Mo and Sb content was increasing. The Mo content is bound in dated molybdenite and Sb in garavellite, jamesonite and tetrahedrite (Figs. 21, 22).

Sb sulfides-rich tourmaline-Fe carbonate mineralization in chlorite-apatite zone in Rozabela vein in the Štofova dolina valley

The Sb sulfides-rich tourmaline-Fe carbonate mineralization in Rozabela vein of Štofova dolina was verified

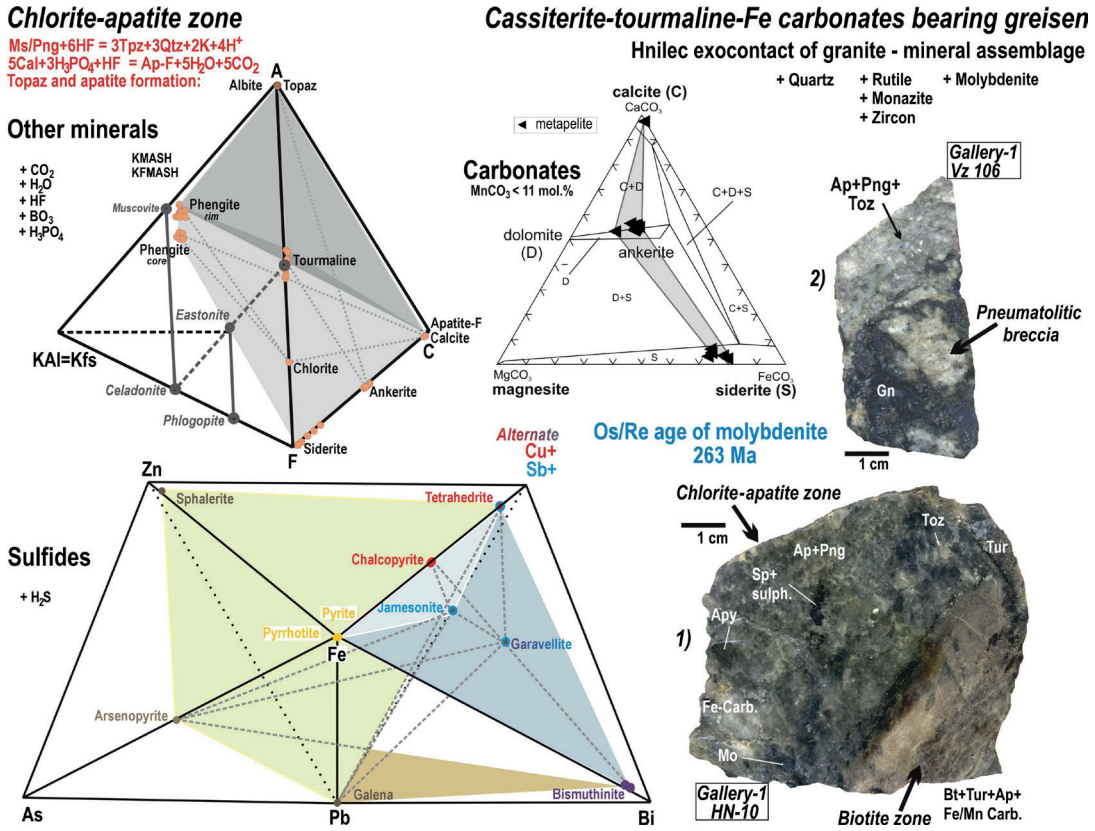

Fig. 22. Projections of positions of mineral asociations of tourmaline-molybdenite-Fe carbonate mineralization with quartz-phengite-topaz-apatite and sulfides in the greisen of chlorite- apatite zone **M1b**. Granite exocontact in locality of Hnilec. Projections of chemical composition of carbonates are in triangle diagram magnesite-siderite-calcite. Position of matrix minerals in KAl=KfsFCA projection. Position of sulfides in FePb(Cu/Sb)Bi, ZnFe(Cu/Sb)Pb and ZnFePbAs projection. Reactions describe the origin of topaz and apatite-F. 1 – in the cross-section the older greisen from the biotite zone is enveloped by younger greisen from chlorite-apatite zone. 2 – pneumatolitic breccia with the galena (Gn) matrix. Abbreviations of minerals are in Fig. 21.

by four small exploration adits located along the whole 500 m length of this vein cropping out. From related small dumps four samples were taken for determination of the contents of 62 elements (Tabs. 3, 4) and mineral association of the vein.

In older literature the above stated mineralization was simply called as stibnite–mineralization or marked as Sb veins (Bartalský et al., 1973; Grecula et al., 1995). This name was due to the target raw material – stibnite, though the main mineral of Sb veins is quartz. Sb veins were found in the southern Čučma-Poproč zone as well as in northern Dobšiná – Helcmanovce – Zlatá Idka zone. These two zones of Sb mineralization are identical with southern and northern hot lines, where originated the metamorphic zones and anatectic granites of S-type in Permian magmatic cycle of Variscan orogenic belt (Fig. 1; Radvanec et al., 2007, 2009; Grecula et al., 2009). According to the amount, the occurrences of Sb veins in southern zone distinctly prevail above occurrences in the northern zone (Bartalský et al., 1973; Grecula et al., 1995). Sb veins were verified by exploration trenches, adits and in numerous places Sb ores were exploited – mainly in the surrounding of Betliar, Poproč and Zlatá Idka villages. Quartz in Sb veins is significantly prevailing over Sb sulfides. The subsidiary minerals represent sulfides, Fe carbonates, albite, phengite, apatite, tourmaline, a.o. The level of geological knowledge on this mineralization type was summed up by Bartalský et al. (1973) and Grecula et al. (1995, 2009). Sb veins always occur close to granite, having variegated length from several tens of meters to 1 km. Vertically they occur close above granites and their depth range is maximum 300 m. Thickness of veins is from several cm in stockworks to veins and lenses of 8 m thickness. Sb veins were tectonically segmented and mylonitized during Alpine orogenesis. They occur in tectonic blocks together with surrounding rocks of biotite zone, or tectonic blocks of epidote-amphibolite facies of Variscan metamorphism **M1b** (Fig. 1; Grecula et al., 2009).

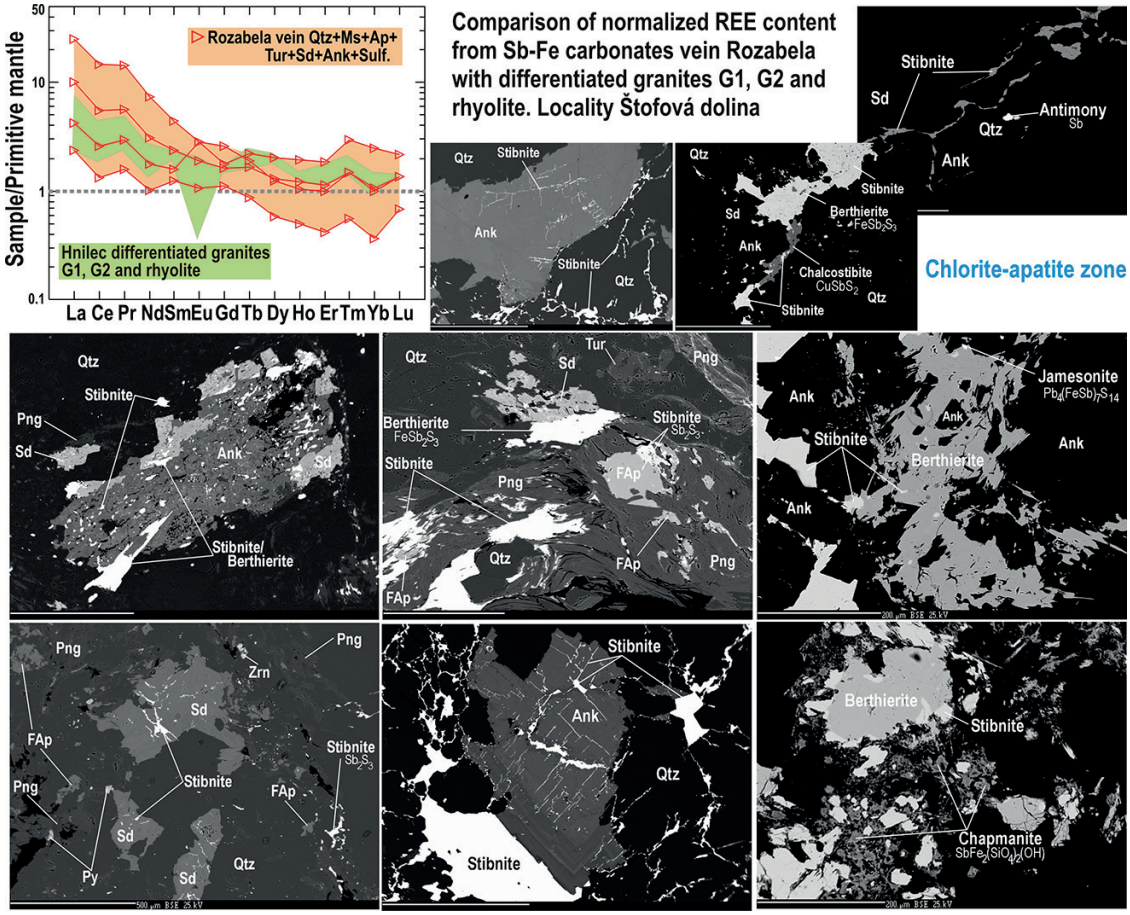

Fig. 23. Sb-sulfides rich tourmaline-Fe carbonate mineralization in Rozabela vein. Association quartz (Qtz), ankerite (Ank), siderite (Sd), apatite-F (FAp), tourmaline (Tur), phengite (Png) with Sb sulfides and albite in chlorite-apatite zone of **M1b** metamorphism in locality of Štofova dolina. BSE image. REE contents from this Sb vein are normalized to primitive mantle and vein belongs to younger Permian mineralization group together with differentiated granites and their volcanic equivalent - rhyolite. Four samples for REE contents were taken from small dumps and represent the whole known superficially cropping out course of the vein.

The Rozabela vein in whole known profile near surface is formed by agglomerates and clusters of ankerite, stibnite, berthierite, phengite, apatite-F, tourmaline, albite, siderite, chalcostibite, chapmanite, senarmontite, fülöppite, pyrite, pyrrhotite, chalcopyrite, arsenopyrite and native antimony in the quartz matrix. These clusters are often bearing zircon. Jamesonite forms in berthierite admixtures and inclusions. Stibnite fills cleavage joints in siderite and ankerite. These small stibnite veinlets do not continue to quartz matrix. It is an evidence that Fe carbonates and Sb sulfides represent coexisting minerals (Figs. 23, 24). Tourmaline belongs to schorl-dravite series. It has the same zonality and chemical composition as in other investigated localities (Jiang et al., 2008). Apatite-F does not contain any admixture of further elements and its chemical formula is $Ca_5(PO_4)_3F$.

The Rozabela vein is characterized by gradual origin of mineral associations, chemically classified in various crystallization systems. Matrix association of phengite, chlorite, tourmaline, apatite-F, ankerite, siderite and albite in KAl=KfsFCA projection, characterizing the chlorite-apatite zone (Fig. 24). Classification triangle diagram magnesite-siderite-calcite shows projection of ankerite and siderite chemical composition. The projections of sulfides chemical composition are visualized in connected triangles FePbAs and Fe(Sb/Cu)Pb. The equilibrium reaction describes the origin of apatite-F (Fig. 24). Applying the classification of minerals and equilibrium reactions there was derived that residual fluid phase in chlorite-apatite zone contained H_2S, H_2O, CO_2, HF, BO_3, H_3PO_4, Na, K, Ca, Al, Si, Fe, As, Pb, Cu and Sb. Comparison of composition with residual fluid phase in chlorite-apatite zone of Hnilec locality we found that in the fluid phase in the Rozabela vein the REE, Zn, Bi and Mo are missing. The other components are equally represented.

Siderite-sulfidic mineralization of the Strieborná and Konštancia veins in the chlorite zone of metamorphism

The Strieborná and Konštancia veins were selected to this study as etalons of the vein siderite-sulfidic mineralization in the Gemeric unit. This mineralization is

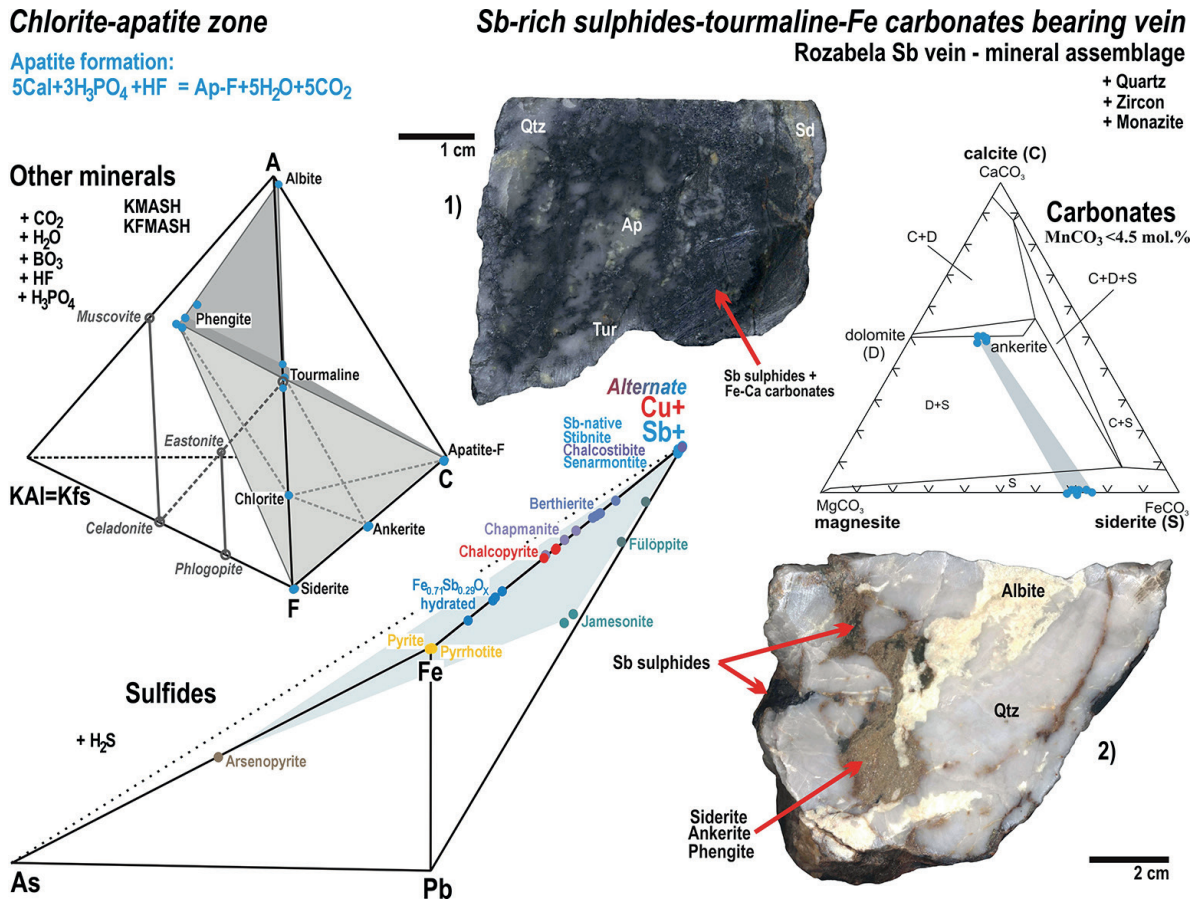

Fig. 24. Mineral associations of Sb-vein Rozabela in classification diagrams for carbonates, sulfides and further minerals. Chemical formula of the association phengite, apatite-F, chlorite, siderite, ankerite and albite are identical with chemical composition of corresponding minerals in studied localities of chlorite-apatite zone of Gemeric unit. 1 – cut sample shows the relation of apatite (Ap), tourmaline (Tur), quartz (Qtz) and Fe carbonates. 2 – cut sample shows the relation of albite, quartz and Sb sulfides with Fe carbonates. Reaction describes the origin of apatite-F.

represented by ca 1200 veins, being explored and numerous of them also exploited. The depth range of the veins is around 1000 m and their thickness ranges from several cm to 50 m. Detail description of mineral associations of these veins and their location were summed up in works by Bartalský et al. (1973) and Grecula et al. (1995), as well as numerous other studies and reports from their survey. Veins and vein systems of quartz-siderite-sulfidic mineralization are located in chlorite zone of greenschists facies (Grecula et al., 2009). Genetic model of the origin of this mineralization is derived from the origin of fluid phase in amphibolite, epidote-amphibolite facies and in biotite zone of metamorphism, acting from Upper Carboniferous, but mainly in Permian on hot line of Variscan orogenesis in Paleo-Gemericum. This fluid phase migrated from the zone of ductile overprint into colder area of greenschists facies, where it crystallized in cracks formed in the brittle deformation conditions. Source of elements for this fluid phase is represented by Devonian stratiform sulfidic mineralization, Silurian organogene sediments and lydites of Betliar Fm., all metamorphosed and melted in amphibolite facies conditions (Grecula et al., 1995, 2009; Žák et al., 2005; Radvanec et al., 2004, 2010; Radvanec & Grecula, 2016).

Representative samples of quartz-siderite-sulfidic mineralization were taken from the 6th mining level of the Strieborná vein, not reaching the surface. The Konštancia vein represents the same mineralization located in the Betliar Fm.

The veins Strieborná and Konštancia are characterized by the origin of mineral associations, being chemically classified in crystallization systems. The KAl=KfsFCA projection demonstrates the matrix association of phengite, chlorite, apatite-F, siderite and albite. Apatite-F and tourmaline in these veins occurs in their bottom parts. In the quartz siderite matrix occur accessoric minerals. Main matrix association phengite-chlorite-siderite characterizes the chlorite zone (Fig. 25). In classification triangle diagram magnesite-siderite-calcite are shown projections of siderite chemical composition. Siderite from the Strieborná vein has 10–20 mol.% $MgCO_3$ content and siderite from the Konštancia vein the content 2–3 mol. %. Projections of chemical composition of sulfides are shown in connected systems of ZnFePbAs,

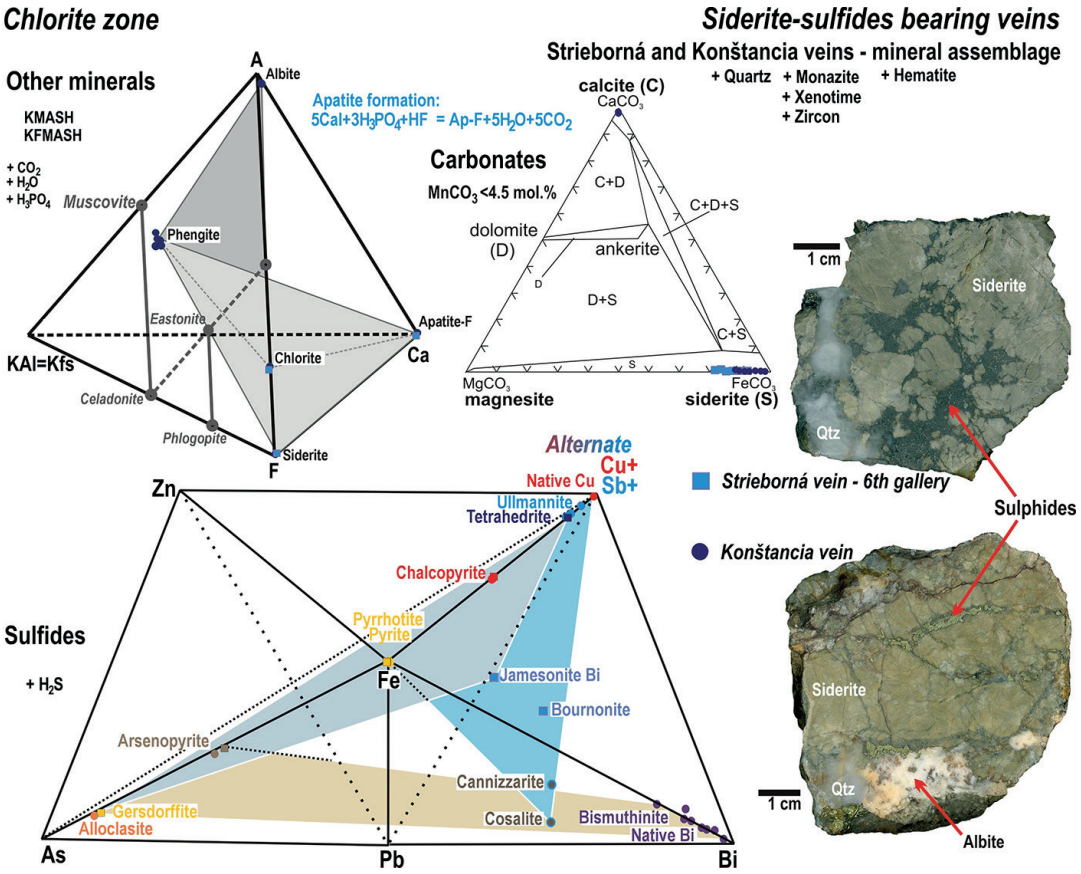

Fig. 25. Mineral association of siderite-sulfidic mineralization in veins of Konštancia and Strieborná in classification diagrams for carbonates, sulfides, arsenides and other minerals. Chemical formula of the association phengite, apatite-F, chlorite, siderite and albite corresponds with chemical composition of the same minerals in studied localities of chlorite-apatite zone of Gemeric unit. Reaction describes the origin of apatite-F.

Zn(Cu/Sb)FePb and Fe(Cu/Sb)PbBi. The Konštancia vein contains the native Bi, bismuthinite, cannizzarite, cosalite and alloclasite, native Cu and ullmannite, missing in the Strieborná vein. The Strieborná vein contains Bi jamesonite, boulangerite and gersdorffite, missing in the Konštancia vein. Other sulfides – pyrite, pyrrhotite, arsenopyrite, chalcopyrite, tetrahedrite and quartz, monazite, xenotime, zircon and hematite have the same chemical composition and found they were in both veins, forming their main sulfidic association. The equilibrium reaction describes the origin of apatite-F (Fig. 25). Applying these classifications and the equilibrium reaction we have derived the composition of residual fluid phase, containing H_2S, H_2O, CO_2, Na, K, Ca, Al, Si, Fe, Ni, Co, As, Pb, Bi, Cu, Sb ± HF, BO_3 and H_3PO_4. The REE contents from both veins of Konštancia (four samples with various ratios of sulfides, siderite, quartz and albite) and Strieborná are normalized in good agreement with primitive mantle. This classification ranks them to younger mineralization group of Permian, together with differentiated granites and their volcanic equivalent – rhyolite (Fig. 26).

Disseminated sedimentary-exhalation U-SedEx mineralization from chlorite-apatite zone in Permian volcanosedimentary sequences in locality of Krompachy, Kurišková and in tectonic breccia in the Poráč locality

The disseminated sedimentary-exhalation phengite-apatite-carbonate-U-Mo-Cu-Fe SedEx mineralization (in further text U-SedEx) is known from numerous localities from Novoveská Huta to Košice along the northern margin of Gemeric unit and is genetically interconnected with Permian andesite-rhyolite volcanism (Novotný & Mihál', 1987; Vozárová & Vozár, 1988; Grecula et al., 2009).

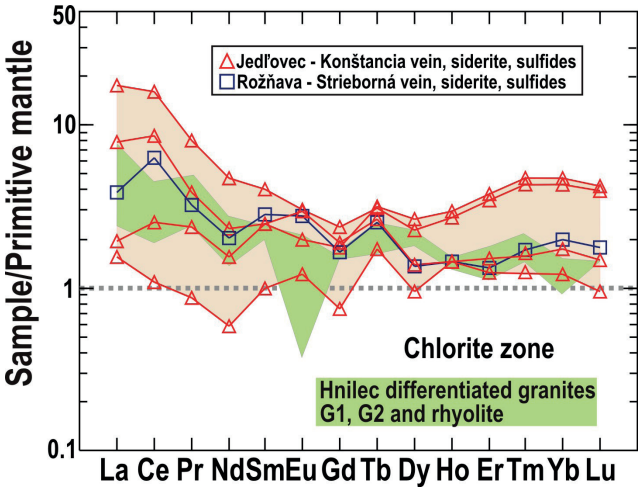

Fig. 26. Normalization of REE to primitive mantle of siderite-sulfidic mineralization of the Konštancia and Strieborná veins.

U-SedEx mineralization was newly studied in volcano-sedimentary sequences and andesite tuff in Kurišková locality. Besides a new mineralogical investigation we have completed the missing data about evolution and chemical composition of minerals in this locality, as well as compared and comprehensively evaluated until published analyses of minerals from works by Ferenc & Maťo (2006), Ferenc & Demko (2007; 2010), Demko & Ferenc (2007), Demko et al., (2007, 2011) and Ferenc et al. (2008).

In the Poráč locality the mineralogical investigation of U-SedEx mineralization studied the matrix of tetonic breccia. In Krompachy locality the pneumatolitic breccia in andesite tuff was found in borehole 953, 103.3 m, which matrix is formed by Fe-Ca carbonates, phengite, apatite-F, chlorite and pyrite. In borehole 1113, 454.8 m in this locality a stockwork of Fe-Ca carbonates in andesite was found (Fig. 27 and Table 3). This mineralization belongs to the process of the origin of U-SedEx mineralization. According to normalization of REE contents the mineralization from pneumatolitic breccia is corresponding with normalization of the contents on upper crust, so belongs to earlier Permian mineralization cycle, with the origin of porphyric granite and andesite (Fig. 27).

In the Kurišková locality we have newly studied samples from the borehole LE-K-29, where the U-SedEx mineralization was revealed in phengite-chlorite shale and in the borehole KGJ-21A-165, where it occurs in the andesite tuff. U-SedEx mineralization forms impregnations or it was found in concordant stockworks and veins with thickness of several tens of µm up to 1 cm. It is formed by pyrite, apatite-F, orthobrannerite, albite, rutile, quartz, phengite, dolomite, chlorite and coffinite (Fig. 28). The mixture of chlorite and phengite or apatite-F is often rimmed by the mixture of albite, coffinite and quartz (Figs. 28a, 28e). Concerning the U-SedEx mineralization in Poráč locality, quartz in the matrix of tectonic breccia encloses the association of phengite, pyrite and molybdenite (Fig. 29).

The projections of chemical composition of the matrix association are in the KAl=KfsFCA system completed by K-feldspar, tourmaline and actinolite from above stated earlier studies. Mineral associations gradually originated in the KAl=KfsFCA system. Association of K-feldspar, phengite-1 and albite relates with the origin of andesite tuff and volcanosediments during effusions of andesite lava. Association phengite-2, tourmaline, chlorite, actinolite, coffinite, apatite-F, ankerite, dolomite and Mg siderite crystallized from residual fluid phase, which altered and infiltrated the unsolidified sediments and volcanic products to U-SedEx mineralization (Fig. 30). Apatite-F similarly as in other investigated localities does not contain any admixture of other elements and its chemical formula is $Ca_5(PO_4)_3F$. Matrix association in KAl=KfsFCA system indicates that U-SedEx mineralization originated

at chlorite-apatite zone conditions. The projections of chemical composition of the mineral assemblages of U-SedEx mineralization are shown in PCaUREE system with projected positions of florencite, monazite, apatite-F, dolomite, ankerite, Mg siderite, uraninite, metacalciouranoite, calciouranoite and coffinite. In PCaUTi system it is association uraninite, orthobrannerite and rutile. In the frame of U-SedEx mineralization the assemblages in PCaUREE and PCaUTi systems are named as REE-P-U-Ti mineralization correspondingly as in other studied localities (Figs. 9, 11, 18, 20, 30). Sulfides from U-SedEx mineralization are shown in ZnFePbAs system. It is an association of sphalerite, pyrite, galena, arzenopyrite and gersdorffite. In ZnFePbCu/Sb system it is tennantite, chalcopyrite, bournonite, tetrahedrite, bornite, chalcocite, roxbylite and covellite. Coexisting carbonates from U-SedEx mineralization – calcite, dolomite, ankerite and Mg siderite/Fe magnesite are visualized in triangle diagram magnesite-siderite-calcite. Unclassified minerals of U-SedEx mineralization in the systems are represented by quartz, molybdenite, zircon, goethite, barite, organic substance (C), hematite and magnetite (Fig. 30). Projections of chemical formula of minerals in classification diagrams correspond with chemical composition of the same minerals, which originated in studied localities in chlorite-apatite zone of **M1b** metamorphism.

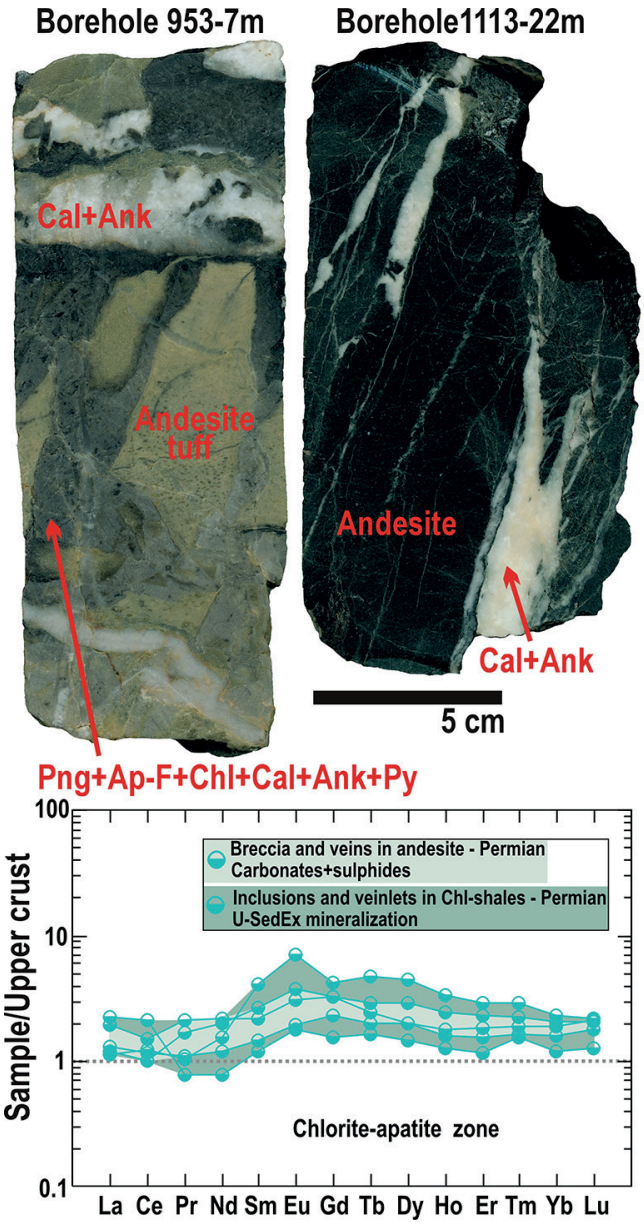

Fig. 27. Pneumatolitic breccia in Permian andesite tuff – borehole 953-7 and stockwork of carbonates in andezite, borehole 1113-22. Boreholes are from the Krompachy locality. Abbreviation: Calcite (Cal), ankerite (Ank), phengite (Png), chlorite (Chl), apatite-F (Ap-F), pyrite (Py). Normalizations of REE contents from carbonate mineralization of boreholes 953-7 and 1113-22 are consistent with normalization of the REE contents from U-SedEx mineralization, found in chlorite schists in locality of Kurišková. The REE normalizations are in good agreement with upper crust. Chlorite-apatite zone.

Using the above stated classification systems, it has been found that residual fluid phase, forming U-SedEx mineralization contained H_2S, H_2O, CO_2, HF, BO_3, H_3PO_4, Na, K, Ca, Al, Si, Fe, Mg, REE, U, Ti, Zn, Pb, Ni, As, Cu, Sb, Mo and Ba (Fig. 30). Composition of this fluid phase is in good agreement with the composition of residual fluid from apatite-chlorite and stilpnomelane-chlorite zone in localities of Hnilec, Dlhá dolina (skarn and greisen), Čučma and Rozabela vein. In fluid phase of U-SedEx the contents of Y, Te, Bi, In, Sr and Co are missing in this total comparison of the fluid phase composition. In U-SedEx fluid phase there occurred also Ba content (Fig. 30). The age of U-SedEx mineralization is according to Re-Os molybdenite dating 257–256 Ma (Kohút et al., 2013).

The normalization of the REE contents in locality of Kurišková confirms that U-SedEx mineralization is identical with the mineralization of pneumatolytic breccia from the locality of Krompachy and correspond with REE contents normalization to upper crust (Fig. 27). According to this characteristic both localities belong to older mineralization cycle, when in Permian originated the porphyric granite and andesite. U-SedEx mineralization with molybdenite from the matrix of tectonic breccia in locality of Poráč belongs to younger granite-rhyolite cycle with characteristic REE normalization to primitive mantle (Fig. 29).

Mineralization source in Permian metamorphic-magmatic-hydrothermal cycle

The source of elements for mineralization of Permian metamorphic-magmatic cycle is represented by pre-Permian rocks, having in Lower Paleozoic Paleo-

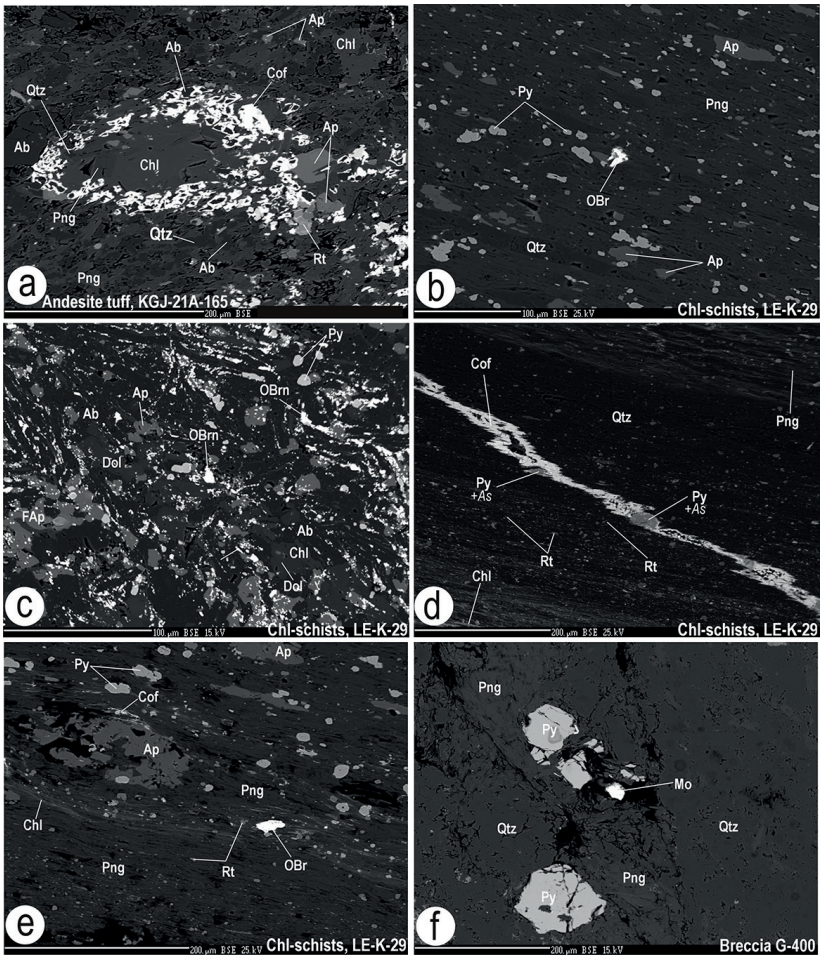

Fig. 28. Disseminated sedimentary-exhalative U-SedEx mineralization in Permian chlorite schist in locality of Kurišková ***(a–e)***. Abbreviations: Albite (Ab), dolomite (Dol), phengite (Png), chlorite (Chl), apatite-F (Ap), pyrite (Py), quartz (Qtz), rutile (Rt), orthobrannerite (OBrn), coffinite (Cof). BSE image.

Gemericum significant areal/volume spread. This condition is fulfilled by Devonian disseminated and stratabound sulfidic mineralization of the Smolník Fm. and phyllites with organic substance and interbeds of lydites/volcanosilicites of Silurian Betliar Fm. (Grecula et al., 2009). Stratabound sulfidic mineralization originated during bimodal basalt-keratophyre magmatism in the rift zone of oceanic floor. Both formations – Smolník Fm with stratabound sulfidic mineralization and Betliar Fm. with organic substance and lydites – were on Permian hot line metamorphosed and underwent anatectic melting. Hence, the Betliar Fm. became a source of CO_2 and the stratabound sulfidic mineralization of Smolník Fm. became a source of elements forming oxidic-sulfidic and Fe-Mn-Ca carbonatic mineralization. The process of mobilization of CO_2 from the rocks of Betliar Fm. and elements from stratiform sulfidic mineralization of Smolník Fm. to residual fluid phase was found by Radvanec (1988), Grecula et al. (1995), Radvanec et al. (2004), Žák et al. (2005) and Radvanec et al. (2010).

The occurrences of primary stratabound sulfidic mineralization are still well preserved in greenschists facies sequences not degrading it and its areal spread together with rocks of Betliar Fm. is significant also in recent Gemeric unit.

Etalon of stratabound sulfidic mineralization is represented by the Smolník locality (Fig. 1). Considering the position to former effusive center of ore-bearing fluids on sea bottom, three representative samples of basalts and one sample of keratophyre were taken from the Pech adit. These samples have distinctly prevailing sulfidic impregnations over host basalt and keratophyre. Mineralogical and geochemical investigation revealed that chalcopyrite- pyrite/pyrrhotite Fe-Cu ± Ni, B mineralization forms in basalt the central part around the former hydrothermal vent and this mineralization of the sea floor originated from the black smoke at ca 370 °C. Disseminated Fe-Zn-Pb ± Rb, As, Ag, Co mineralization forms transitional, more external part from the vent and besides pyrite there crystallized mainly sphalerite and galena. External part of effusion is formed by Fe-Ba-Sn-Mo dissemination mineralization in keratophyres, where the former ore-bearing fluid generated in the rift of Silurian-Devonian ocean crust and significantly was diluted with the

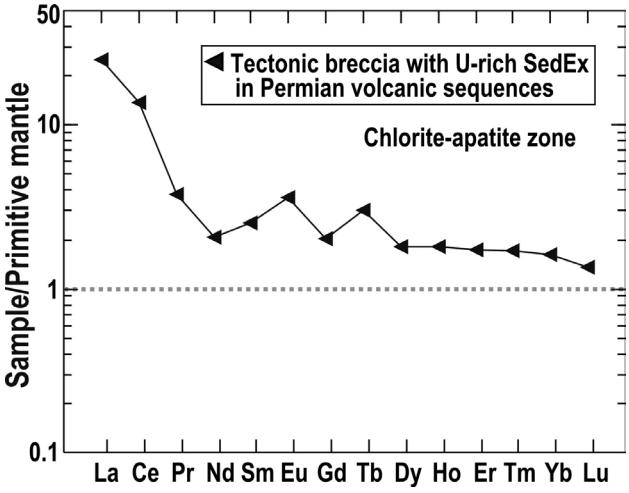

Fig. 29. The REE contents from tectonic breccia in locality of Poráč are normalized to primitive mantle. Contents of La and Ce are enriched in comparison with the mantle and mineralization belongs to younger mineralization group together with differentiated granite and its volcanic equivalent – rhyolite.

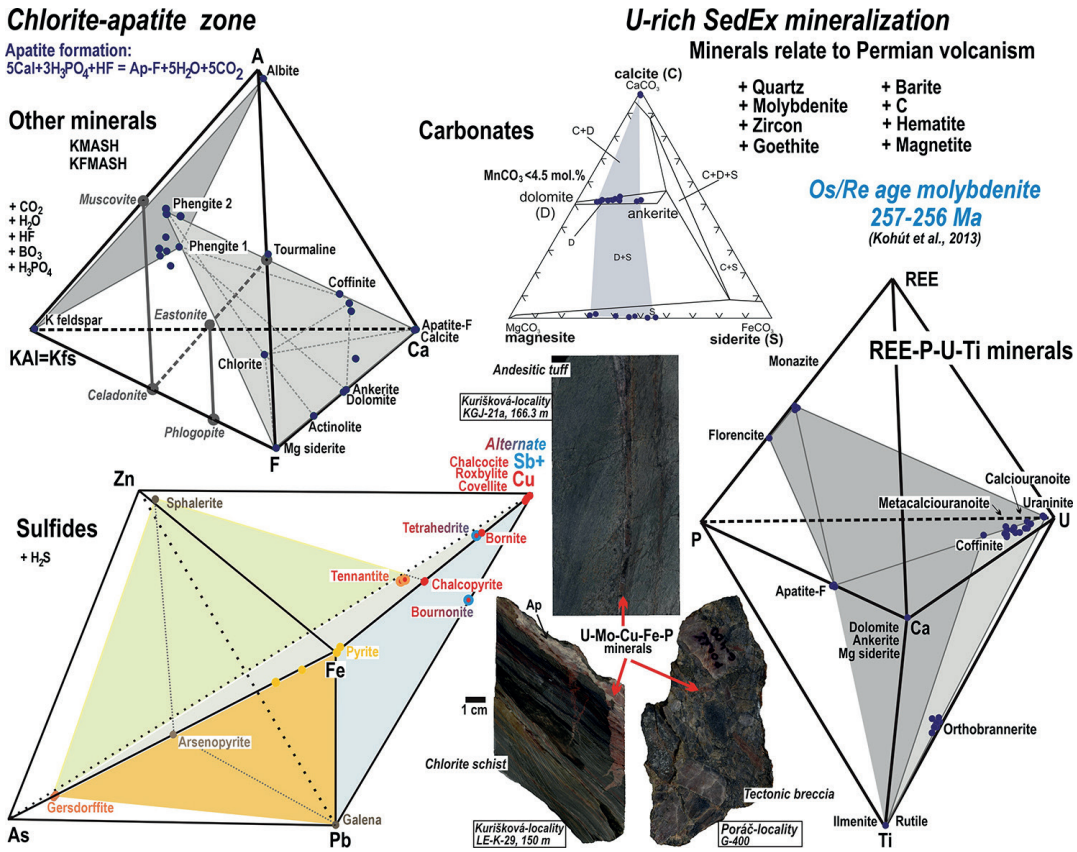

Fig. 30. Mineral associations of sedimentary-exhalative phengite-apatite-carbonate U-Mo-Cu-Fe mineralization of SedEx type in Permian volcanosedimentary sequences from chlorite- apatite zone. Classification diagrams show separately projections of carbonates, sulfides and REE-P-U-Ti minerals. The molybdenite age is 257–256 Ma (Kohút at al., 2013).

sea water (Bartalský et al., 1993; Radvanec et al., 1993; Grecula et al., 1995). In this external part the molybdenite was found in association with pyrite in metakeratophyre and Sn contents in metabasalt reach 960 mg/kg (Radvanec & Grecula, 1985).

The main mineral association of stratabound sulfidic mineralization in locality of Smolník is represented by pyrite, significantly prevailing over chalcopyrite, sphalerite, galena, pyrrhotite and arsenopyrite. Besides the main association also subsidiary minerals were found: glaucodote, arsenolite, claudetite, bismuthinite, native Bi, boulangerite, bournonite, jamesonite, bornite, tetrahedrite, ullmanite, stibnite, native Cu, chalcotite (Bartalský et al., 1993). Projections of these minerals are shown in systems ZnFePbAs, ZnPbCu/SbFe and FePbCu/SbBi (Fig. 31). Besides the main and subsidiary mineral association in the stratabound sulfidic mineralization also other minerals were found: quartz, K-feldspar, K-SO minerals, gypsum, phengite, chlorite, albite, cassiterite, hematite, molybdenite, sulphur, gold, anatase, apatite, fluorite, biotite, epidote, graphite, ilmenite, uraninite, scheelite, tourmaline, magnetite, topaz, zircon, ankerite, Mn ankerite, siderite and calcite (l.c.). It is probable that some mineral associations originated in former stratabound sulfidic mineralization and by auto-metamorphogenic process in the greenschists facies respectivelly (Fig. 31). The locality of Smolník is metamorphosed in this facies (Grecula et al., 2009). According to above stated mineralogical composition, the stratabound sulfidic mineralization is a source of S, F, B, Sn, K, Ca, As, Fe, U, Ti, Cu, Bi, Pb, Zn, Mo, Li and U entering the residual fluid phase (Fig. 31).

Lydites in localities of Smolník-Úhorná and Jedľovec (Fig. 1) are formed prevailingly of quartz, phengite, graphite and pyrite. Next minerals in the quartz matrix of lydite are represented by chlorite, allanpringite, rutile, hematite and white mica with the V content. According to mineralogical composition, lydites are a source of P, Ti, Si, Fe, U and CO_2, entering into residual fluid phase (Fig. 32).

The REE contents from the central, transitional and external part of the stratabound sulfidic mineralization and lydite are after normalization in good agreement with the etalon of upper crust (Figs. 31, 32).

Classification of Permian metamorphic-magmatic-hydrothermal cycle according to normalization of REE contents and ages

The normalization of REE contents from granites, volcanites and various above stated mineralizations classifies Permian metamorphic-magmatic-hydrothermal (MMH)

cycle into two groups. First group corresponds with upper crust and second group with primitive mantle (Fig. 33). Dating of granites, volcanites and mineralizations indicates gradual origin of two Permian parallel hot lines in Paleo-Gemericum (Figs. 1, 2; Radvanec et al., 2007, 2009). Older hot line metamorphosed and anatectically melted upper crust and classifies this older evolution of MMH cycle as upper crustal. The S-type porphyric granites and andesite as their effusive equivalent originated in this line. The stratabound sulfidic mineralization of the Smolník type of Smolník Fm. and lydites of the Betliar Fm. were a source of mineralization in this anatectic-hy-

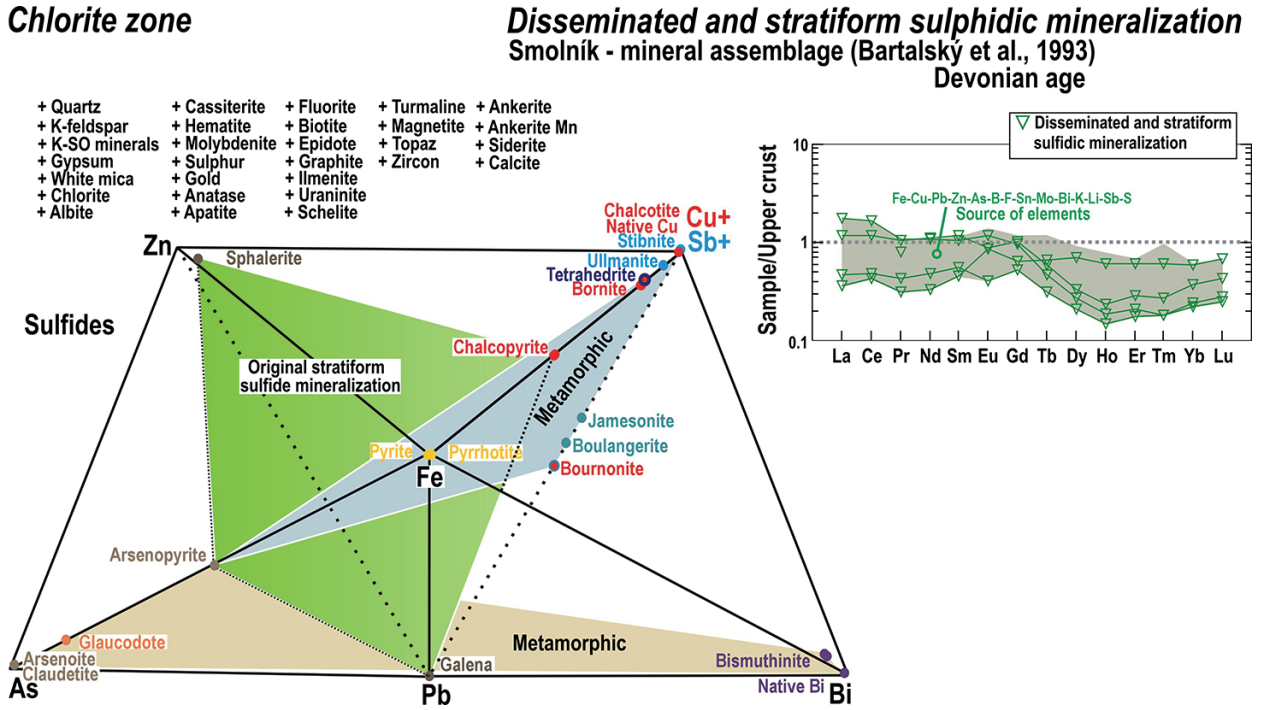

Fig. 31. Mineral association of Devonian stratabound sulfidic mineralization in the Smolník locality (Bartalský et al., 1993) with greenschists facies overprint, belonging to Smolník Fm. (Grecula et al., 2009). The REE contents normalization is in agreement with that of lydites and upper crust.

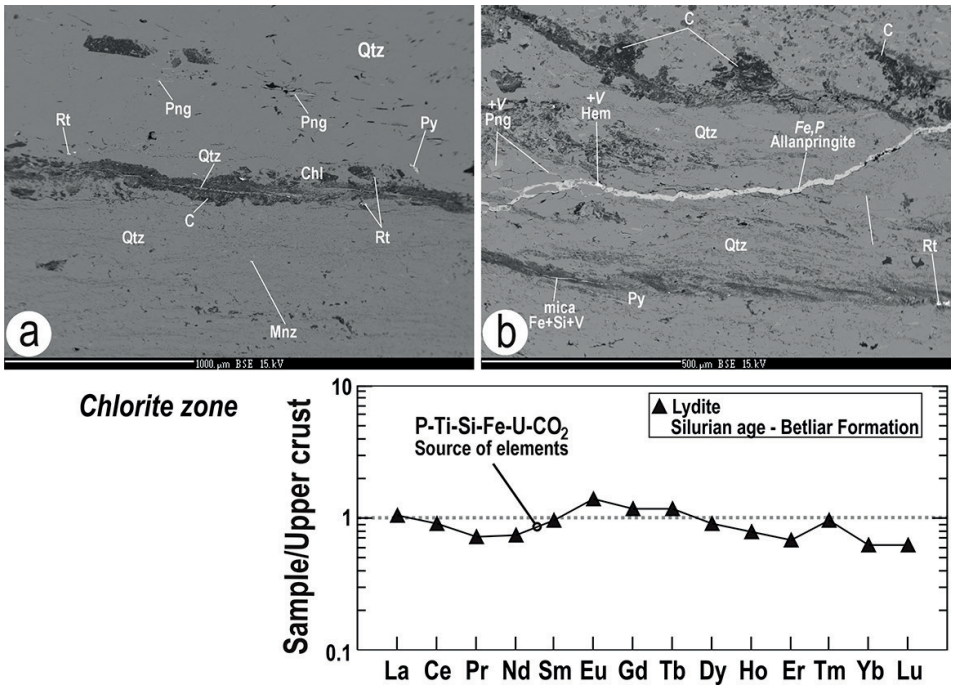

Fig. 32. Mineral association of lydite: quartz (Qtz), phengite (Png), pyrite (Py), chlorite (Chl), graphite (C), rutile (Rt), hematite with V content (Hem + V), allanpringite and mica with V content. BSE image. Lydite belonging to Silurian Betliar Fm. underwent the greenschists facies overprint (Grecula et al., 2009). The REE contents normalization in lydite agrees with the upper crust. Localities Smolník-Úhorná and Jedľovec.

drothermal cycle (Fig. 33). The related hydrothermal mineralization was found in biotite zone and chlorite-apatite zone in etalon localities of Hnilec, Dlhá dolina, Čučma, Betliar, Krompachy and Kurišková (Fig. 33). This older Permian upper crustal MMH cycle was active within the period of 281–268 Ma and its termination is indicated by the cassiterite age 268 Ma from the greisen at the Hnilec village (Kohút, personal information; Fig. 33).

Permian MMH cycle gradually continued by the evolution within younger hot line (Figs. 1, 2; Radvanec et al., 2007, 2009). The magmatites and mineralization were influenced by the primitive mantle (Fig. 33), which has reflected in the differentiated S-type granites, rhyolites and mineralization of chlorite-stilpnomelane zone, chlorite-apatite zone and chlorite zone. It was revealed in type localities of Hnilec, Dlhá dolina, Jedľovec (Konštancia vein), Rožňava (Strieborná vein), Štofova dolina (Rozabela vein) and Poráč (Fig. 33.). According to zircon, monazite and uraninite dating, the younger differentiated granites originated within an interval of 263–256 Ma (Radvanec et al., 2007, 2009). The molybdenite Re-Os ages of 263–256 Ma (Fig. 33) confirm that the mineralization with the primitive mantle influence is coeval with differentiated granites. The age of the Hnilec molybdenite is 263 Ma and the Kurišková molybdenite 256 Ma (Kohút & Stein, 2005; Kohút et al., 2013). The molybdenite ages together with the ages of both – differentiated granites and dacite-rhyolite – put younger MMH cycle to the Middle–Upper Permian (263–251 Ma; Fig. 33; Radvanec et al., 2007, 2009; Kohút & Stein, 2005; Kohút et al., 2013; Vozárová et al., 2015).

Isoconcetrations, anomalous and deficient contents of elements in reference rocks and type mineralizations of metamorphic-magmatic-hydrothermal cycle in Permian

The content of 62 elements was analysed from numerous reference granites, lydites, andesites, rhyolites and etalon

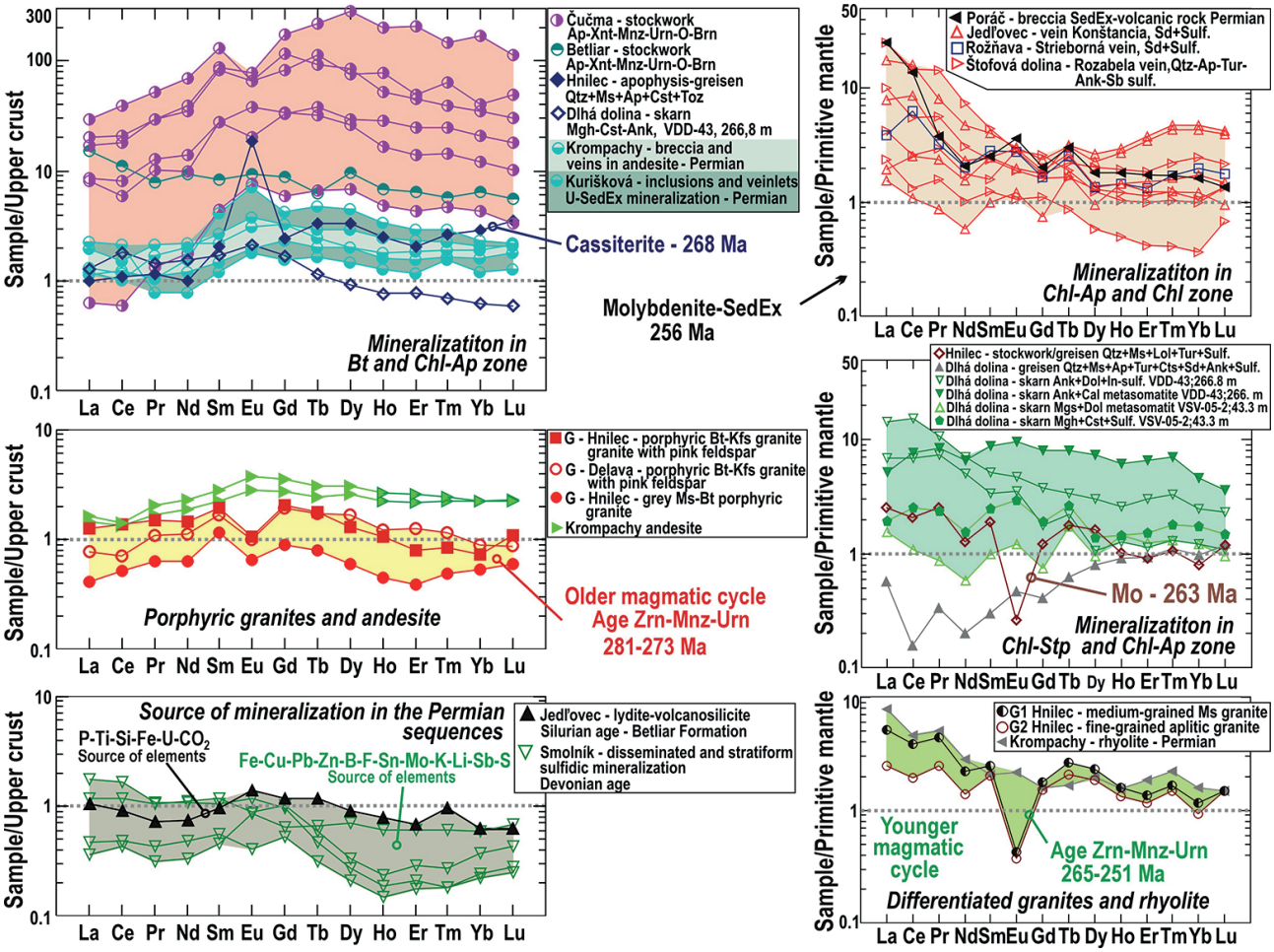

Fig. 33. Classification of Permian metamorphic-magmatic-hydrothermal cycle with the REE contents normalization and related ages. First group is classified by the REE normalization as a group identical with the upper crust and having Lower to Middle Permian age. Second group is according to contents and REE normalization identical with primitive mantle, hawing Middle to Upper Permian age. Normalization on upper crust and primitive mantle is according to Sun and McDonough (1989).

mineralizations. Applyning the normalization of the element contents to those in reference rocks, the deficient and anomalous contents were revealed, being visualized in logarithmic scale. After the normalization of the element content to reference rock, the isoconcentration (in further text – the isocone) in compared sample is the same in the case of their ratio equal to 1. In good agreement with the reference granite an isocone falls within the range 0.1–10. Values beneath 0.1 represent a deficiency and above 10 the enrichment against the reference rock (Figs. 34–37). The contents of 62 elements have colour division and division to groups, respecting the results of mineralogical investigation and binding of elements in mineral associations, found in type localities by mineralogical-geochemical investigation. Part of the main components of analyses and unclassified element contents occur in the black group. The red and green groups belong to elements prevailingly from apophyses, greisens and stockworks. Yellow group is formed by elements from the stockwork mineralization and blue group belongs to elements of vein mineral association (Figs. 36, 37).

As already expressed earlier, two groups of rocks and etalon mineralizations were divided according to REE classification, ages and mineralogical results. First group of samples is Lower and Middle Permian and identical with the upper crust, second Middle and Upper Permian group is identical with primitive mantle (Fig. 33). The grey muscovite-biotite (Ms/Bt) porphyric anatectic granite G from the Hnilec locality is a reference rock of the first group – according to normalized REE contents identical with upper crust. It has indistinct negative Eu anomaly, indicating the plagioclase origin from anatectic melt not differentiated in hot line (Fig. 4). So the contents of elements in grey Ms/Bt porphyric granite G represent the reference upper crust, which underwent anatectic melting without magmatic differentiation. To this crust were normalized and compared in isocones the samples of hydrothermal mineralization as well as andesite samples from the Permian MMH cycle (Figs. 34, 35).

The reference rock for the second group of samples with the primitive mantle influence is represented by fine-grained aplitic granite G2 from the Hnilec locality (Fig. 4). Contents of normalized REE in this granite, identical with primitive mantle, show a distinct negative Eu anomaly, related to the origin of plagioclase – albite from differentiated anatectic magma. The element contents in this fine-grained aplitic granite G2 represent a rock which underwent magmatic differentiation. Analyses of hydrothermal mineralization with the primitive mantle nature and rhyolite analyses were compared to this granite in isocones (Figs. 36, 37).

Concordantly with the methodology described above, on the contents of reference grey porphyric granite G of the upper crust, the elements contents in lydites and stratabound sulfidic mineralization of the Smolník type were normalized. According to zonality of stratabound mineralization from the vent centre on the sea floor, the metabasalt samples with dissemination mineralization were separately normalized in the central, transitional and external zones. From external zone of the effluence the disseminations in metakeratophyre were analysed and in the isocone of this mineralization also two incomplete analyses (taken from Radvanec and Grecula, 1985) are included – one from the metabasalt and one from metakeratophyre (Fig. 34). In metakeratophyre were rich molybdenite disseminations and in metabasalt the Sn contents reach the value of 960 mg/kg (l.c.).

The normalized isocones show that the lydite represents a source of Si, P, Rb, Cu, Cr, Ni, Ba, Sc, V, Cd and Se, entering to the Permian MMH cycle, and according to frequent occurrence of carbon being also a source of CO_2 (Fig. 32). Lydite from Jedľovec locality is a source of HREE and lydite from Smolník-Úhorná is a source of Ti, Fe, Mg, U, Zn, Pb, Sb, Tl and Hf (Fig. 34). Normalized isocones express the element potential of Silurian lydites much more precise than primarily derived from mineralogical investigation (Fig. 32).

Mineral associations and chemical composition of analysed samples of stratiform sulfidic mineralization confirms that the Devonian mineralization is a main source of elements to Permian MMH cycle (Fig. 34). Central and transitional zone of stratabound sulfidic mineralization is a source of Fe, Mn, Mg, Li, S, Bi, In, Cu, Zn, Pb, Cr, Ni, Co, Ag, Ga, Cd and Se. External zone is a source of Rb, Nb, Sn, B, Mo and As. According to isocone, the F high content 600–700 mg/kg in stratabound sulfidic mineralization represents an equivalent of the content in reference granite G, similarly like in lydite from the area of Smolník-Úhorná. The source of F in MMH cycle is stratibound sulfidic mineralization and lydite (Fig. 34). Normalized isocone of stratabound sulfidic mineralization specifies the elemental potential derived by mineralogical research in Fig. 31.

The magmatic differentiation of S-type granites was compared and evaluated in isocones, aiming to reveal the enrichment or deficiency of elements in individual granite varieties. The enrichment or deficiency in contents in differentiation succession of granites from Bt/Kfs porphyric to medium-grained granite G with pink feldspar (in further text Bt/Kfs granite G) through the medium-grained Ms granite G1 (Ms granite G1) to fine-grained aplitic granite G2 (granite G2), determines that granite type, where the residual fluid phase was separated (Figs. 3, 5). The element associations of enrichment or deficiency determine in isocones also composition of separated fluid phase, which according to the change of P-T conditions has crystallized in metamorphic zones. By this way the various anomalous element associations, characterizing greisens,

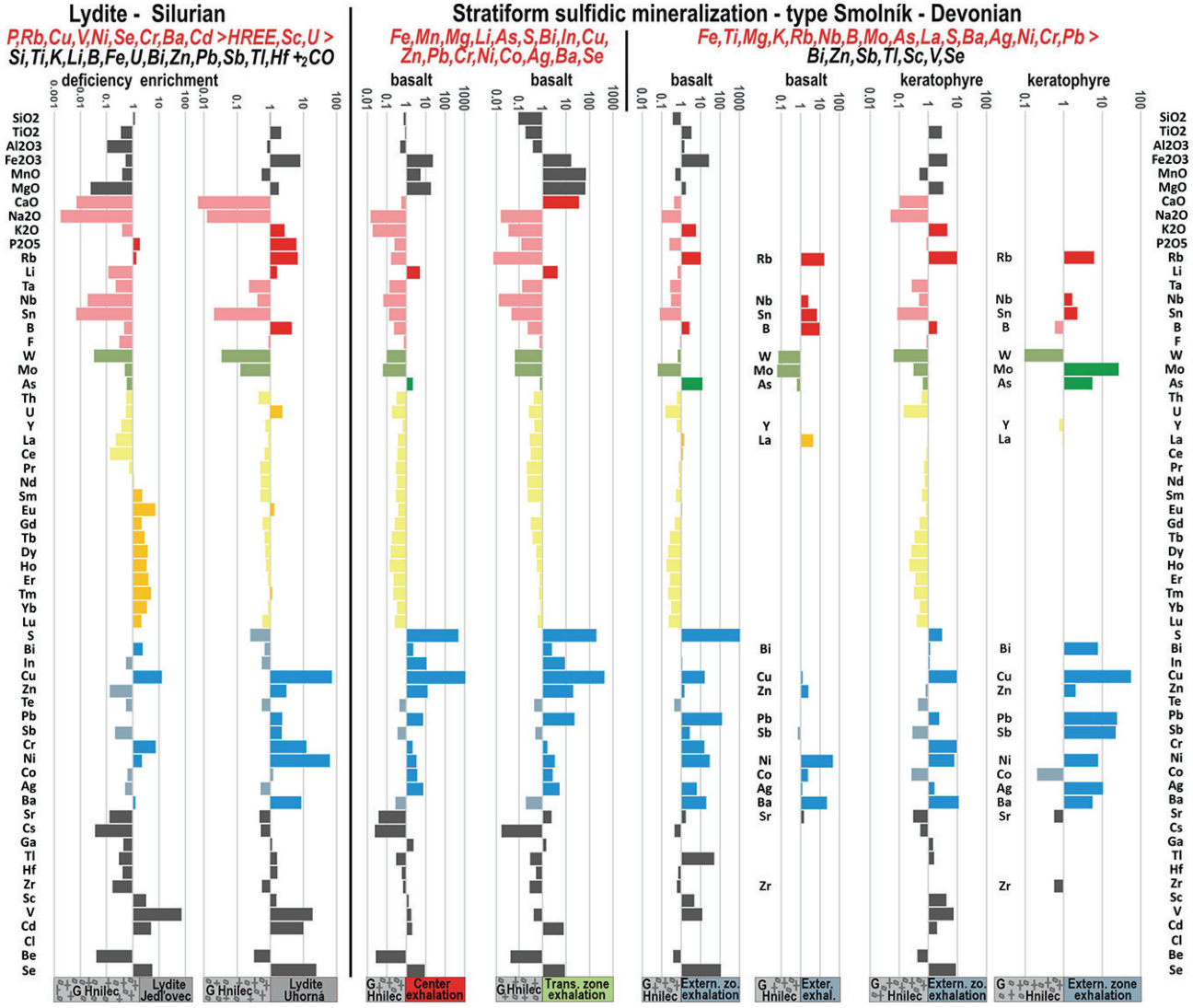

Fig. 34. Enrichment, deficiency or isoconcentratiom – isocone of the element content after normalization of contents of 62 elements in lydites and samples of zonal stratabound sulfidic mineralization of the Smolník type. According to sample classification by REE contents normalization to upper crust, the normalization logarithmically visualized the relation with the reference grey Ms/Bt porphyric granite G from the Hnilec locality. This normalization to granite G shows, which elements from lydites and stratabound mineralization were mobilized to metamorphic-magmatic-hydrothermal cycle in Permian.

skarns, stockworks, veins and SedEx mineralization were found (Figs. 35–37).

The evolution of Permian granite magma started with melting of upper crust with the origin of grey Ms/Bt porphyric granite G and Bt/Kfs granite G (Fig. 5). The younger differentiation varieties of Ms granite G1 and granite G2 were influenced by the mantle at their origin (Figs. 3, 4). The granite differentiates were normalized by the elements contents in reference Ms/Bt granite G (Fig. 35). Differentiated Bt/Kfs granite G and younger granites G1 and G2 are enriched by association of elements K, P, Rb, Li, Ta, Nb, Sn, B, F, S, Sb, Ba, Cs, Ga, Tl, Cl ± U and depleted by Ti, Mg, Na, W, Mo, As, Y, REE, Bi, Cr, Co, Ag, Sr, Zr and V. The gradual differentiation of granite melt caused the deficiency of REE contents in all melt varieties and in younger granites G1 and G2 also deficieny of Y content. It means that the residual fluid phase with the content of Y and REE has separated from granite melt during first differentiation, when in localities Hnilec and Delava originated the bodies of pink Bt/Kfs granite G in the grey Ms/Bt granite G (Figs. 4, 5). The separated fluid phase with the content of Y and REE partially crystallized in the greisen of biotite zone and mainly crystallized in stockworks of chlorite-apatite zone. The Y and REE contents in the greisen and stockworks represent a part of xenotime, monazite and REE goyazite (Figs. 19, 20, 35). Separated fluid phase with a significant content of Y and REE has preserved the geochemical characteristic

of upper crust, similarly as reference grey Ms/Bt granite G. Reference grey porphyric granite and fluid phase with Y-REE belong to older Permian MMH cycle (Fig. 33). From the viewpoint of raw materials, the isocones comparison revealed that Permian gemeric granites of S-type are bearers of K, P, Rb, Li, Ta, Nb and mainly Sn, B and Sb (Fig. 35).

A pair of grey Ms/Bt granite G and its effusive equivalent andesite, represent melting of upper crust in Permian hot line. The ratios of Sn, W, Mo, As, Bi and Te contents are in andesite isocone in deficience in relation to reference Ms/Bt granite (Fig. 35). Other values of elements ratios are in the range of 0.1–10, which is in good agreement with reference Ms/Bt granite and in andesite isocone are not considered as deficits or anomalies. Reference Ms/Bt granite and its effusive equivalent andesite are besides the association Sn, W, Mo, As, Bi and Te by the range of enrichment and depletion of elements the same rocks and represent the magmatic end members of older granite – andesite cycle with Permian ages 281–273 Ma.

Besides the reference grey Ms/Bt granite G and andesite into the first older group with the signs of upper crust there belong also greisen from the apophysis in Hnilec, stockworks from Čučma and Betliar, skarn from Dlhá dolina and SedEx mineralization from Kurišková and Petrova hora localities at the town of Krompachy (Fig. 35). These mineralizations originates or gradually are localized in epidote-amphibolite facies, in biotite zone, chlorite- apatite zone and in stilpnomelane-chlorite zone (Fig. 35). They originated and crystallized from residual fluid phase gradually in relation on the temperature decrease in metamorphic facies from the zone of anatectic melting in hot line towards the surface. Greisen from apophysis in Hnilec concentrates Ca, P, Rb, Nb, Sn, F, Eu, Se and is deficit with the content of Na and Co (Fig. 35). According to mineralogical investigation and this element association, the Hnilec greisen is characterized by apatite-topaz-columbite-cassiterite mineralization without the origin of albitu. According to cassiterite age, this mineralization is dated to 268 Ma (Figs. 7–9, 35). Anomalous Eu content in this greisen is a part of indistinct enrichment of this greisen by REE. Position of greisen in biotite zone and its direct genetic relation with the origin of granites indicate that mobilized REE in locality of Hnilec are from granite melt transported by residual fluid phase to area of biotite zone or epidote-amphibolite facies (Fig. 35). In these facies the elements REE are bound to crystallization of xenotime, REE goyazite and monazite (Figs. 8, 9). The distinct Eu enrichment in greisen apophysis in Hnilec relates with the Eu deficiency during differentiation of granite melt, when during the fractionation of granite melt the Na plagioclase – albite originates (Figs. 4, 7). Differentiation of the granite melt has mobilized Eu and transported by residual fluid phase, and from it followingly at the temperature decrease in the biotite zone or in epidote-amfibolite facies around 550 °C crystallized in the greisen the association of REE-P-Ca minerals with anomalous content of Eu (Figs. 9, 35). The remnant residual fluid phase from this zone migrated in the granite exocontact to colder chlorit-apatite zone. From it the REE-P-U-Ti mineralization has crystallized: xenotime, REE goyazite, monazite, allanite, vyacheslavite, apatite-F, meta-autunite, uraninite and orthobrannerite in the stockwork form. This mineralization is known from the Čučma and Betliar area (Figs. 19, 20). Isocone of the stockwork mineralization from the Čučma and Betliar areas is in comparison with reference Ms/Bt granite G anomalous by Ca, P, U, Y, REE, Bi, Cu, Te, Ni and Se contents. Deficit contents of Na, Sn and W indicate that residual fluid phase did not contain theses elements (Fig. 35). In the stockwork with REE-P-U-Ti mineralization from the Čučma and Betliar areas, albite and Sn mineralization were not found (Figs. 19, 20). Skarn from the borehole V-DD-43 in stilpnomelane-chlorite zone in the Dlhá dolina locality has, according to normalization to reference grey Ms/Bt granite G, the anomalous contents of Fe, Mn, Mg, Sn, S, In and Cu (Fig. 35). Residual fluid phase containing these elements has crystallized in the contact with the limestone tectonic block from Holec Beds and in this contact originated maghemite, cassiterite and In sulfidic mineralization in the range of stilpnomelane stability from 370 to 300 °C (Figs. 17, 18).

The SedEx mineralization of the older group, having upper crust signs, originated and is located in Permian volcanic sequences of chlorite-apatite zone (Fig. 35). In locality of Petrova hora at the Krompachy town it was a shallow sea in the immediate surrounding of the andesite lava outflow centers. Isocones of SedEx mineralization from localities of Petrova hora and Kurišková represent disseminated mineralization, which is anomalous to the reference grey Ms/Bt porphyric granite G by the contents of Rb, B, U, S, Cu, Cr, Ni, Co, Ba and Tl. The contents of Ca, Sn and W are deficient. The area of residual fluid outflow into sediments in the Kurišková locality is characteristic with Mo enrichment. In the area near the andesite effusion, in the andesite tuff, the Mo content is deficient (Fig. 35). It means that the U-Mo-Cu-Fe SedEx mineralization is zonal concerning molybdenite, and similarly it is also in Early Paleozoic stratabound sulfidic mineralization of the Smolník type. Molybdenite in SedEx mineralization crystallized in the external part of the vent on sea bottom, where the residual fluid phase mixed with the sea water.

Second group, where isocones were calculated, has REE normalization identical with primitive mantle and its age, revealed by the dating of differentiated granites and molybdenite, is Middle to Upper Permian (Fig. 33). Second group represents younger magmatic cycle

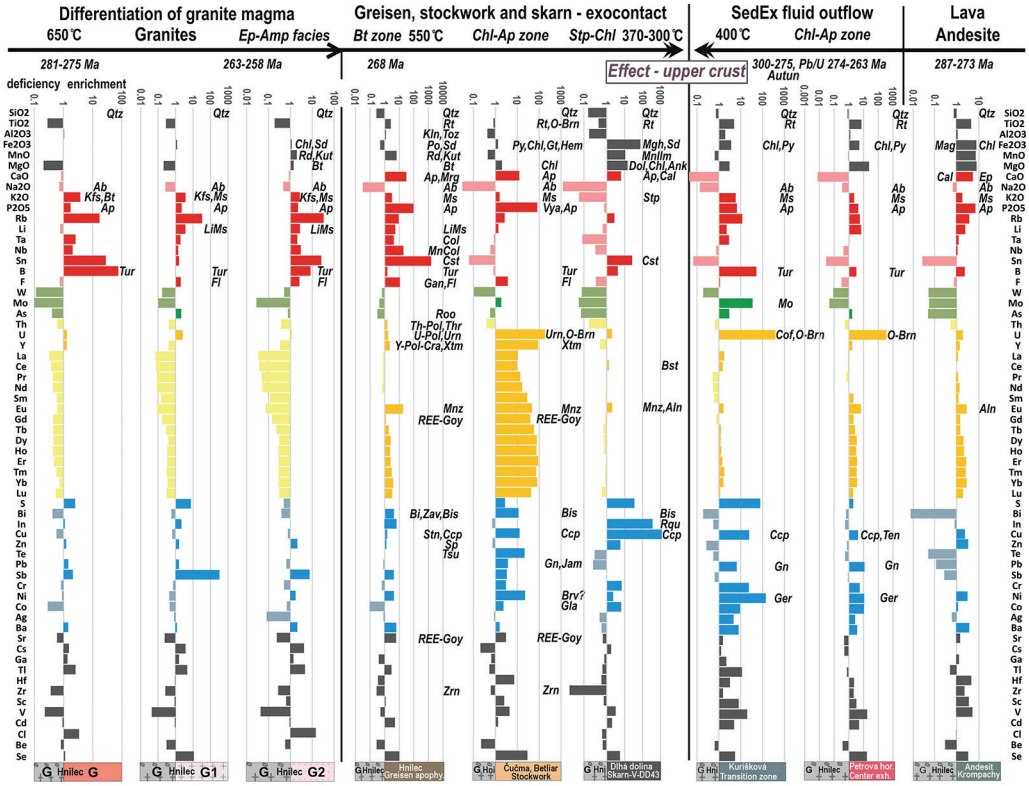

Fig. 35. Enrichment, deficiency or isoconcentration – isocone of the elements contents are expressed by the ratio in logarithmic scale after normalization of 62 elements contents of those in grey Ms/Bt porphyric to medium-grained granite G, representing melting of upper crust. The principle of isoconcentration – isocone values is explained in the text. According to samples classification, which are the same after the REE contents were normalized to upper crust, the isocones were calculated in the greisen sample in the Hnilec apophysis, stockworks in Čučma and Betliar localities, in the skarn of borehole V-DD-43 in Dlhá dolina and in fluid effluences of SedEx type in Permian volcanic sequences of Kurišková and Krompachy localities. These type mineralizations are located in epidote-amphibole facies, in biotite zone, in chlorite-apatite zone and in stilpnomelane-chlorite zone. Isocones were calculated in normalization to grey Ms/Bt porphyric granite G to Bt/Kfs porphyric granite G with pink phenocrysts of feldspar, in medium-grained Ms granite G1, fine-grained aplitic granite G2 and andesite. According this normalization there was found that granites of S-type have increasing contents of K, P, Rb, Li, Ta, Nb, but mainly Sn, B and Sb. Andesite is depleted by association Sn, W, Mo, As, Bi and Te, characterizing greisens. Anomalous ratios in isocone are marked by the abbreviation of mineral – the main bearer of anomalous element. Abbreviations are explained in mineralogical figures.

with differentiated Ms granite G1 and granite G2, as well as rhyolite as their effusive equivalent (Figs. 4, 33). Type mineralizations of this group encompass greisens, skarns and veins, located in chlorite-apatite, stilpnomelane-chlorite and chlorite zone. Reference rock for the second group isocones is a fine-grained aplitic granite G2. Its effusive equivalent – rhyolite is depleted by P, Rb, Nb, Sn, W, As, Bi, In, Zn, Te, Pb, Sb and Tl after normalization to reference granite G2 and enriched by U and V (Fig. 37). It is interpreted by finding that rhyolite magma does not contain elements, being in the anatectic process and in magmatic chambers of rhyolite magma separated into residual fluid phase. This element association separated in residual fluid phase was bound in mineralizations from epidote-amphibolite facies to chlorite zone (Figs. 36, 37).

Greisen from chlorite-apatite zone in locality of Dlhá dolina is in comparison to reference granite G2 enriched by Nb, Sn, Bi, Ag and Se, but depleted by the contents of Na, P, LREE, Cs, Tl and Be. According to mineral association and isocone, this greisen type is characterized by columbite and cassiterite (Figs. 10, 36). According to molybdenite Re-Os age of 263 Ma, the greisen from the chlorite-apatite zone in locality of Hnilec is younger than in this locality present older apatite-topaz-columbite-cassiterite greisen from epidote-amphibolite facies and biotite zone. The age of older greisen is according to cassiterite 268 Ma and has the source characteristic in the upper crust (Figs. 8, 9, 33). According to isocone, the younger greisen from chlorite-apatite zone in the locality of Hnilec is enriched by B, F, Mo, As, S, Bi, Ag and Cd and depleted by Na, K, Rb, Sn, In, Cs and Tl contents (Fig. 36). According to mineral association and isocone, this type of greisen is characterized by association of tourmaline-topaz-apatite and As-Bi-Mo sulfides, as well as Fe-Ca carbonates (Figs. 21, 22, 36).

The skarn samples of stilpnomelane-chlorite zone were taken from the Dlhá dolina – the borehole V-DD-43, 266,8 m and underground borehole VSV 05-2, 43,2 m, drilled in the Elisabeth gallery in the magnesite and talc deposit (Fig. 1). The skarn isocone from the borehole VSV 05-2, 43,2 m is enriched by Fe, Mo, Bi, Cu, Cr and Cd, but depleted by Si, Ti, Al, Na, K, P, Rb, Li, Nb, B, W, As, Th, U, Sb, Sr, Cs, Zr and Be in the ratio to reference granite G2. Sulfidic zone from the skarn contact with former

limestone in borehole V-DD-43, 266,8 m is according to REE normalization influenced by primitive mantle, so this part of the skarn belongs to the second - younger group of Permian mineralization development (Figs. 16, 17). Isocone of this sulfidic zone is depleted by Fe, Mn, Mg, Ca, LREE, S, Bi, In, Cu, Co, Sr, V and Cd and enriched by Si, Al, Na, K, Rb, Ta, Nb, W and Tl. Other elements are in good agreement with reference fine-grained granite G2 (Fig. 36). Comparison of skarn mineralization and its isocones demonstrates that the skarn mineralization is zonal and characterized by maghemite-cassiterite-Bi-In-sulfidic mineralization (Figs. 12-18, 36).

Isocones of the vein mineralization were calculated in Fe-Ca carbonate Rozabela vein with Sb sulfides, in siderite veins with sulfides Konštancia and Strieborná, as well as in SedEx mineralization from tectonic breccia in Poráč (Figs. 1, 37). These mineralizations are located in chlorite-apatite zone and in chlorite zone, and according to REE normalization they are influenced by primitive mantle, likewise the reference granite G2 (Fig. 33). Isocone of Fe-Ca carbonate vein with Sb sulfides is enriched by Ti, Ca, Mo, S, Pb, Sb, V, Cd and Se and depleted by Na, P, Rb, Ta, Nb, Sn, In, Cs and Zr (Fig. 37). This mineralization in chlorite-apatite zone represents the transition from the skarn and stockwork form of crystallization of residual fluid phase to the vein form. The origin of veins with Fe-Ca carbonates and Sb sulfides was facilitated by the brittle deformation, originating after doming of rocks above hot line in termination of Variscan orogenesis. These veins have variegated depth range from 50 to 300 m (Grecula et al, 1995).

The isocone of the Konštancia siderite vein with sulfides is enriched by Fe, Mn, W, Mo, As, S, Bi, Cu, Pb, Ni, Co, Ag, V, Cd and Se, but depleted by Ca, K, Rb, Nb, Sn, B, Th, U, Cs, Tl and Be. The isocone of the Strieborná siderite vein with sulfides, similarly as the Konštancia vein is enriched by Fe, Mn, As, S, Cu, Zn, Pb, Sb, Ag and Cd, being depleted by Si, Ti, Al, Na, K, Rb, Li, Nb, Sn, B, W, Th, U, Cs and Be (Fig. 37). Both type mineralizations represent siderite mineralization with sulfides, forming the main raw material potential of Gemeric unit. The origin of veins was allowed by the brittle deformation in the chlorite zone of greenschists facies during Variscan orogenesis. Vein structures have variegated depth ranging to 1000 m and originated with the doming of rocks above hot line in external part of the zone of amphibolite facies and the area of anatectic melting (Grecula et al., 1995).

SedEx mineralization is genetically related to rhyolite phase of Permian volcanism in the chlorite-apatite zone. It was studied by normalization to granite G2 in tectonic breccia in locality of Poráč. The isocone of this mineralization is enriched by Mo, U, S, Cu, Cr, Ni, Ag, V and Cd, but depleted by Mn, Mg, Ca, Na, Sn, W and In. The comparison of isoconcentration of vein mineralization with isocone of SedEx mineralization in tectonic breccia show their good trend concordance (Fig. 37).

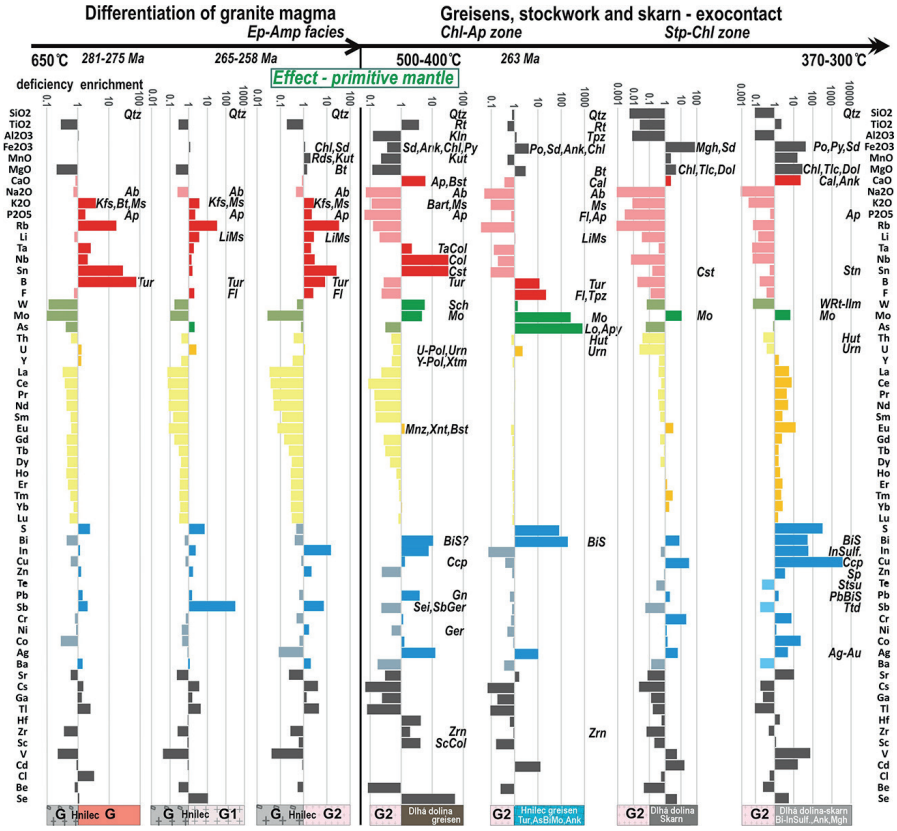

Fig. 36. Enrichment and deficiency of the elements content expressed by the ratio of 62 normalized elements in logarithmic scale to elements in fine-grained aplitic granite G2, representing the differentiation of granite melt with REE characteristic of primitive mantle. According to classification of samples, corresponding after normalization of REE contents to primitive mantle, the isocones were calculated in the Dlhá dolina greisen, the greisen with molybdenite and ankerite from Hnilec, in the skarn from the borehole VSV 05-2 in Elisabeth gallery – talc and magnesite deposit in Dlhá dolina and in the skarn of sulfidic zone in borehole V-DD-43 from the Dlhá dolina. These etalon mineralizations are located in chlorite- apatite and stilpnomelane-chlorite zones. Anomalous ratios in isocone are marked by the abbreviation of mineral – the main bearer of anomalous element. Abbreviations are explained in mineralogical figures.

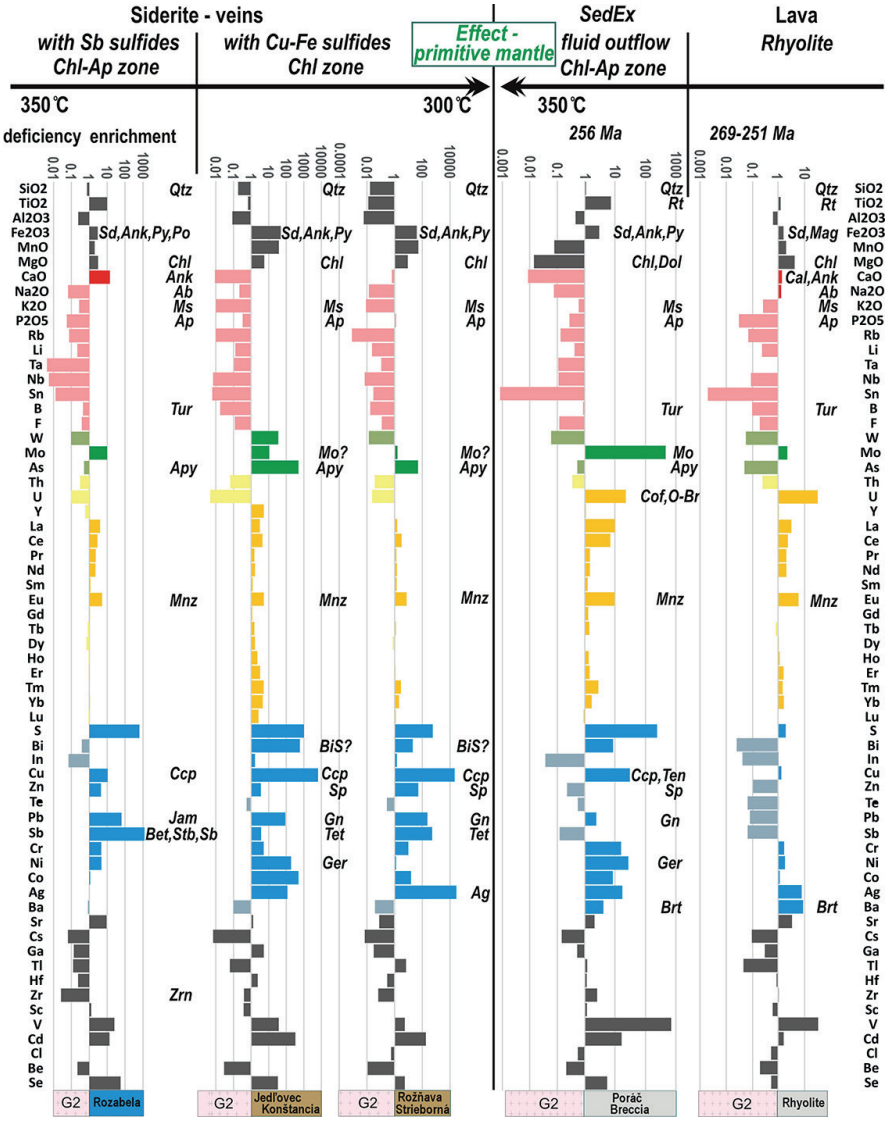

Fig. 37. Enrichment and deficiency of the elements content expressed by the ratio of 62 normalized elements in logarithmic scale to elements in fine-grained aplitic granite G2, representing the differentiation of granite melt with REE characteristic of primitive mantle. Isocones were calculated for type mineralizations influenced by primitive mantle: Fe carbonate vein Rozabela with Sb sulfides, siderite veins Konštancia and Strieborná with sulfides and SedEx mineralization from tectonic breccia in Poráč, all being localized in chlorite-apatite and chlorite zone. Normalization of element contents in rhyolite to reference granite G2 shows that rhyolite is depleted by P, Rb, Nb, Sn, W, As, Bi, In, Zn, Te, Pb, Sb and Tl, but enriched by U and V. Rhyolite does not contain elements, deliberating to residual fluid phase in the anatectic process.

Genetic model of metamorphic-magmatic-hydrothermal cycle in Permian

The reconstruction of geotectonic background of Permian evolution in Gemeric unit summarizes the results of mineralogical and geochemical study. This reconstruction takes into account the principles of previous Lower Paleozoic and Carboniferous evolution. Mineralization process in Permian is based on thickening of continental crust in Upper Carboniferous, producing orogenic collapse related to subduction that culminated by the transfer of heat, volatiles and magma from the boundary of asthenosphere. The heat transfer caused metamorphism in amphibolite facies, leading to anatectic melting of a part of upper crust with dominant granitoid magmatism in Lower and Middle Permian and on the surface corresponding with andesite volcanism. In the Middle and Upper Permian the differentiation of granite magma caused the rhyolite volcanism on the surface. This younger magmatism influenced the transfer of heat, volatilies and magma from the melting of subducted material in the asthenosphere. Differentiated granites and rhyolite have the upper mantle geochemical characteristics. In the upper crust this gradual Permian metamorphism and magmatic activity was arranged in two hot lines, trending E-W. They caused doming of Early Paleozoic sequences of metasediments, metabasalts and metarhyolites in the overlier of anatectic granite (Figs. 1, 2; Grecula et al., 2009, Radvanec et al., 2010, Radvanec & Grecula, 2016). In the collision zone of Paleo-Gemeric and Paleo-Veporic units this megaanticlinal setting (doming) of sediments has produced the intensive unroofing, being confirmed also by the beds of conglomerates and detritic sediments (Novotný & Mihál', 1987). The detritus of conglomerates consists of rocks from surrounding Early Permian sequences and volcanic rhyolite-andesite interbeds.

Doming of rocks above hot line caused the fan like opening of brittle-ductile structures above granite and towards the surface opening of brittle structures. In all these structures, from greisens, through stockworks, skarns to veins, the same main or matrix mineral association of phengite, quartz, apatite-F, tourmaline and Mn/Fe/Mg/Ca carbonates was found. According to chemical formula, phengite, apatite-F, tourmaline and carbonates have the same composition (Tabs. 1-3). The crystallization of

this matrix association is not related on the decrease of temperature from the anatectic zone ~ 650 °C to greenschists facies ~ 300 °C in the extension area above granite. In the coexistence with this matrix mineralization various associations have crystallized from residual metamorphic-magmatic fluid phase in relation to temperature decrease towards the surface. Nearest to granite the greisen mineralization originated in epidote-amphibolite facies of biotite zone with minerals, crystallizing from residual fluid phase with the content of H_2S, H_2O, CO_2, HF, BO_3, $SnCl_2$, H_3PO_4, Na, K, Ca, Al, Si, Ni, Co, As, Fe, Mn, Mg Sn, REE, U, Ti, Y, Ta, Nb, Cu, Te, Bi, Pb and Sr (locality of Hnilec). Towards the surface, in colder chlorite-apatite zone the greisen originated from the fluid phase of following composition: H_2S, H_2O, CO_2, HF, BO_3, Cl_2, H_3PO_4, Na, K, Ca, Al, Si, Ni, Co, As, Fe, Mg Sn, REE, U, Ti, Y, Ta, Nb, Cu, Sb, Te, Bi, Pb and Zn (locality of Dlhá dolina). In stilpnomelane-chlorite zone the skarn mineral association originated from the fluid phase of H_2S, H_2O, CO_2, HF, BO_3, $SnCl_2$, H_3PO_4, K, Ca, Al, Si, Fe, Mg, REE, U, Ti, Y, Cu, Sb, Te, Bi, Zn and In (locality of Dlhá dolina). In the stockwork of chlorite-apatite zone there originated the mineral association from the fluid phase of H_2S, H_2O, HF, BO_3, H_3PO_4, K, Ca, Al, Si, Fe, REE, U, Ti, Ni, Co, As, Pb, Cu, Sb and Sr (locality of Čučma). In the greisen of chlorite-apatite zone the mineral association originated from the fluid phase of H_2S, H_2O, CO_2, HF, BO_3, H_3PO_4, Na, K, Ca, Al, Si, Fe, REE, As, Pb, Zn, Cu, Bi, Mo and Sb (locality of Hnilec). Veins in chlorite-apatite zone consist of mineral association from the fluid phase of H_2S, H_2O, CO_2, HF, BO_3, H_3PO_4, Na, K, Ca, Al, Si, Fe, As, Pb, Cu and Sb (Rozabela vein, Štofova dolina). Veins of chlorite zone bear mineralization from the fluid phase consisting of H_2S, H_2O, CO_2, Na, K, Ca, Al, Si, Fe, Ni, Co, As, Pb, Bi, Cu, Sb ± HF, BO_3 and H_3PO_4 (Konštancia vein and Strieborná vein). Towards the surface and on sea bottom of Permian evaporitic basins the SedEx

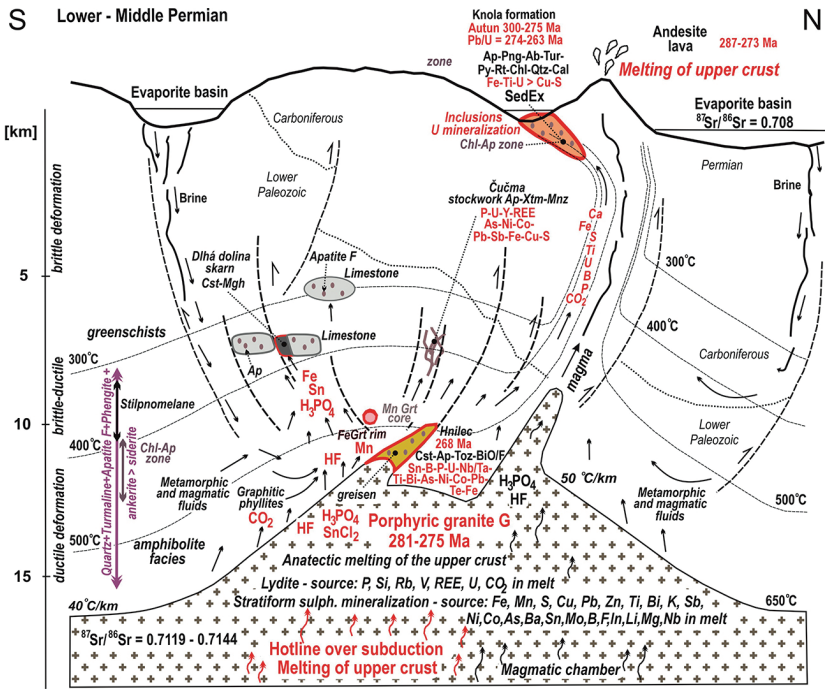

Fig. 38. Model of the origin of metamorphic-magmatic-hydrothermal cycle in Lower to Middle Permian. Mineralization and magmatism have their source in upper crust. Ratios of Sr isotopes and ages are from the works by Radvanec et al. (2004, 2007, 2009, 2010, 2016), Vozárová & Vozár (1988), Vozárová et al. (2015). The cassiterite age (Kohút, personal information).

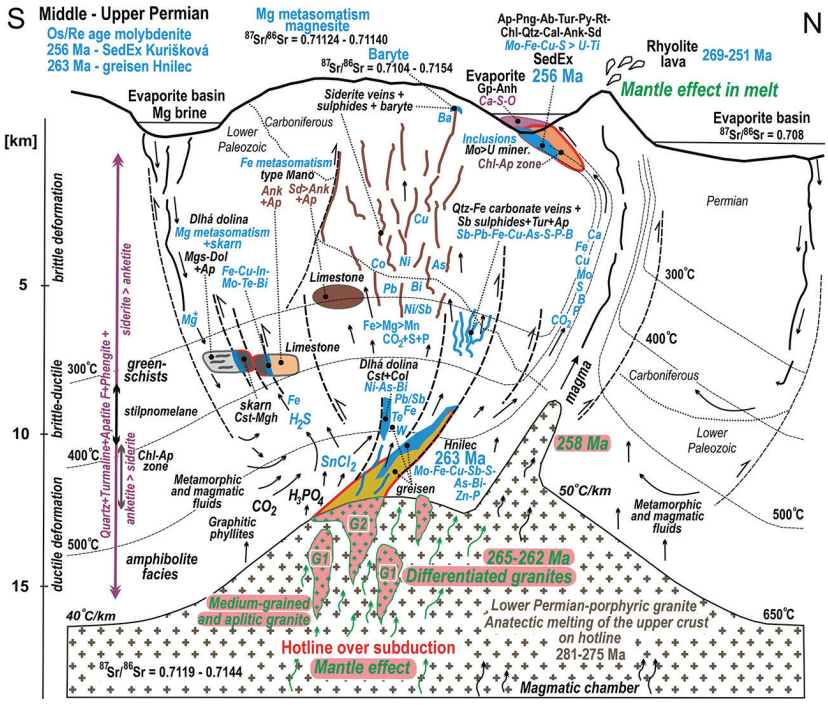

Fig. 39. Model of the origin of metamorphic-magmatic-hydrothermal cycle in Middle to Upper Permian. Mineralization and magmatism is influenced by primitive mantle. Ratios of Sr isotopes and ages are from the works by Radvanec et al. (2004, 2007, 2009, 2010, 2016), Vozárová & Vozár (1988), Vozárová et al. (2015). The molybdenites age (Kohút & Stein, 2005; Kohút et al 2013).

mineralization originated on chlorite-apatite zone from the fluid phase of H_2S, H_2O, CO_2, HF, BO_3, H_3PO_4, Na, K, Ca, Al, Si, Fe, Mg, REE, U, Ti, Zn, Pb, Ni, As, Cu, Sb, Mo and Ba (localites of Kurišková and Poráč).

In above stated zones, the boundaries of the occurrence of individual mineral associations are not strictly delimited and composition of the fluid phase changed in relation on the age of mineralization and its source. The geotectonic background of metallogenetic evolution in Lower and Middle Permian is derived from metamorphism and anatectic melting of upper crust. The metallogenetic evolution from the Middle to Upper Permian is connected with the influence of upper mantle – both in magmatites and fluid phase (Figs. 38, 39).

Acknowledgement. Authors express their thanks to Ministry of Environment of Slovak Republic for funding the metallogenetic research, based on the project "Raw material potential of Slovak Republic – analysis and prognostic re-evaluation of critical raw materials". The study of greisens, granites and skarn would not be possible without accurate localized samples from mining works and boreholes – we thank to L. Drnzíková and O. Rozložník for maintaining these excelent and important samples. The remarks and suggestions of reviewer P. Uher and one anonymous reviewer are greatly appreciated. This comprehensive paper greatly benefited by the contribution of Z. Németh.

References

Bartalský, J., Grecula, P., Bárta, R., Rozložník, L., Snopko, L., Varček, C., Varga, J., Ilavský, J. & Ťapák, M., 1973: Geologicko-ložisková štúdia Spišsko-gemerského rudohoria. *Spišská Nová Ves, Geol. prieskum.*

Bartalský, J., Ilavský, J., Bartalský, B., Čiško, V., Grecula, P., Hock, M., Kellner, M., Kladivík, E., Magula, R., Návesňák, D., Popreňák, J., Radvanec, M., Szabó, R. a Žifčák, F., 1993: Smolník mesto medenorudných baní. Geológia ložiska polymetalických rúd, ich využitie a vplyv na mesto a okolie. *Bratislava, Miner. Slov., ISBN 80-967010-0-0.*

Broska, I. & Uher, P., 2001: Whole-rock chemistry and genetic typology of the West-Carpathian, Variscan Granites. *Geol. Carpath., 52, 2, 79–90.*

Cambel, B., Bagdasarjan, G. P., Gukasjan, R. Ch. & Veselský, J., 1989: Rb-Sr geochronology of leucocratic granitoid rocks from the Spišsko-gemerské rudohorie Mts. and Veporicum. *Geol. Zbor. Geol. carpath., 40, 323–332.*

Cloos, M., 1993: Lithospheric buoyancy and collisional orogenesis: subduction of oceanic plateaus, continental margins, island arcs, spreding ridges, and seamonts. *Geol. Soc. Amer. Bull., 105, 715–737.*

Demko, R. & Ferenc, Š., 2007: Petrografický a petrochemický výskum horninových komplexov z ložiska Košice I. *Manuscript. Spišská Nová Ves, archive Ludovika Energy, 94 pp.*

Demko, R., Ferenc, Š., Novotný, L. & Bartalský, B., 2007: Geochemical-petrographical and mineralogical study of U-Mo ore deposits Košice I – Jahodná. *In: Ďurža, O. & Rapant, S. (Eds.): Geochemia 2007. Konf., Symp., Sem. Bratislava, St. Geol. Inst. D. Štúr, 106–108 (in Slovak).*

Demko, R., Ferenc, Š. & Biroň, A., 2011: Syntéza poznatkov mineralogického a petrografického výskumu na ložisku Košice I. – Kurišková za roky 2006–2010. *Manuscript. Spišská Nová Ves, archive Ludovika Energy, 91 pp.*

Drnzík, E. et al., 1981: ZS z úlohy Hnilec, cínové rudy. *Manuscript. Spišská Nová Ves, archive Geol. prieskum.*

Drnzík, E., 1982: Factor controls of the tin mineralization in the Hnilec tin ore field. PhD thesis. *Manuscript. Košice, archive Technical University, 1–142 p.*

Donát, A., 1998: Ocenenie výskytov anomálií prvkov vzácnych zemín v perme a gelnickej skupine SGR. *Manuscript. Bratislava, archive St. Geol. Inst. D. Štúr.*

Ferenc, Š. & Maťo, Ľ., 2006: Mineralogické a petrologické zhodnotenie vzoriek vrtov KG-J-1, KG-J-1a, KG-J-2 U-Mo ložiska Košice I pri Košiciach. *Manuscript. Spišská Nová Ves, archive Ludovika Energy, 61 pp.*

Ferenc, Š. & Demko, R., 2007: Komplexné zhodnotenie U-Mo mineralizácie ložiska Košice I. *Manuscript. Spišská Nová Ves, archive Ludovika Energy, 151 pp.*

Ferenc, Š., Demko, R., Mikušová, J. & Janega, A., 2008: Aplikovaný mineralogicko-geochemický výskum U-Mo mineralizácie na ložisku Košice I. – Kurišková. *Manuscript. Spišská Nová Ves, archive Ludovika Energy, 152 pp.*

Ferenc, Š. & Demko, R., 2010: Doplňujúci mineralogický a petrografický výskum na ložisku Košice I. – Kurišková. *Manuscript. Spišská Nová Ves, archive Ludovika Energy.*

Grecula, P., Abonyi, A., Abonyiová, M., Antaš, J., Bartalský, B., Bartalský, J., Dianiška, I., Drnzík, E., Ďuďa, R., Gargulák, M., Gazdačko, Ľ., Hudáček, J., Kobulský, J., Lörincz, L., Macko, J., Návesňák, D., Németh, Z., Novotný, L., Radvanec, M., Rojkovič, L., Rozložník, O., Varček, C. & Zlocha, J., 1995: Mineral deposit of the Slovak Ore Mountains. Vol. 1. *Bratislava, Miner. Slov. – Monogr., 834 pp.*

Grecula, P. (ed.), Kobulský, J., Gazdačko, Ľ., Németh, Z., Hraško, Ľ., Novotný, L. & Maglay, J., 2009: Geologická mapa Spišsko-gemerského rudohoria 1 : 50 000. *Bratislava, Ministerstvo život. prostr. Slovenskej republiky – Št. Geol. Úst. D. Štúra.*

Gubač, J., 1977: Premeny okolných hornín na ložiskách Spišsko--gemerského rudohoria. *Západ. Karpaty, Sér. Mineral. Petrogr. Geochém. Metalogen., 4, 9–279.*

Henry, D. J. & Guidotti, C. V., 1985: Tourmaline as a petrogenetic indicator mineral: an example from the staurolite-grade metapelites of NW Maine. *Amer. Mineralogist, 70, 1–15.*

Jiang, S. Y., Radvanec, M., Nakamura, M., Palmer, M., Kobayashi, K., Zhao, H. X. & Kui, D. Z ., 2008: Chemical and boron isotopic variations of tourmaline in the Hnilec granite-related hydrothermal system, Slovakia: Contrains on magmatic and metamorphic fluid evolution. *Lithos, 106, 1–2, 1–11.*

Kantor, J., 1957: A^{40}/K^{40} method of absolute age dating of rocks and its application to Betliar granite. *Geol Práce, Spr, 11, 188–200 (in Slovak with German summary).*

Kantor, J., 1959: Contribution to age knowledge of some granites and its related deposits of the Western Carpathians. *Acta geol. geogr. Univ. Comen. 2, 63–73 (in Slovak).*

Kantor, J. & Rybár, M., 1979: Radiometric ages and polyphasis character of Gemeride granites. *Geol. Zbor. Geol. carpath. 4, 433–448.*

Kamenický, J. & Kamenický, L., 1955: Gemeric granites and ore mineralisation of Zips-Gömör Ore Mountains. *Geol Práce, Zoš., 47, 1–73 (in Slovak).*

Kilík, J. et al., 1995: Gemerská Poloma – mastenec, VP, Surovina: mastenec, Stav k 31. 3. 1995. *Manuscript. Bratislava, archive St. Geol. Inst. D. Štúr..*

Koděra, P. & Radvanec, M., 2002: Comparative mineralogical and fluid inclusion study of the Hnúšťa-Mútnik talc--magnesite and Miková-Jedľovec magnesite deposit (Western Carpathians, Slovakia). *Bol. paranaense Geocienc., 50, 131–150.*

Koděra, P. & Radvanec, M., 2003: Fluid inclusion and mineralogical data from the Hnúšťa-Mútnik talc-magnesite and Miková-Jedľovec magnesite deposits (Slovakia) *In: Eliopoulos et al. (eds): Mineral exploration and sustainable development, Proc. 7th SGA meeting, 899–902. (Millpress).*

Kohút, M., Kovach, V. P., Kotov, A. B., Salnikova, E. B. & Savatenkov, V. M., 1999: Sr and Nd isotope geochemistry of Hercynian granitic rocks from the Western Carpathians – implications for granite genesis and crustal evolution. *Geol. Carpath., 50, 477–487.*

Kohút, M., Nabelek, P. & Recio, C., 2001: Stable isotopes. In: Petrík, I., Kohút, M., Broska, I. (eds.): Granitic plutonism of the Western Carpathians. *Bratislava, Veda, 33–35.*

Kohút, M. & Recio, C., 2002: Sulphur isotope study of selected Hercynian granitic and surrounding rocks from the Western Carpathians (Slovakia). *Geol. Carpath., 53, 3–13.*

Kohút, M. & Stein, H., 2005: Re-Os molybdenite dating of granite-related Sn-W-Mo mineralization at Hnilec, Gemeric Superunit, Slovakia. *Mineral. Petrol., 85, 117–129.*

Kohút, M., Trubač, J., Novotný, L., Ackerman, L., Demko, R., Bartalský, B. & Erban, V., 2013: Geology and Re-Os molybdenite geochronology of the Kurišková U-Mo deposit (Western Carpathians, Slovakia). *J. Geosci., 58, 271–282, DOI: 10.3190.*

Kovách, Á., Svingor, E. & Grecula, P., 1979: Nové dáta o gemerických granitoch. *Miner. Slov., 11, 71–77.*

Kovách, Á., Svingor, E. & Grecula, P., 1981: Isotopic age relationships of the granitoid rocks in the Spiš-Gemer metalliferous Mts., Eastern Slovakia. *Bucurest, Abstracts, XI. Congres CBGA, 600–601.*

Kovách, Á., Svingor, E. & Grecula, P., 1986: Rb/Sr isotopic ages of granitoide rocks from the Spiš-Gemer metalliferous Mts., West Carpathians, Eastern Slovakia. *Miner. Slov., 18, 1–14.*

Kusák, B. et al., 1981: ZS Delava-Peklisko, Sn-W rudy, VP, stav k 1. 9. 1981. *Manuscript. Spišská Nová Ves, archive Geol. prieskum.*

Malachovský, P., Dianiška, I., Matula, I., Kamenický, J., Kobulský, J., Hodermarský, J., Fabian, M., Radvanec, M., Kozáč, J., Vlasák, M., Mihalič, A., Ščerbáková, A., Seliga, J. & Novoveský, M., 1983: SGR – high temperature mineralization – Sn, W, Mo ores. Open file report. *Manuscript. Bratislava, archive St. Geol Inst. D. Štúr, 1–248 (in Slovak).*

Malachovský, P., Turanová, L. & Dianiška, I., 1992: Final report on mineral exploration from Gemerská Poloma. Open file report. *Manuscript. Bratislava, archive St. Geol Inst. D. Štúr, 1–180 (in Slovak).*

Malachovský, P., Uher, P. & Ďuďa, R., 2000: Nb-W minerals in rare granites, Dlhá dolina Spišsko Gemerské Rudohorie Mts. *Natura Carpat., 41, 7–14 (in Slovak).*

Németh, Z., Putiš, M. & Hraško, Ľ., 2016: The relation of metallogeny to geodynamic processes – the natural prerequisite for the origin of mineral deposits of public importance (MDoPI): The case study in the Western Carpathians, Slovakia. *Miner. Slov., 48, 2, 119–134.*

Novotný, L. & Miháľ, F., 1987: New lithostratigraphic units of the Krompachy Group. *Miner. Slov. 19, 97–113 (in Slovak).*

Petrík, I. & Kohút, M., 1997: The Evolution of Granitoid Magmatism During the Hercynian Orogen in the Western Carpathians. In: Grecula, P., Hovorka, D., Putiš, M. (eds.): Geological evolution of the Western Carpathians. *Bratislava, Miner. Slov. – Monogr., 235–252.*

Poller, U., Uher, P., Broska, I., Plašienka, D. & Janák, M., 2002: First Permian-Early Triassic ages for tin-bearing granites from the Gemeric unit (Western Carpathians, Slovakia): connection to the post-collisional extension of the Variscan orogen and S-type granite magmatism. *Terra Nova, 14, 41–48.*

Putiš, M., Sergeev, S., Ondrejka, M., Larionov, A., Siman, P., Spišiak, J., Uher, P. & Paderin, I., 2008: Cambrian--Ordovician metaigneous rocks associated with Cadomian fragments in the West-Carpathian basement dated by SHRIMP on zircons: a record from the Gondwana active margin setting. *Geol. Carpath., 59, 1, 3–18.*

Putiš, M., Ivan, P., Kohút, M., Spišiak, J., Siman, P., Radvanec, M., Uher, P., Sergeev, S., Larionov, A., Méres, Š., Demko, R. & Ondrejka, M., 2009: Metaigneous rocks of the West--Carpathian basement, Slovakia: indicators of Early Paleozoic extension and shortening events. *Bull. Soc. géol. France, 180, 6, 461–471.*

Radvanec, M. & Grecula, P., 1985: Geochemické anomálie Sn a Mo v rudonosnom vulkanickom horizonte staršieho paleozoika gemerika. *Miner. Slov., 17, 563–568.*

Radvanec, M., 1988: Mobilizácia prvkov v regionálnej metamorfóze staršieho paleozoika gemerika. Kandidátska dizertačná práca. *Manuscript. Praha, archive ČSAV.*

Radvanec, M., Grercula, P., Návesňák, D. & Kobulský, J., 1993: Zonálnosť submarinno-exhalačnej mineralizácie v oblasti Mníška nad Hnilcom a Prakoviec, staršie paleozoikum gemerika. *Miner. Slov., 25, 249–262.*

Radvanec, M. & Iró, S., 1994: Distribúcia a spôsob kryštalizácie Fe karbonátov s ohľadom na výskyt sírnikov a zistenie zdroja SO_2 v dobývacom priestore ložiska Manó v Nižnej Slanej. *Manuscript. Spišská Nová Ves, archive St. Geol. Inst. D. Štúr, 3–34.*

Íro, S. & Radvanec, M., 1997: Chemical and Mineralogical Research of Carbonate Minerals at Nižná Slaná – Mano Deposit (Gemericum, Western Carpathians). *Acta geol. geogr. Univ. Comen., 52, 19–28.*

Radvanec, M. & Prochaska, W., 2001: Successive replacement of Upper Carboniferous calcite to dolomite and magnesite in Dúbrava magnesite deposit (Western Carpathians, Slovakia). *Miner. Slov., 33, 517–525.*

Radvanec, M., Grecula, P. & Žák, K., 2004a: Siderite mineralization of the Gemericum superunit (Western Carpathians, Slovakia): review and revised genetic model. *Ore. Geol. Rev., 24, 3–4, 267–298.*

Radvanec, M., Koděra, P. & Prochaska, W., 2004b: Mg replacement at the Gemerská Poloma talc-magnesite deposit, Western Carpathians, Slovakia. *Acta Petrol. Sin., 20, 4, 773–790.*

Radvanec, M., Konečný, P., Németh, Z. & Grecula, P., 2007: P-T-t dráha a lokálne anatektické tavenie metapelitu s prímesou psamitického kremeňa vo variskej metamorfóze gemerika. *Miner. Slov., 39, 1–44.*

Radvanec, M., Konečný, P., Ondrejka, M., Putiš, M., Uher, P. & Németh, Z., 2009: Granity gemerika ako indikátor extenzie kôry nad neskorovariskou subdukčnou zónou a pri ranoalpínskej riftogenéze (Západné Karpaty): interpretácia podľa veku monazitu a zirkónu datovaného metódou CHIME a SHRIMP. *Miner. Slov., 41, 381–394*.

Radvanec, M., Németh, Z. & Bajtoš, P. (eds.), Koděra, P., Prochaska, W., Roda, Š., Tréger, M., Baláž, P., Grecula, P., Cicmanová, S., Kráľ, J. & Žák, K., 2010: Magnesite and Talc in Slovakia – Genetic and Geoenvironmental Models: Magnezit a talk na Slovensku, genetický a geoenvironmentálny model. *Bratislava, Št. Geol. Úst. D. Štúra, 189 p., ISBN 978-80-89343-31-7.*

Radvanec, M. & Grecula, P., 2016: Geotectonic and metallogenetic evolution of Gemericum (Inner Western Carpathians) from Ordovician to Jurassic. *Miner. Slov., 48, 104–118.*

Radvanec, M., Néhmeth, Z., Kráľ, J. & Pramuka, S., 2017: Variscan dismembered metaophiolite suite fragments of Paleo-Thetys in gemeric unit, Western Carpathians. *Miner. Slov., 49, 1–48.*

Radvanec, M. & Németh, Z., 2018: Variscan epidote-eclogite, blueschists and pumpellyite actinolite facies Cpx/Sr-rich epidote-metagabbro blocks exhumed in Carboniferous, with Permian amphibolite facies overprint (Gemeric unit, Western Carpathians). *Miner. Slov., 50, 55–99.*

Spear, F. S., 1995: Metamorphic Phase Equilibria and Pressure--Temperature-Time Paths. *Monogr. Mineral. Soc. Amer.*

Steiger, R. H. & Jäger, E., 1977: Subcommission on geochronology: convention on the use of decay constants in geo- and cosmochronology. *Earth planet. Sci. Lett., 36, 359–362.*

Sun, S. S. & McDonough, W. F., 1989: Chemical and isotopic systematics of oceanic basalts; implications for mantle composition and processes. In: Saunders, A. D. & Norry, M. J. (eds.): Magmatism in the ocean basins. *London, Geol. Soc. London, 42, 313–345.*

Tauson, L. B., Kozlov, V. D., Cambel, B. & Kamenický, L., 1977: Geochemistry and the problem of ore-bearing capacity of the Gemeride granites of Slovakia. *Geol. Zbor. Geol. carpath., 28, 261–267 (in Russian with English Abstract).*

Taylor, S. R. & McLennan, S. M., 1985: The continental crust: its composition and evolution. *Blackwell, Oxford, 312 p.*

Tropper, P. & Piber, A., 2012: Geothermobarometry of quartzphyllites, orthogneisses and greenschists of the Austroalpine basement nappes in the northern Zillertal (Innsbruck Quartzphyllite Complex, Kellerjochgneiss, Wildschönau Schists; Tyrol, Eastern Alps). *Austrian J. Earth Sci., 105, 3, 80–94.*

Uher, P., Ondrejka, M. & Konečný, P., 2009: Magmatic and post-magmatic Y-REE-Th phosphate, silicate and Nb-Ta-Y--REE oxide minerals in A-type metagranite: an example from the Turčok massif, the Western Carpathians, Slovakia. *Min. Mag., 73, 6, 1009–1025.*

Vozárová, A. & Vozár, J., 1988: Late Paleozoic in West Carpathians. *Bratislava, Geol. Úst. D. Štúra, 1–314.*

Vozárová, A., Šmelko, M. & Paderin, I., 2009: Permian single crystal U-Pb zircon ages of the Rožňava Formation volcanites (Southern Gemeric Unit, Western Carpathians, Slovakia). *Geol. Carpath., 60, 6, 439–448.*

Vozárová, A., Ebner, F., Kovács, S., Kräutner, H.-G., Szederkenyi, T., Krstić, B., Sremac, J., Aljinović, D., Novak, M. & Skaberne, D., 2009a: Late Variscan (Carboniferous to Permian) environments in the Circum Pannonian Region. *Geol. Carpath., 60, 71–104.*

Vozárová, A., Lepekhina, E., Vozár, J. & Rodionov, N., 2010: In situ U-Pb (SHRIMP) zircon age dating from the Permian volcanites of the Northern Veporicum. In: Kohút, M. (ed.): Dating 2010. Dating of minerals and rocks, metamorphic, magmatic and metallogenic processes, as well as tectonic events. Conference Proc., *Bratislava, St. Geol. Inst. D. Štúr, 49 p.*

Vozárová, A., Šmelko, M., Paderin, I. & Larionov, A., 2012: Permian volcanics in Northern Gemericum and Bôrka Nappe system: U-Pb zircon dating and implication to geodynamic evolution (Western Carpathians, Slovakia). *Geol. Carpath., 63, 191–200.*

Vozárová, A., Laurinc, D., Šarinová, K., Larionov, A., Presnyakov, S., Rodionov, N. & Paderin, I., 2013: Pb ages of detrital zircons in relation to geodynamic evolution: Paleozoic of the Northern Gemericum (Western Carpathians, Slovakia). *J. Sed. Res., 83, 915–927.*

Vozárová, A., Presnyakov, S., Šarinová, K. & Šmelko, M., 2015: First evidence for Permian-Triassic boundary volcanism in the Northern Gemericum: geochemistry and U-Pb zircon geochronology. *Geol. Carpath., 66, 5, 375–391.*

Wiedenbeck, M., Allé, P., Corfu, F., Griffin, W. L., Meier, M., Oberli, F., von Quadt, A., Roddick, J. C. & Spiegel, W., 1995: Three natural zircon standards for U-Th-Pb, Lu-Hf, trace element and REE analyses. *Geostandards Newsletter, 19, 1–23.*

Williams, I. S., 1998: U-Th-Pb geochronology by ion microprobe. In: Applications in microanalytical techniques to understanding mineralizing processes. *Rev. Econ. Geol., 7, 1–35.*

Žák, K., Radvanec, M. & Grecula, P., 2005: Siderite mineralization of the Gemericum Superunit (Western Carpathians, Slovakia): review and a revised genetic model (Ore Geol. Rev., 24, 267–298) – a reply. *Ore Geol. Rev., 26, 173–180.*

Analyses of minerals, rocks and mineralizations are in Tabs. 1–12 of the Supplement to this study.

Genetický model permskej hydrotermálnej mineralizácie gemerika od zóny anatektického tavenia v hĺbke po vulkanicko-exhalačnú SedEx mineralizáciu na povrchu

Prezentovaný model vzniku mineralizácie gemerika v permskom uzavretom metamorfno-magmaticko-hydrotermálnom cykle bol vytvorený na základe nového mineralogického, petrologického a geochemického štúdia. Model hodnotí a dopĺňa výsledky doterajšieho poznania vývoja hydrotermálnej mineralizácie a geo-tektonického vývoja gemerika v čase (Radvanec et al., 2010; Radvanec a Grecula, 2016).

Na typových lokalitách Hnilec, Delava, Dlhá dolina, Čučma, Štofova dolina-Rozabela, Strieborná žila, žila Konštancia, Poráč, Krompachy a Kurišková sa hydrotermálne minerálne asociácie permského metamorfno-magmaticko-hydrotermálneho cyklu študovali v granite, v horninách priameho kontaktu s granitom, v horninách exokontaktu granitu, v širšom plášti granitu a vo vulkanitoch a vulkanických brekciách permu (obr. 1). Na presne lokalizovaných vzorkách z vrtov, banských diel a odkryvov sa na týchto typových lokalitách zisťoval vzťah metamorfózy granitov a reziduálnej fluidnej fázy, petrologicky sa hodnotili rovnaké indexové minerály matrixu na horúcej línii (turmalín, sľudy, Mn/Fe/Ca karbonáty, F-apatit ± albit, chlorit, stilpnomelán, topás, goyazit, allanit a kaolinit) a zisťovala sa postupnosť kryštalizácie minerálnych asociácií v závislosti od P-T podmienok ich vzniku. Bola pri tom zohľadnená normalizácia obsahu vzácnych zemín, izokoncetrácia a anomálny a deficitný obsah 62 prvkov v referenčných granitoch a typových mineralizáciách metamorfno-magmaticko-hydrotermálneho cyklu v perme (obr. 2 – 30).

Etalóny rôzneho typu mineralizácie sa vybrali podľa postupnosti ich výskytu a vzdialenosti ich lokalizácie od zóny anatexie v amfibolitovej fácii (amfibolit, granit) cez epidotovo-aktinolitovú fáciu alebo biotitovú zónu s greisenmi (obr. 1). Predmetom detailného štúdia boli greisen z biotitovej zóny a z epidotovo-amfibolitovej línie v zóne anatektického tavenia na typovej lokalite Hnilec, greisenová mineralizácia v chloritovo-apatitovej zóne na typovej lokalite Dlhá dolina, skarn s In sulfidmi v stilpnomelánovo-chloritovej zóne na lokalite Dlhá dolina, žilníková apatitovo-kremeňovo-fengitovo-turmalínová a REE-P-U-Ti mineralizácia v chloritovo-apatitovej zóne metamorfózy na lokalite Čučma, kremeňovo-fengitovo-topásovo-apatitovo-turmalínovo-železitý karbonát, sulfidická mineralizácia v greisene chloritovo-apatitovej zóny z exokontaktu granitu na lokalite Hnilec, kremeňovo-Fe, karbonátovo-apatitovo-turmalínovo-fengitová a Sb sulfidická mineralizácia v chloritovo-apatitovej zóne na žile Rozabela v Štofovej doline, kremeňovo-sideritovo-sulfidická mineralizácia Striebornej žily a žily Konštancia v chloritovej zóne metamorfózy a vtrúseninová sedimentárno-exhalačná fengitovo-apatitovo-karbonátová U-Mo-Cu-Fe SedEx (sedimentárno-exhalačná) mineralizácia z chloritovo-apatitovej zóny vo vulkanicko-sedimentárnych sekvenciách permu na lokalite Krompachy, Kurišková a v tektonickej brekcii na lokalite Poráč. Nové zistenia vysvetľujú vzťah hydrotermálno-exhalačnej uránonosnej SedEx mineralizácie v permských vulkanických sekvenciách gemerika k ostatnej metamorfno-anatektico-hydrotermálnej mineralizácii, ktorá sa v gemeriku vyskytuje v greisene, skarne, žilníkoch a žilách (Bartalský et al., 1973; Grecula et al., 1995). Uránonosná SedEx mineralizácia sa buď geneticky priamo viaže na andezitovo-ryolitový vulkanizmus, alebo sa vyskytuje vo vulkanicko-sedimentárnych sekvenciách v sedimentačných bazénoch, alebo tvorí matrix vo vulkanogénno-pneumatolitických a tektonických brekciách permu (Novotný a Mihál', 1987; Vozárová a Vozár, 1988; Grecula et al., 1995).

O výsledky mineralogického a geochemického štúdia sa opiera aj rekonštrukcia geotektonického vývoja permu v gemeriku, pričom sa vychádza z poznatkov o predchádzajúcom spodnopaleozoickom a karbónskom vývoji. Vývoj mineralizácie v perme gemerika bol najprv podmienený zhrubnutím kontinentálnej kôry kolíziou vo vrchnom karbóne a následným orogénnym kolapsom. V perme bola kolízia vyvrcholením subdukčného procesu s prenosom tepla, volatílií a magmy zo zóny tavenia v hĺbke okolo 100 km, najprv do litosféry a následne z hranice astenosféry (obr. 2; Radvanec, et al., 2007, 2009; Putiš et al., 2009). Tento postupný prenos tepla spôsobil na dvoch paralelných horúcich líniách metamorfózu, ktorá v amfibolitovej fácii vyvrcholila anatektickým tavením vrchnej kôry s dominantným granitovým magmatizmom v spodnom a strednom perme a na povrchu korešpondujúcim andezitovým vulkanizmom (obr. 2). V strednom a vrchnom perme došlo k diferenciácii granitovej magmy s vulkanickým ryolitovým ekvivalentom na povrchu (obr. 3 až 6). Tento mladší magmatizmus bol ovplyvnený prenosom tepla, volatílií a magmy z tavenia subdukovaného materiálu v astenosfére (obr. 2). Diferencované granity a ryolit majú podľa normalizácie obsahom REE geochemickú charakteristiku vrchného plášťa (obr. 4). Táto postupná permská metamorfná a magmatická aktivita mala vo vrchnej kôre sukcesívne usporiadanie v dvoch dominantných horúcich líniách s priebehom V – Z, pričom teplo spôsobilo vyklenutie staropaleozoických sekvencií metasedimentov a metavulkanitov v nadloží anatektického granitu (obr. 1 a 2; Grecula et al., 2009; Radvanec et al., 2010; Radvanec a Grecula, 2016). Vyklenutie horninových sekvencií v osi

gemerika sa prejavilo intenzívnym odstrešovaním od osi vyklenutia smerom na sever aj juh, pričom v severogemerickej zóne otváranie nového bazénu dokladajú polohy zlepencov knolského a petrovohorského súvrstvia krompašskej skupiny a postupne jemnozrnnejších detritických sedimentov (cf. Novotný a Miháľ, 1987). Detrit zlepencov v knolskom súvrství pozostáva z okolitých starších sekvencií a v petrovohorskom súvrství z klastov permských ryolitov a andezitov.

Vyklenutie hornín nad horúcou líniou spôsobilo vejárovité otvorenie krehko-duktilných štruktúr nad granitom a smerom na povrch otvorenie krehkých štruktúr. Vo všetkých týchto štruktúrach od greisenov cez žilníky, skarny až po žily sa zistila rovnaká matrixová minerálna asociácia fengit, kremeň, apatit-F, turmalín a Mn/Fe/Mg/Ca karbonáty ± albit, chlorit, stilpnomelán, topás, goyazit, allanit a kaolinit (obr. 9, 11, 15, 18, 20, 22, 24, 25 a 30). Fengit, apatit-F, turmalín a karbonáty majú podľa chemických vzorcov rovnaké zloženie (tab. 1 – 3). Na kryštalizáciu tejto matrixovej asociácie nemá vplyv pokles teploty od zóny anatexie ~ 650 °C po fáciu zelených bridlíc ~ 300 °C v extenznej oblasti od granitu. V koexistencii s touto matrixovou mineralizáciou z reziduálnej metamorfno-magmatickej fluidnej fázy v závislosti od poklesu teploty smerom k povrchu kryštalizovali rôzne asociácie. Najbližšie ku granitu vznikla mineralizácia greisenov v epidotovo-amfibolitovej fácii a v biotitovej zóne s minerálmi, ktoré vznikli z reziduálne fluidnej fázy s obsahom H_2S, H_2O, CO_2, HF, BO_3, $SnCl_2$, H_3PO_4, Na, K, Ca, Al, Si, Ni, Co, As, Fe, Mn, Mg, Sn, REE, U, Ti, Y, Ta, Nb, Cu, Te, Bi, Pb a Sr (lokalita Hnilec). V chladnejšej chloritovo-apatitovej zóne smerom na povrch bolo zloženie fluidnej fázy, z ktorej vznikol greisen, H_2S, H_2O, CO_2, HF, BO_3, $SnCl_2$, H_3PO_4, Na, K, Ca, Al, Si, Ni, Co, As, Fe, Mg Sn, REE, U, Ti, Y, Ta, Nb, Cu, Sb, Te, Bi, Pb a Zn (lokalita Dlhá dolina). V stilpnomelánovo-chloritovej zóne vnikla minerálna asociácia skarnu z fluidnej fázy H_2S, H_2O, CO_2, HF, BO_3, $SnCl_2$, H_3PO_4, K, Ca, Al, Si, Fe, Mg, REE, U, Ti, Y, Cu, Sb, Te, Bi, Zn a In (lokalita Dlhá dolina). V žilníku v chloritovo-apatitovej zóne vznikla minerálna asociácia z fluidnej fázy H_2S, H_2O, HF, BO_3, H_3PO_4, K, Ca, Al, Si, Fe, REE, U, Ti, Ni, Co, As, Pb, Cu, Sb a Sr (lokalita Čučma). V greisene chloritovo-apatitovej zóny vznikla minerálna asociácia z fluidnej fázy H_2S, H_2O, CO_2, HF, BO_3, H_3PO_4, Na, K, Ca, Al, Si, Fe, REE, As, Pb, Zn, Cu, Bi, Mo a Sb (lokalita Hnilec). V žilách chloritovo-apatitovej zóny vznikla minerálna asociácia z fluidnej fázy H_2S, H_2O, CO_2, HF, BO_3, H_3PO_4, Na, K, Ca, Al, Si, Fe, As, Pb, Cu a Sb (žila Rozabela, Štofova dolina). V žilách chloritovej zóny vnikla mineralizácia z fluidnej fázy H_2S, H_2O, CO_2, Na, K, Ca, Al, Si, Fe, Ni, Co, As, Pb, Bi, Cu, Sb ± HF, BO_3 a H_3PO_4 (žily Konštancia a Strieborná žila). Blízko povrchu a na morskom dne evaporitových bazénov vo vulkanickom perme vznikla v chloritovo-apatitovej zóne SedEx mineralizácia z fluidnej fázy H_2S, H_2O, CO_2, HF, BO_3, H_3PO_4, Na, K, Ca, Al, Si, Fe, Mg, REE, U, Ti, Zn, Pb, Ni, As, Cu, Sb, Mo a Ba (lokalita Kurišková a Poráč).

V uvedených zónach hranice výskytu minerálnych asociácií nie sú striktne vymedzené a zloženie fluidnej fázy sa menilo v závislosti od veku mineralizácie a jej zdroja. Geotektonické pozadie metalogenetického vývoja v spodnom a strednom perme je odvodné od metamorfózy a anatektického tavenia vrchnej kôry a metalogenetický vývoj od stredného po vrchný perm je spojený s vplyvom vrchného plášťa v magmatitoch a vo fluidnej fáze (obr. 38 a 39).

Analýzy minerálov, hornín a mineralizácií sú v tabuľkách 1 až 12 v prílohe tejto štúdie.

Doručené / Received: 15. 7. 2019
Prijaté na publikovanie / Accepted: 2. 12. 2019

Tab. 1
Representative analyses of tourmaline in Permian metamorphic-magmatic-hydrothermal (MMH) cycle in Gemeric unit.

Mineral	Tourmaline	Tourmaline	Tourmaline	Tourmaline	Tourmaline	Tourmaline	Tourmaline	Tourmaline	Tourmaline	Tourmaline	Tourmaline	Tourmaline	Tourmaline	Tourmaline
Locality	Hnilec	Hnilec	Hnilec	Hnilec	Hnilec	Hnilec	Dlhá dolina	Dlhá dolina	Dlhá dolina	Dlhá dolina	Čučma	Čučma	Rozabela	Kurišková
Sample	HD-41	HN-1253	HN-1253	HG-3	HG-3	HG-3	DD-3a	DD-3a	V-DD-43	V-DD-43	CU-1	CU-1	ROZ-4-2	LE-K-29
Place	in Act+Adr	core	rim	core	rim	rim-rim	core	rim	core	rim	matrix	matrix	in Sd	U-SEDEX
Location	Cracks	Greisen	Greisen	Greisen	Greisen	Greisen	Greisen	Greisen	Skarn	Skarn	Vein swarm	Vein swarm	Vein	Chl schist
Zone	Bt/EpAmp	Bt/EpAmp	Bt/EpAmp	Chl-Ap	Chl-Ap	Chl-Ap	Chl-Ap	Chl-Ap	Stp-Chl	Stp-Chl	Chl-Ap	Chl-Ap	Chl-Ap	Chl-Ap
SiO_2	37.26	36.12	37.21	35.29	37.68	37.46	34.91	38.65	35.65	36.53	36.88	35.94	36.20	36.56
TiO_2	0.05	0.37	0.07	0.03	0.10	0.22	0.15	0.10	0.45	0.25	0.27	0.28	0.05	0.06
Al_2O_3	35.28	32.40	34.09	33.13	33.39	32.31	34.33	31.55	34.93	31.94	35.33	32.31	31.58	26.85
FeO	6.98	12.28	4.53	15.69	6.74	6.06	14.90	2.49	14.08	8.83	10.05	13.31	9.09	19.50
MnO	0.00	0.13	0.00	0.33	0.03	0.00	0.19	0.00	0.22	0.04	0.00	0.00	0.28	0.08
MgO	5.57	3.47	8.38	0.02	6.81	7.98	0.75	10.81	0.33	6.53	3.47	3.34	6.30	3.12
CaO	0.10	0.18	0.52	0.04	0.09	0.15	0.14	0.08	0.05	0.09	0.00	0.07	0.35	2.00
Na_2O	1.58	2.06	2.23	1.83	2.09	2.47	2.09	2.10	1.87	2.48	1.92	2.41	2.55	1.90
K_2O	0.02	0.05	0.02	0.03	0.02	0.02	0.01	0.01	0.02	0.04	0.06	0.00	0.00	0.03
V_2O_5	0.00	0.00	0.00	0.00	0.00	0.00	0.00	0.00	0.00	0.00	0.00	0.00	0.05	0.00
B_2O_3	10.78	10.44	10.86	10.17	10.77	10.74	10.34	10.90	10.38	10.60	10.69	10.47	10.51	10.35
F	0.00	0.00	0.00	0.88	0.12	0.20	0.00	1.15	0.00	0.00	0.00	0.00	0.57	0.12
Cl	0.00	0.00	0.00	0.00	0.00	0.00	0.00	0.00	0.00	0.00	0.00	0.00	0.00	0.08
Cr_2O_3	0.01	0.00	0.01	0.00	0.00	0.00	0.00	0.00	0.00	0.00	0.00	0.00	0.00	0.01
H_2O	1.90	1.85	1.91	1.80	1.90	1.90	1.82	1.92	1.83	1.87	1.89	1.85	1.86	1.83
SPOLU	99.53	99.37	99.85	99.23	99.75	99.51	99.63	99.77	99.82	99.21	100.56	99.98	99.39	98.78
Si	6.008	6.011	5.955	6.029	6.083	6.063	5.869	6.16	5.968	5.987	5.993	5.967	5.985	6.141
Al	6.704	6.355	6.429	6.672	6.352	6.164	6.801	5.927	6.891	6.17	6.767	6.323	6.154	5.317
Ti	0.006	0.046	0.009	0.004	0.012	0.027	0.019	0.012	0.056	0.031	0.033	0.035	0.006	0.008
Fe_2	0.941	1.709	0.607	2.242	0.91	0.82	2.094	0.332	1.971	1.211	1.366	1.848	1.257	2.739
Cr	0.001	0	0.001	0	0	0	0	0	0	0	0	0	0	0.001
Mn	0	0.019	0	0.048	0.004	0	0.027	0	0.032	0.006	0	0	0.039	0.012
Mg	1.339	0.861	1.999	0.005	1.639	1.926	0.189	2.569	0.081	1.595	0.841	0.827	1.553	0.782
Ca	0.018	0.033	0.09	0.007	0.016	0.026	0.025	0.014	0.009	0.016	0	0.012	0.062	0.36
Na	0.495	0.665	0.692	0.605	0.653	0.775	0.682	0.648	0.608	0.787	0.605	0.776	0.816	0.618
K	0.004	0.011	0.004	0.007	0.004	0.004	0.002	0.002	0.004	0.008	0.012	0	0	0.007
F	0	0	0	0.477	0.062	0.102	0	0.582	0	0	0	0	0.297	0.066
Cl	0	0.006	0	0	0	0	0	0	0	0	0	0	0	0.024
V	0	0	0	0	0	0	0	0	0	0	0	0	0.005	0
B	3	3	3	3	3	3	3	3	3	3	3	3	3	3
OH	2	2	2	2	2	2	2	2	2	2	2	2	2	2
AlZ	6	6	6	6	6	6	6	6	6	6	6	6	6	6
AlY	0.712	0.366	0.384	0.701	0.435	0.227	0.670	0.087	0.860	0.158	0.760	0.290	0.140	0
X-side vacancy	0.494	0.304	0.236	0.386	0.334	0.201	0.299	0.341	0.384	0.194	0.388	0.215	0.130	0.024
Al/(Al+Fe+Mg)	0.746	0.712	0.712	0.748	0.714	0.692	0.749	0.671	0.771	0.687	0.754	0.703	0.687	0.602
Na/(Na+Ca)	0.965	0.953	0.885	0.989	0.976	0.968	0.965	0.979	0.985	0.980	1.000	0.985	0.929	0.632
Mg/(Mg+Fe)	0.587	0.335	0.767	0.002	0.643	0.701	0.083	0.886	0.040	0.569	0.381	0.309	0.553	0.222

Tab. 2

Representative analyses of biotite, phengite, margarite, topaz, kaolinite, chlorite and stilpnomelane in Permian MMH cycle in Gemeric unit.

Mineral	Biotite	Biotite	Biotite	Phengite	Margarite	Phengite	Topaz	Topaz	Kaolinite	Chlorite	Phengite	Phengite	Phengite	Phengite	Chlorite	Chlorite	Kaolinite	Phengite	Phengite	Stilpnomelane	Phengite	Chlorite	Chlorite	Chlorite	Phengite	Phengite	Phengite	Phengite	Phengite	Phengite	Phengite	Phengite	Chlorite
Locality	Hnilec	Hnilec	Hnilec	Hnilec	Hnilec	Hnilec	Hnilec	Hnilec	Hnilec	Hnilec	Hnilec	Hnilec	Dlhá dolina	Dlhá dolina	Dlhá dolina	Dlhá dolina	Dlhá dolina	Dlhá dolina	Dlhá dolina	Dlhá dolina	Dlhá dolina	Dlhá dolina	Dlhá dolina	Dlhá dolina	Čučma	Čučma	Čučma	Rozabela vein	Poráč	Poráč	Kurišková	Kurišková	Kurišková
Sample	HD-28	HNL-1	VHS-61/54.5	HN-1253	HN-1253	HN-6	HN-6	HN-1253	HN-1253	HN-1253	HG-3	HG-3	DD-2	DD-2	DD-3a	DD-3a	DD-3a	DD-3a	DD-3a	V-DD-43	V-DD-43	V-DD-43	V-DD-43	V-DD-43	CU-1	CU-1	CU-1	ROZ-4-2	G-400	G-400	KGJ-21a	LE-K-29	KGJ-21a
Place	core	matrix	matrix	matrix	matrix	matrix	in Png+Mrg	in Png+Mrg	in Tpz	rim Tpz	in Qtz+ Ank	in Qtz+ Ank	in Qtz+ Ank	in Qtz+ Ank	in Qtz+ Ank	in Qtz+ Ank	in Qtz+ Ank	in Qtz+ Ank	in Qtz+ Ank	matrix	matrix	matrix	matrix	in Py	in matrix+Ap	in matrix+Ap	in matrix+Ap	in Sd	SedEx	SedEx	SedEx	SedEx	SedEx
Location	G1 granite	Greisen	Greisen	Greisen	Greisen	Greisen	Greisen	Greisen	Greisen	Greisen	Greisen	Greisen	Greisen	Greisen	Greisen	Greisen	Greisen	Greisen	Greisen	Skarn	Skarn	Skarn	Skarn	Skarn	Vein swarm	Vein swarm	Vein swarm	Vein	Tect. Brec.	Tect. Brec.	Ands. Tuf	Chl-schist	Ands. Tuf
Zone	Bt/ EpAmp	Bt/ EpAmp	Bt/ EpAmp	Bt/ EpAmp	Bt/ EpAmp	Bt/ EpAmp	Bt/ EpAmp	Bt/ EpAmp	Bt/ EpAmp	Bt/ EpAmp	Chl-Ap	Chl-Ap	Chl-Ap	Chl-Ap	Chl-Ap	Chl-Ap	Chl-Ap	Chl-Ap	Chl-Ap	Chl-Stl	Chl-Stl	Chl-Stl	Chl-Stl	Chl-Stl	Chl-Ap	Chl-Ap	Chl-Ap	Chl-Ap	Chl-Ap	Chl-Ap	Chl-Ap	Chl-Ap	Chl-Ap
SiO_2	34.44	34.67	37.99	49.04	30.27	48.77	32.06	31.75	45.06	26.89	50.16	48.25	48.58	49.88	24.8	36.1	35.19	50.89	52.32	48.79	51.31	27.46	31.1	29.31	48.6	48.14	48.05	46.96	46.42	49.28	47.73	46.33	31.57
TiO_2	2.13	1.77	0	0.19	0	0.01	0.01	0	0	0	0.07	0.01	0.07	0.09	0.02	0	0.01	0.08	0.07	0.02	0.03	0.03	0	0.04	0.26	0.28	0.27	0.22	0.8	0.1	0.19	0.08	0.05
Al_2O_3	17.42	17.27	24.3	28.04	51.21	33.22	56.07	55.71	35.32	17.72	30.22	30.25	32.59	31.34	21.34	37.45	36.96	33.1	29.51	5.59	32.71	17.64	19.78	22.54	31.69	32.03	32.22	35.45	30.61	31.03	30.15	32.7	23.2
Cr_2O_3	0.01	0.09	0.03	0	0.02	0	0	0	0.04	0	0.02	0.03	0.03	0.01	0.01	0	0	0.01	0.02	0	0	0	0	0	0	0.01	0	0.05	0	0.04	0.28	0.01	0.13
FeO	28.43	23.57	20.4	1.9	0.16	0.31	0	0.07	3.52	37.37	1.23	4.88	0.69	0.92	28.26	7	2.21	0.71	1.47	10	0.32	24.15	3.06	5.1	1.75	1.06	1.05	1.31	4.18	1.85	3.58	3.78	14.57
MnO	0.22	0.17	1.32	0.01	0	0	0	0	0.03	0.2	0	0.05	0.03	0	0.25	0.05	0	0	0	0.17	0.04	0.22	0.02	0.02	0.01	0.02	0.01	0	0	0	0.04	0.01	0.05
MgO	2.14	8.16	0.06	3.79	0.05	1.7	0	0	0.73	3.36	2.37	0.88	2.1	2.4	12.17	3.52	1.9	1.62	2.95	7.06	2.87	16.86	32.5	29.46	1.84	2.11	2	0.64	1.25	1.71	2.83	2.3	16.61
CaO	0.02	0.02	0.07	0.04	10.58	0.04	0	0	0.27	0.15	0.06	0.02	0.03	0.04	0.04	0.09	0.16	0.15	0.16	0.22	0.55	0.07	0	0.01	0.09	0.03	0.06	0.05	0.06	0.1	0.05	0.14	0.07
Na_2O	0.04	0.02	0.12	0.1	1.82	0.2	0	0.01	0	0.06	0.12	0.22	0.41	0.26	0.02	0.07	0.06	0.33	0.1	0.25	0.61	0.03	0.02	0.02	0.32	0.37	0.4	0.9	0.36	0.4	0.2	0.59	0
K_2O	9.39	9.14	9.64	9.59	0.05	10.05	0.01	0.01	0.79	0.02	10.62	10.88	10.41	10.23	0	0.89	0.66	8.49	9.41	1.6	9.46	0	0	0.01	10.15	10.44	10.3	9.24	10.36	9.29	9.81	8.99	1.69
F	1.35	0.77	0.12	0.86	0.06	0.85	20.35	19.93	0	0	0.28	0.23	0	0.12	0	0	0	0	0.44	0	0.89	0	0.27	0.24	0	0	0	0	0	0	0	0	0
Cl	0.13	0.11	0.03	0.03	0	0	0	0	0.01	0	0	0	0.01	0	0.02	0.02	0.04	0	0	0.02	0.02	0	0	0	0	0	0	0.01	0	0	0	0	0
H_2O				3.99	5.07	4.11	0.14	0.27	13.49	10.43	4.38	4.32	4.51	4.48	11.08	12.87	12.08	4.62	4.39	2.66	4.27	11.29	12.57	12.46	4.49	4.48	4.48	4.52	4.38	4.47	4.45	4.46	12.21
Total	95.05	95.37	94.02	97.58	99.29	99.26	108.64	107.75	99.26	96.2	99.53	100.02	99.46	99.77	98.01	98.06	89.27	100	100.84	96.91	103.08	97.75	99.32	99.21	99.2	98.97	98.84	99.35	98.42	98.27	99.31	99.39	100.15
O_F_Cl	0.6	0.35	0.06	0.37	0.03	0.36	8.57	8.39	0	0	0.12	0.1	0	0.05	0	0	0.01	0	0.19	0	0.38	0	0.11	0.1	0	0	0	0	0	0	0	0	0
C_{Total}	94.45	95.02	93.96	97.21	99.26	98.9	100.07	99.36	99.26	96.2	99.41	99.92	99.46	99.72	98.01	98.06	89.26	100	100.65	96.91	102.7	97.75	99.21	99.11	99.2	98.97	98.84	99.35	98.42	98.27	99.31	99.39	100.15
Si	5.567	5.427	5.82	6.682	4.003	6.474	0.982	0.979	4.006	6.183	6.672	6.526	6.449	6.591	5.365	6.725	1.746	6.611	6.817	8.229	6.551	5.835	5.875	5.591	6.491	6.44	6.431	6.229	6.361	6.605	6.436	6.228	6.202
Al^{IV}	2.433	2.573	2.18	1.318	3.997	1.526	0.018	0.021	0	1.817	1.328	1.474	1.551	1.409	2.635	1.275	2.16	1.389	1.183	0	1.449	2.165	2.125	2.409	1.509	1.56	1.569	1.771	1.639	1.395	1.564	1.772	1.798
Al^{VI}	0.883	0.611	2.204	3.182	3.979	3.667	2.004	2.003	3.698	2.981	3.406	3.345	3.544	3.468	2.802	6.941	0	3.675	3.345	1.11	3.47	2.249	2.275	2.655	3.475	3.486	3.51	3.766	3.301	3.503	3.224	3.404	3.569
Ti	0.259	0.208	0	0.019	0	0.001	0	0	0	0	0.007	0.001	0.007	0.009	0.003	0	0	0.008	0.007	0.003	0.003	0.005	0	0.006	0.026	0.028	0.027	0.022	0.082	0.01	0.019	0.008	0.007
Fe^{2+}	3.843	3.086	2.614	0.217	0.018	0.034	0	0.002	0.262	7.186	0.137	0.552	0.077	0.102	5.113	1.091	0.092	0.077	0.16	1.41	0.034	4.291	0.483	0.814	0.195	0.119	0.118	0.145	0.479	0.207	0.404	0.425	2.394
Cr	0.001	0.011	0.004	0	0.002	0	0	0	0.003	0	0.002	0.003	0.003	0.001	0.002	0	0	0.001	0.002	0	0	0	0	0	0	0.001	0	0.005	0	0.004	0.03	0.001	0.02
Mn	0.03	0.023	0.171	0.001	0	0	0	0	0.002	0.039	0	0.006	0.003	0	0.046	0.008	0	0	0	0.024	0.004	0.04	0.003	0.003	0.001	0.002	0.001	0	0	0	0.005	0.001	0.008
Mg	0.516	1.904	0.014	0.77	0.01	0.336	0	0	0.097	1.152	0.47	0.177	0.416	0.473	3.925	0.978	0.141	0.314	0.573	1.775	0.546	5.34	9.153	8.378	0.366	0.421	0.399	0.127	0.255	0.342	0.569	0.461	4.864
Ca	0.003	0.003	0.011	0.006	1.499	0.006	0	0	0.026	0.037	0.009	0.003	0.004	0.006	0.009	0.018	0.009	0.021	0.022	0.04	0.075	0.016	0	0.002	0.013	0.004	0.009	0.007	0.009	0.014	0.007	0.02	0.015
Na	0.013	0.006	0.036	0.026	0.467	0.051	0	0.001	0	0.027	0.031	0.058	0.106	0.067	0.008	0.025	0.006	0.083	0.025	0.082	0.151	0.012	0.007	0.007	0.083	0.096	0.104	0.231	0.096	0.104	0.052	0.154	0
K	1.936	1.825	1.884	1.667	0.008	1.702	0	0	0.09	0.006	1.802	1.877	1.763	1.725	0	0.212	0.042	1.407	1.564	0.344	1.541	0	0	0.002	1.729	1.782	1.759	1.564	1.811	1.588	1.688	1.542	0.424
Cations	15.484	15.677	14.938	13.888	13.983	13.797	3.004	3.006	8.184	19.428	13.864	14.022	13.923	13.851	19.908	17.273	4.196	13.586	13.698	15.62	13.824	19.953	19.921	19.867	13.888	13.939	13.927	13.867	14.033	13.772	13.998	14.016	19.301
CF	1.38	0.762	0.116	0.741	0.05	0.714	3.941	3.889	0	0	0.236	0.197	0	0.1	0	0	0	0	0.363	0	0.719	0	0.323	0.29	0	0	0	0	0	0	0	0	0
CCl	0.071	0.058	0.016	0.014	0	0	0	0	0.003	0	0	0	0.005	0	0.015	0.013	0.007	0	0	0.011	0.009	0	0	0	0	0	0	0.004	0	0	0	0	0
OH	0	0	0	3.622	4.475	3.643	0.029	0.056	7.998	16	3.882	3.902	3.998	3.95	15.993	15.994	3.997	4	3.819	2.994	3.636	16	15.839	15.855	4	4	4	3.998	4	4	4	4	16
O	22	22	22	24	24	24	6	6	18	36	24	24	24	24	36	36	9	24	24	27	24	36	36	36	24	24	24	24	24	24	24	24	36
Mg/(Fe+Mg)	0.12	0.38	0.01	0.78	0.36	0.91	0.00	0.00	0.27	0.14	0.77	0.24	0.84	0.82	0.43	0.47	0.61	0.80	0.78	0.56	0.94	0.55	0.95	0.91	0.65	0.78	0.77	0.47	0.35	0.62	0.58	0.52	0.67

Tab. 3
Representative analyses of apatite in Permian MMH cycle in Gemeric unit.

Mineral	Ap-F	Ap-F	Ap-F	Ap-F	Ap-F	Ap-F	Ap-F	Ap-F	Ap-F	Ap-F	Ap-F	Ap-F
Locality	Hnilec	D. dolina	D. dolina	Hnilec	Hnilec	Čučma	D. dolina	D. dolina	Rozabela	Poráč	Kurišková	Kurišková
Sample	HN-1253	DD-2	DD-3a	HN-133	HN-133	Cu-17-1	VSV-05-2	V-DD-43-1	ROZ-4-2	G-400	KGJ-21A	LE-K-29
Place	Cst-Ms	Cst-sulf.	Cst-sulf.	core	rim	Mnz-Xtm-U	Mgh-Cst	Mgh-Cst	Mgh-Cst	U-SedEx	U-SedEx	U-SedEx
Location	Greisen	Greisen	Greisen	Greisen	Greisen	Vein swarm	Skarn	Skarn	Vein Sb	Tec. breccia	Andesite	Chl. schist
Zone	Bt	Chl-Ap	Chl-Ap	Chl-Ap	Chl-Ap	Chl-Ap	Chl-Stp	Chl-Stp	Chl-Ap	Chl-Ap	Chl-Ap	Chl-Ap
SiO_2	0	0.21	0.01	0.09	0.02	0	0.05	0	0.27	0	0	0
Al_2O_3	0	0.02	0.01	0.03	0	0	0	0.02	0.01	0	0	0.11
FeO	0.08	0.12	0.13	0.3	0	0.14	0.64	0.17	0.25	0	0.32	0.21
MnO	0.85	6.54	0	3.41	0.1	0.06	0.03	0.05	0.18	0.04	0.04	0.01
MgO	0.01	0	0.01	0	0	0	0	0	0	0	0	0
SrO	0.29	0	0.06	0	0	0.14	0	0.09	0	0.14	0.16	0.14
Y_2O_3	0	0.03	0	0.17	0.16	0.07	0	0	0.09	0	0.13	0
UO_2	0	0.64	0	0	0.02	0.07	0	0	0.02	0	0.03	0.14
ThO_2	0	0.47	0	0.01	0	0	0	0	0	0	0.02	0
CaO	55.44	47.95	55.22	51.83	55.69	55.57	55.51	54.98	54.53	55.69	54.7	56.17
Na_2O	0.06	0.19	0	0.06	0.03	0	0	0	0.13	0	0	0
K_2O	0	0	0	0	0	0	0	0	0	0	0	0
P_2O_5	41.88	40.41	41.56	40.54	40.91	42.42	42.3	42.79	40.97	41.7	43.28	42.88
La_2O_3	0.02	0	0	0	0.03	0	0	0	0.22	0	0.14	0
Ce_2O_3	0	0	0	0.1	0	0.1	0	0	0.56	0	0.57	0.03
Nd_2O_3	0.02	0.03	0	0.03	0.03	0.07	0	0	0.32	0	0.35	0
SO_3	0	0	0.03	0	0	0	0.15	0.02	0	0	0	0
F	3.73	3.69	4.05	4.53	4.64	3.79	3.2	4.34	4.02	4.5	2.85	3.7
Cl	0.02	0.05	0	0.08	0.01	0.02	0.04	0	0.03	0.04	0.32	0.12
Total	102.4	100.35	101.08	101.18	101.64	102.45	101.92	102.46	101.6	102.1	102.91	103.51
O_F_Cl	1.58	1.56	1.71	1.93	1.96	1.6	1.36	1.83	1.7	1.9	1.27	1.58
C_{Total}	100.82	98.79	99.37	99.25	99.68	100.85	100.56	100.63	99.9	100.2	101.64	101.93
Fe_2	0.006	0.009	0.009	0.022	0	0.01	0.045	0.012	0.018	0	0.022	0.014
Mn	0.06	0.482	0	0.249	0.007	0.004	0.002	0.004	0.013	0.003	0.003	0.001
Mg	0.001	0	0.001	0	0	0	0	0	0	0	0	0
Sr	0.014	0	0.003	0	0	0.007	0	0.004	0	0.007	0.008	0.007
Ca	4.98	4.468	5.018	4.788	5.088	4.97	4.956	4.916	4.973	5.038	4.842	4.966
Na	0.01	0.032	0	0.01	0.005	0	0	0	0.021	0	0	0
K	0	0	0	0	0	0	0	0	0	0	0	0
Si	0	0.018	0.001	0.008	0.002	0	0.004	0	0.023	0	0	0
P	2.973	2.976	2.984	2.959	2.954	2.998	2.984	3.023	2.952	2.981	3.027	2.996
Y	0	0.001	0	0.008	0.007	0.003	0	0	0.004	0	0.006	0
Th	0	0.009	0	0	0	0	0	0	0	0	0	0
U	0	0.012	0	0	0	0.001	0	0	0	0	0.001	0.003
La	0.001	0	0	0	0.001	0	0	0	0.007	0	0.004	0
Ce	0	0	0	0.003	0	0.003	0	0	0.017	0	0.017	0.001
Nd	0.001	0.001	0	0.001	0.001	0.002	0	0	0.01	0	0.01	0
Al	0	0.002	0.001	0.003	0	0	0	0.002	0.001	0	0	0.011
S	0	0	0.002	0	0	0	0.009	0.001	0	0	0	0
Cations	8.046	8.01	8.019	8.051	8.065	7.998	8	7.962	8.039	8.029	7.94	7.999
CF	1.978	2.03	2.172	2.47	2.503	2.001	1.687	2.291	2.164	2.401	1.489	1.931
CCl	0.006	0.015	0	0.023	0.003	0.006	0.011	0	0.009	0.011	0.09	0.034
O	13	13	13	13	13	13	13	13	13	13	13	13

Tab. 4
Representative analyses of carbonates in Permian MMH cycle in Gemeric unit.

	Mineral	Locality	Sample	Place	Location	Zone	FeO	MnO	MgO	CaO	CO_2	Total	Fe	Mn	Mg	Ca	$CaCO_3$	$MgCO_3$	$FeCO_3$	$MnCO_3$
	Dolomite	Hnilec	HD-28	matrix+Ab	Granite G1	Bt/EpAmp	3.86	0.47	19.21	29.57	46.65	99.76	0.05	0.006	0.448	0.495	49.5	44.8	5	0.6
	Ankerite	Hnilec	HD-28	matrix+Qtz	Granite G1	Bt/EpAmp	7.57	2.94	12.67	31.92	45.24	100.33	0.102	0.04	0.305	0.553	55.3	30.5	10.2	4
	Siderite	Hnilec	HD-28	matrix+Png	Granite G1	Bt/EpAmp	53.32	0.35	6.08	0.63	40.02	100.39	0.816	0.005	0.166	0.012	1.2	16.6	81.6	0.5
	Calcite	Hnilec	HN-6	in Png	Greisen	Bt/EpAmp	0.95	0.56	0.33	54.59	44.01	100.44	0.013	0.008	0.008	0.971	97.1	0.8	1.3	0.8
	Kutnahorite	Hnilec	HN-6	in Png+Tur	Greisen	Bt/EpAmp	18.21	6.91	5.09	27.46	42.43	100.10	0.262	0.101	0.131	0.506	50.6	13.1	26.2	10.1
	Kutnahorite	Hnilec	HN-1253	in Png+Tur	Greisen	Bt/EpAmp	12.31	13.38	4.99	26.79	42.42	99.72	0.178	0.196	0.129	0.497	49.7	12.9	17.8	19.6
	Rhodochrosite	Hnilec	HN-6	in Png+Tur	Greisen	Bt/EpAmp	10.73	46.18	3.14	0.49	39.25	99.78	0.168	0.734	0.088	0.01	1	8.8	16.8	73.4
	Dolomite	Hnilec	HD-41	in Tur+Ap	Greisen	Bt/EpAmp	5.46	2	15.52	31.52	46.21	100.71	0.072	0.027	0.366	0.535	53.5	36.6	7.2	2.7
	Ankerite	Hnilec	HN-6	Ab+Tur+Qtz	Greisen	Bt/EpAmp	11.83	0.67	14.33	27.6	44.89	99.32	0.161	0.009	0.348	0.482	48.2	34.8	16.1	0.9
	Ankerite	Dlhá dolina	DD-3a	in Png+Tur	Greisen	Chl-Ap	15.71	1.21	10.55	28.31	44.10	99.88	0.218	0.017	0.261	0.504	50.4	26.1	21.8	1.7
	Siderite	Dlhá dolina	DD-3a	in Png+Tur	Greisen	Chl-Ap	48.38	0.59	9.7	0.65	41.11	100.43	0.721	0.009	0.258	0.012	1.2	25.8	72.1	0.9
	Calcite	Hnilec	HG-3	relict	Greisen	Chl-Ap	1.04	0.63	0.14	54.43	43.98	100.23	0.014	0.009	0.004	0.973	97.3	0.4	1.4	0.9
	Dolomite	Hnilec	HG-3	in Png	Greisen	Chl-Ap	8.91	1.52	13.42	30.65	45.33	99.83	0.121	0.021	0.325	0.533	53.3	32.5	12.1	2.1
	Ankerite Mn	Hnilec	HG-3	in Mo	Greisen	Chl-Ap	15.36	7.22	5.47	29.11	42.75	99.91	0.22	0.105	0.14	0.535	53.5	14	22	10.5
	Ankerite Mn	Hnilec	HG-3	Ap+Qtz	Greisen	Chl-Ap	17.7	5.4	5.45	28.79	42.69	100.03	0.254	0.078	0.139	0.529	52.9	13.9	25.4	7.8
	Siderite	Hnilec	HG-3	In Png+Tur	Greisen	Chl-Ap	51.1	0.73	7.02	1.3	40.49	100.64	0.774	0.011	0.19	0.025	2.5	19	77.4	1.1
	Calcite	Dlhá dolina	V-DD-43	Limest.-rel.	Skarn	Chl-Stp	0.83	1.05	0.34	54.11	43.79	100.11	0.012	0.015	0.008	0.966	96.6	0.8	1.2	1.5
	Dolomite	Dlhá dolina	V-DD-43	contact	Skarn	Chl-Stp	2.16	0.29	20.68	29.45	47.17	99.75	0.028	0.004	0.478	0.489	48.9	47.8	2.8	0.4
	Ankerite	Dlhá dolina	V-DD-43	contact	Skarn	Chl-Stp	14.48	0.88	11.70	28.74	44.60	100.39	0.198	0.012	0.285	0.504	50.4	28.5	19.8	1.2
	Magnesite Fe	Dlhá dolina	V-DD-43	in Py	Skarn	Chl-Stp	34.99	1.21	19.96	0.15	44.02	100.33	0.486	0.017	0.494	0.003	0.3	49.4	48.6	1.7
	Sidrite	Dlhá dolina	V-DD-43	matrix+Cst	Skarn	Chl-Stp	50.15	0.33	8.71	0.36	40.77	100.32	0.754	0.005	0.234	0.007	0.7	23.4	75.4	0.5
	Dolomite	Dlhá dolina	VSV-05-2	contact	Skarn	Chl-Stp	2.77	0.27	20.91	28.89	47.21	100.04	0.036	0.004	0.482	0.479	47.9	48.2	3.6	0.4
	Dolomite	Dlhá dolina	VSV-05-2	contact	Skarn	Chl-Stp	5.88	0.19	18.59	28.69	46.70	100.05	0.077	0.003	0.436	0.484	48.4	43.6	7.7	0.3
	Ankerite	Dlhá dolina	VSV-05-2	contact	Skarn	Chl-Stp	11.83	0.67	14.33	27.6	44.89	99.32	0.161	0.009	0.348	0.482	48.2	34.8	16.1	0.9
	Magnesite	Dlhá dolina	VSV-05-2	contact	Skarn	Chl-Stp	3.73	0.24	44.31	0.71	51.37	100.36	0.044	0.003	0.942	0.011	1.1	94.2	4.4	0.3
	Magnesite Fe	Dlhá dolina	VSV-05-2	contact	Skarn	Chl-Stp	16.33	1.05	34.38	0.09	48.25	100.11	0.207	0.013	0.777	0.002	0.2	77.7	20.7	1.3
	Magnesite Fe	Dlhá dolina	VSV-05-2	contact	Skarn	Chl-Stp	21.46	0.53	30.67	0.13	46.90	99.69	0.279	0.007	0.712	0.002	0.2	71.2	27.9	0.7
	Magnesite Fe	Dlhá dolina	VSV-05-2	contact	Skarn	Chl-Stp	29.61	0.76	24.21	0.08	45.23	99.89	0.402	0.011	0.586	0.001	0.1	58.6	40.2	1.1
	Siderite Mg	Dlhá dolina	VSV-05-2	contact	Skarn	Chl-Stp	38.68	1.32	16.75	0.47	43.08	100.3	0.549	0.019	0.424	0.009	0.9	42.4	54.9	1.9
	Siderite Mg	Dlhá dolina	VSV-05-2	contact	Skarn	Chl-Stp	44.12	0.55	12.68	0.77	41.97	100.09	0.646	0.008	0.331	0.014	1.4	33.1	64.6	0.8
	Siderite	Dlhá dolina	VSV-05-2	matrix+Cst	Skarn	Chl-Stp	54.29	0.36	5	0.31	39.17	99.13	0.849	0.006	0.139	0.006	0.6	13.9	84.9	0.6
	Ankerite	Rozabela	ROZ-4-2	in Sb sulp.	Vein	Chl-Ap	13.55	0.36	13.44	27.88	45.08	100.30	0.184	0.005	0.325	0.485	48.55	32.53	18.42	0.5
	Siderite	Rozabela	ROZ-1-2	in Sb sulp.	Vein	Chl-Ap	48.39	1.63	8.87	0.18	40.49	99.56	0.732	0.025	0.239	0.003	0.3	23.92	73.27	2.5
	Siderite	Konštancia	53-150-5	in Sulp.	Sd vein	Chl	53.72	3.03	3.81	0.34	39.12	100.02	0.839	0.048	0.106	0.007	0.7	10.6	83.9	4.8
	Siderite	Konštancia	53-150-5	in Sulp.	Sd vein	Chl	59.01	1.08	1.67	0.15	38.73	100.64	0.932	0.017	0.047	0.003	0.3	4.7	93.2	1.7
	Siderite	Strieborná	STZ-6-2	in Sulp.	Sd vein	Chl	50.76	2.62	6.33	0.23	40.05	99.99	0.781	0.041	0.174	0.005	0.5	17.4	78.1	4.1
	Siderite	Strieborná	STZ-6-2	in Sulp.	Sd vein	Chl	55.96	2.66	2.39	0.06	38.65	99.72	0.888	0.043	0.068	0.001	0.1	6.8	88.8	4.3

Tab. 5
Representative analyses of oxides in Hnilec locality. Permian MMH cycle in Gemeric unit.

Mineral	Uraninite	U-Polycrase	U-Polycrase	Nb-Rutile	Mn-Columbite	Ta-Polycrase	Ta-Polycrase	Th-Crasite(?)	U-Kobeite	Cassiterite	Cassiterite
Locality	Hnilec	Hnilec	Hnilec	Hnilec	Hnilec	Hnilec	Hnilec	Hnilec	Hnilec	Hnilec	Hnilec
Sample	HN-1253	HN-1253	HN-1253	HN-1253	HN-1253	HN-1253	HN-1253	HN-1253	HN-1253	HN-1253	HN-1253
Place	in Cst	core	core	core	in Cst	in Cst	in Cst	rim	rim	matrix	matrix
Location	Greisen	Greisen	Greisen	Greisen	Greisen	Greisen	Greisen	Greisen	Greisen	Greisen	Greisen
Zone	Bt/EpAmp	Bt/EpAmp	Bt/EpAmp	Bt/EpAmp	Bt/EpAmp	Bt/EpAmp	Bt/EpAmp	Bt/EpAmp	Bt/EpAmp	Bt/EpAmp	Bt/EpAmp
CaO	0	1.44	2	0.01	0	1.56	1.96	0.47	0.63	0	0
Ta_2O_5	0	2.81	3.69	1.07	16.5	30.74	24.8	0.01	4.8	0.48	0
WO_3	0	1.44	1.09	0	2.89	1.14	1.15	0.4	0.19	0	0
TiO_2	0	28	27.1	89.45	2.42	18.99	19.85	3.72	44.59	0.83	0.74
FeO	0	2.87	3	2.57	8.88	0	0	1.23	3.88	0.18	0.16
Fe_2O_3	0	0	0	0	0	1.17	2.63	0	0	0	0
MnO	0	0.36	0.31	0	10.85	0.05	0.19	0.17	0.13	0	0
ZnO	0	0	0.03	0	0	0	0.01	0.04	0.11	0.09	0
Sc_2O_3	0	0	0	0	0.25	0.05	0.04	0	0.03	0.03	0
SnO2	0	0.05	0.03	0	0.31	0.07	0.04	0.18	0.12	97.35	97.65
Y_2O_3	0.12	7.25	7.1	0	0	15.41	12.23	0.52	0.37	0	0
UO_2	89.80	29.77	26.48	0	0.15	3.12	7.73	35.72	18.33	0	0
ZrO_2	0	0.06	0.14	0.05	0.21	0.02	0.1	0.09	0.29	0	0.08
Nb_2O_5	0	13.14	14.3	5.44	58.6	13.94	13.36	3.92	12.54	0.39	0.14
MgO	0	0	0	0	0.01	0	0	0.04	0.09	0.14	0.16
ThO_2	5.94	2.17	2.84	0	0	0.83	2.3	35.64	2.34	0	0
SiO_2	0.06	0.15	0.28	0	0	0	0	9.46	4.71	0	0
La_2O_3	0	0	0	0	0	0.01	0	0	0.03	0	0
Ce_2O_3	0.07	0.15	0.11	0	0	0.14	0.08	0.12	0.39	0	0
Pr_2O_3	0.33	0.2	0.17	0	0	0.27	0.21	0.22	0.14	0	0
Nd_2O_3	0	0.12	0.13	0	0	0.76	0.25	0.05	0.13	0	0
Sm_2O_3	0.16	0.34	0.45	0	0	1.6	0.88	0.09	0.04	0	0
Eu_2O_3	0.24	1.05	0.37	0	0	0.44	0.53	0.26	0.25	0	0
Gd_2O_3	0.04	0.99	1.13	0	0	3.08	2.24	0.2	0.16	0	0
Tb_2O_3	0.04	0.33	0.4	0	0	0.6	0.66	0.11	0.04	0	0
Dy_2O_3	0.05	2.24	2.83	0	0	3.14	4.09	0.23	0.13	0	0
Ho_2O_3	0.00	0.29	0.36	0	0	0.27	0.46	0.04	0	0	0
Er_2O_3	0.49	1.52	1.69	0	0	1.03	1.68	0.5	0.32	0	0
Tm_2O_3	0.08	0.37	0.42	0	0	0.87	0.8	0.14	0.18	0	0
Yb_2O_3	0.18	1.15	1.27	0	0	0.99	1.46	0.36	0.17	0	0
Lu_2O_3	0.10	0.44	0.25	0	0	0.25	0.24	0.13	0.09	0	0
BaO	0	0	0	0	0	0	0	0	0	0	0
PbO	2.25	0	0	0	0	0	0	0	0	0	0
Sb_2O_3	0	0	0	0	0	0	0	0	0	0.29	0.26
H_2O	0	1.16	1.29	0	0	0	0	0.41	0	0	0
Total	99.99	99.86	99.26	98.59	101.07	100.54	99.97	94.47	95.22	99.78	99.19
Ti	0	1.359	1.307	0.937	0.108	0.953	1.007	0.253	1.841	0.016	0.014
Fe_3	0	0	0	0	0	0.059	0.133	0	0	0	0
Fe_2	0	0.155	0.161	0.03	0.442	0	0	0.093	0.178	0.004	0.003
Ta	0	0.049	0.064	0.004	0.267	0.558	0.455	0	0.072	0.003	0
Mn	0	0.02	0.017	0	0.547	0.003	0.011	0.013	0.006	0	0
Mg	0	0	0	0	0.001	0	0	0.005	0.007	0.005	0.006
Ca	0	0.1	0.137	0	0	0.111	0.142	0.046	0.037	0	0
W	0	0.024	0.018	0	0.045	0.02	0.02	0.009	0.003	0	0
Zn	0	0	0.001	0	0	0	0	0.003	0.004	0.002	0
Sc	0	0	0	0	0.013	0.003	0.002	0	0.001	0.001	0
Sn	0	0.001	0.001	0	0.007	0.002	0.001	0.006	0.003	0.967	0.976
Y	0.003	0.249	0.242	0	0	0.546	0.438	0.025	0.011	0	0
U	0.897	0.427	0.378	0	0.002	0.046	0.116	0.718	0.224	0	0
Zr	0	0.002	0.004	0	0.006	0.001	0.003	0.004	0.008	0	0.001
Nb	0	0.383	0.414	0.034	1.577	0.42	0.407	0.16	0.311	0.004	0.002
Th	0.061	0.032	0.041	0	0	0.013	0.035	0.733	0.029	0	0
Si	0.003	0.01	0.018	0	0	0	0	0.855	0.259	0	0
La	0	0	0	0	0	0	0	0	0.001	0	0
Ce	0.001	0.004	0.003	0	0	0.003	0.002	0.004	0.008	0	0
Pr	0.005	0.005	0.004	0	0	0.007	0.005	0.007	0.003	0	0
Nd	0	0.003	0.003	0	0	0.018	0.006	0.002	0.003	0	0
Sm	0.003	0.008	0.01	0	0	0.037	0.02	0.003	0.001	0	0
Eu	0.004	0.02	0.01	0	0	0.01	0.01	0.01	0	0	0
Gd	0.001	0.021	0.024	0	0	0.068	0.05	0.006	0.003	0	0
Tb	0.001	0.007	0.008	0	0	0.013	0.015	0.003	0.001	0	0
Dy	0.001	0.047	0.058	0	0	0.067	0.089	0.007	0.002	0	0
Ho	0	0.006	0.007	0	0	0.006	0.01	0.001	0	0	0
Er	0.007	0.031	0.034	0	0	0.022	0.036	0.014	0.006	0	0
Tm	0.001	0.007	0.008	0	0	0.018	0.017	0.004	0.003	0	0
Yb	0.003	0.023	0.025	0	0	0.02	0.03	0.01	0.003	0	0
Lu	0.001	0.009	0.005	0	0	0.005	0.005	0.004	0.001	0	0
Ba	0	0	0	0	0	0	0	0	0	0	0
Pb	0.027	0	0	0	0	0	0	0	0	0	0
Sb	0	0	0	0	0	0	0	0	0	0.003	0.003
Cations	1.020	3.002	3.002	1.005	3.015	3.029	3.065	2.998	3.029	1.005	1.005
OH	0	0.5	0.55	0	0	0	0	0.25	0	0	0
O	2	6	6	2	6	6	6	6	6	2	2

Tab. 6
Representative analyses of U-Ti-Sr-P minerals in Čučma and Kurišková localities. Permian MMH cycle Gemeric unit.

Mineral	Ort-brannerite	Monazite	Xenotime	Goyazite	Goyazite	Met-Aunite	Met-Aunite	Vyacheslavite	New	Uraninite	Met-Ca uranite	Met-Ca uranite	Ca uranoite	Coffinite	Ort-brannerite
Locality	Čučma	Čučma	Čučma	Čučma	Čučma	Čučma	Čučma	Čučma	Čučma	Kurišková	Kurišková	Kurišková	Kurišková	Kurišková	Kurišková
Sample	CU-17-1	CU-1	CU-17-1	CU-17-1	CU-17-1	CU-1	CU-1	CU-17-1	CU-1	KGJ-21a	KGJ-21a	KGJ-21a	KGJ-21a	LE-K-29	LE-K-29
Place	in Png	in matrix+Ap	in matrix+Ap	in Xtn	in Xtn	in matrix+Ap	in matrix+Ap	in Xtn	in matrix+Ap	matrix	in Png	matrix	in Png	matrix	in Png
Location	Vein swarm	Vein swarm	Vein swarm	Vein swarm	Vein swarm	Vein swarm	Vein swarm	Vein swarm	Vein swarm	SedEx	SedEx	SedEx	SedEx	SedEx	SedEx
Zone	Chl-Ap	Chl-Ap	Chl-Ap	Chl-Ap	Chl-Ap	Chl-Ap	Chl-Ap	Chl-Ap	Chl-Ap	Chl-Ap	Chl-Ap	Chl-Ap	Chl-Ap	Chl-Ap	Chl-Ap
CaO	1.01	0.35	0.30	0.34	0.53	6.72	6.72	0.07	2.41	0.92	4.49	5.24	5.07	3.11	1.73
TiO_2	36.19	0	0.05	0.01	0	0	0	0.02	38.01	0.11	0.28	0.05	0.11	0.23	35.22
FeO	0.00	0	0	0.13	0.12	0	0	0	6.11	0.08	0.01	0.22	0.38	0.49	1.09
Fe_2O_3	3.99	0	5.10	0.00	0	0	0	0	0	0	0	0	0	0	0
SrO	0	0.01	0	13.14	6.67	0.37	0.37	0	0.18	0	0	0	0	0	0
Al_2O_3	0	0	0.07	30.37	30.33	0	0	0.09	0	0.01	0.22	1.09	3.37	1.58	0.16
P_2O_5	0	29.54	32.90	30.05	29.43	16.12	16.12	18.12	11.21	0.05	0.52	0.98	2.82	0.95	0.03
MnO	0.08	0	0.03	0.04	0.02	0	0	0	0.03	0.02	0.22	0.04	0.04	0.08	0
ZnO	0	0	0	0	0	0	0	0	0	0	0	0	0	0	0
Y_2O_3	0.27	1.11	40.11	0.01	0.01	0.03	0.03	0.03	0.13	0.23	0.20	0.14	0.32	0.47	0
UO_2	53.52	0.19	1.59	0.02	0.05	68.82	68.82	67.72	14.41	94.49	85.32	80.41	71.94	73.38	55.91
Nb_2O_5	0	0	0	0	0	0	0	0	0	0	0	0	0	0	0
MgO	0	0	0	0.01	0.05	0	0	0.04	0.12	0.04	0	0.14	0.50	0.14	0.06
ThO_2	0	0	0.02	0	0.01	0	0	0	0.05	0	0	0	0	0	0
La_2O_3	0	7.94	0	1.77	3.56	0	0	0	0	0	0	0	0	0	0
Ce_2O_3	0.15	23.46	0.09	5.08	9.06	0	0	0.03	0.28	0.13	0.21	0.10	0.20	0.10	0.14
Pr_2O_3	0.34	4.21	0.10	0.82	1.37	0.21	0.21	0.22	0.13	0.25	0.32	0.32	0.36	0.44	0.20
Nd_2O_3	0.09	22.30	0.10	3.67	6.17	0	0	0	0.11	0	0.04	0	0.15	0.02	0
Sm_2O_3	0.14	6.02	0.87	0.94	1.58	0	0	0.01	0.09	0	0.01	0.02	0.01	0.10	0
Eu_2O_3	0.40	0.21	0.11	0.11	0.12	0.15	0.15	0.27	0.12	0.08	0.34	0.27	0.24	0.44	0.14
Gd_2O_3	0.30	2.17	4.03	0.26	0.29	0.14	0.14	0.08	0.17	0.25	0.23	0.28	0.25	0.24	0.14
Tb_2O_3	0.05	0.17	0.97	0	0	0.07	0.07	0.04	0.10	0.05	0.05	0.03	0.11	0	0.02
Dy_2O_3	0.03	0.56	6.69	0.04	0.05	0.03	0.03	0.06	0.08	0.05	0.01	0	0.01	0	0
Ho_2O_3	0.12	0	0.83	0.03	0.04	0	0	0.02	0.04	0.05	0.00	0	0.15	0.01	0.04
Er_2O_3	0.36	0.33	3.53	0.16	0.08	0.16	0.16	0.26	0.25	0.66	0.52	0.42	0.61	0.45	0.55
Tm_2O_3	0.12	0.11	0.61	0	0	0.03	0.03	0.11	0.11	0.11	0.08	0.15	0.02	0.11	0.07
Yb_2O_3	0.35	0.15	2.81	0.08	0.09	0.05	0.05	0.06	0.27	0.29	0.28	0.13	0.30	0.15	0.06
Lu_2O_3	0.25	0.02	0.15	0.17	0.27	0	0	0	0	0	0	0.13	0.10	0.20	0.10
CuO	0	0	0	0	0	0	0	0	0	0	0	0	0	0	0
As_2O_5	0	0	0	0	0	0	0	0	0	0	0	0	0	0	0
SO_3	0	0.07	0	0	0	0	0	0	0	0	0	0	0	0	0
SiO_2	0	0.21	0	0	0	0	0	0	0	0	0	0	0	15.99	0
PbO	0.85	0	0	0.02	0	0	0	0	8.74	2.18	1.38	0	0.04	0	1.21
F	0	0	0	0.46	0	0	0	0	0	0	0	0	0	0	0
Cl	0	0	0.01	0.01	0.02	0	0	0.03	0.05	0.05	0.01	0.01	0.02	0.00	0.03
H_2O	1.12	0	0.00	8.10	7.89	5.79	5.79	2.57	7.03	0	0	0	0	1.19	1.89
Total	99.73	99.12	101.07	95.84	97.81	98.69	98.69	89.85	90.23	100.12	94.75	90.20	87.10	99.85	98.79
Ti	1.826	0	0.001	0.001	0	0	0	0.001	6.085	0.004	0.009	0.006	0.011	0.009	4.194
Fe_3	0.201	0	0.129	0	0	0	0	0	0	0	0	0	0	0	0
Fe_2	0	0	0	0.009	0.008	0	0	0	1.087	0.003	0	0.027	0.043	0.021	0.144
Mn	0	0	0.001	0.003	0.001	0	0	0	0.005	0.001	0.008	0.006	0.004	0.004	0
Mg	0.005	0	0	0.001	0.006	0	0	0.004	0.038	0.003	0	0.032	0.099	0.010	0.014
Ca	0.073	0.089	0.011	0.030	0.046	0.392	0.392	0.005	0.550	0.044	0.207	0.837	0.729	0.168	0.293
P	0	5.948	0.938	2.063	2.035	0.742	0.742	0.983	2.020	0.002	0.019	0.124	0.320	0.040	0.004
Zn	0	0	0	0	0	0	0	0	0	0	0	0	0	0	0
Al	0	0	0.003	2.900	2.917	0	0	0.007	0	0.001	0.011	0.192	0.532	0.094	0.030
Y	0.01	0.141	0.718	0	0	0.001	0.001	0.001	0.015	0.005	0.005	0.011	0.023	0.013	0
U	0.799	0.010	0.012	0	0.001	0.833	0.833	0.966	0.682	0.930	0.817	2.667	2.149	0.824	1.970
Sr	0	0.001	0	0.618	0.316	0.012	0.012	0	0.022	0	0	0	0	0	0
Nb	0	0	0	0	0	0	0	0	0	0	0	0	0	0	0
Th	0	0	0	0	0	0	0	0	0.002	0	0	0	0	0	0
La	0	0.697	0	0.053	0.107	0	0	0	0	0	0	0	0	0	0
Ce	0.004	2.043	0.001	0.151	0.271	0	0	0.001	0.022	0.002	0.003	0.005	0.010	0.002	0.008
Pr	0.008	0.365	0.001	0.024	0.041	0.004	0.004	0.005	0.010	0.004	0.005	0.017	0.018	0.008	0.012
Nd	0.002	1.894	0.001	0.106	0.180	0	0	0	0.008	0	0.001	0	0.007	0	0
Sm	0.003	0.494	0.010	0.026	0.044	0	0	0	0.007	0	0	0.001	0.001	0.002	0
Eu	0.009	0.017	0.001	0.003	0.003	0.003	0.003	0.006	0.009	0.001	0.005	0.014	0.011	0.007	0.008
Gd	0.007	0.171	0.045	0.007	0.008	0.003	0.003	0.002	0.012	0.004	0.003	0.014	0.011	0.004	0.007
Tb	0.001	0.013	0.011	0	0	0.001	0.001	0.001	0.007	0.001	0.001	0.002	0.005	0	0.001
Dy	0.001	0.043	0.073	0.001	0.001	0.001	0.001	0.001	0.005	0.001	0	0	0.001	0	0
Ho	0.003	0	0.009	0.001	0.001	0	0	0	0.003	0.001	0	0	0.006	0	0.002

Tab. 6 – continuation
Representative analyses of U-Ti-Sr-P minerals in Čučma and Kurišková localities. Permian MMH cycle in Gemeric unit.

Mineral	Ort-brannerite	Monazite	Xenotime	Goyazite	Goyazite	Met-Aunite	Met-Aunite	Vyacheslavite	New	Uraninite	Met-Ca uranite	Met-Ca uranite	Ca uranoite	Coffinite	Ort-brannerite
Locality	Čučma	Čučma	Čučma	Čučma	Čučma	Čučma	Čučma	Čučma	Čučma	Kurišková	Kurišková	Kurišková	Kurišková	Kurišková	Kurišková
Sample	CU-17-1	CU-1	CU-17-1	CU-17-1	CU-17-1	CU-1	CU-1	CU-17-1	CU-1	KGJ-21a	KGJ-21a	KGJ-21a	KGJ-21a	LE-K-29	LE-K-29
Place	in Png	in matrix+Ap	in matrix+Ap	in Xtn	in Xtn	in matrix+Ap	in matrix+Ap	in Xtn	in matrix+Ap	matrix	in Png	matrix	in Png	matrix	in Png
Location	Vein swarm	Vein swarm	Vein swarm	Vein swarm	Vein swarm	Vein swarm	Vein swarm	Vein swarm	Vein swarm	SedEx	SedEx	SedEx	SedEx	SedEx	SedEx
Zone	Chl-Ap	Chl-Ap	Chl-Ap	Chl-Ap	Chl-Ap	Chl-Ap	Chl-Ap	Chl-Ap	Chl-Ap	Chl-Ap	Chl-Ap	Chl-Ap	Chl-Ap	Chl-Ap	Chl-Ap
Er	0.008	0.025	0.037	0.004	0.002	0.003	0.003	0.005	0.017	0.009	0.007	0.019	0.026	0.007	0.027
Tm	0.003	0.008	0.006	0	0	0.001	0.001	0.002	0.007	0.002	0.001	0.007	0.001	0.002	0.003
Yb	0.007	0.011	0.029	0.002	0.002	0.001	0.001	0.001	0.018	0.004	0.004	0.006	0.012	0.002	0.003
Lu	0.005	0.001	0.002	0.004	0.007	0	0	0	0	0	0	0.006	0.004	0.003	0.005
Pb	0.015	0	0	0	0	0	0	0	0.501	0.026	0.016	0	0.001	0	0.052
Cu	0	0	0	0	0	0	0	0	0	0	0	0	0	0	0
S	0	0.012	0	0	0	0	0	0	0	0	0	0	0	0	0
Si	0	0.049	0	0	0	0	0	0	0	0	0	0	0	0.807	0
As	0	0	0	0	0	0	0	0	0	0	0	0	0	0	0
Cations	2.99	12.032	2.039	6.007	5.997	1.997	1.997	1.991	11.132	1.048	1.122	3.993	4.024	2.027	6.777
CF	0		0	0.236	0	0	0	0	0	0	0	0	0	0	0
CCl	0		0.001	0.003	0.006	0	0	0.007	0.036	0.008	0.002	0.006	0.011	0	0.016
OH	0.5		0	4.381	4.297	2.100	2.100	1.097	9.982	0	0	0	0	0.400	1.992
O	6	24	4.000	13.000	13.000	5.000	5.000	5.000	26.000	2.000	2.000	7.000	7.000	4.000	14.000
O_F_Cl	0	0	0	0.200	0	0	0	0.010	0.010	0.010	0	0	0	0	0.010
O_F	0	0	0	0.190	0	0	0	0	0	0	0	0	0	0	0
O_Cl	0	0	0	0	0	0	0	0.010	0.010	0.010	0	0	0	0	0.010

Tab. 7
Representative analyses of oxides in Dlhá dolina locality. Permian MMH cycle in Gemeric unit.

Mineral	Ta-Columbite	Ta-Columbite	Ta-Columbite	Fe-Columbite	U-Polycrase	U-Polycrase	U-Kobeite	U-Kobeite	Rutile	Scheelite	Cassiterite	Cassiterite
Locality	Dlhá dolina	Dlhá dolina	Dlhá dolina	Dlhá dolina	Dlhá dolina	Dlhá dolina	Dlhá dolina	Dlhá dolina	Dlhá dolina	Dlhá dolina	Dlhá dolina	Dlhá dolina
Sample	DD-2	DD-2	DD-2	DD-2	DD-2	DD-2	DD-2	DD-2	DD-3a	DD-2	DD-2	V-DD-43-1
Place	core	core	core-rim	rim	core	core	rim	rim	matrix	core	matrix	with Mgh
Location	Greisen	Greisen	Greisen	Greisen	Greisen	Greisen	Greisen	Greisen	Greisen	Greisen	Greisen	Skarn
Zone	Chl-Ap	Chl-Ap	Chl-Ap	Chl-Ap	Chl-Ap	Chl-Ap	Chl-Ap	Chl-Ap	Chl-Ap	Chl-Ap	Chl-Ap	Chl-Stp
CaO	0	0.01	0.02	0	2.61	3.8	0.42	0.23	0	17.15	0.27	0
Ta_2O_5	25.73	20.3	13.08	3.62	6.18	5.67	5.91	6.17	0	0.31	0.00	0
WO_3	3.07	0.81	2.53	4.64	2.26	4.65	1.69	1.21	0	71.59	0.00	0.01
TiO_2	7.24	4.4	4.67	3.69	25.53	27.14	41.71	35.71	97.64	0.33	0.00	0
FeO	7.32	14.62	17.3	17.52	0.00	0	4.08	2.4	1.77	2.02	0.03	1.29
Fe_2O_3	0	0	0	0	4.12	4.08	0	0	0	0	0	0
MnO	8.8	2.55	1.02	1.51	0.11	0.1	0.05	0	0.04	0.11	0.04	0
ZnO	0.03	0	0.04	0	0.04	0	0	0	0	0	0	0
Sc_2O_3	0.69	0.98	0.76	0.89	0.04	0.07	0.03	0.05	0	0.1	0	0
SnO_2	1.81	0.65	0.6	0.33	0.12	0.32	0.62	0.66	0	0.33	99.13	98.3
Y_2O_3	0	0.07	0.04	0	8.41	4.58	1.04	1.23	0	0	0	0
UO_2	0	0.09	0.18	0.07	24.21	26.69	18.14	23.55	0	0	0	0
ZrO_2	0.4	0.27	0.13	0.11	0.02	0	0.22	0.34	0	0	0	0
Nb_2O_5	42.02	52.14	57.57	66.2	17.00	13.91	12.7	12.35	0	8.53	0	0.18
MgO	0	0.35	0.37	0.41	0.00	0	0	0	0.13	0.02	0	0.13
ThO_2	0.02	0	0.02	0	1.48	1.75	1.54	2.04	0	0.01	0	0
SiO_2	0	0	0	0	0.16	1.07	1.53	4.09		0	0	0
La_2O_3	0	0.02	0	0	0.00	0	0	0.02	0	0	0	0
Ce_2O_3	0.07	0.06	0.04	0	0.11	0.11	0.32	0.41	0	0	0	0
Pr_2O_3	0.17	0.2	0.24	0.17	0.21	0.24	0.26	0.31	0	0	0	0
Nd_2O_3	0	0.01	0	0	0.38	0.27	0.25	0.48	0	0	0	0
Sm_2O_3	0.01	0.06	0.03	0.06	0.41	0.38	0.25	0.5	0	0	0	0
Eu_2O_3	0.6	0.55	0.55	0.55	0.32	0.34	0.26	0.28	0	0	0	0
Gd_2O_3	0.08	0.11	0.12	0.08	0.80	0.72	0.37	0.61	0	0	0	0
Tb_2O_3	0.08	0.06	0.08	0.07	0.22	0.2	0.11	0.19	0	0	0	0
Dy_2O_3	0.02	0.04	0	0	1.40	1.3	0.53	0.82	0	0	0	0
Ho_2O_3	0	0	0	0	0.26	0.17	0	0.09	0	0	0	0
Er_2O_3	0.13	0.18	0.22	0.27	1.29	1.14	0.53	0.66	0	0	0	0
Tm_2O_3	0.58	0.47	0.31	0.15	0.37	0.29	0.24	0.25	0	0	0	0
Yb_2O_3	0.14	0.14	0.11	0.1	0.96	0.81	0.35	0.41	0	0	0	0
Lu_2O_3	0.14	0.08	0.09	0.19	0.16	0.21	0.17	0.12	0	0	0	0
Total	99.15	99.22	100.12	100.63	99.18	100.01	93.32	95.18	99.59	100.5	99.47	99.91
Ti	0.342	0.203	0.208	0.158	1.237	1.295	1.854	1.626	0.998	0.011	0	0
Fe_3	0	0	0	0	0.199	0.195	0	0	0	0	0	0
Fe_2	0.384	0.748	0.855	0.834	0	0	0.202	0.121	0.02	0.078	0.001	0.027
Ta	0.439	0.338	0.21	0.056	0.108	0.098	0.095	0.102	0	0.004	0	0
Mn	0.468	0.132	0.051	0.073	0.006	0.005	0.003	0	0	0.004	0.001	0
Mg	0	0.032	0.033	0.035	0	0	0	0	0.003	0.001	0	0.005
Ca	0	0.001	0.001	0	0.18	0.258	0.027	0.015	0	0.849	0.007	0
W	0.05	0.013	0.039	0.068	0.038	0.076	0.026	0.019	0	0.856	0	0
Zn	0.001	0	0.002	0	0.002	0	0	0	0	0	0	0
Sc	0.038	0.052	0.039	0.044	0.002	0.004	0.002	0.003	0	0.004	0	0
Sn	0.045	0.016	0.014	0.007	0.003	0.008	0.015	0.016	0	0.006	0.996	0.981
Y	0	0.002	0.001	0	0.288	0.154	0.033	0.04	0	0	0	0
U	0	0.001	0.002	0.001	0.347	0.377	0.238	0.317	0	0	0	0
Zr	0.012	0.008	0.004	0.003	0.001	0	0.006	0.01	0	0	0	0
Nb	1.192	1.443	1.539	1.704	0.495	0.399	0.339	0.338	0	0.178	0	0.002
Th	0	0	0	0	0.022	0.025	0.021	0.028	0	0	0	0
Si	0	0	0	0	0.01	0.068	0.09	0.248	0	0	0	0
La	0	0	0	0	0	0	0	0	0	0	0	0
Ce	0.002	0.001	0.001	0	0.003	0.003	0.007	0.009	0	0	0	0
Pr	0.004	0.004	0.005	0.004	0.005	0.006	0.006	0.007	0	0	0	0
Nd	0	0	0	0	0.009	0.006	0.005	0.01	0	0	0	0
Sm	0	0.001	0.001	0.001	0.009	0.008	0.005	0.01	0	0	0	0
Eu	0.01	0.01	0.01	0.01	0.01	0.01	0.01	0.01	0	0	0	0
Gd	0.002	0.002	0.002	0.002	0.017	0.015	0.007	0.012	0	0	0	0
Tb	0.002	0.001	0.002	0.001	0.005	0.004	0.002	0.004	0	0	0	0
Dy	0	0.001	0	0	0.029	0.027	0.01	0.016	0	0	0	0
Ho	0	0	0	0	0.005	0.003	0	0.002	0	0	0	0
Er	0.003	0.003	0.004	0.005	0.026	0.023	0.01	0.013	0	0	0	0
Tm	0.011	0.009	0.006	0.003	0.007	0.006	0.004	0.005	0	0	0	0
Yb	0.003	0.003	0.002	0.002	0.019	0.016	0.006	0.008	0	0	0	0
Lu	0.003	0.001	0.002	0.003	0.003	0.004	0.003	0.002	0	0	0	0
Ba	0	0	0	0	0	0	0	0	0	0	0	0
Cations	3.011	3.025	3.033	3.014	3.085	3.093	3.026	2.991	1.011	1.991	1.005	1.015

Tab. 8
Representative analyses of In-rich sulfides in skarn. Dlhá dolina area, V-DD-43 borehole. Permian MMH cycle in Gemeric unit.

Mineral	Sphalerite	Sphalerite-In	Sphalerite-In	Sphalerite-In	Sphalerite-In	Ishiharaite-Zn	Ishiharaite-Zn	Ishiharaite-Zn	Ishiharaite-Zn	Ishiharaite-Zn	Ishiharaite-Zn	Ishiharaite-Zn	Ishiharaite-Zn	Ishiharaite-Zn	Ishiharaite-Zn	Ishiharaite-Zn	Ishiharaite	Sakuraiite	Ishiharaite-Fe	Roquesite	Roquesite	Roquesite	Roquesite	Roquesite	Ishiharaite-Cu	Ishiharaite-Cu	Stannite-In	Chalcopyrite-In	Chalcopyrite
Locality	Dlhá dolina	Dlhá dolina	Dlhá dolina	Dlhá dolina	Dlhá dolina	Dlhá dolina	Dlhá dolina	Dlhá dolina	Dlhá dolina	Dlhá dolina	Dlhá dolina	Dlhá dolina	Dlhá dolina	Dlhá dolina	Dlhá dolina	Dlhá dolina	Dlhá dolina	Dlhá dolina	Dlhá dolina	Dlhá dolina	Dlhá dolina	Dlhá dolina	Dlhá dolina	Dlhá dolina	Dlhá dolina	Dlhá dolina	Dlhá dolina	Dlhá dolina	Dlhá dolina
Sample	V-DD-43	V-DD-43	V-DD-43	V-DD-43	V-DD-43	V-DD-43	V-DD-43	V-DD-43	V-DD-43	V-DD-43	V-DD-43	V-DD-43	V-DD-43	V-DD-43	V-DD-43	V-DD-43	V-DD-43	V-DD-43	V-DD-43	V-DD-43	V-DD-43	V-DD-43	V-DD-43	V-DD-43	V-DD-43	V-DD-43	V-DD-43	V-DD-43	V-DD-43
Location	matrix Ccp. Py	in CCp+Ank	in CCp+Ank	in CCp+Ank	in CCp+Ank	in CCp+Ank	in CCp+Ank	in CCp+Ank	in CCp+Ank	in CCp+Ank	in CCp+Ank	in CCp+Ank	in CCp+Ank	in CCp+Ank	in CCp+Ank	in CCp+Ank	in CCp+Ank	in CCp+Ank	in CCp+Ank	in CCp+Ank	in CCp+Ank	in CCp+Ank	in CCp+Ank	in CCp+Ank	in CCp+Ank	in CCp+Ank	in Py	matrix Py. Sp	matrix Py. Sp
Zone	Stp-Chl	Stp-Chl	Stp-Chl	Stp-Chl	Stp-Chl	Stp-Chl	Stp-Chl	Stp-Chl	Stp-Chl	Stp-Chl	Stp-Chl	Stp-Chl	Stp-Chl	Stp-Chl	Stp-Chl	Stp-Chl	Stp-Chl	Stp-Chl	Stp-Chl	Stp-Chl	Stp-Chl	Stp-Chl	Stp-Chl	Stp-Chl	Stp-Chl	Stp-Chl	Stp-Chl	Stp-Chl	Stp-Chl
S	32.80	31.90	31.76	32.70	30.91	31.23	30.03	30.38	29.35	31.10	28.66	30.04	31.02	29.83	29.38	28.92	30.79	28.51	32.07	26.08	25.57	26.64	24.90	25.24	30.97	29.21	29.38	32.71	34.12
Cd	2.57	0.64	0.61	0.62	0.27	0.28	0.28	0.30	0.74	0.80	0.86	0.63	0.61	0.60	0.77	0.33	0.25	0.45	0.08	0.14	0.07	0.06	0.11	0.08	0.48	0.02	0.16	0.11	0.02
Ag	0	0	0	0.02	0.02	0.02	0	0.02	0	0	0.01	0	0	0	0.02	0.03	0.02	0.02	0.06	0.02	0	0	0.08	0.08	0.04	0.06	0	0.03	0.03
Zn	60.80	59.31	57.53	52.37	54.76	50.56	47.07	45.95	38.71	36.69	32.47	31.59	31.41	30.38	28.73	27.54	27.60	18.43	0.78	3.10	0.33	0.44	5.17	1.08	16.10	0.12	5.18	3.50	0.06
Fe	1.96	3.62	2.37	2.08	0.97	1.05	1.66	1.73	2.76	3.01	4.55	2.13	6.90	2.64	6.95	1.03	14.24	8.39	13.15	2.64	2.72	4.04	1.36	2.06	15.73	17.30	11.27	26.58	30.65
Mn	0.09	0	0.01	0	0	0.01	0	0.01	0	0	0	0.01	0	0	0	0.10	0.03	0	0	0.08	0	0	0.03	0	0	0	0	0	0
Cu	1.17	1.80	3.20	4.80	4.59	6.05	7.96	8.16	10.44	10.99	13.59	13.17	14.07	13.61	15.60	14.91	9.38	20.23	19.83	24.07	25.45	24.27	25.47	25.64	24.04	30.34	30.15	31.99	34.68
In	0.34	2.35	4.32	7.04	7.99	10.49	13.07	13.74	17.49	18.01	19.56	22.64	16.12	23.44	18.37	27.84	17.52	23.84	33.14	43.28	45.46	44.30	42.86	45.55	12.23	22.47	4.71	5.16	0.15
Sn	0	0	0	0	0	0	0	0	0	0	0	0	0	0	0	0	0	0	0	0	0	0	0	0	0	0	18.98	0	0
Sb	0.05	0	0.02	0	0	0	0.03	0	0.02	0	0.03	0	0	0	0	0	0	0.01	0	0	0	0	0	0	0	0	0	0	0
Te	0	0.01	0.02	0	0	0	0	0	0.01	0	0	0	0	0	0.03	0	0	0	0	0	0	0	0	0	0	0	0.05	0	0
Pb	0.15	0.13	0.13	0.15	0.13	0.15	0.14	0.21	0.16	0.07	0.12	0	0.10	0	0.13	0.12	0.20	0	0.10	0.08	0.10	0.15	0.10	0.12	0.21	0.17	0.18	0.13	0.25
Bi	0.03	0	0.01	0	0.09	0.02	0	0.03	0.01	0	0	0	0.02	0	0	0.05	0	0	0.08	0.03	0.31	0	0	0.02	0	0.07	0	0	0.05
Total	99.96	99.76	99.98	99.78	99.72	99.85	100.24	100.53	99.69	100.67	99.83	100.21	100.25	100.50	99.97	100.88	100.02	99.88	99.29	99.52	99.68	99.90	100.10	99.85	99.80	99.76	100.05	100.20	100.01
S	1.005	0.984	0.987	1.019	0.981	0.996	0.971	0.980	0.973	1.009	0.959	1.003	0.998	0.997	0.968	0.988	0.989	0.960	1.081	1.951	1.933	1.979	1.875	1.916	0.974	0.960	3.908	0.972	1.968
Cd	0.022	0.006	0.005	0.006	0.002	0.003	0.003	0.003	0.007	0.007	0.008	0.006	0.006	0.006	0.007	0.003	0.002	0.004	0.001	0.003	0.001	0.001	0.002	0.002	0.004	0	0.006	0.001	0
Ag	0	0	0	0	0	0	0	0	0	0	0	0	0	0	0	0	0	0	0.001	0	0	0	0.002	0.002	0	0.001	0	0	0.001
Sn	0	0	0	0	0	0	0	0	0	0	0	0	0	0	0	0	0	0	0	0	0	0	0	0	0	0	0.682	0	0
Cu	0.018	0.028	0.050	0.075	0.074	0.097	0.130	0.133	0.175	0.180	0.229	0.222	0.228	0.230	0.259	0.257	0.152	0.344	0.337	0.909	0.971	0.910	0.968	0.983	0.381	0.503	2.024	0.480	1.009
Zn	0.914	0.897	0.877	0.801	0.853	0.791	0.747	0.727	0.630	0.584	0.533	0.517	0.496	0.498	0.464	0.462	0.435	0.305	0.013	0.114	0.012	0.016	0.191	0.040	0.248	0.002	0.338	0.051	0.002
Mn	0.002	0	0	0	0	0	0	0	0	0	0	0	0	0	0	0.002	0.001	0	0	0.003	0	0	0.001	0	0	0	0.001	0	0
Fe	0.034	0.064	0.042	0.037	0.018	0.019	0.031	0.032	0.053	0.056	0.087	0.041	0.127	0.051	0.131	0.020	0.263	0.162	0.255	0.113	0.118	0.172	0.059	0.090	0.284	0.327	0.861	0.453	1.015
In	0.003	0.020	0.037	0.061	0.071	0.093	0.118	0.124	0.162	0.163	0.183	0.211	0.145	0.219	0.169	0.266	0.157	0.224	0.312	0.905	0.960	0.920	0.901	0.966	0.107	0.206	0.175	0.043	0.002
Sb	0	0	0	0	0	0	0	0	0	0	0	0	0	0	0	0	0	0	0	0	0	0	0	0	0	0	0	0	0
Te	0	0	0	0	0	0	0	0	0	0	0	0	0	0	0	0	0	0	0	0	0	0	0	0	0	0	0.002	0	0
Pb	0.001	0.001	0.001	0.001	0.001	0.001	0.001	0.001	0.001	0	0.001	0	0	0	0.001	0.001	0.001	0	0.001	0.001	0.001	0.002	0.001	0.001	0.001	0.001	0.004	0.001	0.002
Bi	0	0	0	0	0	0	0	0	0	0	0	0	0	0	0	0	0	0	0	0	0.004	0	0	0	0	0	0.001	0	0
Sum	1.999	2.000	1.999	2.000	2.000	2.000	2.001	2.000	2.001	1.999	2.000	2.000	2.000	2.000	1.999	1.999	2.000	2.000	2.001	3.999	4.000	4.000	4.000	4.000	1.999	2.000	8.002	2.001	3.999
Fe+Cu	0.052	0.092	0.092	0.112	0.092	0.116	0.161	0.165	0.228	0.236	0.316	0.263	0.355	0.280	0.390	0.277	0.415	0.506	0.592	1.022	1.089	1.082	1.027	1.073	0.665	0.830	2.885	0.933	2.024
In+Fe	0.917	0.917	0.914	0.862	0.924	0.884	0.865	0.851	0.792	0.747	0.716	0.728	0.641	0.717	0.633	0.728	0.592	0.529	0.325	1.019	0.976	0.936	1.092	1.006	0.355	0.208	0.514	0.094	0.004
Suma	0.969	1.009	1.006	0.974	1.016	1.000	1.026	1.016	1.020	0.983	1.032	0.991	0.996	0.997	1.023	1.005	1.007	1.035	0.917	2.041	2.065	2.018	2.119	2.079	1.020	1.038	3.399	1.027	2.028

Tab. 9
Representative analyses of sulfides in greisen and skarn. Dlhá dolina area. Permian MMH cycle in Gemeric unit.

Mineral	Gersdorffite	Gersdorffite-Sb	Gersdorffite-Co	Gersdorffite	Galena	Pyrite	Pyrite	Pyrite	Pyrrhotite	Pyrrhotite	Paarite	Paarite	Native Bi	Gladite	Gladite	Gladite-Pb	Ustarasite-Bi	Tetradymite	Tetrahedrite	Tetrahedrite
Locality	**D. dolina**	**D. dolina**	**D. dolina**	**D. dolina**	**D. dolina**	**D. dolina**	**D. dolina**	**D. dolina**	**D. dolina**	**D. dolina**	**D. dolina**	**D. dolina**	**D. dolina**	**D. dolina**	**D. dolina**	**D. dolina**	**D. dolina**	**D. dolina**	**D. dolina**	**D. dolina**
Sample	**DD-3a**	**DD-3a**	**DD-3a**	**DD-3a**	**DD-3a**	**DD-3a**	**VSV-05-2**	**V-DD-43-1**	**VSV-05-2**	**V-DD-43-1**	**VSV-05-2**	**V-DD-43-1**	**VSV-05-2**	**VSV-05-2**	**VSV-05-2**	**VSV-05-2**	**V-DD-43-1**	**V-DD-43-1**	**V-DD-43-1**	**V-DD-43-5**
Place	**in Ccp+Sp**	**in Ccp+Sp**	**in Ccp+Sp**	**in Ccp+Sp**	**in Ccp+Sp**	**matrix**	**in Dol**	**in Ank**	**in Py**	**in Py**	**in Dol**	**in Ank**	**in Mgh**	**in MgSd**	**in MgSd**	**in Dol**	**in Gladite**	**rim Ustara.**	**in Cal/Ank**	**in Ank**
Location	**Greisen**	**Greisen**	**Greisen**	**Greisen**	**Greisen**	**Greisen**	**Skarn**	**Skarn**	**Skarn**	**Skarn**	**Skarn**	**Skarn**	**Skarn**	**Skarn**	**Skarn**	**Skarn**	**Skarn**	**Skarn**	**Skarn**	**Skarn**
Zone	**Chl-Ap**	**Chl-Ap**	**Chl-Ap**	**Chl-Ap**	**Chl-Ap**	**Chl-Ap**	**Chl-Stp**	**Chl-Stp**	**Chl-Stp**	**Chl-Stp**	**Chl-Stp**	**Chl-Stp**	**Chl-Stp**	**Chl-Stp**	**Chl-Stp**	**Chl-Stp**	**Chl-Stp**	**Chl-Stp**	**Chl-Stp**	**Chl-Stp**
S	19.28	18.22	19.28	18.51	13.63	53.07	53.63	53.1	39.36	39.88	18.95	18.55	0.02	18.86	18.86	18.83	18.57	4.65	25.08	24.5
Cd	0	0	0	0	0	0	0	0.02	0	0.03	0.02	0.1	0.04	0.09	0.03	0.04	0.04	0.01	0.19	0.23
Ag	0	0	0	0	0	0.03	0	0.02	0	0.05	0.04	0	0	0	0.03	0	0	0.02	1.42	0.36
Zn	0	0	0	0	0	0	0	0	0	0.12	0.02	0	0.05	0.02	0.01	0	0	0	3.62	4.7
Fe	5.37	1.35	5.33	10.71	0.39	44.06	46.38	46.2	60	60.09	2.27	0.79	5.75	3.71	4.21	1.41	0.04	0	3.38	2.51
Mn	0	0	0	0	0	0	0	0.01	0	0	0.12	0	0	0.04	0.01	0	0	0	0	0
Cu	0.09	0.37	0.08	0.02	0.31	0.03	0	0	0	0.21	4	4.26	0	0.98	0.41	2.8	0.76	0.02	37.76	38.66
In	0	0	0	0.02	0	0	0	0.01	0	0.02	0	0.03	0.03	0.01	0.03	0.04	0.03	0	0.05	0.03
Sn	0	0	0	0	0	0	0	0	0	0	0	0.04	0.05	0	0	0.07	0	0	0.04	0.02
Sb	2.66	12.8	1.08	0	0.19	0	0	0	0	0	1.66	1.88	0.07	1.54	1.19	1.46	1.18	0	26.3	27.28
Te	0	0	0	0	0	0	0	0	0	0.01	0	0.03	0	0	0	0.01	0.01	36.09	0	0
Co	0.15	0.06	14.27	10.67	0.03	1.79	0	0	0	0	0	0	0	0	0	0	0	0	0	0
Ni	30.22	33.28	16.32	14.35	0.02	0.79	0	0	0	0	0	0	0	0	0	0	0	0	0	0
As	41.94	33.7	42.18	45.73	0.01	0.05	0	0	0	0	0	0	0	0	0	0	0	0	0	0
Pb	0.1	0.16	2.34	0.1	85.09	0.42	0	0	0	0.27	13.54	13.89	0.05	3.57	1.32	9.32	2.39	0.05	0.13	0.14
Bi	0	0.06	0.13	0.03	1.58	0	0	0	0	0	59.96	59.92	96.53	71.1	74.64	67.61	76.6	59.44	1.22	1.24
Total	99.81	100	101.01	100.14	101.25	100.24	100.01	99.36	99.36	100.68	100.58	99.49	102.59	99.92	100.74	101.59	99.62	100.28	99.19	99.67
S	1.003	0.99	1.001	0.959	0.991	1.993	2.005	2	1.066	1.069	12.002	12.011	0.001	9.03	9.01	9.048	10.043	1.017	13.107	12.838
Cd	0	0	0	0	0	0	0	0	0	0	0.004	0.018	0.001	0.012	0.004	0.005	0.006	0.001	0.028	0.034
Ag	0	0	0	0	0	0	0	0	0	0	0.008	0	0	0	0.004	0	0	0.001	0.221	0.056
Sn	0	0	0	0	0	0	0	0	0	0	0	0.007	0.001	0	0	0.009	0	0	0.006	0.003
Cu	0.002	0.01	0.002	0.001	0.011	0.001	0	0	0	0.003	1.279	1.392	0	0.237	0.099	0.679	0.207	0.002	9.959	10.224
Zn	0.001	0	0	0	0	0	0	0	0	0.002	0.006	0	0.001	0.005	0.002	0	0	0	0.928	1.208
Mn	0	0	0	0	0	0	0	0	0	0	0.044	0	0	0.011	0.003	0	0	0	0	0
Fe	0.16	0.042	0.159	0.319	0.016	0.95	0.995	0.999	0.934	0.925	0.826	0.294	0.181	1.02	1.155	0.389	0.012	0	1.014	0.755
In	0	0	0	0	0	0	0	0	0	0	0	0.005	0	0.001	0.004	0.005	0.005	0	0.007	0.004
Sb	0.036	0.183	0.015	0	0.004	0	0	0	0	0	0.277	0.321	0.001	0.194	0.15	0.185	0.168	0	3.621	3.765
Te	0	0	0	0	0	0	0	0	0	0	0	0.005	0	0	0	0.001	0.001	1.983	0	0
Co	0.004	0.002	0.403	0.301	0.001	0.037	0	0	0	0	0	0	0	0	0	0	0	0	0	0
Ni	0.859	0.988	0.463	0.406	0.001	0.016	0	0	0	0	0	0	0	0	0	0	0	0	0	0
As	0.934	0.784	0.937	1.014	0	0.001	0	0	0	0	0	0	0	0	0	0	0	0	0	0
Pb	0.001	0.001	0.019	0.001	0.958	0.002	0	0	0	0.001	1.327	1.392	0	0.265	0.098	0.693	0.2	0.002	0.011	0.011
Bi	0	0.001	0.001	0	0.018	0	0	0	0	0	5.828	5.954	0.813	5.224	5.472	4.985	6.357	1.994	0.098	0.1
Sum	2.999	3.001	3	3.001	2	3	3	2.999	2	2	21.601	21.399	0.999	15.999	16.001	15.999	16.999	5	29	28.998

Tab. 10
Representative analyses of minerals in Rozabela Sb-rich vein. Permian MMH cycle in Gemeric unit.

Mineral	Jamesonite	Jamesonite	Fülöppite	Fülöppite	Berthierite	Berthierite	Berthierite	Chalcostibite	Stibnite	Stibnite	Senarmontite	Native Sb
Locality	Rozabela	Rozabela	Rozabela	Rozabela	Rozabela	Rozabela	Rozabela	Rozabela	Rozabela	Rozabela	Rozabela	Rozabela
Sample	ROZ-1-2	ROZ-1-2	ROZ-1-2	ROZ-1-2	ROZ-4-2	ROZ-4-2	ROZ-1-2	ROZ-4-2	ROZ-1-2	ROZ-4-2	ROZ-4-2	ROZ-4-2
Place	in Stb	in Stb	in Sd+Ank	in Ank+Tur	in Ank+Stb	in Qtz	in Sd+Ank	in Qtz	in Png+Sd	in Ank	in Qtz	in Qtz
Location	Vein	Vein	Vein	Vein	Vein	Vein	Vein	Vein	Vein	Vein	Vein	Vein
Zone	Chl-Ap	Chl-Ap	Chl-Ap	Chl-Ap	Chl-Ap	Chl-Ap	Chl-Ap	Chl-Ap	Chl-Ap	Chl-Ap	Chl-Ap	Chl-Ap
S	21.84	22.18	23.91	25.67	30.10	29.97	30.73	26.22	28.64	29.12	0	0
Ag	0	0	0	0	0	0.01	0.01	0.01	0	0	0.01	0
Fe	2.57	3.41	1.55	1.03	9.81	12.78	12.91	0.02	0.14	0.64	0.00	0.04
Cu	0	0.01	0.05	0.04	0.00	0.03	0.03	26.43	0	0.04	0	0.05
Sb	36.03	34.32	50.65	58.89	59.14	56.71	55.69	46.79	68.91	70.10	88.83	98.93
Co	0.04	0	0	0	0	0.03	0.02	0	0	0	0	0.01
Ni	0.01	0.01	0.01	0	0.03	0.01	0	0	0	0	0.01	0.01
Pb	38.96	40.19	23.49	14.40	0.63	0.26	0.30	0.15	1.97	0.21	0	0
Bi	0.04	0.08	0.07	0.02	0.02	0	0	0	0	0	0.03	0.05
Total	99.50	100.20	99.73	100.05	99.73	99.80	99.69	99.62	99.65	100.10	88.88	99.10
S	3.933	3.938	4.002	4.082	4.097	4.009	4.068	2.020	3.035	3.033	0	0
Ag	0	0	0	0	0	0	0	0	0	0	0	0
Cu	0	0.001	0.004	0.003	0	0.002	0.002	1.028	0	0.002	0	0.001
Fe	0.266	0.348	0.149	0.094	0.767	0.982	0.981	0.001	0.009	0.038	0	0.001
Sb	1.709	1.605	2.233	2.466	2.120	1.998	1.942	0.950	1.924	1.923	0.999	0.997
Co	0.004	0	0	0	0	0.002	0.001	0	0	0	0	0
Ni	0.001	0.001	0.001	0	0.002	0.001	0	0	0	0	0	0
Pb	1.086	1.105	0.608	0.354	0.013	0.005	0.006	0.002	0.032	0.003	0	0
Bi	0.001	0.002	0.002	0	0	0	0	0	0	0	0	0
Sum	7.000	7.000	6.999	6.999	6.999	6.999	7.000	4.001	5.000	4.999	0.999	0.999

Tab. 11

Representative analyses of sulfides and native Bi in Konštancia and Strieborná (Stz) - siderite and sulfide bearing veins. Permian MMH cycle in Gemeric unit.

Mineral	Cannizzarite	Cosalite	Native Bi	Bisnuthinite	Jamesonite-Bi	Bournonite	Alloclasite	Ullmannite	Chalcopyrite	Pyrrhotite	Tetrahedrite	Arsenopyrite	Arsenopyrite	Gersdorffite
Locality	Konštancia	Konštancia	Konštancia	Konštancia	Strieborna	Strieborna	Konštancia	Konštancia	Konštancia	Konštancia	Stz-6	Stz-6	Konštancia	Stz-6
Sample	53-150	53-150	53-150	53-150	Stz-6	Stz-6	53-150	53-150	53-150	53-150	Stz-6	Stz-6	53-150	Stz-6
Place	in siderite	in siderite	in siderite	in siderite	in siderite	in siderite	in siderite	in siderite	in siderite	in siderite	in siderite	in siderite	in siderite	in siderite
Location	siderite-vein	siderite-vein	siderite-vein	siderite-vein	siderite-vein	siderite-vein	siderite-vein	siderite-vein	siderite-vein	siderite-vein	siderite-vein	siderite-vein	siderite-vein	siderite-vein
Zone	Chlorite	Chlorite	Chlorite	Chlorite	Chlorite	Chlorite	Chlorite	Chlorite	Chlorite	Chlorite	Chlorite	Chlorite	Chlorite	Chlorite
S	17.73	16.58	0.04	18.69	19.73	19.68	21.24	15.05	34.93	40.12	25.18	20.88	19.73	19.57
Cd	0.05	0.11	0.07	0.08	0.02	0.05	0	0	0	0	0.01	0	0	0
Ag	0.05	0.08	0.03	0	0.02	0	0	0	0	0.02	1.05	0.02	0	0
Zn	0.01	0	0.01	0	0.02	0	0.01	0.02	0.04	0	1.33	0	0.03	0
Fe	1.72	0.39	0.71	0.64	0.46	0.31	5.07	4.34	30.32	59.65	5.56	34.54	30.65	6.10
Mn	0	0.01	0.03	0.04	0	0	0	0	0	0	0	0	0	0
Cu	1.07	0.24	0	0.11	2.01	13.02	0.60	1.09	34.41	0.47	37.70	0.16	0.20	0.06
In	0	0.01	0.03	0.03	0.00	0	0	0	0	0	0	0	0	0
Sn	0.06	0	0.08	0	0.05	0	0	0	0	0	0.08	0	0	0
Sb	6.95	2.73	0.42	1.38	20.50	23.25	0	53.61	0.02	0.01	29.38	0.18	0.08	1.18
Te	0.02	0.01	0	0.01	0	0	0	0	0	0.00	0	0	0	0
Co	0	0	0	0	0	0	28.81	0.02	0.02	0.00	0	0.15	4.79	0.33
Ni	0	0	0	0	0	0	2.62	25.79	0	0.02	0	0.69	0.06	29.40
As	0	0	0	0	0	0	41.47	0	0.03	0.07	0	43.43	44.01	43.89
Pb	35.95	41.56	0.04	1.07	36.48	41.64	0	0	0	0	0.08	0	0	0
Se	0	0	0	0	0	0	0	0.20	0	0	0	0.01	0.02	0
Bi	36.26	38.35	99.81	77.64	21.58	1.92	0	0	0	0	0.21	0	0	0
Total	99.87	100.06	101.27	99.69	100.87	99.86	99.82	100.10	99.77	100.36	100.58	100.06	99.57	100.53
S	12.638	4.969	0.003	2.956	3.901	3.004	1.074	0.973	2.003	1.075	13.000	1.046	1.004	1.005
Cd	0.010	0.009	0.001	0.004	0.001	0.002	0	0	0	0	0.001	0	0	0
Ag	0.010	0.007	0.001	0	0.001	0	0	0	0	0	0.161	0	0	0
Sn	0.011	0	0.001	0	0.003	0	0	0	0	0	0.011	0	0	0
Cu	0.386	0.036	0	0.009	0.201	1.003	0.015	0.035	0.996	0.006	9.823	0.004	0.005	0.002
Zn	0.003	0	0	0	0.002	0	0	0.001	0.001	0	0.337	0	0.001	0
Mn	0	0.002	0.001	0.004	0	0	0	0	0	0	0	0	0	0
Fe	0.702	0.068	0.026	0.058	0.052	0.027	0.147	0.161	0.999	0.918	1.648	0.993	0.896	0.180
In	0	0.001	0.001	0.001	0	0	0	0	0	0	0	0	0	0
Sb	1.305	0.215	0.007	0.058	1.068	0.935	0	0.913	0	0	3.995	0.002	0.001	0.016
Te	0.003	0.001	0	0	0	0	0	0	0	0	0	0	0	0
Co	0	0	0	0	0	0	0.793	0.001	0.001	0	0	0.004	0.133	0.009
NI	0	0	0	0	0	0	0.072	0.911	0	0	0	0.019	0.002	0.825
As	0	0	0	0	0	0	0.898	0	0.001	0.001	0.006	0.931	0.959	0.964
Pb	3.966	1.929	0	0.026	1.116	0.984	0	0	0	0	0.006	0	0	0
Se	0	0	0	0	0	0	0	0.005	0	0	0	0	0	0
Bi	3.965	1.764	0.960	1.885	0.655	0.045	0	0	0	0	0.017	0	0	0
Sum	22.999	9.001	1.001	5.001	7.000	6.000	2.999	3.000	4.001	2.000	28.999	2.999	3.001	3.001

Tab. 12
Representative analyses of rock and mineralizations. Permian MMH cycle in Gemeric unit.

Locality	Jedľovec	Smolník-Uhorná	Smolník	Smolník	Smolník	Smolník	Hnilec	Hnilec	Delava	Hnilec	Hnilec	Hnilec	Čučma	Dlhá dolina	Kurišková	Petrová hora	Krompachy	Dlhá dolina	Hnilec	Dlhá dolina	Dlhá dolina	Štofova dolina	Jedľovec	Rožňava	Poráč	Krompachy
Rock	Lydite	Lydite	Stratabound	Stratabound	Stratabound	Keratophyre	Porphyric	Porphyric	Porphyric	Medium grained	Aplitic	Greisen	Stockwork	Skarn	U-SedEx	U-SedEx	Andesite	Greisen	Greisen	Skarn	Skarn	Vein	Vein	Vein	SedEx-U-Mo	Rhyolite
			sulfidic miner.	sulfidic miner.	sulfidic miner.	Smolník Fm.	Ms/Bt granite	Medium grained	Medium grained	Ms granite	granite	Cst-Toz-Tur		Mgh-Cst-Ank				Outcrop	As-Png-Ank		Sulfidic rim	Sb-Ank-Sd	Sd+sulfides	Sb+sulfides	breccia	
			Center exhal.	Trans. zon. exhal.	Extern zo. exhal.	Extern zo. exhal.	grey (G)	Bt/Kfs granite (G)	Bt/Kfs granite (G)	(G1)	(G2)															
Sample	PF/53-149.2 m	PF/61-119.2 m	SM-3	SM-1	SM-2	PF 59/9	HD-41-1037.9 m	HD-41-1092.3 m	DP-1-553 m	Hn-28-380 m	1st level	HN-1253	CU-17-1	V-DD-43-266.8 m	LE-K-29-150 m	gallery-55	1113-24 m	DD-1	HN-133	VSV-05-2	V-DD-43-266.8	Rozabela-1	PF/53-150.6 m	STR-VI-gallery	G-400	1113/7 m
Age - Ma	Silurian	Silurian	Devonian	Devonian	Devonian	Devonian	281-275	281-275	281-275	265-258	265-258	268			300-275. 274-263	300-275. 274-263	300-275. 274-263		263						256	263-258
Zone	Chl	Chl	Chl	Chl	Chl	Chl	Bt/EpAmp	Bt/EpAmp	Bt/EpAmp	Bt/EpAmp	Bt/EpAmp	Bt/EpAmp	Chl-Ap	Chl-Stl	Chl-Ap	Chl-Ap	Chl-Ap	Chl-Ap	Chl-Ap	Chl-Stl	Chl-Stl		Chl	Chl	Chl-Ap	Chl-Ap
SiO_2 wt.%	92	73.3	55.5	6.88	28.2	72.6	75.9	74.4	73.1	74	76.1	20.4	71.8	4.8	55.8	61.8	55	77.5	59.2	0.42	5.13	56.7	14	1.28	84.4	79.5
TiO_2	0.075	0.45	0.18	0.04	0.71	0.61	0.21	0.06	0.22	0.06	0.04	0.55	0.02	0.074	1.043	1.495	0.98	0.15	0.02	0.001	0.091	0.4	0.027	0.001	0.297	0.05
Al_2O_3	1.42	10.6	6.47	5.15	19.1	12.8	13.2	14.1	13.5	13.6	13.5	16.3	2.87	1.38	25.7	16.6	15.3	1.67	16.7	0.11	0.9	3.25	1.17	0.08	6.22	8.47
Fe_2O_3	0.56	8.4	24.2	17.5	27.5	4.66	1.04	1	1.97	1.28	1.22	0.51	1.06	79.2	3.8	5.36	9.08	0.43	4.91	93.5	51.5	3.63	59.8	48.7	3.73	1.97
MnO	0.008	0.011	0.11	1.39	0.01	0.01	0.02	0.02	0.03	0.02	0.04	0.13	0.008	0.215	0.013	0.018	0.17	0.009	0.02	0.095	0.633	0.08	1.538	2.11	0.003	0.08
MgO	0.005	0.43	4.42	16.1	0.41	0.79	0.24	0.05	0.5	0.05	0.34	0.24	0.27	3.56	0.74	5.68	2.29	0.04	1.02	1.65	9.71	1.04	1.93	3.07	0.005	1.42
CaO	0.005	0.005	0.37	24	0.29	0.07	0.67	0.56	0.61	0.71	0.57	20.7	11.8	4.2	0.005	0.005	4.13	3.43	0.21	1.35	13.3	8.07	0.005	0.36	0.005	0.8
Na_2O	0.01	0.07	0.09	0.09	0.6	0.31	6.1	4.4	3.2	4.1	2.9	0.19	0.2	0.01	0.83	2.13	3.4	0.19	0.19	0.003	0.01	0.19	0.63	0.04	0.16	3.8
K_2O	0.42	2.84	0.02	0.04	6.13	4.81	1.06	4.06	5.77	3.98	2.94	3.39	0.54	0.06	6.33	2.43	2.03	0.33	0.28	0.025	0.04	0.8	0.03	0.025	1.76	0.75
P_2O_5	0.15	0.49	0.02	0.01	0.02	0.07	0.08	0.14	0.15	0.18	0.18	7.59	9.46	0.058	0.54	0.35	0.63	0.01	0.13	0.001	0.107	0.01	0.06	0.229	0.05	0.005
St. zih	4.78	3.98	0	25.3	0	2.76	1.17	0.56	0	0.83	1.42	1.94	0.77	4.6	3.12	3.62	6.81	4.28	4.76	2.55	14	6.17	4.2	26.1	1.6	3.03
Suma wt.%	99.433	100.576	91.38	96.5	82.97	99.49	99.69	99.35	99.05	98.81	99.25	71.94	98.798	98.157	97.921	99.488	99.82	88.039	87.44	99.704	95.421	80.34	83.39	81.995	98.23	99.875
Rb mg/kg	25	122	3	0.15	182	177	18	312	261	608	602	164	27	49	212	100	70	75	23	0.5	21	45	6	0.5	79	39
Li	2	27	85.6	74.3	11	16.9	16.9	13.1	28	62.8	47.3	91.3	22	10	39	115	55	9.5	51.1	1.6	6.6	10.1	6	1.1	20	11
Ta	0.25	0.25	0.15	0.15	0.3	0.3	1.1	2.9	1.9	2.1	2.3	4.6	0.8	0.1	3.2	1.2	1.4	5.1	0.3	0.9	0.1	0.01	0.25	0.25	0.25	2.2
Nb	0.25	4.9	0.8	0.15	3.6	5.8	12	25	11	17	36	233	2.5	2.8	9.1	5.1	13.3	1199	7	0.25	0.9	0.2	0.25	0.25	4	3.1
Sn	1	3	18	7	11	12	139	3967	9	222	3686	217500	5	3592	7	4	4	122000	337	568	2065	48	23	109	3	6
B	8	76	4	4	45	34	17	1303	14	18	143	26	12	71	900	56	40	39	1686	2.5	24	64	2.5	2.5	124	13
F	250	700	10	10	10	10	800	600	400	1600	2100	8900	800	200	900	250	600	490	47000	250	800	800	250	250	250	400
W	5	5	14	9	93	9	140	16	5	24	73	91	6	5	27	12	8	419	100	5	5	7	2595	1	5	5
Mo	16	4	2	2	2	10	32	3.2	2	3.3	0.9	13.8	45	1	1113	1.5	2	4.2	229	10	6	8.9	10	1.5	413	2
As	64	108	234	84	1342	70	108	44	6	228	84	34	56	7	322	178	6	26	68550	5	71	43	41897	4220	45	5
Th	10.3	7.93	5.7	7.7	10.9	10.7	18	10.9	18.7	7.4	6.8	27.9	2.08	1.82	11.9	9.8	9.26	3.3	5	0.25	1.76	2.1	0.45	0.25	2.4	1.66
U	5	21	1.7	2.4	1.4	1.3	9.1	11.9	62.8	23.5	10.5	15.7	1169	17.8	3516	3216	24.2	5.8	23.3	0.25	4.09	1	0.05	0.25	237	326

Tab. 12 – continuation
Representative analyses of rock and mineralizations. Permian MMH cycle in Gemeric unit.

Locality	Jedľovec	Smolník-Uhorná	Smolník	Smolník	Smolník	Smolník	Hnilec	Hnilec	Delava	Hnilec	Hnilec	Hnilec	Čučma	Dlhá dolina	Kurišková	Petrová hora	Krompachy	Dlhá dolina	Hnilec	Dlhá dolina	Dlhá dolina	Štofova dolina	Jedľovec	Rožňava	Poráč	Krompachy
Rock	Lydite	Lydite	Stratabound	Stratabound	Stratabound	Keratophyre	Porphyric	Porphyric	Porphyric	Medium grained	Aplitic	Greisen	Stockwork	Skarn	U-SedEx	U-SedEx	Andesite	Greisen	Greisen	Skarn	Skarn	Vein	Vein	Vein	SedEx-U-Mo	Rhyolite
			sulfidic miner.	sulfidic miner.	sulfidic miner.	Smolník Fm.	Ms/Bt granite	Medium grained	Medium grained	Ms granite	granite	Cst-Toz-Tur		Mgh-Cst-Ank				Outcrop	As-Png-Ank		Sulfidic rim	Sb-Ank-Sd	Sd+sulfides	Sb+sulfides	breccia	
			Center exhal.	Trans. zon. exhal.	Extern zo. exhal.	Extern zo. exhal.	grey (G)	Bt/Kfs granite (G)	Bt/Kfs granite (G)	(G1)	(G2)															
Sample	PF/53-149.2 m	PF/61-119.2 m	SM-3	SM-1	SM-2	PF 59/9	HD-41-1037.9 m	HD-41-1092.3 m	DP-1-553 m	Hn-28-380 m	1st level	HN-1253	CU-17-1	V-DD-43-266.8 m	LE-K-29-150 m	gallery-55	1113-24 m	DD-1	HN-133	VSV-05-2	V-DD-43-266.8	Rozabela-1	PF/53-150.6 m	STR-VI-gallery	G-400	1113/7 m
Age - Ma	Silurian	Silurian	Devonian	Devonian	Devonian	Devonian	281-275	281-275	281-275	265-258	265-258	268			300-275. 274-263	300-275. 274-263	300-275. 274-263		263						256	263-258
Zone	Chl	Chl	Chl	Chl	Chl	Chl	Bt/EpAmp	Bt/EpAmp	Bt/EpAmp	Bt/EpAmp	Bt/EpAmp	Bt/EpAmp	Chl-Ap	Chl-Stl	Chl-Ap	Chl-Ap	Chl-Ap	Chl-Ap	Chl-Ap	Chl-Stl	Chl-Stl		Chl	Chl	Chl-Ap	Chl-Ap
Y	13	25	23	16	21	35	35	45	41	14	12	78	4385	15	34	60	52	6	10	5	20	7	64	12	13	13
La	8.5	32	14	11	53	35	37.5	12.2	23	2.7	1.3	29.8	613	39	66	34	44	0.3	1.35	0.5	7.4	5.22	4.1	2	13	4.1
Ce	12	59	31	28	108	76	87.7	33.3	45	6.69	3.37	68.9	1321	116	133	78	84	0.28	3.65	1.9	26.6	9.64	15	11	24	8
Pr	7.62	5.18	3.11	2.25	7.7	7.6	10.5	4.49	7.64	0.91	0.51	8.26	209	10.1	5.44	7.32	11.7	0.07	0.53	0.18	2.21	1.16	0.79	0.67	0.77	1.05
Nd	41.5	19.6	12.5	8.6	28.4	28.7	37.6	16.2	29.4	3.18	1.97	25.8	910	40.5	20.2	39.4	48.3	0.29	1.86	0.83	9.96	4.43	3.31	2.9	2.98	4.06
Sm	19.9	4.38	2.56	2.05	4.69	5.3	8.73	5.11	7.49	1.29	1.05	9.31	369	7.6	5.39	18.4	10	0.16	1	0.52	2.68	1.22	1.28	1.48	1.33	1.07
Eu	6.74	1.23	0.36	0.76	1.05	0.78	0.93	0.57	0.87	0.08	0.07	16.5	57.1	1.88	1.54	6.22	2.48	0.09	0.05	0.23	0.89	0.36	0.37	0.52	0.68	0.41
Gd	16.9	4.55	1.99	2.46	3.65	3.95	7.71	3.35	7.34	1.3	1.13	9.24	311	6.54	5.8	16.1	10.4	0.31	0.92	0.55	2.77	1.19	1.32	1.24	1.49	1.18
Tb	3.16	0.75	0.2	0.43	0.3	0.38	1.12	0.5	1.1	0.33	0.26	2.15	71.8	0.73	1.4	2.96	1.57	0.08	0.23	0.22	0.43	0.21	0.4	0.32	0.38	0.21
Dy	17	3.19	0.74	2.49	0.97	1.19	4.55	2.09	5.92	1.77	1.43	11.7	265	3.25	5.5	15.7	9.07	0.63	1.26	0.73	2.34	1	2.4	1.05	1.4	1.52
Ho	2.84	0.63	0.12	0.49	0.15	0.19	0.85	0.36	0.97	0.29	0.24	2.02	63.1	0.62	1.1	2.66	1.8	0.17	0.19	0.26	0.47	0.22	0.54	0.26	0.33	0.28
Er	7.1	1.56	0.41	1.4	0.49	0.67	1.84	0.88	2.89	0.62	0.53	4.74	112	1.78	2.66	6.6	4.97	0.44	0.43	0.7	1.39	0.52	1.72	0.61	0.79	0.86
Tm	1.4	0.32	0.06	0.2	0.06	0.09	0.28	0.16	0.38	0.09	0.08	0.86	20.9	0.23	0.5	0.95	0.74	0.07	0.07	0.24	0.18	0.08	0.42	0.23	0.23	0.12
Yb	5.51	1.37	0.54	1.32	0.5	0.83	1.61	1.17	1.94	0.57	0.46	6.28	88.9	1.37	2.63	5.8	4.88	0.49	0.4	0.84	1.22	0.49	2.13	0.98	0.8	0.77
Lu	0.74	0.2	0.09	0.22	0.08	0.14	0.35	0.19	0.28	0.11	0.11	1.13	15.8	0.19	0.4	0.69	0.74	0.09	0.09	0.11	0.17	0.1	0.29	0.13	0.1	0.11
S	200	50	84800	38800	169000	600	200	500	400	1500	100	200	200	7300	15800	400	200	100	8400	100	32300	62400	102000	56200	24100	200
Bi	12.3	3.5	12	13	5	6	5.2	2.2	0.8	3.1	2.1	23.5	83	5.7	1	3.3	0.05	21.8	390	16.7	113	0.8	1255	43.1	18.4	0.05
In	0.05	0.05	1	0.8	0.1	0.1	0.09	0.1	0.11	0.2	1.3	0.6	0.04	33.2	0.05	0.05	0.08	9.8	0.1	0.7	74.7	0.09	2.16	1.9	0.05	0.05
Cu	51	288	4423	1702	65	38	4	2.3	4	2.6	3.1	6	102	4805	98	17	11	4	1.2	100	11160	33.3	20020	67100	96	4
Zn	2.5	57	233	374	27	15	18.6	23	34	30.7	39.6	25.1	22	111	5	14	15	9.3	30.9	34	140	181	143	2032	9	4
Te	0.5	0.5	0.4	0.4	0.4	0.4	0.9	0.9	0.5	0.9	0.9	0.9	36	0.2	0.5	0.5	0.05	0.9	0.9	0.25	0.2	0.9	0.5	0.25	0.5	0.05
Pb	9	21	68	213	1162	22	9.3	13.5	22.9	14.8	6.1	7.5	32.2	1.7	62	110	1.1	24.5	4	12.1	9.9	384	544	1423	15	0.4
Sb	3	31	5	7	39	4	14	29	1.5	4584	107	59	79	14	9	12	4	25	85	6	19	130600	402	54383	13	6
Cr	42	68	12	9	87	53	5.6	4.6	15	4.1	2.9	3.6	31	37	132	31	6	3.4	2.1	62	22	13.5	15	29	46	5
Ni	2	56	3	3	27	7	0.9	0.8	3	0.4	1.6	3.9	40	2	127	10	3	0.8	0.8	2	2	7.7	304	2	44	3

Tab. 12 – continuation
Representative analyses of rock and mineralizations. Permian MMH cycle in Gemeric unit.

Locality	Jedľovec	Smolník-Uhorná	Smolník	Smolník	Smolník	Smolník	Hnilec	Hnilec	Delava	Hnilec	Hnilec	Hnilec	Čučma	Dlhá dolina	Kurišková	Petrová hora	Krompachy	Dlhá dolina	Hnilec	Dlhá dolina	Dlhá dolina	Štofova dolina	Jedľovec	Rožňava	Poráč	Krompachy
Rock	Lydite	Lydite	Stratabound	Stratabound	Stratabound	Keratophyre	Porphyric	Porphyric	Porphyric	Medium grained	Aplitic	Greisen	Stockwork	Skarn	U-SedEx	U-SedEx	Andesite	Greisen	Greisen	Skarn	Skarn	Vein	Vein	Vein	SedEx-U-Mo	Rhyolite
			sulfidic miner.	sulfidic miner.	sulfidic miner.	Smolník Fm.	Ms/Bt granite	Medium grained	Medium grained	Ms granite	granite	Cst-Toz-Tur		Mgh-Cst-Ank				Outcrop	As-Png-Ank		Sulfidic rim	Sb-Ank-Sd	Sd+sulfides	Sb+sulfides	breccia	
			Center exhal.	Trans. zon. exhal.	Extern zo. exhal.	Extern zo. exhal.	grey (G)	Bt/Kfs granite (G)	Bt/Kfs granite (G)	(G1)	(G2)															
Sample	PF/53-149.2 m	PF/61-119.2 m	SM-3	SM-1	SM-2	PF 59/9	HD-41-1037.9 m	HD-41-1092.3 m	DP-1-553 m	Hn-28-380 m	1st level	HN-1253	CU-17-1	V-DD-43-266.8 m	LE-K-29-150 m	gallery-55	1113-24 m	DD-1	HN-133	VSV-05-2	V-DD-43-266.8	Rozabela-1	PF/53-150.6 m	STR-VI-gallery	G-400	1113/7 m
Age - Ma	Silurian	Silurian	Devonian	Devonian	Devonian	Devonian	281-275	281-275	281-275	265-258	265-258	268			300-275. 274-263	300-275. 274-263	300-275. 274-263		263						256	263-258
Zone	Chl	Chl	Chl	Chl	Chl	Chl	Bt/EpAmp	Bt/EpAmp	Bt/EpAmp	Bt/EpAmp	Bt/EpAmp	Bt/EpAmp	Chl-Ap	Chl-Stl	Chl-Ap	Chl-Ap	Chl-Ap	Chl-Ap	Chl-Ap	Chl-Stl	Chl-Stl		Chl	Chl	Chl-Ap	Chl-Ap
Co	6.2	11.9	36.1	26.9	9.6	2.6	9.8	2.8	5	4.6	6.8	0.9	13	62	92.8	105	10	8.7	6.1	9.6	159	7.7	3383	106	57.9	8
Ag	0.25	0.25	3.6	2.6	3.1	0.8	0.49	0.49	0.3	0.4	0.04	0.4	0.5	0.2	2.3	1.3	0.3	0.49	0.4	0.25	0.2	0.04	4.7	1155	0.7	0.3
Ba	78	523	17	12	1182	688	61	89	195	74	130	392	83	32	488	222	100	23	48	17	23	109	13	5	550	1163
Sr	7	25	2	129	91	16	53	32	38	13	13	330	324	33	82	25	48	4	21	1	135	121	17	1	28	45
Cs	0.25	4.3	0.2	0.15	3.8	4.4	8.3	12.7	4.83	32.4	35.9	8.4	1.53	15	10.6	4.1	14.1	2.6	2.4	0.8	6.5	2.3	0.25	0.25	5.2	3.43
Ga	7	18	38	23	17	23	15.9	21.9	21	26.1	22.7	6.4	2	11.9	35	17	21	5.6	4.3	2.9	5.6	3.1	120	0.7	12	7
Tl	0.15	0.8	0.15	0.15	24.9	0.8	0.5	1.3	1.3	2.4	2.4	1.5	0.2	0.3	5.72	0.37	0.3	0.2	0.2	0.4	0.2	0.3	0.15	15.9	2.95	0.1
Hf	0.7	2.8	1	0.9	1.2	1.7	1.7	1.7	4	1.6	1.7	0.6	17	0.9	5.5	3.8	8.7	7.4	1.1	1	3.2	0.4	4.1	0.5	2	1.5
Zr	23	75	91	38	81	131	134	49	120	36	38	38	36	2	209	286	343	75	35	2.5	19	1	15	2.5	100	42
Sc	12.3	5.89	5	4	18	16	3.8	3.8	4	3.3	2.4	4.3	6.9	2.7	30.8	12.2	14.1	10.3	0.4	0.5	2.9	3.1	0.91	2.6	2.88	1.5
V	674	177	17	4	114	71	9.4	2.1	10	0.45	0.45	4.7	57	30	186	164	45	0.45	0.45	2.5	33	11.4	17	2.5	317	15
Cd	0.5	1	0.2	0.8	0.1	0.2	0.1	0.03	0.1	0.03	0.03	0.5	0.1	0.2	0.5	0.5	0.1	0.03	0.4	0.5	0.5	0.4	10	5.4	0.5	0.05
Cl	90	90	90	90	90	90	90	300	90	90	90	90	90	50	90	90	80	90	90	50	50	90	90	50	50	50
Be	0.3	2.5	0.21	0.33	2.98	3.25	7.72	6.14	4.1	2.32	4.43	2.09	1.9	4.7	4.97	2.9	2.3	0.34	1.17	0.2	1.1	0.96	0.13	0.05	0.94	0.9
Se	0.5	2.2	0.8	0.8	10	0.8	0.09	0.1	0.5	1	0.09	0.9	2	0.5	0.5	1.5	0.05	5	0.09	0.5	0.5	5	3	0.5	0.5	0.05
Sum mg/kg	1773.21	2752.73	90329.29	41733.35	174003.42	2347.87	2201.76	7534.03	1974.56	9278.43	7428.85	228586.78	12220.35	16757.51	24824.00	5776.92	2047.04	124717.98	127159.74	1280.46	47364.66	195039.14	173252.47	187184.14	26716.45	2411.08
Suma total	99.61	100.85	100.41	100.67	100.37	99.72	99.91	100.10	101.02	99.74	99.99	94.80	100.02	99.83	100.40	100.07	100.02	100.51	100.16	99.83	100.16	99.84	100.72	100.71	100.902	100.116

Mineralia Slovaca, Web ISSN 1338-3523, ISSN 0369-2086
51 (2019), 157 – 174, © Authors 2019. CC BY 4.0

Mineralogical and geochemical proxies for the Middle Eocene oil shales from the foothills of the Greater Caucasus, Azerbaijan: Implications for depositional environments and paleoclimate

ADIL A. ALIYEV and ORHAN R. ABBASOV

Azerbaijan National Academy of Sciences, Institute of Geology and Geophysics, AZ1143, Azerbaijan, Baku, H. Javid ave., 119; ad_aliyev@mail.ru, ortal80@bk.ru

Abstract: The sedimentary environment of the Middle Eocene oil shales in the foothills of the Greater Caucasus (Shamakhi-Gobustan region and Absheron Peninsula), including the salinity, redox, and climate conditions were restored using mineralogical and bulk-rock geochemical signatures of 10 samples taken from the outcrop sections and ejecta of mud volcanoes. Obtained results are in agreement with the evolutionary history of the Middle Eocene sediments, being described in the literature. The samples demonstrate their formation feature within the aquatic environments - lagoons and lakes, having a depth of 10 meters. With the exception of some areas of the Absheron Peninsula, all samples can be associated with freshwater, mixed redox (mostly reducing), and arid/semi-arid environments.

Key words: oil shales, mineralogy, geochemistry, depositional environment, paleoclimate, Greater Caucasus

Graphical abstract

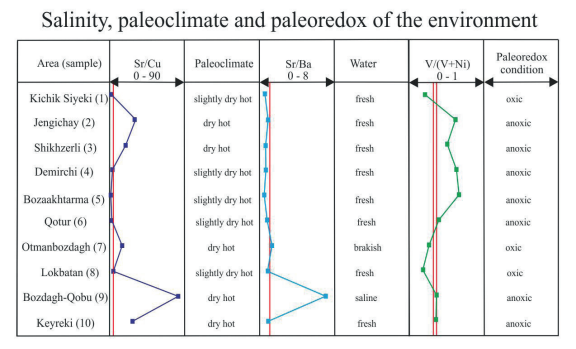

Highlights

- The gradual transition of the sedimentary environment from continental to marine is typical for genesis of Middle Eocene oil shales.
- The depositional conditions of the Middle Eocene oil shales most likely correspond to isolated coastal-marine zones - lagoons and lakes with a depth of 10 meters.
- Except of some samples of the studied regions, oil shales are associated with freshwater, mixed paleoredox (mostly reducing) and arid/semi-arid environments.

Introduction

The Shamakhi-Gobustan region and Absheron Peninsula at the foothills of the Greater Caucasus (Fig. 1a) are located in the collision zone between the Arabian and the Eurasian lithospheric plates (Aliyev & Abbasov, 2019). The specific geodynamic and depositional environments provided favorable conditions for the formation of rich oil and gas fields, mud volcanoes and especially oil shales in the Eastern Azerbaijan, including the adjacent Caspian Sea (Aliyev et al., 2019).

Oil shales are very important for Azerbaijan, being considered as an alternative source of energy and raw materials (Sultanov & Sultanov, 1947; Ali-zade et al., 1962; Salaev et al., 1990; Aliyev et al., 2002, 2015; Abbasov et al., 2013; Aliyev & Abbasov, 2019). It was determined that the main qualitative parameters (organic matter 15–31 %, sulfur 0.4–1.2 %, ash content 65–85 % and caloric value 6.0–12 MJ . kg^{-1}) in oil shale deposits such as Guba, Diyally, Jengichay, Kichik Siyeki and others in Azerbaijan exceed low-caloric deposits of some other countries, like Germany, Romania, China, etc. (Abbasov, 2015; Aliyev et al., 2015a; Aliyev & Abbasov, 2018). In addition, this shale in Azerbaijan has a great potential as a source rock of oil (Abbasov et al., 2012, 2015; Abbasov, 2016a). The beds of oil shales in Central Gobustan, located at relatively shallow depths, are considered as future sources of shale gas for the country (Abbasov, 2016a).

In the Upper Cretaceous–Middle Miocene sedimentary sequences in Eastern Azerbaijan, about 60 oil shale outcrop sections were recorded (Aliyev et al., 2014). However, the main deposits of Middle Eocene oil shales are very thick and have wide spatial distribution (Abbasov, 2009). Oil shales were also found in the ejecta of mud volcanoes (Abbasov et al., 2012; Aliyev & Abbasov, 2018). In these rocks, the Globigerina bulloides (Orbigny), Cibicides sp., Globigerina triloculinoides (Plummer), benthos and planktonic foraminifers, as well as fish teeth and bones were found, belonging also to Middle Eocene.

In the published literature, an extended research was devoted to the general geological, organic-geochemical, and other characteristics of oil shales in Azerbaijan

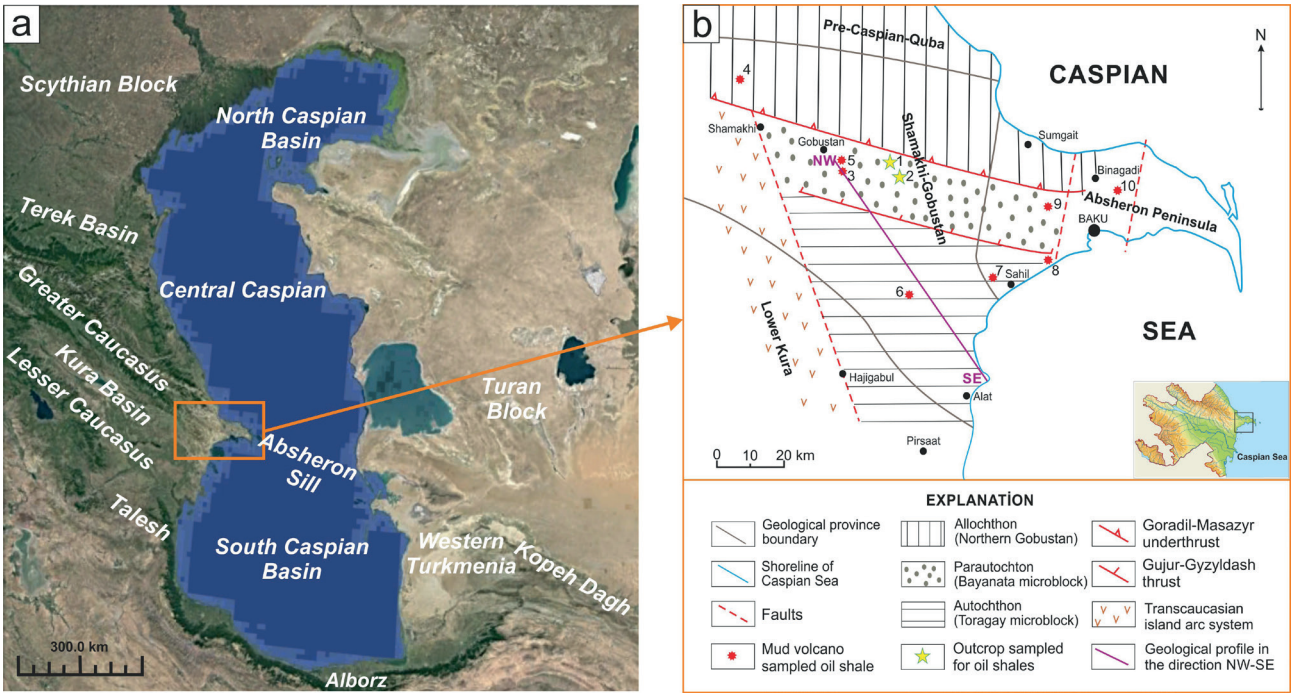

Fig. 1. Location maps (after Aliyev & Abbasov, 2019; Aliyev et al., 2015b) of study regions and samples collected from outcrop sections (1 – Kichik Siyeki, 2 – Jengichay) and ejecta of mud volcanoes (3 – Shikhzarli, 4 – Demirchi, 5 – Bozaakhtarma, 6 – Qotur, 7 – Otmanbozdagh, 8 – Lokbatan, 9 – Bozdagh-Qobu, 10 – Keyreki).

(Sultanov & Sultanov, 1945; Sultanov, 1948; Ali-zade et al., 1962; Salaev et al., 1990; Aliyev et al., 2002, 2014, 2015, 2018a; Aliyev & Abbasov, 2018; Abbasov, 2009, 2016, 2017; Abbasov et al., 2013). Because the studies of depositional environments and paleoclimate conditions were insufficient, this study is devoted to the reconstruction of depositional environments and paleoclimate conditions in relation to the mineralogical and geochemical proxies for the Middle Eocene oil shales of researched areas.

Geology and tectonics: a general overview

The Shamakhi-Gobustan region, located in south-eastern side of the Greater Caucasus, is built of Mesozoic and Cenozoic sediments. About 40 oil shale outcrop sections were registered in the region (Sultanov, 1948; Salaev et al., 1990; Abbasov, 2009; Aliyev et al., 2014). The oil shale interbeds are associated with the sediments of the Upper Cretaceous–Upper Miocene (Sultanov & Sultanov, 1947; Salaev et al., 1990; Aliyev & Abbasov, 2018).

The Middle Eocene sediments are also very important for Azerbaijan (Sachsenhofer et al., 2018), including the Shamakhi-Gobustan region in terms of oil shales-bearing lithofacies (Aliyev & Abbasov, 2019). Besides the outcrops, the Middle Eocene oil shale samples were collected also from the mud volcanoes (Shikhzarli, Demirchi, Bozaakhktarma and Qotur), which brought additional information. In the region, the thickness of Middle Eocene sediments varies from 1.7 km (Central Gobustan) to 3.8 km (Southern Gobustan; Fig. 2).

The variability of the Middle Eocene lithofacies in this region is characteristic. The basal sequence is made up of black shales with interbeds of light brown oil shales (Sultanov & Sultanov, 1947; Aliyev & Abbasov, 2019). The thickness of the interbeds of oil shales found on the wings and ridges of anticlines and synclines, such as Kichik-Siyeki, Jengichay, Jengidagh, a.o., varies from a few centimeters to about 10 meters (Salaev et al., 1990; Abbasov, 2009).

The tectonic block identified between the Altyagaj--Kurqachidagh fault and the Goradil-Masazyr underthrust is called the Northern Gobustan allochthon. This allochthon is related to the Baskal overthrust mass that the Cretaceous flyschoid sequences cover the Paleogene--Miocene sediments (Aliyev & Bayramov, 1999). A microblock located south of the Goradil-Masazyr underthrust and bounded by the Gujur-Qyzyldash thrust is Bayanata parautochthon (Fig. 1). The total thickness of the Paleogene-Miocene sediments in this microblock is 2.5–4.5 km (Fig. 2), and it is the largest exposed area (Boyuk Siyeki, Kichik Siyeki, Jengichay, a.o.) of the Middle Eocene oil shale in the Shamakhi-Gobustan region (Sultanov & Sultanov, 1947; Abbasov, 2009). A microblock located south of the Gujur-Qyzyldash thrust is named Toragay autochthon (Fig. 1b) that made up of

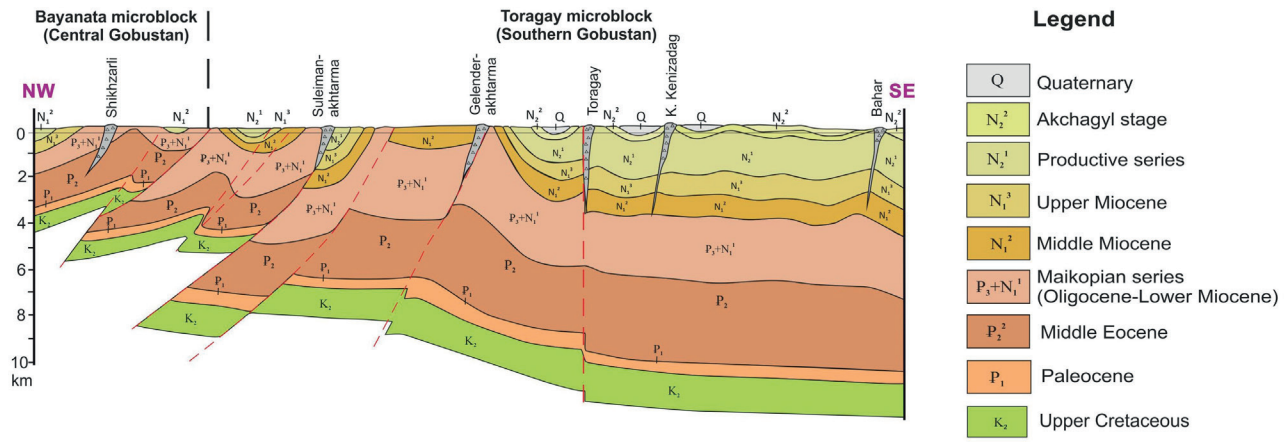

Fig. 2. Geological profile of the Bayanata and Toragay microblocks (after Aliyev et al., 2015b).

the Cenozoic sediments. In this microblock, the top of the Upper Cretaceous lies at a depth of 8–11.5 km (Fig. 2). In addition, the largest and active mud volcanoes (Toragay, Boyuk Kenizadagh, Qotur, a.o.) of the region crop out here (Aliyev et al., 2015b). The ejected mud of these mud volcanoes typically originates from the Maikopian series (Inan et al., 1997; Aliyev et al., 2015) and Middle Eocene sediments (Aliyev et al., 2015b) that have been buried to depths of 4–10 km (Odonne et al., 2020).

On the Absheron Peninsula, which is the southeastern end of the Greater Caucasus, 18 oil shale outcrops have been discovered (Sultanov, 1948; Aliyev et al., 2002). The Peninsula is built of Upper Cretaceous-Cenozoic sediments (Aliyev et al., 2015). The oil shale outcrops related to the Middle Eocene have been found only in Goytepe and Govundagh areas, and they associated mainly with the Upper Maikop and the Upper Miocene (Abbasov, 2016b, 2017).

The tectonic zones studied here dip to the southeast, in the direction of the extension of the Greater Caucasus. The Mesozoic complex in the south of the Absheron Peninsula abruptly descends (Aliyev et al., 2015). The Paleogene--Pliocene sediments dominate in the geological structure of the uplifts, which was found in some outcrop sections (Khirdalan, Zigilpiri, a.o.).

Four tectonic zones have been established in the Peninsula, and there is a morphological connection between the anticlines and the synclines. The dislocations in the Peninsula are indicated also by mud volcanoes Keyreki, Lokbatan, Bozdagh-Qobu, etc. (Aliyev et al., 2015).

Sampling and methods

Sampling collected two samples of oil shales from the outcrops (1 – Kichik Siyeki, 2 – Jengichay) and eight samples from ejecta of mud volcanoes (3 – Shikhzarli, 4 – Demirchi, 5 – Bozaakhtarma, 6 – Qotur, 7 – Otmanbozdagh, 8 – Lokbatan, 9 – Bozdagh-Qobu, 10 – Keyreki; Fig. 1b). The samples were black, grey and brown in colour, having laminated structure.

Mineralogical composition of rocks. Bulk rock mineralogical composition of oil shale samples was determined by XRD "MiniFlex 600" at the Institute of Geology and Geophysics, Azerbaijan National Academy of Sciences. The samples were first wet-ground to fine powders (~5 µm), and then they were loaded onto a zero-background sample holder. After running on the XRD, the resulting diffraction patterns were scanned over the 2θ range of 5 to 65° using Cu–Kα radiation (accelerating voltage of 40 kV and current of 15 mA) with a D/tex high-speed detector using 0.02° steps and a scan rate of 2° per minute. XRD patterns were analysed with the CRYSTAL IMPACT software Match!, and mineral abundances were determined by the RockJock XRD pattern fitting program.

Bulk rock geochemistry. The major elements were determined by X-ray fluorescence spectrometry with wavelength energy dispersion on the S8 TIGER Series 2 WDXRF. The sample was prepared via a hydraulic press at 25 tons. The fire loss was determined at 1000 °C. The quality of the data was verified by analysing the certified sample SRM 2709 (NIST, 2002).

The trace elements were analysed using an Agilent 7700 Series ICP-MS. All samples were finely ground until they could be sieved through a 75 µm sieve. A total of 50 mg of the powder of each sample was dissolved by cleavage with ultrapure acids in three stages. The solutions were transferred to clean flasks and diluted with 1 % HNO_3 to 50 ml. Acids were purified using acid purification equipment. Analytical uncertainties (relative standard deviations) related to measuring elements were less than 5 %. The analyses of major oxides and trace elements were also performed at the Institute of Geology and Geophysics, Azerbaijan National Academy of Sciences.

Age of rocks. The ages of samples collected from the mud volcanic areas were studied at the Integrated Engineering Exploration Production, Department of Geophysics and Geology, SOCAR. The studied samples were carefully grounded and washed to remove sludge and clay particles. The dried powder samples is scattered on a black board measuring 9 x 12 cm. Microfaunas were studied at magnification x200–300, using the Loupe Zoom Paralux XTL 745 and МБС-10 microscopes. Microscope images were transferred to a computer using a digital camera OptixCam.

Mineralogy

The provenance and tectonic setting of used 10 samples were widely discussed in previous papers (Aliyev & Abbasov, 2019; Aliyev et al., 2019).

In this study, related to the bulk rock mineralogical composition, it should be briefly noted that 11 minerals of 5 classes were found in the samples. The samples consist mainly of silicates, as well as carbonates and sulphates. Only one sample contains 1 % of halite. Hematite was found in three samples taken from mud volcano areas Demirchi, Bozdagh-Qobu and Keyreki.

Quantitative analysis of clay minerals shows that montmorillonite (mean = 15.1 %) and chlorite (mean = 16.2 %) are more abundant than illite (mean = 10.9 %). As for silicates, the value of quartz is 25.8 %, and feldspar – anorthite (Fig. 3a, c) and albite (Fig. 3b, d) – 8.2 %. Calcite was determined in eight samples (mean = 7.0 %), and siderite only in two areas (mean

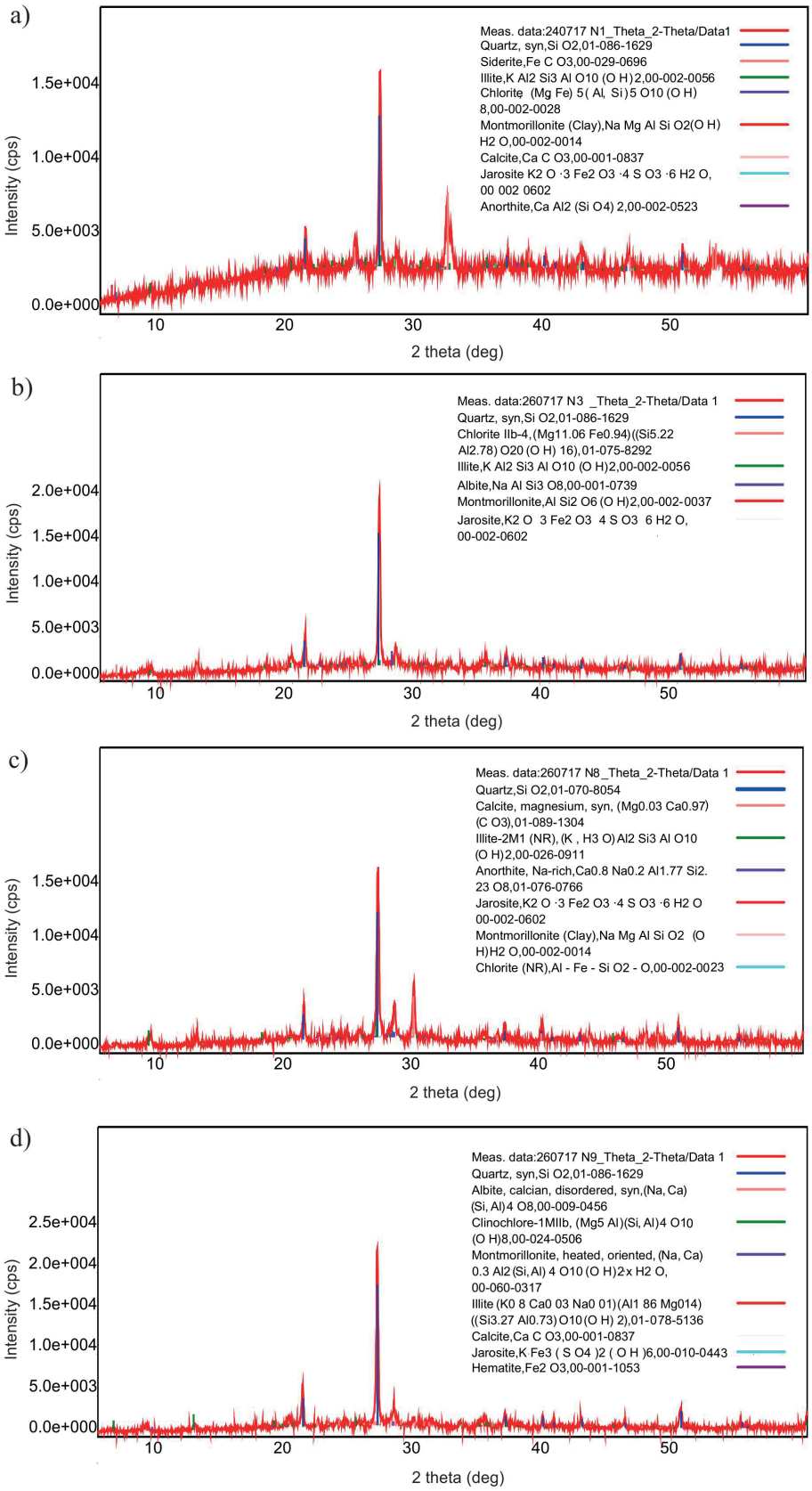

Fig. 3. XRD images of oil shale samples: a – Kichik Siyeki (1), b – Shikhzarli (3), c – Lokbatan (8), d – Bozdagh-Qobu (9).

Tab. 1
Mineralogical composition of samples [wt.%].

	Area (sample)	Quartz	Feldspar	Calcite	Illite	Montmorillonite	Chlorite	Jarosite	Halite	Siderite	Hematite	Gypsum
Shamakhi – Gobustan region	Kichik Siyeki (1)	26.7	10.0	2.0	9.0	10.0	15.0	1.5	–	25.8	–	–
	Jengichay (2)	28.0	6.0	8.0	10.0	13.0	20.0	15.0	–	–	–	–
	Shikhzarli (3)	23.0	7.0	–	15.0	15.0	20.0	20.0	–	–	–	–
	Demirchi (4)	28.0	13.0	4.0	15.0	15.0	18.0	4.0	–	–	3.0	–
	Bozaakhtarma (5)	27.0	5.0	–	7.0	26.0	10.0	22.0	–	3.0	–	–
	Qotur (6)	23.0	5.0	12.0	10.0	12.0	16.0	16.0	1.0	–	–	5.0
Absheron Peninsula	Otmanbozdagh (7)	20.0	15.0	9.0	12.0	17.0	17.0	7.0	–	–	–	–
	Lokbatan (8)	23.0	5.0	14.0	10.0	16.0	15.0	17.0	–	–	–	–
	Bozdagh-Qobu (9)	35.0	8.0	3.0	11.0	12.0	16.0	12.0	–	–	3.0	–
	Keyreki (10)	24.0	8.0	18.0	10.0	15.0	15.0	4.0	–	–	6.0	–
Mean		25.8	8.2	7.0	10.9	15.1	16.2	11.8	0.1	2.9	1.2	0.5

= 2.9 %) with carbonates (Tab. 1). The most common sulphate in the samples is jarosite (mean = 11.8 %). In addition, 5 % of gypsum was defined in the Qotur sample. The mean value of hematite is 1.2 %.

Major oxides

The value of SiO_2 ranges from 45.72 to 55.55 %, with an average value of 49.81 %. Compared to the mud volcanoes of the Shamakhi-Gobustan region, the value of this major oxide differs in samples taken from the outcrop sections (Kichik Siyeki and Jengichay) in some regions. The maximum values were recorded in the Northern Gobustan allochthon. The concentration of Al_2O_3 varies from 12.69 to 16.81 % (with an average value of 14.64 %) and the same regularity can be given for this major oxide. The highest Fe_2O_3 value was determined only in Kichik Siyeki, and in the remaining nine samples its value is much lower (Fig. 4).

The compositions of Na_2O (0.97–1.76 %, average value 1.34 %), MgO (2.25–3.20 %, aver. 2.65 %), P_2O_5 (0.03–0.39 %, aver. 0.17 %), SO_3 (0.35–7.37 %, aver. 2.93 %), K_2O (2.06–3.89 %, aver. 3.36 %), CaO (0.29–9.67 %, aver. 3.97 %), TiO_2 (0.61–0.90 %, aver. 0.76 %) and MnO (0.02–0.18 %, aver. 0.09 %) are shown in Tab. 2. The regularity of the abundance of oxide compounds in the samples was as follows: $SiO_2 > Al_2O_3 > Fe_2O_3 > CaO > K_2O > SO_3 > MgO > Na_2O > TiO_2 > P_2O_5 > MnO$.

Trace elements

The maximum Zr values were recorded in the samples of the mud volcanoes Lokbatan and Bozdagh-Qobu (317 and 419 ppm). Unlike the Otmanbozdagh sample, the Sr

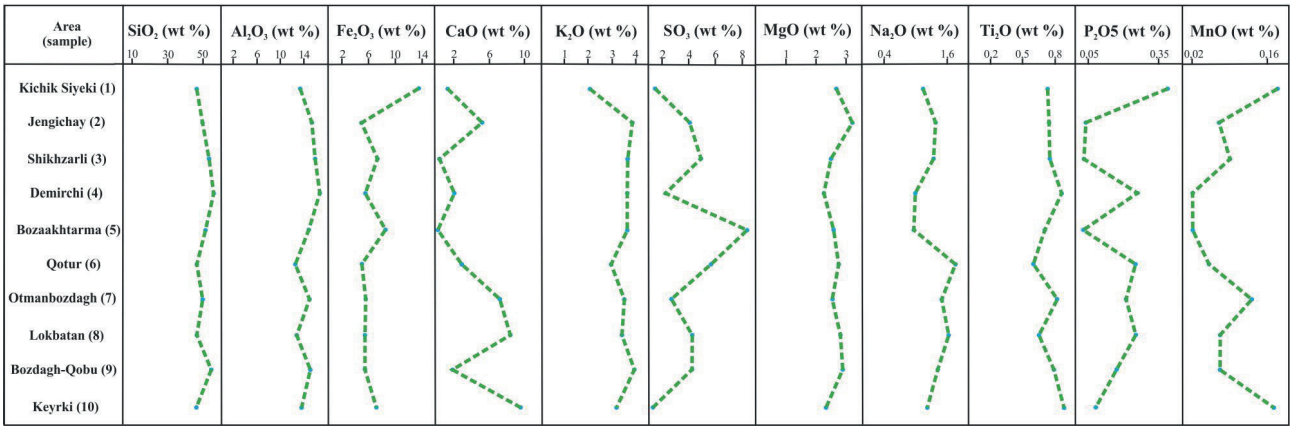

Fig. 4. Variation of major oxides in the samples.

value is higher in samples from three other mud volcanoes (426 ppm in Lokbatan and Keyreki, and 1000 ppm in Bozdagh-Qobu) of the Absheron Peninsula. According to the distribution of Mo, an absolute superiority of the Shamakhi-Gobustan region was established. The value of Zn reaches 112 ppm in the sample of mud volcano Demirchi, 100 ppm in the Lokbatan, 114 ppm in the Keyreki and 541 ppm in the Bozdagh-Qobu. The Absheron Peninsula has a significant advantage in the Cr content distribution. The highest value of V was recorded in the sample of the Bozaakhtarma mud volcano. In addition, the value of this element in other samples, such as Jengichay reaches 104 ppm, Demirchi – 241 ppm and Shikzarli – 246 ppm. The values of Ga and U are characterized by low concentrations. The regularity of the abundance of trace elements in the samples was as follows: Ba > Sr > Zr > Rb > V > Cr > Zn > Ni > Mo > Cu > Pb > Br > Ga > As > U = Se (Tab. 2).

Tab. 2
Major and trace element concentrations of oil shale samples.

Area (sample)	Kichik Siyeki	Jengichay	Shikhzarli	Demirchi	Bozaakhtarma	Qotur	Otmanbozdagh	Lokbatan	Bozdagh-Qobu	Keyreki	Mean
Major oxide [wt %]											
SiO_2	46.04	49.55	53.39	55.55	51.23	46.43	49.71	46.07	54.39	45.72	49.81
Al_2O_3	13.36	15.36	16.06	16.81	14.93	12.69	15.10	12.96	15.27	13.82	14.64
Fe_2O_3	13.54	4.92	7.29	5.53	8.54	4.97	5.63	5.42	5.46	7.12	6.84
FeO	12.18	4.43	6.56	4.98	7.68	4.47	5.07	4.88	4.91	6.41	6.16
CaO	1.37	5.22	0.37	2.09	0.29	2.97	7.32	8.47	1.97	9.67	3.97
Na_2O	1.15	1.38	1.34	1.00	0.97	1.76	1.50	1.63	1.42	1.23	1.34
K_2O	2.06	3.84	3.65	3.61	3.61	2.93	3.47	3.38	3.89	3.15	3.36
MgO	2.67	3.20	2.49	2.25	2.58	2.76	2.56	2.81	2.89	2.34	2.65
TiO_2	0.74	0.75	0.76	0.87	0.71	0.61	0.83	0.66	0.80	0.90	0.76
P_2O_5	0.39	0.04	0.03	0.26	0.03	0.25	0.21	0.25	0.17	0.08	0.17
SO_3	0.45	3.06	3.90	1.26	7.37	4.69	1.69	3.30	3.20	0.35	2.93
MnO	0.18	0.07	0.09	0.02	0.02	0.05	0.13	0.07	0.07	0.17	0.09
Trace element [ppm]											
Ba	235	405	426	555	384	412	241	516	142	434	375
Zr	116	196	215	142	184	214	117	419	317	154	207.4
Br	8	12	5	1	5	72	5	5	8	3	12.4
Mo	80	77	64	48	126	5	19	16	34	12	48.1
Sr	116	325	214	317	134	294	295	426	1000	426	354.7
Cu	49	11	11	83	94	88	19	89	12	15	47.1
Cr	87	112	141	84	96	214	216	212	134	142	143.8
Rb	53	218	191	94	175	184	710	114	41	81	186.1
Zn	83	71	86	112	85	84	77	100	541	114	135.3
Ni	74	16	102	31	75	34	41	176	60	74	68.3
Se	0.4	0.1	0.6	0.3	11.6	0.7	0.3	0.5	0.1	0.4	1.5
As	5	3	5	8	2	7	23	3	9	7	7.2
Ga	17	8	15	11	7	12	14	5	8	12	10.9
V	31	104	246	241	964	41	24	61	61	71	184.4
U	3	1	2	1	1	1	1	1	3	1	1.5
Pb	7	34	12	19	19	18	9	18	11	21	16.8

Interpretation of analytical data based on knowledge from earlier researches

Depositional environments. The mineralogical assemblages of the studied areas have provided information on the depositional environments during the Middle Eocene age.

Mason and Moore (1982) considered illite as the applicable mineral for the marine environment analysis. Illite associates with a K-rich alkaline environment. A decrease in water depth leads to a decrease in illite concentration (Freed, 1980). Powers (1957) found the genesis of chlorite in a marine environment. However, in addition to an open sea, Weaver (1956) believed this mineral may also be associated with sedimentation occurring in a freshwater environment. Parham (1966) suggested a general clay zonation from a coast to deep ocean environment in the following order: kaolinite, illite, chlorite, palygorskite, and sepiolite. Together with montmorillonite, mixed I/S minerals can be formed at almost all paleodeposition ranges. A typical pattern of distribution of clay minerals from shore to open sea is determined as follows: kaolinite – illite – smectite (Galán, 2006). Transformation of smectite to illite occurs due to the absorption of K^+ and the release of Na^+. Removed Na^+ leads to albitization, which was found in some samples (Fig. 3b, d). Hence, replacing Na^+ with K^+ contributes to albitization in sandstones and shales. The process of converting of kaolinite to illite requires a relatively high temperature (100–130 °C), which leads to removal of a certain amount of K^+ (Saigal et al., 1988).

The genesis of calcite is associated with shallow phreatic zones (De Ros et al., 1994). In addition, there is an evidence that calcite occurs in alluvial environment (Leeder, 1975; Wright & Tucker, 1991).

Jarosite occurs in an aqueous and acidic environment (Singh et al., 2016). Hematite is more susceptible to oxidation and can be considered a replacement product of magnetite. In many igneous rocks, this mineral is a solid solution in the composition of ilmenite. Higher contents of hematite produce a strip-like iron formation. The origin of this mineral is related to geothermal waters, as well as to a stagnant water environment at the bottom of lakes, sometimes also anhydrous conditions and volcanic activity (Nelson, 2014). Zolotov and Shock (2005) considered that the genesis of hematite spherules is associated with mineral deposition in an aqueous environment. They concluded that the occurrence of a jarosite-goethite-gypsum assemblage is a result of precipitation of acidic solutions formed through near-surface aqueous oxidation of pyrite mineral. Unlike a marine environment, the content of Ca and Mn in siderite mineral, associated with the deposition of freshwater, is relatively higher. Such a difference is explained by various activities of Fe^{2+}, Mg^{2+}, Ca^{2+}, and Mn^{2+} in a marine environment and porous meteoric water (Mozley, 1989). In addition, the formation condition of halite, which was found in lower concentrations in two samples, is associated with an evaporite deposition occurring in a saline lake.

Geochemical proxies of lithofacies assemblages provide useful information on paleodepositional environments. Some ratios and plots based on the major oxides, such as Al_2O_3, K_2O, Na_2O, CaO, Fe_2O_3, etc., and trace elements, were used to reconstruct the deposition processes of oil shale samples during the Middle Eocene.

Englund and Jørgensen (1973) established a ternary classification diagram based on a study of soil and shale samples from different geographical regions of the world to ascertain the depositional environments of the sediments. The position of samples, associated with various geochemical, mineralogical and paleoweathering conditions, in various parts of AKF ternary diagram [Al_2O_3 – (K_2O + Na_2O + CaO) – (Fe_2O_3 + MgO)] reveals whether

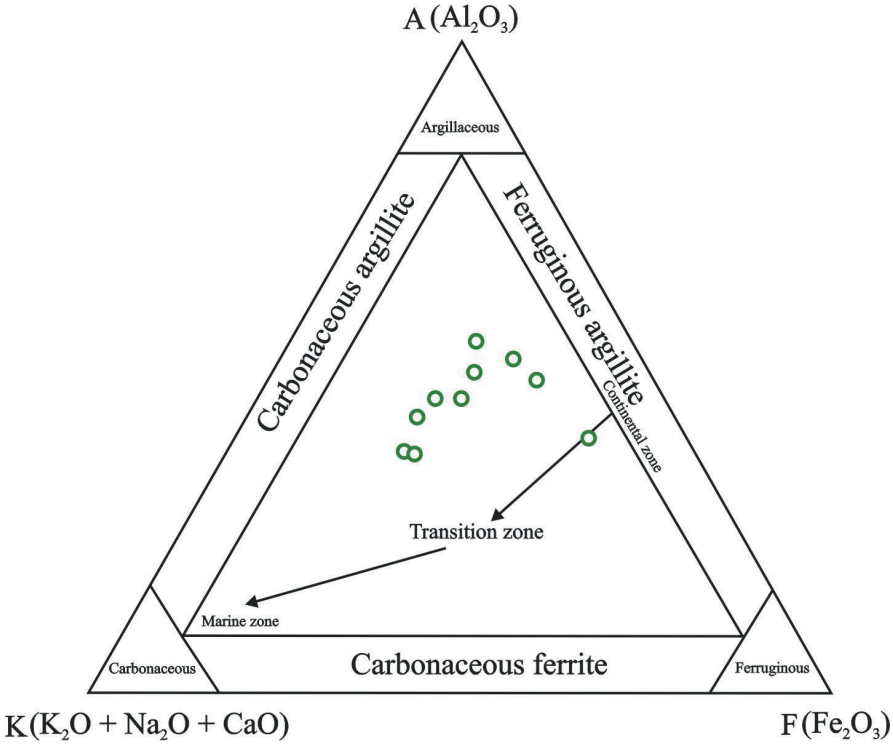

Fig. 5. Oil shale samples in AKF diagram (after Englund and Jørgensen, 1973).

the sediments were deposited in continental, transition and/or marine zone. Fig. 5 shows a gradual transition of sediments of the basin from freshwater to marine environment, majorly falling within the transition zone.

Na is often transported in the form of a solvent. Its high concentration indicates a continental sedimentary environment and arid climate. However, within the sea and lake conditions, this element is associated with a humid climate. Low amount of Na is considered typical for a coastal marine condition. The amount of Al increases when this clay-forming element relates to an open sea environment (Engalychev & Panova, 2011). In addition, the ratio of Na_2O/Al_2O_3 provides information on the relationship of rocks with clay minerals or plagioclase (Ratcliffe et al., 2007). Such a specific feature creates this ratio to be a favorable indicator for assessing a paleodepositional environment. The Na_2O/Al_2O_3 values are characterized by an increased tendency from the Northern Gobustan to Absheron.

Since a high MgO value indicates marine lithofacies, then an increase in this major oxide in the samples characterizes a broad transition from the terrestrial to marine lithofacies. The use of the binary diagram MgO vs. Fe_2O_3 and the ternary diagram (MgO – SiO_2/Al_2O_3 – Fe_2O_3) excludes a formation condition associated with the nonmarine assemblages (Fig. 6a, b).

K is mainly transported as solvent in a humid climate condition. Lower concentration of this element is associated with a coastal-sea basin environment (Engalychev & Panova, 2011). Taking into account the role of K in the reconstruction of a paleodepositional environment of sedimentary rocks, Roaldest (1978) established a classification diagram based on K_2O/Al_2O_3 vs. log MgO/Al_2O_3. Our samples in the diagram confirm the marine provenance of studied oil shales (Fig. 6c).

An important issue represents a determination of the water type (seawater or freshwater), as well as the structure (delta, coastal, lagoon, etc.) and depth of the paleobasin of the studied oil shale. To clarify these parameters, detailed chemical characteristics are investigated. Mn and Fe are mobile in the water, Fe^{+2} oxidizes more easily than Mn^{+4}. Mg tends to be reduced faster than Fe. In addition, these two elements, mobile in water, freely transfer from the rock to a reducing environment. Vertical and horizontal flows occurring in a water column cause a separation of Fe and Mg ions from the sediment, so no precipitation of these ions occurs in sediment. However, Fe precipitates in a colloidal form in a low saline environment, while Mn

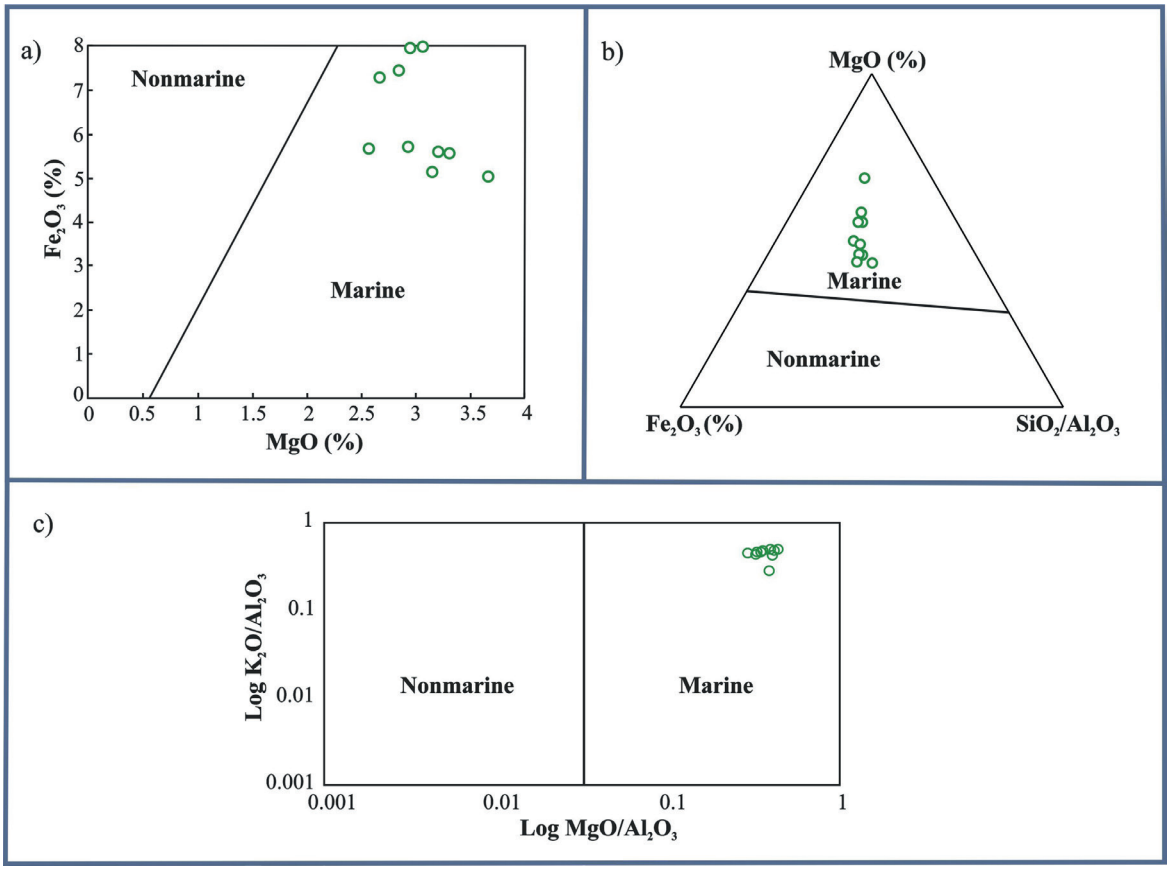

Fig. 6. Diagrams showing depositional conditions of samples: a) MgO vs. Fe_2O_3; b) MgO SiO_2/Al_2O_3 – Fe_2O_3 (after Ratcliffe et al., 2007); c) log K_2O/Al_2O_3 vs. log MgO/Al_2O_3 (after Roaldest, 1978).

is more stable and its precipitation occurs only when an environment is too saline (Liang et al., 2014). Lower Fe values indicate a sedimentation environment associated with a pelagic zone, but higher values represent a zone close to a shelf. The value of Fe/Mn indicates that the studied samples correspond to sedimentation occurring at shallow depths (Fig. 7).

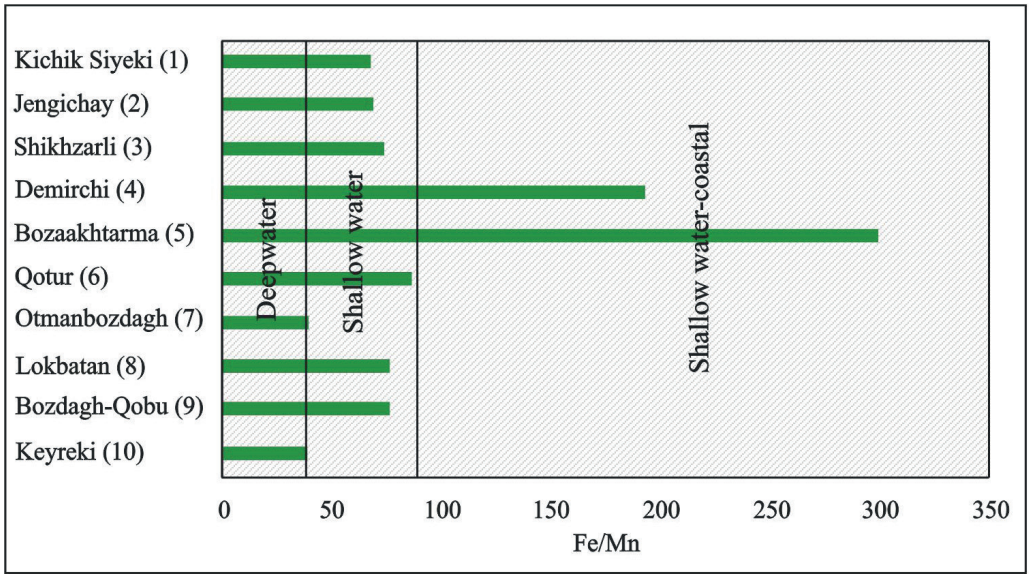

Fig. 7. Paleodepositional conditions of oil shales based on the Fe/Mn ratios of samples.

In sedimentary rocks, a Ti/Mn ratio increases in a nonmarine zone. Resistance to chemical weathering of Ti mineral leads to association with an alluvial and coastal marine region. Ti concentration in saline water basins is characterized by low values, which is associated with the absence of their solutions (Engalychev & Panova, 2011). For the samples studied, the Ti/Mn ratio ranges from 3.14 to 21.5. The obtained results are well-correlated with a shallow water basin.

Indicators such as Mn/Ni and Mn/Ga are widely used to determine a sedimentation conditions. Genetic significance of these indicators is based on a migration characteristics of these elements. As mentioned above, a rich Mn content is characteristic for pelagic zone located far from the coast, but Ga most likely precipitates close to coast, and its value decreases sharply in the direction of deep sea. From the point of view of nickel, a rich concentration of this element is associated with a closed basin – a lagoon, which is rich in organic matter. As a pyroxene exchange product, Ni is incorporated with high concentrations of chloride (Ratcliffe et al., 2007). Therefore, it is used as a facial indicator of a coastal-marine environment to explain the sedimentation process in published literature (Engalychev & Panova, 2011). For the studied samples, the value of Mn/Ni ranges from 2.67 to 31.25, and Mn/Ga from 18.18 to 108.33.

Ti/Zr ratio provides information on the transportation of terrigenous material. Such an estimate is based on the better preservation of Zr in comparison to Ti. A higher value of this ratio corresponds to deep water, a lower – to coastal marine environment (l.c.). The ratio values for samples range from 9.55 to 42.74. Sr and Ba as alkaline earth metals reflect a similar chemical feature. However, Br salts have a lower solubility than those of Sr. On the other hand, the radius of its ion is larger. In the process of paleoweathering and sedimentation, Ba containing clay minerals can easily be adsorbed by colloids and organic particles (l.c.; Liang et al., 2014). In mixed marine and freshwater environments, the main part of this element is deposited as $BaSO_4$. A higher Ba concentration is associated with coastal-marine environment, including an outflow of large rivers. However, the presence of this element in an open sea is very limited (Engalychev & Panova, 2011). In contrast to Sr, an increase in salinity leads to early precipitation of Ba (Liang et al., 2014). However, Sr has the same feature as a crisis limit of salinity. Thus, this element is practically not chemically precipitated, since a salinity becomes higher in seawater. Also, the Sr migration occurs together with Ca (Engalychev & Panova, 2011). Based on the specific chemical characteristics of both elements, a Sr/Ba ratio is considered as an favorable indicator for assessing the water salinity. It was established that the ratio >1 indicates seawater (saltwater) and <1 − freshwater (Couch, 1971; Miknis & McKay, 1983). Except for two samples (Otmanbozdagh and Bozdagh-Qobu), the calculated values of this ratio for oil shales are lower than one.

Paleoredox conditions. Inorganic contents provide indicators of oxygenation of bottom sediment and water column. A number of indices and plots have been identified for the reconstruction of paleoredox conditions of sedimentary rocks, some of which are associated with metals (Jones & Manning, 1994). The value of V in the composition of oil shales increases sharply from the

center to the north in Gobustan. A downward trend was established for oil shale sampled from the Absheron Peninsula (Tab. 2). The general analysis shows that, the V value of oil shale (mean = 184 ppm) is much higher than that of NASC (130 ppm; Gromet et al., 1984), PAAS (150 ppm; Taylor & McLennan, 1985) and UCC (97 ppm; l.c.). Such enrichment corresponds to a marine environment (Ernst, 1970). From the point of view of the incorporation of V^{4+} into porphyrins, V binds to rich organic matter, including oil shale. Such incorporation is the result of substitution for Mg in porphyrins, which are degradation products of chlorophyll (Emerson & Huested, 1991). V is not always correlated with organic matter, and Glikson et al. (1985) found it may be physically hosted by detrital silicate sources (Jones & Manning, 1994). Mangini et al. (2001) explained the richness of U and V during sedimentation due to an anoxic-euxinic environment in bottom sediment and water column. Organic compounds rich in V and other metals are always correlated with Type I and II kerogens. This is due to the organic origin of these kerogens, including their relationship with phytoplankton. However, Type III kerogen is not rich in metals (less than 100 ppm), such as V and Ni. The high stability of V and Ni in organic compounds plays a key role in their connection with tetrapyrrole complexes. The preservation of organic matter associated with tetrapyrroles is also favored under anaerobic conditions. In general, the abundance of these metals in organic matter depends on the concentration of tetrapyrrole complexes contained in organic composition (highly aliphatic material of algal origin). The amount of preservation of such complexes in organic compounds is a function of exposure time to aerobic conditions (Lewan & Maynard, 1982). Huerta-Diaz and Morse (1992) believed that in reducing conditions, which sulfate reduction is more efficient, V accumulates preferentially over Ni (Watitemsu et al., 2014). Emerson and Huested (1991) note that the content of Mo and V in a water column of anoxic condition are usually lower than in oxic seawater environment due to uptake into highly anoxic sediments. Anderson et al. (1989) also established this pattern for U. Shaw et al. (1968) made a conclusion that during early diagenesis under oxygen conditions, V is mobilized from biogenic material, although its mobilization is limited under anoxic environments (Watitemsu et al., 2014). V is more likely to be enriched under acidic conditions, while Ni can be enriched in both basic and acidic conditions (Lewan & Maynard, 1982). In addition, Hatch and Levental (1992) note that high Mo, U, V, Zn and S contents provide an indication on the presence of dissolved H_2S in a strongly stratified water column. Their low contents indicate a weakly stratified, dysoxic water column. Organic sediments are rich in heavy metals such as Cu and Cr. They are well-uptaken and stored by organic matter (Glikson et al., 1985). Cu^{2+} can be reduced to Cu_2S and precipitates in an environment bound to reducing state (Liang et al., 2014). Cr is always bound to detrital fractions of sedimentary rocks.

The tendency to a decrease in Ni/V ratio indicates that the genesis of sedimentation environment associated with hydrocarbons is more reductive (Telnaes et al., 1991). This is bound to the fact that the unavailability of V under oxic conditions, and the removal of nickel as sulfide under anoxic environments (Jones & Manning, 1994). Unlike the Kichik Siyeki sample, the Ni/V ratio is characterized by lower values in the samples of Central Gobustan compared to the Absheron Peninsula.

In general, the suboxic and anoxic intermediate environments show an average V/Cr value >4.25, while the dysoxic state ranges from 2 to 4.25, and the oxic condition <2. The values around 1 suggesting the O_2–H_2S interface is within the sediment (Jones & Manning, 1994). Interpretation of this ratio shows the distinctive features of two studied regions. Thus, with a few exceptions, there is a tendency showing that the oxic state dominates on the Absheron Peninsula compared to the Shamakhi-Gobustan region (Fig. 8).

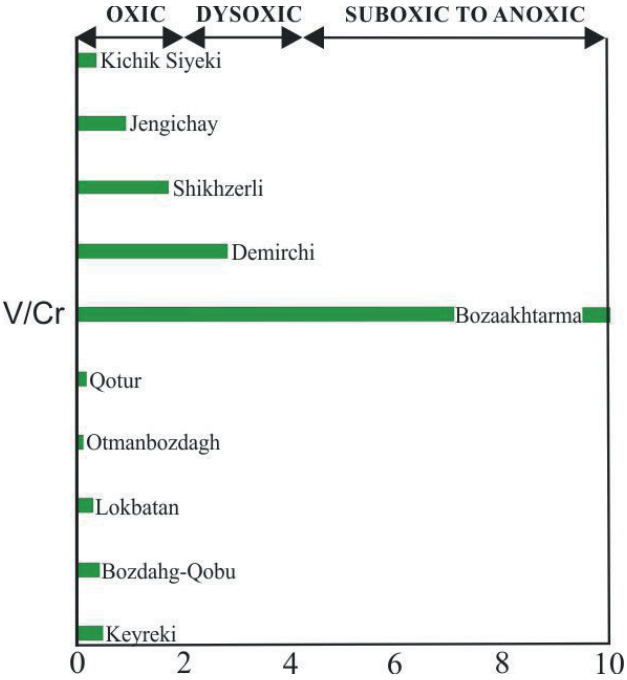

Fig. 8. V/Cr plot showing paleoredox conditions of oil shale samples.

Depending on the content of some metals in sedimentary rocks, the V/(V + Ni) value ≥ 0.84 presents a significant indicator of dissolved H_2S in the deeper part of a strongly stratified water column, which corresponds to euxinic, while the value is between 0.54 and 0.72 indicating minimal dissolved H_2S (anoxic) and a less strongly stratified water column. The dysoxic, weakly

stratified water column shows an average V/(V + Ni) value of 0.46–0.60 (Hatch & Leventhal, 1992). In addition, some other researchers have almost similar classifications on the same ratio (Lewan & Maynard, 1982; Lewan, 1984; Hoffman et al., 1998; Rimmerr, 2004). The values of V/(V + Ni) for the samples range from 0.26 to 0.93, suggesting that except for Kichik Siyeki and Qotur, the reducing anoxic states are characteristic in other areas of the Shamakhi-Gobustan region. A (Cu + Mo)/Zn ratio is proposed as an indicator for the oxidation of bottom waters (Hallberg, 1982). In the process of sedimentation that occurs in the presence of H_2S, Cu precipitates more than Zn. The abundance of Mo in the water content, which is rich in H_2S, led to its inclusion in this ratio. In addition, under anoxic and sulfide (euxinic) conditions, the adsorption nature of Mo on humic substances provides a favorable environment to transfer this element to the sediment–water interface (Hoffman et al., 1998). The (Cu + Mo)/Zn values increase in reducing conditions (Hoffman et al., 1998). Unlike the sample taken from the Lokbatan mud volcano, the calculated values of this ratio are higher in the samples of the Shamakhi-Gobustan region compared to the whole Absheron Peninsula.

Paleoclimate. Study of the nature of mineral formation is only informative in assessing of paleoclimatic conditions. Westermann et al. (2013) found that in marine settings, the variations in bulk-rock mineralogical proxies may record paleoenvironmental changes and/or diagenetic overprint (Madhavaraju et al., 2016). On the other hand, variations in paleoclimate affect the water basin, including pH, redox conditions, etc. Therefore the general paleoclimate characteristics of some minerals, discovered in the content of oil shale samples, are reviewed. Chamley (1977) made a conclusion that sediments rich mainly in chlorite and quartz relate to arid climates, while humid periods lead to an alteration in primary minerals, and formation of kaolinite and degraded mixed layers (Singer, 1984). In relatively low-relief areas, arid climatic conditions replaced by short-term humid seasons are characteristic by high concentrations of smectites (l.c.). Chamley (1979) found in semi-arid conditions the smectite bound to moderately hot and only periodically wet seasons. Keller (1970) noted that the formation of smectites of detrital origin is more associated with the semi-arid conditions. Like smectite and chloride, illite is one of the major minerals forming in arid or semi-arid climates (Khormali & Abtahi, 2003). The widespread distribution of chlorite and illite in sedimentary rocks formed during the initial stage of weathering (Nesbitt & Young, 1989), associated with rapid erosion, occurring in source area (Fursich et al., 2005). This condition is considered as a typical change in the paleoclimate from warm and humid (seasonal) to arid or semi-arid one (Madhavaraju et al., 2016).

The dominance of semi-arid climatic conditions is favourable for carbonate minerals, including calcite (Emadi et al., 2008). Like potassium and iron hydroxide, jarosite demonstrates the genesis of the weathering associated with arid climate conditions. Diagenetic processes and semi-arid fluid environments occurring at shallow depth are characteristic for hematite (Walker, 1976). Paleoclimate environment of calcium is bound to semi-arid zones (Leeder, 1975).

Liu et al. (1984) noted the relative lower mobile properties of Al, Fe, and Mg, and leaching of the other more-easily and more-rapidly deliberating elements, which provides very useful information in assessing paleoclimatic conditions (Chandra et al., 2016). K and Na are the most rapidly and easily deliberating, which leads to their accumulation in dry climatic condition (l.c.). Transient climatic conditions, such as sub-arid and sub-humid, influence some properties of Ca (dissolution, accumulation, etc.; Shang et al., 2013). The arid/semi-arid paleoclimatic states in the above-mentioned mineralogical properties should prevail in the case of higher concentrations of Al, Fe, Mg and Ca (Gao et al., 2011) (Tab. 2).

Suttner and Dutta (1986) established a binary diagram based on (Al_2O_3 + K_2O + Na_2O) versus SiO_2 to constrain the paleoclimatic condition during sedimentation of siliciclastic rocks. The result of this plot confirms the arid climatic conditions for the studied oil shale samples (Fig. 9).

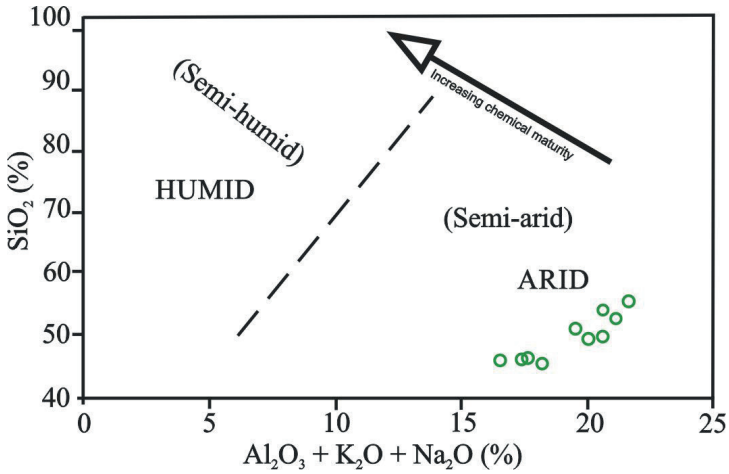

Fig. 9. Discriminant diagram showing paleoclimatic properties of oil shale samples (after Suttner & Dutta, 1986).

In our study we used various ratios such as Na_2O/Al_2O_3, Na_2O/K_2O, Na_2O/CaO, and Na_2O/TiO_2 to get more information on paleoclimate changes. Fig. 10 shows that there are some variations for the curves depending on the areas in which the analysed samples are located. Commonly, in response to chemical weathering and precipitation, the values of these ratios decrease as a result of rapid loss of

Na^+ (Chandra et al., 2016). In addition, depletion in CaO, MgO, TiO_2, and K_2O, and enrichment in these ratios are also interpreted as an indicator of cold and arid climatic conditions. The detailed analysis of the research areas shows that values of Na_2O/Al_2O_3, Na_2O/K_2O and Na_2O/TiO_2 ratios for samples taken from the northern part of Gobustan (Demirchi) and the adjacent Central Gobustan (Bozaakhtarma) are relatively lower (Fig. 10), which is typical for hot and comparatively humid conditions. For some samples (Qotur and Lokbatan), the depletion in values of some major oxides, such as Al_2O_3, TiO_2, and enrichment in these ratios indicate the prevalence of colder and arid climatic conditions.

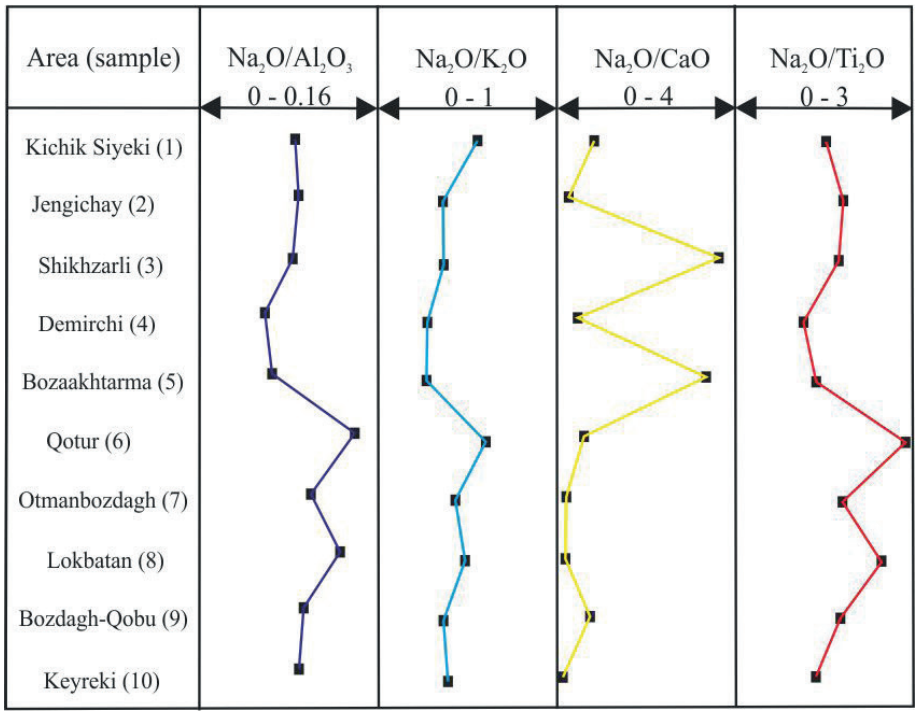

Fig. 10. Profiles of selected ratios, showing the paleoclimatic conditions of the samples.

An eluvial coefficient is used to obtain information on weathering of sediments (Zhang et al., 2013). In its formula

$$Ki = R_2O_3/(RO + R_2O)$$

RO represents the value of CaO and MgO in the sample and R_2O is a sum of Na_2O and K_2O. R_2O_3 indicates trivalent oxides, including Al_2O_3 and Fe_2O_3. The calculated values for the samples range from 6.1 to 13.15, indicating weak to moderate leaching of elements, which corresponds to semi-arid climatic conditions.

Concerning specific features of trace elements, various ratios are used to understand paleoclimate environments. Thus, the Sr, found in the samples, represents one of the most active trace elements – easily dissolving in the content of weathered rocks. Its higher concentration indicates the salty environment of the basin in arid season, which limits the flow of seawater in it (Couch, 1971). Accumulation of Cu is favourable for oil shale, which is enriched in organic matter, deposited in warm and humid climates (Liang et al., 2014). The Sr/Cu ratio is used to reveal paleoclimatic conditions: a warm humid climate is manifested by the value of 1.3–5.0, whereas Sr/Cu >5.0 suggests a hot arid climate (Abraham, 1978). In our case, the Sr/Cu ratio is expressed by the much higher values (1.4–83.33), which suggests a hot arid climatic conditions for the majority of samples.

Discussion

The genetic properties of clay mineral assemblages and also calcite, jarosite, hematite, etc., found in the samples indicate that the studied oil shales were formed in an aqueous environment. The determined values of illite suggest an idea that the samples are associated with peripheral zones. Also, the presence of calcite in the composition of mineral complexes (Tab. 1) indicates a condition of sedimentation related to shallow water zones. Studied oil shales are rich in chlorite (Tab. 1), which indicates both – marine and freshwater sedimentary conditions, so the freshwater basin conditions should not be excluded in our interpretation.

Since the lagoon systems are characterized by a high concentration of smectite, illite, chlorite, calcite, and quartz (Sabatier et al., 2010; Abidi et al., 2019), data on the bulk-rock mineralogy of our samples (Tab. 1) confirm the idea that the paleodepositional conditions in studied areas are associated with isolated coastal marine areas.

The AKF diagram indicates that the paleosedimentation conditions of oil shale can be associated with transition zones located between continental and marine areas (Fig. 5). The use of classification diagrams based on the chemical composition of oil shales clearly indicates the bound of samples to aqueous environments (Fig. 6a, b, c).

Moreover, published works (Sultanov & Sultanov, 1945; Aliyev & Abbasov, 2018) show the traces of fauna, such as fish larvae and planktonic crustaceans, often

recorded in oil shale-containing assemblages located in both studied regions, which provide a sign of aquatic faunas. This fact is confirmed by the fauna (benthos, planktonic foraminifers, as well as the teeth and bones of fish), determined in recent studies and providing the age of samples from mud volcanoes. The values of Fe/Mn ratio suggest the shallow Middle Eocene sedimentation basin during the deposition of oil shale samples (Fig. 7). The comparison of these values from the Absheron Peninsula, located in a short distance from the South Caspian Basin, as well as from the Central and South Gobustan, manifests an increasing tendency of the water column in the direction to North Gobustan, which is situated at a high hypsometric level. The values of Fe/Mn ratio in the samples from the mud volcanoes of Bozaakhtarma and Demirchi are higher, which indicates the shallow-coastal water conditions (Fig. 7).

The maximum values of Ti/Mn were also recorded for the samples of the Bozaakhtarma (21.5) and Demirchi (26) mud volcanoes, which confirms the finding of the relatively shallow water column in comparison with other areas. The Mn/Ni and Mn/Ga values indicate that the paleodepositional environments of oil shale collected from Kichik Siyeki (Mn/Ni = 18.92; Mn/Ga = 82.35), Jengichay (Mn/Ni = 31.25; Mn/Ga = 62.5), Otmanbozdagh (Mn/Ni = 24.39; Mn/Ga = 71.43) and Keyreki (Mn/Ni = 17.57; Mn/Ga = 108.33) areas are associated with relatively deeper water levels.

Based on values obtained for the Ti/Zr ratio, it can be assumed that the transfer distance of terrigenous materials derived from the source terrains to the sedimentary basin was relatively long.

Aliyev and Abbasov (2019) found that the Middle Eocene sedimentation was probably associated with the final Eocene basin, which represented the northern branch of Meso-Tethys in the Crimea-Greater Caucasus-Kopet Dagh system. The evolution of that independent deepwater basin, fed on the left – north branch of Meso-Tethys (Rustamov, 2005, 2008) is associated with areas covering the shale-flysch trough of the axial zone, which formed as a result of Jurrasic rifting (Zonenshain & Le Pichon, 1986; Khain, 1995; Babayev et al., 2015) in the North Crimea-Greater Caucasus-Kopet Dagh system, and extended to the east of Kopet Dagh. The shale-flysch and non-compensated (Babayev et al., 2015; Rustamov, 2015) deep basin played a role as a border between the Scythian-Turan plate of the Eurasian continent and the intra-Transcaucasian plate (Rustamov, 2005). The beginning of the late Alpine tectogenesis corresponds to the period of regional uplift in the Caucasus-Caspian region and Iran (Shixalibeyli, 1967; Rustamov, 2008; Babayev et al., 2015). The flysch basin of Meso-Tethys covered the southern slopes of the Greater Caucasus and the Absheron Sill, playing a role in transporting terrigenous material during the Tufan and Vandam uplifts, and being completely closed in the Upper Eocene (Brunet et al., 2003; Rustamov, 2015). The intensification of regional uplift processes in the transitional phase of the Upper Cretaceous-Paleogene (in the tectonic phase of Laramie; Babayev et al., 2015) probably led to a decrease in the depth of the final Eocene basin (Aliyev & Abbasov, 2019). Such an interpretation corresponds well with the results obtained in the present study for the depths of the Middle Eocene sedimentary basin and the transport distance of terrigenous materials.

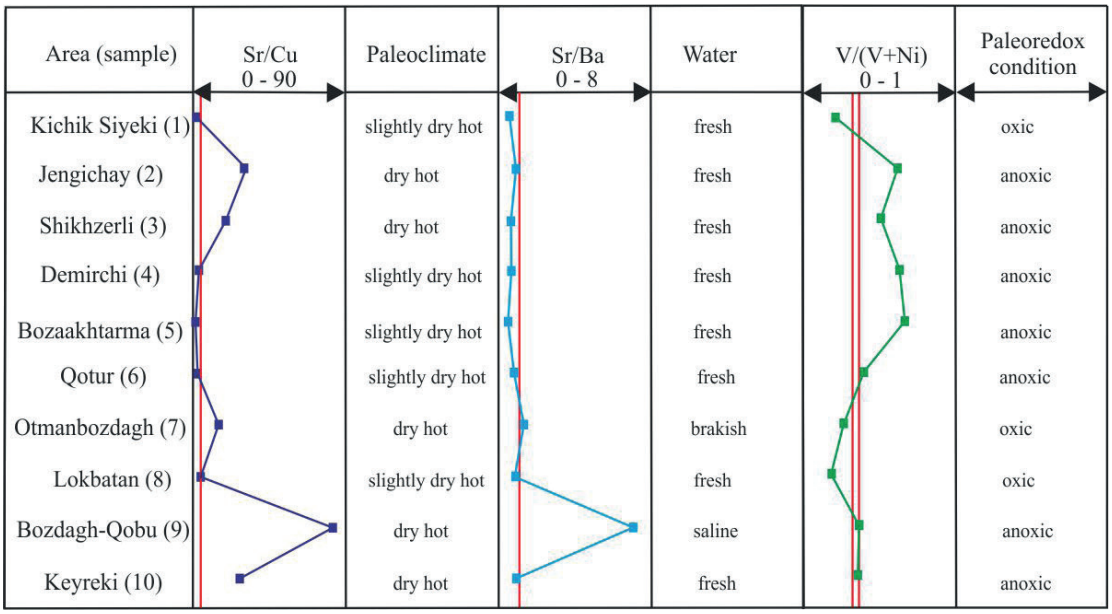

Fig. 11. Vertical profiles showing salinity, paleoclimate and paleoredox of samples.

Taking into account an analog (Engalichev & Panova, 2011) of the obtained results, the paleodepositional conditions for the Middle Eocene oil shales are most likely associated with isolated coastal-marine zones, in more detail, lagoons and lakes, which depth was 10 meters.

The results of the well-known approaches used in the reconstruction of the paleo-redox conditions of oil shales do not coincide. In more detail, although the amount of V determined in oil shales exceeds 100 ppm (mean = 184.4 ppm) but the average value of Ni is lower than this indication (mean = 68.3 ppm). In addition, it was established that the kerogen of oil shale samples is a mixture of type II and III (Aliyev et al., 2018b).

Unlike the Kichik Siyeki area in Central Gobustan and all areas of the Absheron Peninsula, the reducing conditions were established based on lower Ni/V values for the Shamakhi-Gobustan region. The same result was also recorded for the V/Cr ratio (Fig. 8). Except for the Lokbatan sample, the (Cu + Mo)/Zn values are lower in the Absheron samples. Jones and Manning (1994) found that the Ni/V and (Cu + Mo)/Zn are not reliable ratios in the interpretation of the palaeo-redox conditions.

The study of the nature of the minerals found in oil shales, which related to paleoclimatic conditions shows the samples are more strongly associated with arid/semi-arid seasons. In addition, the results of the widely used diagram (Al_2O_3 + K_2O + Na_2O) vs. SiO_2 (Fig. 9), Na_2O/Al_2O_3, Na_2O/K_2O, Na_2O/CaO, and Na_2O/TiO_2 ratios (Fig. 10), and also the eluvial coefficient confirm the dominance of arid paleoclimatic conditions.

In general, the obtained results of the map of vertical variabilities of salinity, paleoclimate and paleoredox of samples (Fig. 11) can be considered as characteristic features of oil shale from the foothills of the Greater Caucasus.

Conclusion

The nature of the clay minerals found in the samples and the results of used ratios and diagrams based on the analysis of the bulk rock geochemistry data indicate that the oil shale is associated with the paleodepositional environment bound to a transition zone located between continental and marine zones. The AKF plots show a gradual transition of the sediments of the basin from continental to marine environment. The process of sedimentation in the aquatic environments was probably associated with the final Eocene basin, which was the northern branch of Meso-Tethys in the Crimea-Greater Caucasus-Kopet Dagh system. The intensification of regional uplift movements in the Upper Cretaceous-Paleogene periods probably led to a decrease in the depth of the final Eocene basin. The paleodepositional conditions of the Middle Eocene oil shales most likely correspond to isolated coastal- marine zones, in more detail, lagoons and lakes, which depth was 10 meters.

The mineralogical and geochemical proxies of the Middle Eocene oil shales suggest an idea that except for some samples of the Apsheron Peninsula, all oil shales can be associated with freshwater, mixed paleo-redox (mostly reducing), and arid/semi-arid environments.

Acknowledgement

Authors express their thanks to reviewers Prof. Y. Shnyukov (Ukraine), Dr. M. Pereszlényi (Czech Republic), Dr. E. H. Hasanov (Azerbaijan), Dr. M. Vďačný (Slovakia) and one anonymous reviewer, as well as scientific editor of Mineralia Slovaca Z. Németh for valuable remarks and suggestions, increasing the quality of primary manuscript.

References

Abbasov, O. R., 2009: Distribution regularities of shales of Paleogene-Miocene sediments in Gobustan. *Abstract of PhD thesis, Baku.*

Abbasov, O. R., 2015: Oil shale of Azerbaijan: geology, geochemistry and probable reserves. *Int. J. Res. Stud. Sci., Eng. Technol., 2, 9, 31–37.*

Abbasov, O. R., 2016a: Geological and geochemical properties of oil shale in Azerbaijan and petroleum potential of deep-seated Eocene-Miocene deposits. *Eur. J. Natur. Hist., 2, 31–40.*

Abbasov, O. R., 2016b: Distribution regularities of oil shale in Azerbaijan. *ISJ Theor. Appl. Sci., 3, 35, 165–171.*

Abbasov, O. R., 2017: Distribution regularities and geochemistry of oil shales in Azerbaijan. *Miner. Res. Ukraine, 2, 22–30.*

Abbasov, O. R., Ibadzadeh, A. C. & Mammadova, A. N., 2012: Hydrocarbon generation potential of the deeper sediments of Azerbaijan. *Baku, Integrated approach for unlocking hydrocarbon resources, 1–48.*

Abbasov, O. R., Mamedova, A. N., Huseynov, A. R. & Baloglanov, E. E., 2013: Some new data of geochemical researches of combustible slates of Azerbaijan. *Geol., Geophys. Develop. Oil Gas Fields, 2, 32–35.*

Abbasov, O. R., Baloglanov, E. E. & Akhundov, R. V., 2015: Organic compounds in ejected rocks of mud volcanoes as geological and geochemical indicators: a study from Shamakhi-Gobustan region (Azerbaijan). *Azerbaijan, Baku: International Multidisciplinary Forum "Academic Science Week 2015".*

Abidi, M., Amor, R. Ben & Gueddari, M., 2019: Sedimentary dynamics of the South Lagoon of Tunis (Tunisia, Mediterranean Sea). *Estud. geol., 75, 1, e086.*

Aliyev, Ad. A. & Bayramov, A. A., 1999: Some aspects of the tectonics of the Gobustan mud volcanic zones. Proc. ANAS, Earth Sci., 1, 129–131.

Aliyev, Ad. A., Belov, I. S. & Ibadzade, A. J., 2002: Oil shale of Azerbaijan (geology, geochemistry and use). *Proc. Inst. Geol., Azerbaijan Nation. Acad. Sci., 30, 5–24.*

Aliyev, Ad. A., Bayramov, A. A., Abbasov, O. R. & Mammadova, A. N., 2014: Reserves of oil shale and natural bitumen. National Atlas of the Republic of Azerbaijan, *Map (Scale 1:1000000), 101.*

Aliyev, Ad. A., Aliyev, Ch. S., Feyzullayev, A. A., Huseynov, D. A., Isayeva, M. I., Gadirov, F. A., Guliyev, I. S., Latifova, Y. N., Muxtarov, A. Sh., Novruzov, N. A. & Abbasov, O. R., 2015a: Geology of Azerbaijan. *In: Academician Ali-zadeh, Ak. A. (ed): Baku, Publishing house "Elm", II, 341 p.*

Aliyev, Ad. A., Guliyev, I. S., Dadashev, F. G. & Rahmanov, R. R., 2015b: Atlas of mud volcanoes in the world. In: Academician Alizadeh, Ak. A. (ed): Baku: *Publishing house "Nafta-Press" and "Sandro Teti Editore", 361 p.*

Aliyev, Ad. A. & Abbasov, O. R., 2018: Organic geochemical characteristics of oil shale in Azerbaijan. *Tehran, Iran: The 36th National and the 3rd International Geosciences Congress.*

Aliyev, Ad. A., Abbasov, O. R., Ibadzade, A. J. & Mammadova, A. N., 2018a: Genesis and organic geochemical characteristics of oil shale in Eastern Azerbaijan. *SOCAR Proc., 3, 4–15.*

Aliyev, Ad. A., Abbasov, O. R., Ibadzade, A. J. & Mammadova, A. N., 2018b: Organic-geochemical study of oil shales in Pre-Caspian-Guba region (Azerbaijan). *Miner. Resour. Ukraine, 3, 13–18.*

Aliyev, Ad. A. & Abbasov, O. R., 2019: Nature of the provenance and tectonic setting of oil shale (Middle Eocene) in the Greater Caucasus southeastern plunge. *Geodynamics, 1, 26, 43–59.*

Aliyev, Ad. A., Abbasov, O. R. & Agayev, A. M., 2019: Mineralogy and geochemistry of oil shale in Azerbaijan: classification, palaeoweathering and maturity features. *Visnyk V. N. Karazin Kharkiv Nation. Univ., ser. Geol. Geogr. Ecol., 50, 11–26.*

Ali-zade, A. A., Ahmedov, G. A. & Zeynalov, M. M., 1962: Oil shale of the Miocene in Azerbaijan. *Azerbaijan Oil Industry, 1, 5–8.*

Anderson, R. F., Fleisher, M. Q. & Le Huray, A. P., 1989: Concentration, oxidation state, and particulate flux of uranium in the Black Sea. *Geochim. cosmochim. Acta, 53, 9, 2215–2224.*

Babayev, Sh. A., Bagmanov, M. A., Aliyeva, E. H.-M., Ali-zade, Kh. A., Kengerli, T. N., Latifova, Y. N. & Zohrabova, V. R., 2015: Geology of Azerbaijan. *In: Academician Ali-zadeh, Ak. A. (ed): Baku: Publishing house Elm, II, 532 p.*

Brunet, M.-F. Korotaev, M. V., Ershov, A. V. & Nikishin, A. M., 2003: The South Caspian Basin: a review of its evolution from subsidence modeling. *Sedimentary Geol., 156, 119–148.*

Jones, B. & Manning, D. A. C., 1994: Comparison of geochemical indices used for the interpretation of palaeoredox conditions in ancient mudstones. *Chem. Geol., 111, 1–4, 111–129.*

Chamley, H., 1989: Clay sedimentology. Berlin, Springer, 116 p.

Chandra, R., Ahmad, I. & Qurashi, A., 2016: Pedological and geochemical characterization of loess-paleosol sediments of Karewa Basin: Implications for paleoclimatic reconstruction of Kashmir Valley. *Spec. Publ. Geol. Soc. India, 4, 38–54.*

Couch, E. L., 1971: Calculation of palaeosalinities from boron and clay mineral data. *Bull. Amer. Assoc. Petrol. Geol., 55, 1829–1839.*

De Ros, Luiz F., Morad, S. & Paim, P. S. G., 1994: The role of detrital composition and climate on the diagenetic evolution of continental molasses: evidence from the Cambro-Ordovician Guaritas Sequence, southern Brazil. *Sedimentary Geol., 92, 197–228.*

Emadi, M., Baghernejad, M. & Maftoun, M., 2008: Assessment of some soil properties by spatial variability in saline and sodic soils in Arsanjan plain Southern Iran. *Pakistan J. Biol. Sci., 11, 2, 238–243.*

Emerson, S. R. & Huested, S. S., 1991: Ocean anoxia and the concentrations of molybdenum and vanadium in seawater. *Mar. Chem., 34, 3–4, 177–196.*

Engalychev, S. Yu. & Panova, E. G., 2011: Geochemistry and origin of sandstones of the eastern part of Main Devonian field in the north-west of Russian Plate. *Lithosphere, 5, 16–29.*

Englund, J. O. & Jørgensen, Dr. P., 1973: A chemical classification system for argillaceous sediments and factors affecting their composition. *Geol. Fören. Förh. (Stockholm), 95, 1, 87–97.*

Ernst, W., 1970: Geochemical facies analysis, methods in geochemistry and geophysics. *Amsterdam, Elsevier, 158 p.*

Freed, R. L., 1980: Clay minerals as indicators for depositional environment ın the South Hallettsville Field, Lavaca County, Texas. *Gulf Coast Assoc. Geol. Soc. Trans., 30, 347–350.*

Fürsich, F. T., Singh, I. B., Joachimski, M., Krumm, S., Schlirf, M. & Schlirf, S., 2005: Palaeoclimate reconstructions of the Middle Jurassic of Kachchh (Western India): an integrated approach based on palaeoecological, oxygen isotopic, and clay mineralogical data. *Palaeogeogr. Palaeoclimatol. Palaeoecol., 217, 3/4, 289–309.*

Galán, E., 2006: Genesis of clay minerals. *Handbook Clay Sci., Chap. 14, 1129–1162.*

Gao, Z. L., Kang, Y. S., Liu, R. H. & Bai, W. H., 2011: Geological features and developmental controlling factors of Lucaogou oil shale in the southern margin of Junggar Basin. *Xinjiang Geol., 29, 189–193.*

Glikson, M. W., Chappell, R., Freeman, S. & Webber, E., 1985: Trace elements in oil shales, their source and organic association with particular reference to Australian deposits. *Chem. Geol., 53, 1–2, 155–174.*

Gromet, L. P., Dymek, R. F., Haskin, L. A. & Korotev, R. L., 1984: The "North American shale composite" its compilation, major, and trace elements characteristics. *Geochim. cosmochim. Acta, 48, 2469–2482.*

Hallberg, R. O., 1982: Diagenetic and environmental effects on heavy-metal distribution in sediments: A hypothesis with an illustration from the Baltic Sea. *In: Fanning, K. A. & Manheim, F. T. (ed.): The dynamic environment of the ocean floor. Lexington Books, Lexington, Mass., 305–316.*

Hatch, J. R. & Leventhal, J. S., 1992: Relationship between inferred redox potential of the depositional environment and geochemistry of the Upper Pennsylvanian (Missourian) Stark Shale Member of the Dennis Limestone, Wabaunsee County, Kansas, U.S.A. *Chem. Geol., 99, 1–3, 65–82.*

Hoffman, D. L., Algeo, T. J., Maynard, J. B., Joachimski, M. M., Hower, J. C. & Jaminski, J., 1998: Regional and stratigraphic variation in bottom water anoxia on offshore core shales of Upper Pennsylvanian cyclothems from the Eastern Midcontinent Shelf (Kansas), USA. *In: Schieber, J., Zimmerle, W., Sethi, P. (ed): Shales and mudstones I, E. Stuttgart, Schweizerbart. Verlagsbuchhandl., 243–269.*

Huerta-Diaz, M. A. & Morse, J. W., 1992: Pyritization of trace metals in anoxic marine sediments. *Geochim. cosmochim. Acta, 56, 2681–2702.*

Inan, S., M., Yalçin, M. N., Guliev, I. S., Kuliev, K. & Feizullayev, A. A., 1997: Deep petroleum occurrences in the Lower Kura Depression, South Caspian Basin, Azerbaijan: an organic geochemical and basin modeling study. *Mar. Petrol. Geol., 14, 7–8, 731–762.*

Keller, W. D., 1970: Environmental aspects of clay minerals. *J. Sed. Res., 40, 3, 788–813.*

Khain, V. E., 1995: Geology of the Northern Eurasia (USSR). Second Part of the Geology of the USSR. Phanerozoic Fold Belts and Young Platforms. *Berlin, Gebrüder Borntraeger, 404 p.*

Khormali, F. & Abtahi, A., 2003: Origin and distribution of clay minerals in calcareous arid and semi-arid soils of Fars Province, southern Iran. *Mineral. Soc. Great Britain Ireland, 38, 4, 511–527.*

Leeder, M. R., 1975: Pedogenic carbonates and flood sediment accretion rates: a quantitative model for alluvial arid-zone lithofacies. *Geol. Mag., 112, 3, 257–270.*

Lerman, A., 1978: Lakes: Chemistry, geology, physics. *New York, Springer-Verlag, 363 p.*

Lewan, M. D., 1984: Factors controlling the proportionality of vanadium to nickel in crude oils. Geochim. cosmochim. Acta, 48, 11, 2231–2238.

Lewan, M. D. & Maynard, J. B., 1982: Factors controlling enrichment of vanadium and nickel in the bitumen of organic sedimentary rocks. *Geochim. Cosmochim. Acta, 46, 12, 2547–2560.*

Liang, J., Tang, D., Xu, H., Tao, S., Li, Ch. & Gou, M., 2014: Formation conditions of Jimusaer oil shale at the northern foot of Bogda Mountain, China. *Oil Shale, 31, 1, 19–29.*

Liu, Y. J., Cao, L. M., Li, Z. L., Wang, H. N., Chu, T. Q. & Zhang, J. R., 1984: Element Geochemistry. *Sci. Press (Beijing), 6–86.*

Madhavaraju, J., Ramírez-Montoya, E., Monreal, R. A., González-León, C. M., Pi-Puig, T., Espinoza-Maldonado, I. G. & Grijalva-Noriega, F. J., 2016: Paleoclimate, paleoweathering and paleoredox conditions of Lower Cretaceous shales from the Mural Limestone, Tuape section, northern Sonora, Mexico: Constraints from clay mineralogy and geochemistry. *Rev. Mexic. Cienci. Geol., 33, 1, 34–48.*

Mangini, A., Jung, M. & Laukenmann, S., 2001: What do we learn from peaks of uranium and of manganese in deep sea sediments? *Mar. Geol., 177, 1–2, 63–78.*

Mason, B. & Moore, C. B., 1982: Principles of geochemistry. *New York, Wiley, 344 p.*

Miknis, F. P. & McKay, J. F., 1983: Geochemistry and chemistry of oil shales. *Washington, Amer. Chem. Soc., 230, 565 p.*

Mozley, P. S., 1989: Relation between depositional environment and the elemental composition of early diagenetic siderite. *Geology, 17, 8, 704–706.*

Nelson, S. A., 2014: Tectosilicates, carbonates, oxides, and accessory minerals. *Mineralogy, USA, 1–15.*

Nesbitt, H. W. & Young, G. M., 1989: Formation and diagenesis of weathering profiles. *J. Geol., 97, 129–147.*

Odonne, F., Imbert, P. Dupuis, M. et al., 2020: Mud volcano growth by radial expansion: Examples from onshore Azerbaijan. *Mar. Petrol. Geol., 112, 104051.*

Parham, W. E., 1966: Lateral variations of clay mineral assemblages in modern and ancient sediments. In: Heller, L., Weiss, A. (ed.): Proceedings of the International Clay Conference, *Jerusalem, Israel Program for Scientific Translation, 1, 135–145.*

Powers, M. C., 1957: Adjustment of land derived clays to the marine environment. *J. sed. Res., 27, 4, 355–372.*

Ratcliffe, K. T., Morton, A. C., Ritcey, D. H. & Evenchick, C. A., 2007: Whole-rock geochemistry and heavy mineral analysis as petroleum exploration tools in the Bowser and Sustut basins, British Columbia, Canada. *Bull. Canad. Petrol. Geol., 55, 4, 320–336.*

Rimmer, S. M., 2004: Geochemical paleoredox indicators in Devonian-Mississippian black shales, central Appalachian Basin (USA). *Chem. Geol., 206, 3–4, 373–391.*

Roaldest, E., 1978: Mineralogical and chemical changes during weathering, transportation and sedimentation in different of Kashmir Valley. *Spec. Publ. Geol. Soc. India, 4, 38–54.*

Rustamov, M. I., 2005: South Caspian Basin – geodynamic events and processes. *In: Academician Ali-zadeh, Ak. A. (ed): Baku, Nafta-Press, 345 p.*

Rustamov, M. I., 2008: Geodynamics and magmatism of the Caspian–Caucasian segment of the Mediterranean belt in the Phanerozoic. Abstract of Sci. *Doctor thesis, Baku.*

Rustamov, M. I., 2015: Main indicators of the collisional geodynamics of Zagros-Caucasian segment of Mediterranean belt. *Proc. Azerbaijan Nation. Acad. Sci., Earth Sci., 1, 3–14.*

Sabatier, P., Dezileau, L., Briqueu, L., Colin, Ch. & Siani, G., 2010: Clay minerals and geochemistry record from northwest Mediterranean coastal lagoon sequence: Implications for paleostorm reconstruction. *Sedimentary Geol., 228, 3–4, 205–217.*

Sachsenhofer, R. F., Popov, S. V., Coric, S., Mayer, J., Misch, D., Morton, M. T., Pupp, M., Rauball, J. & Tari, G., 2018: Paratethyan petroleum source rocks: An overview. *J. Petrol Geol., 41, 3, 219–246.*

Saigal, G. C., Morad, S., Bjorlykke, K., Egeberg, P. K. & Aagaard, P., 1988: Diagenic albitization of detrital K-feldspars in Jurassic, Lower Cretaceous, and Tertiary clastic reservoirs from offshore Norway, I. Textures and origin. *J. sed. Res., 58, 6, 1003–1013.*

Salaev, S. G., Kravchinsky, Z. Y., Selimkhanov, A. I. et al., 1990: Oil sands and oil shale in Azerbaijan. *Baku, Elm, 129 p.*

Shang, Y., Lu R. J., Jia, F. F., Tian, L. H., Tang Q. L., Chen, Y., Zhao, Ch. & Wu W. Y., 2013: Paleoclimatic evolution

indicated by major geochemical elements from aeolian sediments on the east of Qinghai Lake. *Sci. Cold Arid Regions, 5, 3, 301–308.*

Shaw, D. M., 1968: A review of K-Rb fractionation trends by covariance analysis. *Geochim. cosmochim. Acta, 32, 573 – 601.*

Shikhalibeyli, E. Sh., 1967: Geological structure and history of the tectonic development of the eastern part of the Lesser Caucasus. *In: Academician Khain, V. E., (ed.): Baku, Publ. house Acad. Sci. USSR, 235 p.*

Singh, M., Rajesh, V. J., Sajinkumar, K. S., Sajeev, K. & Kumar, S. N., 2016: Spectral and chemical characterization of jarosite in a palaeolacustrine depositional environment in Warkalli Formation in Kerala, South India and its implications. *Spectrochim. Acta, A: Molecular Biomolecular Spectrosc., 168, 86–97.*

Singer, A., 1984: The paleoclimatic interpretation of clay minerals in sediments – a review. *Earth Sci. Rev., 21, 4, 251–293.*

Sultanov, R. G., 1948: Oil shale of south-eastern Caucasus and geological conditions of their distribution. *Baku, Fund IGANA.*

Sultanov, A. D. & Sultanov, R. G., 1945: Oil shales of the southeastern tip of the Main Caucasian Range in Azerbaijan. *DAN Az. SSR. 1, 11–13.*

Sultanov, A. D. & Sultanov, R. G., 1947: Materials on oil shales in Azerbaijan. *Proc. Azerbaijan Acad. Sci. SSR, 2, 18–20.*

Suttner, L. J. & Dutta, P. K., 1986: Alluvial sandstone composition and paleoclimate; I, Framework mineralogy. *J. sed. Res., 56, 3, 329–345.*

Taylor, S. R. & McLennan, S. M., 1985: The continental crust: its composition and evolution. *Oxford, Blackwell, 312 p.*

Telnaes, N., Cooper, B. S. & Jones, B., 1991: Kerogen facies, biomarkers, trace metal contents, and spectral logs as indicators of oxicity and salinity, Upper Jurassic, North Sea. *In: Manning, D. A. C. (ed.): Organic Geochemistry, Advances and Applications in Energy and the Natural Environment. Manchester, Manchester University Press, 391–393.*

Walker, T. R., 1976: Diagenetic origin of continental red beds. In: Falke, H. (ed): The continental Permian in Central, West and South Europe. *Dordrecht, D. Reidel, 240–482.*

Watitemsu, I. W., Thong, G. T. & Pongen, T., 2014: Provenance, tectonic setting and age of the sediments of the Upper Disang Formation in the Phek District, Nagaland. *J. Asian Earth Sci., 88, 11–27.*

Weaver, Ch. E., 1956: A discussion on the origin of clay minerals in sedimentary rocks. *Clays and Clay Minerals, 5, 1, 159–173.*

Westermann, S., Duchamp-Alphonse, S., Fiet, N., Fleitmann, D., Matera, V., Adatte, T. & Follmi, K. B., 2013: Paleoenvironmental changes during the Valanginian: New insights from variations in phosphorous contents and bulk- and clay mineralogies in the Western Tethys. *Paleogeogr. Paleoclimatol. Paleoecol., 392, 196–208.*

Wright, V. P. & Tucker, M. E., 1991: Calcretes: introduction. *International Assoc. Sed. Reprint Ser., 3, 1–22.*

Zhang, W., Shi, Z., Chen, G., Liu, Y., Niu, J., Ming, Q. & Su, H., 2013: Geochemical characteristics and environmental significance of Talede loess-paleosol sequences of Ili Basin in Central Asia. *Environ. Earth Sci., 70, 5, 2191–2202.*

Zolotov, M. Y. & Shock, E. L., 2005: Formation of jarosite-bearing deposits through aqueous oxidation of pyrite at Meridiani Planum, Mars. *Geophys. Res. Lett., 32, L21203.*

Zonenshain, L. P. & Le Pichon, X., 1986: Deep basins of the Black Sea and Caspian Sea as remnants of Mesozoic back-arc basins. *Tectonophysics, 123, 181–211.*

Aplikácia mineralogických a geochemických údajov zo strednoeocénnych roponosných bridlíc na úpätí Veľkého Kaukazu v Azerbajdžane pri rekonštrukcii environmentálnych a paleoklimatických podmienok ich genézy

Produktívna oblasť na úpätí Veľkého Kaukazu je situovaná v kolíznej zóne medzi arabskou a euroázijskou litosférickou platňou. Špecifické geodynamické a depozičné podmienky v tejto zóne prispeli k vytvoreniu bohatých akumulácií ropy a zemného plynu (cf. Aliyev & Abbasov, 2019).

Roponosné bridlice v Azerbajdžane sa vyznačujú vysokou kvalitou (energetická hodnota 6,0 – 12 MJ . kg^{-1}, zastúpenie organickej substancie 15 – 31 %, síry 0,4 – 1,2 % a popola 65 – 85 %), prevyšujúcou kvalitu roponosných bridlíc v iných štátoch. Keďže vystupujú v hrubých polohách s veľkým plošným rozšírením, predpokladá sa, že sa v tejto krajine v budúcnosti stanú dôležitým zdrojom ropy a zemného plynu (Abbasov, 2015, 2016a, b).

Tento článok má za cieľ preklenúť doterajší nedostatok poznatkov o depozičnom prostredí a paleoklimatických podmienkach počas strednoeocénnej evolúcie roponosných bridlíc. Výskum sa realizoval na 10 vzorkách z odkryvov a bahenných vulkánov v oblasti medzi lokalitami Gobustan a Baku, nachádzajúcimi sa na polostrove Abšeron na východnom úpätí Veľkého Kaukazu v susedstve Kaspického mora (obr. 1). Produktívne strednoeocénne súvrstvie je v tejto zóne situované v hĺbke len niekoľko stoviek metrov, prípadne vychádza až na povrch (obr. 2).

Metodika výskumu zahŕňala štúdium mineralogického a geochemického zloženia hornín (hlavné oxidy a stopové prvky; tab. 1 a 2, obr. 3 – 6) spojené s datovaním. Depozičné prostredie bridlíc sa určovalo na základe pomerov determinujúch prvkov (obr. 7 – 11), pričom pri interpretácii sa brali do úvahy aj publikované zistenia a rekonštrukcie iných autorov aj z iných častí sveta.

Výsledkom výskumu je doloženie sedimentačných podmienok strednoeocénnych roponosných bridlíc v prostredí izolovaných príbrežno-morských oblastí – lagún a jazier – s hĺbkou okolo 10 m. Doložený bol postupný prechod z kontinentálneho sedimentačného prostredia do morského. Roponosné bridlice v študovanom regióne, s výnimkou niekoľkých vzoriek, vznikali dominantne v sladkovodnom a prevažne redukčnom prostredí v aridných a poloaridných podmienkach.

Doručené / Received: 19. 7. 2019
Prijaté na publikovanie / Accepted: 2. 12. 2019

Mineralia Slovaca, Web ISSN 1338-3523, ISSN 0369-2086
51 (2019), 175 – 186, © Authors 2019. CC BY 4.0

Block rotations in the Carpathian Shear Corridor – a paleomagnetic record

FRANTIŠEK MARKO[1], †IGOR TÚNYI[2] and EMÍLIA BENIAKOVÁ[2]

[1] Comenius University in Bratislava, Faculty of Natural Sciences, Department of Geology and Paleontology, Ilkovičova 6, SK-842 15 Bratislava, Slovakia; *frantisek.*
[2] Slovak Academy of Sciences, Earth Science Institute, Dúbravská cesta 9, SK-845 28 Bratislava, Slovakia

Abstract: So far realized paleomagnetic research describes uniform, approximately 60–90° declination of the Early Miocene paleomeridians as a result of en-bloc rotation of the ALCAPA plate. After this en-bloc rotation, during the Neo-Alpine (Cenozoic) tectonic evolution an important role belonged to a strike-slip brittle shear zone, the Carpathian Shear Corridor. It represents the lateral ramp transform boundary of an extruded crustal segment and within this zone extensive counterclockwise rotation of small blocks is expected due to sinistral shearing. To detect and to measure exactly anomalous block rotations a paleomagnetic research was applied and focussed to localities situated inside the shear corridor. Gained declinations of paleomeridians from the Eggenburgian and Late Oligocene sediments indicate large 120–240° CCW block rotations within this wide shear corridor. These results support the existence and the geodynamic role of the Carpathian Shear Corridor as a prominent dynamic strike-slip boundary of an extruded Inner Carpathians crustal block.

Key words: block rotation, paleomagnetic data, strike-slip tectonics, Neo-Alpine evolution, Western Carpathians

Graphical abstract

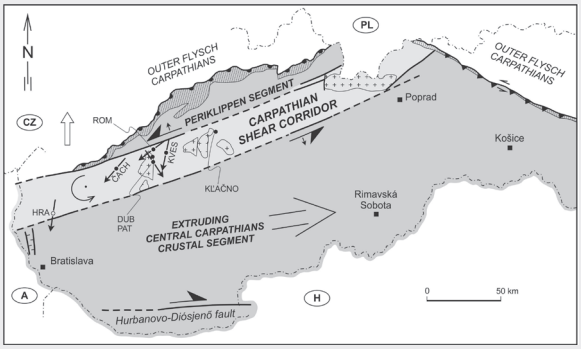

Highlights

- The domino-style rotations of small blocks inside a prominent sinistral strike-slip brittle shear zone – the Carpathian Shear Corridor, related to eastward escape of the Inner Western Carpathians crustal segment, is interpreted applying the paleomagnetic data.
- In contrast to until known average 60–90° declinations of magnetic paleomeridians due to ALCAPA en-bloc rotation, 120–240° ranging declinations of magnetic paleomeridians were detected inside the wrench corridor, supporting the interpretation of additional rotation of the blocks.

Introduction

The extensive block rotations and tilting cannot be avoided at reconstruction of the Western Carpathians structure evolution. Except of an en-bloc rotation of the Internides of Western Carpathians (e.g. Balla, 1987; Kováč et al., 1989; Kováč and Túnyi, 1995; Márton and Fodor, 1995; Fodor, 1995; Fodor et al., 1998; Márton et al., 2013), the large domino-style rotations inside the strike-slip shear zones, rimming moving individual blocks, are expected (e.g. Kováč et al., 1997). Just the Carpathian Shear Corridor (CSC, sensu Marko et al., 2017) should represent such a zone with rotated blocks inside it due to an extensive Miocene rotation (Marko et al., 1991, 2013, 2017; Marko, 2012), uplift/subsidence, tilting and contemporaneous blocks exhumation at different erosional levels. The Carpathian Shear Corridor, a wide ENE-WSW trending strike-slip brittle shear zone creates a dynamic boundary, controlling eastward escape of the Inner Western Carpathians crustal segment during the Neo-Alpine oblique collision of the Western Carpathians with foreland. This structure was recognized in the 1990s (Janků et al., 1984; Doktór et al., 1985) and dynamically interpreted as a strike-slip structure (Pospíšil et al., 1986, 2012; Pospíšil, 1989, 1990; Nemčok et al., 1998; Vass, 1998). The rotation and tilting of individualized blocks inside the corridor accomodated long distance escape (extreme strike-slip separation) of the Central Western Carpathians crustal segment (along CSC) and resulted in formation of the basin and range-like tectonic style – the alternation of intramountaine basins and horsts, roughly corresponding with the belt of outer core mountains.

Except of structural-tectonic arguments, aiming to detect exactly and quantify block rotations and tilting expected within the strike-slip corridor, a paleomagnetic research was applied. Samples measurements were realized

in 2013–2014 within the paleomagnetic laboratory of the Geophysical Institute of the Slovak Academy of Science in Bratislava.

According the generally accepted geodynamic scenario for the Western Carpathians morphostructural evolution, the shear corridor ought to be active during the Miocene period. So the most appropriate rocks recording the dynamics of the corridor seems to be the Early Miocene sediments. Limiting factors for sampling were the occurences and physical properties of measured rocks. We had to face the problem of the grain size of clastic sediments, because coarse grained sediments represent the most frequent transgressive facies of the Early Miocene period. Psephitic-psammitic rocks are not ideal for a paleomagnetic procedure, but even in such cases we succeeded and we gained acceptable results.

Analysed samples

The sampling was focussed on the Eggenburgian sediments, relics of inverted and destroyed wrench furrow basin, whose origin was related to Carpathian Shear Corridor, inside which these remnants exclusively occur. Five localities of the Eggenburgian sediments, exhumed remnants of wrench furrow basin fill were selected within the corridor to detect current paleomeridians orientation – Čachtice, Rožňové Mitice, Patrovec, Dubodiel, Krásna Ves. One sampled locality – Hrabník (near village of Sološnica) – is situated within the Uppermost Oligocene sediments of the Buková furrow (**Fig. 1, 3a–e**).

Čachtice (ČACH)

N 48° 43′ 41.6″, E 17° 47′ 40.6″, 255 m a.s.l.

A large active quarry where the Mesozoic carbonates (Hronic unit) are covered by transgressive facies of Eggenburgian sediments. A samples were extracted from the Eggenburgian thick layered calcarenites (S_o 140/25°) and micro-conglomerates exposed at the first exploitation site (**Fig. 3a**). Locality is situated at the southeastern edge of the Čachtické Karpaty Mts. horst.

Rožňové Mitice (ROM)

N 48° 48′ 39.4″, E 18° 06′ 24.2″, 354 m a.s.l.

A large active quarry in Mesozoic dolomites and limestones (Hronic unit). Samples were extracted from the very probably Eggenburgian (R. Marschalko, pers. com.) conglomerates (**Fig. 3b**) – a tiny relic of Early Miocene wrench furrow basin fill (Marko, 2012). Although the conglomerates are massive and bedding is not clear, as the S_o 155/42° was detected one from the contacts of

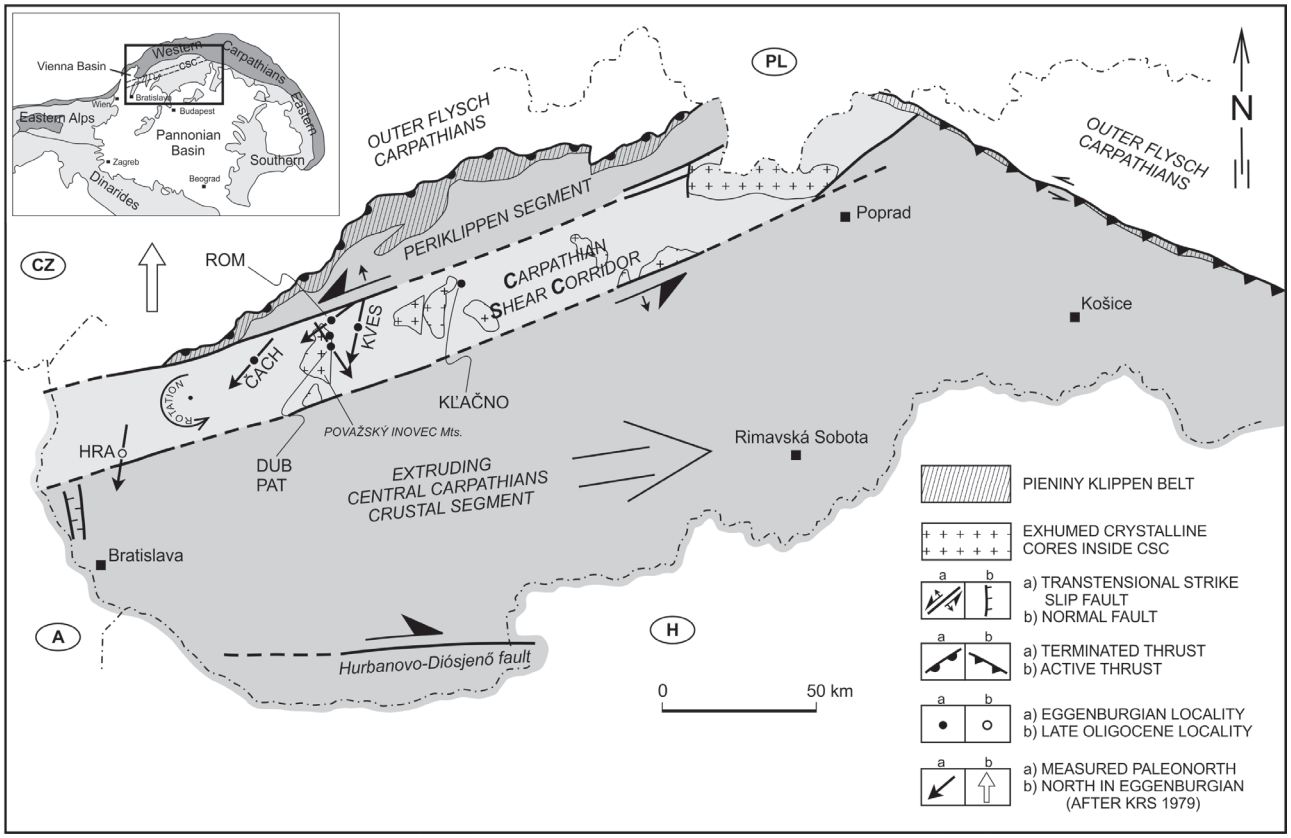

Fig. 1. Position of selected and paleomagnetically analysed rock samples within the Carpathian Shear Corridor and a synopsis of gained main results and tectonic interpretation for the Miocene period.

conglomerate body with the basement. Other contacts are faults. Locality is situated at the horst of the Strážovské vrchy Mts.

Dubodiel (DUB)

N 48° 45′ 55.5″, E 18° 05′ 49.6″, 362 m a.s.l.

Unpawed road cut nearby small dam at the stream Inovec in the village Dubodiel. There are exposed the Eggenburgian sandstones and carbonatic conglomerates of Čausa Formation (Ivanička et al., 2007). The stratification is not clear, ca S_o 60/40°. Locality is situated at the western rim of the Považský Inovec Mts. horst, affected by the Závada-Dubodiel fault, which separates Považský Inovec Mts. horst from the Miocene fill of the Bánovská kotlina depresion. The influence of this marginal fault dynamics to recent position of sampled rocks is highly probable. Bedrock represents carbonates of the Tatric cover unit cut by N-S Závada-Dubodiel fault.

Fig. 3. Sampling on studied sites. a – Sampling of Eggenburgian calcareous micro-conglomerates in the active Čachtice quarry; b – Sampling of Eggenburgian(?) calcareous fine-grained conglomerates in the active Rožňové Mitice quarry; c – Sampling of weakly lithified fine to medium-grained Eggenburgian calcareous conglomerates for the paleomagnetic analysis (I. Túnyi) and FT analysis (J. Kráľ) in the abandoned Krásna Ves quarry; d – Marked oriented samples of grey Oligocene sandstones for paleomagnetic analysis in the active Hrabník quarry before extraction; e – So we remember Igor, tireless and loving field works, just taking samples from the Eggenburgian sediments at locality Kľačno, which ones he has already missed to analyse.

Tab. 1

Results of paleomagnetic measurements. Good results with low scatter are marked bold. For samples localization see Fig. 1.

Locality code	Locality name & rock age	N	Average Paleo-north azimuth after bedding correction	Declination CCW	Inclination after bedding correction	Results scattering	Bedding S_0
ČACH	Čachtice Eggenburgian	30	**223°**	**130°**	73° °	8°	138/25°
ROM	Rožňové Mitice Eggenburgian?	30	236°	122°	58°	15°	180/45°
KVES	Krásna Ves Eggenburgian	16	ca 195°	173° 119°	29°	21°	150/55°
DUB	Dubodiel Eggenburgian	17	**151°**	**210°**	56°	7°	60/40°
PAT	Patrovec Eggenburgian	5	**120°**	**245°**	55°	9°	60/27°
HRA	Hrabník Latest Oligocene	10	188°	173°	23°	14°	150/45°

Patrovec (PAT)

N 48° 46′ 35.4″, E 18° 06′ 07.8″, 363 m a.s.l

Small outcrop beside road connecting Dubodiel and Trenčianske Jastrabie villages. There are exposed massive Eggenburgian carbonatic conglomerates and sandstones of Čausa Formation (Ivanička et al., 2007), latest one were sampled. As bedding (S_o 60/30°) was identified contact of sandstones and conglomerates. Locality is situated at the western rim of the Považský Inovec Mts. horst.

Krásna Ves (KVES)

N 48° 50′ 08.8″, E 18° 13′ 33.2″, 283 m a.s.l.

A large abbandoned quarry in the Krásna Ves village. There are exposed basal Eggenburgian sediments transgressed over dolomites of the Hronic unit. Observed successions are faulted and individual blocks are tilted (Marko, 2012). Locality is situated near the N-S Timoradza fault affecting the northern rim of the Bánovská kotlina depression (Danube basin). Sampled were well lithified beds of medium-grained conglomerates (**Fig. 3c**) dipping due to block tilting to the NE (S_o 150/55°). Locality is situated at the northern periphery of the Bánovská kotlina depression.

Hrabník (HRA)

N 48° 27′ 26.0″, E 17° 13′ 36.8″, 257 m a.s.l.

Currently active excavation pit Hrabník is situated close to the Sološnica village at the Buková furrow filled with the Paleogene sediments. The sample (**Fig. 3d**) was extracted from the upper, not folded part of the Hrabník Formation (H. F., sensu Marko et al., 1990) that is built up by the sandstone-calcarenite beds, intercalated by weakly indurated claystones (S_o 150/45°). The age of H. F. was determined (l. c.) according to the nanoplankton and foraminifers as the Uppermost Oligocene, the Kiscellian (NP 22). Locality is situated in the realm of the Malé Karpaty Mts. horst (Polák et al., 2011).

Kľačno (KLA)

N 48° 53′ 20.4″, E 18° 38′ 15.8″, 368 m a.s.l.

A short defilé at the road cut, nearby entrance to agricultural farm. Neokomian limestones of the Fatric unit are covered by transgressive facies of the Eggenburgian sediments – Kľačno conglomerates and microconglomerates of the Čausa Formation (Ivanička et al., 2007), bedding is ca S_o 265/33° (**Fig. 3e**). Locality is situated in the northern termination of the Horná Nitra depression.

Method of magnetic parameters measurements and gained results

To measure magnetic characteristics of investigated rocks a well-established methodology was applied, being developped in Geophysical Institute of the Slovak Academy of Sciences in Bratislava, including self-construction of original measurement and supporting devices. This methodology was verified by a long lasting practice.

Subsamples for further paleomagnetic analysis were extracted in laboratory by core drilling (up to 25.4 mm in diameter) from oriented field samples. The volume of each sample was established and by the susceptibilitymeter KL-Y2 and RMP spinner magnetometer JR-5 was used to measure the magnetic susceptibility (kappa) and natural remanent magnetic polarization (NRM). Gained values were recalculated in relation to the volume of the sample. After that the samples were demagnetized by step-wise procedure and before each measurement in given temperature (approximately 14 steps with ca 50 °C temperature increment up to the highest temperature

650 °C) was external magnetic field compensated automatically by means of MAVACS system, as well as manually to exclude eventual problems with the automatic system. The period of sample warming was ca 30 min. After cooling the samples to laboratory temperature the magnetic susceptibility and remanent magnetization RM were measured. Magnetic data gained from measurement devices were processed by a specialized software, and magnetic parameters for each sample were calculated. As the final software output was Zijderveld diagram in stereographic projection with the evaluation of relation between magnetic susceptibility and intenzity of RM and temperature; and changes of RM with the changing temperature. Selected measured data were processed by means of Fisher`s statistics and mean magnetic vector (paleonorth direction for given sample) was constructed.

Analysed samples situated inside CSC rendered remarkable paleomagnetic results (**Tab. 1, Fig. 2**). They show 120–240° declination of paleomeridians (**Fig. 1**) interpreted as a value of CCW rotation. So far gained paleomagnetic data from the Inner Western Carpathians declare generally ca 60–90° declinations (e.g. Túnyi and Márton, l996; Kováč and Túnyi, 1995; Márton et al., 1999).

a) – cach1

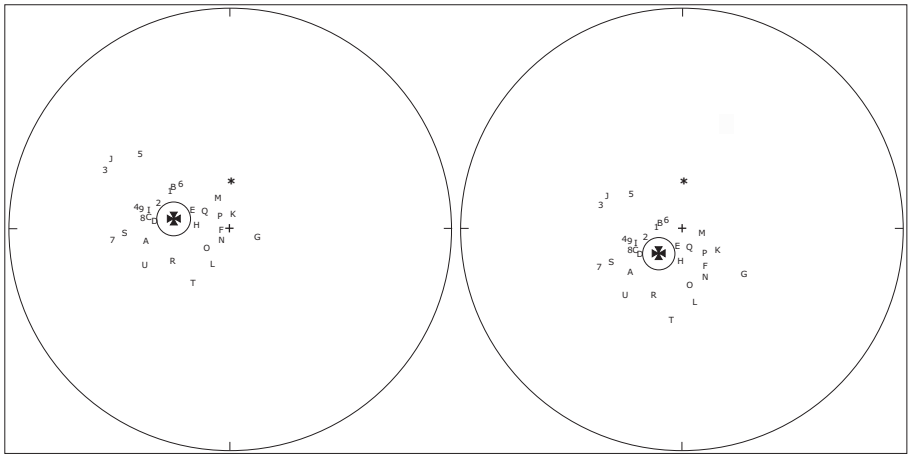

CACH1.fis, number of vectors: 30, parameters BBC (left), ABC (right):

D	I	R	k	alfa	Js	dJ	KAPs	dKAP
279.91	61.26	27.5199	11.693	8.03	0.089	0.101	5.330	12.546
222.70	72.66	27.5199	11.693	8.03	0.089	0.101	5.330	12.546

Chosen samples, demagnetization fields, marking:

12f1 150 1	12f2 300 2	12f3 50 3	12f2 200 4	12f5 100 5	12f6 200 6	13f1 150 7	13f2 400 8
13f3 150 9	13f4 350 A	13f5 200 B	13f6 250 C	13f7 450 D	14f1 300 E	14f2 150 F	14f3 200 G
14f4 150 H	14f5 150 I	14f6 100 J	14f7 50 K	15f1 100 L	15f2 100 M	15f3 150 N	15f4 150 O
15f5 50 P	15f6 50 Q	16f1 50 R	16f2 250 S	16f3 350 T	16f4 50 U		

a) – cach2

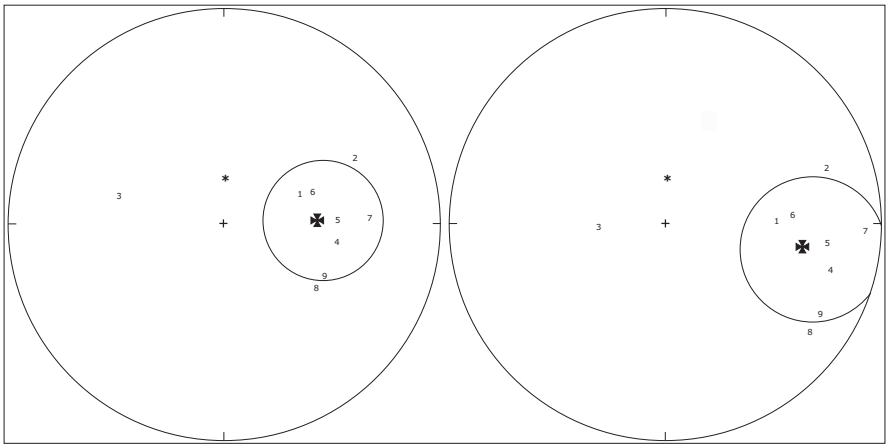

CACH2.fis, number of vectors: 9, parameters BBC (left), ABC (right):

D	I	R	k	alfa	Js	dJ	KAPs	dKAP
87.66	43.54	7.3439	4.831	26.16	0.073	0.037	2.944	10.736
99.39	24.86	7.3366	4.809	26.23	0.073	0.037	2.944	10.736

Chosen samples, demagnetization fields, marking:

11f1 150 1	11f2 200 2	16f5 50 3	17f1 350 4	17f2 300 5	17f3 350 6	17f4 50 7	17f5 100 8
17f6 100 9							

b) – kves1

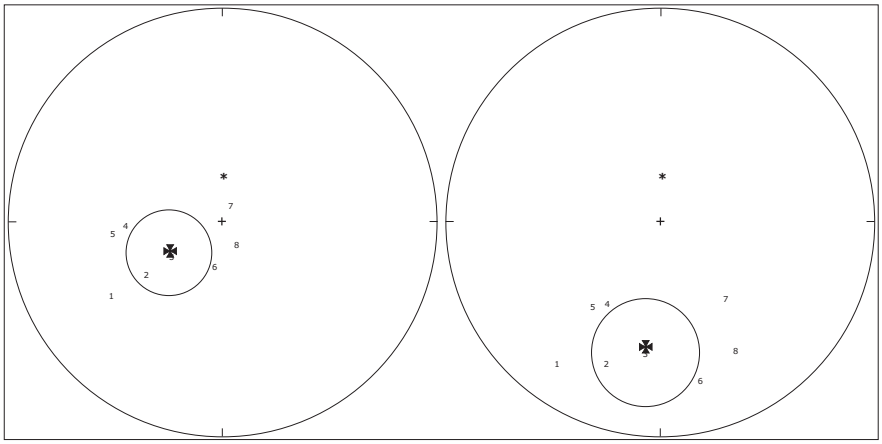

KVE1.fis, number of vectors: 8, parameters BBC (left), ABC (right):

D	I	R	k	alfa	Js	dJ	KAPs	dKAP
239,64	59,20	7.1164	7.922	20.98	0.606	1.137	2.725	1.021
185.97	29.34	7.1164	7.922	20.98	0.606	1.137	2.725	1.021

Chosen samples, demagnetization fields, marking:

7f1 100 1 7f2 350 2 7f3 150 3 7f4 200 4 7f5 150 5 7f8 150 6 9f4 400 7 9f6 350 8

b) – rom

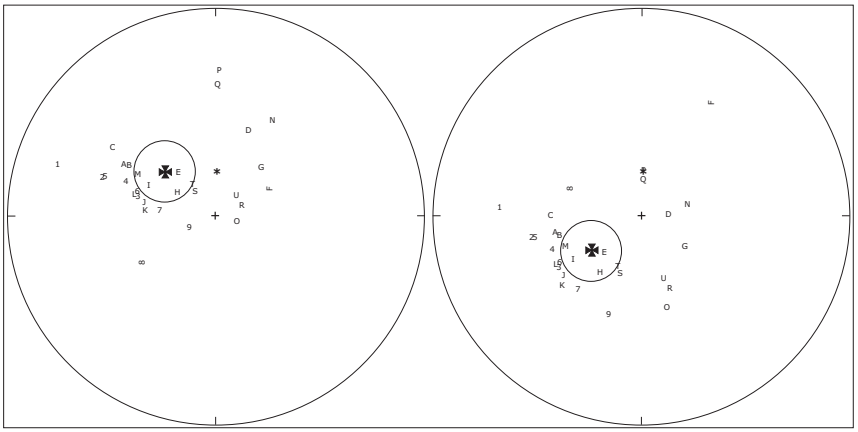

ROM.fis, number of vectors: 30, parameters BBC (left), ABC (right):

D	I	R	k	alfa	Js	dJ	KAPs	dKAP
311.62	54.24	22.7315	3.990	15.16	1.083	0.830	-0.257	1.551
235.58	58.02	22.7315	3.990	15.16	1.083	0.830	-0.257	1.551

Chosen samples, demagnetization fields, marking:

1f1 350 1	1f2 350 2	1f3 350 3	2f1 350 4	2f2 350 5	2f3 400 6	2f4 350 7	2f6 150 8
2f7 100 9	3f1 400 A	3f2 350 B	3f3 450 C	3f6 100 D	4f1 450 E	4f2 250 F	4f3 100 G
4f4 400 H	4f5 450 I	5f1 350 J	5f2 350 K	5f3 100 L	5f4 350 M	5f5 100 N	5f6 150 O
6f1 300 P	6f2 350 Q	6f3 450 R	6f4 150 S	6f5 200 T	6f6 150 U		

Below are presented results of paleomagnetic measurements for single localities displayed in the lower hemispehere of streographic projection. For each sample – locality the diagram has marked calculated mean vector direction with the circle of results reliability, and magnetic north direction estabilished for the Neogene period (after Krs, 1979).

Tectonic interpretation of paleomagnetic results

Anomalous declinations in Eggenburgian and Late Oligocene sediments inside the Carpathian Shear Corridor points to large blocks rotation due to the post-Eggenburgian sinistral strike-slip regime. Nevertheless, such extreme rigid body block rotations can be hardly realized inside one shear zone due to geometrical limits of rotations. We expect combination of succeeding events (Marko et al., 2014), during which the blocks gradually rotated to present position. First rotation took place due to CCW *en-bloc* rotation of ALCAPA (Balla, 1987). This event could has been followed by CCW domino-style rotation inside wide sinistral N-S trending shear zone, separating already stacked Eastern Alpine units from still northward moving Carpathians units. The final part of CCW block rotations took place inside ENE-WSW trending Carpathian Shear Corridor operating in sinistral regime. It drove the eastward escape of the Central Carpathians crustal

c) – kves2

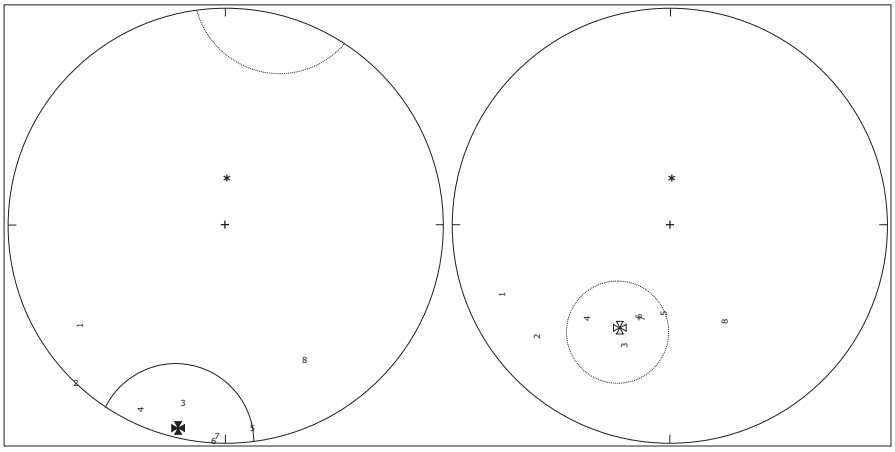

KVES2.fis, number of vectors: 8, parameters BBC (left), ABC (right):

D	I	R	k	alfa	Js	dJ	KAPs	dKAP
192.81	2.39	7.1413	8.151	20.65	1.906	2.253	2.588	2.238
206.20	-35.20	7.1413	8.151	20.65	1.906	2.253	2.588	2.238

Chosen samples, demagnetization fields, marking:

8f1 350 1 8f2 350 2 8f3 100 3 8f4 350 4 8f5 150 5 9f1 250 6 9f2 150 7 9f3 50 8

c) – kves3

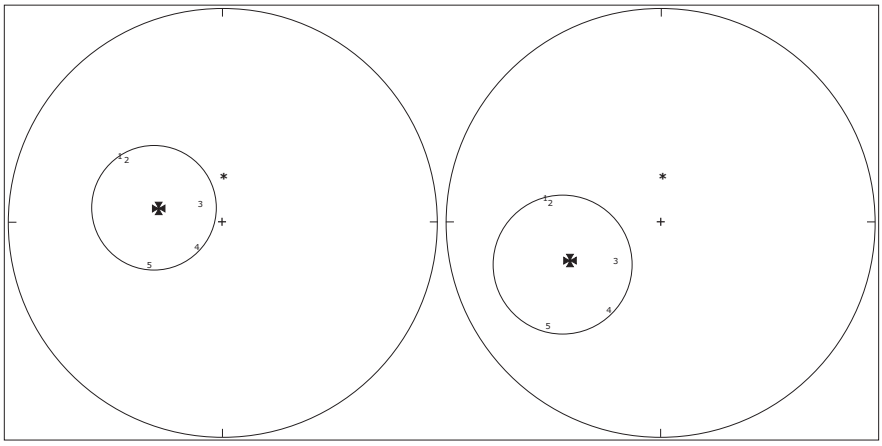

KVES3.fis, number of vectors: 5, parameters BBC (left), ABC (right):

D	I	R	k	alfa	Js	dJ	KAPs	dKAP
282,20	55,83	4.4700	7.547	29.79	0.724	0.957	-1.200	11.970
247.24	40.72	4.4700	7.547	29.79	0.724	0.957	-1.200	11.970

Chosen samples, demagnetization fields, marking:

10f1 350 1 10f2 350 2 10f3 650 3 10f4 350 4 10f9 350 5

segment. The highest values of block rotation (ca 240° CCW) was measured in localities Dubodiel and Patrovec. Both localities are situated at the zone of N-S trending Závada-Dubodiel fault, a marginal fault of the Považský Inovec Mts. horst. These extreme values of rotation could be a result of superposed rotational events within sinistral N-S trending shear zone, followed by rotation within sinistral Carpathian Shear Corridor.

Simultaneuously with block rotations around vertical axes due to sinistral strike-slip regime inside CSC, block tilting (**Fig. 4**) took place. It is evident from inclinations of formerly horizontally laying cover and nappe units in asymmetrical horsts (core mountains). This process is well described e.g. by Jaroszewski (1980) and Zolnai (1995). Block tilting is a reason of high-angle paleomeridians inclinations observed inside CSC.

The Carpathian Shear Corridor is a zone of Late Miocene exhumation of crystalline basement in individual blocks; where the AFT data from the Strážovské vrchy Mts. inside the corridor point to two uplift and exhumation phases, with moderate to slow cooling 24–22 Ma ago and fast cooling approximately 10–7 Ma ago (Marko et al., 2017). These processes were driven by shear zone activity. The rigid body block rotation and tilting, resp. blocks uplift/subsidence inside strike-slip zones are usually coeval processes. However, the ages of two uplift events in CSC are different from the published Lower/Middle Miocene ages of rotations in the Western Carpathians

d) – dub

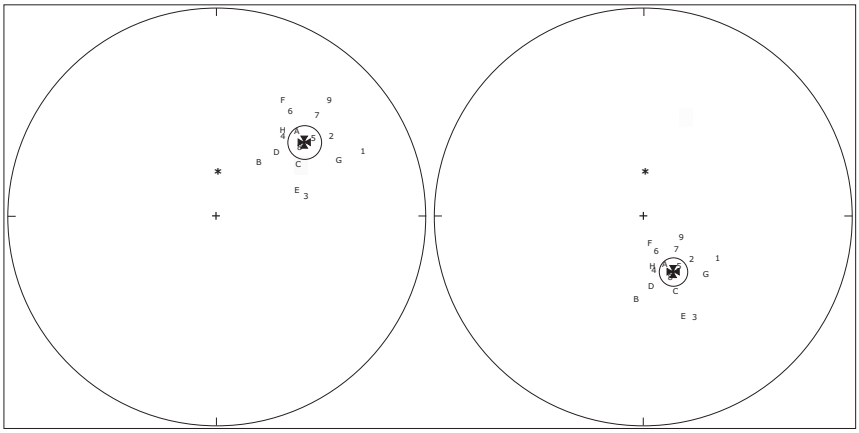

DUB.fis, number of vectors: 17, parameters BBC (left), ABC (right):

D	I	R	k	alfa	Js	dJ	KAPs	dKAP
49.59	32.86	16.3902	26.239	7.10	0.015	0.005	-12.982	17.555
151.29	56.49	16.3902	26.239	7.10	0.015	0.005	-12.982	17.555

Chosen samples, demagnetization fields, marking:

18f1 350 1 18f2 150 2 18f3 100 3 18f4 50 4 18f5 150 5 19f2 200 6 19f3 150 7 19f4 200 8
19f5 200 9 20f1 300 A 20f2 400 B 21f1 400 C 21f2 350 D 21f3 150 E 21f4 100 F 21f5 150 G
22f1 350 H

d) – pat

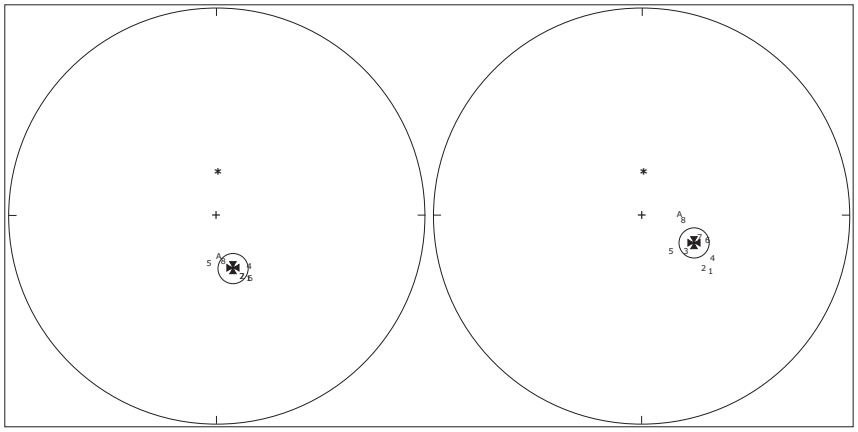

PAT.fis, number of vectors: 10, parameters BBC (left), ABC (right):

D	I	R	k	alfa	Js	dJ	KAPs	dKAP
162.53	60.32	9.8940	84.880	5.27	0.106	0.015	55.560	6.218
117.93	58.68	9.7840	41.660	7.57	0.106	0.015	55.560	6.218

Chosen samples, demagnetization fields, marking:

23f1a 150 1 23f2a 150 2 24f1a 200 3 24f2a 200 4 24f3a 100 5 23f1b 150 6 23f2b 150 7 24f1b 200 8
24f2b 200 9 24f3b 150 A

(e.g. Králiková et al., 2016). One explanation of this contradiction involves rotations inside the corridor ca 8 Ma ago, contemporaneously with the last AFT related uplift event. We prefer this alternative. Other explanation involves rotations inside the corridor, taking place at the same age (15–17 Ma) as has been already declared, but in this case the rotations were realized withouth uplift of the blocks.

Rotations revealed in localities in Eggenburgian sediments and one in Late Oligocene sediments, all situated inside the corridor, are large, but not exactly the same in each locality. It can be explained by strain heterogeneity, resp. deformation as well rotation partitioning. Individual localities are probably situated in blocks of different dimensions, which were affected by different intensity of rotation. Differences in magnetic fabric of core mountains (Hrouda et al., 2002) is desctribed as a result of not uniform Neo-Alpine rotation of individual blocks (l. c.) as well.

Discussion

Paleomagnetic measurements from several studied localities display more scattered results, but others are well clustered (loc. ČACH, DUB, PAT, HRA – **Fig. 1**). Nevertheless we gained usable results, which correspond to our earlier interpretation of CSC as a dynamic strike-slip zone. Despite that some of the gained paleomagnetic data are not perfect, our preliminary results of paleomagnetic measurements reflect what happened inside the CSC – the

e) – hra

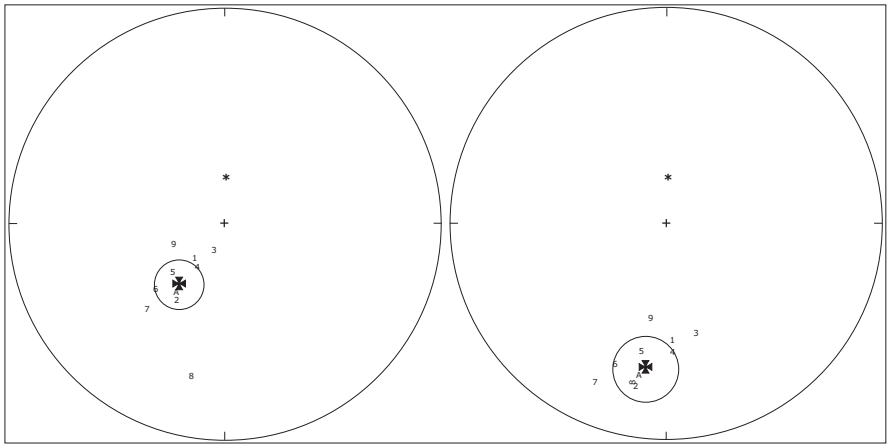

HRA.fis, number of vectors: 10, parameters BBC (left), ABC (right):

D	I	R	k	alfa	Js	dJ	KAPs	dKAP
216.64	51.94	9.4916	17.704	11.81	0.145	0.075	133.180	88.854
187.80	22.57	9.4916	17.704	11.81	0.145	0.075	133.180	88.854

Chosen samples, demagnetization fields, marking:

hpm1_1 300 1 hpm1_2 300 2 hpm1_3 200 3 hpm1_4 350 4 hpm1_5 300 5 hpm1_6 400 6 hpm1_7 400 7 hpm1_9 150 8

hpm1_11 300 9 hpm1_12 400 A

Fig. 2a–e. Diagrams (stereographic projection, lower hemisphere) with magnetic paleo-poles directions of single measurements (alphabets and numbers) and mean paleomagnetic direction (gothic cross) with the circle of reliability calculated for localities Čachtice (ČACH), Rožňové Mitice (ROM), Krásna Ves (KVES), Dubodiel (DUB), Patrovec (PAT) and Hrabník (HRAB) (compare with Tab. 1) before bedding correction (BBC) and after bedding correction (ABC) was done. Star represents an orientation of the North magnetic pole for the Neogene period (after Krs, 1979). Normal and reversal magnetic polarization are distinguished by single measurements symbols position – normal position means normal magnetic polarization, sloping position of symbol means reversal polarization.

large block rotation and tilting. It is difficult to explain such large rigid body block rotations, but we have examples for even larger rotations from the nature, which are quite usual and effective in mineral dimensions within metamorphic processes (e.g. porphyroblast rotations). If we accept the scale invariance principle (*see also* Marko, 2012), equivalent rotations can be expected in all scales. The step-wise rotation in superposed shear zones can explain the extreme values of block roatation as well. Similar idea was suggested also in pioneering work by Grecula et al. (1990).

There is a linear relation between magnitude of strike-slip separation and magnitude of blocks rotation inside a shear zone. A map view domino-style model simplifies and explains evolution of observed real structures, but not in 3D. Question is what happens in depth during the rotaion, whether and where are individualized and rotated blocks detached from the basement. Towards the depth we can expect transition from brittle to ductile rheology of deformation. In the case of moderate rigid body block rotation in the schizosphere, there is a gradual transition to rotation in ductile conditions in plastosphere and no detachement is necessary. Blocks are rooted in depth. However, extreme 180° and even more block rotations due to extreme strike-slip separation identified along the CSC needs total detachement of rotated blocks from the basement. Detachment of rotated blocks from the basement should be somewhere at the brittle-ductile transitional zone, or could be situated at the basal thrust plane of the Western Carpathians micro-plate.

We explain declinations of paleomeridians tectonically, as a result of CCW Early/Middle Miocene rigid-body block rotations due to sinistral shearing in the wrench corridor. However, there exist another, non tectonic hypothesis explaining extreme values of declinations by autoreversal of remanent magnetization of minerals (Orlický, 2018). This eventuality declaring the complexity of the physical principles of magnetism has not been taken into considerartion in our tectonic concept based on classical field-reversal theory.

Conclusions

An important block rotations occurred during the Western Carpathians Neo-Alpine tectonic evolution. Paleomagnetic data were so far tectonically interpreted as a proof of counter-clockwise ALCAPA micro-plate rotation during its invasion into the North-European Platform embayment of subducting thin oceanic crust in the early stages of the Neo-Alpine tectonic evolution.

We suggest that subsequent domino-style rotations of small blocks took place inside a prominent sinistral strike-slip brittle shear zone – a strike-slip corridor controlling eastward escape of the Inner Western Carpathians crustal segment and inside this shear zone the high values of block rotations are expected. To confirm this concept five oriented samples of Eggenburgian sediments and one

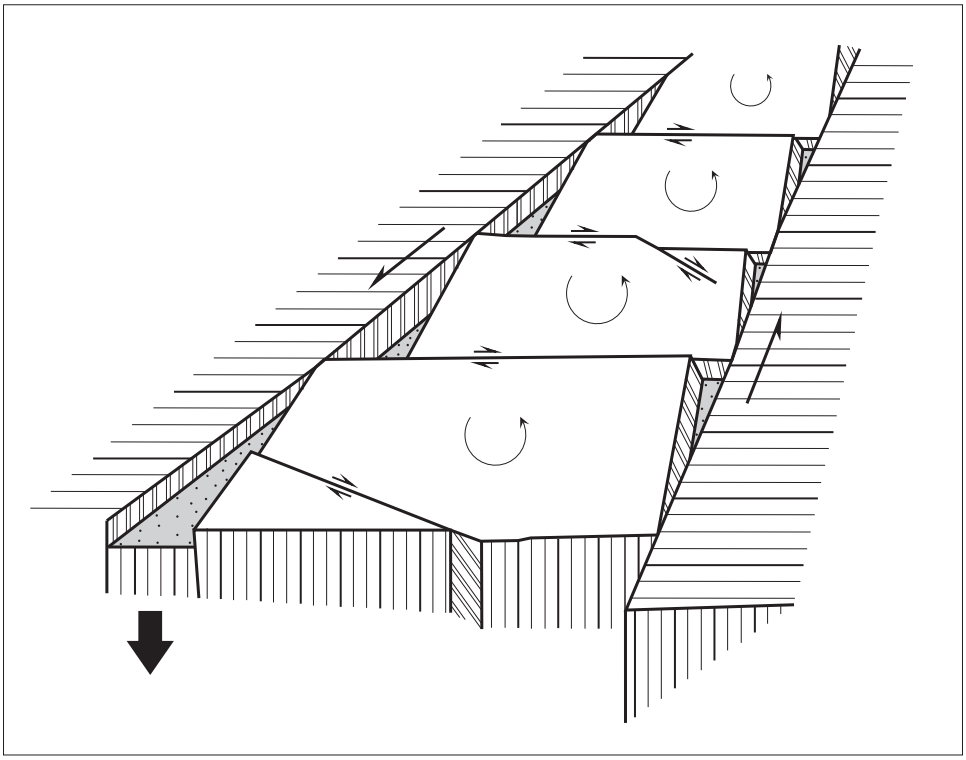

Fig. 4. Model of domino-style rigid-body blocks rotation and tilting, accommodated by antithetic Riedel's shears inside sinistral strike-slip brittle shear zone with arrow indicating subsided marginal parts (after Jaroszewski, 1980).

Late Oligocene sample from the localities situated inside the wrench corridor were selected and declinations of magnetic paleomeridians were detected.

In contrast to so far known average 60–90° declinations of magnetic paleomeridians due to ALCAPA en-bloc rotation, 120–240° ranging declinations of magnetic paleomeridians were detected inside the wrench corridor. It is an evidence of the occurrence and the geodynamic role of the Carpathian Shear Corridor inside which the subsequent CCW rotation took place after the ALCAPA en-bloc rotation. Although the paleomagnetic results are preliminary and some gained data are not perfect, these are important, because they reflect what happened inside the CSC – the excessive block rotations.

Acknowledgements

This work is dedicated in memory of Igor Túnyi, genuine and empathetic friend, pioneer and top authority of paleomagnetic studies in the Western Carpathians, whose research and opinions were substantial for the paper compilation and are still so inspirative for all of us. We are indebted to Oto Orlický for processing, measurements of paleomagnetic samples and especially for fundamental consultations concerning methodology and gained results. Thanks are expressed also to reviewers/consultants Lubomír Pospíšil, Čestmír Tomek, František Hrouda, Dušan Plašienka and particularly to Zoltán Németh, all improving quality of the original manuscript. Ladislav Bittó is acknowledged for illustrations processing. This work was realized in the frame of the APVV-16-0146 project and benefited also from the data gained during research on VEGA 1/0712/11 project.

References

Balla, Z., 1987: Tertiary paleomagnetic data for the Carpatho--Pannonian region in the light of Miocene rotation kinematics. *Tectonophysics, 139, 67–98.*

Doktór, S., Dornič, J., Graniczny, M. & Reichwalder, P., 1985: Structural elements of Western Carpathians and their Foredeep on the basis of satellite interpretation. *Kwart. Geol., 29, 1, 129–138.*

Fodor, L., 1995: From transpression to transtension: Oligocene--Miocene structural evolution of the Vienna basin and the East Alpine-West Carpathians junction. *Tectonophysics, 242, 151–182.*

Fodor, L., Jelen, B., Márton, E., Skaberne, D., Čar, J. & Vrabec, M., 1998: Miocene-Pliocene tectonic evolution of the Slovenian Periadriatic fault: Implications for Alpine--Carpathian extrusion models. *Tectonics, 17, 5, 690–709.*

Grecula, P., Návesňák, D., Bartalský, B., Gazdačko, Ľ., Németh, Z., Ištván, J. & Vrbatovič, P., 1990: Shear zones and arc structure of Gemericum, the Western Carpathians. *Miner. Slov., 22, 2, 97–110.*

Hrouda, F., Plašienka, D. & Gregorová, D., 2002: Assumed Neogene deformation in the Central Western Carpathiansas inferred from magnetic anisotropy investigations. *EGU Stephan Mueller Spec. Publ. Ser., 1, 125–136.*

Ivanička, J., Havrila, M., Kohút, M., Kováčik, M., Madarás, J., Olšavský, M., Hók, J., Polák, M., Filo, I., Elečko, M., Fordinál, K., Maglay, J., Pristaš, J., Buček, S. & Šimon, L., 2007: Geological map of the Považský Inovec Mts. and SE part of the Trenčianska kotlina depression. *Bratislava, MŽP SR, Št. Geol. Úst. D. Štúra.*

Janků, J., Pospíšil, L. & Vass, D., 1984: Príspevok diaľkového prieskumu Zeme k poznaniu stavby Západných Karpát (západný úsek). *Miner. Slov., 16, 2, 121–137.*

Jaroszewski, W., 1980: Tektonika uskokow i faldow. *Warszawa, Wyd. Geol., 360 pp.*

Kováč, M., Baráth, I., Holický, I., Marko, F. & Túnyi, I., 1989: Basin opening in the Lower Miocene strike-slip zone in the SW part of the Western Carpathians. *Geol. Zbor. Geol. Carpath., 10, 1, 37–62.*

Kováč, M., Bielik, M., Lexa, J., Pereszlényi, J., Šefara, J., Túnyi, I. & Vass, D., 1997: The Western Carpathian intramountane basins. *In: Grecula, P., Hovorka, D. & Putiš, M. (eds.): Geological evolution of the Western Carpathians. Bratislava, Miner. Slov., Monogr., 43–64.*

Kováč, M. & Túnyi, I., 1995: Interpretácia paleomagnetických údajov zo západnej časti Centrálnych Západných Karpát. *Miner. Slov., 27, 213–220.*

Králiková, S., Vojtko, R., Hók, J., Fügenschuh, B. & Kováč, M., 2016: Low-temperature constraints on the Alpine thermal evolution of the Western Carpathian basement rock complexes. *J. struct. Geol., 91, 144–160.*

Krs, M., 1979: An analysis of the paleomagnetic field. *Stud. Geophys. Geod., 22, 4, 368–389.*

Marko, F., 2012: Kenozoické napäťové pole a zlomová aktivita severného okraja Dunajskej panvy (Západné Karpaty, Slovensko). *Miner. Slov., 44, 3, 213–230.*

Marko, F., Kováč, M., Fodor, L. & Šútovská, K., 1990: Deformácie a kinematika miocénnej strižnej zóny severnej časti Malých Karpát (Bukovská brázda, hrabnícke súvrstvie). *Miner. Slov., 22, 5, 399– 410.*

Marko, F., Fodor, L. & Kováč, M., 1991: Miocene strike--slip faulting and block rotation in Brezovské Karpaty Mts. (Western Carpathians). *Miner. Slov., 23, 189–200.*

Marko, F., Andriessen P. A. M., Tomek, Č., Bezák, V., Fojtíková, L., Bošanský, M., Piovarči, M. & Reichwalder, P., 2017: Carpathian Shear Corridor – A strike-slip boundary of an extruded crustal segment. *Tectonophysics, 703–704, 119–134.*

Marko, F., Túnyi, I., Andriessen, P. A. M., Fojtíková, L., Piovarči, M. & Králiková, S., 2013: Carpathian Shear Corridor – a zone of blocks uplift, tilting, rotation and recent seismic activity (Western Carpathians). GEEWEC 2013 *Geological evolution of the Western Carpathians: new ideas in the field of inter-regional correlations, Smolenice, Slovakia, October 16.–19. 2013. Abstract book, ISBN 978--80-971442-5-8, 59–60.*

Marko, F., Túnyi, I., Tomek, Č., Andriessen, P. A. M., Králiková, S., Fojtíková, L., Piovarči, M., Orlický, O. & Bučová, J., 2014: Structural, remote sensing, FT, paleomagnetic and seismic record of the Central Carpathians crustal segment extrusion. Environmental, Sedimentary & Structural Evolution of the Western Carpathians. *Abstract book. Bratislava, Geophys. Inst. Slovak Acad. Sci., ISBN 978-80-85754-31-5, 38–39.*

Márton, E. & Fodor, L., 1995: Combination of paleomagnetic and stress data – a case study from North Hungary. *Tectonophysics, 242, 99–114.*

Márton, E., Grabowski, J., Plašienka, D., Túnyi, I., Krobicki, M., Haas, J. & Pethe, M., 2013: New paleomagnetic results from the Upper Cretaceous red marls of the Pieniny Klippen Belt, Western Carpathians: evidence for general CCW rotation and implications for the origin of the structural arc formation. *Tectonophysics, 592, 1–13.*

Márton, E., Mastella, L. & Tokarski, A., 1999: Large Counterclockwise Rotation of the Inner West Carpathian Paleogene Flysch – Evidence from Paleomagnetic Investigations of the Podhale Flysch (Poland). *Phys. Chem. Earth (A), 24, 8, 645–649.*

Márton, E., Vass, D. & Túnyi, I., 1996. Rotation of the South Slovak Paleogene and Lower Miocene rocks indicated by paleomagnetic data. *Geol. Carpath., 47, 1, 31–41.*

Nemčok, M., Pospíšil, L., Lexa, J. & Donelick, R. A., 1998: Tertiary subduction and slab break-off model of the Carpathian-Pannonian region. *Tectonophysics, 295, 307–340.*

Orlický, O., 2018: A new original conception in rock magnetism, paleomagnetism and geomagnetism: An origin of the reversed magnetization of rocks on Earth. *Contr. Geophys. Geol., 48, 1, 75–112.*

Polák, M., Plašienka, D., Kohút, M., Putiš, M., Bezák, V., Filo, I., Olšavský, M., Havrila, M., Buček, S., Maglay, J., Elečko, M., Fordinál, K., Nagy, A., Hraško, Ľ., Németh, Z., Ivanička, J. & Broska, I., 2011: Geological map of the Malé Karpaty Mts. region in scale 1 : 50 000 (in Slovak). *Bratislava, MŽP SR, Št. Geol. Úst. D. Štúra.*

Pospíšil, L., 1989: Nové geofyzikální mapy Západních Karpat a možnosti jejich využití (přehled). *Miner. Slov., 21, 5, 403–420.*

Pospíšil, L., 1990: Současné možnosti identifikace střižných zón v oblasti Západních Karpat. *Miner. Slov., 22, 1, 19–31.*

Pospíšil, L., Hefty, J. & Hipmanová, L., 2012: Risk and geodynamically active areas of the Carpathian lithosphere on the base of geodetical and geophysical data. *Acta Geod. Geophys. Hung. (online), 47, 3, 287–309 (ISSN: 1 587–1 037).*

Pospíšil, L., Nemčok, J., Graniczny, M. & Doktór, S., 1986: Příspěvek metod dálkového průzkumu k identifikaci zlomů s horizontálním posunem v oblasti Západních Karpat. *Miner. Slov., 19, 385–402.*

Túnyi, I. & Márton, E., 1996: Indication for large Tertiary rotation in the Carpathians and Northern Pannonian region outside the North Hungarian paleogene basin. *Geol. Carpath., 47, 1, 43–49.*

Vass, D., 1998: Neogene geodynamic development of the Carpathian arc and associated basins. In: Rakús, M. (ed.): Geodynamic development of the Western Carpathians. *Bratislava, GS SR, Dionýz Štúr Publishers, 155–158.*

Zolnai, G., 1995: Different types of orogens and orogenic processes, with reference to Southern and Central Europe. *Acta geol. hung., 38, 2, 131–184.*

Rotácie blokov v karpatskom strižnom koridore – paleomagnetický záznam

Paleomagnetické štúdie realizované v Západných Karpatoch (napr. Balla, 1987; Kováč et al., 1989; Kováč a Túnyi, 1995; Márton a Fodor, 1995; Fodor, 1995; Fodor et al., 1998; Márton et al., 2013) dokladajú odklon spodnomiocénnych magnetických paleomeridiánov od neogénneho magnetického meridiánu definovaného Krsom zhruba 60 – 90° (1979). Tieto deklinácie sa interpretujú ako dôsledok CCW *en-bloc* rotácie mikroplatne ALCAPA prenikajúcej do zálivu severoeurópskej platformy, tvoreného tenkou oceánskou kôrou subdukujúcou pod Karpaty. Domnievame sa, že v období neoalpínskej tektonickej evolúcie po rotácii karpatskej mikroplatne zohral pri postupe samostatných menších kôrových blokov interníd Západných Karpát dôležitú úlohu karpatský strižný koridor (CSC sensu Marko et al., 2017). Dynamiku tohto rozhrania identifikovaného zo snímok diaľkového prieskumu Zeme (DPZ) (Janků et al., 1984; Doktór et al., 1985) opísali Pospíšil et al. (1986, 2012) a Pospíšil (1989, 1990). CSC reprezentoval smernoposunovú laterálnu rampu kôrového segmentu interníd Západných Karpát extrudujúceho na východ (**obr. 1**). Podľa tohto modelu bolo vysúvanie centrálnokarpatského kôrového segmentu relaxované v zóne CSC intenzívnou strižnou deformáciou s CCW rotáciou a tiltovaním mikroblokov (**obr. 4**) v sinistrálnom smernoposunovom, pravdepodobne transtenznom režime. Výsledkom stredno- až vrchnomiocénnej dynamiky je špecifický stavebný štýl v zóne karpatského strižného koridoru, charakteristický striedaním vyzdvihnutých (jadrové pohoria) a poklesnutých (sedimentárne vnútrohorské bazény) rotovaných a tiltovaných blokov. Načrtnutý koncept predpokladá anomálne ľavostranné (CCW) rotácie mikroblokov vnútri karpatského strižného koridoru. Aby sme overili túto predstavu, zamerali sme sa na štúdium orientácie magnetických paleomeridiánov v ranomiocénnych sedimentoch na niektorých dostupných lokalitách v priestore karpatského strižného koridoru. Orientované vzorky boli odobrané z 5 lokalít v egenburských sedimentoch, jedna lokalita bola vo vrchnooligocénnych sedimentoch (**obr. 1, 3a – e**). Vzhľadom na nie ideálnu zrnitosť meraných sedimentov a technické komplikácie s meracou aparatúrou považujeme výsledky meraní (**obr. 2**) za predbežné. Výsledky sú však výpovedné, odrážajú dynamiku strižného koridoru a podporujú našu tektonickú koncepciu. Zistené hodnoty deklinácií magnetických paleomeridiánov potvrdzujú náš predpoklad a CCW rotácie blokov v rozmedzí 120 – 240° (**tab. 1**) vyplývajúce z orientácie paleomeridiánov sú anomálne. Tento poznatok podporuje existenciu a geodynamickú úlohu karpatského strižného koridoru ako prominentného smernoposunového rozhrania extrudujúceho vnútrokarpatského kôrového segmentu.

Rozdielne hodnoty deklinácií meraných na rôznych lokalitách situovaných v tej istej strižnej zóne môžu byť vysvetlené deformačnou, resp. rotačnou heterogenitou, ktorá mohla byť spôsobená aj odlišnou mierou rotácie blokov rôznych rozmerov. Okrem rotácií okolo vertikálnych osí bloky zároveň tiltovali. Tilting je evidentný z tektonického štýlu asymetrických hrastí jadrových pohorí a halfgrabenov sedimentárnych bazénov. Tilting je aj príčinou vysokých hodnôt inklinácií magnetických vektorov na niektorých lokalitách.

Prezentované výsledky paleomagnetických meraní v CSC sú síce predbežné, ale dôležité pri verifikácii tektonickej koncepcie CSC. Tieto cenné údaje sme získali vďaka nasadeniu a entuziazmu priekopníka spolupráce medzi geológmi a geofyzikmi Igora Túnyiho, ktorému aj týmto vzdávame hold.

Doručené / Received: 26. 9. 2019
Prijaté na publikovanie / Accepted: 2. 12. 2019

Mineralia Slovaca, Web ISSN 1338-3523, ISSN 0369-2086
51 (2019), 187 – 204, © Authors 2019. CC BY 4.0

Hidden groundwater inflows from the Slovenský kras Mts. to the Slaná River identified by thermometric and resistivimetric measurements

PETER MALÍK[1], BRANISLAV MÁŠA[2], FRANTIŠEK BOTTLIK[1], JAROMÍR ŠVASTA[1], NATÁLIA BAHNOVÁ[1], ALEXANDRA VASILENKOVÁ[1], PETER BAJTOŠ[1] and RADOVAN ČERNÁK[1]

[1] State Geological Institute of Dionýz Štúr, Division of Hydrogeology and Geothermal Energy, Mlynská dolina 1, SK-817 04 Bratislava 11, Slovak Republic; peter.malik@geology.sk;
[2] HES-Comgeo, spol. s r. o.; Kostiviarska cesta 4, SK-974 01 Banská Bystrica, Slovak Republic; branislav.masa@hes-comgeo.sk

Abstract: Longitudinal profile measurement of specific electric conductivity (resistivimetry) and water temperature (thermometry) along the watercourse of a surface stream, if performed in sufficient density of measuring points, can reveal position of hidden groundwater inflows in a surprisingly detailed scale. Contrary to flow accretion survey, i.e. discharge measurements on appropriately distanced locations of streams that are able to quantitatively define hidden surpluses or losses of discharge, but their evaluator can attribute these to stream segments only, outputs of thermometry and resistivimetry have potential of precise location identification of groundwater outlets. The best season for such measurements is culminating summer or winter with naturally highlighted contrast in surface water and groundwater temperatures. In our case, thermometric and resistivimetric measurements were performed on the watercourse of the Slaná River (SE Slovakia), segment between Brzotín and Gombasek municipalities, where the river is cutting two major karstic plateaus (Silická planina and Plešivská planina) in a form of several hundred meters wide and several hundred meters deep canyon. Three major karstic springs are found in this area, but hidden dewatering of karst water resources directly into the Slaná River remained unknown. Measurements were performed within 5 summer days from 21/06/2016 until 25/06/2016 on an 8300 meters long rivercourse section. The basic footage step of measurements was 1.0 meter. Mesurements were performed in the streamline of active flow and also along its left and right side, 20 cm aside the stream-bank. Both parameters – water temperature and specific electric conductivity – were measured near the streambed, ~5 cm above the bottom, in the ~20 to 40 cm distance from the left or right bank, and also in the main streamline. No major karstic groundwater inlets were found here, but small-scale inflows were mostly found on the left bank pointing to groundwater flow from the east – from the Silická planina Plateau. It seems that at least on the Brzotín-Gombasek watercourse segment of the Slaná River, Plešivská planina Plateau is dewatered only through already registered karstic springs west from the river.

Key words: hidden groundwater surpluses, Slaná River surface stream, longitudinal profile measurements, water electric conductivity, resistivimetry, thermometry

Graphical abstract

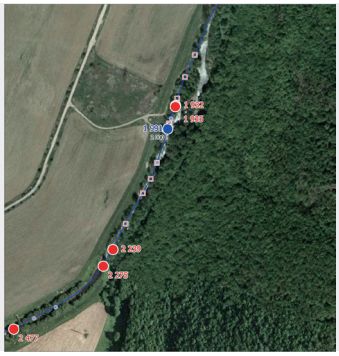

Highlights

- Hidden groundwater inflows to the river were verified by water temperature and electric conductivity measurements.
- Major karst groundwater inputs were not registered.
- River section between Brzotín and Gombasek had low incidence of right-sided anomalies, more inflows were from the left bank from the Silická planina Plateau.
- Hidden dewatering of the Plešivská planina Plateau was not verified.

Introduction

The use of longitudinal profile measurements of temperature and specific electrical conductivity (EC, also described as electrolytic conductivity, which is a reciprocal value of specific electrical resistance) in the investigation of quantitative-qualitative relationships between groundwater and surface waters has long been considered a proven geophysical method in Slovak hydrogeological practice. This simple, less costly but very effective method has been applied initially to surface streams in karst areas since the early 1980s (Husák and Lizoň, 1980; Lizoň, 1980; Foltán, 1983; Kullman et al., 1985). Later, it was also successfully applied in hydrogeological surveys for mineral water sources (e.g. Ferenc et al., 1986). Resistivimetric and thermometric measurements were used to locate hidden groundwater inflows into surface streams (Filo and Švastová, 1994; Švastová in Malík et al., 2000;

Vojtková and Malík, 2005). These measurements utilize the temperature and conductivity contrast between surface water and groundwater, when the groundwater is considerably colder in summer time and considerably warmer in winter time than surface water. Therefore, periods of extreme air temperatures (culminating winter or summer) are usually most preferable for such measurements. The EC contrast depends on the differences in the geochemical nature of the rocks in the whole source watershed of the surface stream and in the immediate surroundings of the measurements, where groundwater is supposed to originate. In this (EC) case, one should also consider possible presence of anthropogenic influences (usually contaminants). The groundwater inflow rate is reflected over the surface streamflow course in the range of temperature and specific electric conductivity anomalies, taking into account the total flow discharge of the investigated stream/river. Correlation of both data (temperature/EC) allows qualitative identification of hidden groundwater surpluses as anomalies caused by inflowing groundwater and excludes possible false anomalies caused by other factors.

Resistivimetric and thermometric measurements were also applied to detect hidden water increments inside cave spaces, respectively in underground hydrological systems of caves (Malík et al., 2010a, 2010b, 2011; Gregor et al., 2017). In karst hydrogeology, such methods are even more effective in the cases of combination of surface and underground parts of streams in karst areas (Auxt et al., 2012; Malík et al., 2013; Malík et al., 2016). Performing resistivimetric and thermometric measurements inside the cave, the thermal contrast rate is usually suppressed due to the constant temperature inside the underground spaces, and the detection of inflows relies on EC anomalies unless a significant inflow from the ground surface enters the underground hydrological system. If in this case there is limited time for temperature equalisation, water temperature measurements can be helpful as well. From a speleological point of view, lateral, hydraulically active branches of the karst systems can be inspected for in hidden water inflows from unknown places. For karst hydrologists and hydrogeologists, these results are important in assessment of hydraulic and hydrodynamic conditions of water flow in open karst conduits. Great importance of such a knowledge is valuable especially in the design and refinement of caves' protection zones or recharge areas/protection zones of (exploited) karstic springs.

Another interesting contribution of the longitudinal profile measurements of water temperature and EC may also be their indirect impact on the water balance calculation as it was in the case of Kopa karstic hydrogeological structure (NW part of the Veľká Fatra Mts., northern Slovakia). Balance closure of this hydrogeological structure was verified by thermometric and resistivimetric measurements carried out directly from the boat to reveal signs of hidden groundwater inflows into the surface water of the Krpeľany Reservoir (Švasta and Malík, 2006). Identification of places of hidden groundwater inflows remains the main goal of resistivimetric and thermometric measurements, however, their quantification, i.e. the determination of the hidden groundwater amounts must already be done by other methods – mostly by hydrometric measurements. On the other hand, interval (sectional) hydrometric measurements are usually performed by measuring stream cross-section in profiles distanced each from other in the order of hundreds of meters, if not more. For this reason, only combination of both methodologies is currently able to reliably determine both – the size and location of hidden groundwater inflows existing in the form of streamflow surpluses.

In the current paper, we present the results of measurements of temperature and specific electrical conductivity of surface water carried out along both banks of the surface stream of the Slaná River in its section between Brzotín and Gombasek, in the Slovenský kras Mts. (Fig. 1). In this section, Slaná River preserves relatively low total dissolved solids (TDS) content characteristic for phyllites, sandstones and metarhyolites of the low-grade metamorphic Gemeric sequences (Hanzel in Bajaník et al., 1983). TDS of natural waters here is usually in the range between 100 and 200 mg.l^{-1} while in karstic waters of Silická planina Plateau it is ranging from 400 to 700 mg.l^{-1} (Haviarová et al., 2010; Fľaková et al., 2018). In the past, a geophysical thermometric survey was carried out here (Džuppa and Husák, 1976), but measurements applied shallow probes of 0.5 to 1.0 m depth in a regular network of 4 × 4 m in the surroundings of major karstic springs of Gyepű/Brzotínska vyvieračka, Pisztráng/Pstruhová vyvieračka and Vyvieračka pod Veľkou skalou springs. In total, 503 measurements were carried out here in February 1976, focusing only on the immediate surroundings of the aforementioned three karstic springs, and leaving the surface flow of the Slaná River without measurements. The presence of such karst water outflows in this area encouraged also our measurements, aiming to verify the existence of possible hidden groundwater inflows to the Slaná River. The Slaná River in the Brzotín area enters a deep but also wide canyon, where both canyon slopes are formed by light-grey Wetterstein limestones of the Silica unit (Mello – ed., 1996, 1997). The obtained and interpreted results contributed to the better understanding of water communication between Slaná River as the main surface recipient in the area and the karstic groundwater accumulated in the extensive karstic plateaus of the Silická planina and Plešivská planina plateaus.

Data acquisition methodology

The suitability of resistivity measurements usage is based on the assumed differences in TDS of surface water

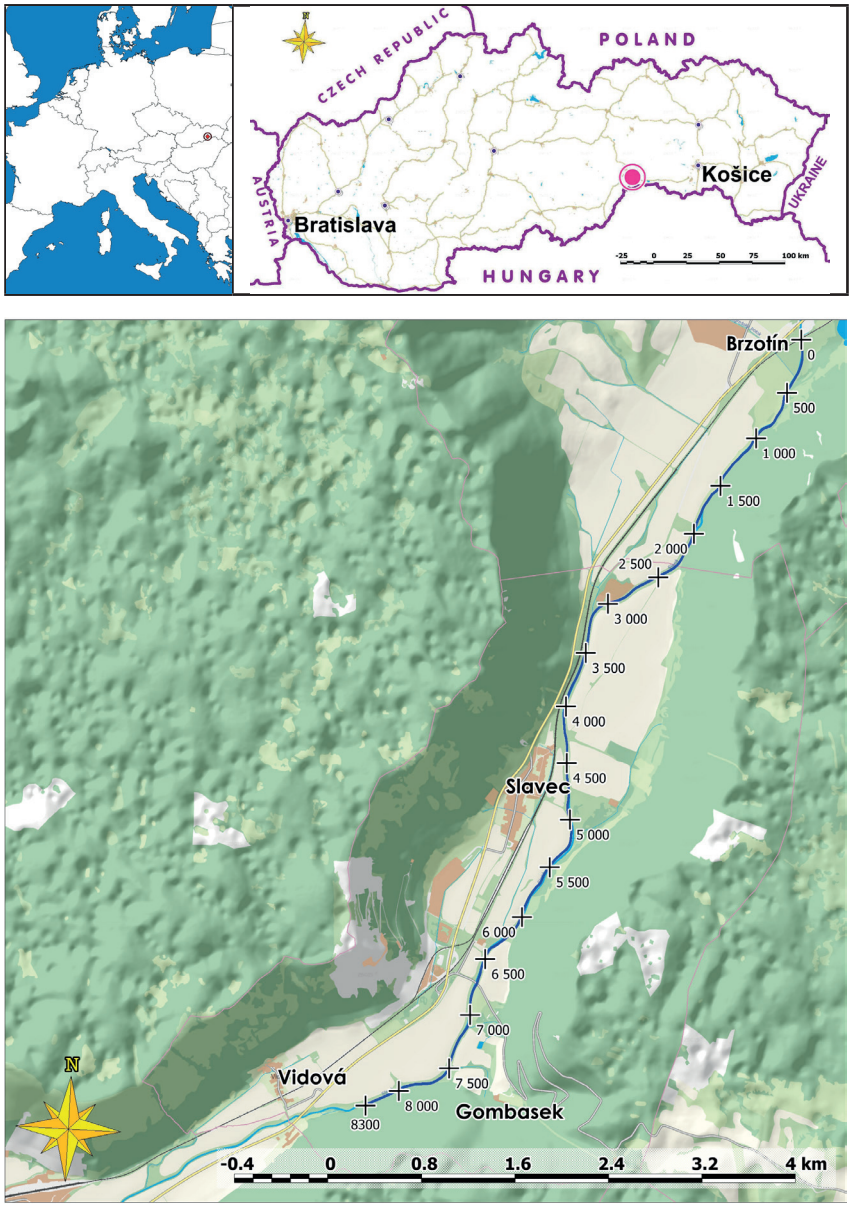

Fig. 1. Location of the investigated area on the territory of Slovak Republic and location of thermometric and resistivimetric measurements performed in the period between 21/06/2016 – 25/06/2016 on the Slaná River on the Brzotín – Gombasek section.

and groundwater and thus the places of hidden groundwater inflows are manifested by local change of specific electric conductivity (in our case, the entry of groundwater into the surface water should be signalised by its increase). The inflow rate (its discharge) is reflected in the course and range of temperature and conductivity anomalies, taking into account the total discharge of the investigated river watercourse. Correlation of both (temperature and EC anomalies) allows qualitative interpretation of hidden tributaries and enables exclusion of false anomalies caused by other phenomena like sewage or drainage channels. To obtain appropriate dataset for the Slaná River between Brzotín and Gombasek, side measurement of the stream electrolytic conductivity and water temperature were performed near the river bottom, about 5 cm above its level and in the distance of 20 to 40 cm from the bank on both sides of the river. EC and water temperature values were also taken from the streamline (flow nozzle) at the same footage, where measuring point was also some 5 cm above the river bottom (Fig. 2a, b). The measurement step was set to 1.0 m, and before taking, a footage path was drawn up using the measuring tape following the streamline (Fig. 2c). All the measurement records, present in the detailed documentation for both river banks, are then related to this uniform footage of river axis/streamline.

Measurements were performed by two WTW ProfiLine Cond 197i field conductivitymeters (Fig. 2b), allowing the water temperature measurement accuracy of 0.1 °C and the accuracy of EC measurements of 0.1 $\mu S.cm^{-1}$. In the second case, 1.0 $\mu S.cm^{-1}$ resolution of EC data records was applied. Thermometric and resistivimetric measurements on the Slaná River were carried out from 21/06/2016 to 25/06/2016. The measurements were performed by two closely cooperating measuring groups moving independently but in coordination along both banks of the river (Fig. 2d) following the footage measuring tape. Each measuring group consisted of a data recording person equipped with waterproof notebook, and a surveyor, equipped with a conductivitymeter. Conductivitymeter probe was placed on the measuring rod to keep the probe constantly submerged in the water and to avoid fluctuations in the probe measurements caused by its transfer through the air. It was verified by practical experience that each probe emergence above the water level caused time-consuming stabilization of measured parameters. There were two measuring groups, each for the left resp. right bank, and one "geometer" group equipped with measuring tape and GPS device following the river streamline and thus marking the footage of measurements. Garmin 60 CSx GPS instruments were used here to measure the position of the endpoints of the band, i.e. to mark the measured section by point of every 50 m (Fig. 2c). The measured section had a total length of 8300 m and consisted of the

Fig. 2a. Measurements of water temperature and specific electric conductivity performed along the Slaná River left bank on 23/06/2016.

Fig. 2b. Measurements of water temperature and specific electric conductivity performed along the Slaná River left bank on 25/06/2016.

Fig. 2c. Fixing of the measuring tape for positioning of thermometric and resistivimetric measurements of the Slaná River on 25/06/2016.

Fig. 2d. Thermometric and resistivimetric measurements of the Slaná River on 24/06/2016 – coordination of measuring groups on both right and left river bank.

same number of footage measurements (8300) along the left bank and right bank of the river. Taking into account the river width, EC and water temperature measurements for the streamline were separately measured by each measuring group. Therefore the group moving along the right bank marked its streamline measurements as center-right and a group moving along the left bank referred respective measurements as center-left.

Obtained data and discussion

The first measurement on the footage of 0 m in the area under the railway bridge over the Slaná River near Brzotín was carried out on 21/06/2016 at 10 : 10, the last measurement in the alluvium in the middle of fields under the Gombasek municipality, respectively in between Slavec-Vidová and Plešivec municipalities took place on 25/06/2016 at 15 : 10. During each day of measurements, systematic daily changes in water temperature were observed – a gradual increase by 2.3 to 4.3 °C (3.2 °C in average) depending on the weather conditions. Systematic daily increase in the specific electric conductivity values was not as significant, ranging from 1 to 8 $\mu S.cm^{-1}$ (4.2 $\mu S.cm^{-1}$ in average), but in the meantime a slight decrease in conductivity was observed, associated with a noticeable increase in discharge in the afternoons, which was possibly related to the water manipulation at the upstream hydro-power plant in Dobšiná. Data on water temperatures and EC at the beginning and at the end of the day are summarized in Table 1. An overview presentation of the thermometric and resistivimetric measurement results of the Slaná River in the section between Brzotín and Gombasek, along with the footage indication of individual measured sections is shown in Figs. 4 and 5. Course of water temperatures and EC values measured on both river banks as well as in the middle of the river (streamline), indicating some important anomalies, are depicted here.

A detailed description of the results of water temperature and EC measurements in the Slaná River streamline and its right and left banks by both measurement groups is presented in the following text from the beginning to the end of measurements, thus from the footage 0 to 8300 m. After the start of measurements on the "zero point" located under the railway bridge south of Brzotín, an anomaly of a hidden tributary from

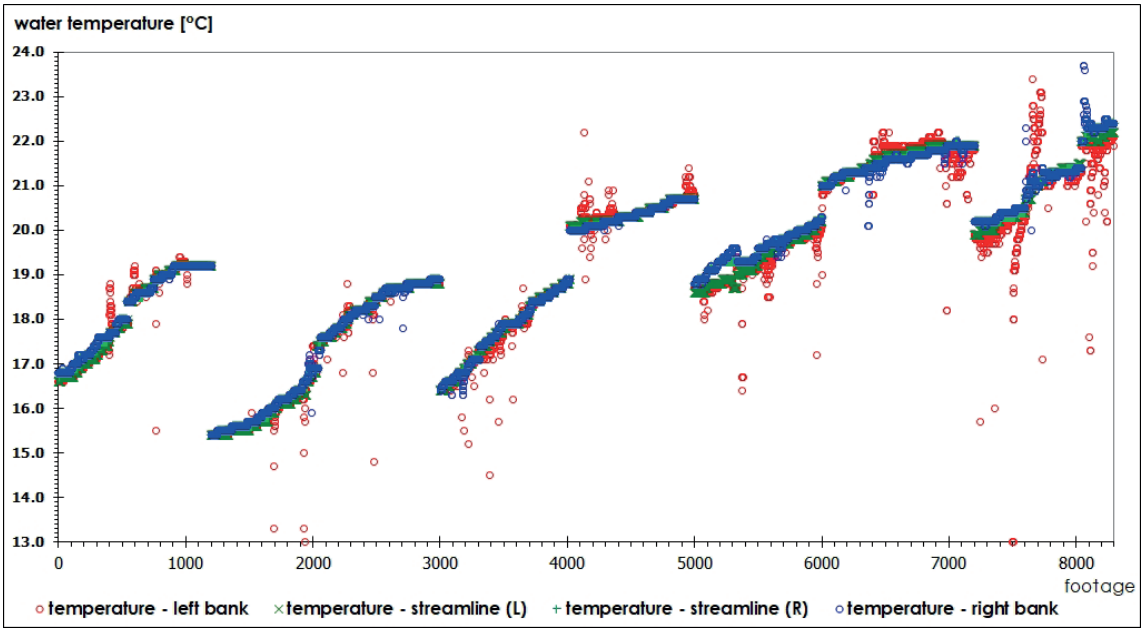

Fig. 3. Graphical representation of the water temperatures observed at both – right and left banks of the Slaná River and in the middle of the river ("left middle – L" or "right middle – P" according to the measuring working group) during thermometric and resistivimetric measurements in the section between Brzotín and Gombasek during 21/06/2016 – 25/06/2016.

the right side was observed on the 95 m footage. This anomaly is not shown in temperature response, but significantly affects the EC for a few meters on the right bank of the Slaná River. The recorded EC increase was from 299 to 335 µS.cm^{-1}. On the left bank, a decrease of temperature and an EC increase between the 388 and 395 m footage reflects a hidden groundwater inflow into the surface water flow of Slaná River (decrease of temperature by 0.2 resp. 0.3 °C, increase of EC by 20 resp. 29 µS.cm^{-1}). We assume that this is groundwater circulating in the alluvium of the Čremošná stream, which enters into the Slaná River on the footage of 405 m. Here, surface water of the Čremošná stream had a conductivity of 409 µS.cm^{-1} and a water temperature of 18.9 °C (Slaná River: 302 µS.cm^{-1} and 17.7 °C). Although Čremošná stream is considerably warmer (probably the effect of water storage in the Brzotín ponds), groundwater in its alluvium accompanying its surface stream maintains a lower (more stable) temperature, and shows a higher conductivity than Slaná River. A display of an interpretation graph of measurements on the footages 0 to 500 m is shown in Fig. 5.

Tab. 1

Data on the initial and final values of water temperatures and EC during the individual measurement days and the corresponding values of the measured footage in the Slaná River.

Date	Measured footage	Streamflow temperature at the beginning of daily measurements [°C]	Streamflow temperature at the end of daily measurements [°C]	Streamflow EC at the beginning of daily measurements [µS.cm^{-1}]	Streamflow EC at the end of daily measurements [µS.cm^{-1}]
21/06/2016	0–1200 m	16.6	19.2	299	300
22/06/2016	1200–3000 m	15.4	18.8	300	303
23/06/2016	3000–5000 m	16.4	20.7	314	320
24/06/2016	5000–7200 m	18.6	21.9	334	342
25/06/2016	7200–8300 m	19.9	22.2	326	331

On 614 m footage, there is a smaller hidden anomaly on the left bank, manifested by an isolated temperature drop of 0.2 °C and an increase in conductivity of 4 µS.cm^{-1}. The already visible spring on the left bank on 765 m footage causes a high increase in EC, from 305 to 388 µS.cm^{-1} and a drop in temperature from 18.9 to 15.5 °C, but its influence on these values on the left bank quickly resembles. In 29 meters downstream (footage of 794 m) there is a smaller left-bank anomaly of the hidden inflow (temperature decrease by 0.4 °C, increase of EC by 7 µS.cm^{-1}), also without significant influence on the surrounding water flow. Similarly, there is an anomaly on the right bank (footage 871 m) with a temperature drop of 0.1 °C and an increase in EC of 6 µS.cm^{-1}. The hidden groundwater surplus from the left bank is then manifested by a minor anomaly at 1006 m footage (temperature drop of 0.4 °C from 19.2 to 18.8 °C, EC increase of 7 µS.cm^{-1} from 303 to 310 µS.cm^{-1}). Another, almost 500 m long section of Slaná River is without any significant sudden changes in temperature or specific electric conductivity. A smaller visible spring, manifested also by an increase in water temperature of 0.3 °C and an EC of 8 µS.cm^{-1}, is found on footage 1515 m on the left. An overview of the measurement results on the 0 to 2000 m meter is shown in Fig. 6.

As very pronounced there can be then considered the manifestation of a visible spring on the Slaná River left bank of on the footage of 1687 m (values measured directly in the spring were 10.3 °C and 555 µS.cm^{-1}, which is in 5.9 °C less and in 260 µS.cm^{-1} more than the respective values in the

stream). This spring, named Hradná vyvieračka/Várforrás (Castle Spring), leaves a significant mixing track along the left bank on a stretch of more than 25 m. Smaller visible springs on the left side of the river on footages 1826 and 1871 m are manifested by an increase of EC values by 12 resp. 14 µS.cm^{-1} and by increasing the water temperature by 0.1 °C without significantly affecting the properties of the river water. These are probably parts of larger drainage area of already

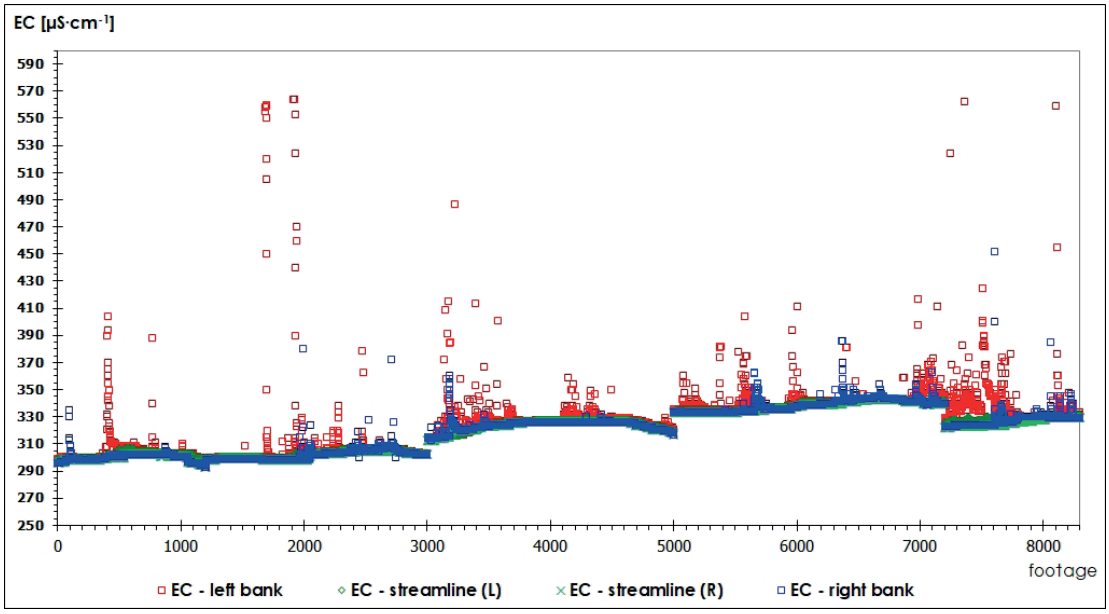

Fig. 4. Graphical representation of the specific electric conductivity observed at both – right and left banks of the Slaná River and in the middle of the river ("left middle – L" or "right middle – P" according to the measuring working group) during thermometric and resistivimetric measurements in the section between Brzotín and Gombasek during 21/06/2016 – 25/06/2016.

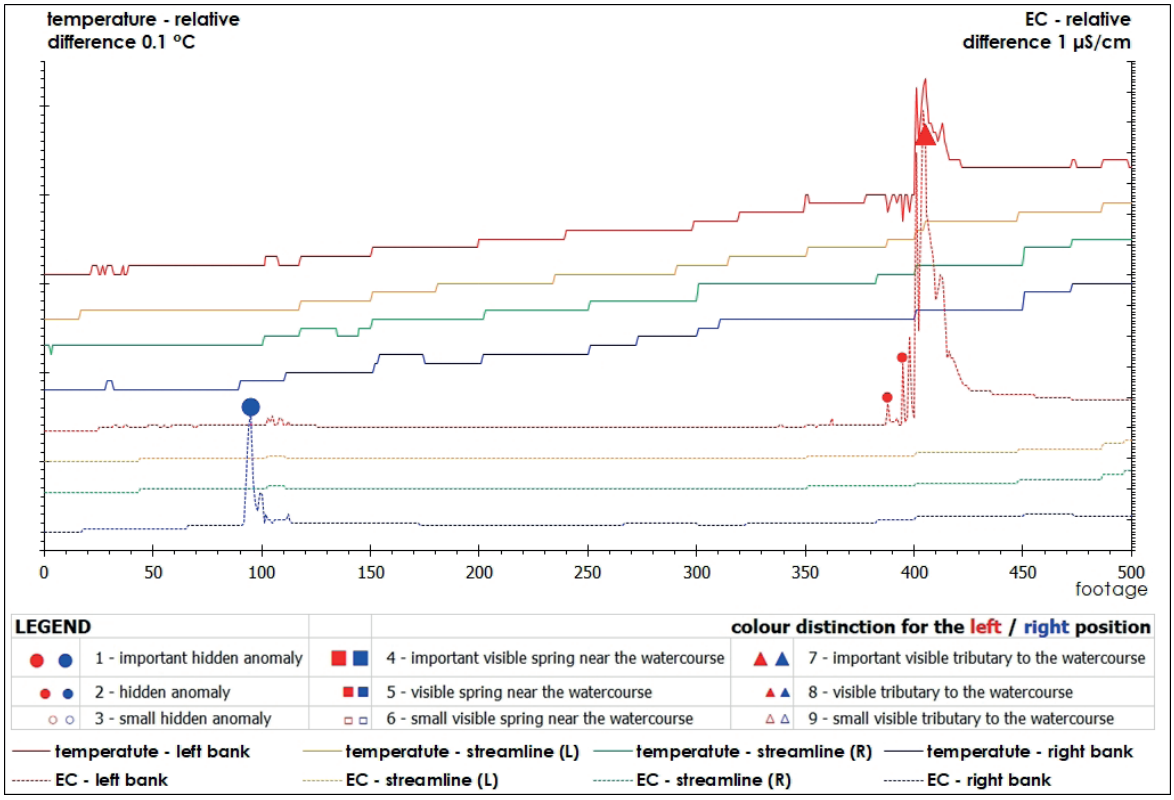

Fig. 5. Relative changes in the course of the water temperature of the Slaná River [°C] and its specific electric conductivity [µS.cm^{-1}] at both right and left banks, and in the middle of the river ("left middle – L" or "right middle – P" according to the measuring working group) in the footage 0–500 meters based on measurements from 21/06/2016.

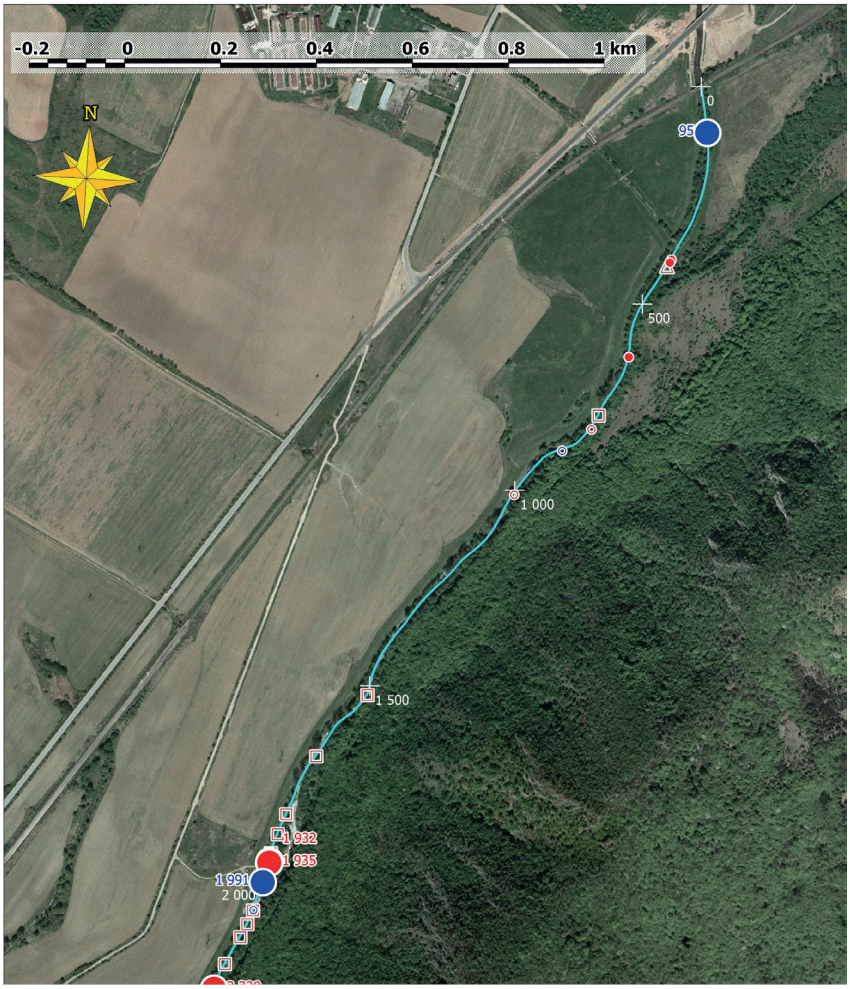

Fig. 6. Location of anomalies detected by thermometric and resistivimetric measurements on the Slaná River in the Brzotín – Gombasek section, 0 to 2000 m footage. For explanation of symbols see Fig. 5.

mentioned Hradná vyvieračka/Várforrás spring system, which itself also appears on the ground surface in the form of three seemingly independent spring outlets. In the past in this area, pretty productive hydrogeological exploration boreholes were drilled, of which the 507.6 m deep RC-12C borehole (Orvan, 1992) is currently exploited for a drinking water supply. In addition, there are also other unexploited boreholes in the same area – HR-1 (419 m deep) on the right and R-29 (25 m deep) on the left side of the Slaná River. Significant manifestation of the main Hradná vyvieračka/Várforrás spring, discharging approximately 5 $l.s^{-1}$ at the time of measurements, was visible on the left bank on the 1915 m footage by reducing the water temperature by 6.5 to 9.9 °C and increasing the specific electric conductivity in 264 to 564 $\mu S.cm^{-1}$. Significant persistence of this signal along the left bank and a decrease in water temperature of 0.1 °C even in the river streamline was registered here. Behind this place, two significant anomalies were found on the left bank in 1932 and 1935 m footages (drop in water temperature by 6.4 and 3.8 °C respectively; increase in EC by 253 and 166 $\mu S.cm^{-1}$, respectively). On this site, a steel waterworks pipeline is crossing the river bed, and it is not possible to exclude the influence of possible water leaks from this pipeline on the water properties in the river. Slightly lower, on the 1963 m footage, two smaller right-side anomalies were detected, probably originating in a hidden surface inflow (increase in water temperature by 0.3 and 0.5 °C, increasing of EC values by 17 and 8 $\mu S.cm^{-1}$ respectively). Similarly, anomalies of elevated water temperature (rise of 0.4 °C in water temperature and of 26 $\mu S.cm^{-1}$ in EC values) were also detected on the left bank on the footage from 1980 to 1982 m, originating in visible water leakage from the left bank. On the right bank, a significant anomaly appeared on the 1991 m footage with a drop in water temperature of 0.9 °C and a rise in conductivity of 82 $\mu S.cm^{-1}$ (here, a visible water inflow of 13.9 °C and 512 $\mu S.cm^{-1}$ was recorded). Slightly warmer water (by 0.3 °C) with slightly increased conductivity (by 7 $\mu S.cm^{-1}$) was spotted on the opposite bank (footage 1998 m). At the same place, dry tributary outlet was found with already abandoned gauging by Thomson weir. At the time of measurements, it was without any runoff and stagnant water was found in the small pools along the river bank. So far (i.e. from the footage 1687 m to the footage of 1998 m), we can observe both visible and hidden large drainage area around the group of springs Hradná vyvieračka/Várforrás, where karstic groundwater of the Silická planina Plateau is feeding the surface flow of the Slaná River.

An overview of the measurement results on the footage interval 2000–4000 m is shown in Fig. 7. On the 2052 m footage, a hidden anomaly was identified on the right bank (water temperature in 0.2 °C lower and EC in 22 $\mu S.cm^{-1}$ higher than surface water in the river), whereas on the opposite left bank a small groundwater inflow was also recognized, responsible for a 0.2 °C drop in the water temperature. This was followed by a number of minor anomalies along the left bank of the river. A small groundwater outflow on the 2083 m footage causing a local 10 $\mu S.cm^{-1}$ EC increase on the left river bank was registered, and on the 2113 m footage a similar visible flow caused not only an increase in EC of 6 $\mu S.cm^{-1}$, but also a drop in water tem-perature of 0.5 °C. On the 2181 m footage, a visible groundwater outlet on the left bank caused an increase of EC in 10 $\mu S.cm^{-1}$ and a drop in the water temperature of 0.1 °C. The hidden anomaly was identified in the deep pool of the river water course at 2239 m footage, this caused a more intense change in the properties of the Slaná River water on the left bank – decrease in water temperature by 1.1 °C and an increase in specific electrical conductivity by 15 $\mu S.cm^{-1}$. This clearly recognizable feature was accompanied by smaller anomalies in 5 to 7 meters upstream. Down-stream, in the distance of 35 to 40 m, another two anomalies signalizing hidden inflows to Slaná River from its left bank were found: on footage 2275 m with water temperature drop by 0.2 °C and EC increase by 33 $\mu S.cm^{-1}$; on footage 2281 m with water temperature drop by 0.2 °C and increase of EC by 23 $\mu S.cm^{-1}$.

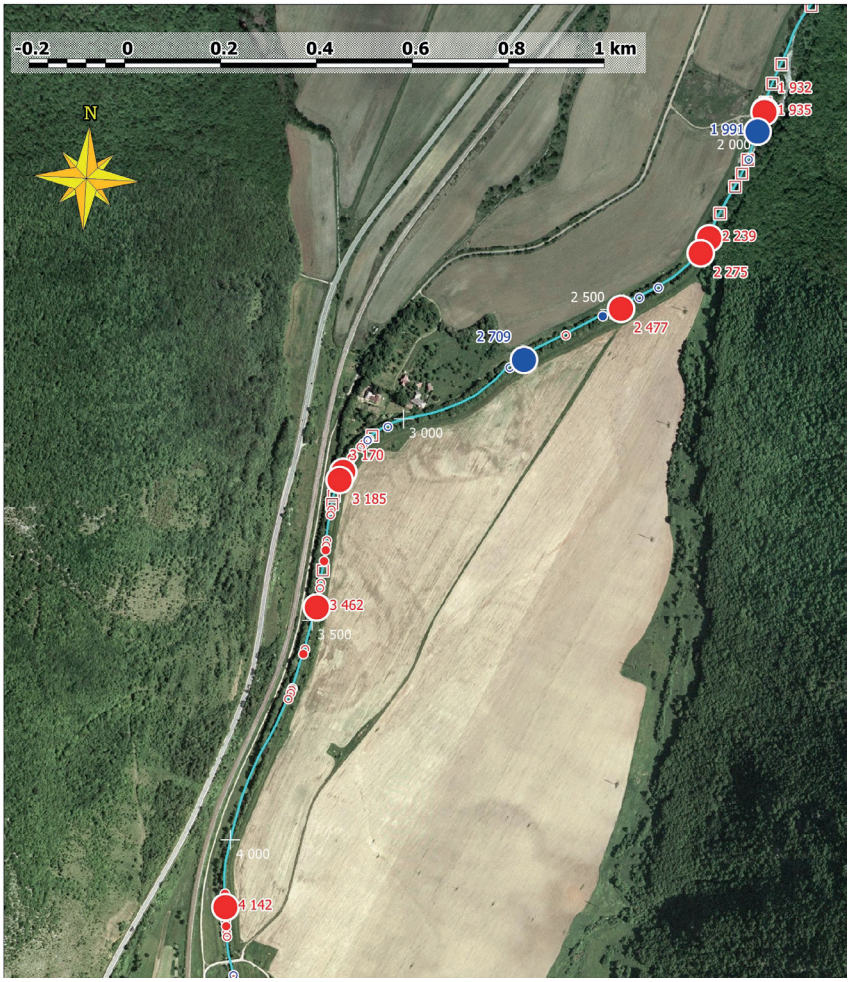

Fig. 7. Location of anomalies detected by thermometric and resistivimetric measurements on the Slaná River in the Brzotín – Gombasek section, footage of 2000–4000 m. For explanation of symbols see Fig. 5.

Approximately at the 2300 m footage, the Slaná River watercourse changes its position from the foot of the Silická planina Plateau towards the foot of the Plešivská planina Plateau (the transition watercourse segment is up to the footage of approximately 3100 m). At these places then the Slaná River crosses its own alluvium from northeast to southwest. If we suppose the groundwater flow in the Quaternary alluvial sediments to be parallel with the general course of river alluvia, one should expect anomalies pointing to groundwater inflows mostly (if not only) on the right bank of the Slaná River in this section. This assumption has been fulfilled by two small hidden anomalies on the 2388 m footage (local water temperature drop of 0.1 °C and EC increase of 4 μS.cm^{-1}) and on the 2436 m footage (here the water temperature on the right bank was by 0.3 °C less and EC by 14 μS.cm^{-1} more than the water in the main stream). Very surprising was then the discovery of a 1.6 °C drop in the water temperature on the left bank and an increase of EC by 72 μS.cm^{-1} (footage 2471 m), and of a water temperature drop of up to 3.6 °C and an EC increase in 50 μS.cm^{-1} (footage 2478 m, also on the left bank). The temperature and the specific electrical conductivity on the left bank of the river in these places of the left bank were significantly affected on a larger section. The origin of this anomalies can only be explained by the entry of groundwater directed from the foot of the Silická planina Plateau towards the west – but such an assumption can only be verified by otherwise conceived field work. Right-side anomalies of different levels were then registered along the footage 2520 m (local temperature drop by 0.5 °C and EC increase of 23 μS.cm^{-1} on the most significant anomaly). Signs of groundwater inflow from the left-bank were again discovered at a footage of 2607 m – by a presence of minor anomaly indicated by temperature drop of 0.2 °C an EC increase of 6 μS.cm^{-1}. Further downstream there are four anomalies on the right bank – on the footages 2709 m, 2714 m, 2727 m and 2742 m. On the first, the highest one (footage 2709 m), water temperature compared to the main river flow was in 0.9 °C less and the EC there was in 67 μS.cm^{-1} higher. On the next anomalies below, the water temperature was found identically to be only in 0.1 °C lower, and the difference in the specific electrical conductivity was found to be in 6 or 21 μS.cm^{-1}. Only after the change of the direction of the Slaná River watercourse to the south, along the edge of the Plešivská planina Plateau (footage of 3176 m with visible inflow of the tributary from the Gyepü/Brzotínska vyvieračka karstic spring), two smaller right-side anomalies (3035 m and 3088 m footages) were identified. The lower anomaly influenced also the surface flow temperature by 0.3 °C (the EC values has been increased, compared to the main flow, in both anomalies – by 8 and 9 μS.cm^{-1} respectively). Significant visible inflow of water from the Gyepü/Brzotínska vyvieračka karstic springs, where the water temperature 13.6 °C and EC 516 μS.cm^{-1} were directly measured at the footage of 3176 m, was influencing the water temperature along the right side of the Slaná River watercourse at a section of about 40 m and EC values even at a section of about 60 m long. The right bank was then found to be without any major changes in measured values up to footage of 3460 m.

Much more varied data have been registered along the left bank of the Slaná River since its approach to the foot of the Plešivská planina Plateau, approximately from the footage of 3070 m. A small visible spring was found on the left bank (footage 3073 m), which influenced only difference in EC by 3 μS.cm^{-1}. Downstream, three smaller anomalies without visible inflow were identified at footages of 3084 m, 3099 m and 3110 m. In all three cases, the temperature difference (drop) was only up to 0.2 °C and EC rise up to 11 μS.cm^{-1}. Further on, on footages 3137 and 3142 m, the EC was raised in 55 and 99 μS.cm^{-1} (at equally small temperature differences), and several significant EC fluctuations were also recorded on footages 3150 m, 3164 m and 3170 m. At the latter point (footage 3170 m), a water temperature drop of 1.0 °C (EC

increase in 97 μS.cm^{-1}) was also registered. This place on footage 3170 m therefore represents a more significant left-side anomaly, together with an analogous point on the footage of 3185 m (water temperature decrease by 1.3 °C and EC increase by 67 μS.cm^{-1}), also found along the left bank. A visible groundwater outlet on the left bank (15.2 °C; 487 μS.cm^{-1}) was then found on the 3225 m footage, a smaller one also on the 3246 m footage (16.7 °C; 338 μS.cm^{-1}). The left-side anomalies at footage points of 3195 m, 3258 m, 3270 m, 3327 m, 3339 m, 3349 m and 3371 m are likely to belong to the same groundwater flow that is invisibly drained by the surface flow of the Slaná River. Later, this is also evidently reflected in the 3390 m footage visible spring (14.5 °C, 414 μS.cm^{-1}) and by minor hidden anomalies at 3416 m and 3427 m footages (temperature drops of 0.4 and 0.2 °C, respectively, and an EC increase in 27 and 20 μS.cm^{-1}, respectively). Also a significant anomaly was detected on the 3462 m footage (water temperature drop by 1.9 °C and EC was found higher by 44 μS.cm^{-1}). The whole left-bank groundwater transfer front probably ends with small anomalies on footages 3476 m and 3479 m (local temperature drops of 0.3 °C and increase of EC by 10 μS.cm^{-1} and 26 μS.cm^{-1} respectively). There is also a small right-bank anomaly in this area (3460 m footage, water temperature increase in 0.2 °C and conductivity increase 9 μS.cm^{-1}).

Despite the fact that the watercourse of the Slaná River is in direct contact with the important compact karst area of Plešivská planina Plateu foothills in these places, no sign of visible or hidden groundwater inflow into the river was noticed on its right bank. Only the left river bank was active, where there was a minor hidden anomaly on the 3560 m footage (0.5 °C water temperature drop, EC increase of 29 μS.cm^{-1}), followed by a larger 3571 m footage anomaly (temperature drop of 1.7 °C with EC increase of 75 μS.cm^{-1}). A series of minor detected anomalies between footages of 3647 and 3673 m (3647 m, 3651 m, 3658 m and 3673 m) was associated with an increase of water temperature on the left bank (0.2 and 0.5 °C, later a 0.2 respectively 0.1 °C decrease) associated with a slight increase in EC from 5 to 13 μS.cm^{-1}, which, however, was still recognizable along the left bank up to the footage of 3700 m. From this section, water of the Slaná River showed a uniform temperature increase within the usual daily variation without records of significant temperature and conductivity anomalies up to approximately 4100 m footage. The difference (increase) of water temperature by 1.1 °C on footage 4021 m was recorded during approximately hour-long lunch break, and the specific electric conductivity values remained unchanged. Fig. 8 shows the overall situation of measurement results on the footage from 4000 to 6000 m.

In the immediate area of the Slavec municipality, the first major anomaly was found on the 4118 m footage, where the 0.9 °C drop of water temperature and the local EC value increase by 8 μS.cm^{-1} was detected on the left river bank. The following section of the river, more than 100 m wide up to 4230 m footage, is characterized by an intensive variation in water temperature (decreases, but also significant increases) on the left bank of the Slaná River. However, elevated temperatures were recorded in the shallow water by the river bank, possibly heated by the sun, while the decreases were as high as 1.6 °C (4142 m footage). This significant temperature anomaly was also accompanied by an increase in conductivity of 29 μS.cm^{-1}, which is also the largest measured difference in this section. Other left-bank anomalies were located on footages of 4131 m, 4171 m (change in EC with rising temperature), 4177 m (drop in water temperature by 0.6 °C, increase in EC by 18 μS.cm^{-1}), and 4187 m (drop in water temperature by 0.5 °C, EC increase of 22 μS.cm^{-1}); partly also on footages of 4201 m and 4210 m (lowering of temperature in 0.4 °C and increasing EC by 16 μS.cm^{-1}). It should be stated that the values in the streamflow remained unchanged, however, a slight decrease of 0.1 °C was registered in the section between footages 4251 m and 4217 m. The values along the right bank of the Slaná River remained unchanged for the whole described section (water temperature 20.0 to 20.1 °C; EC value 326 μS.cm^{-1}). The river section up to the 4290 m footage was then found without any changes of both parameters along the both river banks.

After an approximately 80 m long section without manifestations of anomalies in EC and water temperature, another section with signs of hidden groundwater inflows begins in footages approx. 4290 to 4400 m, starting in the area of the cart-road bridge across the Slaná River (the cart-road leads to the captured spring Pisztráng/Pstruhová vyvieračka). This section starts with a slight increase in conductivity at the right bank (from 326 to 330 μS.cm^{-1}) and a decrease in water temperature (from 20.2 to 20.0 °C) on the 4292 m footage. Then, a series of slightly more pronounced anomalies, but only at the left bank, follows. On the 4300 m footage the temperature drop by 0.5 °C and the EC increase by 7 μS.cm^{-1} were recorded, on the 4314 m by 0.3 °C and 9 μS.cm^{-1}, on footages of 4325 and 4358 m EC was increased by 18 resp. 17 μS.cm^{-1}, but also the temperature was increased by 0.6 resp. 0.5 °C, what points to shallow water circulation in these places. The whole series of aforementioned anomalies is then terminated again on the right bank and again only by slightly increasing conductivity on the right bank (by 3 μS.cm^{-1}, from 326 to 329 μS.cm^{-1}) and by lowering the water temperature (by 0.2 °C, from 20.3 to 20.1 °C) on 4404 m footage. The left-bank change in EC value of 21 μS.cm^{-1} on 4489 m footage did not have a temperature changing effect and was caused by a visible inflow of low yield (from behind a stone).

By following river course section, about 800 m long, the Slaná River gradually returns from the foothills of the Plešivská planina Plateau back to the foothills of the Silická planina Plateau, again crossing the entire width of its alluvium. However, up to 5000 m footage, this section is significantly hydraulically passive – for more than 500 m, no sudden drop in the water temperature of the surface stream has been recorded, either in the middle of the stream or at its edge. On the footage around 4930 m, there was a slight increase in the EC values at the left bank by 6 resp. 4 μS.cm^{-1} (from 323 to 329 and from 322 to 326 μS.cm^{-1} respectively), but these were accompanied by an increase in the water temperature (by 0.5 and 0.6 °C respectively). These increased temperature anomalies had some persistence along the river bank but did not occur in the middle of the stream. Measurement on 23/06/2016 was completed on footage of 5000 m at air temperature of 27 °C and water temperature in the river of 20.7 °C.

The next day of measurement (24/06/2016) began with 18.7 °C at the main flow (2.0 °C lower than at the end of the previous day measurement), but specific electric conductivity changed even more significantly – it was 334 μS.cm^{-1} compared to 320 μS.cm^{-1} measured at the end of the previous day. Stable values of water parameters, similarly as in the previous section, continued up to the 5070 m footage. Then there were five left-bank anomalies on the 110 m long section, two of which more significant. These can be found on footages 5074 and

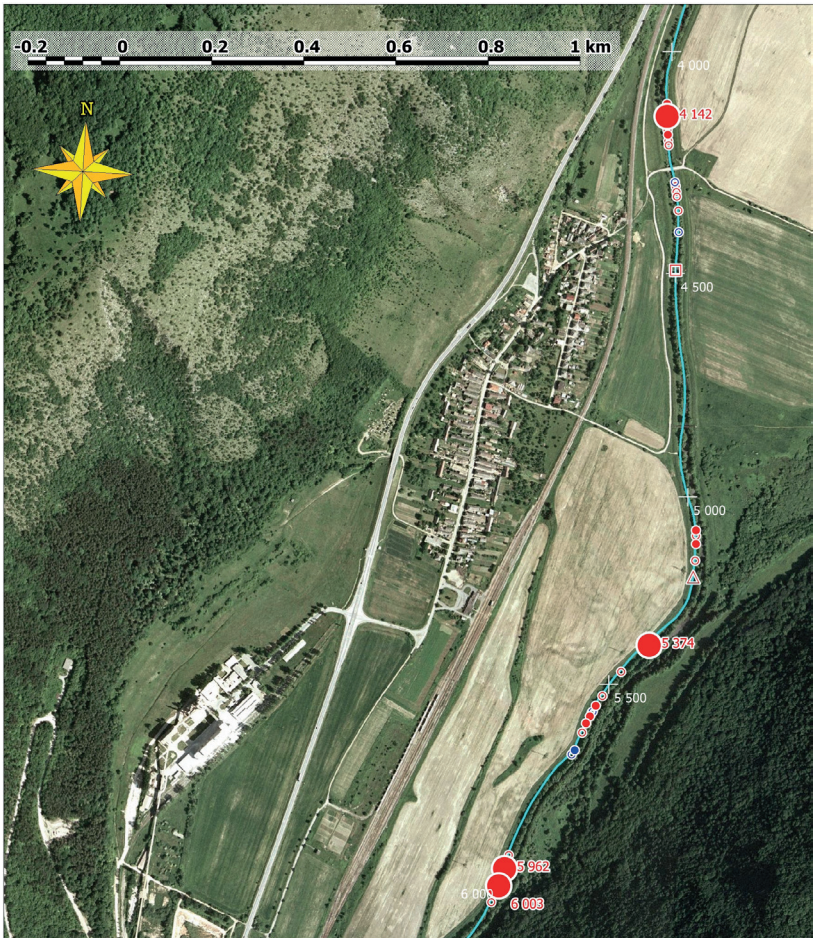

Fig. 8. Location of anomalies detected by thermometric and resistivimetric measurements on the river Slaná in the Brzotín – Gombasek section, 4000 to 6000 m footages. For explanation of symbols see Fig. 5.

5104 m, where the water temperature drops by 0.6 and 0.5 °C respectively and EC increases in 25 and 19 µS.cm^{-1} respectively. On footages 5086 and 5137 m, without water temperature change, only the specific electric conductivity is increased by 10, resp. 7 µS.cm^{-1}. On the footage 5174 m, the EC increase of 15 µS.cm^{-1} was registered as a manifestation of the visible water inflow into the stream, tributary from the 0.5 km distanced Pisztráng/Pstruhová vyvieračka karstic spring. It is interesting that the water temperature on the left bank reacts only in a drop by 0.1 °C. The left-side anomaly found on the footage 5374 m is more pronounced, where the water temperature has dropped by 2.6 from 19.0 to 16.4 °C and the conductivity has risen from 336 to 381 µS.cm^{-1} (by 45 µS.cm^{-1}). After this significant fluctuation of water properties of the Slaná River, the measured values up to 5520 m footage showed then only a stable course of values, with the exception of a small anomaly (again left-side) on footage 5452 m (water temperature drop by 0.1 °C, EC increase by 7 µS.cm^{-1}).

Between the 5525 and 5646 m footages, there is a frequent manifestation of temperature and specific electric conductivity anomalies on the appro-ximately 120 m long section on the Slaná River left bank. This situation is also illustrated in the interpretative graph of measurements on footages 5500–6000 m in Fig. 9. Its effect can be observed on this relatively long section for both variables along the shore, but the main streamflow remains unaffected. Anomalies in footages 5526 m, 5565 m and 5609 m are manifested only by a significant increase in EC – by 42, 30 and 10 µS.cm^{-1} – without sufficient parallel decrease in water temperature (or only by 0.1, 0.3 and 0.2 °C). Therefore, anomalies detected here are classified as minor hidden anomalies, compared to the more pronounced anomalies in footages 5550 m, 5573 m and 5588 m. The anomaly on footage 5550 m is characterized by a drop in the water temperature by 0.5 °C (from 19.4 to 18.9 °C) and increase of EC value by 25 µS.cm^{-1} (from 336 to 361 µS.cm^{-1}). On the footage 5573 m, the water temperature dropped by 0.5 °C and the EC increased by 64 µS.cm^{-1}, on the footage 5588 m by 0.7 °C and 29 µS.cm^{-1}. Interestingly, as soon as the above-described occurrence of anomalies on the left bank diminishes approximately on footage 5646 m, similar changes in water properties appear on the right river bank on approximately 55 to 60 m long section roughly between footage of 5651 and 5706 m. Influence of the lowered water temperature and increased EC can be observed here in the whole aforementioned section, but the most significant is the anomaly on 5655 m footage, where the temperature difference was found in 0.4 °C (decrease from 19.8 to 19.4 °C) and conductivity difference of 29 µS.cm^{-1} (increase from 334 to 363 µS.cm^{-1}). A less contrasting, but long-lasting anomaly was found on footage 5672 m (temperature drop by 0.1 °C and increase in EC by 17 µS.cm^{-1}). There were no phenomena documented by the hydrogeological mapping (Malík et al., 2013) to which the hidden inflows could be related.

After weakening of right-side anomalies approximately from the 5707 m footage, the stable water temperature of 20.0 °C and its EC value of 337 µS.cm^{-1} are maintained in the stream and along the banks of the Slaná River for approx. 230 m long section up to footage 5934 m. This state is eventually interrupted by fluctuations of values in small anomaly on 5934 m footage on the left bank (water temperature drop by 0.2 °C and increase in EC by 6 µS.cm^{-1}). Behind it, about 20 m long stone paved bottom stretches along the right bank of the river, and downstream a small left-bank anomaly on footage of 5954 m (water temperature drop of 0.5 °C and EC increase by 5 µS.cm^{-1}) signalizes the onset of very significant change of water properties at the left bank on the 5962 m footage. At this significant anomaly, a drop in water temperature of 2.4 °C and a rise in EC of 56 µS.cm^{-1} were measured, followed by a smaller anomaly on footage 5968 m (0.4 °C/20 µS.cm^{-1}). Manifestations of lowered temperature and increased EC are then following the left bank on approximately 80 to 90 m long section and can be considered to completely diminish on the 6050 m footage. Surface water properties of the Slaná River remained unchanged in EC but its temperature has increased from 20.2 to 21.0 °C (by 0.8 °C) during one-hour lasting lunch break (13 : 40 – 14 : 40). On the left bank, on 6003 m footage, another significant anomaly was then detected

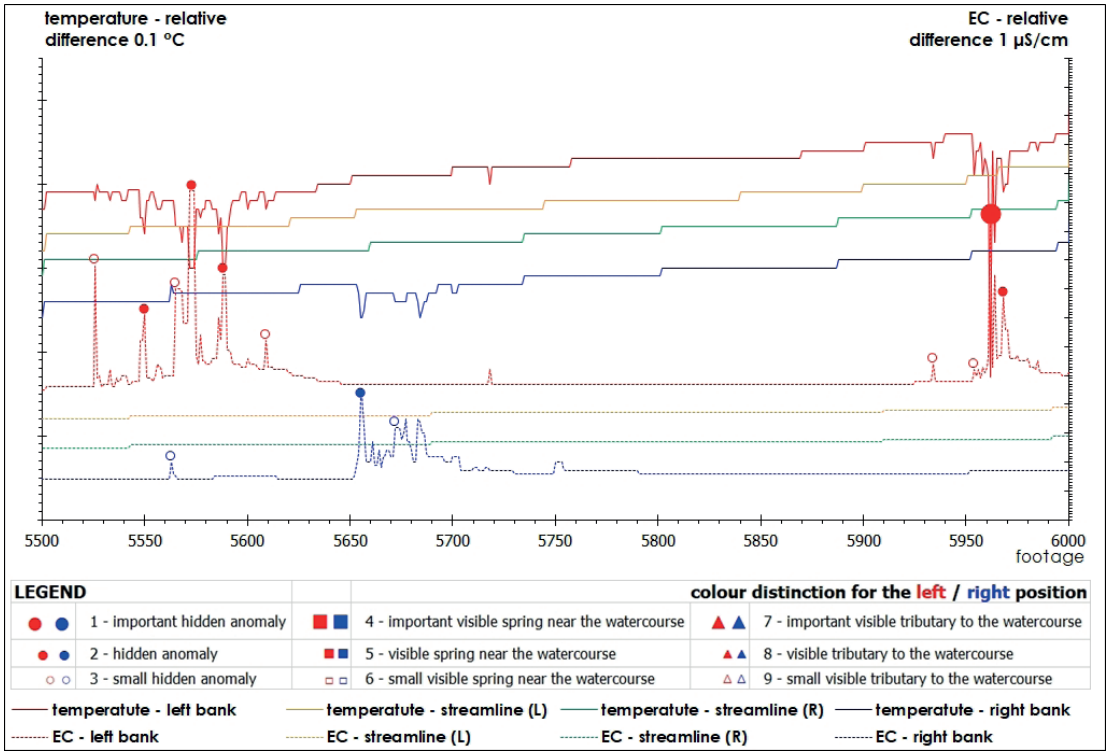

Fig. 9. Relative changes in the course of the water temperature of the Slaná River [°C] and its specific electric conductivity [µS.cm^{-1}] at both right and left banks, and in the middle of the river ("left middle – L" or "right middle – P" according to the measuring working group) in the footage 5500–6000 meters based on measurements from 24/06/2016.

by water temperature decreased in 1.8 °C and EC increase by 57 µS.cm^{-1}. This was followed by another minor anomaly 5 meters downstream (footage 6008 m; water temperature drop by 0.5 °C, conductivity increase by 20 µS.cm^{-1}). The whole section of left-side anomalies (in the 5950–6050 m footages) was then finally terminated by a small left-side anomaly at 6047 m (water temperature drop of 0.1 °C, EC increase of 6 µS.cm^{-1}). This part of the Slaná River watercourse can be considered as affected by the most significant manifestations of hidden groundwater inflows to the surface flow in the area south of the Slavec municipality, and here too, previous hydrogeological investigations on the ground surface did not document any phenomena pointing to groundwater – surface water interaction in these places.

An overview of the measurement results of the Slaná River on the footages from 6000 to 8300 m is shown in Fig. 10. After the smooth section of the stable water temperature and its specific electrical conductivity both in the streamflow and on the river banks, which follows from 6050 m footage and reaches approximately to 6360 m footage and is interrupted by only one small right-side anomaly on 6188 m footage (isolated drop of water temperature by 0.4 °C and increase of EC by 8 µS.cm^{-1}), the first significant right-side anomaly was detected on the 6367 m footage. It is situated approximately at the previously existing, in the meantime dry outflow intermittent stream from Slavec municipality between the Slaná River and the railroad, bringing water from the occasional karst spring Pri cintoríne ("Near the cemetery"), active only during higher water levels. The tributary riverbed is on the bank of the Slaná River terminated by a concrete building with a shut-off valve. At the time of measurement, this bed was dry, but a visible flow of surface water was observed on the bank of Slaná River. This was manifested by the above-mentioned anomaly on the 6367 m footage by decreasing the water temperature by 1.3 °C and increasing the EC by 46 µS.cm^{-1}. It is likely that there is still a hidden drainage of groundwater in the area from the right side, from the Plešivská planina Plateau (Pri cintoríne spring), although in small quantities. Low flow conditions at that time of measurements let this anomaly to resolve relatively quickly, after about 20 m. Continuation of thermometric and resistivimetric measurements revealed a visible water flow on the left bank on the 6402 m footage, in a small pool close to the streamflow. This visible inflow resulted in a decrease in the water temperature of 0.7 °C and an increase in its specific electrical conductivity by 39 µS.cm^{-1}. Several minor anomalies were found on the right bank, successively on footages of 6432 m, 6440 m, 6462 m and 6480 m where changes in 0.3 °C/11 µS.cm^{-1}; 0.1 °C/2 µS.cm^{-1}; 0.3 °C/9 µS.cm^{-1} resp. 0.1 °C/7 µS.cm^{-1} were detected, all for water temperature drop and EC increase. Shallow water exposed to the sun on the left bank contributed to the increase of the water temperature between footages of 6406 to 6494 m, while the EC value on the left bank in this section as well as the water temperature in the streamflow remained unchanged.

The following nearly 500 meters of the watercourse remain without significant anomalies. At the 6533 m footage, there was a small visible spring on the left bank, which was manifested by an increase in water temperature of 0.3 °C and an increase in EC of 5 µS.cm^{-1}, which was then accompanied by two smaller hidden anomalies on 6521 and 6536 m footages (EC increase by 2 and 5 µS.cm^{-1} respectively, water temperature decreased by 0.1 °C in both cases). On the 6673 m footage, a right-side anomaly was detected, indicated by a decrease in water temperature by 0.1 °C and an increase in its specific

electrical conductivity by 9 µS.cm^{-1}. In the area of anomaly there is also a water management object on the right bank, a flood damper signalizing surface water communication, and perhaps also hidden groundwater communication, which may also lead to appearance of a hidden anomaly on the 6673 m footage. Between 6415 and 6720 m footages, there is a road bridge for the road leading to the Gombasecká jaskyňa Cave and the village of Silica. Another anomaly (left-bank) was detected on footage 6865 m and is characterized by a 0.3 °C drop in water temperature (from 22.1 to 21.8 °C) and an increase in EC value of 18 µS.cm^{-1} (from 341 to 359 µS.cm^{-1}).

The section between footage 6935 and 7166 m is accompanied by a series of minor anomalies on the left bank, part of which (footages 6935 m, 6948 m and 6983 m) is a manifestation of visible groundwater outflows on the left bank of the Slaná River (temperature decrease by 0.6, 0.1 and 3.5 °C and an increase in the EC of 7 µS.cm^{-1}, 3 µS.cm^{-1} and 67 µS.cm^{-1}). Anomalies representing possible hidden groundwater inflows to the surface stream were indicated on footages of 6962 m, 6,973 m and 6978 m. Here, a temperature decrease of 0.3 °C, 0.5 °C and 0.6 °C and an increase in the specific electrical conductivity of 8 µS.cm^{-1}, 19 µS.cm^{-1} and 21 µS.cm^{-1} were recorded. Nearby, a karstic spring of Biela vyvieračka ("White Spring")/ Margitin prameň ("Margita's spring") is lo-cated, and it is possible that the water in anomalies is coming from this source, moving in the underground in the alluvium of an old, no longer existing trough. The currently existing inflow from the Biela vyvieračka/Margitin prameň spring was recorded on footage of 7143 m. Its estimated discharge rate at the mouth was approximately 4 l.s^{-1}; the measured EC value directly in the inflow was 572 µS.cm^{-1} and the inlet water temperature was 15.2 °C. Directly at the mouth of the tributary, it was possible to observe the formation of recent travertines and travertine mass connecting gravel pebbles in the river alluvium. However, between this visible tributary and 7000 m footage there were even more anomalies indicating hidden groundwater inflows to the surface stream from its left side: on 7008 m footage there was a minor anomaly (water temperature drop of 0.4 °C and EC increase of 14 µS.cm^{-1}), bigger anomaly was on footage of 7023 m (water temperature drop by 0.6 °C and EC increase by 16 µS.cm^{-1}), and finally a smaller anomaly on the footage 7040 m (water temperature drop by 0.2 °C and EC increase by 13 µS.cm^{-1}). Still on the left bank, these were followed by three major anomalies on footages of 7064 m, 7087 m and 7107 m. On these temperature decreases of 0.5 °C, 0.6 °C and 0.4 °C were recorded with an increase in EC of 18 µS.cm^{-1}, 19 µS.cm^{-1} and 24 µS.cm^{-1}. In the case of the last of these anomalies, there was a visible groundwater inflow from the gravel paved by travertine to the Slaná River. At the same time, anomalies were also indicated on the right bank of the river – on footages 7094 and 7109 m. The first was manifested by a decrease in water temperature by 0.1 °C and an increase in EC by 23 µS.cm^{-1}; in the second case the water temperature drop was more pronounced (by 0.4 °C) and EC increase was less (by 12 µS.cm^{-1}). In the case of a minor anomaly found on the left bank on the 7166 m footage of the Slaná River (already below the mouth of the Biela vyvieračka/Margitin prameň spring), a drop in water temperature of 0.3 °C and an increase in EC by 12 µS.cm^{-1} was accompanied by a visible spring on the river bank.

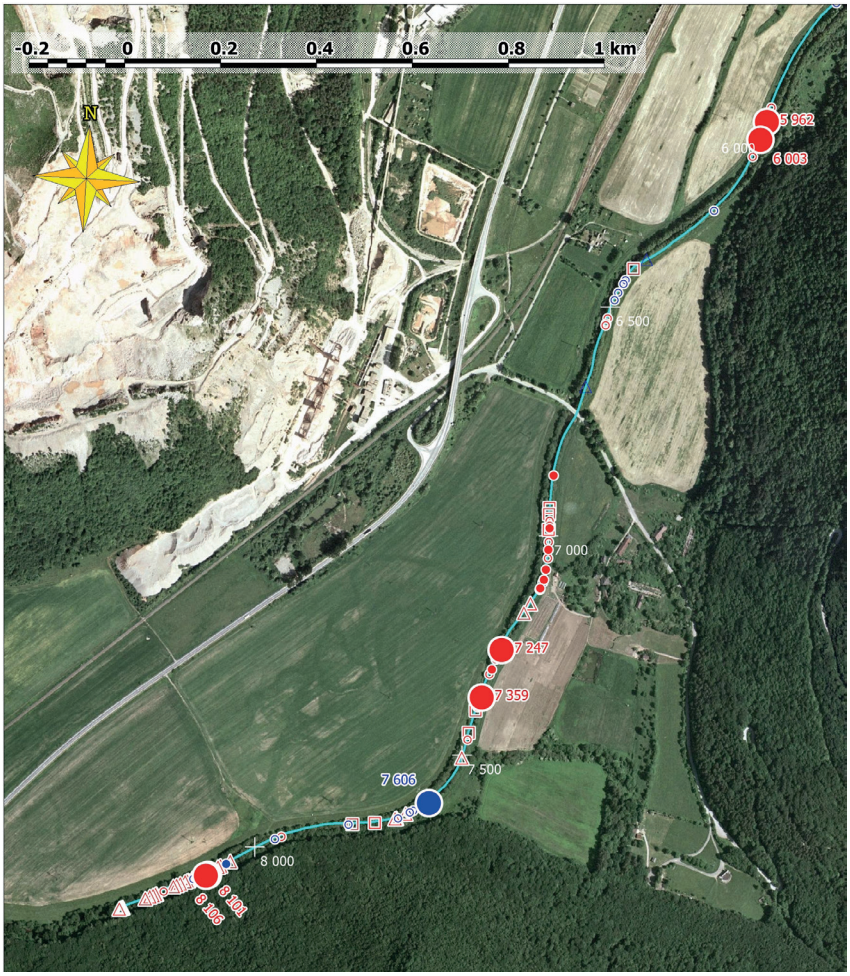

Fig. 10. Location of anomalies detected by thermometric and resistivimetric measurements on the river Slaná in the Brzotín – Gombasek section, 6000 to 8300 m footages. For explanation of symbols see Fig. 5.

The measurement on 24/06/2016 was completed on 7200 m footage at a water temperature in the river of 21.9 °C and its specific electrical conductivity of 340 µS.cm^{-1}. At the onset of measurements the next day (25/06/2016), the main water temperature was 20.2 °C (in 1.7 °C lower), and EC was 322 µS.cm^{-1} (in 18 µS.cm^{-1} less than the value measured at the end of the previous day). On that day, two significant anomalies were detected in the section between 7200 and 7500 m footages: on 7247 m, where a significant hidden anomaly was indicated by the measurement, accompanied by a 4.2 °C drop in the water temperature and a 194 µS.cm^{-1} specific electrical conductivity rise, and on footage 7359 m, where the water

temperature drop by 3.7 °C and the EC increase by 220 μS.cm^{-1} were also accompanied by a visible manifestation of water output from the left bank of the Slaná River. In the meantime, both these significant anomalies were (always on the left bank) accompanied by several minor anomalies – in the section that recorded their onset were footages 7236 and 7244 m, which preceded the above-mentioned more significant hidden inflow on the 7247 m footage. In the case of 7236 m footage only EC increased by 7 μS.cm^{-1}, in the case of 7244 m footage, in addition to an EC increase of 20 μS.cm^{-1}, a temperature drop of 0.3 °C was also observed. This significant anomaly (footage 7247 m) was followed by indications of hidden groundwater inflows on footages 7254 m, 7259 m, 7270 m, 7275 m, 7299 m and 7311 m. Water temperature decreases of 0.3 °C/0.2 °C/0.2 °C/0.3 °C/0.4 °C and 0.3 °C were recorded there, as well as an increase in the EC values of 26 μS.cm^{-1}/7 μS.cm^{-1}/17 μS.cm^{-1}/18 μS.cm^{-1}/32 μS.cm^{-1} and 20 μS.cm^{-1}. Significant anomaly on footage 7359 m with visible manifestation of groundwater output was preceded by smaller anomaly on footage 7345 m (water temperature drop by 0.2 °C and EC increase by 44 μS.cm^{-1}), followed by cloud of smaller left-bank anomalies on footages of 7372 m, 7389 m, 7399 m, 7446 m and 7460 m. Decreases in water temperature of 0.3 °C/0.2 °C/0.3 °C/0.0 °C and 0.1 °C, and an increase in the specific electrical conductivity of 20 μS.cm^{-1}/20 μS.cm^{-1}/29 μS.cm^{-1}/18 μS.cm^{-1} and 30 μS.cm^{-1}. Of the five anomalies, two (on footages 7399 and 7446 m) were accompanied by a smaller visible groundwater inlet to the Slaná River.

On the footage of 7502 m, a visible tributary of the flow from the karstic spring Čierna vyvieračka ("Black spring"), previously an underground flow through the Gombasecká jaskyňa Cave, enters the Slaná River from the left. Its temperature at the mouth was 13.0 °C and a specific electrical conductivity of 624 μS.cm^{-1} was recorded here. The flow rate of this inflow was estimated to be about 10 l.s^{-1}. Mixing of the spring water with the river water along the left bank was evident up to the footage of 7539 m, may last beyond in high water stages. The flow of the Slaná River is already influenced by the backwater of a small hydroelectric power plant, deep water in many places made the continuous measurements impossible. The footage 7600 m is then assigned to the dam body, which divides a part of the Slaná River into an upper artificial derivation channel supplying the turbines of the power plant, closer to the foot of the slope eastwards, and the original old riverbed. The measurements took place in the old riverbed, again along both its banks. An anomaly was reported on footage 7606 m, associated with an increase in water temperature of 1.6 °C and an increase in conductivity of 128 μS.cm^{-1}. Due to its temperature, we assume that this is a manifestation of surface water leakage. In the continuation of the old Slaná riverbed, several other minor anomalies were found on 7676 m, 7654 m and 7681 m footages at the right bank. Changes of 1.1 °C/5 μS.cm^{-1}; 0.1 °C/7 μS.cm^{-1} resp. 0.2 °C/5 μS.cm^{-1} were recorded here where there was a decrease in water temperature and an increase in its EC value. Along the left bank, anomalies are found on the opposite section (footages of 7657 m, 7663 m, 7684 m and 7687 m). The biggest anomaly found there (footage 7657 m) was associated with a 0.3 °C water drop in water temperature and an increase in the specific electrical conductivity by 34 μS.cm^{-1}. The other three have already been associated with a higher water temperature than in the surface stream and are therefore associated with water leaking through the embankment of the uppermost derivation channel, and in the last three cases these leaks were directly visible by the naked eye. The observed changes in EC in footages of 7663 m, 7684 m and 7687 m were 40 μS.cm^{-1}; 21 μS.cm^{-1} and 17 μS.cm^{-1}, with temperatures varying within the range of 2.4 from 21.0 to 23.4 °C (Slaná River streamline temperature was 21.0 °C). A small inflow with a discharge rate of about 0.04 l.s^{-1} was visually observed on footage 7733 m, but this caused an extremely strong drop of 5.1 °C on the left bank water temperature and an EC rise by 46 μS.cm^{-1}. On the continuing course of water temperature records on the left bank of the Slaná River downstream we find only minor anomalies on footages 7778 and 7932 m. On its right bank, up to footage 8000 m (nearby the AK-15 hydrogeological borehole) only smaller anomalies were found on footages of 7786 and 7948 m. Aforementioned left-bank anomalies (on 7778 and 7932 m footage) can be characterized by a drop in water temperature by 0.7 and 0.3 °C; as well as increasing the EC value by 16 and 4 μS.cm^{-1}. A smaller groundwater inflow was also visually observed on 7,778 m footage in connection with the registered anomaly. Concerning right-bank anomalies (footage 7786 and 7948 m), a drop in water temperature by 0.2 resp. 0.1 °C and an EC increase by 3 and 6 μS.cm^{-1} were recorded – these were really small anomalies.

Along the left bank, a series of leaks from the more and more higher (with greater height difference between the levels) derivation channel of the power plant, whose step with turbines is located on the Slaná River near the Vidová-Rima osada area. The 8040 m footage shows a shift in water temperatures (an increase by 0.6 °C) during an approximately 1 hour lunch break while maintaining the specific electrical conductivity values. Visible leaks were observed in large quantities at the foot of the derivation channel. On 8051 m footage, leakage with EC parameters of 344 μS.cm^{-1}, temperature 18.6 °C and discharge rate of about 0.3 l.s^{-1} was manifested only by a small left-bank anomaly of EC increase by 1 μS.cm^{-1} and without change of water temperature. Much more pronounced was the hidden anomaly on the right bank on 8061 m footage (increase of water temperature by 1.7 °C and increase of EC by 56 μS.cm^{-1}). According to the water temperature, this is probably surface water input. From the leakages on footages of 8072 m, 8078 m and 8095 m (8072 m: EC 338 μS.cm^{-1}, water temperature 20.7 °C, discharge 0.5 l. s^{-1}; 8078 m: EC 342 μS.cm^{-1}, water temperature 20.2 °C, discharge approximately 0.5 l.s^{-1}; 8095 m: EC 352 μS.cm^{-1}, water temperature 21.1 °C, negligible discharge), only that from 8078 m footage can be considered as left-side groundwater inflow (water temperature drop by 1.7 °C, EC increase by 12 μS.cm^{-1}). However, the two adjacent left-hand anomalies on the footages 8101 and 8106 m were much more significant. They were characterized by a high temperature drop (by 4.4 and 4.6 °C) as well as by a steep change in conductivity (increase by 229 and 124 μS.cm^{-1}). In the area of the first anomaly, there was a small spring with a yield of about 0.05 l.s^{-1}, the spring in the area of the second anomaly had a discharge of up to about 1.0 l.s^{-1}, a conductivity of 592 μS.cm^{-1} and a water temperature of 11.0 °C. Given these parameters, it was obviously not a seepage water from the derivation channel, but a real manifestation of the transiting groundwater. Series of visible leaks from the derivation channel foot, with its position along the foot of the Silická planina Plateau slope continued also in the next sections. Leakage of approximately 0.1 l.s^{-1}

on footage 8126 m had the same EC as the river water, but the water temperature dropped by 2.3 °C. On footage 8132 m, there was a similar drop in water temperature of 2.0 °C, without conductivity change at the leak registered here. The leakage on the 8137 m had an EC value of 339 μS.cm^{-1}, the same as in the Slaná River stream, but its water temperature of 20.4 °C was in 1.1 °C decreased. In these places, finally a small anomaly of the hidden groundwater inflow was detected by lowering the water temperature by 1.0 °C and increasing the conductivity by 16 μS.cm^{-1} at the right bank. Along the left bank, leaks from the dam were visually observed on footages of 8147 m, 8150 m and 8155 m, but they did not affect the water properties on the left bank of the old riverbed. Electric conductivity values measured here were 337 μS.cm^{-1}; 340 μS.cm^{-1} and 395 μS.cm^{-1}, the water temperatures were 21.2 °C, 20.3 °C and 18.7 °C. The leak on meter 8150 m had an estimated discharge of 0.15 l.s^{-1}. Similarly, undetected in the river, was the impact of leaks from 8166 and 8182 m footages (although the first had a discharge of 0.1 l.s^{-1}, a temperature of 17.3 °C and an EC of 350 μS.cm^{-1} and the second one, even discharge of approximately 0.8 l.s^{-1}, temperature 20.9 °C and EC of 338 μS.cm^{-1}). On the other hand, the leakage on the footage 8175 m between the aforementioned two, although at the surface of negligible yield, caused a decrease in water temperature of 0.9 °C and an increase in conductivity of 11 μS.cm^{-1}. On the footage 8205 m, an anomaly of a hidden groundwater inflow from the left bank, but without visible leaks from the derivation channel was detected by a decrease in water temperature of 1.0 °C and an increase in conductivity by 15 μS.cm^{-1}. The series of leaks from the channel above the left bank of the Slaná River old riverbed between footages of 8218 and 8240 m was manifested only by temperature drops, the difference in EC is (due to its similar source) only very slight. For the leakage on the footage 8218 m the EC value of 334 μS.cm^{-1} and the water temperature of 21.7 °C were found, the large leakage on the footage 8220 m had 338 μS.cm^{-1} and 21.0 °C and a discharge of about 0.2 l.s^{-1}, similar leakage on 8225 m had a discharge of approximately 0.4 l.s^{-1}, EC 338 μS.cm^{-1} and a temperature of 20.5 °C. Between these two leakages, another water amount of approximately 1.0 l.s^{-1} was seeping into the old riverbed. The leakage on the 8231 m footage had a temperature of 21.8 °C and a conductivity of 333 μS.cm^{-1}, and the last one in this section was the leakage on the 8240 m footage of about 0.2 l.s^{-1}, 20.2 °C and 340 μS.cm^{-1}. Temperature manifestations of these leakages in the Slaná River stream resulted in a significant decrease in water temperature by 1.5 °C on 8224 m footage and by 2.0 °C on 8242 m footage. Similarly to the section between 8140 and 8160 m footages, visually observed leaks from the derivation channel of the hydropower plant between footages 8290 and 8300 m did not affect the water properties on the left bank of the old riverbed. Gradually, a leakage of about 0.05 l.s^{-1} of water at 18.9 °C with an EC value of 345 μS.cm^{-1} was observed on footage 8290 m; 0.03 l.s^{-1} of water with a temperature of 21.2 °C and an EC value of 338 μS.cm^{-1} on the footage 8293 m and leakage with a water temperature of 21.9 °C and EC of 333 μS.cm^{-1}. On a footage of 8296 m it was about 0.4 l.s^{-1} of water with a temperature of 21.3 °C and an EC value of 336 μS.cm^{-1}; on the 8298 m then there was a leak with a water temperature of 21.1 °C and an EC value of 339 μS.cm^{-1}. At that time, the temperature of the water stream in the Slaná River had a temperature of 22.2 °C and a specific electric conductivity of 331 μS.cm^{-1}. On the footage 8300 m, the measurements of 25/06/2016 as well as all measurements in the section between Brzotín and Gombasek were completed. The list and location of the most significant hidden anomalies

Tab. 2

List of the most important hidden anomalies detected by thermometric and resistivimetric measurements in the Brzotín – Gombasek section of the Slaná River within the 21/06/2016 – 25/06/2016 period and coordinates of their location (S-JTSK coordinate system).

Footage	Anomaly position	Date of detection	X – SJTSK coordinates	Y – SJTSK coordinates
95	right-hand	21/06/2016	–319 298.411	–1 247 663.155
1932	left-hand	22/06/2016	–320 210.395	–1 249 183.652
1935	left-hand	22/06/2016	–320 210.956	–1 249 185.734
1991	right-hand	22/06/2016	–320 225.100	–1 249 226.696
2239	left-hand	22/06/2016	–320 326.176	–1 249 449.714
2275	left-hand	22/06/2016	–320 344.190	–1 249 480.750
2477	left-hand	22/06/2016	–320 509.375	–1 249 596.989
2709	right-hand	22/06/2016	–320 712.472	–1 249 703.060
3170	left-hand	23/06/2016	–321 089.051	–1 249 936.888
3185	left-hand	23/06/2016	–321 096.591	–1 249 953.836
3462	left-hand	23/06/2016	–321 143.573	–1 250 219.787
4142	left-hand	23/06/2016	–321 334.789	–1 250 845.376
5374	left-hand	24/06/2016	–321 373.394	–1 251 993.740
5962	left-hand	24/06/2016	–321 687.469	–1 252 478.810
6003	left-hand	24/06/2016	–321 700.782	–1 252 516.582
7247	left-hand	25/06/2016	–322 240.598	–1 253 580.874
7359	left-hand	25/06/2016	–322 281.701	–1 253 679.324
7606	right-hand	25/06/2016	–322 392.022	–1 253 899.883
8101	left-hand	25/06/2016	–322 852.895	–1 254 049.285
8106	left-hand	25/06/2016	–322 857.149	–1 254 051.279

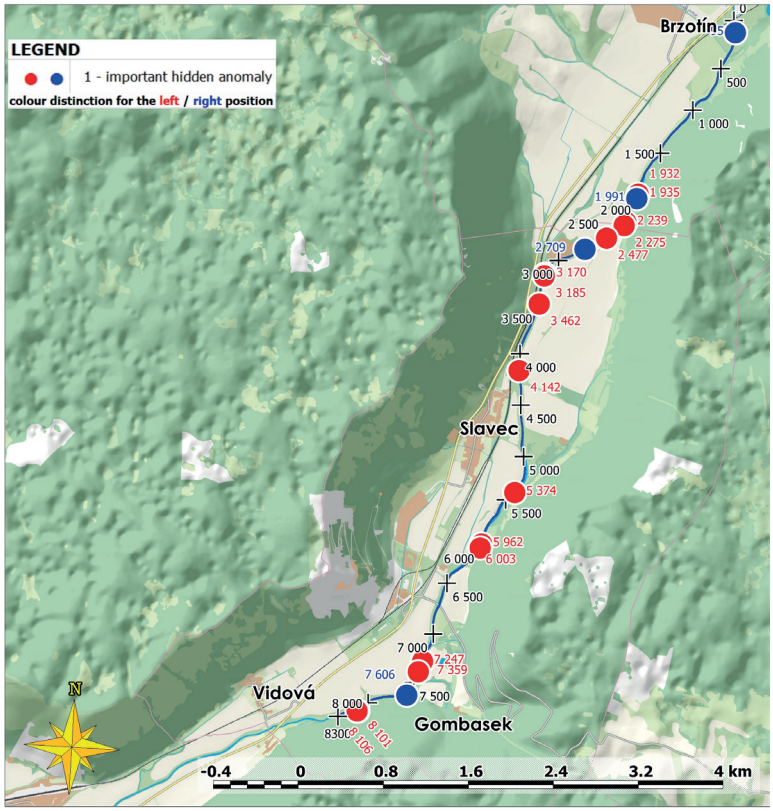

Fig. 11. Overview of the most important anomalies detected by thermometric and resistivimetric measurements performed within the period 21/06/2016 – 25/06/2016 in the Brzotín – Gombasek section of the Slaná River.

detected by thermometric and resistivimetric measurements in the Slaná River between Brzotín and Gombasek within the period 21/06/2016 – 25/06/2016 are shown in Tab. 2 and their overview in Fig. 11.

Conclusion

Results of longitudinal profile measurement of specific electric conductivity (resistivimetry) and water temperature (thermometry) along the watercourse of the Slaná River in its segment between Brzotín and Gombasek municipalities during 5 summer days from 21/06/2016 until 25/06/2016 enabled identification of hidden groundwater inflows position. Although many small anomalies were found, no major karstic groundwater inlets that would be able to influence water temperature and its specific electric conductivity were found here.

More pronounced hidden groundwater inflows to the Slaná River were found in several sections between the footages of 1900 and 8000 m. Detected hidden inflows mostly correspond to the position of already known important karstic springs rising from the foot of the western slopes of the Silická planina Plateau. Such significant left-side anomalies from the footages of 1932 and 1935 m correlate with their location to the visible springs of Hradná vyvieračka/Várforrás. Downstream, also left-side ano-malies of footages 2239 m, 2275 m and 2477 m are also interesting as these can point to hidden groundwater flow from the karstified Triassic limestones of the Silická planina Plateau towards Slaná River through gravels of Quaternary alluvia. However, right-hand anomalies from the footages of 1991 and 2709 m can be considered as also interesting, as quite distanced from the Plešivská planina Plateau and from the Brzotínska vyvieračka/Gyepü spring, the only karst water outlet is in these places. However, the highest right-hand anomaly on 95 m footage which does not manifest itself in temperature (only the value of specific electrical conductivity is increased), can be attributed to the passage of groundwater previously circulating in alluvium which could be partially affected by human polluting activity. Much more interesting is the origin of large left-side anomalies, which were registered along the left bank of the Slaná River on footages of 3170 m, 3185 m, 3462 m and 4142 m. Despite the fact that Slaná River watercourse in these places directly touches the foot of the Plešivská planina Plateau, any indication of visible or hidden groundwater inlet into the surface stream was recorded here. The presence of left-sided anomalies on these places suggests that groundwater flow here must cross a wide alluvium between the river and the foot of the Silická planina Plateau, while the side of Plešivská planina Plateau remains hydraulically inactive. The last of these anomalies (on the footage of 4142 m) could correspond by its location to the position of the karst spring Pod Veľkou skalou, which is known for strong variations in yield. It is possible that at minimum water stages these karstic waters are invisibly entering the alluvium and after passing this Quaternary gravely aquifer they feed the river. The point of their inlet can be marked by the anomaly found on footage 4142 m.

Similarly to the Hradná vyvieračka/Várforrás spring near Brzotín situation, where anomalies were found several hundred meters below it, we can possibly attribute left-hand anomalies on footages 5374 m, 5962 m and 6003 m to residual karstic groundwater that are visible rise in the Pstruhová vyvieračka/Pisztráng spring. This is already captured and exploited drinking water source, but remains of uncaptured waters are possibly invisibly feeding alluvial gravels and only after flowing here in direction parallel to the Slaná River course, they finally appear on its left bank. In the area of Gombasek, along the left bank of the Slaná River on the stretch between footages 6850 to 7500 m, a series of small anomalies located between the springs Biela vyvieračka spring (also known as Margitin prameň spring) and Čierna vyvieračka spring (outflow from the underground hydrologic system

of the Gombasecká jaskyňa Cave) is clearly visible. It is obvious that part of waters here either re-enters the Quaternary sediments from the short streams bellow the springs, or is directly fed in the underground by karstic groundwater of Triassic limestones, and later in groups of scattered inlets subsidize the Slaná River from its left bank. The most prominent points of these surpluses were indicated by anomalies on footages of 7247 and 7359 m. This makes the presence of a right-side anomaly at these places (footage 7606 m) even more interesting. The 7606 m footage anomaly is associated with an increase in water temperature (in 1.6 °C) with parallel EC increase in 128 $\mu S.cm^{-1}$, so we assume that this is a manifestation of surface water or the water that had previously been in contact with the ground surface.

During the measurements in the old riverbed of the Slaná River, numerous left-side inflows from the body of the supply channel embankment belonging to the small hydroelectric power plant were observed. The river step equipped with turbines is several hundred meters downwards around the Vidová-Rima osada site. These anomalies did not show any significant indication of groundwater inlets, but the presence of such a number of leaks is likely to jeopardize the stability of the embankment of this supply channel. However, this falls within the competence and responsibility of the Slovak Water Management Company to assess the seriousness of our findings. Karst groundwater outflows in these places were contrasting with the characteristics of the aforementioned seepages. These (karst groundwater outflows) were found in two adjacent left-hand anomalies (footages 8101 and 8106 m). Inlets of karstic groundwater was characterized by a high temperature drop (by 4.4 and 4.6 °C) as well as by a step change in EC (increase by 229 and 124 $\mu S.cm^{-1}$, respectively). In the area of the first mentioned anomaly, also a small spring with discharge rate of about 0.05 $l.s^{-1}$ was registered, and the spring found in the area of the second anomaly had a discharge of nearly 1.0 $l.s^{-1}$, electric conductivity of 592 $\mu S.cm^{-1}$ and water temperature 11.0 °C. In the vicinity of these groundwater inlets, there is no other natural karstic spring (visible groundwater outlet) at the foot of the Silická planina karstic Plateau, and the anomalies thus indicate the presence of an intense hidden surpluses of karst groundwater from limestones covered by alluvial gravels here.

Acknowledgement

The results of this study could be obtained thanks to the project, coordinated by the European Commission as LIFE11ENV/SK/001023, entitled *Implementation of Sustainable Groundwater Use in the Underground Karst System of the Krásnohorská jaskyňa Cave* (acronym: KRASCAVE). The aim of this project was to reduce the risk of contamination of drinking water in the underground karst ecosystem of Krásnohorská jaskyňa Cave through the implementation of innovation activities, the outputs of the project should also serve to reduce the risk of environmental impairment fragile ecosystems, depending on the quantity and quality groundwater. In the KRASCAVE project, the State Geological Institute of Dionýz Štúr Bratislava was acting as coordinating beneficiary and civic association Envi Slovakia Bratislava as associated beneficiary. In addition to the European Commission, also the Ministry of Environment of Slovak Republic participated in the project co-financing.

References

Auxt, A., Malík, P., Klačanová, Z., Pristaš, P., Filo, J., Šuchová, M., Gretsch, J., Gregor, M., Bottlik, F., Mikita, S., Pažická, A., Buček, S., Černák, R., Nagy, A., Michalko, J., Maglay, J., Máša, B., Švasta, J. & Danko, D., 2012: Doplnkový hydrogeologický prieskum a monitoring ramsarskej lokality – jaskyne Demänovskej doliny. *Manuscript. Bratislava, archive of SGIDŠ, arch. No. 91991, 1–181.*

Bajaník, Š., Hanzel, V., Ivanička, J., Mello, J., Pristaš, J., Reichwalder, P., Snopko, L., Vozár, J. & Vozárová, A., 1983: Vysvetlivky ku geologickej mape Slovenského rudohoria – východná časť v mierke 1 : 50 000. *Bratislava, Geol. Úst. D. Štúra, Veda – vyd. Slov. Akad. Vied, 1–225.*

Džuppa, P. & Husák, Ľ., 1976: Správa z geofyzikálneho prieskumu na akcii Slavec, hydrogeologický prieskum. Geofyzika Bratislava. *Manuscript. Bratislava, archive SGIDŠ, arch. No. 36139, 1–16.*

Ferenc, P., Szalayová, V. & Vrúbel, I., 1986: Lipovce – Salvátor, minerálne pramene. Záverečná správa z geofyzikálnych prác. *Manuscript. Bratislava, archive SGIDŠ, arch. No. 63017.*

Filo, J. & Švastová, D., 1994: Termometrické merania na vybraných lokalitách, záverečná správa za geofyzikálny prieskum. *Manuscript. Bratislava, archive SGIDŠ, arch. No. 79239.*

Foltán, J., 1983: Geofyzikálny výskum povodia Hrona, Hornádu, Podhradského potoka a Necpalského potoka – hydrogeológia, záverečná správa za rok 1982, termometrické merania. *Manuscript. Bratislava, archive SGIDŠ, arch. No. 55112, 1–11.*

Gregor, M., Malík, P., Švasta, J. & Haviarová, D., 2017: Interpretácia rezistivimetrických a termometrických meraní podzemného vodného toku jaskyne Milada (Slovenský kras). In: Bottlik, F. & Malík, P. (eds.), 2017: Zborník príspevkov zo seminára Podzemná voda v regiónoch Slovenska. *Bratislava, Slovenská asociácia hydrogeológov, ISBN 978-80-972651-0-6, 81–87.*

Haviarová, D., Fľaková, R., Seman, M. & Ženišová, Z., 2010: Formovanie chemického zloženia vôd v jaskyni Domica. *Podzemná voda, 16, 1, 54–72.*

Fľaková, R., Gavuliaková, B., Haviarová, D. & Ženišová, Z., 2018: Izotopový výskum krasových vôd Silickej planiny. *Bratislava, Slovenská asociácia hydrogeológov, ISBN 978--80-972651-2-0, 1–126.*

Husák, Ľ. & Lizoň, I., 1980: Jasenie – Horná Lehota – termometrické merania v rokoch 1978, geofyzikálny prieskum. *Manuscript. Bratislava, archive SGIDŠ, arch. No. 44471, 1–10.*

Lizoň, I., 1980: Základný hydrogeologický výskum Belianskych Tatier. Termometrické a vodivostné merania v Belianskej

doline – technická správa. *Manuscript. Bratislava, archive SGIDŠ, arch. No. 47489, 1–17.*

Malík, P., Bodiš, D. & Mello, J., 2000: Mezozoikum západnej časti Slovenského krasu, Železníckeho podhoria a časti Licinskej pahorkatiny, hydrogeologický rajón M 130 – vyhľadávací hydrogeologický prieskum. Final Report. *Manuscript. Bratislava, archive SGIDŠ, arch. No. 84809, 1–307.*

Malík, P., Gregor, M., Švasta, J., Haviarová, D. & Gaál, Ľ., 2010a: Rezistivimetrické a termometrické merania pozemného vodného toku v Gombaseckej jaskyni. *Podzemná voda, XVI, 2 (ISSN 1335-1052), 193–203.*

Malík, P., Gregor, M., Švasta, J. & Haviarová, D., 2010b: Rezistivimetrické a termometrické merania podzemného vodného toku v Drienovskej jaskyni. *Aragonit, 15, 2, 71–76.*

Malík, P., Gregor, M., Švasta, J. & Haviarová, D., 2011: Interpretácia meraní teploty a mernej elektrickej vodivosti v profile podzemného toku Krásnohorskej jaskyne. *Slov. Kras, 49, 1, 41–56.*

Malík, P., Haviarová, D., Gregor, M., Švasta, J., Bottlik, F., Černák, R., Mikita, S., Pažická, A. & Auxt, A., 2013: Demänovská dolina: vzťah povrchových a podzemných vôd. *Aragonit, 18, 2 (ISSN 1335-213X), 3–14.*

Malík, P., Haviarová, D., Švasta, J., Gregor, M., Černák, R., Pažická, A. & Auxt, A., 2016: Výsledky termometrických a rezistivimetrických meraní na podzemných a povrchových tokoch Demänovskej doliny. *Slov. Kras – Acta Carsol. Slovaca, 54, 1 (ISSN 0560-3137), 33–52.*

Mello, J. (ed.), Elečko, M., Pristaš, J., Reichwalder, P., Snopko, L., Vass, D., Vozárová, A., Gaál, Ľ., Hanzel, V., Hók, J., Kováč, P., Slavkay, M. & Steiner, A., 1996: Geologická mapa Slovenského krasu 1 : 50 000. *Bratislava, GS SR (map sheet).*

Mello, J. (ed.), Elečko, M., Pristaš, J., Reichwalder, P., Snopko, L., Vass, D., Vozárová, A., Gaál, Ľ., Hanzel, V., Hók, J., Kováč, P., Slavkay, M. & Steiner, A., 1997: Vysvetlivky ku geologickej mape Slovenského krasu 1 : 50 000. *Bratislava, GS SR, Vyd. D. Štúra, 1–255.*

Orvan, J., Vrábľová, M., Drahoš, M., Kovařík, K. & Kullman, E., 1992: Slavec – hlboké vrty, podrobný hydrogeologický prieskum. Ingeo Žilina. *Manuscript. Bratislava, archive SGIDŠ, arch. No. 78665.*

Švasta, J. & Malík, P., 2008: Vzťah podzemných a povrchových vôd v oblasti hydrogeologickej štruktúry karbonátov hronika Kopy vo Veľkej Fatre. *Podzemná voda, XIV, 2 (ISSN 1335--1052), 151–160.*

Vojtková, S. & Malík, P., 2005: Vzájomná komunikácia podzemných krasových vôd a povrchového toku Hrdzávka na Muránskej Planine. *Podzemná voda, XI, 2 (ISSN 1335-1052), 145–151.*

Skryté prestupy podzemných vôd Slovenského krasu do rieky Slaná medzi Brzotínom a Gombasekom identifikované termometrickými a rezistivimetrickými meraniami

Merania mernej elektrickej vodivosti (rezistivimetria) a teploty vody (termometria) pozdĺž povrchového vodného toku vykonávané v dostatočne zahustenej sieti meracích bodov dokážu identifikovať polohu skrytých prítokov podzemnej vody do povrchového toku v prekvapivo podrobnej miere detailu. Pri intervalových meraniach prietoku, t. j. meraní a vzájomnom porovnávaní prietoku na vhodne vzdialených miestach tokov, dokážeme kvantitatívne definovať skryté prestupy do toku alebo straty prietokového množstva, ale veľkosť prestupu môžeme priradiť iba k istému segmentu toku s dĺžkou rovnajúcou sa vzdialenosti meraní. Na rozdiel od toho, výstupy termometrie a rezistivimetrie majú potenciál presnej identifikácie polohy prestupov, a to aj bez ich kvantifikácie. Časovo najvhodnejšie obdobia na termometrické a rezistivimetrické merania sú vrcholiace leto alebo zima, ktoré prirodzene zvýrazňujú teplotný kontrast povrchovej a podzemnej vody. V našom prípade sa termometrické a rezistivimetrické merania uskutočnili na toku rieky Slaná v jeho úseku medzi obcami Brzotín a Slavec, časť Gombasek. Rieka sa tu vo forme kaňonu širokého aj hlbokého niekoľko sto metrov prerezáva pomedzi dve veľké krasové planiny (Silickú planinu a Plešivskú planinu). V tejto oblasti sú známe tri veľké krasové pramene, ale skryté odvodňovanie krasovej podzemnej vody priamo do rieky Slaná nebolo doteraz preskúmané. Merania na danom úseku rieky v dĺžke 8 300 m sa uskutočnili počas 5 letných dní od 21. do 25. 6. 2016. Základný krok meraní bol 1,0 m, jednotlivé zámery sa realizovali 20 cm od okraja toku pozdĺž ľavého a pravého brehu, ako aj v prúdnici aktívneho toku Slanej. Oba parametre, teplota vody a merná elektrická vodivosť, sa merali v blízkosti dna ~ 5 cm nad ním a vo vzdialenosti ~ 20 až 40 cm od brehu. Na celom úseku toku rieky Slaná medzi Brzotínom a Gombasekom dlhom 8 300 m sa však nezistili žiadne významné skryté prítoky krasovej podzemnej vody. Malé prítoky boli väčšinou situované na ľavom brehu a naznačovali smer prúdenia skryto prestupujúcej podzemnej vody z východu – od priestorov Silickej planiny. Zdá sa, že prinajmenšom v nami overovanom úseku sa Plešivská planina odvodňuje len cez známe krasové pramene, registrované západne od rieky Slaná.

Z celkového priebehu termometrických a rezistivimetrických meraní (teploty vody a jej mernej elektrickej vodivosti) realizovaných v dňoch 21. až 25. 6. 2016 na rieke Slanej v úseku medzi Brzotínom a Gombasekom možno určiť polohu významnejších anomálií, ktoré by mohli byť spôsobené skrytými prestupmi podzemnej vody do povrchového toku. Treba však konštatovať, že k skutočne výrazným prestupom veľkého množstva podzemnej vody, ktoré by ovplyvnilo aj teplotu vody a vodivosť celého toku meraného v prúdnici, tu nedochádza. Významnejšie prestupy sme zaznamenali na niekoľkých úsekoch

medzi 1 900 a 8 000 m. V porovnaní s pomerne malým výskytom pravostranných anomálií boli v oveľa väčšej miere anomáliami indikované skryté prestupy podzemnej vody do ľavého brehu Slanej (v smere od Silickej planiny). Tie vo veľkej miere svojou polohou zodpovedajú polohe významných známych krasových prameňov vystupujúcich z úpätia západných svahov Silickej planiny. Významné ľavostranné anomálie z úsekov 1 932 a 1 935 m svojou polohou korelujú s viditeľnými vývermi prameňa Hradná vyvieračka/Várforrás. Zaujímavé sú aj ľavostranné anomálie nachádzajúce sa nižšie po toku z úsekov 2 239, 2 275 a 2 477 m, ktoré by mohli indikovať pohyb krasovej vody z vápencov budujúcich Silickú planinu do Slanej prostredníctvom aluviálnych náplavov, do ktorých skryto vstupujú z planiny. Zaujímavé sú ale aj pravostranné anomálie z úsekov 1 991 a 2 709 m, ktoré sú dosť vzdialené od Plešivskej planiny, resp. od Brzotínskej vyvieračky/Gyepü, ktorá ju v týchto miestach odvodňuje. Najvyššie sa nachádzajúcu pravostrannú anomáliu na úrovni 95 m, ktorá sa teplotne neprejavuje (stúpla len hodnota mernej elektrickej vodivosti), môžeme priradiť k prestupu vôd infiltrovaných a obiehajúcich v alúviu. Tie mohli byť čiastočne ovplyvnené (znečisťujúcou) činnosťou človeka. Oveľa zaujímavejší je pôvod veľkých ľavostranných anomálií, ktoré boli registrované popri ľavom brehu Slanej na úsekoch 3 170, 3 185, 3 462 a 4 142 m. Napriek tomu, že tok rieky Slanej sa v týchto miestach dotýka úpätia Plešivskej planiny, z jej strany nebol na pravom brehu toku Slanej zaznamenaný žiaden náznak viditeľného alebo skrytého vstupu podzemnej vody do povrchového toku. Prítomnosť ľavostranných anomálií naznačuje, že prúd podzemnej vody tu musí križovať široké alúvium smerom od úpätia Silickej planiny, kým zo strany Plešivskej planiny k jej odvodňovaniu nedochádza. Posledná z uvedených anomálií (na úseku 4 142 m) by svojou polohou mohla zodpovedať polohe krasového prameňa Pod Veľkou skalou, ktorý je známy silným rozkyvom výdatnosti (je možné, že pri minimálnych vodných stavoch voda vstupuje iba skryto do alúvia a až neskôr do rieky, čo môže byť signalizované anomáliou zistenou na úseku 4 142 m).

Podobne ako v prípade brzotínskej Hradnej vyvieračky (prameňa Várforrás) sa anomálie zistili aj niekoľko stoviek metrov pod ňou. Ľavostranné anomálie na úsekoch 5 374, 5 962 a 6 003 m môžeme pravdepodobne priradiť k zvyškovej krasovej vode, ktorá viditeľne nevystupuje v prameni Pstruhový/Pisztráng (tiež „Pstružia“ alebo „Vodovodná“ vyvieračka, ktorý je v súčasnosti vodárensky zachytený), ale pravdepodobne sa pod známou úrovňou výstupov skryto „vlieva“ do aluviálnych náplavov a až po pretečení (v prúde paralelnom s tokom rieky) skryto prestupuje do Slanej. V oblasti Gombaseka potom možno popri ľavom brehu Slanej zhruba na úseku medzi 6 850 až 7 500 m sledovať sériu malých anomálií, ktoré sa nachádzajú medzi prameňmi Biela vyvieračka (tiež Margitin prameň) a Čierna vyvieračka (vyústenie krasového podzemného toku pretekajúceho Gombaseckou jaskyňou). Je zjavné, že časť tu vyvierajúcich vôd buď spätne vstupuje do kvartérnych sedimentov, alebo do nich priamo vteká z prostredia skrasovatených vápencov a rozptýlene dotuje rieku Slanú z jej ľavého brehu. Najvýraznejšie miesta týchto prestupov boli indikované anomáliami na úsekoch 7 247 a 7 359 m. O to zaujímavejšia je prítomnosť pravostrannej anomálie v týchto miestach (7 606 m). Pretože je však táto anomália spojená so zvýšením teploty vody (o 1,6 °C) pri zvýšení jej vodivosti o 128 µS . cm^{-1}, predpokladáme, že ide o prejav povrchovej vody, resp. vody, ktorá už bola v predchádzajúcom čase v kontakte s povrchom terénu. Počas meraní na starom koryte Slanej sme pozorovali množstvo prítokov z telesa hrádze prívodného kanála malej vodnej elektrárne, ktorej stupeň (stavba s turbínami) sa nachádza na rieke Slanej v oblasti Vidovej, osady Rima. Vzhľadom na obeh podzemnej vody zväčša nemali významný indikačný význam, no prítomnosť takého množstva miest presakovania môže pravdepodobne ohrozovať stabilitu telesa hrádze tohto prívodného kanála. To však patrí do kompetencie Slovenského vodohospodárskeho podniku, ktorý by mal posúdiť reálnu závažnosť daných zistení. Vývery krasovej podzemnej vody v týchto miestach, ktorá je z hľadiska vlastností v kontraste so spomínanou presakujúcou vodou, sa zistili na dvoch susediacich ľavostranných anomáliách (úseky 8 101 a 8 106 m). Táto voda bola charakteristická vysokým poklesom teploty (o 4,4, resp. 4,6 °C), ako aj skokovou zmenou vodivosti (nárast o 229, resp. 124 µS . cm^{-1}). V oblasti prvej z nich sa navyše vyskytoval malý prameň s výdatnosťou zhruba 0,05 l . s^{-1}. Prameň v oblasti druhej anomálie mal výdatnosť až okolo 1,0 l . s^{-1}, vodivosť 592 µS . cm^{-1} a teplotu vody 11,0 °C. V blízkosti uvedených prestupov podzemnej vody sa na povrchu terénu (pri úpätí krasovej planiny) nevyskytuje žiaden viditeľný prirodzený výver (prameň). Dané anomálie tak indikujú prítomnosť intenzívneho skrytého výstupu krasovej podzemnej vody z krasových priestorov prekrytých alúviom.

Doručené / Received: 7. 10. 2019
Prijaté na publikovanie / Accepted: 2. 12. 2019

Mineralia Slovaca, Web ISSN 1338-3523, ISSN 0369-2086
51 (2019), 205 – 2016, © Authors 2019. CC BY 4.0

Removal of toxic elements from the minerals particles of contaminated soil by chemical and biological leaching

IVETA ŠTYRIAKOVÁ[1], ZUZANA DANKOVÁ[1,*], MARIÁN KOŠUTH[1], JAROSLAV ŠUBA[1], JARMILA NOVÁKOVÁ[2] and VIERA KOLLÁROVÁ[3]

[1]State Geological Institute of Dionýz Štúr, Regional Centre Košice, Department of Applied Technology of Raw Materials, Jesenského 8, SK-040 01 Košice, Slovak Republic; iveta.styriakova@geology.sk
[2]State Geological Institute of Dionýz Štúr, Regional Centre Spišská Nová Ves, Division of Geoanalytical Laboratories, Slovak Republic
[3]State Geological Institute of Dionýz Štúr, Department of Special Laboratories, Bratislava, Slovak Republic

Abstract: Four experiments of chemical (CHL) and biological (BL) leaching of toxic elements from the contaminated soil using chelants Ethylenediaminetetraacetic acid disodium salt dihydrate (Na_2EDTA), Ethylenediamine-*N*,*N'*-disuccinic acid trisodium salt (Na_3EDDS) and heterotrophic indigenous bacteria was realized with the aim to remove mobile toxic elements from the contaminated soil. The first test of chemical extraction using 10 mM chelants was effective for toxic metal removal in order Cu(II) > Zn(II) > Pb(II), but was very low for the As(V), Sb(III) and Ba(II) extraction. Next the chemically leached sample was treated in the second test combining CHL and BL with 2 mM chelants and nutrients. The second test allowed to enhance the Pb and As extraction to 4 and 6 %, respectively. The extraction of Cu(II) and Ba(II) decreased. Therefore the sample originated from the abiotic control was next treated in the third test only by bioleaching. The effect of leaching was similar as in previous combined test and the As extraction reached 44 %. Based on the obtained result technological method of leaching of contaminants was tested and verified. The effect of Cu(II) and Zn(II) extraction reached 68 and 59 %, respectively. For Zn(II) it was 49 %, for As(V) and Sb(III) 40 and 31 %, respectively and for Ba(II) only 22 %.

Key words: soil, toxic elements, chelants, bacteria, bioremediation

Graphical abstract

Highlights

- The study verified the intensification of toxic elements extraction from the contaminated soils.
- Higher As concentration in soil required longer time of bioleaching and higher nutrients concentration during the leaching cycle.
- The As mobility was influenced by the mineralogical composition of particular soil samples.
- Chemical leaching for metals removal following by bioleaching for maximum As removal seems to be a promising method.

Introduction

Metal pollution of soils is widespread across the globe, as caused by many anthropogenic activities, including mining operations, smelting, waste disposition, coal combustion, application of pesticides, etc. Most hazardous sites are contaminated with mixed heavy metals and metalloids rather than a single heavy metal. One major concern is the treatment of soil contaminated by arsenic. Arsenic as a toxic metalloid occurs in the environment in several oxidation states (–3, 0, +3, +5). Major As species in common environments are predominantly oxyanions, trivalent arsenite and pentavalent arsenate and their mobility differs from other heavy metals (Chatain et al., 2005; Lee et al., 2013). Many methods have been suggested to eliminate contaminants from soil: stabilization/solidification, vitrification, electrical process, but require long term monitoring and appropriate controls and are limited because of high material costs, regeneration of sludge, high energy requirements, etc. (Yamamura et al., 2005; Yao et al., 2012; Torres et al., 2012; Wang et al., 2009; Bahemmat et al., 2015; Tandy et al., 2004). The detailed overview of different methods for soil remediation and their combination is described by Peng et al. (2018). Soil washing offers a permanent remediation alternative for metal-polluted sites. Washed out metals can

also be recovered from leachate, and then reintroduced into the social material cycle instead of being landfilled (Li et al., 2015). Chemical-enhanced soil washing has shown promising results in removing heavy metals. Soil washing with chelating agents is considered to be an emerging remedial method for removal contaminants from soil rapidly and/or efficiently relative to other methods (Wang et al., 2018). Use of organic metal chelants in the wash formulation offer the advantages of high potential extraction, efficiencies, homogenous treatment of the polluted matrix and specificity for metals. Scientists remain uncertainty as to the optimal choice of chelating agents. Degradability and residues, potential adverse health effects, cost, extraction effect and possibility of chelant recovery need to be considered (Vandevivere et al., 2001). Also, ratio of chelating agent to toxic metals, pH, quantity of major cations extracted and source of contamination should be regarded (Tandy et al., 2004). Ethylenediaminetetraacetic acid (EDTA) is the most popular chelating agent and is used in various industrial fields. EDTA is nominated as a chemical unlikely to be removed during biological sewage treatment even after prolonged exposure. The reason for this might be that it has a slow biodegradation rate under conventional treatment conditions, which usually results in deterioration of soil function (Takahashi et al., 1997; Wang et al., 2018). [S, S]-stereoisomer of ethylenediamine disuccinic acid (EDDS) is a strong transition metal chelant which was originally developed for application in laundry detergents. It was tested as an agent for metal extraction based on its biodegradability, low toxicity, high affinity for most heavy metals ions and low sorption tendency which makes it perspective for environmentally sustainable treatment process (Takahashi et al., 1997; Vandevivere et al., 2001). The extraction of Cu, Zn and Pb using bioedegradable chelant EDDS was studied by Hauser et al. (2005). While the Cu extractability was higher in batch experiments, the Zn and Pb extraction was higher in column experiments. Between 18 and 42 % of the applied EDDS was lost through biodegradation after 7 weeks. Kim et al. (2015a, b, 2016) studied the reductive arsenic extraction from soils with various reducing agents in order to remediate arsenic-contaminated soils. Oxalate and ascorbic acid were effective only at extracting arsenic associated with amorphous iron oxide. Extraction by dithionite was not effective because of re-adsorption of arsenic to the newly formed iron oxide phase. But the addition of oxalate enhanced the As extraction. Also, combination of chelating agents (EDTA) with reducing agents greatly improved the As extraction from the soil samples. The increase of the enhancement of EDTA extraction was greatly affected by the reducing conditions and soil-metal binding characteristics. The reductant and chelating agent were applied to remove arsenic and chromium in soil by electrokinetic technology coupled with permeable reactive barrier (Xu et al., 2019). The pretreatment with reductant (ascorbic acid) enhanced arsenic removal but reduced chromium removal. Moreover, pretreating with chelating agent (EDTA-2Na) slightly enhanced arsenic and chromium removals. For such co-contaminated soils, pretreatment with sodium citrate was a relatively good way, because sodium citrate had both chelation and reducibility. Hashem et al. (2015) studied the effect of phosphate on arsenic mobilization from the contaminated sediment. The leached amount of As(V) was strongly depended on the phosphate concentration. It was expected that during long time leaching under anaerobic, leached As(V) will be reduced to As(III) but after 24 h of the leaching As(III) concentration was decreased. However, EDDS is more expensive than EDTA, therefore the possibility to combine these chelants could be promising for remediation technology.

Bioleaching is second promise technique generally used at industrial scale for low-grade ores. Microbial-based technologies for metal extraction have become attractive because of great potential for future development due to environmental compatibility and possible cost-effectiveness (Chatain et al., 2005; Wang and Zhao, 2009). Bioleaching may be applicable for a large number of inorganic pollutants and can be carried out under either anaerobic or aerobic conditions following specific microbial metabolisms. The stimulation of biochemical processes in decontamination is possible, if resistant bacteria are present in the soil (Štyriaková et al., 2015). Zeng et al. (2015) studied the removal of Cu, Pb and Zn from the contaminated sediment using *Aspergillus niger* strain SY1. The bioleaching efficiencies of heavy metals in the two-step bioleaching were better than that in one-step bioleaching. After the bioleaching, metals remaining in the sediment were mainly found in the stable fractions, and the toxicity of it was reduced to a level for it to be used safely in landfill or in land application. Anaerobic heterotrophic bioleaching batch tests with indigenous bacteria and carbon source addition showed that a fraction of arsenic could be extracted using appropriate biostimulation. When carbon source was added, release of arsenic increased 28-fold (Chatain et al., 2005). Arsenic bioleaching can be a result of direct reduction of arsenite associated with a solid phase to more mobile arsenate, the bio-oxidation of arsenic-containing sulfides or the reductive dissolution of iron hydroxides (Wang et al., 2009). Dissimilatory arsenate-reducing bacterium (DARB), *Bacillus* sp. SF-1 was able to effectively extract arsenic from various arsenic-laden solid via the reduction of solid-phase arsenate to arsenite. Extraction of As from the soil was a little more efficient with rotary shaking than without it. On the other hand, maximum extraction can be achieved even under static conditions by prolonged treatment (Yamamura et al., 2005).

Vaxevanidou et al. (2008) reported that bacterial activity of *Desulfuromonas palmitatis* can induce the reductive dissolution of Fe(III)-oxides in the contaminated soil and thus enhanced the release the retained arsenic without its reduction. However the pure chemical treatment by EDTA extracted only one third of the arsenic contamination.

The aim of this work is to suggest a method for toxic elements, mainly As(III)/(V), extraction from the contaminated soils, considering the environment and costs requiremnts. The chemical and biological leaching of soil samples using heterotrophic indigenous bacteria and resistant heterotrophic bacteria from sediments was studied in different leaching tests. Finally, the experiment with higher amounts of contaminated soils were performed to compare and verify the particular results and defined the method of mobile As(III)/(V) extraction.

Materials and Methods

Chemical analyses of soil samples

The soil samples of 20 kg were sampled from three sites of Richnava locality (denoted as R1, R2 and R3). The one of the sampling site was a garden (R1) often flooded by the river Hornád, being through the localities hard loaded by the anthropogenic activities, especially after mining and metallurgical industry. The soils were sieved to grain size < 4 mm. The oversized product consisted of anthropogenic sludge and larger rock grains. The grains below 4 mm were used for the experimental purposes.

X-ray diffraction analysis

The powder X-ray diffraction (XRD) patterns of R1, R2 and R3 soil samples were recorded using a diffractometer D2 Phaser (Bruker, Germany), equipped with a CuKa radiation source (30 kV, 10 mA) and Lynxeye detector. The data were qualitatively and quantitatively analysed using Software DIFFRAC.EVA with PDF-2 Database.

Electron probe micro analyzer

The particular soil grains were observed by electron micro analyzer CAMECA SX-100, allowing to provide the point chemical analyses, line profiles, RTG quantitative and qualitative maps, backscattered electron (BEI) and secondary electron (SEI) images.

Bioleaching experiments

For the bioleaching experiments the heterotrophic bacteria *Bacillus* spp. isolated from the sediment of Ružín water dam were used. The samples were heated at 80 °C for 15 min to kill vegetative cells. The sediment contained the spore-forming bacteria at a concentration of 10^5 CFU/g active in Fe dissolution (Štyriaková et al., 2016). The isolates were grown in Trypton soya broth at 28 °C for 18 h. Next the cells were centrifuged at 4000 rpm for 15 min and washed twice with saline solution (0.9 wt % NaCl). These bacteria were inoculated into parallel columns before the medium percolation (to ensure the activity of autochthonous bacteria). The stimulation of indigenous heterotrophic bacteria using nutrients in form of fertilizers verified the mobilization of toxic elements from the soil samples.

Leaching tests

The first chemical leaching was performed in ex-situ conditions. 600 ml of media percolated through the 300 g of contaminated sample for 5 days. For the experiments three types of media containing different chelants (solution of 10 mM) were used: Na_2EDTA (ch1), Na_3EDDS (ch2) and combination of both chelants in ratio 1 : 1 (ch3). The combination of chelants was used with the aim to decrease EDTA non-degradability according to the Beiyuan et al. (2018). From the chemical analyses of the solutions (leachates) the cumulative concentrations of extracted elements were calculated and compared. The effect of chemical leaching by different chelants was evaluated.

In the second series of experiments the percolation cycle combining CHL and BL in six steps was tested and compared with abiotic control (chemical leaching). The sample from the previous CHL represented the first step of this cycle. Following the medium of 300 mL containing 2 mM chelant and nutrients was percolated through the column (Scheme 1). For the abiotic control, chemical leaching by 10 mM chelant was performed. Also, the chemical leaching using 2 mM chelant as an abiotic control was tested, but the effect of As(III)/(V) extraction was approximately half in comparison with use of 10 mM chelant. The media percolated through the soil sample for 15 and 3 days for BL and CHL steps, respectively. The soil sample contained less than 5 % of clay fraction to ensure sufficient percolation of used media.

In the third series of bioleaching the soil sample after previous leaching in abiotic control (soil leached by 10 mM chelants) was treated in the percolation of 4 steps, Scheme 2. Media of 100 ml with 2 mM chelant with nutrients percolated through the 100 g of soil sample in four cycles during two months. The extraction was controlled after the finish of the experiment. The concentration of toxic elements were compared with abiotic control (CHL) using 2 mM chelants in the same time intervals.

Finally, according to the obtained results from the previous tests, the combination of particular leaching steps was tested and verified. Through the glass column of 80 mm in diameter and 340 mm high containing 1 kg of contaminated soil percolated 2 l of media with 10 mM Na_2EDTA (to eliminate the most content of contaminants such as Cu(II), Zn(II) and Pb(II)). Then,

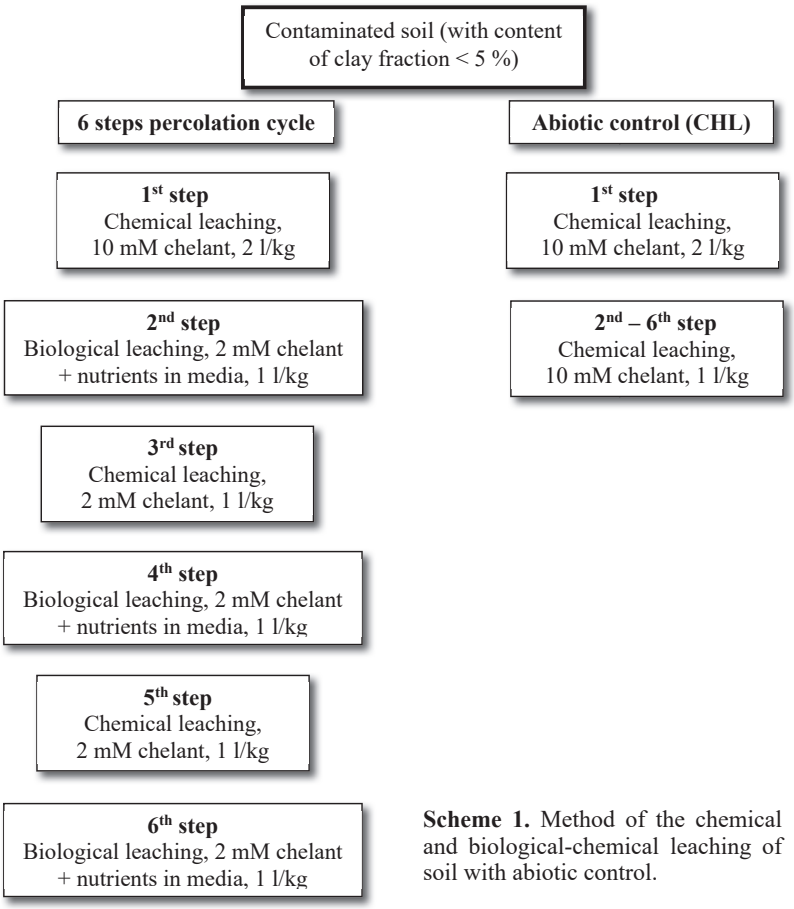

Scheme 1. Method of the chemical and biological-chemical leaching of soil with abiotic control.

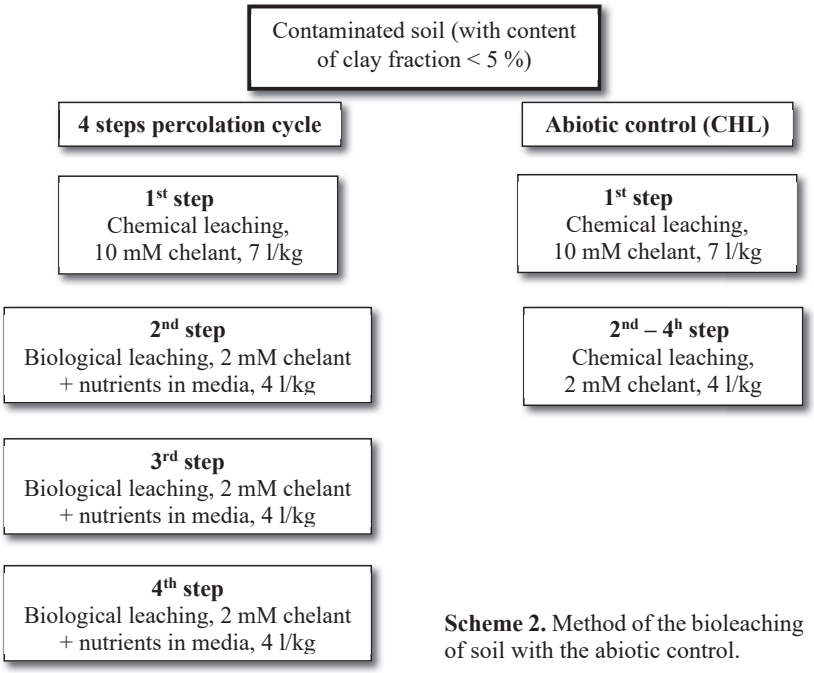

Scheme 2. Method of the bioleaching of soil with the abiotic control.

1.5 l of medium with Na_3EDDS percolated through the glass bottle contained 800 g of chemically leached soil with the aim to remove the non-biodegradable chelant from the soil (and remaining content of inorganic contaminants). After that 700 g of pretreated soil was bioleached using 3 l of media with 2 mM chelant and nutrients.

The percolation rate of the medium was not studied during the experiments, more important for each cycle was the volume of percolated media.

Results

Chemical and mineralogical analyses

Chemical analysis of soil samples showed higher contamination by toxic elements for the sample R1, Table 1, in the order Ba(II) > As(III)/(V) > Sb(III)/(V) > Cu(II). The sites of sampling R2 and R3 soils are far from the flooded locality, where the soil is contaminated by minerals particles of alluvial deposits containing studied heavy metals and metalloids.

The chemical analysis of the plants (onion and potatoes) from the locality R1 showed the presence of over limited concentration of As(III)/(V) (0.7 ppm). Other toxic elements were present in admissible concentrations Cu(II) (0.7–1.5 ppm), Ba(II) (0.5–0.7 ppm), Sb(III (< 0.1 ppm). From the reason of the highest contamination of R1 sample, the leaching tests were performed with this soil. Because the concentration of Zn(II), Pb(II), Ni(II) and Cd(II) did not exceed the values of permissible limits of their concentration, the leaching of As(III)/(V), Cu(II), Sb(III)/(V) and Ba(II) was studied more detailed and discussed.

Knowledge of the mineralogical composition of soil is important to better explain the mobility of toxic elements in the process of biological treatment. For example, As(III)/(V) is bonded by various bonds in different minerals (arsenopyrite, tetrahedrite, gersdorffite or in the secondary phases of grains coatings), what can influence its liberation into the solution. Therefore, the detailed study of mineralogy of different soil fraction is needed to obtain the information about the As(III)/(V) bonding and mobility in contaminated

Tab. 1
Basic chemical composition of soil sample and concentration of contaminants in studied soil samples.

	As(III)/(V) [mg.kg^{-1}]	Cu(II) [mg.kg^{-1}]	Zn(II) [mg.kg^{-1}]	Pb(II) [mg.kg^{-1}]	Ni(II) [mg.kg^{-1}]	Cd(II) [mg.kg^{-1}]	Sb(III)/(V) [mg.kg^{-1}]	Ba(II) [mg.kg^{-1}]
ID	65	500	1500	250	180	10	25	900
IT	70	600	2500	300	250	20	40	1000
R1	**364**	**692**	541	143	86	1	**61**	3303
R2	56	104	329	80	54	< 1	17	465
R3	40	600	187	46	49	< 1	40	478

ID – permissible limit of contaminant concentration in soils IT – critical limit of contaminant concentration in soils

Tab. 2
Amount of magnetic and non-magnetic fraction in soil sample.

Grain size	Mass yield		Magnetic (MP)	Mass yield of products in relation with grain fraction
[mm]	[g]	[%]	Non-magnetic (NP) fraction	[%]
> 0.5	7.62	2.51	MP1	0.96
			NP1	1.55
< 0.5	295.77	97.49	MP2	16.82
			NP2	80.67

soil. For the mineralogical analysis the soil sample was separated to fractions (< 0.5 mm, > 0.5 mm), magnetically and gravitationally separated. The amount of magnetic and non-magnetic fraction is listed in Table 2. The soil fraction of grain size below 0.5 mm was used for the following XRD analysis.

The XRD analysis confirmed the presence of main mineral phase quartz, creating more than 70 % of soil, 12 % of siderite and Mg-siderite (especially siderite grains coated by Fe oxides should be the key factor for As(III)/(V) bioleaching from the soil), next lower content of plagioclase (4.3 %), muscovite (2.4 %), K-feldspar and chlorite (both approximately 1 %), calcite (1.8 %), dolomite (1.4 %) and below 1 % of barite, hematite and illite. The magnetic fraction below 0.5 mm composed of 76 % siderite, 13.5 % quartz and 1.4 % hematite.

In the grains of non-magnetic fraction the point chemical analysis confirmed the content of Fe(III) (almost 50 wt.%), next toxic elements mainly Zn(II) and Co(II), whose content together with other elements (As(III)/(V), Cu(II), Sb(III)/(V)) was more than 0.5 wt.%. The self-standing particles of sulphide minerals (chalcopyrite and pyrite) coated by Fe(II)/(III) layers were observed in the magnetic fraction (Fig. 1). They represented 30–65 % of total content with 1.5 wt.% As(III)/(V). The Ba(II) was bonded in the form of barite, which is very resistant towards chemical and biological leaching (Fig. 2).

On the basis of XRD and electron microanalyses it can be concluded that the mobile form of As(III)/(V) is preferentially bonded on Fe(II)/(III) oxides coating the grains of silicate minerals and carbonates. In the case of Fe(II)/(III) coatings of sulphides more resistant bondings of As(V) towards chemical and biological leaching can be expected (Wolthers et al., 2007).

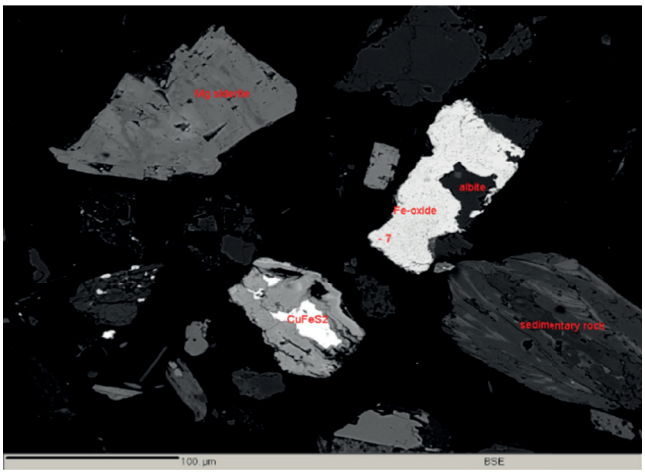

Fig. 1. Electron probe BSI image of selected chalcopyrite grain in magnetic fraction of soil sample.

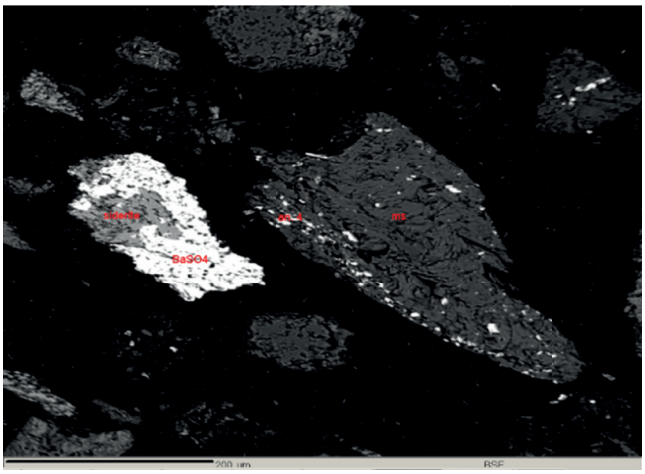

Fig. 2. Electron probe BSI image of selected barite grain in magnetic fraction of soil sample.

Chemical leaching of soil

Using the chemical leaching the extraction of studied elements decreased in the order Cu(II) > Zn(II) > Pb(II). However, the concentration of extracted As(III)/(V), Ba(II) and Sb(III)/(V) was very low. Higher effect of extraction of Pb(II) was observed for chelant ch1, while for the Zn(II) and Cu(II) leaching the chelant ch2 was more effective. Effect of extraction of other elements decreased in order Mn(II) > Fe(III) > Ni(II) > As(III)/(V) > Cd(II) > Ba(II) > Sb(III)/(V). The chelant ch2 was more effective for Mn(II), Fe(III), Ni(II), As(III)/(V) and Sb(III)/(V) extraction (Fig. 3). Ba(II) and As(III)/(V) are strongly bonded in minerals, their cumulative amount was below 1 mg.kg^{-1} after the first cycle of media percolation. The highest effect of extraction was obtained for Cu(II) removal. For Sb(III)/(V) and As(III)/(V) leaching more washing cycles are needed to decrease their over-limited concentrations in soil.

Chemical and biological-chemical leaching of soil

The 3 days chemical leaching with medium of 2 mM chelant was combined with 15 days bioleaching (Scheme 1). The toxic elements extraction was studied after each step and compared with the abiotic control (chemical leaching of soil sample using 10 mM chelant in the same time intervals). In the abiotic control the extraction of Cu(II) decreased after the second percolation cycle for all chelants. The effect of bioleaching was very low, the extraction decreased after the first step of chemical leaching and leaching by bacteria was not effective (Fig. 4). After the last step, the Cu(II) concentration in the soil sample was decreased up to 36 %, what was at 4 % less than in case of abiotic control. Similarly, the effect of Zn(II) removal was lower in comparison with CHL (Tab. 3). Also, biological extraction of Sb(III)/(V) and Ba (II) was very low. The effect of extraction slightly increase in the 3rd and in the 5th step (after the nutrients addition in the previous BL step) for chelants ch1 and ch3, but it was comparable with CHL (Figs. 5 and 6). The combination of CHL and BL resulted in 43 % effect of As(III)/(V) extraction, what was at 6 % higher in comparison with CHL using 10 mM chelant. Positive running of the extraction curve can be observed especially in the 3rd and 5th step (Fig. 7). Addition of nutrients in BL step enhanced the mobilization of toxic elements by bacteria and they were following removed in CHL step in higher amounts. The process of bioleaching seems to be effective only for As(III)/(V) and Pb(II) (Tab. 3). But, comparing the results from CHL and BL, the concentrations of extracted toxic elements and heavy metals are similar, what pointed at the propriety of combined method of soil leaching, mainly from the reason of using of lower amounts of chelants (especially non-biodegradable EDTA).

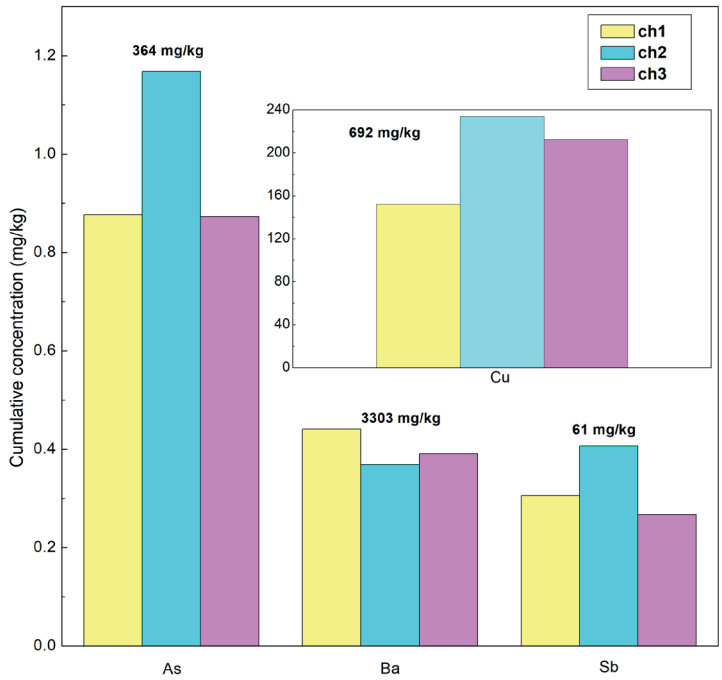

Fig. 3. Cumulative amounts of extracted toxic elements Cu, Sb, As and Ba.

Bioleaching of soil

The sample after chemical leaching using 10 mM chelant (from the previous abiotic control) was bioleached in 4 steps by percolation of medium containing 2 mM chelant and nutrients during 2 months and compared with the abiotic control (according to the Scheme 2). The partial Cu(II) extraction was observable only in the first step of bioleaching. The concentration of extracted Cu(II) was minimal (Fig. 8). In spite of relatively high concentration of Ba(II) in the as-obtained sample, the concentration of extracted Ba(II) was only 2 mg/L (Fig. 9). The highest extraction was observed for chelant ch1 after the first step of bioleaching. Then the extraction decreased for ch1 and ch2. In the next steps it has slightly increased. For chelant ch3, the Ba(II) extraction increased for the 2nd and the 3rd step of BL. As was mentioned above, Ba(II) is strongly bonded in the mineral phase of barite, that is resistant towards chemical and biological leaching. The mobile phase of Ba(II) in the tested sample represents only 20 %. The extraction of As(III)/(V) increased in the 2nd step for chelant ch1 and ch2. The most expressive increase of extraction can be observed for the 3rd step of BL for chelant ch3. Comparing the extraction curves with the abiotic control, BL of As(III)/(V) is more effective in each BL step for each used chelant (Fig. 10). The concentration of As(III)/(V) 24 mg.l^{-1} was obtained after the

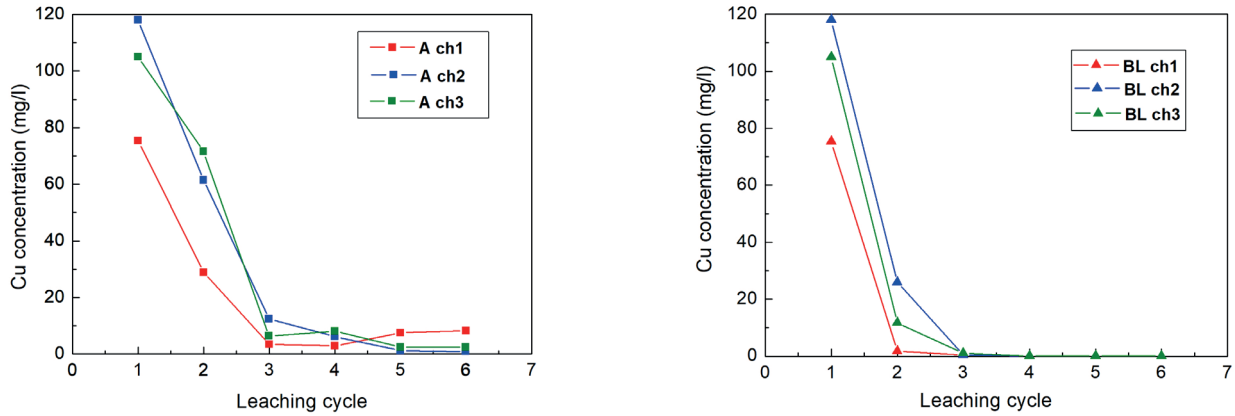

Fig. 4. Chemical (A) and biological-chemical (BL) extraction of Cu from the soil sample.

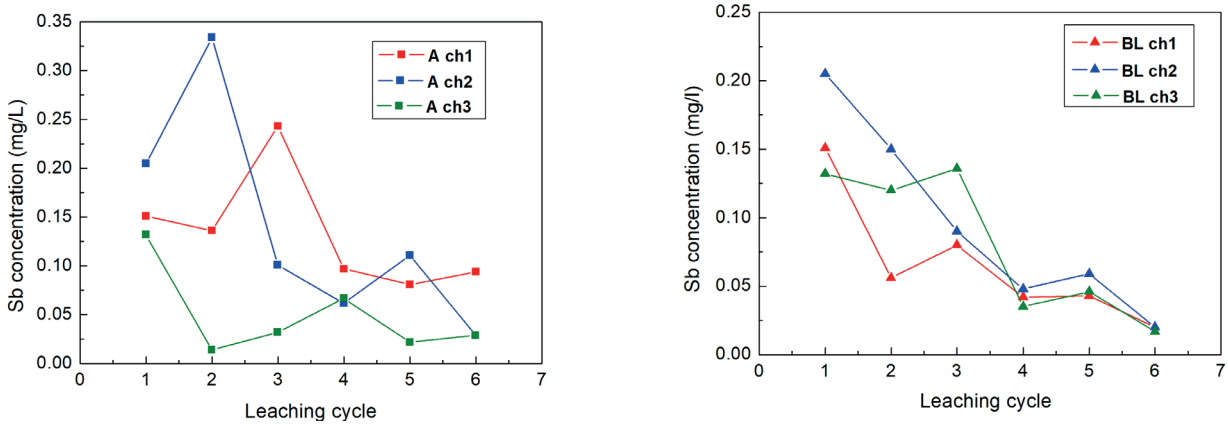

Fig. 5. Chemical (A) and biological-chemical (BL) extraction of Sb from the soil sample.

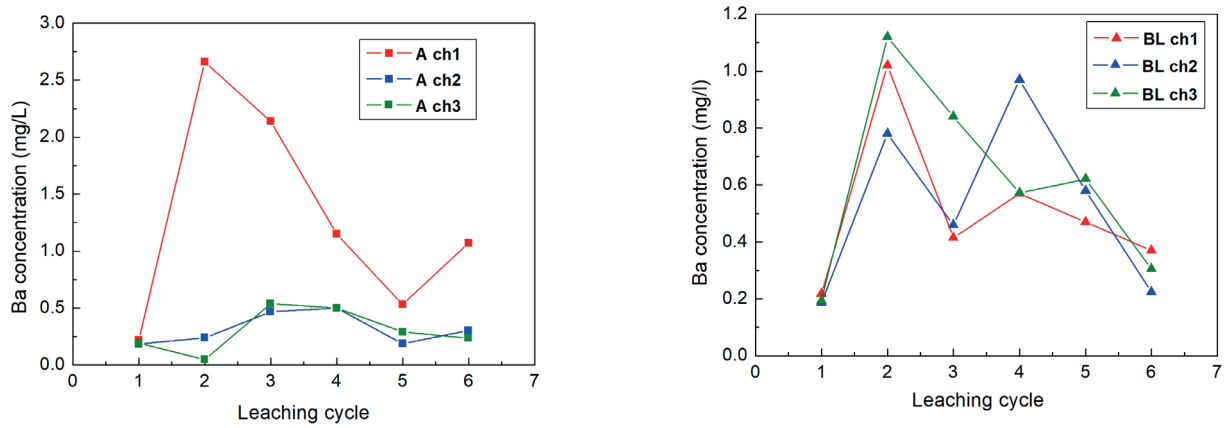

Fig. 6. Chemical (A) and biological-chemical (BL) extraction of Ba from the soil sample.

leaching of soil using chelant ch3. The maximal effect of As(III)/(V) removal was 44 %, what confirmed that the BL enhanced the effect of As(III)/(V) extraction from the contaminated soil.

The over-limited concentration of Cu(II) and partially Sb(III)/(V) in soil can be decreased by chemical and biological leaching. Also, the decrease of other toxic elements and heavy metals was observed, such as Pb(II), Zn(II), Ni(II), Co(II). The concentration of these elements did not exceed the permissible values. After the CHL and BL the toxic elements As(III)/(V) and Ba(II) are still present in the over-limited concentrations in the soil. Effect of their extraction was 44 and 21 %, respectively (Tab. 4). By the combination of biological and chemical leaching as an activity of heterotrophic bacteria and chelants it is possible to remove only mobile amounts of elements, whose can come into food chain through the plant growing in the contaminated soil.

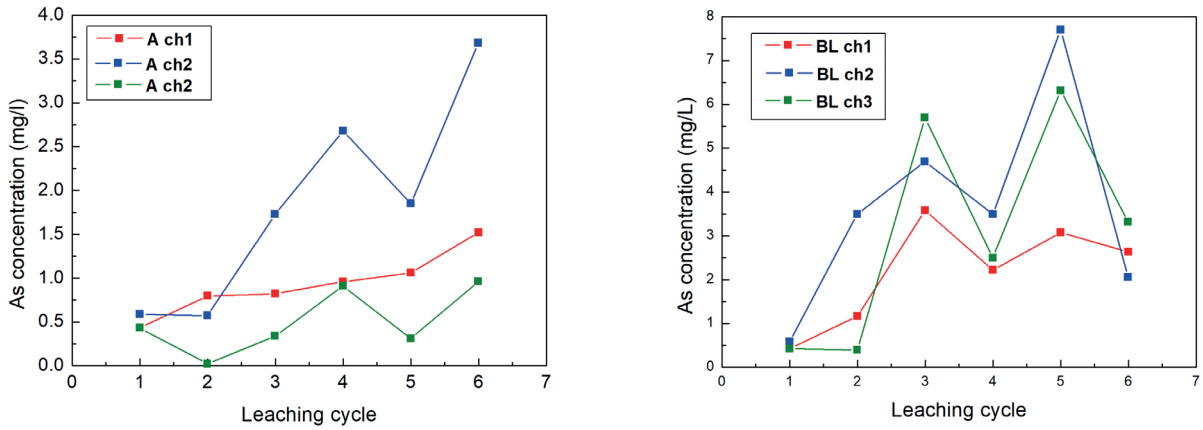

Fig. 7. Chemical (A) and biological-chemical (BL) extraction of As from the soil sample.

Tab. 3

Effect of toxic elements extraction by chemical leaching using ch2 chelant in comparison with bioleaching.

	Initial concentration [mg.kg^{-1}]	Concentration after CHL [mg.kg^{-1}]	Effect of CHL [%]	Concentration after BL [mg.kg^{-1}]	Effect of BL [%]	Difference in CHL and BL [%]
Cu(II)	692	219	68	267	64	– 4
Zn(II)	541	261	52	287	47	– 5
Sb(III)/(V)	61	43	30	43	30	0
Ba(II)	3303	2592	22	2632	20	– 3
As(III)/(V)	364	229	37	208	43	**+ 6**
Pb(II)	143	88	39	82	43	**+ 4**

Verification of the process of chemical and biological leaching of soil

On the basis of the results obtained from the previous test the verification of the CHL and BL of soil sample of weight 1 kg was performed. The applied volume of solution was equal with previous tests, but during the CHL leaching it was decreased up to half (with the aim to decrease amounts of used chelants). It was shown above that the extraction of Cu(II) (partially also Pb(II)) is inhibited by heterotrophic bacteria. On the other hand, higher As(III)/(V) extraction was achieved by BL. For that reason the soil was at first leached by chelant ch1 with the aim to extract heavy metals. Subsequently the chelant ch2 was used to remove the non-biodegradable chelant ch1 as well as the rest of toxic elements from the soil. Finally, the BL was performed to ensure the maximal possible extraction of mobile As(III)/(V).

The chemical analyses of leachates after each cycle pointed at the chemical extraction of Cu(II), Zn(II) and Pb(II). Higher extraction of As(III)/(V), Sb(III)/(V), Ba(II) and Ni(II) was obtained by BL (Fig. 11). The effect of Ba(II) extraction was minimal in comparison with its concentration in the soil. Because the barite is very stable form towards the CHL and BL, and as such is not accessible for plants, it should not be dangerous for underground waters.

This test of chemical and biological leaching in three steps showed the enhance of Cu(II) extraction at 5 %, but a small decrease in As(III)/(V), Ni(II) and Co(II) extraction in comparison with the biological leaching (previous 4 steps test; Tab. 5). The chemical leaching, using chelant ch2, did not influence the As(III)/(V) and Sb(III)/(V) extraction. On the other hand, the bioleaching enhanced the As(III)/(V) removal at 7 %. The effect of leaching obtained from this test is a little bit lower in comparison with 4 steps bioleaching. Considering the decrease of chelants consumption, the difference is not so significant. The concentration of toxic elements As(III)/(V), Ba(II) and Sb(III)/(V) remained still over limited in the soil. But, their mobile phases, whose are the potential source of the contamination of groundwater and agricultural plants were removed successfully.

Conclusion

The study was focused on testing the chemical and chemical-biological methods of toxic elements extraction from the soil. The aim of the study was to outline environmentally friendly as well as cost effective method of the soil decontamination. Four different leaching tests showed that Cu(II), Zn(II) and Pb(II) can be removed by chemical leaching. The biological leaching combined

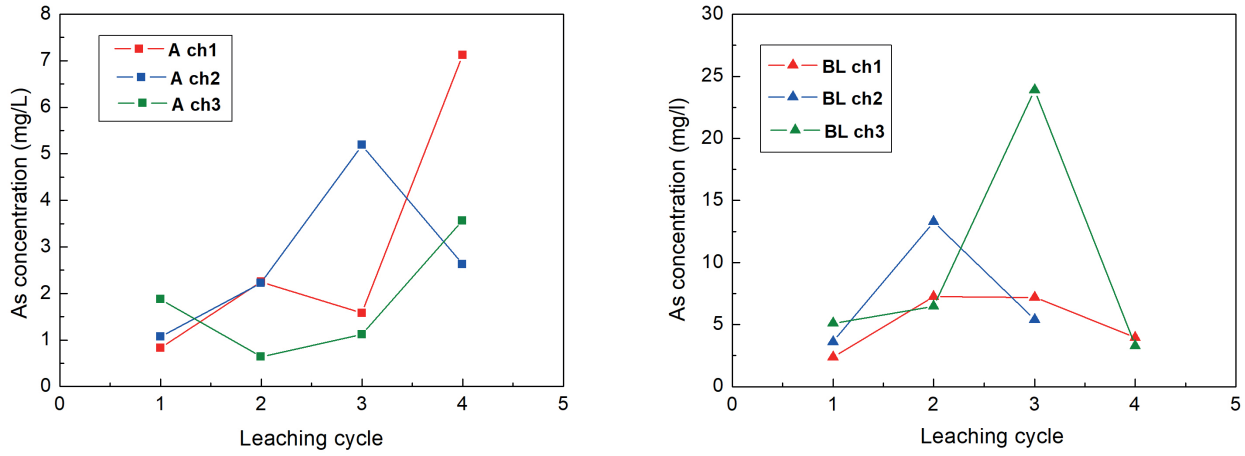

Fig. 8. Extraction of Cu from the soil sample during the bioleaching (BL) in comparison with abiotic control (A).

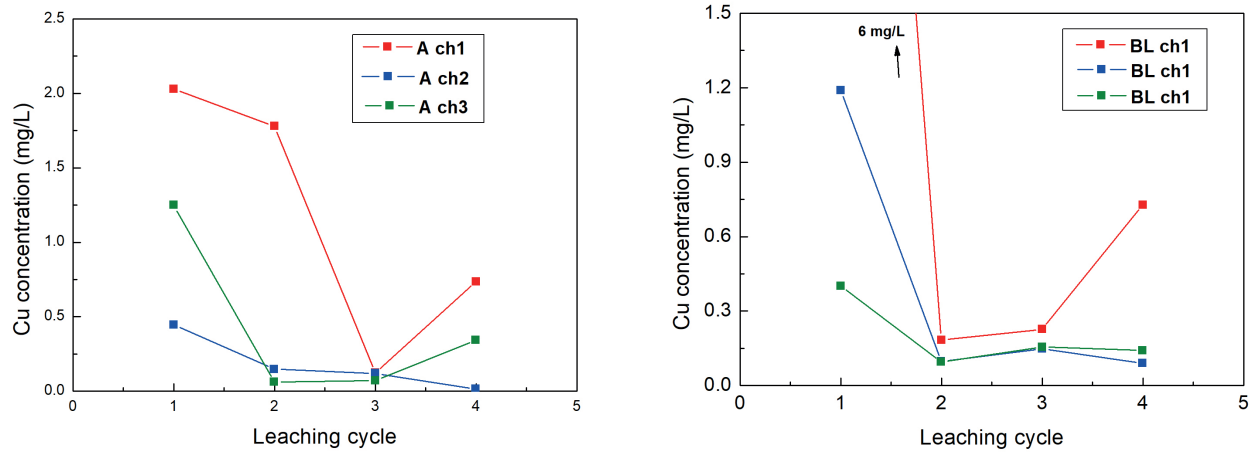

Fig. 9. Extraction of Ba from the soil sample during the bioleaching (BL) in comparison with abiotic control (A).

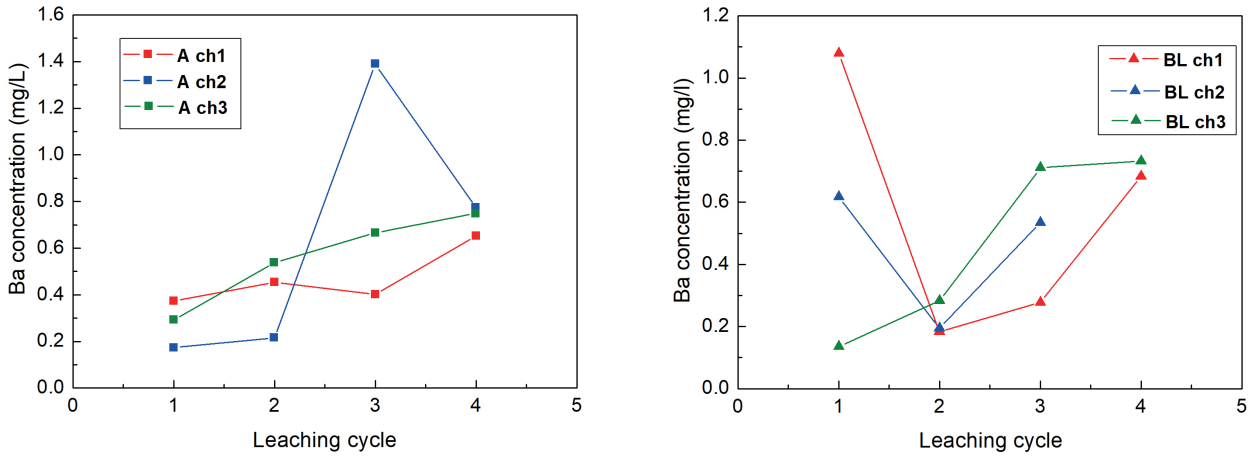

Fig. 10. Extraction of As from the soil sample during the bioleaching (BL) in comparison with abiotic control (A).

Tab. 4
Effect of chemical and biological leaching in extraction of different toxic elements concentrations.

	As(III)/(V) [mg.kg^{-1}]	Cu(II) [mg.kg^{-1}]	Zn(II) [mg.kg^{-1}]	Pb(II) [mg.kg^{-1}]	Ni(II) [mg.kg^{-1}]	Co(II) [mg.kg^{-1}]	Sb(III)/(V) [mg.kg^{-1}]	Ba(II) [mg.kg^{-1}]
Soil	**364**	**692**	541	143	86	25	**61**	**3303**
CHL + BL	**204**	258	276	57	50	7	**42**	**2598**
Effect [%]	**44**	63	49	60	42	72	**31**	21

with the chemical leaching resulted in increase of As(III)/(V) extraction, its mobile forms were leached from the soil. Moreover, for this test, lower amounts of chelants were needed, what decreases the costs on treatment of the contaminated soil. On the basis of obtained results, simply method of bioremediation was draft and tested with positive results:

- chemical leaching with Na_2EDTA [with the aim to remove Cu(II), Zn(II) and Pb(II)],
- chemical leaching with Na_3EDDS (with the aim to remove non-biodegrable chelant and rest of the toxic elements and heavy metals),
- bioleaching of the contaminated soil using less concentrated chelant in the leaching medium with nutrients for the maximal removal of mobile As(III)/(V).

These three steps of soil decontamination should be realized on heaps, where the contaminated soil would be sprinkled by media. The leachates would be collected in basins for further leaching media recycling and heavy metals concentration.

Acknowledgement

The authors are thankful for financial support by the Ministry of Environment of the Slovak Republic based on geological task GT 02 18 *Development of technologies during the remediation process of the contaminated environment*.

References

Bahemmat, M., Farahbakhsh, M. & Shabani, F., 2015: Compositional and metabolic quotient analysis of heavy metal contaminated soil after electroremediation. *Environ. Earth Sci., 74, 4639–4648.*

Beiyuan, J., Tsang, D. C. W., Vali, X. M., Baek, K., Ok, Y. S., Zhang, W., Bolan, N. S., Rinklebe, J. & Li, X.-D., 2018: Combined application of EDDS and EDTA for removal of potentially toxic elements under multiple soil washing schemes. *Chemosphere, 205, 178–187.*

Chatain, V., Bayard, R., Sanchez, F., Moszkowicz, P. & Gourdon, R., 2005: Effect of indigenous bacterial activity on arsenic mobilization under anaerobic conditions. *Environ. Inter., 31, 221–226.*

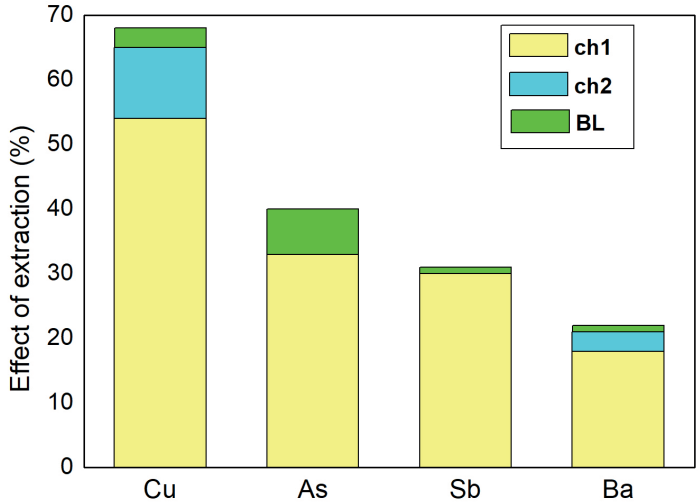

Fig. 11. Effect of chemical and biological leaching on extraction of studied toxic elements.

Tab. 5
Chemical analysis of soil sample after the chemical leaching with chelants ch1 and ch2 and after the biological leaching.

	As(III)/(V) [mg.kg^{-1}]	Cu(II) [mg.kg^{-1}]	Zn(II) [mg.kg^{-1}]	Pb(II) [mg.kg^{-1}]	Ni(II) [mg.kg^{-1}]	Co(II) [mg.kg^{-1}]	Sb(III)/(V) [mg.kg^{-1}]	B(II) [mg.kg^{-1}]
Soil	**364**	**692**	541	143	86	25	**61**	**3303**
CHL, ch1	**244**	317	296	70	65	14	**43**	**2721**
Effect [%]	**33**	54	45	51	24	44	**30**	**18**
CHL, ch2	**245**	242	281	63	68	11	**42**	**2618**
Effect [%]	**33**	65	48	56	21	56	**31**	**21**
BL	**218**	224	275	59	53	8	**42**	**2562**
Effect [%]	**40**	68	49	59	38	68	**31**	**22**

Hashem Md. A., Toda, K. & Ichi-Ohira, S., 2015: Leaching behaviour of arsenite and arsenate from the contaminated sediment by the effect of phosphate ion under anaerobic conditions. *Environ. Earth Sci., 74, 737–743.*

Hauser, L., Tandy, S., Schulin, R. & Nowack, B., 2005: Column extraction of heavy metals from soils using the biodegradable chelating agent EDDS. *Environ. Sci. Technol., 39, 6819–6824.*

Kim, E. J., Lee, J.-Ch. & Baek, K., 2015: Abiotic reductive extraction of arsenic from contaminated soils enhanced by complexation: Arsenic extraction by reducing agents and combination of reducing and chelating agents. *J. Hazard. Mater., 283, 454–461.*

Kim, E. J. & Baek, K., 2015: Enhanced reductive extraction of arsenic from contaminated soils by a combination of dithionite and oxalate. *J. Hazard. Mater., 284, 19–26.*

Kim, E. J., Jeon, E.-K. & Baek, K., 2016: Role of reducing agent in extraction of arsenic and heavy metals from soils by use of EDTA. *Chemosphere, 152, 274–283.*

Lee, K.-Y., Moon, D. H., Lee, S.-H., Kim, K.-W., Cheong, K.-H., Park, J.-H., Ok, Y. S. & Chang, Y.-Y., 2013: Simultaneous stabilization of arsenic, lead, and copper in contaminated soil using mixed waste resources. *Environ. Earth Sci., 69, 1813–1820.*

Li, J.-S., Xue, Q., Wang, P. & Zhang, T.-T., 2015: Enhanced washing for Cr(VI) removal from contaminated soil using EDTA and microwave radiation. *Environ. Earth Sci., 74, 2167–2172.*

Peng, W., Li, X., Xiao, S. & Fan, W., 2018: Review of remediation technologies for sediments contaminated by heavy metals. *J. Soils Sediments, 18, 1701–1719.*

Štyriaková, D., Štyriaková, I., Štyriak, I., Šuba, J., Danková, Z. & Gešperová, D., 2015: Inhibition effect of heterotrophic microorganisms on Cu and Zn cations mobilization from contaminated soil and sediment. *Proc. Earth Planet. Sci. 15, 866–871.*

Štyriaková, I., Štyriak, I., Balestrazzi, A., Calvio, C., Faè, M. & Štyriaková, D., 2016: Metal leaching and reductive dissolution of iron from contaminated soil and sediment samples by indigenous Bacteria and *Bacillus* Isolates. *Soil Sediment Contamin., 25, 519–535.*

Takahashi, R., Fujimoto, N., Suzuki, M. & Endoab, T., 1997: Biodegradabilities of Ethylenediamine-N,N'-disuccinic Acid (EDDS) and other chelating agents. *Biosci. Biotec. Biochem., 61, 1957–1959.*

Tandy, S., Bossart, K., Mueller, R., Ritschel, J., Hauser, L., Schulin, R. & Nowack, B., 2004: Extraction of heavy metals from soils using biodegradable chelating agents. *Environ. Sci. Technol. 38, 937–944.*

Torres, L. G., Lopez, R. B. & Beltran, M., 2012: Removal of As, Cd, Cu, Ni, Pb and Zn from a highly contaminated industrial soil using surfactant enhanced soil washing. *Phys. Chem. Earth, 37–39, 30–36.*

Vandevivere, P., Hammes, F., Verstraete, W., Feijtel, T. & Schowanek, D., 2001: Metal decontamination of soil, sediment, and sewage sludge by means of transition metal chelant [S,S]-EDDS. *J. Environ. Eng. 127, 802–811.*

Vaxevanidou, K., Papassiopi, N. & Paspaliaris, I., 2008: Removal of heavy metals and arsenic from contaminated soils using bioremediation and chelant extraction techniques. *Chemosphere, 70, 1329–1337.*

Wang, S. & Zhao, X., 2009: Review on the potential of biological treatment for arsenic contaminated soils and groundwater. *J. Environ. Manage., 90, 2367–2376.*

Wang, G., Zhang, S., Zhong, Q., Xu, X., Li, T., Jia, Y., Zhang, Y., Peijnenburg, W. J. G. M. & Vijver, M. G., 2018: Effect of soil washing with biodegradable chelators on the toxicity of residual metals and soil biological properties. *Sci. Total Environ., 625, 1021–1029.*

Wolthers, M., Butler, I. B. & Rickard, D., 2007: Influence of arsenic on iron sulfide transformations. *Chem. Geol., 236, 217–227.*

Xu1, Y., Li J., Xia, W., Sun, Y., Qian, G. & Zhang, J., 2019: Enhanced remediation of arsenic and chromium co-contaminated soil by electrokinetic-permeable reactive barriers with different reagents. *Environ. Sci. Pollut. Res. Int., 26, 3392–3403.*

Yamamura, S., Yamamoto, N., Ike, M. & Fujita, M., 2005: Arsenic extraction from solid phase using a dissimilatory arsenate-reducing bacterium. *J. Biosci. Bioeng., 100, 219–222.*

Yao, Z., Li, J., Xie, H. & Yu, C., 2012: Review on remediation technologies of soil contaminated by heavy metals. *Proc. Environ. Sci., 16, 722–729.*

Zeng, X., Wei, S., Sun, L., Jacques, D. A., Tang, J., Lian, M., Ji, Z., Wang, J., Zhu, J. & Xu, Z., 2015: Bioleaching of heavy metals from contaminated sediments by the Aspergillus niger strain SY1. *J. Soils Sed., 15, 1029–1038.*

Odstraňovanie toxických prvkov z minerálnych častíc kontaminovanej pôdy chemickým a biologickým lúhovaním

S cieľom odstrániť toxické prvky z kontaminovanej pôdy z lokality Richnava sa realizovali testy chemického a biologického lúhovania pôdy. Vzorky pôdy boli odobrané z lokality Richnava (R1, R2 a R3). Vzorka pôdy R1 pochádzala z oblasti kontaminovanej nánosmi rieky Hornád, ktorá preteká lokalitami zaťaženými metalurgickým priemyslom, ako aj niekdajšou banskou činnosťou. Chemická analýza poukázala na jej znečistenie toxickými prvkami v poradí Ba > As > Hg > Sb > Cu. Koncentrácia Zn, Pb, Cd a Ni neprekračovala hodnotu stanovených koncentračných limitov. V ďalších dvoch vzorkách sledované toxické prvky neprekračovali

povolené limitné hodnoty ich koncentrácie v pôde (tab. 1). Preto na ďalšie experimenty bola zvolená vzorka pôdy R1. Röntgenovodifrakčná (rtg.) analýza a elektrónová mikroanalýza ukázali, že As sa prioritne viaže s oxidmi železa (hydroxidmi) pokrývajúcimi zrná silikátových a karbonátových minerálov (obr. 1 a 2). Na základe uvedených analýz sa predpokladala aj vyššia odolnosť Fe povlakov sulfidov proti chemickému a biologickému lúhovaniu. Chemické lúhovanie sa realizovalo použitím troch rôznych chelátov: Na_2EDTA (médium ch1), Na3 EDDS (ch2) a ich zmes v pomere 1 : 1 (ch3). Počas chemického lúhovania klesala koncentrácia extrahovaných sledovaných prvkov v poradí Cu > Zn > Pb, pričom v prípade As a Ba sa získala vo výluhoch len veľmi nízka koncentrácia. Pri lúhovaní chelátom ch1 sme pozorovali viac extrahovaného Pb, zatiaľ čo pri lúhovaní Cu a Zn bol účinnejší chelát ch2. Výsledky extrakcie pri ostatných prvkoch klesali v poradí Mn > Fe > Ni > As > Cd > Ba > Sb, pričom vyšší účinok odstránenia Mn, Fe, Ni, As a Sb bol dosiahnutý pri použití chelátu ch2 (obr. 3). Väzby Ba a As v mineráloch boli silné a ich kumulatívna koncentrácia v roztoku po prvej perkolácii média predstavovala hodnotu nižšiu ako 1 mg . kg^{-1}. Najvyššia účinnosť lúhovania sa dosiahla pri Cu. Na zníženie nadlimitnej koncentrácie Sb a As v pôde by bolo potrebné opakovanie niekoľkých cyklov chemického lúhovania.

Druhý lúhovací test sa realizoval použitím autochtónnych baktérií a heterotrofných baktérií izolovaných zo sedimentov (Štyriaková et al., 2016). Extrakcia ťažkých kovov a toxických prvkov sa sledovala kombinovaným testom 15-dňového biolúhovania a 3-dňového chemického lúhovania s 2 mM chelátom. Výsledky sa porovnávali s abiotickou kontrolou (chemické lúhovanie pôdy 10 mM chelátom) v rovnakých časových intervaloch (schéma 1). V prvých dvoch perkolačných cykloch sa prejavil výrazný vplyv chemického lúhovania na odstránenie Cu. Počas biolúhovania koncentrácia Cu poklesla už v druhom perkolačnom cykle. Kombinácia chemického a následného biologického lúhovania umožnila pokles obsahu Cu vo vzorke pôdy o 64 %. Účinnosť odstránenia Sb a Ba bola rovnaká ako pri použití 10 mM chelátu v chemickom lúhovaní. Kombinované lúhovanie však umožnilo odstránenie 43 % As, čo predstavovalo o 6 % viac ako pri úprave pôdy chemickým lúhovaním 10 mM chelátom (tab. 3). Aj keď účinnosť odstránenia sledovaných prvkov touto kombinovanou metódou bola porovnateľná s účinnosťou chemického lúhovania pôdy, kombinovaná metóda je oveľa vhodnejšia. Dôvodom je použitie menšieho množstva chelátov, čo je dôležité z environmentálneho hľadiska, najmä pri použití biologicky nedegradovateľného Na_2EDTA (Takahashi et al., 1997; Wang et al., 2018).

Vzorka po chemickom lúhovaní 10 mM chelátom z predchádzajúceho testu (abiotickej kontroly) sa počas dvoch mesiacov biologicky lúhovala v štvorstupňovom perkolačnom cykle s použitím média obsahujúceho 2 mM chelát a živiny a porovnávala sa s abiotickou kontrolou (chemické lúhovanie 2 mM chelátom; schéma 2). Iba v prvom lúhovacom cykle sme pozorovali čiastočnú extrakciu Cu (obr. 8). Koncentrácia Ba aj napriek jeho vysokému obsahu v pôde dosiahla iba 2 mg . l^{-1} (obr. 9). Bárium je pevne viazané v minerálnej fáze baritu, ktorý je veľmi odolný proti biologickému lúhovaniu. Mobilná fáza v testovanej vzorke predstavovala iba 20 % Ba. Najvyššia koncentrácia As bola extrahovaná pri použití média ch3 (obr. 10). Maximálna účinnosť odstránenia As dosiahla 44 %. Chemické a biologické lúhovanie viedlo k poklesu koncentrácie Cu v pôde a k čiastočnému poklesu koncentrácie Sb, Pb, Zn, Ni a Co. As a Ba naďalej ostávali v koncentrácii prekračujúcej ich dovolené limitné hodnoty v pôde (tab. 4). Biologicko-chemické lúhovanie ukázalo, že týmto spôsobom je možné odstrániť iba kontaminanty v mobilnej fáze, ktoré môžu vstupovať do potravinového reťazca prostredníctvom plodín pestovaných v kontaminovanej pôde.

Posledný test sa uskutočnil na overenie výsledkov získaných z predchádzajúcich lúhovacích experimentov. Realizoval sa na vzorke pôdy s hmotnosťou 1 kg, pričom objem jednotlivých médií korešpondoval s objemom v predchádzajúcich testoch. Pri chemickom lúhovaní sa však použil polovičný objem roztokov s cieľom znížiť spotrebu chelátov. Vzorka sa najprv lúhovala chemicky chelátom ch1 s cieľom odstrániť ťažké kovy ako Cu, Zn a Pb. Následne sa použilo médium s chelátom ch2, aby sa odstránili zvyšné mobilné fázy kontaminantov, ale najmä, aby sa z pôdy odstránil biologicky nedegradovateľný chelát. Posledným krokom bolo biologické lúhovanie zameraná na maximálne odstránenie As z pôdy. Opakovaný trojstupňový test na jednej strane zvýšil extrahované množstvo Cu o 5 % v porovnaní so štvorstupňovým perkolačným testom, na druhej strane sme pozorovali čiastočný pokles v extrakcii As, Ni a Co po chemickom lúhovaní. Biologické lúhovanie zvýšilo odstránenie As ešte o 7 % (tab. 5). Táto kombinovaná metóda je veľmi perspektívna, pretože na extrakciu toxických prvkov využíva menšie množstvo chelátov. Navyše, je aj finančne nenáročná a umožňuje odstránenie mobilných fáz kontaminantov z pôdy, ktoré sú potenciálnym zdrojom znečistenia vody a kontaminácie rastlín.

Doručené / Received: 7. 10. 2019
Prijaté na publikovanie / Accepted: 2. 12. 2019

Mineralia Slovaca, Web ISSN 1338-3523, ISSN 0369-2086
51 (2019), 217 – 232, © Authors 2019. CC BY 4.0

Geochemicko-mineralogický prieskum pôd ovplyvnených banskou činnosťou v oblasti opusteného Sb ložiska Čučma

ĽUBOMÍR JURKOVIČ[1], JANA JUHÁSOVÁ[2], TATIANA KULIKOVA[1], TOMÁŠ FARAGÓ[1], ŠTEFAN MÉRES[1], TOMÁŠ KLIMKO[1], PETER ŠOTTNÍK[3], EDGAR HILLER[1], LUCIA NEMČEK[4] a MAREK BUJDOŠ[4]

Univerzita Komenského v Bratislave, Prírodovedecká fakulta, Ilkovičova 6, 842 15 Bratislava
[1]Katedra geochémie, [2]Katedra environmentálnej ekológie, [3]Katedra ložiskovej geológie,
[4]Ústav laboratórneho výskumu geomateriálov, lubomir.jurkovic@uniba.sk

Geochemical and mineralogical exploration of soils affected by mining activities at the abandoned Sb-deposit Čučma

Abstract: One of the most important sources of soil contamination with metals and metalloids is mining and processing of mined ores. Old tailing ponds and dumps affect the surrounding environment mainly by releasing potentially toxic trace elements, and thus contribute to contamination of the natural environment, including soils. The area of abandoned antimony deposit Čučma (eastern Slovakia) with unliquidated and unsecured mining wastes belongs to environmental burden, which should be monitored and eventually remediated. The main objective of this article was to (i) determine the basic physicochemical properties of mining soils at the former Čučma antimony deposit and total concentrations of selected trace elements with the emphasis on antimony (Sb) and arsenic (As), (ii) characterize mineralogy of these soils and (iii) evaluate the mobility of the two metalloids by means of extraction experiments with distilled water. The soils of the former antimony deposit Čučma showed a wide range of pH values (2.84 – 7.45 for a soil depth of 0 – 15 cm and 2.82 – 7.74 for a soil depth of 15 – 30 cm) and the organic carbon content varied from 0.13 wt. % to 19.1 wt. % with a median value of 3.67 wt. % in the soil surface layer, with a decrease to a median value of 1.21 wt. %. Total concentrations of the main contaminants Sb and As in the soils from 0 – 15 cm were in the range from 6.2 mg . kg^{-1} to 142 322 mg . kg^{-1} with a median of 433 mg . kg^{-1} and 16 – 2 253 mg . kg^{-1} with a median of 116 mg . kg^{-1}, respectively, and significantly correlated with each other ($R^2 = 0.87$ at $p < 0.000\ 1$). The indication (ID = 65 mg . kg^{-1} for As and 25 mg . kg^{-1} for Sb) and intervention (IT = 140 mg . kg^{-1} for As and 80 mg . kg^{-1} for Sb) criteria for industrial areas were exceeded in most soil samples and the median concentrations of Sb and As were far higher than their median concentrations within the soils of Slovakia (0.70 mg . kg^{-1} and 7.20 mg . kg^{-1} for Sb and As in A-horizon, respectively). Despite the high total concentrations of these metalloids in some soils irrespective of depth, the extractable proportions of Sb and As were low (median of 0.46 % and 0.50 % for Sb and 0.60 % and 0.70 % for As at soil depths of 0 – 15 cm and 15 – 30 cm, respectively). The low mobility of Sb and As has been interpreted as a result of their incorporation into stable secondary mineral phases under oxidizing conditions, in particular Fe-oxy-hydroxides and, in the case of Sb, also due to the formation of separate secondary mineral phases such as romeite ($Ca_2Sb_2O_7$), cervantite (Sb_2O_4) and stibiconite [$Sb_3O_6(OH)$]. The presence of all these secondary solid phases in the investigated soils was confirmed by optical microscopy, X-ray diffraction and electron micro-probe analyses. Slightly higher mobility of As and Sb in soils from 15 – 30 cm depth than their mobility in soils from the top layer does not exclude the influence of organic matter on the release of these elements into natural waters.

Key words: antimony, arsenic, contamination, mine, mineralogy, mobility, soil

Graphical abstract

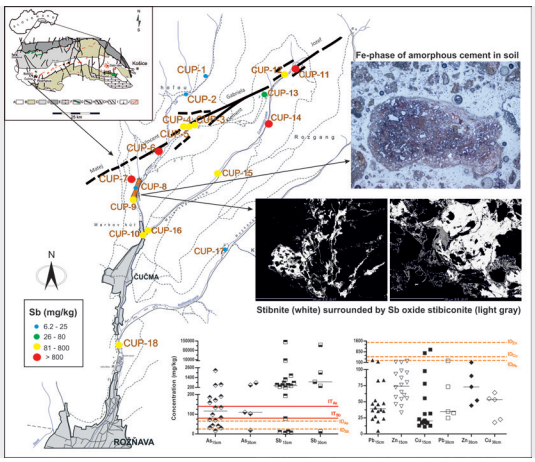

Highlights

- The soils at former antimony mines in Čučma (Eastern Slovakia) are contaminated mainly with antimony (Sb) and arsenic (As)
- Secondary Sb minerals and Fe oxy-hydroxides with variable contents of Sb and As commonly occur and together with organic matter control the metalloid mobility in the soils
- Water-soluble portion of Sb and As is low despite their high total contents in the soil

Úvod

Jedným z významných geochemických a environmentálnych problémov súčasnosti je exaktné hodnotenie kontaminácie životného prostredia, ktorá je často odrazom prirodzených geologických procesov v krajine v kombinácii s nevhodnými ľudskými aktivitami. Medzi časté príčiny nadmerného výskytu potenciálne toxických prvkov v prostredí patrí ťažba a spracovanie nerastných surovín. Napriek svojej pomerne malej rozlohe patrí Slovensko medzi krajiny s vysokou početnosťou environmentálnych záťaží, ktoré sú viazané na intenzívnu banskú a úpravnícku činnosť. Opustené oblasti rudných ložísk zostávali dlhé roky nepovšimnuté, pričom sa len pomerne málo vedelo o možných environmentálnych rizikách pre životné prostredie vyplývajúcich z geochemicko-mineralogických osobitostí týchto oblastí. Staré banské diela, haldy a odkaliská ovplyvňujú svoje okolie v dôsledku uvoľňovania prítomných potenciálne toxických stopových prvkov a prispievajú ku kontaminácii prírodného prostredia (Bajtoš et al., 2012; Šottník et al., 2015). Ťažobné a spracovateľské aktivity sa často vyznačujú rozsiahlym negatívnym dosahom na všetky zložky životného prostredia. Znečistenie pôdnych substrátov, vodných zdrojov, ovzdušia, ako aj celkové zmeny v krajine patria medzi najzávažnejšie dôsledky banskej činnosti, ktorých prejav nadobúda regionálny charakter. Po skončení ťažby a spracovania nerastných surovín predstavuje deponovaný ťažobný odpad významné riziko a potenciálny zdroj znečistenia. V dôsledku vystavenia veternej erózii a prirodzeným procesom zvetrávania minerálnych fáz môžu prispievať k tvorbe kyslých banských výluhov v procese drenáže (Helios Rybicka, 1996; Brusseau et al., 2006). Postupná mobilizácia rizikových látok môže negatívne ovplyvňovať pôdne substráty a prírodné vody v oblastiach opustených ložísk (Jurkovič et al., 2010, 2016; Mangová a Lintnerová, 2015; Bajtoš, 2016; Fľaková et al., 2017 a i.).

Baníctvo na Slovensku má veľmi dlhú históriu. Na väčšine bývalých ložísk boli práce pozastavené už pomerne dávno. V súčasnosti sa ložiská spomínajú hlavne ako oblasti environmentálnych záťaží so špecifickými kontaminantmi, ako sú napríklad potenciálne toxické stopové prvky (PTSP). Medzi také prvky patrí aj arzén (As) a antimón (Sb), ktoré sú známe svojimi karcinogénnymi a mutagénnymi účinkami a schopnosťou spôsobovať chronické ochorenia ľudí. Prítomnosť kovov, a hlavne ich zvýšeného množstva (aj v dôsledku lokálnej prirodzenej vysokej koncentrácie v horninovom prostredí), môže predstavovať vážny environmentálny problém (Rapant et al., 2006; Ženišová et al., 2009). K takýmto potenciálnym zdrojom znečistenia patrí aj lokalita opusteného Sb ložiska Čučma ležiaca v oblasti Spišsko-gemerského rudohoria, ktoré predstavuje najvyššiu koncentráciu rudných ložísk na Slovensku (Rojkovič, 2003).

Opustené Sb ložisko Čučma leží v južnom pruhu Spišsko-gemerského rudohoria. Ťažobná činnosť sa začala už v 13. storočí, najväčší rozsah však dosiahla v 19. storočí. V čase pred 2. svetovou vojnou bolo vďaka tejto ložiskovej oblasti bývalé Československo na šiestom mieste vo svete v ťažbe antimónových rúd. Širšia oblasť ložiska patrila k najvýznamnejším producentom Sb v rámci Európy (najmä žily Vincent, Gabriela, Klement a Matej) (Rozložník et al., 1987). Hlavným minerálom kremenných žíl bol antimonit, sprevádzaný mnohými ďalšími minerálmi (napríklad siderit, pyrit, arzenopyrit, sfalerit a iné). Ťažba Sb na ložisku sa skončila v roku 1952, pričom neskoršie geologické prieskumy oblasti nezaznamenali priaznivé výsledky (Grecula et al., 1995; Rojkovič, 2003).

V súčasnosti je časť lokality opusteného Sb ložiska Čučma zaradená v Registri environmentálnych záťaží (REZ) medzi pravdepodobné environmentálne záťaže. V REZ je evidovaná pod označením RV (003)/Čučma – bývalý banský závod (SK/EZ/RV/777) a je evidovaná aj v registri úložísk (IS NTO) ako Čučma – Odkalisko Čučma. Predchádzajúce prieskumné a vedecké práce potvrdili, že za hlavný zdroj znečistenia v oblasti sa považujú výtoky banskej vody a odpadový materiál zanechaný na území (Hiller et al., 2012). Uvoľňovanie Sb a As v dôsledku zvetrávania antimonitu a arzenopyritu zo spracovaného horninového materiálu aj dnes spôsobuje šírenie stopových prvkov do okolitého životného prostredia (Lalinská et al., 2010).

Cieľom článku je detailné geochemické a mineralogické štúdium pôdnych substrátov z územia opusteného Sb ložiska v Čučme a experimentálna kvantifikácia mobilizovateľného podielu potenciálne toxických stopových prvkov v zmysle hodnotenia environmentálnych záťaží na Slovensku. Výsledky prezentované v štúdii majú význam pri exaktnom vyhodnotení aktuálnej kontaminácie pôdnych substrátov, ktorá je výsledkom prirodzených zvetrávacích procesov materských hornín tejto časti Slovenského rudohoria v kombinácii s dlhodobou ťažobnou činnosťou a nevhodným deponovaním ťažobného odpadu v oblasti.

Geologická stavba študovanej oblasti

Opustené Sb ložisko Čučma je situované vo východnej časti Slovenského rudohoria a patrí do gemerickej tektonickej jednotky Západných Karpát. Gelnická skupina, ktorá má v tejto oblasti najväčší rozsah, predstavuje vývojovú etapu od vrchného kambria po spodný devón. Tvorí ju nízko metamorfovaný staropaleozoický komplex sedimentárnych a vulkanických hornín, do ktorých intrudujú permské granitoidné telesá. Sedimentárne súbory pozostávajú z hrubnúcich flyšových megacyklov s terigénnym, a hlavne vulkanogénnym materiálom (smerom nahor). Bázy cyklov sú tvorené pelagickými silicitmi (lyditmi),

anoxickými bridlicami a miestami aj karbonátmi. Vulkanity, prevažne vulkanoklastiká, majú kyslý, bázický, prevažne však intermediárny charakter (Bajaník et al., 1983; Kobulský et al., 2006; Šimurková et al., 2016). Kremeno-antimonitové žily (obr. 1) vytvárajú oblúkovitú líniu východno-západného smeru dlhú približne 50 km, ktorá sa tiahne od mesta Rožňava (ložiská Betliar a Čučma) po Košice (ložisko Zlatá Idka).

Najvýraznejšie a najvýznamnejšie antimonitovo-zlatonosné ložiská sa nachádzajú v čučmianskej rudonosnej štruktúre. Minerálna výplň antimonitových žíl je prevažne kremeňovo-sulfidická. Pozostáva najmä z kremeňa a antimonitu, častý je aj pyrit, menej arzenopyrit, zriedkavejšie sú sulfidy Pb, Zn, As a karbonáty (Chovan et al., 1994; Bakoš et al., 2004). Podľa Rojkoviča (2003) na základe paragenetických štúdií sa vyčlenili 4 mineralizačné periódy: kremenná, karbonátová, kremeňovo-sulfidická a kalcitová. Kremenná perióda je v závislosti od bezprostrednej blízkosti granitovej intrúzie vyššie termálna a minerálna asociácia potvrdzuje topominerálny vplyv granitov a porfyroidov pri jej vzniku (kremeň, albit, chlorit, turmalín, sericit). Karbonátová perióda je vyvinutá len na lokalite Straková. Kremeňovo-sulfidická perióda má samostatnú tektonickú pozíciu a jej zloženie je najpestrejšie (polymetalická a antimonitová mineralizácia). Klimko et al. (2009) opísali predpokladaný vývoj hydrotermálnej mineralizácie

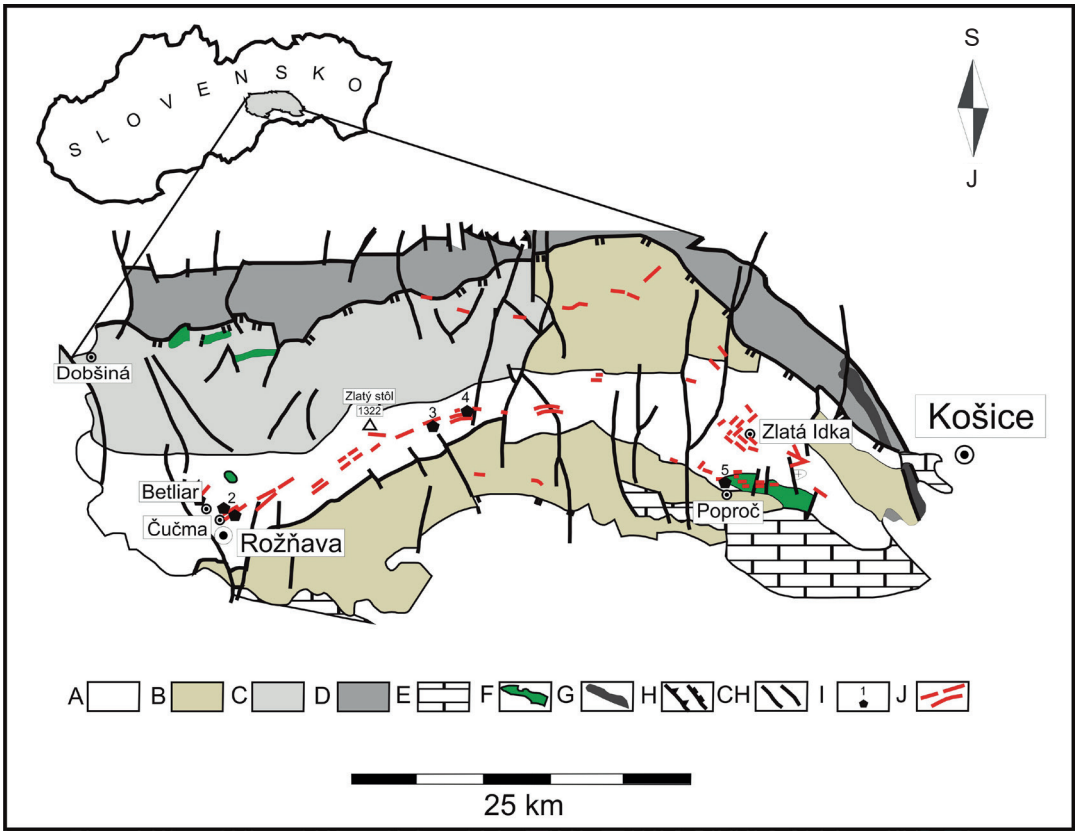

Obr. 1. Geologická mapa južnej časti Spišsko-gemerského rudohoria s vyznačeným priebehom antimonitových žíl (antimonitový pás). A – metapieskovce, fylity, karbonáty, lydity a kyslé vulkanity (súvrstvie Bystrého potoka; ordovik – silúr); B – metapieskovce, fylity, karbonáty a kyslé vulkanity (drnavské súvrstvie; silúr – spodný devón); C – sericiticko-chloritické fylity, metapieskovce a zlepence, metavulkanity, karbonáty a lydity (vlachovské súvrstvie; vrchné kambrium – spodný silúr); D – metapieskovce, fylity a spilitovo-keratofýrové vulkanity (smrečinské súvrstvie; spodný až vrchný devón?); E – pestré kaolínové íly, piesky a štrky (pont); F – biotitické až dvojsľudové granity (neskorovariské); G – metamorfované pieskovce a zlepence, fylity, bázické vulkanity, dolomity a magnezity (lubenícke súvrstvie; visén – starší namur); H – plochy násunov 1. a 2. rádu; CH – zlomy; I – antimonitové ložiská (1 – Betliar-Straková; 2 – Čučma; 3 – Bystrý potok; 4 – Štofova dolina; 5 – Poproč); J – antimonitové žily (podľa Klimka et al., 2009).

Fig. 1. Geological map of the southern part of Spiš-Gemer Ore Mts. with course of stibnite veins (stibnite zone). A – metasandstones, phyllites, carbonates, cherts, acid volcanics (Bystrý potok Fm.; Ordovician – Silurian); B – metasandstones, phyllites, carbonates, cherts, acid volcanics (Drnava Fm.; Silurian – Lower Devonian); C – sericite-chlorite phyllites, metasandstones and conglomerates, metavolcanics, carbonates, cherts (Vlachovo Fm.; Upper Cambrian – Lower Silurian); D – metasandstones, phyllites, spilite-keratophyre volcanics (Smrečinka Fm.; Middle – Upper Devonian?); E – variegated kaolinite clayes, sands, gravels, rate lignite seams (Pontian); F – biotite to two-mica granites (Upper Hercynian); G – metamorphosed sandstones and conglomerates, phyllites, mafic volcanics, dolomites and magnesites (Lubeník Fm., Visean – Lower Namurian); H – overthrust lines, first and second order; CH – faults; I – antimony deposits (1 – Betliar-Straková; 2 – Čučma; 3 – Bystrý potok; 4 – Štofova dolina; 5 – Poproč); J – stibnite veins (according Klimko et al., 2009).

od najstaršieho štádia: *1. turmalínové štádium* (kremeň, turmalín a chlorit); *2. pyritové štádium* (kremeň, pyrit a arzenopyrit); *3. sfaleritové štádium* (karbonát, kremeň, sfalerit, chalkopyrit, tetraedrit, bournonit a tintinait); *4. galenitové štádium* (boulangerit a galenit); *5. antimonitové štádium* (kremeň, dolomit, antimonit, bertierit, senarmontit, jamesonit, chalkostibit a zinkenit).

Metodika práce

Pre potreby štúdia geochemických a mineralogických vlastností pôd z oblasti opusteného Sb ložiska Čučma sa počas terénneho výskumu odobrali vzorky pôd v okolí potoka Laz, Čučmianskeho potoka a Rožňavského potoka. Po odstránení rastlinného pokryvu boli vzorky odobrané pôdnym vrtákom v zmysle horizontálneho princípu vzorkovania pôd (Čurlík a Jurkovič, 2012). V závislosti od lokálnych podmienok pôdneho profilu sa odber uskutočnil v dvoch hĺbkových horizontoch: 0 – 15 cm (18 vzoriek) a 15 – 30 cm (5 vzoriek). Schematická lokalizácia odberných miest (18) je uvedená na obr. 2.

Vzorky pôdnych substrátov sa spracúvali v laboratóriu Katedry geochémie PriF UK v Bratislave. Odobraný pôdny materiál sa vysušil (pri laboratórnej teplote zhruba 25 °C, voľne na konštantnú hmotnosť), homogenizoval a preosial (frakcia < 2 mm). Následne podľa záväznej metodiky pre pôdy a zeminy (Fiala et al., 1999) sa zmerali hodnoty pôdnej reakcie (pH) (aktívna, výmenná) a elektrickej vodivosti (EC) pomocou multimetra typu WTW pH 340i. Chemické analýzy pôdnych substrátov sa realizovali v akreditovaných laboratóriách spoločnosti ACME Analytical Laboratories Ltd. (Vancouver, Kanada) metódami ICP-OES, resp. ICP-MS (typ rozkladu pôdnych substrátov – *aqua regia*). Stanovenie obsahu karbonátov a organického uhlíka sa urobilo na základe Ťjurinovej metódy s modifikáciou Nikitina (Fiala et al., 1999). Zrnitostné zloženie pôd sa študovalo pipetovacou metódou s neopakovanou sedimentáciou podľa Nováka (Fiala et al., 1999) v laboratóriách PriF UK v Bratislave.

Na účely mineralogického štúdia pôd sa vybrané vzorky rozdrvili v achátovej miske a preosiali na frakciu < 0,16 mm. Vzorky sa následne mleli s Al_2O_3 (vnútorný štandard) na špeciálnom mlyne (McCrone Micronizing Mill, KLG PriF UK, podľa metodiky Środoňa et al., 2001). Získané vzorky sa zaslali na RTG difrakčnú analýzu (laboratóriá Ústavu vied o Zemi SAV v Bratislave – difraktometer PHILLIPS PW 1710 pri použití CuKα). Na mikroskopické štúdium pôd sa z pevnej fázy vzoriek vytvorili leštené výbrusy, ktoré sa študovali viacerými mineralogickými metódami. Hlavnými mineralogickými metódami boli mikroskopia v odrazenom, prechádzajúcom a polarizovanom svetle. Minerálne fázy sa študovali na prístroji CAMECA SX 100 (metódy EDS, BSE a WDS, ŠGÚDŠ Bratislava) pri nasledujúcich podmienkach: ZAF korekcia, urýchľovacie napätie 15 – 20 kV, vzorkový prúd 20 nA a priemer elektrónového lúča 1 – 10 µm. Použité štandardy merania: Si Kα – SiO_2; Al Kα – ortoklas; Pb Mα – PbS; S Kα – $CuFeS_2$; Fe Kα – $CuFeS_2$; Sb Lß – Sb_2S_3; As Kß – FeAsS; Co Kα – Co; Ni Kα – Ni; Cu Kα – $CuFeS_2$; Zn Kα – ZnS; Mn Kα – rodonit; Ca Kα – wollastonit; P Kα – apatit.

Exaktné hodnotenie kontaminácie pôd bolo rozšírené o štúdium potenciálnej mobilizácie vybraných stopových prvkov prostredníctvom statických lúhovacích experimentov (Hiller, 2003; Vítková et al., 2009; Ettler et al., 2012; Hlodák et al., 2015), ktoré poskytujú dôležité informácie o ich správaní v životnom prostredí. Lúhovacie experimenty sa zrealizovali na 14 vzorkách s preukázanou kontamináciou stopovými prvkami: 10 substrátov z vrchného hĺbkového horizontu a 4 substráty zo spodného hĺbkového horizontu. Experimentálny postup reprezentovali jednokrokové extrakcie pomocou destilovanej vody s cieľom simulácie uvoľňovania ľahko mobilizovateľných podielov prvkov v geologickom prostredí vplyvom prírodných procesov (napríklad zrážková činnosť). Extrahovateľný podiel prvku bol stanovený z vodnej suspenzie v pomere pevná fáza : roztok 1 : 10 (w/v). Získané suspenzie sa premiešavali na laboratórnom multirotátore (Biosan Multi Bio RS-24) počas 2 hodín (60 ot . min^{-1}) a po skončení extrakcie sa centrifugovali a prefiltrovali cez 0,45 µm membránový filter (Pragopor 6). V rámci prevencie proti zrážaniu prvkov sa výluhy stabilizovali pridaním 2 % HNO_3 (Ettler et al., 2007). Z hľadiska zabezpečenia homogenity výsledkov sa všetky extrakcie robili duplicitne. Chemické analýzy získaných výluhov sa urobili na prístroji EcaFlow 150 GLP metódou prietokovej rozpúšťacej chronopotenciometrie.

Získané hodnoty celkovej koncentrácie arzénu a antimónu v študovaných pôdach sa vyhodnotili v súlade so smernicou MŽP SR č. 1/2015-7 na vypracovanie analýzy rizika znečisteného územia, ktorá definuje limitné hodnoty kontaminantov [indikačné kritérium (ID) a intervenčné kritérium (IT) v prípade obytných, resp. priemyselných zón]. ID vyjadruje hraničnú hodnotu koncentrácie znečisťujúcej látky, ktorá predstavuje možné ohrozenie zdravia a životného prostredia. IT je hodnota koncentrácie s vysokou pravdepodobnosťou ohrozenia zdravia a životného prostredia.

Závislosti medzi obsahom prvkov a niektorými fyzikálno-chemickými vlastnosťami pôd vyjadrené pomocou koeficientov korelácie boli vypočítané v prostredí softvéru GraphPadPrism.

Výsledky a diskusia

Fyzikálno-chemické vlastnosti pôd

Z výsledkov laboratórnych analýz pôdnych substrátov je zrejmé, že odobrané vzorky vykazujú významnú heterogenitu prejavujúcu sa v prípade jednotlivých sledovaných parametrov (tab. 1). Hodnoty pôdnej reakcie pri pôdach

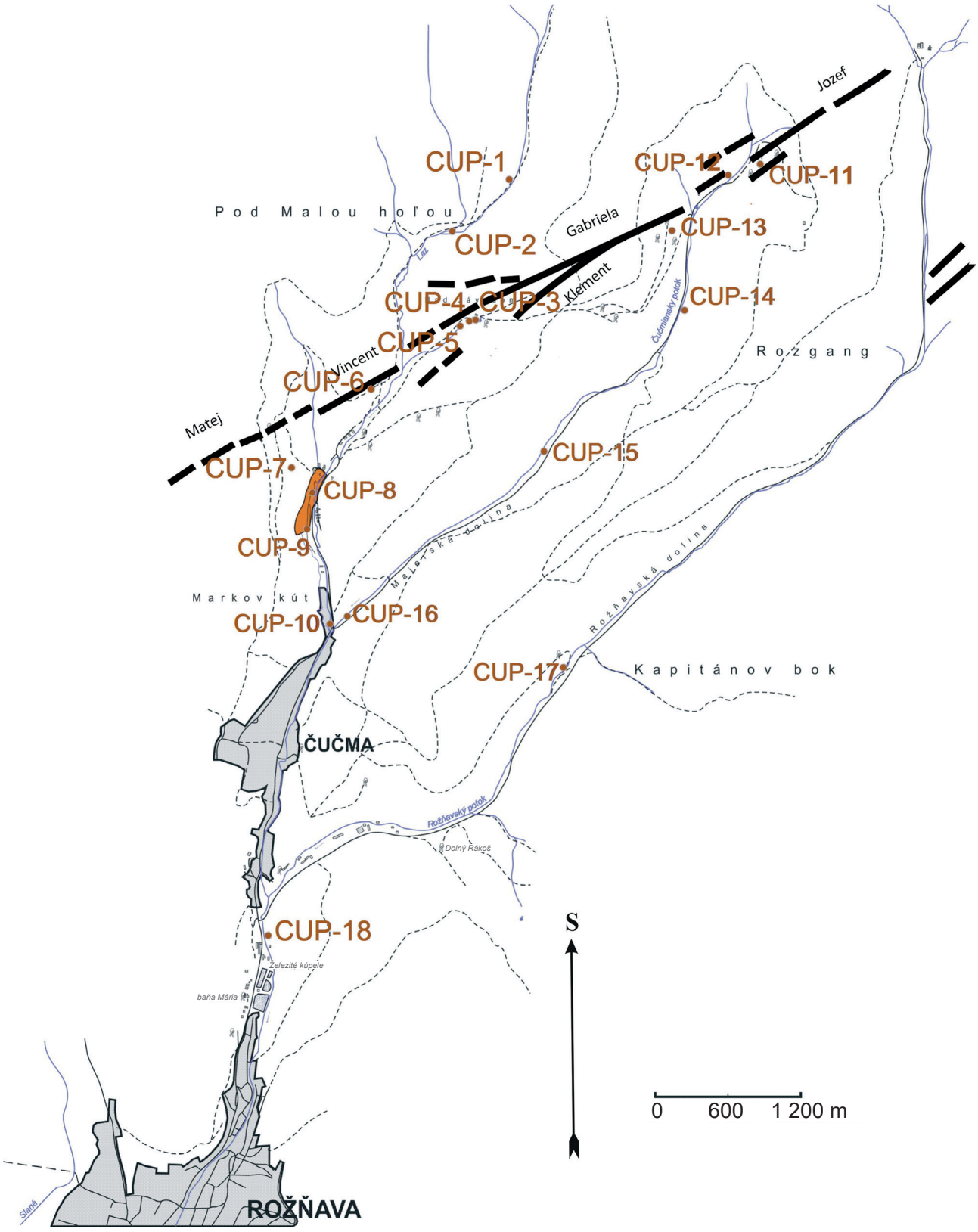

Obr. 2. Mapa odberných miest pôdnych vzoriek a výskytu antimonitových žíl na lokalite Čučma.
Fig. 2. Map of soil sampling sites and stibnite veins at the Čučma deposit.

z hĺbky 0 až 15 cm sa nachádzajú vo veľmi širokom rozsahu: 2,84 – 7,45, resp. 2,06 – 7,13 v príslušnom poradí v prípade pH(H_2O) a pH(KCl). Na základe stupnice USDA (Šefčík et al., 2012) na hodnotenie aktívneho pH pôd spadajú skúmané substráty do kategórií od ultra kyslých až po slabo alkalické pôdy, s mediánom hodnôt patriacim do kategórie silne kyslých pôd. Rovnakú tendenciu pozorujeme aj v prípade substrátov odobraných z hĺbky 15 až 30 cm. Percentuálne zastúpenie karbonátov v pôdnych substrátoch kolíše rovnakým spôsobom ako hodnoty pH, pričom najvyšší obsah bol preukázaný v pôdach s vyššími hodnotami pH. Elektrická vodivosť všetkých odobraných pôd sa pohybuje v rozmedzí od 64 do 718 µS . cm^{-1}.

Na základe výsledkov zrnitostného zloženia je možné klasifikovať odobrané vzorky ako pôdy ľahké až stredne ťažké (SPS VÚPOP, 2014). Spomedzi odobraných pôd boli najviac zastúpené pôdy piesočnato-hlinité a hlinito-piesočnaté (tab. 1). Výnimku tvorí len niekoľko vzoriek pôdnych substrátov antrozemí odobraných z priestoru odkaliska, ktoré sa vyznačujú vyšším obsahom ílu a predstavujú triedu ílovito-hlinitých pôd. Z hľadiska pôdnej skupiny v študovanej oblasti išlo predovšetkým o iniciálne pôdy bez prítomnosti horizontov alebo s prítomnosťou ťažko rozlíšiteľných horizontov, hlavne fluvizeme a antrozeme.

Z hľadiska hodnotenia špecifických kontaminantov v študovanej oblasti je očividná veľmi vysoká koncentrácia niektorých stopových prvkov, hlavne Sb a As. V prípade antimónu bola koncentrácia v rozsahu 6,2 až 142 322 mg . kg^{-1}, s mediánmi 433 mg . kg^{-1} (v hĺbke do 15 cm) a 882 mg . kg^{-1} (v hĺbke do 30 cm), s evidentným nárastom hodnôt mediánu, ako aj priemernej koncentrácie Sb smerom do hĺbky (8 525 mg . kg^{-1} vs. 24 872 mg . kg^{-1}). Obohatenie spodnejších hĺbkových horizontov iniciálnych pôd oproti vrchným v prípade banských oblastí súvisí na jednej strane so zvetrávaním materských hornín a na druhej strane s lúhovaním stopových prvkov z povrchových vrstiev vplyvom kyslého prostredia (napríklad banských výtokov z háld) (Jung, 2008). Obsah As v pôdnych matriciach vo významnej miere koreluje s obsahom antimónu (R^2 = 0,87 pri p < 0,000 1). Pozorovali sme súčasne vysokú koncentráciu obidvoch prvkov, no na rozdiel od Sb, obsah As s hĺbkou klesá. Distribúcia rizikových stopových prvkov vyjadrená formou bodovej mapy (obr. 3) poukazuje na výskyt pôdnych substrátov s vysokým obsahom prvkov (Sb_{max} 142 322 mg . kg^{-1}, $As_{max.}$ 2 253 mg . kg^{-1}) v blízkosti bezprostredných zdrojov kontaminácie na území, teda bývalých štôlní a háld. Najvyšší obsah Sb a As bol identifikovaný v pôdnych vzorkách na území medzi štôlňami Matej, Gabriela a Jozef (CUP-3, CUP-4, CUP-6, CUP-7, CUP-11, CUP-12). V študovanom území boli pozorované miesta s tzv. kumulatívnym efektom kontaminantov (CUP-10, CUP-16, CUP-18), prejavujúcim sa pri sútoku potokov (Rožňavský potok, Laz, Čučmiansky potok) drénujúcich celú oblasť opusteného Sb ložiska. V týchto vzorkách pôdnych substrátov bol okrem As a Sb stanovený aj vysoký obsah iných prvkov (hlavne Pb, Zn a Cu).

Indikačné kritérium (ID) a intervenčné kritérium (IT) pre pôdy (zeminy) boli v zmysle hodnotenia environmentálnych rizík podľa smernice MŽP SR 1/2015-7 viackrát prekročené (17x ID_{Sb} a 9x IT_{Sb}, resp. 18x ID_{As} a 17x IT_{As}).

Tab. 1
Vybrané fyzikálno-chemické parametre odobraných pôd spolu s príslušnými intervenčnými a indikačnými limitmi a priemernou koncentráciou prvkov v pôdach SR.
Tab. 1
Selected physicochemical parameters of collected soils with corresponding intervention and indication limits and median soil element concentrations for SR.

	As	Sb	Pb	Zn	Cu	pH(H_2O)	pH(KCl)	$CaCO_3$	C_{ox}	Íl	Prach	Piesok
	[mg . kg^{-1}]							[hm. %]		[%]		
	0 – 15 cm											
MIN	16	6,2	4,7	33	11,3	2,84	2,06	0	0,13	3	13	25
MAX	2 253	142 322	253,8	189	997,9	7,45	7,13	14,49	19,07	34	41	82
MED	116	433,3	39,15	74	20,4	5,47	4,67	1,04	3,67	5	28	68
	15 – 30 cm											
MIN	19	13,4	24,7	44	17,9	2,82	2,24	0,50	0,37	4	24	29
MAX	763	121 061	215,8	101	64	7,74	7,42	3,50	17,16	30	41	71
MED	110	882	34,7	73	53,3	5,95	4,84	0,58	1,21	8	28,5	63,5
ID[a]	65	25	250	1 500	500							
IT[a]	140	80	800	5 000	1 500							
Æ SR[b] A/C hor.	7,2/6,6	0,7/0,5	20/14	61/55	17/17							

[a] Limitné hodnoty stopových prvkov predstavujú indikačné kritérium (ID) a intervenčný limit (IT) pre priemyselné oblasti podľa smernice MŽP SR č. 1/2015-7; [b] mediánová koncentrácia v pôdach SR (Čurlík a Šefčík, 1999).

[a] Limit values for trace elements represent an indication criterion (ID) and an intervention limit (IT) for industrial areas according to directive of MoE SR no. 1/2015-7; [b] median soil element concentrations for SR (Čurlík and Šefčík, 1999).

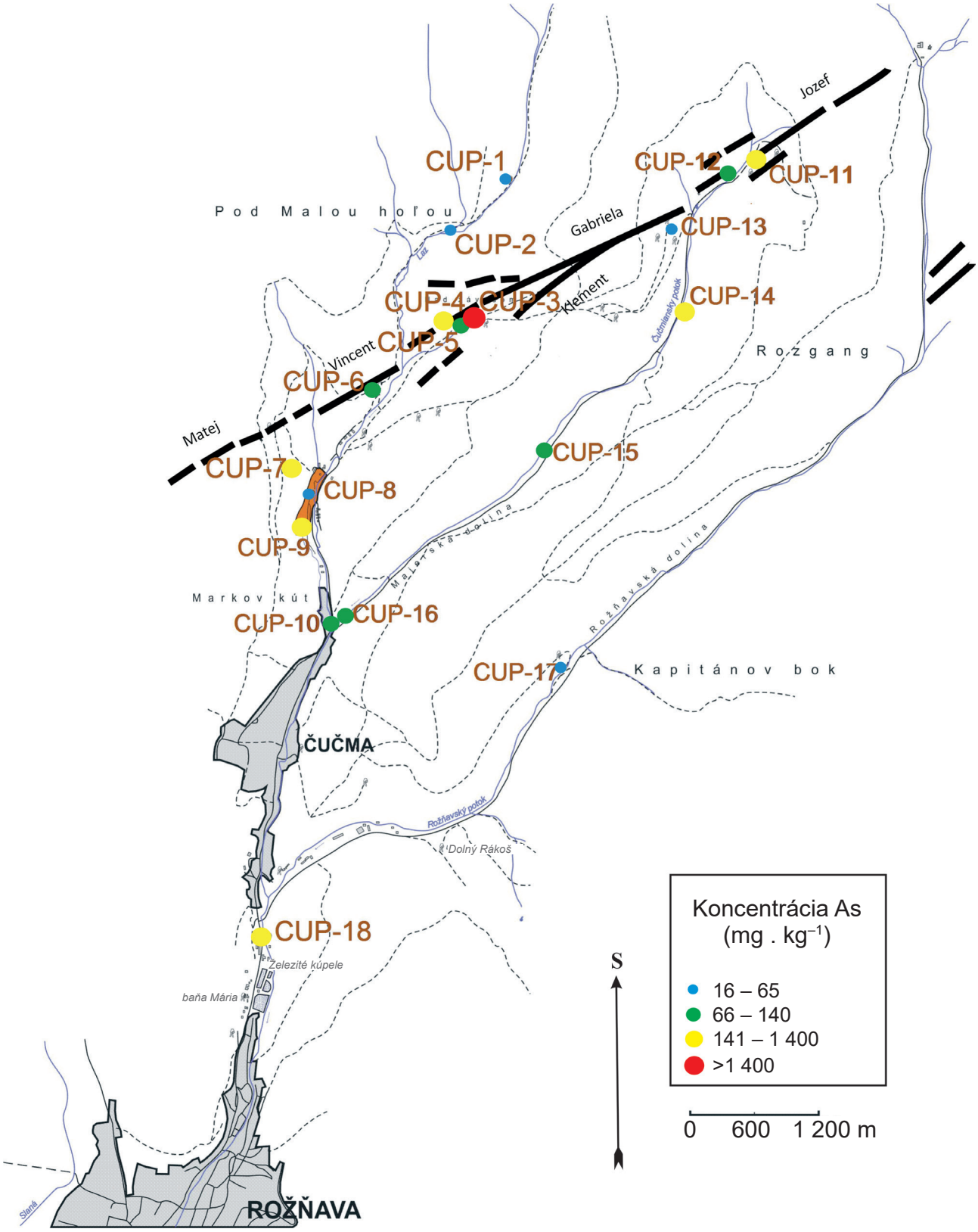

Obr. 3. Distribúcia vybraných kontaminantov (Sb a As) v pôdach študovanej oblasti.
Fig. 3. Distribution of selected contaminants (Sb and As) in soils of the studied area.

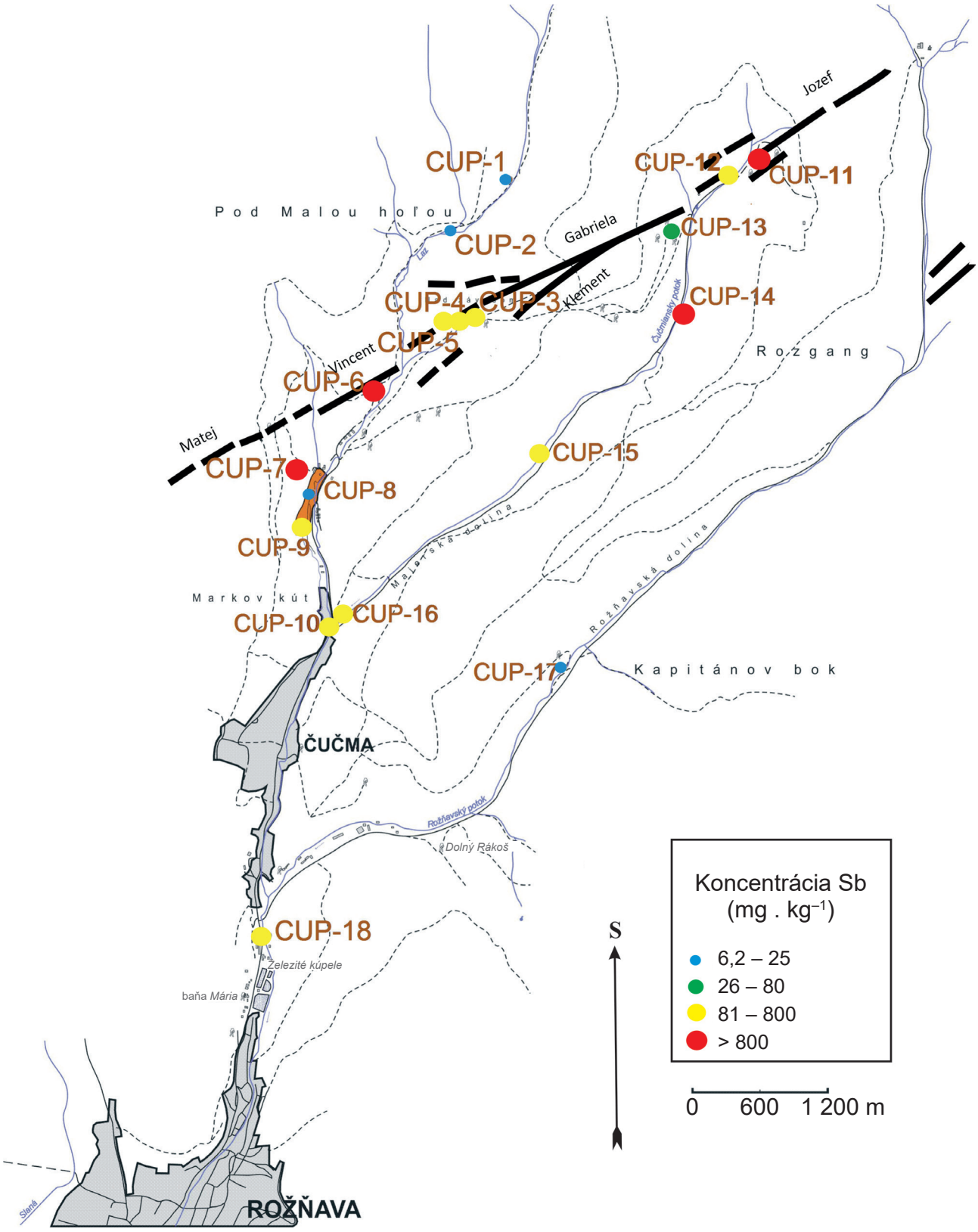

Obr. 3. Distribúcia vybraných kontaminantov (Sb a As) v pôdach študovanej oblasti.
Fig. 3. Distribution of selected contaminants (Sb and As) in soils of the studied area.

Pri väčšine odobraných pôd boli v prípade rizikových stopových prvkov Sb a As stanovené významné prekročenia hraničných hodnôt (obr. 4), pri ktorých sa predpokladá možnosť, resp. vysoká pravdepodobnosť ohrozenia ľudského zdravia a životného prostredia. Spomedzi ďalších stopových prvkov bol pomerne vysoký obsah stanovený aj v prípade Pb, Zn a Cu. Mediánový obsah Pb v pôdach bol niekoľkonásobne vyšší ako medián v rámci pôd Slovenska (Čurlík a Šefčík, 1999). Maximálny obsah Pb prevyšoval ID daného prvku. Podobná situácia bola pozorovaná aj pri Cu, pričom prekročenie ID nastalo pri 2 vzorkách pôd. V prípade výskytu Zn v pôdnych substrátoch bol medián koncentrácie v porovnaní s mediánom v pôdach SR vyšší len nepatrne, ale ojedinele sa vyskytovala aj pomerne vysoká koncentrácia (Zn_{max} 189 mg . kg^{-1}).

Mineralógia pôdnych substrátov

Pri exaktnom hodnotení kontaminácie pôd a potenciálu uvoľňovania rizikových stopových prvkov z prítomných substrátov je nevyhnutné poznať minerálne fázy tvoriace študované substráty (Rochette et al., 1998; Veselská et al., 2013; Hiller et al., 2016). Práve detailné mineralogické štúdium substrátov prináša základné informácie o stabilite prítomných minerálnych fáz a litoklastov tvoriacich pôdnu matricu vrátane pevných zložiek generovaných antropogénnou činnosťou.

Pôdny substrát tvoria litoklasty a kryštaloklasty s rôznou zrnitosťou (Wentworth, 1922) – od hrubých štrkov/brekcií (viac ako 4 – 10 mm) až po ílovce (menej ako 0,003 9 mm; obr. 5). Medzi litoklastami prevládajú veľmi jemnozrnné metapieskovce (obr. 5, A-1, B-1, C-1). Litoklasty sú stmelené červenohnedým až čiernym amorfným tmelom, ktorý často do litoklastov preniká po puklinách (obr. 5, A-3, E-1, F-2). Litoklasty sú zastúpené aj acidnými metavulkanoklastikami (obr. 5, H-1, I-1, J-1) a acidnými metapyroklastikami (obr. 5, K). Červenohnedý až čierny amorfný tmel obsahuje najmä veľmi jemnozrnný kremeň, svetlú sľudu (sericit), ílové minerály, albit a karbonát (obr. 5, C-2, L).

Materskými horninami litoklastov a kryštaloklastov substrátu boli najmä metapieskovce, acidné metavulkanity, metavulkanoklastiká a metapyroklastiká gelnickej skupiny gemerika. Potvrdzujú to zachované štruktúry litoklastov a ich minerálne zloženie (obr. 5, H-1, I-1, J-1, K). V alterovaných litoklastoch je primárny biotit premenený na sericit + Fe oxidy, primárny muskovit je nahradený illitom a živce zastupuje albit. V najjemnozrnnejšej frakcii, ktorá sa nachádza vždy v červenohnedom až čiernom amorfnom tmele, tak prevládajú illit, albit, kremeň, sericit a vzácne sa vyskytuje aj karbonát.

Na základe vyhodnotenia RTG záznamov možno konštatovať, že hlavnými minerálnymi fázami v pôdach študovanej oblasti sú kremeň, kalcit, albit, muskovit a illit. Z rudných minerálov bol vo vzorkách pôd oblasti Čučmy najčastejšie identifikovaný tetraedrit [$(Cu,Fe,Ag,Zn)_{12}Sb_4S_{13}$] a zriedkavo chalkopyrit ($CuFeS_2$). Medzi bežné amorfné minerálne fázy v pôdach patria Fe oxyhydroxidy, ktorých prítomnosť bola dokumentovaná snímkami z polarizačného mikroskopu (obr. 6). Zaznamenali sa železité agregáty a tmely, pričom sekundárne Sb(Fe) minerálne fázy tmelia litoklasty v pôdnom materiáli. Zvýšený obsah Fe vo vrchných horizontoch pôd na lokalite Čučma opisujú aj autori štúdie o opustených Sb ložiskách (Chovan et al., 2010; Lalinská et al., 2010). Dôležitým zistením z vyhodnotenia RTG difrakčných záznamov je identifikácia sekundárnych Sb minerálnych fáz – romeit ($Ca_2Sb_2O_7$) a cervantit (Sb_2O_4), ktoré sú produktmi zvetrávania antimónových rúd a boli opísané na viacerých lokalitách opustených Sb ložísk na Slovensku (Klimko et al., 2011).

Najčastejším nerudným minerálom vo všetkých vzorkách bol kremeň. Tvorí celistvé zrná a obklopuje ostatné minerály, ktoré doň najčastejšie vnikajú v podobe rôznych

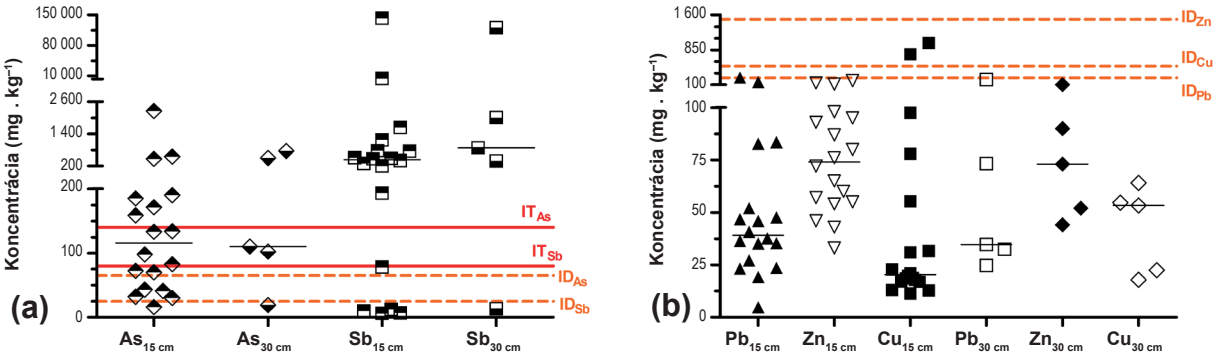

Obr. 4. Koncentrácia Sb a As (a), Pb, Zn a Cu (b) vo vzorkách pôd z dvoch hĺbkových intervalov (0 – 15 cm a 15 – 30 cm) a ich porovnanie s ID a IT.

Fig. 4. Sb and As (a) and Pb, Zn and Cu (b) concentrations in soil samples from two depth intervals (0 – 15 cm and 15 – 30 cm) and their comparison with ID and IT.

žiliek (Klimko et al., 2009). Vo všetkých vzorkách sú často prítomné aj karbonáty. Sú tvorené hlavne sideritom a Fe dolomitmi, pričom po puklinách sú zatlačené oxidmi Fe s prímesou Mn a Mg (Lalinská et al., 2010).

Oxidy Sb sú najfrekventovanejšie minerálne fázy v takmer všetkých vzorkách. Typickým príkladom je identifikovaný oxid Sb stibikonit [$Sb_3O_6(OH)$] (obr. 7). Najvyšší podiel týchto fáz sa zistil vo vzorke pôdneho substrátu v blízkosti štôlne Jozef (až 63 %). Vysoký podiel Sb oxidov bol stanovený aj v substrátoch odkaliskových sedimentov v Čučme. Oxidy Fe a Sb majú veľmi variabilné zloženie, od „čistých“ oxidov Sb a Fe až po zmiešané Fe-Sb oxidy bez prímesí a Sb-Fe oxidy so zvýšeným obsahom iných prvkov, napríklad Ca, As a Pb (Lalinská et al., 2010). Podobný trend platí aj pri celkovom obsahu v pôdnej matrici odobraných vzoriek pôd, kde Fe vystupuje ako dominantný prvok v systéme Ca – Fe – As, resp. Ca – Fe – Sb (obr. 8).

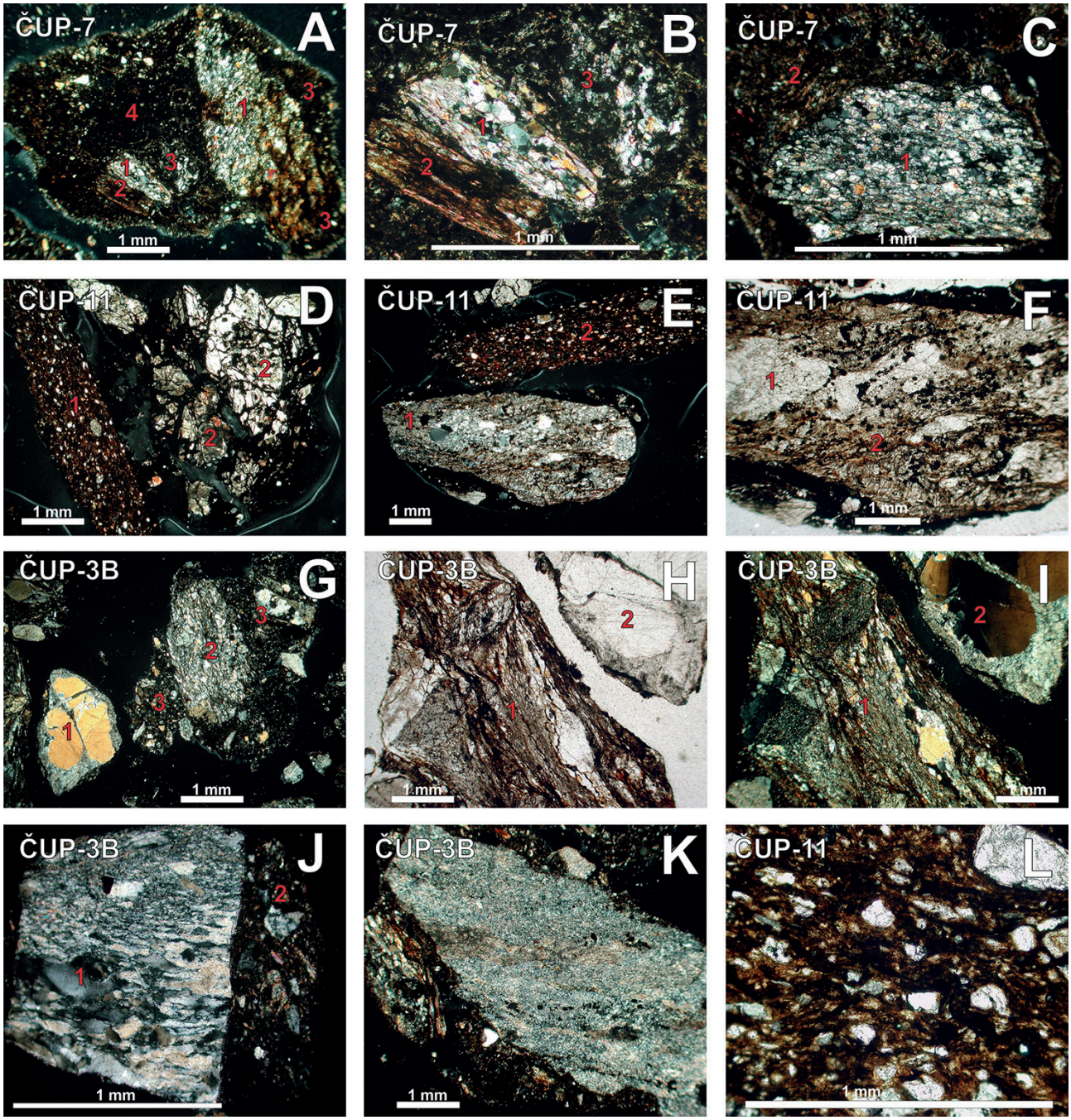

Mobilita stopových prvkov v pôdach

Výsledky extrakčného experimentu s destilovanou vodou (tab. 2) poukázali na relatívne nízky mobilizovateľný podiel Sb a As z celkového obsahu týchto prvkov v pôdnych substrátoch. V prípade antimónu sa z pôd (hĺbka 0 – 15 cm) vylúhovalo 0,14 až 1,42 % Sb z jeho celkovej koncentrácie s mediánom 0,46 %. Podobný trend lúhovania Sb sa zaznamenal aj pri pôdnom substráte z hĺbky 15 – 30 cm, kde bol medián nepatrne vyšší (0,50 %). Vo všeobecnosti sa preukázalo, že koncentrácia extrahovaného Sb bola úmerná jeho celkovému obsahu, teda pri pôdach s vysokým obsahom Sb bola stanovená aj jeho najvyššia mobilná koncentrácia. Vzťah medzi celkovým obsahom Sb v pôdach a extrahovateľnou koncentráciou Sb bol štatisticky veľmi významný (R^2 = 0,93 pri p < 0,000 1). Celkovo nízke percento extrahovaného Sb sa uvádza aj v rámci viacerých predchádzajúcich štúdií (Ettler et al., 2007; Hiller et al., 2012; Nakamaru et al., 2017; Zhang et al., 2018), pričom hlavnou príčinou nízkej mobility Sb je silná adsorpcia alebo koprecipitácia s oxidmi Fe v procesoch zvetrávania (Hammel et al., 2000). Podľa Álvarez-Ayuso et al. (2013) však aj nízky podiel mobilného Sb (< 2 % z celkovej koncentrácie Sb) môže predstavovať značné nebezpečenstvo pre okolité prostredie, najmä rastlinnú biomasu rastúcu na kontaminovaných pôdach v území. Percentuálny podiel uvoľneného As v porovnaní s Sb bol relatívne vyšší. Z pôdy z hĺbky 0 – 15 cm sa do vody uvoľnilo 0,26 – 2,69 % As (medián 0,60 %) a z pôdy z hĺbky 15 – 30 cm to bolo 0,56 – 1,60 % (medián 0,70 %) z celkového obsahu As v pôdach. Nižšie rozpustené po-

Tab. 2
Celkový obsah Sb a As ($C_{celk.}$; mg . kg^{-1}), ich extrahovaná koncentrácia ($C_{výluh}$; mg . kg^{-1}), percentuálny podiel (% mob.) vo vodných výluhoch z pôd a hodnoty pH výluhov.

Tab. 2
Total contents of Sb and As ($C_{celk.}$; mg . kg^{-1}), their extractable concentrations ($C_{výluh}$; mg . kg^{-1}) and proportions (% mob.) in aqueous extracts of soils and leachate pH values.

	Sb			As			pH
	$C_{celk.}$	$C_{výluh}$	% mob.	$C_{celk.}$	$C_{výluh}$	% mob.	
	0 – 15 cm						
MIN	6,9	0,09	0,14	16	0,39	0,26	3,28
MAX	142 322	198	1,42	2 253	5,92	2,69	7,42
MED	620	3,43	0,46	153	0,73	0,60	6,47
	15 – 30 cm						
MIN	13,4	0,1	0,15	19	0,30	0,56	3,20
MAX	121 061	181	0,77	763	5,29	1,60	7,85
MED	1 448	9,03	0,50	304	2,06	0,70	6,54

Obr. 5. Mikrofotografie študovaných pôdnych substrátov (vzorky ČUP-3B, ČUP-7, ČUP-11).
A: 1 – litoklasty veľmi jemnozrnného metapieskovca s prevahou kremeňa; 2 – ílovec s prevahou sericitu, ílových minerálov a amorfného tmelu (hnedý až čierny); 3 – veľmi jemnozrnný metapieskovec s klastami kremeňa a karbonátov v amorfnom tmele; 4 – tmel z amorfných Fe oxyhydroxidov (X polaroidy). **B:** detail A1 (X polaroidy). **C:** 1 – litoklast veľmi jemnozrnného pieskovca (kremeň + sericit + albit + karbonát); 2 – substrát s prevahou tmelu, menej sú zastúpené ílové minerály, kremeň, albit, svetlá sľuda a karbonát s prachovcovou zrnitosťou (X polaroidy). **D:** 1 – veľmi jemnozrnný substrát tvorí kremeň, karbonáty, ílové minerály a prevláda amorfný tmel; 2 – polykryštalický (žilný?) kremeň s amorfným tmelom po puklinách (X polaroidy). **E:** 1 – veľmi hrubý metapieskovec (kremeň + muskovit + albit) s amorfným tmelom Fe oxyhydroxidov na foliačných plochách; 2 – ako D 1 (X polaroidy). **F:** 1 – litoklasty polykryštalického hrubozrnnejšieho metamorfného kremeňa v jemnozrnnejšom substráte (II polaroidy). **G:** 1 – fragmenty kremeňa v submikroskopickom matrixe (kremeň + sľuda + albit); 2 – veľmi jemnozrnný metapieskovec; 3 – rôzne litoklasty v tmele (X polaroidy). **H:** 1 – litoklast alterovaného metavulkanoklastika; 2 – kryštaloklast undulózneho kremeňa v submikroskopickom matrixe (kremeň + karbonát + sericit) (II polaroidy). **I:** ako H (X polaroidy). **J:** 1 – litoklast acidného metavulkanoklastika; 2 – jemnozrnné fragmenty kremeňa, svetlej sľudy, karbonátu a albitu v amorfnom tmele (X polaroidy). **K:** alterované acidné metapyroklastikum (kremeň + karbonát + sericit + albit) (X polaroidy). **L:** veľmi jemnozrnný substrát (kremeň + ílové minerály + albit + amorfný tmel) (II polaroidy).
Fig. 5. Microphotography of studied soil substrates (samples CUP-3B, CUP-7, CUP-11).
A: 1 – very fine-grained metasandstone with a predominance of quartz; 2 – claystone with predominance of sericite, clay minerals and amorphous cement (red-brown to black); 3 – very fine grained metasandstone with quartz and carbonate in amorphous cement; 4 – cement of amorphous Fe-oxyhydroxides (X polaroids). **B:** Detail A1 image (X polaroids). **C:** 1 – very fine-grained metasandstone (quartz + sericite + albite + carbonate); 2 – a substrate in which cement prevails, clay minerals, quartz, albite, light mica and silstone grain size carbonate are less represented (X polaroids). **D:** 1 – a very fine-grained substrate consists of quartz, carbonates, clay minerals and amorphous cement predominates; 2 – polycrystalline (vein?) quartz with amorphous cracks (X polaroids). **E:** 1 – very coarse-grained metasandstone with amorphous Fe-oxyhydroxides cement in foliar areas; 2 – as Fig. D 1 (X polaroids). **F:** 1– lithoclasts of polycrystalline coarse-grained metamorphic quartz in fine-grained substrate (II polaroids). **G:** 1 – quartz fragments in submicroscopic matrix (quartz + mica + albite); 2 – very fine grained metasandstone; 3 – different lithoclasts in cement (X polaroids). **H:** 1 – lithoclast of altered metavulcanoclastics; 2 – crystalloid of undulose quartz in submicroscopic matrix (quartz + carbonate + sericite) (II polaroids). **I:** as Fig. H (X polaroids). **J:** 1 – lithoclast of acid metavulcanoclastics; 2 – fine grained fragments of quartz, light mica, carbonate and albite in amorphous cement (X polaroids). **K:** altered acid metapyclastics (quartz + carbonate + sericite + albite) (X polaroids). **L:** very fine-grained substrate (quartz + clay minerals + albite + amorphous matrix) (II polaroids).

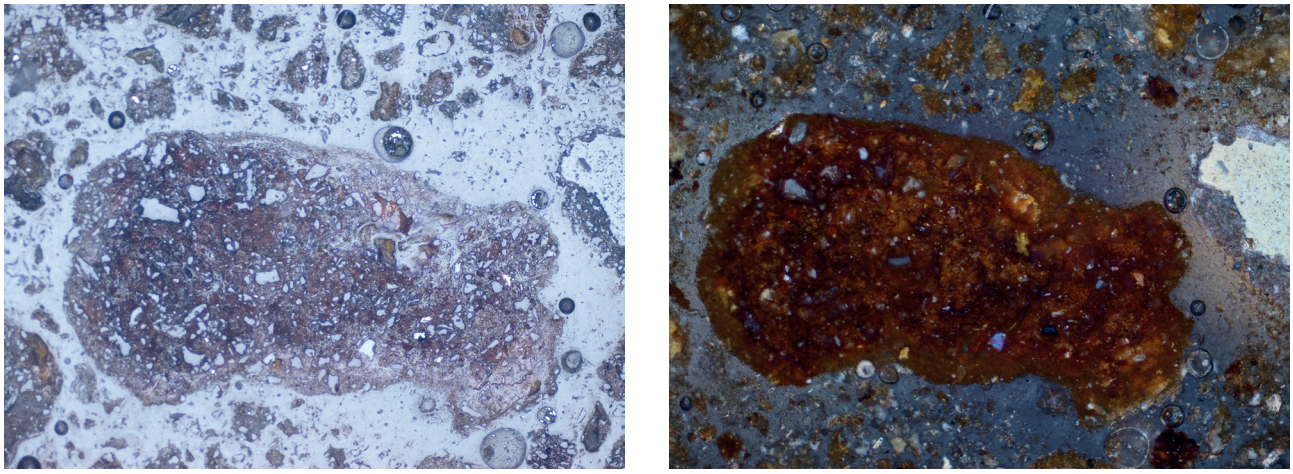

Obr. 6. Fe fázy tmelu litoklastov vo výbruse pôdnej vzorky (vzorka CUP-8, vľavo II polaroidy, vpravo X polaroidy).
Fig. 6. Fe-phase of amorphous cement in soil microscope slice (sample CUP-8, left II polaroids, right X polaroids).

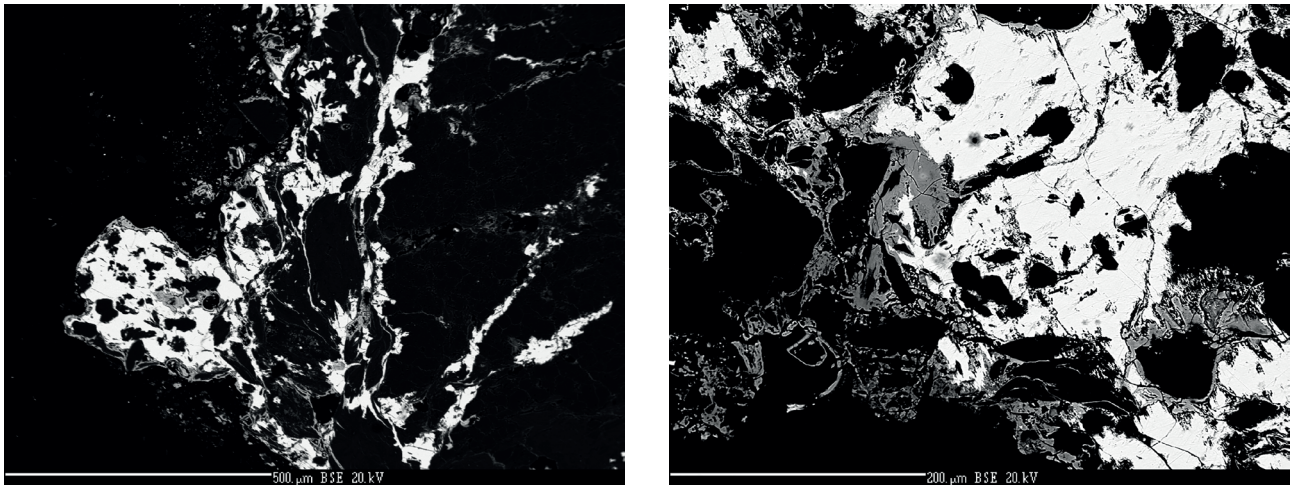

Obr. 7. Antimonit (biely) obklopený oxidom Sb stibikonitom (svetlosivý). Najtmavšie zrná reprezentuje kremeň a muskovit (obrázok vpravo – detailný pohľad).
Fig. 7. Stibnite (white) surrounded by Sb oxide stibiconite (light gray). The darkest grains are quartz and muscovite (picture right – detail view).

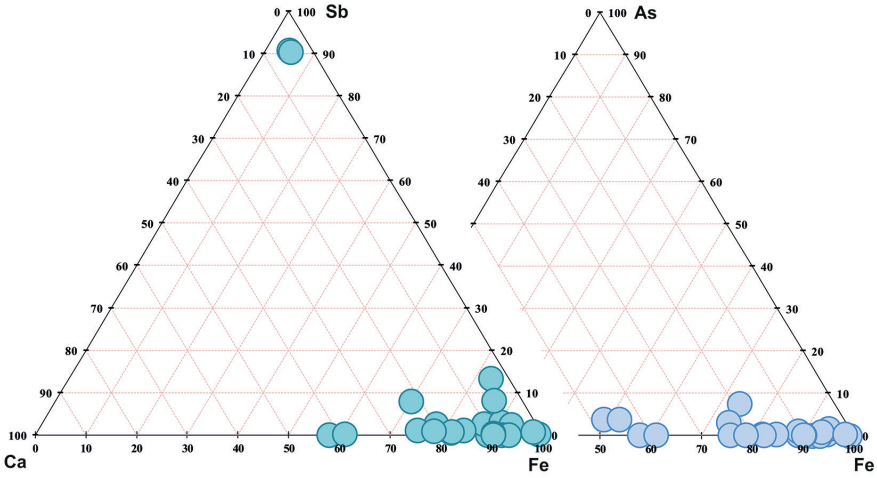

Obr. 8. Diagram chemického zloženia pôdnych substrátov v systéme Ca – Fe – Sb a Ca – Fe – As (v %).
Fig. 8. Diagram of chemical composition of soil substrates in Ca – Fe – Sb and Ca – Fe – As systems (in %).

diely As a Sb v najvrchnejšej vrstve pôd pravdepodobne súvisia s vyšším obsahom organickej hmoty (fulvokyselín a humínových kyselín), ktorá je schopná viazať tieto polokovy prostredníctvom tvorby komplexov (Herath et al., 2017). Štatisticky silný pozitívny vzťah medzi celkovým obsahom a extrahovanou koncentráciou sa rovnako potvrdil aj pri As ($R^2 = 0,95$ pri $p < 0,000\ 1$). Nízke percentuálne podiely mobilného As, rovnako ako v prípade Sb, možno vysvetliť adsorpciou As na povrch sekundárnych oxidov Fe, ako aj jeho inkorporáciou do štruktúry hojne zastúpených oxidov Fe. Potvrdzujú to aj výsledky z mineralogického výskumu týchto pôd.

Na základe výsledkov statických extrakčných experimentov možno konštatovať, že v rámci skúmaného územia EZ v Čučme sú identifikované miesta s extrémnym obsahom rizikových prvkov ako Sb a As v substrátoch iniciálnych pôd, ktoré súčasne predstavujú potenciálne riziko vyplývajúce z mobilizácie Sb a As v procesoch zvetrávania. Sú to hlavne miesta v blízkosti historických štôlní a opustených háld a odvalov.

Záver

Na základe zrealizovaného mineralogicko-geochemického prieskumu pôd v oblasti opusteného Sb ložiska Čučma bola zreteľne preukázaná kontaminácia pôdnych substrátov antimónom a arzénom. Geologická stavba tohto územia, ako aj rozsiahla banská činnosť prebiehajúca v minulosti sú hlavnými príčinami extrémne vysokého obsahu stopových prvkov, ktorých maximá sú pozorované najmä v blízkosti deponovaných háld a odvalov s ťažobným odpadom a bývalých štôlní. Zvetrávanie mechanicky porušených materských hornín so zastúpením sulfidov Sb a As spôsobuje neustále uvoľňovanie týchto dvoch kontaminantov do prostredia. Nízky podiel ľahko mobilizovateľných foriem Sb a As je spojený s ich pomerne stabilnou väzbou v štruktúrach hojne zastúpených sekundárnych oxidov Fe v týchto pôdach. V prípade Sb je to aj vďaka tvorbe samostatných stabilných oxidov Sb (stibikonit, cervantit a roméit) a nemožno vylúčiť ani úlohu pôdnej organickej hmoty. Aj tento nízky extrahovateľný podiel je však stále pre širšie okolie potenciálnym rizikom, pretože bol stanovený v prípade slabého extrakčného činidla (destilovaná voda) a nezohľadňuje v tomto prípade dlhodobý reálny účinok v prostredí. V súvislosti s tým je potrebný ďalší výskum a vyhodnotenie potenciálneho environmentálneho rizika v tejto oblasti zamerané na detailnejšie štúdium podmienok šírenia a bioprístupnosti kontaminantov.

Poďakovanie

Táto práca bola vypracovaná vďaka projektu Agentúry na podporu výskumu a vývoja č. APVV-17-0317 a projektu VEGA 1/0597/17.

Literatúra / References

Álvarez-Ayuso, E., Otones, V. Murciego, A., García-Sánchez, A. & Santa Regina, I., 2013: Mobility and phytoavailability of antimony in an area impacted by a former stibnite mine exploitation. *Sci. Total Environ., 449, 260 – 268.*

Bajaník, Š., Hanzel, V., Ivanička, J., Mello, J., Pristaš, J., Reichwalder, P., Snopko, L., Vozár, J. & Vozárová, A., 1983: Vysvetlivky ku geologickej mape Slovenského rudohoria, východná časť. *Bratislava, Št. Geol. Úst. D. Štúra, 16, 50.*

Bajtoš, P., 2016: Mine waters in the Slovak, part of the Western Carpathians – distribution, classification and related environmental issues. *Slovak Geol. Mag., 16, 139 – 158.*

Bajtoš, P., Záhorová, Ľ., Rapant, S. & Pramuka, S., 2012: Monitoring geologických faktorov vplyvu ťažby nerastov na životné prostredie v rizikových oblastiach na Slovensku v rokoch 2007 – 2011. *Miner. Slov., 44, 375 – 392.*

Bakoš, F., Chovan, M., Bačo, P., Bahna, B., Ferenc, Š., Hvožďara, P., Jeleň, S., Kamhálová, M., Kaňa, R., Knésl, J., Krasnec, Ľ., Križáni, I., Maťo, Ľ., Mikuš, T., Pauditš, P., Sombathy, L. & Šály, J., 2004: Zlato na Slovensku. *Bratislava, Slovenský skauting, 298 s.*

Brusseau, M. L, Mccoll, C. M., Famisan, G. & Artiola, J. F., 2006: Chemical Contaminants. In: Pepper, I. L., Gerba, Ch. P. & Brusseau, M. L. (Eds.): *Environmental & Pollution Science. Second Ed. Amsterdam, Elsevier Academic Press, 532 s.*

Čurlík, J. & Šefčík, P., 1999: Geochemický atlas SR. Časť V. – Pôdy. *Bratislava, VÚPOP, 100 s. + 83 map. príloh.*

Čurlík, J. & Jurkovič, Ľ., 2012: Pedogeochémia. Vysokoškolská učebnica. *Univerzita Komenského v Bratislave, 228 s.*

Ettler, V., Mihaljevič, M., Šebek, O. & Grygar, T., 2007: Assessment of single extractions for the determination of mobile forms of metals in highly polluted soils and sediments – Analytical and thermodynamic approaches. *Anal. Chim. Acta, 602, 131 – 140.*

Ettler, V., Mihaljevič, M., Šebek, O., Valigurová, R. & Klementová, M., 2012: Differences in antimony and arsenic releases from lead smelter fly ash in soils. *Chem. Erde, 72, 15 – 22.*

Fiala, K., Barančíková, G., Brečková, V., Búrik, V., Chomaničová, A., Houšková, B., Kobza, J., Litavec, T., Makovníková, J., Matúšková, L., Pechová, B. & Váradiová, D., 1999: Záväzné metódy pôd. Čiastkový monitorovací systém – Pôda. *Bratislava, Výskumný ústav pôdoznalectva a ochrany pôdy, 139 s.*

Fľaková, R., Ženišová, Z., Krčmář, D., Ondrejková, I. & Sráček, O., 2017: Occurrence of antimony and arsenic at mining sites in Slovakia: Implications for their mobility. *Carp. J. Earth Environ. Sci., 12, 41 – 48.*

Grecula, P., Abonyi, A., Abonyiová, M., Antaš, J., Bartalský, B., Bartalský, J., Dianiška, I., Drzík, E., Ďuďa, R., Gargulák, M., Gazdačko, Ľ., Hudáček, J., Kobulský, J., Lörinz, L., Macko, J., Návesňák, D., Németh, Z., Novotný, L., Radvanec, M., Rojkovič, I., Rozložnák, L., Rozložník, O., Varček, C. & Zlocha, J., 1995: Ložiská

nerastných surovín Slovenského rudohoria, zv. 1. *Bratislava, Geocomplex, 834 s.*

Hammel, W., Debus, R. & Steubing, L., 2000: Mobility of antimony in soil and its availability to plants. *Chemosphere, 41, 1 791 – 1 798*.

Helios Rybicka, E., 1996: Environmental impact of mining and smelting industries in Poland. In: Appleton, J. D, Fuge, R. & Mccall, G. J. H. (Eds.): Environmental Geochemistry and Health with special reference to developing countries. *London, Geol. Soc., 264 s.*

Herath, I., Vithanage, M. & Bundschuh, J., 2017: Antimony as a global dilemma: Geochemistry, mobility, fate and transport. *Environ. Pollut., 223, 545 – 559*.

Hiller, E., 2003: Adsorpcia arzeničnanov na pôdach: štúdium rýchlosti adsorpcie a adsorpčných izoteriem. *J. Hydrol. Hydromech., 51, 288 – 297.*

Hiller, E., Lalinská, B., Chovan, M., Jurkovič, Ľ., Klimko, T., Jankulár, M., Hovorič, R., Šottník, P., Fľaková, R., Ženišová, Z. & Ondrejková, I., 2012: Arsenic and antimony contamination of waters, stream sediments and soils in the vicinity of abandoned antimony mines in the Western Carpathians, Slovakia. *Appl. Geochem., 27, 598 – 614*.

Hiller, E., Tóth, R., Kučerová, G., Jurkovič, Ľ., Šottník, P., Lalinská-Voleková, B. & Vozár, J., 2016: Geochemistry of mine tailings from processing of siderite-Cu ores and mobility of selected metals and metalloids evaluated by a pot leaching experiment at the Slovinky impoundment, Eastern Slovakia. *Mine Water Environ., 35, 447 – 461.*

Hlodák, M., Matúš, P., Urík, M., Kořenková, L., Mikušová, P., Senila, M. & Diviš, P., 2015: Evaluation of various inorganic and biological extraction techniques suitability for soil mercury phytoavailable fraction assessment. *Water Air Soil Pollut., 226, Article num. 198.*

Chovan, M., Háber, M., Jeleň, S., Rojkovič, I., Andráš, P., Antal, B., Bebej, J., Beňka, J., Bőhmer, M., Divinec, Ľ., Ďuďa, R., Határ, J., Hurai, V., Hurný, J., Kotuľák, P., Koděra, P., Kúšik, R., Maťo, Ľ., Onačila, D., Ragan, M., Rojkovič, I. & Rojkovičová, Ľ., 1994: Ore textures in the Western Carpathians. *Bratislava, Slovak Academic Press, 219 s.*

Chovan, M., Lalinská, B., Šottník, P., Jurkovič, Ľ., Ženišová, Z., Fľaková, R., Krčmář, D., Lintnerová, O., Hiller, E., Klimko, T., Jankulár, M., Hovorič, R., Jašová, I., Lux, A., Vaculík, M., Hudáček, M., Michňová, J., Petrák, M., Andráš, P., Milovská, S. & Majzlan, J., 2010: Zhodnotenie vplyvu banskej činnosti na okolie opustených Sb ložísk Slovenska s návrhmi na remediáciu. Záverečná správa o riešení projektu. *Bratislava, PriF UK, 358 s.*

Jung, M. C., 2008: Heavy metal concentrations in soils and factors affecting metal uptake by plants in the vicinity of a Korean Cu-W mine. *Sensors, 8, 2 413 – 2 423*.

Jurkovič, Ľ., Šottník, P., Fľaková, R., Jankulár, M., Ženišová, Z. & Vaculík, M., 2010: Opustené Sb-ložisko Poproč – zdroj kontaminácie prírodných zložiek v povodí Olšavy. *Miner. Slov., 42, 109 – 120.*

Jurkovič, Ľ., Šottník, P., Sekula, P., Peťková, K., Kotúč, J., Leššo, J., Bačik, M., Hiller, E. & Malý, V., 2016: Geochemické hodnotenie environmentálnych rizík na lokalite opusteného Hg ložiska Merník (východné Slovensko). *Miner. Slov., 48, 157 – 170.*

Klimko, T., Lalinská, B., Majzlan, J., Chovan, M., Kučerová, G. & Paul, Ch., 2011: Chemical composition of weathering products in neutral and acidic mine tailings from stibnite exploitation in Slovakia. *J. Geosci., 56, 327 – 340.*

Klimko, T., Chovan, M. & Huraiová, M., 2009: Hydrotermálna mineralizácia na antimonitových žilách Spišsko-gemerského rudohoria. *Miner. Slov., 41, 115 – 132*.

Kobulský, J., Grecula, P., Gazdačko, Ľ., Németh, Z., Hraško, Ľ., Novotný, L., Maglay, J., Pramuka, S., Radvanec, M., Kucharič, Ľ., Bajtoš, P., Záhorová, Ľ., Konečný, P. & Kaličiak, M., 2006: Geologická mapa Spišsko-gemerského rudohoria v mierke 1 : 50 000. *Bratislava, Št. Geol. Úst. D. Štúra.*

Lalinská, B., Chovan, M., Kučerová, G., Šottník, P. & Petrák, M., 2010: Procesy oxidácie sulfidov a migrácia As a Sb v odkalisku na opustenom Sb-Au ložisku Čučma. *Miner. Slov., 42, 79 – 94.*

Mangová, K. & Lintnerová, O., 2015: Environmentálne aspekty transformácie nízko-sulfidického postflotačného kalu na antropogénnu pôdu (Smolník, Slovensko). *Acta Geol. Slov., 7, 195 – 212.*

Nakamaru, Y. M. & Martín Peinado, F. J., 2017: Effect of soil organic matter on antimony bioavailability after the remediation process. *Environ. Pollut., 228, 425 – 432*.

Rapant, S., Dietzová, Z. & Cicmanová, S., 2006: Environmental and health risk assessment in abandoned mining area Zlata Idka, Slovakia. *Environ. Geol., 51, 387 – 397*.

Rojkovič, I., 2003: Rudné ložiská Slovenska. *Bratislava, PriF UK, 180 s*.

Rochette, E. A., Li, G. C. & Fendorf, S. E., 1998: Stability of arsenate minerals in soil under biotically generated reducing conditions. *Soil Sci. Soc. Am. J., 62, 1 530 – 1 537.*

Rozložník, L., Havelka, J., Čech, F. & Zorkovský, V., 1987: Ložiská nerastných surovín a ich vyhľadávanie. *Bratislava, ALFA, 696 s*.

Smernica MŽP SR z 28. 1. 2015 č. 1/2015-7 na vypracovanie analýzy rizika znečisteného územia. *Bratislava, MŽP SR, 96 s.*

SPS VÚPOP, 2014: Morfogenetický klasifikačný systém pôd Slovenska. Bazálna referenčná taxonómia. Druhé upravené vyd. *Bratislava, NPPC – VÚPOP, 96 s*.

Środoń, J., Drits, V. A., McCarty, D. K., Hsieh, J. C. C. & Eberl, D. D., 2001: Quantitative X-ray diffraction analysis of clay-bearing rocks from random preparations. *Clays Clay Miner., 49, 514 – 528.*

Šottník, P., Jurkovič, Ľ., Hiller, E., Kordík, J. & Slaninka, I., 2015: Environmentálne záťaže. Vysokoškolská učebnica. *Banská Bystrica, Slovenská agentúra život. prostr., 301 s.*

Šimurková, M., Ivan, P. & Gargulák, M., 2016: Subsolidus alkali metasomatism in the metamorphosed Ordovician acid volcanics and volcaniclastics of the Gelnica Group (Gemeric Superunit, Western Carpathians). *Acta Geol. Slov., 8, 87 – 98*.

Šefčík, P., Bystrická, G. & Káčer, Š., 2012: Pedogeochemické mapy – vysvetlivky. *Bratislava, Štátny Geologický Ústav Dionýza Štúra, 60 s.*

Veselská, V., Majzlan, J., Hiller, E., Peťková, K., Jurkovič, Ľ., Ďurža, O. & Lalinská-Voleková, B., 2013: Geoche-

mical characterization of arsenic-rich coal-combustion ashes buried under agricultural soils and the release of arsenic. *Appl. Geochem., 33, 153 – 164.*

Vítková, M., Ettler, V., Šebek, O., Mihaljevič, M., Grygar, T. & Rohovec, J., 2009: The pH-dependent leaching of inorganic contaminants from secondary lead smelter fly ash. *J. Hazard. Mater., 167, 427 – 433.*

Wentworth, C. K.,1922: A scale of grade and class terms for clastic sediments. *J. Geol., 30, 377 – 392.*

Zhang, S., Wang, Y., Pervaiz, A., Kong, L. & He, M., 2018: Comparison of diffusive gradients in thin-films (DGT) and chemical extraction methods for predicting bioavailability of antimony and arsenic to maize. *Geoderma, 332, 1 – 9.*

Ženišová, Z., Feaková, R., Jašová, I. & Cicmanová, S., 2009: Antimón a arzén vo vodách ovplyvnených banskou činnosťou vo vybraných oblastiach Slovenska. *Podzemná voda, 15, 100 – 117.*

Geochemical and mineralogical exploration of soils affected by mining activities at the abandoned Sb-deposit Čučma

Abandoned Sb-deposit Čučma is one of the typical mining sites in Slovakia, situated in the southern belt of the Spišsko-gemerské rudohorie Mts. (Western Carpathians) (Fig. 1). At present, part of the locality is classified as probable environmental burden (registered as RV (003)/ Čučma – former mining plant, SK/EZ/RV/777) and the impoundment is registered in the repository register. The main source of environmental contamination (mostly Sb and As) in the area are the outflows of mining waters from old galleries and deposited mining wastes in the area (Hiller et al., 2012). Soil samples were taken at two depth horizons (0 – 15 cm/18 samples and 15 – 30 cm/5 samples) for the study of geochemical and mineralogical properties of soils (Fig. 2).

Laboratory analyses of soil substrates showed their significant heterogeneity (Tab. 1). The soil pH values for samples from a depth of 0 – 15 cm were in the range of 2.84 – 7.45 and 2.06 – 7.13 for pH(H_2O) and pH(KCl), respectively with the same tendency for soil samples from a depth of 15 to 30 cm. The soil substrates fell into the categories from "ultra-acidic" to "weakly alkaline" soils with a median of values belonging to the "strongly acidic" soils based on the USDA scale for the assessment of active soil pH. The soil samples represented primarily initial soils without the presence of horizons or with the presence of hardly distinguishable horizons, mainly fluvisols and technosols.

Total concentrations of potentially toxic trace elements were high in several cases, especially in the case of Sb and As (the range of Sb contents was 6.2 – 142 322 mg . kg^{-1} with a median of 433 mg . kg^{-1} for a depth of 0 – 15 cm and a median of 882 mg . kg^{-1} for a depth 15 – 30 cm). Median and mean Sb (8 525 mg . kg^{-1} *vs*. 24 872 mg . kg^{-1}) concentrations increased with soil depth. The enrichment of the lower depth horizons of the initial soils compared to the upper horizons in mining areas relates to the rock weathering and leaching of trace elements from surface layers due to acidic environments (e.g. mine effluents) (Jung, 2008). The As contents of the soils significantly correlated with antimony ($R^2 = 0.87$ at $p < 0.000\ 1$), however, the As content decreases with depth of soil profiles. The highest total concentrations of Sb and As as well as Pb, Zn and Cu were identified in soil samples of the area between the adits of Matej, Gabriela and Jozef (CUP-3, CUP-4, CUP-6, CUP-7, CUP-11, CUP-12) and at sites with the cumulative effect of contaminants (CUP-10, CUP-16, CUP-18), at the confluence of streams draining the whole area of abandoned Sb deposit (Fig. 3). Indication (ID) and intervention (IT) criteria for soils (according to Directive of Ministry of Environment of the Slovak Republic) were exceeded in 17 samples for ID_{Sb} and in 9 samples for IT_{Sb}, resp. in 18 samples for ID_{As} and 17 samples for IT_{As} (Fig. 4). For most soils, significant exceedances of limit values, assuming the possibility of a high probability of endangering human health and the environment, were assessed.

The soil substrate consists of lithoclasts and crystalloclasts of variable grain size (Wentworth, 1922) – from coarse gravel/breccias (more than 4 – 10 mm) to granularity of claystones (less than 0.003 9 mm). Very fine-grained meta-sandstones predominate among lithoclasts (Fig. 5). Lithoclasts are cemented with red-brown to black amorphous cement, which often penetrates the cracks. The red-brown to black amorphous cement contains especially fine-grained quartz, light mica (sericite), clay minerals, albite and carbonates.

Quartz, calcite, albite, muscovite and illite are the main mineral phases in the soils of the study area. Concerning the ore minerals, tetrahedrite and rarely chalcopyrite were mostly identified in the soil samples. Common amorphous mineral phases in the soils were Fe oxy-hydroxides. Ferric aggregates and cement were recorded (Fig. 6), secondary Sb(Fe) mineral phases cemented lithoclasts in the soil substrates. Secondary Sb mineral phases – romeite ($Ca_2Sb_2O_7$), cervantite (Sb_2O_4) and stibiconite [$Sb_3O_6(OH)$] were identified as products of weathering of antimony ores, mostly stibnite (Fig. 7). Antimony oxides are the most frequent mineral phases in almost all samples. In all samples, quartz was the most common non-ore mineral, which forms whole grains and surrounds other minerals that most often enter it in the form of various

veins (Klimko et al., 2009). Carbonates are also often present in all samples. They are mainly made up of siderite and Fe-dolomites, and the fissures are pushed by Fe oxides with the addition of Mn and Mg (Lalinská et al., 2010).

The results of the extraction experiment with distilled water indicated relatively low mobile proportions of Sb and As (Tab. 2). Only 0.14 to 1.42 % Sb (median of 0.46 %) of its total content was extracted from soils at a depth of 0 – 15 cm. A similar trend of Sb extractability was also observed in the soils taken from a depth of 15 – 30 cm, where the median was slightly higher (0.50 %). In general, extractable Sb concentration was proportional to its total content. The main cause of low Sb mobility was likely a strong adsorption or co-precipitation of Sb with Fe oxides in weathering processes (Hammel et al., 2000) and the formation of individual secondary Sb minerals with low solubility in water under oxidizing conditions. The percentage of extracted As was somewhat higher compared to that of extracted Sb. For soils from 0 – 15 cm depth, 0.26 – 2.68 % As (median of 0.60 %) was released into the water, and for soils from 15 – 30 cm depth, it was 0.56 – 1.60 % (median of 0.70 %) of the total As content in soils. The lower extractable proportions of As and Sb in the surface soil layers are probably related to the higher organic carbon content (fulvic acids and humic acids), which bind these metalloids through complex formation (Herath et al., 2017). The low extractable As proportions, as in the case of Sb, can be explained by the adsorption of As to the surfaces of secondary Fe oxides as well as its incorporation into the structure of abundant Fe oxides, whose presence was confirmed by mineralogical research of these soils. It can be concluded from the results of extraction experiments that there are sites with anomalous concentrations of risk elements, such as Sb and As, in substrates of initial soils within the investigated area of abandoned antimony deposit Čučma, representing a potential risk to the surrounding environment. These sites are mainly places located near historical adits and abandoned heaps and dumps.

Doručené / Received: 6. 11. 2019
Prijaté na publikovanie / Accepted: 2. 12. 2019

Inštrukcie autorom

Etika publikovania, záväzná pri publikovaní v časopise Mineralia Slovaca: *www.geology.sk/mineralia* položka *Publikačná etika*

1. Geovedný časopis Mineralia Slovaca publikuje scientometricky hodnotné recenzované pôvodné vedecké články s vysokým citačným potenciálom. V úvode príspevku musí autor jasne deklarovať, čím konkrétnym je jeho príspevok prínosný pre rozvoj geovied. Rešeršné štúdie sa publikujú len ojedinele.

2. Články na publikovanie (manuskripty) sa do redakcie zasielajú poštou (dva vytlačené exempláre a CD so všetkými súbormi v editovateľnej podobe) alebo e-mailom (editovateľné súbory a kompletná verzia vo formáte PDF).

3. Súčasne s článkom je potrebné redakcii poslať autorské vyhlásenie o originalite textu a obrázkov. Kópie obrázkov z iných publikácií musia byť legalizované získaním práva na publikovanie. Vyhlásenie musí obsahovať meno autora (autorov), akademický titul a trvalé bydlisko.

4. Rozsah manuskriptu na publikovanie je najviac 25 rukopisných strán (MS Word, Times New Roman, veľkosť písmen 12 bodov, riadkovanie 1,5) vrátane literatúry, obrázkov a vysvetliviek. V prípade veľkého odborného prínosu sú v ojedinelých prípadoch povolené aj dlhšie články.

5. Články sú publikované v angličtine alebo v slovenčine. Články v slovenčine musia obsahovať anglický preklad názvu, abstraktu, kľúčových slov, resumé a popisov k obrázkom a tabuľkám. Články písané v angličtine musia obsahovať slovenské resumé.

Text

1. Abstrakt stručne sumarizuje článok. Môže mať najviac 200 slov a nemá obsahovať citácie. Počet kľúčových slov je maximálne 6. Text má mať úvod, charakteristiku (stav) skúmaného problému, použitú metodiku, nové zistenia, ich interpretáciu, diskusiu, záver a zoznam literatúry. Východiskové údaje musia byť zreteľne odlíšené od interpretácií. V texte musia byť odvolávky na všetky použité obrázky a tabuľky.

2. Hierarchiu nadpisov v texte je potrebné vyznačiť ceruzkou na ľavom okraji strany manuskriptu: 1 – najvyššia, 2 – nižšia, 3 – najnižšia.

3. V texte sa uprednostňuje citácia v zátvorke, napr. (Dubčák, 1987; Hrubý et al., 1988), pred formou ... podľa Dubčáka (1987).

4. Pozícia obrázkov a tabuliek v texte sa označí. Nie je vhodné, aby text v editore MS Word obsahoval vložené obrázky, ale náhľadová verzia v pdf ich má obsahovať.

5. Grécke písmená treba identifikovať na ľavom okraji slovom (napr. sigma). Potrebné je odlišovať pomlčku od spojovníka. Symboly, matematické značky, názvy skamenelín a pod., ktoré sa majú vysádzať kurzívou, autor v rukopise podčiarkne vlnovkou.

Obrázky a tabuľky

1. Ilustrácie a tabuľky vysokej kvality bývajú publikované buď **na šírku stĺpca (81 mm), alebo strany (170 mm).** Optimálna veľkosť písma a čísiel v publikovaných obrázkoch je 2 mm. Články v slovenčine musia mať popisy v obrázkoch a tabuľkách v slovenčine, záhlavie tabuliek a texty pod obrázkami a tabuľkami sú v slovenčine a angličtine. Články v angličtine majú všetky texty v angličtine. **Maximálny rozmer ilustrácie a tabuľky vytlačený v časopise je 170 x 230 mm.** Väčšie (skladané) ilustrácie sú publikované len v ojedinelých prípadoch.

2. Pri počítačovej tvorbe obrázkov odporúčame používať programy s vektorovým zobrazením (Corel Draw, Adobe Illustrator a pod.). Čiary tzv. vlasovej hrúbky, softvérová alebo rastrová výplň plôch (napr. v Corel Draw) nie sú prípustné. Výplne v obrázkoch musia pozostávať zo samostatne vysádzaných objektov.

3. Ilustrácie vrátane fotografií musia obsahovať **grafickú mierku** v centimetrovej či metrovej škále, prípadne sa rozmer zobrazených objektov vyjadrí v popise obrázka. Mapy a profily musia mať aj **azimutálnu orientáciu** a jednotné vysvetlivky, ktoré sa uvedú pri prvom obrázku. Zoskupené obrázky, napr. fotografie a diagramy, sa uvádzajú ako jeden obrázok s jednotlivými časťami označenými písmenami (a, b, c atď.).

4. Pri zasielaní fotografií vo forme počítačových súborov (formáty JPG alebo TIF) sa požaduje rozlíšenie minimálne 600 DPI. Publikovanie farebných ilustrácií môže byť spoplatnené.

Literatúra

1. Minimálne 50 % citácií musí reprezentovať publikácie od roku 2000. V zozname literatúry sa v abecednom poradí uvádza len literatúra citovaná v danom článku.

2. Spôsob uvádzania literatúry v zozname literatúry

Knižná publikácia: Gazda, L. & Čech, M., 1988: Paleozoikum medzevského príkrovu. *Bratislava, Alfa, 155 s.*

Časopis: Vrba, P., 1989: Strižné zóny v metapelitoch. *Miner. Slov., 21, 135 – 142.*

Zborník: Návesný, D., 1987: Vysokodraselné ryolity. *In: Romanov, V. (ed.): Stratiformné ložiská gemerika. Špec. publ. Košice, Slov. geol. spol., 203 – 215.*

Manuskript: Radvanský, F., Slivka, B., Viktor, J. & Srnka, T., 1985: Žilné ložiská jedľoveckého príkrovu gemerika. Záverečná správa z úlohy SGR--geofyzika. *Manuskript. Spišská Nová Ves, archív Št. Geol. Úst. D. Štúra, 28 s.*

3. Pri článku viac ako dvoch autorov sa v texte cituje iba prvý autor s dodatkom et al., ale v zozname literatúry sa uvádzajú všetci.

Instructions to authors

Publication ethics, being obligatory for publishing in the journal Mineralia Slovaca: *www.geology.sk/mineralia* item *Publication ethics*

1. Geoscientific journal Mineralia Slovaca publishes scientometrically valuable original peer-reviewed scientific articles with a high citation potential. In the introduction of each article the author(s) must clearly declare, which innovative data the paper brings for the development of geosciences. The retrieval studies are published only exceptionally.

2. The articles for publishing (manuscripts) must be sent to Editorial Office by post (two printed copies and CD with editable files), or by e-mail (editable files plus complete preview version in PDF format).

3. Simultaneously with the article the Editorial Office must receive the author´s proclamation that no part of the manuscript was already published and figures and tables are original as well. Copied illustrations from other publications must contain a copyright.

4. The extent of the manuscript for publishing is limited to 25 manuscript pages (MS Word, 12 points Times New Roman, line spacing 1.5) including figures, tables, explanations and references. In the case of contribution with a high scientific value, the longer manuscripts for publishing are exceptionally permitted.

5. Articles can be published in Slovak or English languages. The title, abstract, key words, shortened text (resumé), as well as description to figures and tables in Slovak articles are published also in English. Articles published in English contain Slovak resumé.

Text

1. Abstract briefly summarizing the article is limited to 200 words, no references are allowed. The maximum number of key words is 6. Text of the article has to contain the introduction, characterization (state) of investigated problem, applied methodology, obtained new data, discussion, conclusion and references. The obtained data must be distinctly separated from interpretations. All applied figures and tables must be referred in the text.

2. The hierarchy of headings in the manuscript must be indicated by a pencil note: 1 – highest level, 2 – lower, 3 – lowermost level.

3. The references in the text prefer parentheses, e.g. (Dubčák, 1987; Hrubý et al., 1988). The form "according to Dubčák (1987)" should be used only exceptionally.

4. Position of figures and tables must be indicated in the manuscript. Editable text of manuscript sent to editorial office must be without figures and tables, though the preview PDF has to contain them in a correct position.

5. Greek letter in the text must be identified at the left margin of the text (e.g. sigma). The text should strictly distinguish the dash from hyphen. Symbols, mathematic signs, names of fossils, etc., which should be printed in italics, must be underlined by the wavy line in the manuscript.

Figures and tables

1. The high quality figures and tables can be published either in **maximum width of column (81 mm) or page (170 mm).** The optimum size of letters and numbers in the camera-ready figure is 2 mm. Articles published in Slovak contain the Slovak descriptions in figures and tables, the tables headings and descriptions beneath figures and tables are in Slovak and English. English articles contain all texts in English. **Maximum dimension of figures and tables in the journal is 170 x 230 mm. Larger (fanfolded)** illustrations are published only exceptionally.

2. For figures drawing the editorial office recommends the vector graphics editors (Corel Draw, Adobe Illustrator, etc.). The very thin lines (hair lines), the pre-defined software or raster fillings of polygons (e.g. in Corel Draw) are not allowed. The filling must consist from separately set objects.

3. Each illustration including photographs must contain graphic (metric) scale, eventually the dimensions of visualized objects have to be stated in the describing text to figure. Maps and profiles must contain also the azimuth orientation, their detail explanations are stated at the first figure. Grouped figures, e.g. photographs and diagrams, are compiled as one figure with separate parts designated by letters (a, b, c, etc.).

4. The photographs sent as JPG of TIF files are required for having minimum 600 DPI resolution. Publishing of colour illustrations can be charged by a fee.

References

1. Minimum 50 % of referred works must represent contemporary publications after 2000. The references in alphanumeric order encompass only literature cited in the article.

2. Examples of referring:

Book: Gazda, L. & Čech, M., 1988: Paleozoic of the Medzev nappe. *Bratislava, Alfa, 155 p.*

Journal: Vrba, P., 1989: Shear zones in the metapelite complexes. *Miner. Slov., 21, 135–142.*

Anniversary volume: Návesný, D., 1987: High-potassium rhyolites. *In: Romanov, V. (ed.): Stratiform deposits of Gemericum. Spec. publ. Košice, Slov. geol. soc., 203–215.*

Manuscript: Radvanský, F., Slivka, B., Viktor, J. & Srnka, T., 1985: Vein deposits of the Jedľovec nappe of Gemericum. Final report from the project SGR-geophysics. *Manuscript. Spišská Nová Ves, Archive Št. Geol. Úst. D. Štúra, 28 p.*

3. The article with more than two authors is referred by the name of the first author with the amendment et al., but the list of references contains names of all authors.

Ďalšie informácie/Further information: mineralia.slovaca@geology.sk; zoltan.nemeth@geology.sk

OBSAH – CONTENT

PÔVODNÉ ČLÁNKY – ORIGINAL PAPERS

Radvanec, M. & Gonda, S.
Genetic model of Permian hydrothermal mineralization in Gemericum (W. Carpathians) from the deep-seated zone of anatectic melting to volcanic-exhalative SedEx mineralization on the surface
Genetický model permskej hydrotermálnej mineralizácie gemerika od zóny anatektického tavenia v hĺbke po vulkanicko-exhalačnú SedEx mineralizáciu na povrchu

Aliyev, A. A. & Abbasov, O. R.
Mineralogical and geochemical proxies for the Middle Eocene oil shales from the foothills of the Greater Caucasus, Azerbaijan: Implications for depositional environments and paleoclimate
Aplikácia mineralogických a geochemických údajov zo strednoeocénnych roponosných bridlíc na úpätí Veľkého Kaukazu v Azerbajdžane pri rekonštrukcii environmentálnych a paleoklimatických podmienok ich genézy

Marko, F., †Túnyi, I. & Beniaková, E.
Block rotations in the Carpathian Shear Corridor – a paleomagnetic record
Rotácie blokov v karpatskom strižnom koridore – paleomagnetický záznam

Malík, P., Máša, B., Bottlik, F., Švasta, J., Bahnová, N., Vasilenková, A., Bajtoš, P. & Černák, R.
Hidden groundwater inflows from the Slovenský kras Mts. to the Slaná River identified by thermometric and resistivimetric measurements
Skryté prestupy podzemných vôd Slovenského krasu do rieky Slaná medzi Brzotínom a Gombasekom identifikované termometrickými a rezistivimetrickými meraniami

Štyriaková, I., Danková, Z., Košuth, M., Šuba, J., Nováková, J. & Kollárová, V.
Removal of toxic elements from the minerals particles of contaminated soil by chemical and biological leaching
Odstraňovanie toxických prvkov z minerálnych častíc kontaminovanej pôdy chemickým a biologickým lúhovaním

Jurkovič, Ľ., Juhásová, J., Kulikova, T., Faragó, T., Méres, Š., Klimko, T., Šottník, P., Hiller, E., Nemček, L. & Bujdoš, M.
Geochemicko-mineralogický prieskum pôd ovplyvnených banskou činnosťou v oblasti opusteného Sb ložiska Čučma
Geochemical and mineralogical exploration of soils affected by mining activities at the abandoned Sb-deposit Čučma

Indexed / Abstracted / Accessed by SCOPUS and EBSCO
Indexované / abstraktované / sprístupňované databázami SCOPUS a EBSCO

www.geology.sk/mineralia